ELSEVIER

NANOLAYER RESEARCH

METHODOLOGY AND TECHNOLOGY FOR GREEN CHEMISTRY

TOYOKO IMAE

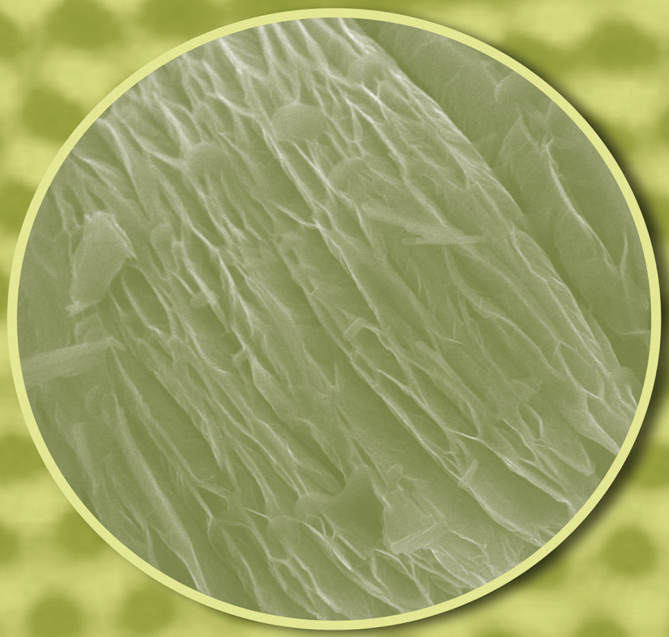

Nanolayer Research

This page intentionally left blank

Nanolayer Research

Methodology and Technology for Green Chemistry

Toyoko Imae

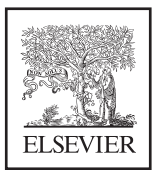

Elsevier
Radarweg 29, PO Box 211, 1000 AE Amsterdam, Netherlands
The Boulevard, Langford Lane, Kidlington, Oxford OX5 1GB, United Kingdom
50 Hampshire Street, 5th Floor, Cambridge, MA 02139, United States

Notices

Knowledge and best practice in this field are constantly changing. As new research and experience broaden our understanding, changes in research methods, professional practices, or medical treatment may become necessary.

Practitioners and researchers must always rely on their own experience and knowledge in evaluating and using any information, methods, compounds, or experiments described herein. In using such information or methods they should be mindful of their own safety and the safety of others, including parties for whom they have a professional responsibility.

To the fullest extent of the law, neither the Publisher nor the authors, contributors, or editors, assume any liability for any injury and/or damage to persons or property as a matter of products liability, negligence or otherwise, or from any use or operation of any methods, products, instructions, or ideas contained in the material herein.

Library of Congress Cataloging-in-Publication Data
A catalog record for this book is available from the Library of Congress

British Library Cataloguing-in-Publication Data
A catalogue record for this book is available from the British Library

ISBN: 978-0-444-63739-0

Publisher: John Fedor
Acquisition Editor: Kostas Marinakis
Editorial Project Manager: Michelle Fisher
Production Project Manager: Maria Bernard
Cover Designer: Mark Rogers

Typeset by SPi Global, India

Contents

Contributors

Mahmoud M.M. Ahmed National Taiwan University of Science and Technology, Taipei, Taiwan
Katsuhiko Ariga National Institute for Materials Science (NIMS), Tsukuba; The University of Tokyo, Kashiwa, Japan
Joseph A. Dura NIST Center for Neutron Research, Gaithersburg, MD, United States
Toyoko Imae National Taiwan University of Science and Technology, Taipei, Taiwan
Paul A. Kienzle NIST Center for Neutron Research, Gaithersburg, MD, United States
Masashi Kunitake Kumamoto University, Kumamoto, Japan
Brian B. Maranville NIST Center for Neutron Research, Gaithersburg, MD, United States
Hidenori Noguchi National Institute for Materials Science, Tsukuba, Japan
Akihiro Ohira National Institute of Advanced Industrial Science and Technology (AIST), Tsukuba, Japan
Hiroyuki Ohshima Tokyo University of Science, Chiba, Japan
Toshiaki Ohta Ritsumeikan University, Kusatsu, Japan
Masaharu Oshima The University of Tokyo, Tokyo, Japan
Eric D. Rus NIST Center for Neutron Research, Gaithersburg, MD, United States
Masaki Ujihara National Taiwan University of Science and Technology, Taipei, Taiwan
Kohei Uosaki National Institute for Materials Science, Tsukuba, Japan
Satoshi Watanabe Kumamoto University, Kumamoto, Japan

This page intentionally left blank

CHAPTER 1

Overview of Nanolayers: Formulation and Characterization Methods

Toyoko Imae

National Taiwan University of Science and Technology, Taipei, Taiwan

1.1 Introduction

The concept of monolayer was established by Irving Langmuir (1881–1957, Nobel Laureate in Chemistry, 1932) after the report regarding the adsorption of gases on plane surfaces [1]. Since then, the fourth phase, "surface" or "interface" at the phase boundary, has been recognized as significant in addition to the traditional three main phases of gas (air), liquid, and solid, and Langmuir earned respect as a pioneer of surface science (chemistry), as it was he who introduced the concept of two-dimensional molecular array, in addition to the concept of two-dimensional thermodynamics, on the interpretation of the surface. Moreover, his establishment of methodology preparing water-insoluble monomolecular film on Langmuir-Blodgett trough enabled the development of not only the basic research of molecular films on surface but also the preparation/modification technology of practically preferable molecular films.

Another important advance in surface science was the development of the scanning probe microscope by G. Binning and H. Rohre in 1981 (Nobel Laureates in Physics, 1986) [2]. This development allows us to see molecular surfaces directly over the estimation. The arrangement of nanolayers including monolayers, bilayers, and multilayers at the interface had formerly been estimated by chemical and physical analyses. However, after the visualization of such molecular arrangement became successfully possible especially as to the thickness of the layers, scientists and engineers expected the strict control of the regularization of nanolayers at the interface and their precision characterization, since they recognized that the characteristics of materials and instrumentation were subjected to the interface. Their expectation encouraged the development of surface analysis methodology based on spectroscopy and electromagnetics. Nowadays, on the strength of these developments, many scientists and engineers in academia and industries have focused on the investigation of surface science. Thus the research is evolving with industrial products relating to adsorption, adhesion, coating, colloidal particles, thin films, chemical reaction, analysis, and separation. Especially notable, such methodologies are currently tactical on high-precision surface processing technology.

Nanolayer Research. http://dx.doi.org/10.1016/B978-0-444-63739-0.00001-3

This chapter gives an overview of nanolayers. Different types of nanolayers including monolayers, bilayers, and multilayers are prepared at different interfaces and with different procedures. The as-prepared nanolayers are analyzed for their structures and properties by means of various methodologies and technologies, which adapt to different scales of specimens and characterizations depending on the particularity of each methodology and technology. For instance, visualization technology by microscope is limited to the resolution by beam wavelengths for optical and electron microscopes and by probes for scanning probe microscopes. In electromagnetic methodology, while light scattering is used for the analyses of structures of larger dimension, X-ray and neutron scattering cover small-scale structures. Spectroscopy is utilized for the analyses of rather fine structures like the orientation or compactness of molecules in the layers. Fig. 1.1 indicates the methodologies of visualization, electromagnetics, and spectroscopy for nanolayers in relation to size scale. In the following section, the formulation of nanolayers at different interfaces and their characterization using microscopy, electromagnetics, and spectroscopy are reviewed.

1.2 Formulation of Nanolayers

1.2.1 Monolayers at Interface

Monolayers are formed at any interfaces between three phases of gas (air), liquid, and solid. Monolayers formed at different interfaces are given different specific names as listed in Table 1.1.

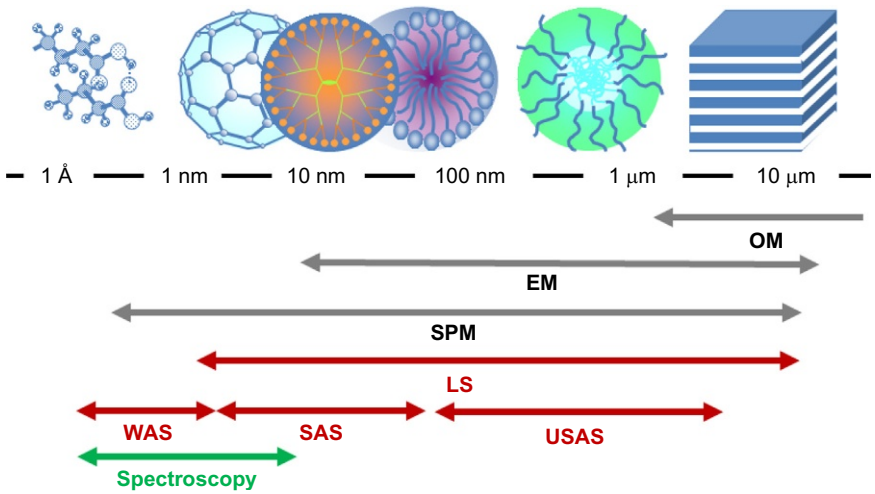

Fig. 1.1

Microscopy, electromagnetics, and spectroscopy for nanolayers sectioned by size scale. OM: optical microscope, EM: electron microscope, SPM: scanning probe microscope, LS: light scattering, WAS: wide angle scattering, SAS: small angle scattering, USAS: ultra-small angle scattering.

Table 1.1 A list of layers and their remarks at different interfaces

Interface	Layer	Remark
Gas-liquid	Gibbs adsorption monolayer	Surface tension
	Langmuir monolayer	Langmuir-Blodgett trough
	Gas micro- or nanobubble	Air and nitrogen bubbles
Gas-solid	Langmuir gas adsorption	Langmuir adsorption isotherm
	BET gas adsorption	BET adsorption isotherm
	Langmuir-Blodgett accumulation film	*X*-, *Y*-, and *Z*-film
Liquid-solid	Self-assembled monolayer	Adsorption
	Solid suspension	Laundry
Gas-gas	Soap bubble (bilayer, multilayer)	Bubble mineral processing
Liquid-liquid	Micro- and macroemulsion	Foods and cosmetics
	Lyotropic liquid crystal	Lamella and bicontinuous phase
Solid-solid	Alloy	Solid solution

1.2.1.1 Monolayer at gas (air)-liquid interface

Based on two-dimensional thermodynamics, the surface free energy F^s at the air-water interface of area A and temperature T is described by

$$dF^s = -S^s dT + \Upsilon dA, \quad \Upsilon = (\partial F^s/\partial A)_T \tag{1.1}$$

where S^s is the surface enthalpy and Υ is the surface tension, that is, surface free energy per unit area. Since the surface tension is positive, the surface always has a tendency to be minimalized. According to Gibbs's definition, the surface excess density of water is zero at the dividing surface (plane) ($\Gamma_w = 0$) (Fig. 1.2A). Then the surface excess density of solute in water is nonzero ($\Gamma_i > 0$: positive adsorption, $\Gamma_i < 0$: negative adsorption [Fig. 1.2A and B]), where Γ_i is the surface excess density of component i.

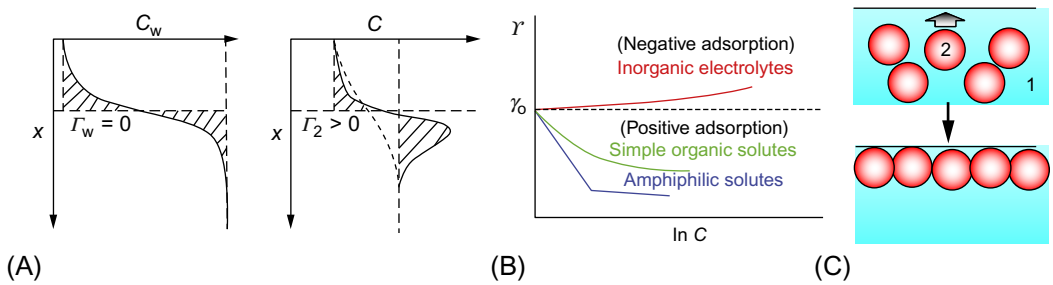

Fig. 1.2

(A) Profiles of surface excess densities of water and solute at Gibbs dividing surface, (B) typical curves of surface tension of a solution as a function of solute concentration, and (C) formation scheme of Gibbs adsorption monolayer.

When component 2 dissolved or dispersed in water, (component 1) is adsorbed at the interface of water with air (Fig. 1.2C), the Gibbs adsorption isotherm is described by

$$-d\Upsilon = \sum \Gamma_i d\mu_i, \quad \Gamma_i = n_i^s/A \tag{1.2}$$

where $i = 1$ and 2, and μ_i and n_i^s are the chemical potential and the number of ith component at the interface, respectively. Thus, Γ_i is the excess number of ith component per unit area at interface. Meanwhile, the differential chemical potential $d\mu_2$ of solute (component 2) in an ideal solution can be described by

$$d\mu_2 = RTd\ \ln C_2 \tag{1.3}$$

where R is the gas constant and C_2 is the concentration of the component 2 in the bulk phase. Thus the Gibbs adsorption isotherm becomes

$$\Gamma_2 = -d\Upsilon/dRT\ \ln C_2 = -(1/RT)(\partial\Upsilon/\partial\ \ln C_2)_{T,P} \tag{1.4}$$

Eq. (1.4) is applicable for one solute system, but other equations must be derived for a multisolute system, the Gibbs adsorption multilayer, and so on [3].

Generally, simple organic solute lowers the surface tension of water with increasing the solute concentration by positive adsorption, but some inorganic electrolytes slightly increase it due to negative adsorption, as described earlier. Amphiphilic solutes (mainly surfactants) initially decrease the surface tension with initial increase of solute concentration, but these keep a constant surface tension above a certain solute concentration (Fig. 1.2B) called critical micelle (aggregate) concentration, where the air-liquid interface is occupied by monolayer of solute molecules. Since micelles of amphiphiles are formed at the critical micelle concentration, this concentration is adopted as a barometer of the micelle formation in bulk. The preparation of Gibbs adsorption monolayer is also possible even by means of amphiphilic polymers [4,5] and nanoparticles [6] besides surfactants [3,7].

Another type of monolayer at air-water interface is well known as the Langmuir monolayer. When water-insoluble molecules dissolved in water-immiscible solvents (chloroform, benzene, and so on) are spread on water surface (subphase) in a trough and solvents are evaporated, monolayer remains on subphase [8]. In this situation, molecules are dispersed throughout whole water subphase and are referred to as gas-state monolayer, as shown in Fig. 1.3. If the area of the subphase is compressed, the surface pressure increases through gas-liquid equilibrium state, liquid state and solid state, and finally the Langmuir monolayer is destroyed at excess compression. Then, surface pressure π ($= \Upsilon_0 - \Upsilon$, Υ_0: surface pressure of water, Υ: surface pressure covered by water-insoluble molecules) is described by $\pi = kT/A$ (k: Boltzmann constant) for gas-state. This equation is comparable to the three-dimensional pressure-volume state equation. When amphiphilic solutes (e.g., surfactants with hydrophilic head and

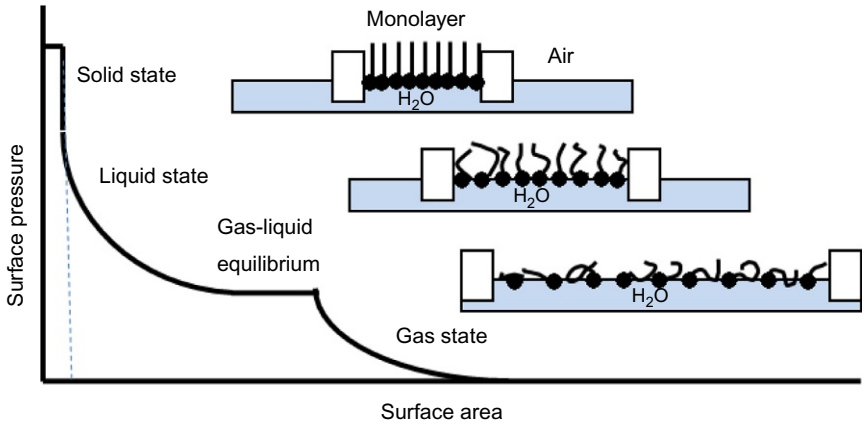

Fig. 1.3
Schematic representation of surface pressure-area isotherm and gas, liquid, and solid states of the monolayer.

hydrophobic tail) are spread, well-packed monolayers can be formed in the solid state. Then the surface area occupied by one molecule can be calculated from surface area at solid state. Incidentally, since the smallest cross-sectional area (critical area) of alkyl chain at a well-packed, solid-state Langmuir monolayer is 20 $Å^2$ [9], which can be attained by eicosanoic acid (arachidic acid, $CH_3(CH_2)_{18}COOH$), the solidity of Langmuir adsorption films can be assessable from the surface area [10,11]. The critical area corresponds to the extrapolation at $\pi = 0$ in a relation of $\pi = b - aA$ for solid state (see Fig. 1.3). When Langmuir monolayer formed at air-water interface is transferred onto solid substrate, one can form Langmuir-Blodgett monolayer film on air-solid interface as described later.

Langmuir adsorption monolayer consisting of the mixture of mutually insoluble components sometimes provides the aspect of two-dimensional phase separation and the uniquely patterned texture as cases of arachidic acid/azo-dye hybrids [12] and perfluorinated/hydrogenated amphiphiles hybrids [9], although patterns vary depending on surface pressure and mixing ratio. Most Langmuir adsorption monolayers are prepared on water subphase, because the subphase of organic solvent with low surface tension is not adequate. The only exceptional subphase besides water is mercury, which is liquid at room temperature. In this case, even thick homogeneous films like 10 μm thickness with smooth surface can also be produced [13].

1.2.1.2 Monolayer at gas-solid interface

The gas adsorption on solid has been investigated as a physical phenomenon since the 18th century. The adsorption is mainly categorized as chemisorption, which is an adsorption concerned by chemical interaction (activated energy), and physisorption, which is an adsorption by weak interaction like van der Waals force, etc. The different types of adsorption

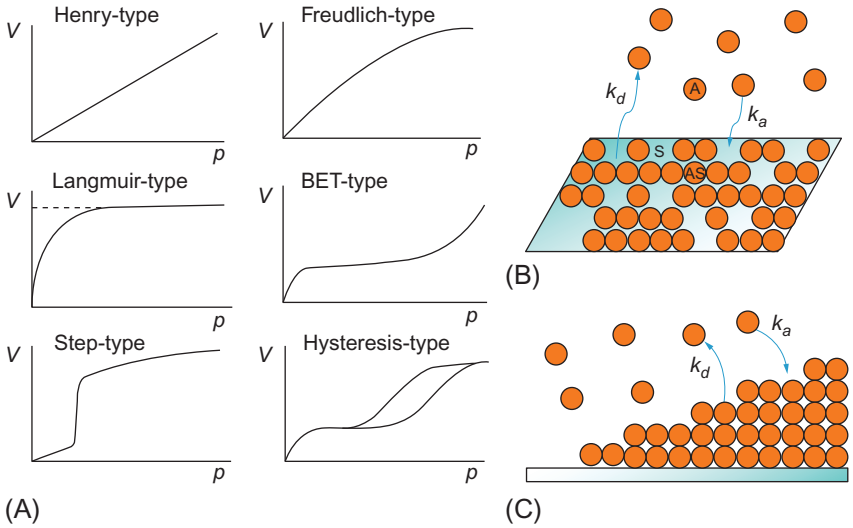

Fig. 1.4
Schematic illustrations of (A) various adsorption isotherms, (B) Langmuir adsorption, and (C) BET adsorption.

have been developed theoretically as well as experimentally, as illustrated in Fig. 1.4A. A simple and convenient equation is called a Freundlich equation, described by

$$v = \alpha p^{1/n} \text{ or } \log v = (1/n)\log p + \log \alpha \tag{1.5}$$

where v is an adsorption amount, p is a partial pressure of adsorbate gas. The α and n are a constant depending on adsorbate and a constant characteristic of adsorbent, respectively, and obtained from a slope and an intercept of the plot of log v as a function of log p, respectively. This equation fits at wide concentration region of adsorbate, but it is an empirical equation as well as a Henry-type adsorption isotherm ($v = \alpha p$).

The physicochemical interpretation of gas adsorption on solid by introducing molecular concept was performed by Langmuir [1]. The theoretical equations derived by Langmuir are called Langmuir adsorption isotherm. The theory takes into account chemisorption of adsorbate on solid, and the concept of binding site on adsorbent surface is introduced on the Langmuir adsorption isotherm (Fig. 1.4B), where the binding site has a same size as adsorbate and one adsorbate can occupy one binding site, indicating that the size and number of binding sites are varied depending on the adsorbate. When equilibrium among free site (S), adsorbate (A), and occupied site ($A-S$) exists (Eq. 1.6), the equilibrium can be described by an Eq. (1.7).

$$A + S \underset{k_d}{\overset{k_a}{\rightleftharpoons}} A - S \tag{1.6}$$

$$k_a p(N_s - N_a) = k_d N_a \tag{1.7}$$

where N_s and N_a are numbers of total site and of adsorbed site (adsorbate), respectively, and k_a and k_d are rate constants of adsorption and desorption, respectively. Thus the adsorption amount of adsorbate v is described by

$$v \equiv N_a = (k_a/k_d)N_s p/[1 + (k_a/k_d)p] \tag{1.8}$$

as a function of a partial pressure of adsorbate p and with constants k_a/k_d and N_s, where N_b corresponds to the saturation adsorption at $p \to \infty$.

The representative theoretical equation as well as Langmuir adsorption isotherm was derived by S. Brunauer, P. H. Emmet, and E. Teller and named the BET adsorption isotherm [14]. The concept is that adsorbates are multiply adsorbed on the adsorbate monolayer on adsorbent surface (see Fig. 1.4C). Then the interaction of adsorbate with adsorbent is different from the interaction between adsorbates. It can be generally assumed that the former is chemisorption and the latter is physisorption. Supposing that the Langmuir adsorption isotherm equation is approved at each adsorption layer, the adsorption amount of adsorbate v is

$$v = v_m cx/(1-x)(1-x-cx), \quad x = p/p_0 \tag{1.9}$$

where v_m is the gas amount adsorbed on first monolayer and c is a BET constant relating to activation energy of adsorption, p and p_o are the gas pressure and saturation gas pressures of adsorbate at the temperature of adsorption. Thus, v_m corresponds to a saturation adsorption N_s in Langmuir adsorption isotherm in Eq. (1.8).

Among profiles of various types of adsorption isotherms illustrated in Fig. 1.4A, the Henry-type isotherm corresponds to the linearly increasing initial adsorption, and the Freundlich-type isotherm covers slightly higher adsorption region deviating from linearity. The Langmuir-type isotherm saturates at limited adsorption, but the BET-type isotherm further adsorbs up to infinity in a theoretical sense. The step-type isotherm occurs on the adsorbent with distinctively shaped pores, and the hysteresis-type isotherm is sometimes observed on mesoporous adsorbents. The gas adsorption is the more common phenomenon possible with high frequency, which is practically utilized in industry in dehumidifiers, deodorants, smoke extraction, gas chromatography, solid catalyst, etc.

Along with Langmuir adsorption isotherm, Langmuir adsorption kinetics is popularly used for investigating kinetics of gas adsorption on solid substrates. On the Langmuir monolayer adsorption described by Eq. (1.6), the rate equation is written by

$$dN_a/dt = k_a p(N_s - N_a) - k_d N_a \tag{1.10}$$

and

$$N_a = \{N_s k_a p/(k_a p + k_d)\}[1 - \exp\{-(k_a p + k_d)t\}] \tag{1.11}$$

This principle can be extended to the adsorption kinetics with multiple binding sites. Thus, the derived equations can exactly fit to gas (CO_2) adsorption with three adsorption sites on layer-by-layer of clay and dendrimer [15].

1.2.1.3 Monolayer at liquid-solid interface

Although Langmuir and BET adsorption isotherm equations are deviated for gas adsorption, the same isotherms are also applicable to the adsorption of solute from a solution on adsorbent solid. In such cases, a partial pressure of gas must be replaced by a concentration of solute. This case belongs to the adsorption at liquid-solid interface, and many layers on solid substrates are prepared by this procedure [16]. Its principle regulates the efficiency of chemical adsorbent, ion exchange resin, chromatography, catalyst, etc.

Incidentally, the self-assembled monolayer (SAM) is a representative monolayer at liquid-solid interface, although it can be regarded as a specific case of Langmuir adsorption of solute in solution on solid. When adsorbate molecules have specific binding functional groups to the substrate solid, molecules adsorb on solid with molecular orientation and it is a monolayer in almost all cases. Thus such an adlayer is called SAM. Thiol and siloxane compounds are most favored for SAM formation on gold and glass substrates, respectively [17,18], and such compounds are strongly immobilized on these substrates (Fig. 1.5). If desirable functional groups are introduced on free terminal of compounds facing to bulk solution, the surface characters of the SAM-substrate can be completely altered. Thus, the formation of SAM is the preferable method for surface modification and nowadays often utilized in academic and industrial researches. The kinetics of the SAM formation on Au surface obeys simple Langmuir (monolayer) kinetics as described by Eqs. (1.10), (1.11), although it is not a case of electrostatic adsorption of cationic surfactant on SAM [19].

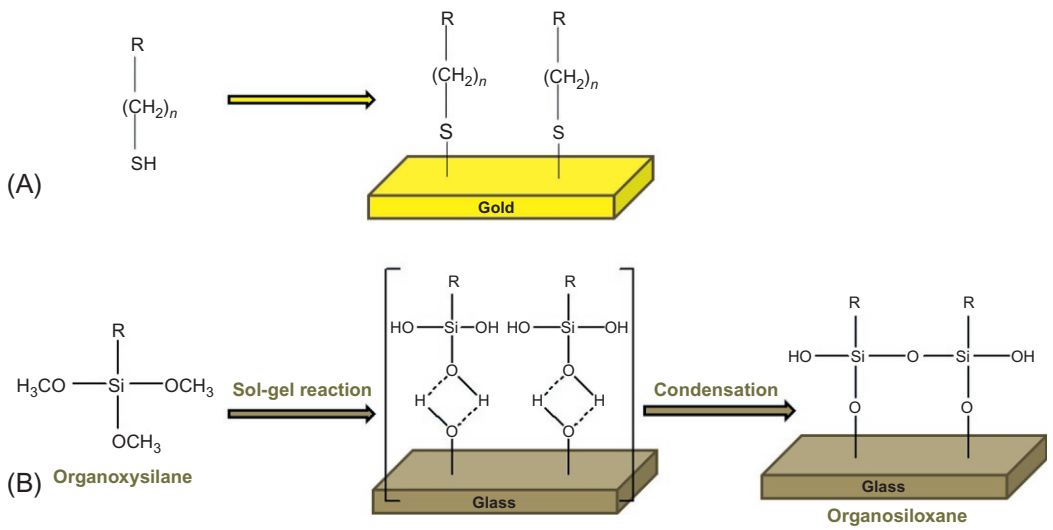

Fig. 1.5
Schematic representation of SAM formation on (A) gold and (B) glass substrates.

1.2.1.4 Monolayer at finite interface

Monolayers are formed even at finite interface between closed phase and surrounding bulk phase. In most cases, amphiphilic molecules (surfactants) are localized at interface and stabilize closed phase in bulk phase. There are three typical cases: gas bubbles (gas in liquid) with gas-liquid interface, emulsions with liquid-liquid interface, and suspensions with liquid-solid interface (see Fig. 1.6). While finite phase larger than micrometer is unstable in bulk phase and causes coagulation, destruction, float, or precipitation, small finite phase such as nanoscale stably disperses in bulk phase. Gas micro- or nanobubbles are a current topic in surface chemistry [20]. Although air macrobubbles in water easily come to the surface and are broken, micro- or nanobubbles are stably dispersed in water without any variation of bulk appearance for a long time.

The research is performed not only as academic investigation but also from necessity on practical applications, since air (oxygen) nanobubbles are useful for the transportation of living water (sea) animals in closed containers and in medical treatment, and nitrogen nanobubbles are available for biocidal and antirust in water. However, the stabilization of nanobubbles in the recently reported cases is not necessarily due to the contribution of monolayer but it can occur by mechanical means in one case, although its stabilization is less. Micro- and nanoemulsions of oil-in-water (o/w) and water-in-oil (w/o) are already utilized in a general way in commercial products, especially in foods and cosmetics. Suspensions are very common on removal or separation of solids, such as in laundering, for example.

1.2.2 Multilayers at Interface

Bilayers are popular in the natural world. The case is the basic structure of cell membranes formed by amphiphilic lipid molecules, which is called liposome (Fig. 1.7A). Lipids form bilayers, where hydrophobic tails are inside and hydrophilic heads locate at the periphery, because they are exposed to aqueous media [21,22]. Similar structures to bio-based liposome

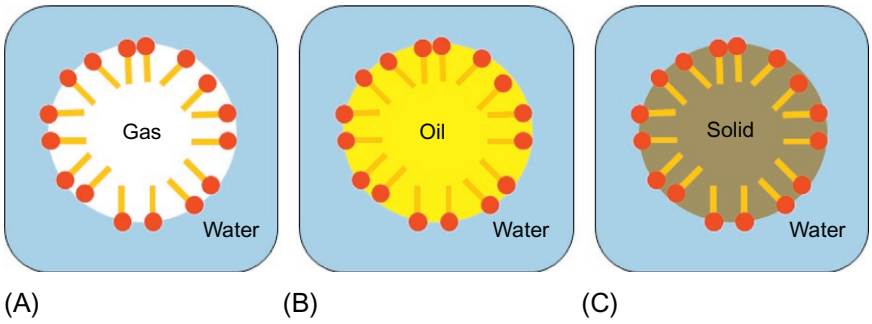

Fig. 1.6
Schematic illustration of monolayers at finite interface: (A) gas bubble, (B) emulsion, and (C) suspension.

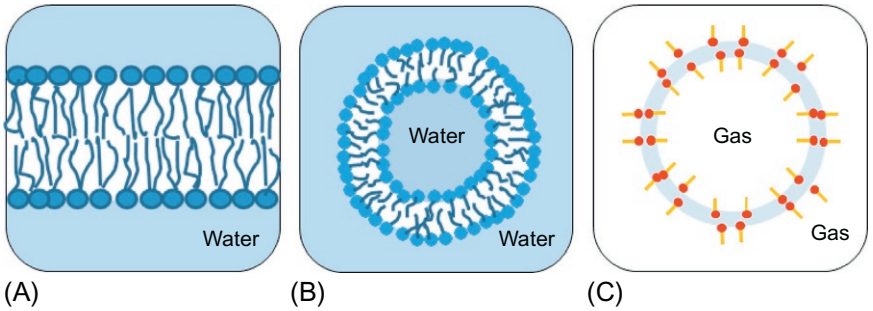

Fig. 1.7
Schematic representation of bilayers: (A) cell membrane bilayer (liposome), (B) vesicle, and (C) soap bubble.

can be formed using artificial amphiphilic molecules (surfactants) and are called vesicles (Fig. 1.7B) [23]. Aggregates of surfactants in solution change their shapes, if the adequate conditions are chosen. For instance, surfactants in solution form micelles in water, and if oil components like hydrocarbon are added to water, they aggregate into microemulsions (o/w microemulsions), subsequently vesicles and lamellar phases. Further addition of oil components results in bicontinuous phase, where continuous water and oil phases are balanced and surfactants are located at the interface of two continuous phases. With further increase of oil components, reversed lamella, reversed vesicles, reversed microemulsions (w/o microemulsions), and finally reversed micelles are formed. In inverse ordering of bilayers, hydrophilic heads are inside and hydrophobic tails locate at the periphery, because water is trapped close to hydrophilic heads in the middle of layers. The aggregates of lamellar, bicontinuous, and reversed lamellar phases are known as lyotropic liquid crystals as well as cubic phase. Aside from bilayers at liquid-liquid interface, bilayers of surfactants at air-air interface are known as soap bubbles (Fig. 1.7C), where hydrophobic tails locate at the periphery of bubbles, because a bubble is surrounded by hydrophobic bulk air. Although water blocked in bubble film is protected by hydrophilic heads, the bubble thickness becomes thinner with time due to the evaporation of water. Thus the color of soap bubbles changes with time and the black bubble just before breaking is a bilayer of surfactants.

Accumulated monolayers can be fabricated using Langmuir-Blodgett accumulation procedure in trough. The fabricated multilayers depend on the deposition process, and *X*-type (↓↓↓), *Y*-type (↑↓↑), and *Z*-type (↑↑↑) films are accumulated, as seen in Fig. 1.8A. Besides the vertical dipping method as shown in Fig. 1.8A, horizontal (flat) adsorption procedure is also possible to prepare *X*-type films. Although the Langmuir-Blodgett accumulation procedure is applicable only for water-insoluble molecules, the Gibbs adsorption monolayer formed by water-soluble molecules is also possible to transfer on solid substrate, if the monolayer is adsorbed on substrate by the horizontal adsorption procedure.

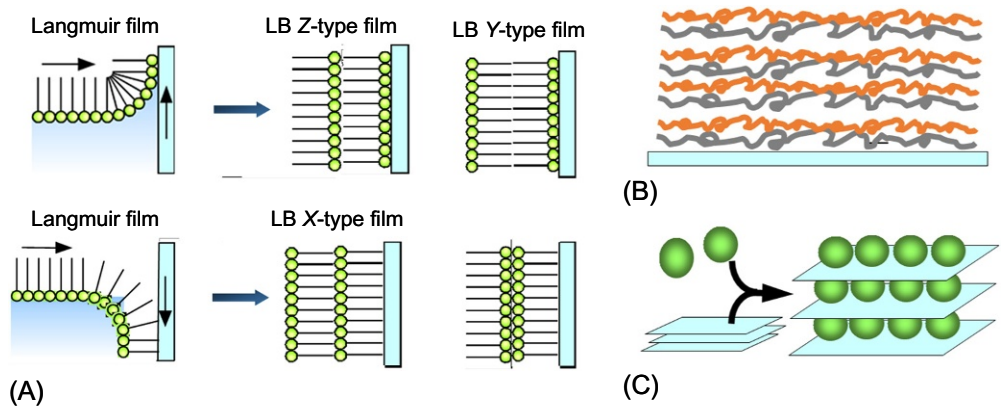

Fig. 1.8
Schematic illustration of (A) accumulation of Langmuir-Blodgett films, (B) layer-by-layer film, and (C) intercalated film.

Layer-by-layer accumulation can be achieved by alternative electrostatic attraction adsorption of inversely charged polymers (or molecules) from solution on substrate (Fig. 1.8B). On the alternative adsorption of polyelectrolytes, a substrate is alternatively dipped into two solutions of cationic and anionic polymers. If the layer-by-layer films are prepared from anionic linear polymer and cationic spherical dendrimer, the average thickness of unit bilayer is about 2 nm [24], being enough large thickness of bilayers compared to bilayers between linear polymers. Another procedure for multilayer preparation is the intercalation method (Fig. 1.8C). Clay has well-ordered sheet structure, and small molecules between sheets can exchange with other molecules (ions). Thus not only surfactants but also polymers can be intercalated between clay layers [25], although intercalated compounds depend on the character of clays, namely, cation-exchange or anion-exchange [26]. Similar intercalation happens for graphite layers, and the products are called graphite intercalation compounds [27]. Two types (accepter type [19] and donor type [28,29]) of graphite intercalation compounds are reported depending on the charge of interaction ions.

Lithography is an excellent technique for the fabrication of three-dimensional heterogeneous nanolayers, which are formed by accumulation of different layers to become devices. In general, the procedure is progressed through the processes of (1) the coating of substrate (wafer) by photoresist (photosensitive organic molecule), (2) the exposure by light after covering by patterned mask, and (3) etching and photoresist removal (Fig. 1.9A). Thus the production of semiconductor device, printed circuit board, printing plate, liquid crystal display panel, plasma display panel, and so on is expected. An alternative procedure is (1) the SAM formation on substrate, (2) the exposure by light after being covered by patterned mask, and (3) the immobilization of another chemical to selected pattern (Fig. 1.9B) [30]. Of course, other options are also available.

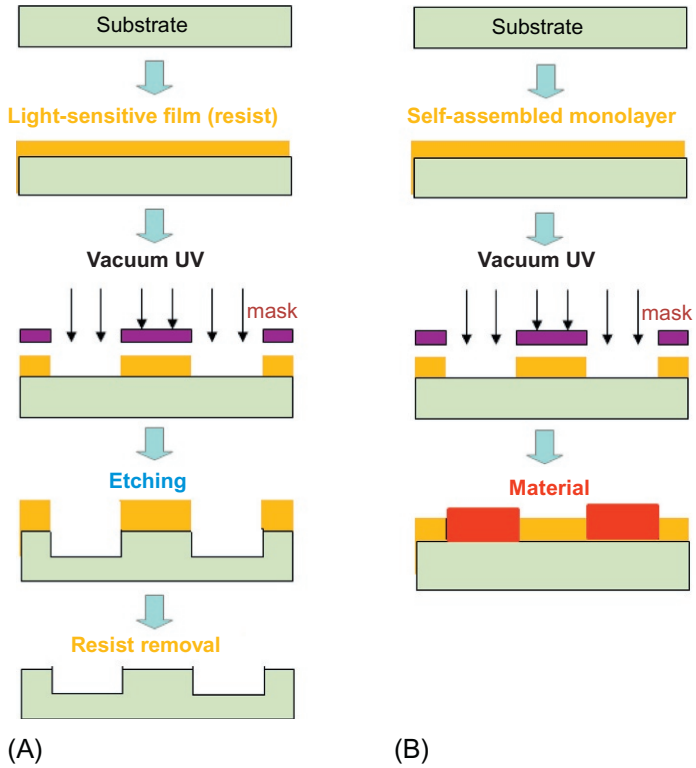

Fig. 1.9

Scheme of photolithography: (A) resist coating, masking, light-irradiating, and etching, and (B) SAM-preparing, masking, light-irradiating, and molecule-immobilizing.

At present, hierarchical structures are required especially for the fabrication of applicable materials [31]. They are roughly classified into planar or nonplanar and homogeneous or heterogeneous. The preparation of well-ordered planar hierarchies can be achieved by means of conventional adsorption [16], casting, SAM, or Langmuir-Blodgett accumulation [32]. Heterogeneous planar hierarchies can be constructed using layer-by-layer accumulation [24] or interlayer intercalation [25,27]. The assemblies by amphiphilic molecules are automatically heterogeneous layers consisting of hydrophilic, hydrophobic, or solvophobic layers [33]. The adsorption of Gibbs monolayer to Langmuir monolayer films on subphase allows the formation of Janus-type hybrid and their accumulation [6,34]. Lithography is the most focused technique for the fabrication of heterogeneous multilayers [30] and the most useful technique for the fabrication of electronic and optical devices. The nonplanar core-shell hierarchies are mainly prepared by self-assembling of surfactants or block copolymers in bulk solvents [35]. Concentric multilayer hierarchies or multilayer tubes/rods/wires can be formed by hierarchic surface modification on core sphere or tube/rod/wire, respectively [17,36]. The resultant hierarchies are potentially or practically applicable to electrical or optical devices, sensing systems, and therapeutic treatments.

1.3 Characterization Methods of Nanolayers

1.3.1 Characterization of Nanolayers by Microscopy

1.3.1.1 Transmission electron microscope

Significant characterizations of nanolayers are the visualization with microscopy and the analyses by electromagnetics and spectroscopy. The observation of morphology is possible using optical microscopes, electron microscopes, and surface probe microscopes. Optical microscopes classified as bright-field, dark-field, phase contrast, polarization, differential interference contrast, and fluorescence microscopes should be used according to the purposes and objectives [37–39]. Compared to these microscopes consisting of a pair of objective lens and eyepiece lens, the Brewster angle microscope is a nonlens optical microscope due to the principle that the reflection intensity of *p*-polarization of laser light is null at an angle of 53.1 degrees to water surface. Thus the texture of materials at water surface can be observed.

Although the resolution of optical microscopes is not so high, the electron microscope is appreciated as the observation tool with rather high resolution. On the transmission electron microscope (TEM), the transmitted photos of structures and electron diffraction are taken. In addition, the ultra-high-resolution TEM enables the resolution of crystal lattice arrangement in metals and pore arrangement in mesoporous particles [40]. Scanning electron microscope (SEM) is adequate for viewing of the surface morphology and equips elemental analysis and elemental mapping functions. Since both TEM and SEM are condensed by electromagnetic lens in high vacuum, the instruments are rather large, expensive, and always require fine alignment. In comparison with TEM, which has enough resolution even for crystal ordering, since the resolution of SEM is less high, the tool for the observation of surface by higher resolution is desired. Moreover, although the specimen must be maintained in vacuum for TEM and SEM observation, the in situ observation at ambient conditions like atmospheric pressure, room temperature, and time interval but at high resolution is also required.

By the way, the various techniques are utilized with TEM observation depending on the situation of specimens. If specimens include elements with high electron density like metals, the images are contrasted sufficiently by their high X-ray absorption (Fig. 1.10(1)). Since many organic molecules do not include such high-contrast elements, the contrast by the negative staining method by spreading heavy metal atoms like uranyl and tungsten ions is helpful (Fig. 1.10(2)). When a large texture like that of a living organism is the objective, this technique is adequate. However, it sometimes makes a texture lacking accuracy. On occasion, the observation of the structure in a medium is required, and thus particles dispersed in water can be observed by the freeze- fracture method or cryo method. In the freeze-fracture method (Fig. 1.10(3)), the solution is instantaneously frozen, the ice is cleaved, the cleavage surface is contrast treated, and the replica is prepared. This method is powerful for the detection of multilayers and determination of the thickness, but not for understanding the morphology of the

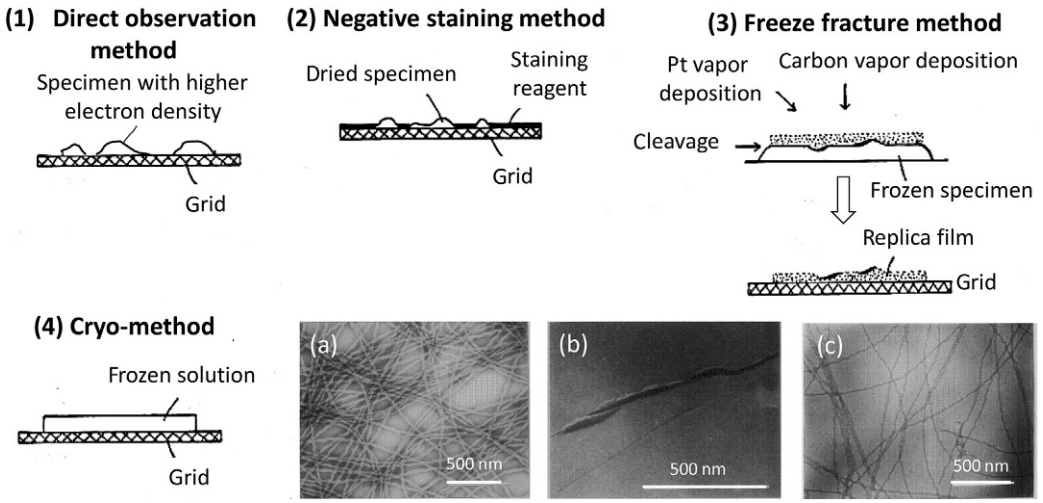

Fig. 1.10

Schematic representation of different preparations of TEM specimens. Insets are TEM images of helical N-hexanoyl-L-aspartic acid fibers in water: (a) negative staining TEM, (b) freeze-fracture TEM, and (c) cryo-TEM. *Reprinted with permission from T. Imae, Y. Takahashi, H. Muramatsu, Formation of fibrous molecular assemblies by amino acid surfactants in water, J. Am. Chem. Soc. 114 (1992) 3414–3419, Copyright 1992, American Chemical Society.*

texture of thin specimens dispersed in water, since the whole texture is difficult to determine. The adequate technique for dispersion in medium is the cryo-TEM method (Fig. 1.10(4)). In this method, the frozen thin film of a solution is directly observed in the instrument with the attachment to keep the liquid nitrogen temperature. This technique provides more exact morphology of the specimen in the solution. Thus, caution should be taken in the selection of an adequate method depending on the specimen. For example, thin fibers can be correctly visible by cryo-TEM, but they appear rather thicker on negative staining TEM, and very few specimens are observed with freeze-fracture TEM, as seen in Fig. 1.10 [41]. However, the freeze-fracture TEM is preferable to other methods for the observation of textures including liquid crystals such as microemulsion, sponge structure, and bicontinuous structure [42].

1.3.1.2 Atomic force microscope

The goal of visualizing the surface at high resolution has been reached by the development of the scanning probe microscope (SPM) by G. Binning and H. Rohre in 1981 (Nobel Prize Laureates in Physics, 1986) [2]. Moreover, the SPM contributed to the viewing of nanolayers. The instruments with different probes are named in connection with the probe such as scanning tunneling (STM), atomic force (AFM), scanning frictional (SFM), magnetic force (MFM), scanning near field (SNFM) microscopes, etc. Among them, although STM is specified only for materials with tunneling effect, AFM is applicable to whole materials, because materials always have any force (attractive or repulsive force) with probe material (Fig. 1.11A). When a tip on cantilever comes close to the specimen in the sample stage, the force between tip and

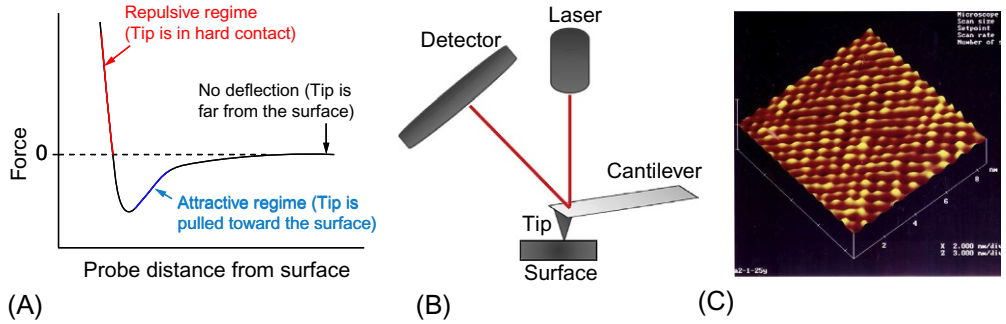

Fig. 1.11

Schematic illustration of (A) force curve, (B) principle of AFM measurement, and (C) AFM image of arachidic acid LB *Z*-type monolayer film on mica (25 mN/m). Full scale of AFM is 9 nm.

molecules in the specimen causes and the cantilever moves. Then the reflection of the laser from the cantilever shifts, and the shift is measured at detector (Fig. 1.11B). Fig. 1.11C shows an AFM image of LB *Z*-type monolayer film of arachidic acid on mica, which was prepared at surface pressure of 25 mN/m of solid state. Each circle indicates methyl terminals. The terminals are well ordered in solid-state Langmuir film with almost hexagonal package.

Table 1.2 lists the comparison of characteristics of microscopies. The resolution of optical and electron microscopes mainly depends on beam wavelength, and thus it is several hundred nm (close to visible light wavelength) and Å (close to X-ray wavelength ~1.5 Å), respectively. The resolution of SPM depends on the probe (force), cantilever (material and shape), and measurement mode, but it is atomic scale (Å) for STM and AFM. Optical microscopes are available for many types of specimens at liquid and solid, in normal pressure, at surface and in dispersion, if the low resolution is not a drawback. On the other hand, it must be noticed that specimens on electron microscope are always put in vacuum, even if the images can be taken at high resolution. Since the scanning probe microscope does not use any electromagnetic beam, the instrument is rather simple and operated at nonspecific conditions (at normal pressure and temperature). Although AFM is now commonly used, especially for getting height profiles superior to other microscopic techniques and from the merits of rather easier operation and higher resolution, this technique can be effective only with surface analysis, not with interior analysis.

Table 1.2 Comparison of characteristics of microscopies

Microscope	Optical	Electron	Scanning Probe (Limited to STM and AFM)
Probe	Light beam	Electron beam	Tunnel current, atomic force
Lens	Optical lens	Electromagnetic lens	No lens
Resolution	Several thousand Å	Several Å	Several Å
Observation	Interior, surface	Interior, surface	Surface
Condition	Solid, liquid	Solid in vacuum	Solid, solid in liquid

As has been described, microscopic images depend on the type of microscope and especially on the magnification. One case is now introduced. Na-[Cr_2(L-tart$_2$H)(phen)$_2$] (tart = tartrate (IV-), phen = 1,10-phenanthroline) formed dinuclear metal complex as expected, but it also showed lyotropic liquid crystal phase in water [38]. Such unique character by a metal complex has rarely or never been reported. On further analysis, the nematic liquid crystal phase was clarified from the observation under polarized optical microscope (Fig. 1.12A), and ribbonlike supramolecular assemblies with crystallographic structure (elucidated from electron diffraction) were displayed by cryo-TEM observation (Fig. 1.12B). Although AFM image at low magnification proved the existence of similar ribbonlike assemblies (Fig. 1.12C), the observation at high magnification revealed the molecularly ordered texture (Fig. 1.12D). The analysis based on chemical structure of the relevant molecule allowed the clarification of the molecular arrangement in supramolecular assembly (Fig. 1.12E).

1.3.2 Characterization of Nanolayers by Electromagnetics

1.3.2.1 Light scattering

Another characterization method of nanolayers is based on electromagnetics, mainly light and X-ray beams. Since Lord Rayleigh has elucidated the phenomenon of static light scattering (elastic light scattering) from smaller particles than the wavelength of the light, the instruments

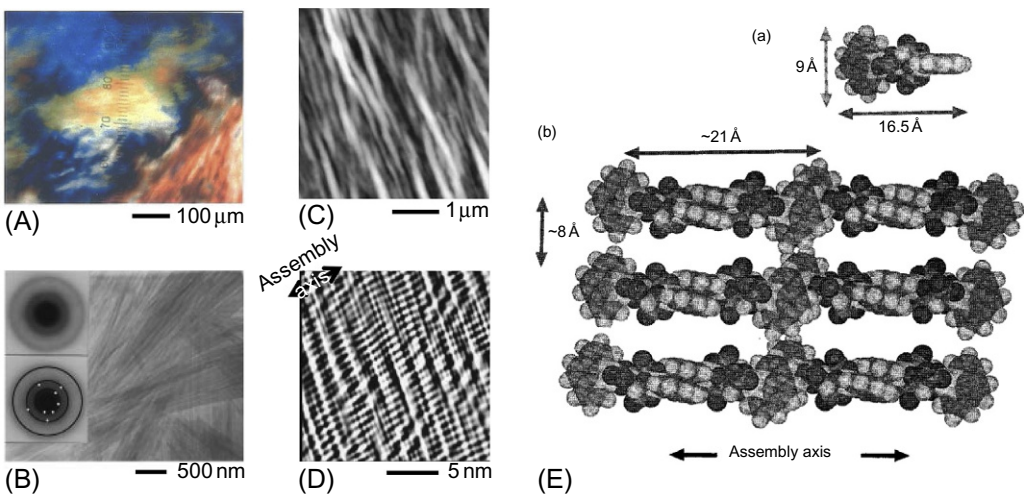

Fig. 1.12

(A) Polarized optical micrograph, (B) transmission electron micrograph, (C) and (D) atomic force micrographs for specimen prepared from an aqueous solution of Na[Cr_2(L-tart$_2$H)(phen)$_2$], and (E) schematic representation of (a) a molecule and (b) molecular arrangement in ribbonlike assembly. *Reprinted with permission from T. Imae, Y. Ikeda, M. Iida, N. Koine, S. Kaizaki, Self-organization of dinuclear metal complex in lyotropic liquid crystal: ribbon-like supramolecular assemblies, Langmuir 14 (1998) 5631–5635, Copyright 1998, American Chemical Society.*

based on Rayleigh scattering theory and the characterization of small particles have been developed. Static scattering intensity $I(q)$ at scattering vector q is contributed by three factors: number density of particle n_p, particle scattering factor $P(q)$, and interparticle scattering factor $S(q)$, in common among light, X-ray, and neutron scattering [43–49].

$$I(q) = n_p P(q) S(q) \tag{1.12}$$

where q $(= (4\pi n_o/\lambda)\sin(\theta/2)$ for light scattering) is a function of incident ray wavelength λ, refractive index of solvent n_o, and scattering angle θ (Fig. 1.13A).

When the concentration of particle is diluted and the scattering angle is small, Eq. (1.12) is developed as [50]

$$Kc/\left(R_\theta - R_\theta^0\right) = (1/M)\left[1 + (1/3)R_G^2 q^2\right] + 2B_2 c \tag{1.13}$$

where $K\left(= 4\pi^2 n_o^2 (\partial n/\partial c)_{Cs}^2 / N_A \lambda^4, (\partial n/\partial c)_{Cs}^2\right.$: specific refractive index increment of a solution at a constant salt concentration (C_s, N_A: Avogadro's number) is the optical constant; c and M are the particle concentration and particle weight (molecular weight), respectively; $R_\theta - R_\theta^0$ is the reduced scattering intensity difference of solute with solvent at a scattering angle θ; R_G is the radius of gyration; and B_2 is the second virial coefficient. When the values of $K_c/\left(R_\theta - R_\theta^0\right)$ are plotted as a function of concentration and angle (called a Zimm plot), the numerical values of R_G and B_2 can be calculated from the slopes at $c \to 0$ and $\theta \to 0$, respectively, and the value of M is obtained from the extrapolation at $\theta \to 0$ and $c \to 0$ (Fig. 1.13B) [51].

The molecular weight of polydisperse molecules (particles) is described by number average $(M_n = \sum N_i M_i / \sum N_i, N_i$ and M_i: number and molecular weight of ith molecule), weight average $(M_w = \sum N_i M_i^2 / \sum N_i M_i)$ and Z average $(M_Z = \sum N_i M_i^3 / \sum N_i M_i^2)$ molecular weight and

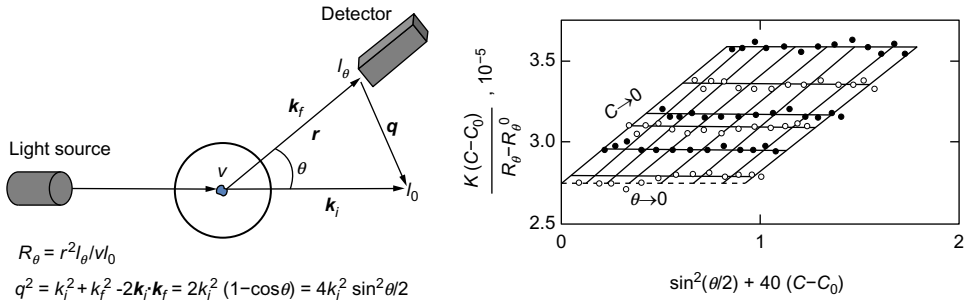

Fig. 1.13

(A) Principle of light scattering and (B) a Zimm plot of light scattering for aqueous 0.5 M NaCl solutions of hexadecyltirmethylammonium chloride at 25°C. The c_0 is the critical micelle concentration. *Reprinted with permission from T. Imae, S. Ikeda, Characteristics of rodlike micelles of alkyltrimethylammonium halides in aqueous sodium halide solutions: their flexibility and entanglement, in: K.L. Mittal (Ed.), Surfactants in Solution, vol. 7, Plenum Publishing Co, New York, NY, 1989, pp. 455–472, Copyright 1989, Plenum Publishing Co.*

$M_n \leq M_w \leq M_z$. The molecular weight obtained from static light scattering is weight average and the radius of gyration is Z average.

Another analysis method based on light scattering is dynamic light scattering (quasielastic light scattering) [44]. The Doppler effect, where the scattered light is slightly deflected from elastic Rayleigh scattering and therefore it widens (see Fig. 1.14A), occurs with the fluctuation of particles and depends on the particle size and shapes. The correlation function of fluctuation $<A(0)A(\tau)>$ is a function of correlation time τ (see Fig. 1.14B), and the first-order correlation function of scattering light electric field $g(q,\tau)$ at scattering vector q is described by Eq. (1.14).

$$g(q,\tau) = \exp(-\Gamma\tau), \quad \Gamma = D|q|^2 \tag{1.14}$$

Decay constant Γ relates to mutual diffusion coefficient D.

For monodisperse system, the correlation function is a simple exponential decay, and its logarithmic plot as a function of correlation time shows a linear decrease with a slope $-\Gamma$ (see Fig. 1.14C). The evaluated diffusion coefficient is a function of scattering vector and solute concentration and described as Eq. (1.15) at the condition of dilute solute concentration and low angle [52].

$$D = (k_B T/6\pi\eta_0 R_H)(1 + k_D c)\left(1 + (2/15)R_G{}^2 q^2\right) \tag{1.15}$$

where k_B is the Boltzmann coefficient, T is the absolute temperature, η_0 is the viscosity of solvent, R_H is the hydrodynamic radius, and k_D is the hydrodynamic virial coefficient. Thus, hydrodynamic radius can be calculated after the extrapolation to $\theta \to 0$ and $c \to 0$, that is, it reaches to Stokes-Einstein equation.

$$\lim_{\theta\to 0,\ c\to 0} D = k_B T/6\pi\eta_0 R_H \tag{1.16}$$

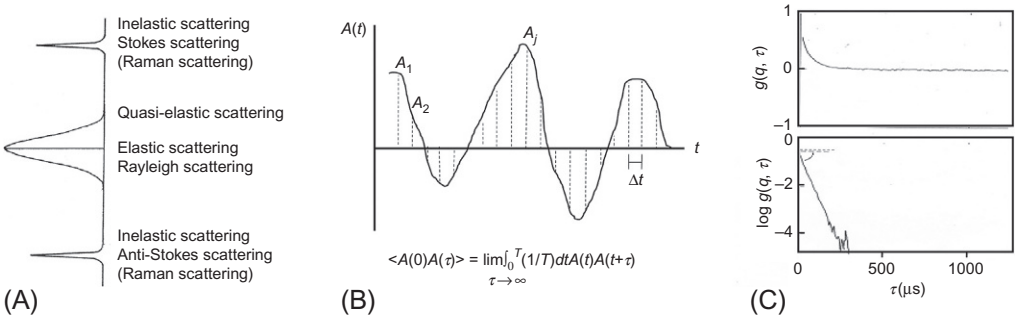

Fig. 1.14

(A) Relation of different scatterings as a function of electric field, (B) principle of correlation function, and (C) plots of simple correlation function of scattering light electric field and its logarithm.

Both the radius of gyration and hydrodynamic radius calculated from static and dynamic light scattering, respectively, depend on particle shape. For instance, the relation for spherical shell structure with outer and inner radius r_o and r_i ($r_o > r_i$) can be described as

$$R_G = \left[3\left(r_o{}^5 - r_i{}^5\right)/5\left(r_o{}^3 - r_i{}^3\right)\right]^{1/2} \quad \text{and} \quad R_H = r_o \tag{1.17}$$

For prolate core shell ellipsoid with long and short hemiaxes (a and b) and shell thickness (x) [44,46],

$$R_G = \left[3\left(a^5 - s^5\right)/5(a^3 - s^3) + 2\left(b^5 - t^5\right)/5(b^3 - t^3)\right]^{1/2}$$
$$R_H = \left(a^2 - b^2\right)^{1/2} / \left[\ \ln\left(a + \left(a^2 - b^2\right)^{1/2}\right)/b\right]$$
$$a = s + x \quad \text{and} \quad b = t + x \tag{1.18}$$

For wormlike chains with contour length L_c and persistence length a [53],

$$R_G^2/a^2 = L_c/3a - 1 + (2a/L_c)\left[1 - (a/L_c)\left(1 - e^{-Lc/a}\right)\right] \tag{1.19}$$

Thus the parameters characteristic to the shape can be evaluated from numerical values of radius of gyration and/or hydrodynamic radius [50,54].

The issue on the data analysis of dynamic light scattering happens for the dispersion of nonhomogeneous particles. Therefore Eq. (1.14) must be rewritten to become Eq. (1.20).

$$g(q, \tau) = \sum A_i \exp\left(-\Gamma_i \tau\right) + \text{constant} \tag{1.20}$$

The analysis of this equation for getting size distribution has been tried by means of the different computation procedures. Using the cumulants method of analysis [55], the average particle size and polydispersity of size distribution are calculated. The analysis by histogram method displays directly the size distribution by histogram. Multiexponential fitting method [56], CONTIN method [57], and maximum entropy method [58], etc., are also proposed. Since the results depend on the analytical method and the different analytical procedures are installed in commercial instruments, users should select adequate instrument and analysis. Although the molecular weight of polydisperse particles can be described by number average, weight average, and z-average, the histogram result is convenient for calculating these averages.

The third notable light scattering technique is an electrophoretic light scattering (ELS). This methodology is based on the theory and procedure initially developed by Ware and Flygare [59]. The principle of the instrumental system is similar to that of dynamic light scattering and only an electrophoretic cell should be attached, not a normal cell, although reference light pass must be equipped (see Fig. 1.15A). When the electric field is applied in a cell, charged particles migrate along positive or negative electrode, depending on applied electric fields. Then the first-order correlation function of scattering intensity at angular frequency ω is written by [60]

$$g(q,\tau,\omega) = \exp(-\Gamma\tau + i(\omega + \Delta\omega)\tau) \tag{1.21}$$

and the power spectrum expression obtained by Fourier transform of correlation function (Fig. 1.15B) is as below:

$$F(q,\omega) = \Gamma / \left[\Gamma^2 + (\omega + \Delta\omega)^2\right] \tag{1.22}$$

Then the Doppler shift $\Delta\omega$ under applied electric field E is described by

$$\Delta\omega = (2\pi n_o/\lambda)EU\sin\theta \tag{1.23}$$

where n_o is the refractive index of solvent, λ is the incident light wavelength, and U is the electrophoretic mobility. Supposing that spherical particles are dispersed in solvent with viscosity η_0 and dielectric constant ε, zeta potential ζ can be calculated from

$$\zeta = 4\pi\eta_0 U/\varepsilon \tag{1.24}$$

The zeta potential is an indispensable parameter in the evaluation of the dispersion of particles in medium. Fig. 1.15C shows the electrophoretic mobility of surfactant micelles [61]. The mobility shifts from negative to positive with increasing degree of protonation, and two differently charged micelles change their amounts at high degree of protonation. Moreover, the evaluation of electrokinetic properties (electrophoretic mobility and surface charge density) from electrophoretic light scattering provides the information relating to adsorption effects of small ions on aggregate surfaces [62]. On the other hand, the evaluation of zeta potential on the flat surface is also requested in nanolayer investigation, but the development of such instrumentation is limited.

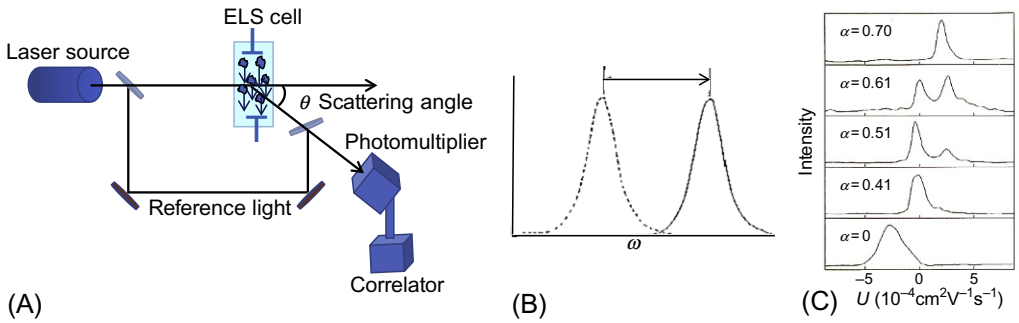

Fig. 1.15

Schematic representation of (A) ELS instrument, (B) power spectrum, and (C) power spectra of 0.05 M NaCl solutions of tetradecyldimethylamine oxide at concentration of 0.5×10^{-2} g cm^{-3} with various degree of protonation. *Reprinted with permission from T. Imae, N. Hayashi. Electrophoretic light scattering of alkyl- and oleyldimethylamine oxide micelles, Langmuir 9 (1993) 3385–3388, Copyright 1993, American Chemical Society.*

1.3.2.2 Small angle scattering

As described, particle weight, radius of gyration, second virial coefficient, or hydrodynamic radius of large particles can be obtained from the analysis of light scattering, but fine structures of small particles or particle-particle interaction are difficult to evaluate from light scattering because of the limitation of scattering vector range, although it is always necessary to analyze such information. For this purpose, small angle X-ray and neutron scattering (SAXS, SANS) is more suitable than light scattering [43–49]. The principle of small angle scattering is the same as light scattering and contributed by number density of particle n_p, particle scattering factor $P(q)$, and interparticle scattering factor $S(q)$. However, the difference is the scattering factor and scattering efficiency. The scattering factor is molecule, atom, and atomic nuclei, and the scattering efficiency is determined by refractive index increment, X-ray scattering amplitude, and neutron scattering length for light scattering, SAXS, and SANS, respectively. Thus, although the scattering equations similar to those of light scattering (Eqs. 1.12, 1.13) are approved even for small angle scattering, small angle scattering can provide more accurate numerical values of particle scattering factor $P(q)$ or radius of gyration of particles [63], and the structures like the short and long axes of ellipsoidal micelles, the diameter of rodlike micelles, and the thickness of multilamellar vesicles and lamellar layers can be numerically determined [64–66]. Moreover, interparticle scattering factor $S(q)$ can be distinguished from particle scattering factor $P(q)$ [65,67].

The neutron scattering length of hydrogen (-0.37×10^{-12} cm) is extremely different from that of deuterium (0.67×10^{-12} cm) and other elements, and this particularity is valuable in neutron-based experiment and analysis. That is, by changing the ratio of H_2O and D_2O in aqueous solution, the internal structure of corresponding particles can be analyzed. This is called the contract variation method. By supposing a five-layer structure with different thicknesses and scattering length densities and assuming the water penetration within dendrimer molecules, segment density and water penetration in each layer can be evaluated from the SANS measurement [68,69]. The distribution of both segment density and water penetration strongly depends on the chemical structure of component of dendrimer.

The dynamic information of particles is also obtained from neutron facility. Normalized intermediate scattering function $I(q,t)/I(q,0)$ at Fourier time t on neutron spin echo is described by

$$I(q,t)/I(q,0) = \exp(-\Gamma t), \quad \Gamma = Dq^2 \tag{1.25}$$

in a single exponential equation. Thus the diffusion coefficient can be obtained in a similar way to dynamic light scattering. The diffusion coefficient obtained by means of the neutron spin echo can be fitted to double exponential equation for poly(amido amine) dendrimer [70]. The diffusion coefficient of the slow mode is close to translational diffusion coefficient regulated by interdendrimer interaction and almost equivalent to translational diffusion coefficient from

dynamic light scattering. The fast mode on the dynamics is originated by microscopic motion, maybe segment motion. It should be noticed that such fast segmental or chain dynamics can be detected by limited techniques like ^{13}C NMR relaxation [71], quasielastic neutron scattering [72], or computer simulation [73–75] besides neutron spin echo but not from dynamic light scattering.

1.3.2.3 Reflectometry

On the nanolayer investigation, the evaluation of layers is requested rather than overall particle structure. Although the nanolayer thickness can be evaluated from AFM, surface plasmon resonance, quartz crystal microbalance, and ellipsometry, these techniques are not sufficient for investigating the internal fine structure in nanolayer. Thus one method that reveals the internal structure is X-ray and neutron reflectometry [76]. When nanolayers are formed by the accumulation of layers, the reflectivity profile responds depending on the existence of such multilayers as seen in Fig. 1.16A. The Kissig fringe and its amplitude reflect the layer thickness and density contrast, and the reflectivity decrease indicates the roughness of the surface (Fig. 1.16B). The reflectivity profile based on the Fresnel equation (Eq. 1.26) can be Fourier transformed to obtain the density-depth profile (Fig. 1.16C).

$$R(q)/R_F(q) = (1/n_0)\int (dn(z)/dz)\exp(iq\cdot z)dz, \quad q = 4\pi\sin\theta/\lambda \tag{1.26}$$

where R is the reflectivity, R_F is the reflectivity at air-substrate interface, n_0 is the reflective index of substrate, and $n(z)$ is the reflectivity density at z depth. The density is the electron density on X-ray reflectivity or scattering length density on neutron reflectivity. Thus, layer properties like thickness, density, and roughness of each layer as well as layer number are able to be determined from reflectometry [77]. Accordingly, the composition, layer structure, and molecular orientation in nanolayers can be determined in nanoscale. This method is applicable to nanolayers at air-solid, liquid-solid, air-liquid, and liquid-liquid interfaces.

For instance, intercalation composites of dendrimer between clay layers in water were adsorbed on arachidic acid Langmuir monolayer at air-water interface and transferred on

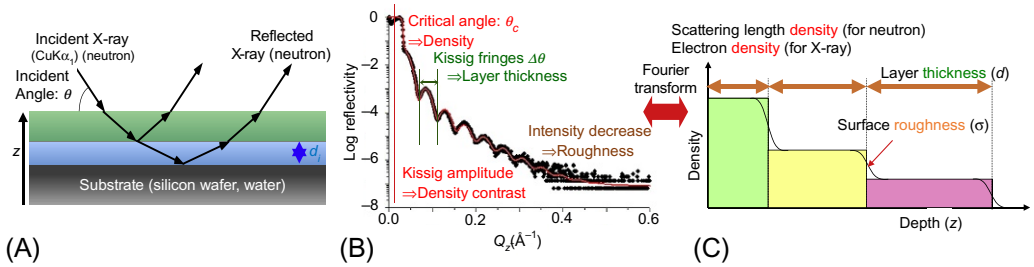

Fig. 1.16

Schematic representation of X-ray and neutron reflectometry: (A) principle of reflection from multilayer, (B) reflectivity plot, and (C) density-depth profile.

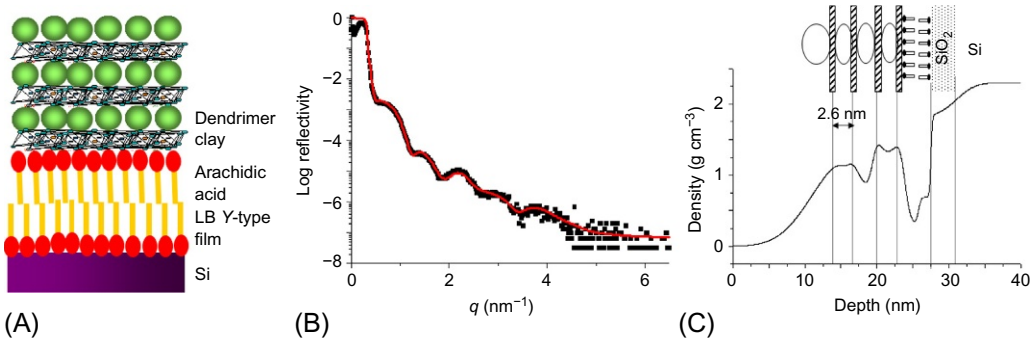

Fig. 1.17

Reflectivity analysis of composite of intercalated film and LB film (A) schematic illustration of a composite of dendrimer/clay intercalated film and arachidic acid *Y*-type LB film on silicone substrate, (B) X-ray reflectivity curve, and (C) density-depth profile. *Reprinted with permission from K. Mitamura, T. Imae, Structure determination of hybrid films of clay and clay/dendrimer nanocomposite on Langmuir-Blodgett film by X-ray reflectometry, Trans. Mater. Res. Soc. Jpn. 28 (2003) 71–74, Copyright 2003, The Materials Research Society of Japan.*

arachidic acid monolayer LB film on silica substrate (Fig. 1.17A), and the layered structure was determined by X-ray reflectometry [78]. Solid multilayer film displayed remarkable Kissig fringe (Fig. 1.17B), and the computational analysis of this reflectivity plot resulted in meaningful layer profile (Fig. 1.17C), where films were distinctly divided into hierarchy layers of dendrimer/clay/arachidic acid/SiO_2/Si. Monolayers at air-water and air-solid interfaces of block copolymers consisting of hydrophobic and perfluoroalkyl side chains were investigated by neutron and X-ray reflectometry [79] and compared to a case of mixture of block copolymers and perfluoroalkanoic acid [33]. Unlike the nonflat arrangement of block copolymers, the mixture presented well-ordered triple hierarchical structure of oleophilic/solvophobic/hydrophilic layers. Neutron reflectivity at air/suspension interface and X-ray reflectivity of the film transferred on a silicon substrate revealed the structure that the dendrimer molecules localized on the upper-half surface of gold nanoparticles, indicating the formation of Janus-type dendrimer/nanoparticle hybrid [6].

1.3.3 Characterization of Nanolayers by Spectroscopy

1.3.3.1 X-ray spectroscopy

Spectroscopy, especially surface spectroscopy, makes a significant contribution for analyzing nanolayers. Three types of surface spectroscopies are notable, since the existence, location, and orientation of elements or molecules in nanolayers can be clarified. One is X-ray spectroscopy. On X-ray photoelectron spectroscopy (XPS) or electron spectroscopy for chemical analysis (ESCA), when soft-X-ray is irradiated on the surface, the electrons of atomic orbital adsorb photo energy and are emitted as photoelectron energy. Thus the elements constituting the

surface are analyzed from intrinsic binding energies as a kind of elemental analysis. Moreover, since a slight shift of binding energy reflects the chemical species and electron states, the chemical bond state and oxidation number can be analyzed from fine spectra of XPS. It must be noted that the detection depth of this analysis is only of several nm.

In X-ray absorption spectroscopy, the electron states of elements and local chemical states are obtained from the analysis of near edge X-ray absorption fine structure (NEXAFS) appearing at absorption edge. In X-ray absorption spectrum at higher energy than NEXAFS up to 1000 EV, extended X-ray absorption fine structure (EXAFS) is observed and the position of atom neighboring to X-ray absorption atom is identified, since the photoelectron irradiated from X-ray absorption atom is scattered by neighboring atom, the photoelectron interferes with scattering wave, and the X-ray absorption coefficient of X-ray absorption atom changes.

1.3.3.2 Vibration spectroscopy

Because the vibration absorption spectroscopy directly involves vibrational level (or vibrational energy) of molecules, this method is an extremely accurate technique for analyzing molecules in nanolayers. Although the transmission mode is the most general technique in infrared absorption spectroscopy, it is not necessarily applicable to all nanolayers, especially to nanolayers on solid substrate. The reflection mode is powerful in surface analysis of nanolayers on substrate. Not only chemical species but also their orientation is also analyzed using this mode. With the reflection absorption (RA) mode, the infrared radiation reflected from the surface of infrared radiation-nontransmitting substrate is observed, when the *p*-polarized infrared ray is radiated at large angle [80]. The infrared absorption bands with transition moment at vertical direction to the substrate surface are intensified a maximum of 20 times at 80 degrees incident angle. In the attenuated total reflection (ATR) mode, the infrared absorption spectra of reflection from the metal (silver or gold)-deposited substrate are measured at larger angle than critical angle. The signal-to-noise (S/N) ratio of ATR mode is better than that of RA mode.

A more powerful technique using infrared absorption spectroscopy is surface enhanced infrared absorption (SEIRA) spectroscopy. Local surface plasmon resonance generated on metal particles (Au, Ag, Cu, Al, etc.) is accumulated on evanescent (incident electromagnetic) field at metal surface and the field is enhanced (see Fig. 1.18A). Then, SEIRA spectroscopy has a selection rule, where the perpendicular transition moment of vibration absorption bands of relevant molecule to metal surface is selectively enhanced. Enhancement factor of Ag is higher than Au and Ag is cheaper than Au, but it is easily sulfureted in air. When plasmon metal particles exist in substrate, the vibration spectra of molecules on such substrate are detected at high sensitivity by this enhanced surface field. SEIRA spectroscopy can be carried out at transmission, RA, and ATR modes. No additional tools are required for transmission mode except an infrared absorption instrument, but a specific attachment must be equipped for both RA and ATR modes. The attachment of Kretschmann optical arrangement for ATR modes is

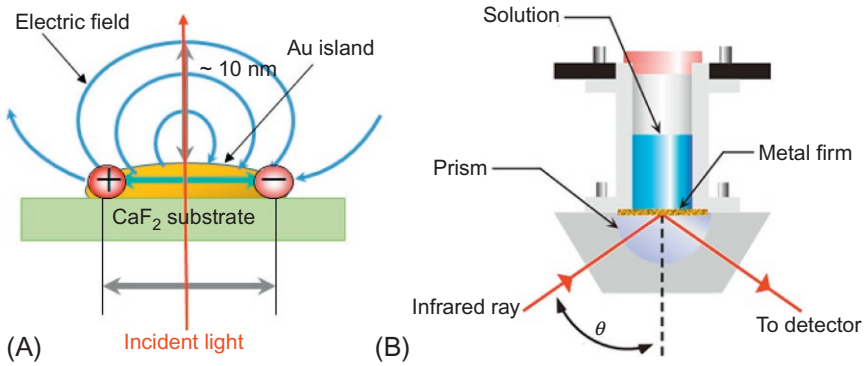

Fig. 1.18

Schematic representation of (A) principle of SEIRA spectroscopy and (B) a solution cell attachment of ATR SEIRA spectroscopy.

illustrated in Fig. 1.18B. In this mode, since a solution cell can be built in, the in situ adsorption of adsorbate on solid surface is possible.

Fig. 1.19A shows ATR infrared absorption spectra measured for solutions of bis(N-octylethylenediamine)zinc(II) chloride:benzene (1:1 w/w) with various water contents up to 30 wt% [42]. While infrared absorption bands of metal complex and benzene remain invariable, bands at 3369, 3261, 1652, 1636, and 1085 cm^{-1} attributed to water (OH group) are intensified by adding water. Thus, by setting a solution cell on a prism-type ATR system, infrared absorption bands of water can be determined. On an ATR-SEIRA system equipped

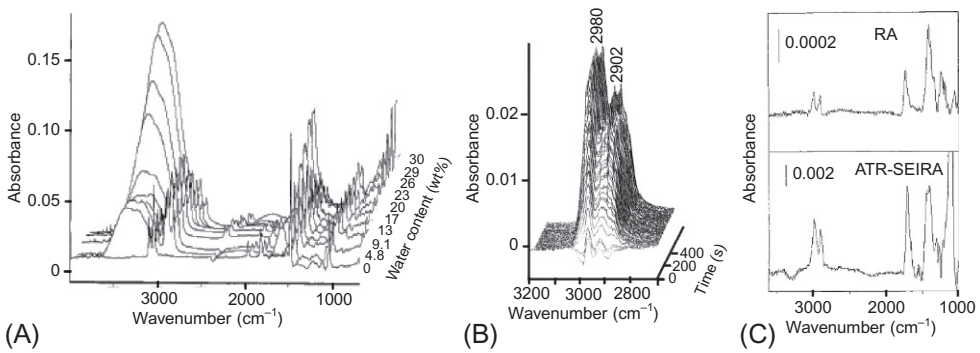

Fig. 1.19

(A) ATR infrared absorption spectra for solutions of bis(N-octylethylenediamine)zinc(II) chloride: benzene (1:1 w/w) with various water contents up to 30 wt% *(Reprinted with permission from Y. Ikeda, T. Imae, J.-C. Hao, M. Iida, T. Kitano, N. Hisamatsu, Structural characterization of microemulsions in a ternary system of Zn(oct-en)$_2$Cl$_2$ complex/benzene/water, Langmuir 16 (2000) 7618–7623, Copyright 2000, American Chemical Society.)*, (B) time-resolved ATR SEIRA spectra, and (C) RA and ATR-SEIRA spectra of adsorption of 3-mercaptopropionic acid from an ethanol solution. *(Reprinted with permission from T. Imae, H. Torii, In situ investigation of molecular adsorption on au surface by surface-enhanced infrared absorption spectroscopy, J. Phys. Chem. B 104 (2000) 9218–9224, Copyright 2000, American Chemical Society.)*

with a solution cell, the fine time-resolved investigation of adsorption of solute on liquid-solid interface is possible. As seen in Fig. 1.19B, the adsorption of 3-mercaptopropionic acid from an ethanol solution on the gold island film can be clarified from time-resolved infrared absorption bands of CH_2 stretching vibration modes at 2980 and 2902 cm^{-1} [19]. Moreover, the absorbance of absorption bands on SEIRA spectrum is 20 times higher than infrared RA spectrum (Fig. 1.19C). As well as the clarification of orientation of molecules on interface, the strength of infrared bands is also a matter of concern for preferable detection of molecules by infrared absorption spectroscopy. Therefore further improvements to the measurement techniques of infrared absorption spectra at interface must be made. Although the reported enhancement factor of SEIRA spectra had been 10–100 [81], a recent report indicated the enhancement factor around 200 on confeito-like gold nanoparticles instead of spherical gold particles [82].

Raman scattering is inelastic scattering against incident radiation (Fig. 1.14A). Raman activity depends on the symmetry of molecules, and therefore it is not necessarily the same as infrared activity [83]. Thus the vibration spectra by Raman scattering should be measured in contradistinction to those by infrared absorption. Moreover, surface enhancement occurs even on Raman scattering, and the effect of surface enhanced Raman scattering (SERS) is also intensified by the resonance Raman effect, where the excited wavelength of laser beam is close to being resonant with electronic absorption bands of relevant molecule, and thus the Raman scattering cross section is remarkably increased [83]. Thus the efficiency of SERS depends on excited wavelength. Since the surface enhancement effect by SERS is remarkably high and superior to the effect by SEIRA, research is mostly focused on the improvement of the enhancement factor. The enhancement factor depends on the size, shape, orientation, and density of plasmon particles. A size of around 20 nm is most effective [84], the rod particle is preferable to sphere [85], perpendicular orientation of rod is superior to horizontal or random orientation [86], and the close arrangement of confeito-like particles are preferable because of the formation of a large amount of active sites (hot spots) [87]. Thus the enhancement factor larger than 100,000 times is achieved by confeito-like gold nanoparticle-adsorbed SAMs [87]. As well as infrared absorption and Raman scattering spectroscopy, ultraviolet-visible absorption and fluorescence spectrometry are also expected to exhibit the surface enhancement effect [88–91]. Surface plasmon fluorescence spectroscopy is preferable to strongly excite fluorescence probe on energy-transfer-controllable organic thin films [91], but the ingenious setup of adequate distance between the probe molecule and the metal surface is required, for example, by layers, bilayers, SAMs, and layer-by-layer accumulation.

1.3.3.3 Surface plasmon resonance spectroscopy

Another methodology for investigating adsorption statics and kinetics belongs to plasmonics by means of the same principle as surface enhanced spectroscopy described earlier but of different phenomenon from it. When the wave vector of the compressional wave of electron propagating

along surface by the assembled energy at interface of metal and dielectric (surface plasmon) is synchronized with parallel component along metal surface of wave vector of incident excitation electromagnetic beam (evanescent wave), surface plasmon resonance (SPR) results (Fig. 1.20A), and the energy of incident radiation is used for the excitation of surface plasmon, inducing the attenuation of the reflection light. This phenomenon is valuable for surface analysis from some advantages.

Suppose that on Kretschmann-type SPR optical cell (Fig. 1.20A), plasmon and evanescent waves with vectors k_{sp} and k_{ev}, respectively, are resonated, if there is no adsorption of molecules on metal. However, when molecules (dielectric constant ε_3) are adsorbed at thickness d_3 on metal (dielectric constant ε_m) from aqueous solution at the interface with water (dielectric constant ε_s), plasmon and evanescent wave vectors vary to k'_{sp} and k'_{ev}, respectively. If an incident radiation at incident angle θ has wave vector of k_p, then, the variation of wave vector is described by

$$\Delta k_{sp} = k'_{sp} - k_{sp} \approx d_3(2\pi/\lambda)^2(\varepsilon_m\varepsilon_s)^{3/2}(\varepsilon_3 - \varepsilon_s)/(\varepsilon_m - \varepsilon_s)^2\varepsilon_3 = d_3(2\pi/\lambda)^2 f(\varepsilon)$$
$$k'_{ev} = k_{ev} + \Delta k_{ev} = k_p \sin(\theta + \Delta\theta) = k_p \sin\theta + k_p\Delta\theta$$
$$k'_{ev} = k'_{sp}, \quad k_{ev} = k_{sp} \quad \text{and} \quad k_p = 2\pi n/\lambda \tag{1.27}$$

from resonance condition. Thus,

$$\Delta\theta \approx d_3(2\pi/n\lambda)f(\varepsilon) \tag{1.28}$$

where n is the dielectric constant of prism.

This phenomenon happens in the vicinity of metal surface (below micrometer) and, incidentally, the strength distribution of surface plasmon is exponentially attenuated in perpendicular direction to surface. Thus, only molecules adsorbed on surface can be selectively detected from reflectance spectrum variation or time-course of angle shift (Fig. 1.20B and C). Its sensitivity is high due to the resonance enhancement effect. Since the methodology is not affected by electric noise and it is possible to introduce optical analysis technology, the methodology can be applicable to photo sensor. The measurement can be carried out in situ and at nondestructive inspection. In fact, this technique is used for the detection of dielectric constant, thickness, molecular orientation, and of reaction as biosensor, chemosensor, and thermosensor. The results of in situ adsorption kinetics of amphiphilic molecules on solid substrates measured by SPR and ATR SEIRA spectroscopy can be analyzed by Langmuir monolayer adsorption and two-step adsorption kinetics [16]. Thus, SPR method is powerful for investigation of nanolayer films [92,93]. Moreover, when the electrochemical cell is set up in SPR system (Fig. 1.20D), the characterization of ultrathin conducting polymer films can be examined as seen in Fig. 1.20E [94]. Then the combination of electrochemistry and SPR methods is better activated for monitoring the growth of polymer films [94–96].

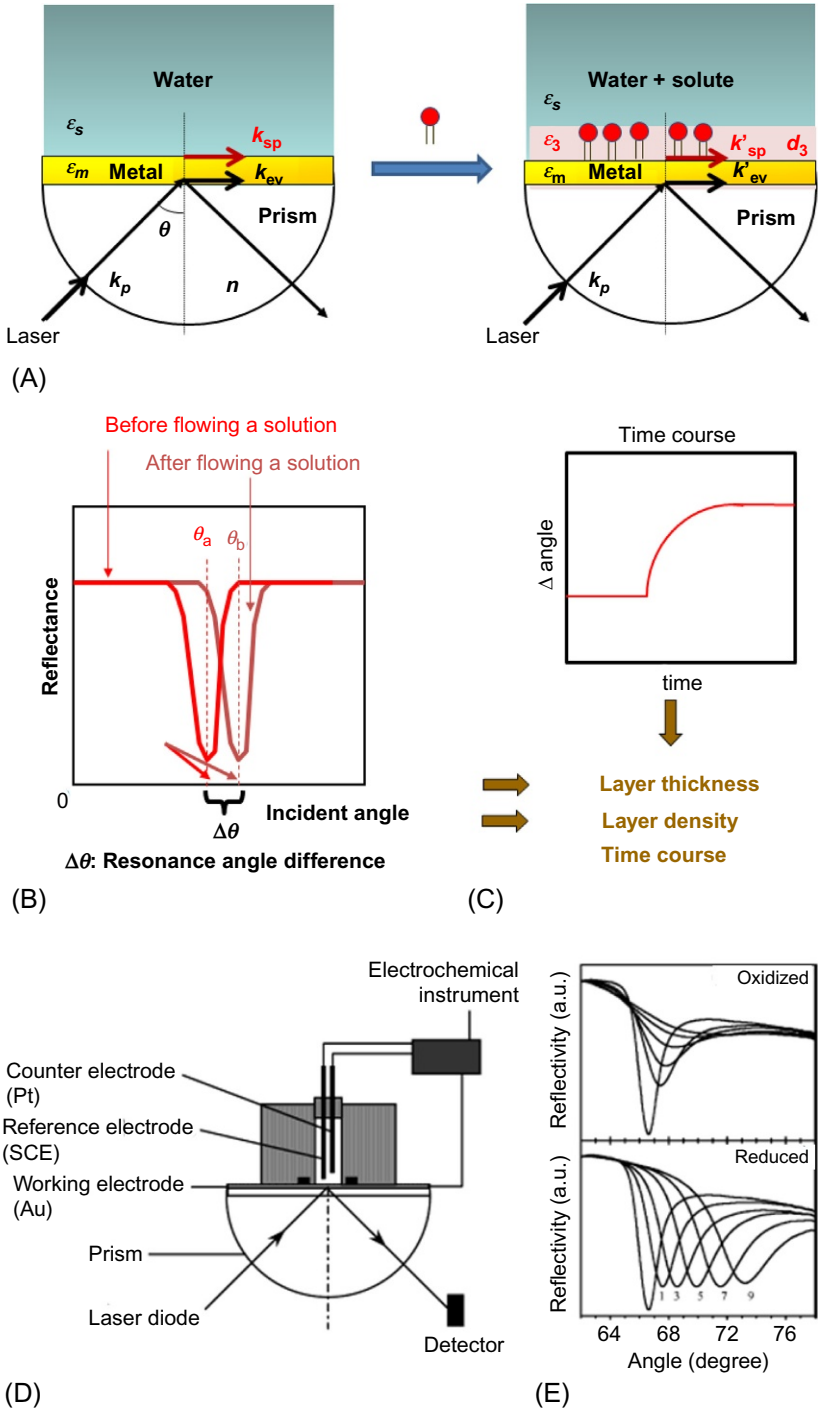

Fig. 1.20

Schematic representation of (A) principle of SPR spectrum, (B) resonance angle shift, (C) time-course angle shift, (D) experimental setup for in situ electrochemical SPR measurement, and (E) SPR angle scan curves at oxidized and reduced states of poly(3,4-ethylenedioxythiophene) films after 1–9 potential cycles under 780-nm laser. *Reprinted with permission from C. Li, T. Imae, Electrochemical and optical properties of the poly(3,4-ethylenedioxythiophene) film electropolymerized in an aqueous sodium dodecyl sulfate and lithium tetrafluoroborate medium, Macromolecules 37 (2004) 2411–2416, Copyright 2004, American Chemical Society.*

Based on the property that the SPR's spectrum sensitivity changes by film thickness and dielectric constant of materials contacting on metal surface, the device for the observation of two-dimensional distribution of dielectic constant or film thickness is developed and named as near field scanning optical microscope [97]. By the interaction of metal surface with electromagnetic field, the optical electric field can be limited in an enough smaller region than light wavelength, and thus nano- and mesoscopic structures can be detected by this high-resolution microscope with resolution of 20 nm. Thus this microscope can be qualified as one of SPM.

1.4 Conclusions

In the first half of this chapter, the formulation of nanolayers was explained. Nanolayers are formed at different interfaces between hetero- or homo-phases of gas, liquid, or solid state. Therefore, they are considerably different in formulation procedures and differently named. Nanolayers vary from monolayer to multilayer and their thickness is controllable to be nanosize, depending on the procedure. The shape of nanolayers is dominated by the shape of interface, namely, flat or finite interface. The nanolayers can be formulated by single components or multiple components and by homogeneous or heterogeneous layers, depending on the purpose.

In the second half of the chapter, the characterization methods of nanolayers were described. The method using microscopy covers the visualization of nanolayers from micrometer to nanometer (or Å) scale. Depending on the type of microscope, different types of nanolayers at liquid and solid states can be visualized and analyzed as to their size, shape, components, crystallization, and ordering. The electromagnetics method yields quantitative characteristics of nanolayers such as the size, shape, and crystallization of nanolayers and, moreover, the ordering and structure of hierarchic layers. The characterization by spectroscopy provides information of molecular basis in detail such as molecular packing, ordering, and orientation.

This chapter provided an overview of formulation and characterization methods of nanolayers. For more detailed descriptions, refer to specialized review articles and books. Books have been published on the chemistry of monolayers at interfaces [98]; SEM [99]; scanning probe microscopy [100]; atomic force microscopy [101]; light, X-ray, and neutron scattering [43–49]; reflectometry [76]; NEXAFS spectroscopy [102]; surface-enhanced Raman spectroscopy [103]; and surface plasmon resonance [104]. The following chapters in this book introduce some specific morphologies and technologies for nanolayers. Nanolayers are nowadays an important material for devices in electronics, mechatronics, and photonics, etc. This information will assist in the engineering of such materials as well as providing the basic science.

Acknowledgments

This chapter was based on the author's study, investigation, and lectures at Nagoya University, Japan; Kieo University, Japan; and National Taiwan University of Science and Technology, Taiwan. The author gratefully acknowledges the encouragement of her colleagues, collaborators, and students in writing this chapter.

References

[1] I. Langmuir, The adsorption of gases on plane surfaces of glass, mica, and platinum, J. Am. Chem. Soc. 40 (1918) 1361–1403, http://dx.doi.org/10.1021/ja02242a004.
[2] G. Binnig, H. Rohrer, Ch. Gerber, E. Weibel, Surface studies by scanning tunneling microscopy, Phys. Rev. Lett. 49 (1982) 57–61.
[3] T. Imae, H. Araki, S. Ikeda, The anomalous behavior of surface tension of aqueous solutions of dimethyloleylamine oxide, and its multimolecular adsorption on aqueous surfaces, Colloids Surf. 17 (1986) 207–219.
[4] K. Aoi, A. Motoda, M. Okada, T. Imae, Novel amphiphilic linear polymer/dendrimer block copolymer: synthesis of poly(2-methyl-2-oxazoline)-block-poly(amido amine) dendrimer, Macromol. Rapid Commun. 18 (1997) 945–952.
[5] K. Aoi, A. Takasu, M. Okada, T. Imae, Synthesis and assembly of novel chitin derivatives having amphiphilic polyoxazoline block copolymer as a side chain, Macromol. Chem. Phys. 200 (1999) 1112–1120.
[6] M. Ujihara, K. Mitamura, N. Torikai, T. Imae, Fabrication of metal nanoparticle monolayers on amphiphilic poly(amido amine) dendrimer langmuir films, Langmuir 22 (2006) 3656–3661.
[7] H. Okuda, T. Imae, S. Ikeda, The adsorption of cetyltrimethylammonium bromide on aqueous surfaces of sodium bromide solutions, Colloids Surf. 27 (1987) 187–200.
[8] A. Pockels, Surface tension, Nature 46 (1891) 437–439.
[9] T. Imae, T. Takeshita, M. Kato, Phase-separation in hybrid Langmuir-Blodgett films of perfluorinated and hydrogenated amphiphiles. Examination by atomic force micorscopy, Langmuir 16 (2000) 612–621.
[10] O. Mori, T. Imae, AFM observation of monolayers of arachidic acid, octadecyldimethylamine oxide, and their mixtures, Langmuir 11 (1995) 4779–4784.
[11] O. Mori, T. Imae, Molecular organization of photoreactive unsaturated carboxylates on Langmuir-Blodgett film, J. Colloid Interface Sci. 198 (1998) 11–17.
[12] T. Imae, K. Aoki, Langmuir-Blodgett films of surface active azodye—investigation by atomic force microscopy, Langmuir 14 (1998) 1196–1200.
[13] S. Ikeda, A. Kito, T. Imae, H. Maeda, Sorption of water vapor on poly-L-lysine hydrobromide, J. Colloid Interface Sci. 48 (1974) 256–262.
[14] S. Brunauer, P.H. Emmet, E. Teller, Adsorption of gases in multimolecular layers, J. Am. Chem. Soc. 60 (1938) 309–319.
[15] K. Shah, T. Imae, Analytical investigation of specific adsorption kinetics of CO_2 gas on dendrimer loaded in organoclays, Chem. Eng. J. 283 (2016) 1366–1373.
[16] M. Ito, T. Imae, K. Aoi, K. Tsutsumiuchi, H. Noda, M. Okada, In situ investigation of adlayer formation and adsorption kinetics of amphiphilic Surface-Block dendrimers on solid substrates, Langmuir 18 (2002) 9757–9764.
[17] K. Mitamura, T. Imae, N. Saito, O. Takai, Fabrication and self-assembly of hydrophobic gold nanorods, J. Phys. Chem. B 111 (2007) 8891–8898.
[18] A. Siriviriyanun, T. Imae, Anti-fingerprint properties of non-fluorinated organosiloxane self-assembled monolayer-coated glass surfaces, Chem. Eng. J. 246 (2014) 254–259.
[19] T. Imae, H. Torii, In situ investigation of molecular adsorption on au surface by surface-enhanced infrared absorption spectroscopy, J. Phys. Chem. B 104 (2000) 9218–9224.

[20] J.S. D'Arrigo, T. Imae, Physical characteristics of ultrastable lipid-coated microbubbles, J. Colloid Interface Sci. 149 (1992) 592–595.
[21] T. Imae, Skin Bioscience: A Molecular Approach, Pan Stanford Publishing Pte. Ltd, Singapore, 2014.
[22] Y. Zhu, T. Imae, T. Saiwaki, T. Oka, Damage/recovery by additive on lipid membrane as a mimicry of human stratum corneum, Langmuir 26 (2010) 4951–4957.
[23] K. Nakazawa, T. Imae, T. Iwamoto, Microscopic observation of vesicles formed by alkene succinic acids, Langmuir 8 (1992) 1878–1880.
[24] C. Li, K. Mitamura, T. Imae, Electrostatic layer-by-layer assembly of poly(amido amine) dendrimer/conducting sulfonated polyaniline: structure and properties of multilayer films, Macromolecules 36 (2003) 9957–9965.
[25] A.S. Costa, T. Imae, Morphological investigation of hybrid Langmuir-Blodgett films of arachidic acid with a hydrotalcite/dendrimer nanocomposite, Langmuir 20 (2004) 8865–8869.
[26] K.J. Shah, A.D. Shukla, T. Imae, Selective capture of CO_2 by poly(amido amine) dendrimer-loaded organoclays, RSC Adv. 5 (2015) 35985–35992.
[27] M. Ujihara, M.M.M. Ahmed, T. Imae, Y. Yamauchi, Massive-exfoliation of magnetic graphene from acceptor-type GIC by long-chain alkyl amine, J. Mater. Chem. A 2 (2014) 4244–4250.
[28] J.M. Englert, C. Dotzer, G. Yang, M. Schmid, C. Papp, J.M. Gottfried, H. P. Steinrück, E. Spiecker, F. Hauke, A. Hirsch, Covalent bulk functionalization of graphene, Nat. Chem. 3 (2011) 279–286.
[29] W. Sirisaksoontorn, A.A. Adenuga, V.T. Remcho, M.M. Lerner, Preparation and characterization of a tetrabutylammonium graphite intercalation compound, J. Am. Chem. Soc. 133 (2011) 12436–12438.
[30] T. Yamazaki, T. Imae, H. Sugimura, N. Saito, K. Hayashi, O. Takai, Photolithographic patterning of dendrimer monolayers and pattern-selective adsorption of linear macromolecules, J. Nanosci. Nanotechnol. 5 (2005) 1792–1800.
[31] M. Ujihara, T. Imae, Hierarchical structures of dendritic polymers, Polym. Int. 59 (2010) 137–144.
[32] A.M. Diyas, T. Hasegawa, J. Nishijo, T. Imae, Y. Ozaki, Structural characterization of Langmuir-Blodgett films of octadecyldimethylamine oxide and dioctadecyldimethylammonium chloride. 1. Reorientation of molecular assemblies during the accumulation of upper layers studied by infrared spectroscopy, Langmuir 15 (1999) 3595–3600.
[33] K. Mitamura, T. Imae, E. Mouri, N. Torikai, H. Matsuoka, T. Nakamura, Structural and morphological changes of monolayers of a block copolymer with dendron and perfluoroalkyl side chains by mixing an perfluorooctadecanoic acid, J. Nanosci. Nanotechnol. 6 (2006) 36–42.
[34] M. Ujihara, J. Orbulescu, T. Imae, R.M. Leblanc, Film structures of poly(amido amine) dendrimers with an azacrown core and long alkyl chain spacers on water or Ag nanoparticle suspension, Langmuir 21 (2005) 6846–6854.
[35] K. Tamano, T. Imae, S. Yusa, Y. Shimada, Structure-selective dye-uptake into aggregate of copolymer with linear polyelectrolyte block and hydrophobic block carrying pendant dendritic moiety in water, J. Phys. Chem. B 109 (2005) 1226–1230.
[36] X. Lu, T. Imae, Size-controlled in situ synthesis of metal nanoparticles on dendrimer-modified carbon nanotubes, J. Phys. Chem. C 111 (2007) 2416–2420.
[37] T. Imae, B. Trend, VEM observation of pH-dependent vesicle formation by single-chain surfactant, Langmuir 7 (1991) 643–646.
[38] T. Imae, Y. Ikeda, M. Iida, N. Koine, S. Kaizaki, Self-organization of dinuclear metal complex in lyotropic liquid crystal: ribbon-like supramolecular assemblies, Langmuir 14 (1998) 5631–5635.
[39] D. Wang, T. Imae, M. Miki, Fluorescence emission from PAMAM and PPI dendrimers, J. Colloid Interface Sci. 307 (2007) 354–360.
[40] W. Tanglumlert, S. Wongkasemjit, T. Imae, Fabrication of dendrimer porogen-capsulated mesoporous silica via sol-gel process of silatrane precursor, J. Nanosci. Nanotechnol. 9 (2009) 1844–1850.
[41] T. Imae, Y. Takahashi, H. Muramatsu, Formation of fibrous molecular assemblies by amino acid surfactants in water, J. Am. Chem. Soc. 114 (1992) 3414–3419.

[42] Y. Ikeda, T. Imae, J.-C. Hao, M. Iida, T. Kitano, N. Hisamatsu, Structural characterization of microemulsions in a ternary system of $Zn(oct\text{-}en)_2Cl_2$ complex/benzene/water, Langmuir 16 (2000) 7618–7623.
[43] A. Guinier, G. Fournet, Small-Angle Scattering of X-rays, Wiley, New York, 1955.
[44] B.J. Berne, R. Pecora, Dynamic Light Scattering: With Applications to Chemistry Biology and Physics, John Wiley & Sons, New York, 1976.
[45] O. Glatter, O. Kratky, Small-Angle X-ray Scattering, Academic Press, London, 1982.
[46] W. Burchard, G.D. Patterson, Light Scattering From Polymers, Springer-Verlang, Berlin, 1983.
[47] L.A. Feigin, D.I. Svergun, G.W. Taylo (Ed.), Structure Analysis by Small-Angle X-ray and Neutron Scattering, Plenum, New York, 1987.
[48] P. Lindner, Th. Zemb, Neutron, X-ray and Light Scattering: Introduction to an InVestigatiVe Tool for Colloidal and Polymeric Systems, North-Holland, Amsterdam, 1991.
[49] T. Imae, T. Kanaya, M. Furusaka, N. Torikai, Neutrons in Soft Matter, John Wiley & Sons Inc., Hoboken, NJ, 2011
[50] T. Imae, S. Ikeda, Sphere-rod transition of micelles of tetradecyltrimethylammonium halides in aqueous sodium halide solutions and flexibility and entanglement of long rodlike micelles, J. Phys. Chem. 90 (1986) 5216–5223.
[51] T. Imae, S. Ikeda, Characteristics of rodlike micelles of alkyltrimethylammonium halides in aqueous sodium halide solutions: their flexibility and entanglement, in: K.L. Mittal (Ed.), Surfactants in Solution, vol. 7, Plenum Publishing Co, New York, NY, 1989, pp. 455–472.
[52] T. Imae, Nonionic rodlike micelles in dilute and semidilute solutions: intermicellar interaction and the scaling law, J. Phys. Chem. 92 (1988) 5721–5726.
[53] H. Benoit, P. Doty, Light scattering from non-Gaussian chains, J. Phys. Chem. 57 (1953) 958–963.
[54] H. Ito, T. Imae, T. Nakamura, M. Sugiura, Y. Oshibe, Self-association of water-soluble fluorinated diblock copolymers in solutions, J. Colloid Interface Sci. 276 (2004) 290–298.
[55] D.E. Koppel, Analysis of macromoleculear polydispersity in intensity correlation spectroscopy: the method of cumulants, J. Chem. Phys. 57 (1972) 4814–4820.
[56] S.W. Provencher, A Fourier method for the analysis of exponential decay curves, Biophys. J. 16 (1976) 27–41.
[57] S.W. Provencher, A constrained regularization method for inverting data represented by linear algebraic or integral equations, Comput. Phys. Commun. 27 (1982) 213. CONTIN: A general purpose constrained regularization program for inverting noisy linear algebraic and integral equations, 27 (1982) 229.
[58] W.H. Press, S.A. Teukolsky, W.T. Vetterlin, B.P. Flanery, Numerical Recipes in FORRAN, 2nd ed., Cambridge University Press, New York, NY, 1992.
[59] B.R. Ware, W.H. Flygare, The simultaneous measurement of the electrophoretic mobility and diffusion coefficient in bovine serum albumin solutions by light scattering, Chem. Phys. Lett. 12 (1971) 81–85. Light scattering in mixtures of BSA, BSA dimers and fibrinogen under the influence of electric fields, J. Colloid Interface Sci. 39 (1972) 670–675.
[60] T. Imae, W. Otani, K. Oka, Electrophoretic light scattering of surfactant micelle colloids, J. Phys. Chem. 94 (1990) 853–855.
[61] T. Imae, N. Hayashi, Electrophoretic light scattering of alkyl- and oleyldimethylamine oxide micelles, Langmuir 9 (1993) 3385–3388.
[62] T. Imae, M. Kakitani, Electrokinetic properties of mixed solutions of dodecyldimethylamine oxide and sodium dodecyl sulfate: specific adsorption effects of small ions, Colloid Polym. Sci. 274 (1996) 1170–1175.
[63] T. Imae, H. Okamura, M. Furusaka, Light scattering and small-angle neutron scattering investigation for the L_1 phase in a terminal system, J. Colloid Interface Sci. 168 (1994) 217–221.
[64] H. Okamura, T. Imae, K. Takagi, Y. Sawaki, M. Furusaka, Small-angle neutron scattering investigation of supramolecular assemblies in ternary system of alkyldimethylamine oxide/cinnamic acid/water, J. Colloid Interface Sci. 180 (1996) 98–105.
[65] T. Imae, M. Kakitani, M. Kato, M. Furusaka, Effect of organic additives or counterions on the supramolecular assembly structures constructed by amphiphiles—small-angle neutron scattering investigation, J. Phys. Chem. 100 (1996) 20051–20055.

[66] T. Imae, SANS investigation of supramolecular assemblies constructed in aqueous alkyldimethylamine oxide solutions with organic additives, Colloids Surf. A Physicochem. Eng. Aspects 109 (1996) 291–304.
[67] M. Kakitani, T. Imae, M. Furusaka, Investigation of mixed micelles of dodecyldimethylamine oxide and sodium dodecyl sulfate by sans: shape, size, charge, and interaction, J. Phys. Chem. 99 (1995) 16018–16023.
[68] T. Imae, K. Funayama, K. Aoi, K. Tsutsumiuchi, M. Okada, M. Furusaka, Small-angle neutron scattering and surface force investigations of poly(amido amine) dendrimer with hydroxyl end group, Langmuir 15 (1999) 4076–4084.
[69] K. Funayama, T. Imae, K. Aoi, K. Tsutsumiuchi, M. Okada, M. Furusaka, M. Nagao, Small-angle neutron scattering investigations of layer-block dendrimers in aqueous solutions, J. Phys. Chem. B 107 (2003) 1532–1539.
[70] K. Funayama, T. Imae, H. Seto, K. Aoi, K. Tsutsumiuchi, M. Okada, M. Nagao, M. Furusaka, Fast and slow dynamics of water-soluble dendrimers consisting of amido-amine repeating units by neutron spin echo, J. Phys. Chem. B 107 (2003) 1353–1359.
[71] A.D. Meltzer, D.A. Tirrell, A.A. Jones, P.T. Inglefield, D.M. Hedstrand, D.A. Tomalia, Chain dynamics in poly (amido amine) dendrimers. A study of ^{13}C NMR relaxation parameters, Macromolecules 25 (1992) 4541–4548.
[72] B. Stark, B. Stühn, H. Frey, C. Lach, K. Lorenz, B. Frick, Segmental dynamics in dendrimers with perfluorinated end groups: a study using quasielastic neutron scattering, Macromolecules 31 (1998) 5415–5423.
[73] P. Welch, M. Muthukumar, Dendrimer-polyelectrolyte complexation: a model guest-host system, Macromolecules 33 (2000) 6159–6167.
[74] P. Chodanowski, S. Stoll, Polyelectrolyte adsorption on charged particles in the Debye-Hückel approximation. A Monte Carlo approach, Macromolecules 34 (2001) 2320–2328.
[75] S. Stoll, P. Chodanowski, Polyelectrolyte adsorption on an oppositely charged spherical particle chain rigidity effects, Macromolecules 35 (2002) 9556–9562.
[76] H.G. Tompkins, W.A. McGaghan, Spectroscopic Ellipsometry and Reflectometry, John Wiley & Sons, Inc., New York, 1999.
[77] A.M. Tikhonov, M.L. Schlossman, Surfactant and water ordering in triacontanol monolayers at the water-hexane interface, J. Phys. Chem. 107 (2003) 3344–3347.
[78] K. Mitamura, T. Imae, Structure determination of hybrid films of clay and clay/dendrimer nanocomposite on Langmuir-Blodgett film by X-ray reflectometry, Trans. Mater. Res. Soc. Jpn. 28 (2003) 71–74.
[79] K. Mitamura, M. Takahashi, S. Hamaguchi, T. Imae, T. Nakamura, Reflectometric investigation of monolayers of copolymers with dendritic and perfluoroalkyl side chains, Trans. Mater. Res. Soc. Jpn. 29 (2004) 255–258.
[80] J. Umemura, T. Kamata, T. Kawai, T. Takenaka, Quantitative evaluation of molecular orientation in thin Langmuir-Blodgett firms by FT-IR transmission and reflection-absorption spectroscopy, J. Phys. Chem. 94 (1990) 62–67.
[81] K. Ataka, J. Heberle, Biochemical applications of surface-enhanced infrared absorption spectroscopy, Anal. Bioanal. Chem. 388 (2007) 47–54.
[82] M. Ujihara, N.M. Dang, C.-C. Chang, T. Imae, Surface-enhanced infrared absorption spectra of eicosanoic acid on confeito-like Au nanoparticle, J. Taiwan Inst. Chem. Eng. 45 (2014) 3085–3089.
[83] P.R. Carey, Biochemical applications of Raman and resonance Raman spectroscopies, Academic Press, New York, 1982.
[84] Z. Zhang, T. Imae, Study of surface enhanced infrared spectroscopy. 2. Large enhancement achieved through metal-molecule-metal sandwich configurations, J. Colloid Interface Sci. 233 (2001) 107–111.
[85] Y.-H. Wu, T. Imae and M. Ujihara, Surface enhanced Plasmon effects by gold nanospheres and nanorods in Langmuir-Blodgett films, Colloids Surf. A Physicochem. Eng. Aspects, 2017, http://dx.doi.org/10.1016/j.colsurfa.2017.05.015.
[86] T. Imae, X. Zhang, Effect of Au nanorod assemblies on surface-enhanced Raman spectroscopy, J. Taiwan Inst. Chem. Eng. 45 (2014) 3081–3084.
[87] C.-C. Chang, T. Imae, L.-Y. Chen, M. Ujihara, Efficient surface enhanced Raman scattering on confeito-like gold nanoparticles-adsorbed self-assembled monolayers, Phys. Chem. Chem. Phys. 17 (2015) 32328–32334.
[88] R. Naumann, A. Jonczyk, R. Kopp, J. Esch, H. Ringsdorf, W. Knoll, P. Gräber, Incorporation of membrane proteins in solid-supported lipid layers, Angew. Chem. 34 (1995) 2056–2058.

[89] D. Kambhampati, P.E. Nielsen, W. Knoll, Investigating the kinetics of DNA-DNA and PNA-DNA interactions using surface plasmon resonance-enhanced fluorescence spectroscopy, Biosens. Bioelectron. 16 (2001) 1109–1118.
[90] S. Krupka, B. Wiltschi, U. Reuning, K. Ho¨lscher, M. Hara, E. Sinner, In vivo detection of membrane protein expression using surface plasmon enhanced fluorescence spectroscopy (SPFS), Biosens. Bioelectron. 22 (2006) 260–267.
[91] K. Mitamura, T. Imae, S. Tian, W. Knoll, Surface plasmon fluorescence investigation of energy transfer-controllable organic thin films, Langmuir 24 (2008) 2266–2270.
[92] W. Knoll, Interfaces and thin films as seen by bound electromagnetic waves, Annu. Rev. Phys. Chem. 49 (1998) 569–638.
[93] T. Imae, Molecular organization in monolayers—surface spectroscopy and sensing, in: A.T. Hubbard (Ed.), Encyclopedia of Surface and Colloid Science, Marcel Dekker, New York, 2002, pp. 3547–3558.
[94] C. Li, T. Imae, Electrochemical and optical properties of the poly(3,4-ethylenedioxythiophene) film electropolymerized in an aqueous sodium dodecyl sulfate and lithium tetrafluoroborate medium, Macromolecules 37 (2004) 2411–2416.
[95] A. Baba, R.C. Advincula, W. Knoll, In situ investigations on the electrochemical polymerization and properties of polyaniline thin films by surface plasmon optical techniques, J. Phys. Chem. B 106 (2002) 1581–1587.
[96] O.A. Raltman, E. Katz, A.F. Böckmann, I. Willmer, Integration of polyaniline/poly(acrylic acid) films and redox enzymes on electrode supports: an in situ electrochemical/surface plasmon resonance study of the bioelectrocatalyzed oxidation of glucose or lactate in the integrated bioelectrocatalytic systems, J. Am. Chem. Soc. 124 (2002) 6487–6496.
[97] U. During, D.W. Pohl, F. Rohner, Near-field optical-scanning microscopy, J. Appl. Phys. 59 (1986) 3318.
[98] T. Imae, Advanced Chemistry of Monolayers at Interfaces—Trends in Methodology and Technology, Elsevier Science Publishers, Amsterdam, 2007.
[99] L. Reimer, Scanning Electron Microscopy, Springer, Berlin, Heidelberg, 1998.
[100] E. Meyer, H.J. Hug, R. Bennewitz, Scanning Probe Microscopy, Springer, Berlin, Heidelberg, 2004.
[101] G. Haugstad, Atomic force Microscopy: Understanding Basic Modes and Advanced Applications, John Willey & Sons, Inc., New York, 2012
[102] J. Stöhr, NEXAFS Spectroscopy, Springer, Berlin, Heidelberg, 1992.
[103] S. Schlücker, Surface Enhanced Raman Spectroscopy: Analytical, Biophysical and Life Science Applications, John Willey & Sons, Inc, New York, 2010.
[104] N.J. Mol, M.J.E. Fisher, Surface Plasmon Resonance, Springer, Berlin, Heidelberg, 2010.

CHAPTER 2

Electrical Double Layer at Nanolayer Interface

Hiroyuki Ohshima

Tokyo University of Science, Chiba, Japan

2.1 Introduction

The surface of charged entities immersed in an electrolyte solution or the interface between two immiscible media can be charged owing to adsorption of ions onto the surface and/or ionization of dissociable groups on the surface. Mobile electrolyte ions with charges of the sign opposite to that of the solid surface charges are called counter ions. They tend to approach the charged solid surface to neutralize the surface charges, but thermal motion of these ions prevents accumulation of the ions so that around the solid surface is formed an ionic cloud. In the ionic cloud the concentration of counterions becomes very high while that of coions (electrolyte ions with charges of the same sign as the particle surface charges) is very low. The ionic cloud together with the solid surface charge forms an electrical double layer, as shown in Fig. 2.1. The electrical double layer plays an essential role in the electric behaviors of charged particles and charged interfaces, including electrostatic interactions between charged particles, the motion of charged particles in an electric field (electrophoresis), and the motion of an electrolyte solution on a charged surface (electroosmosis) [1–14].

Special attention should be paid to the case in which a solid entity is connected to an external power supply such as batteries. In such cases we call this entity an electrode. An electrical double layer is also formed around an electrode immersed in an electrolyte solution. An electrical double layer around an electrode, however, differs from those around other charged entities due to their different surface charging mechanisms. It is possible to regulate the surface charge of an electrode by applying an external electric potential. Fig. 2.2 shows that electrical double layers are formed around two electrodes, anode and cathode when a battery is connected to the electrodes, while they disappear when the battery is disconnected. An electrical double layer formed by the surface charge and counterions can be regarded as an electrical capacitor (Fig. 2.2). The electrical double layer capacitors have attracted growing interest as rechargeable (or secondary) batteries from the viewpoint of green chemistry, since the electrical double layer capacitors do not use chemical reactions unlike usual secondary batteries.

Nanolayer Research. http://dx.doi.org/10.1016/B978-0-444-63739-0.00002-5

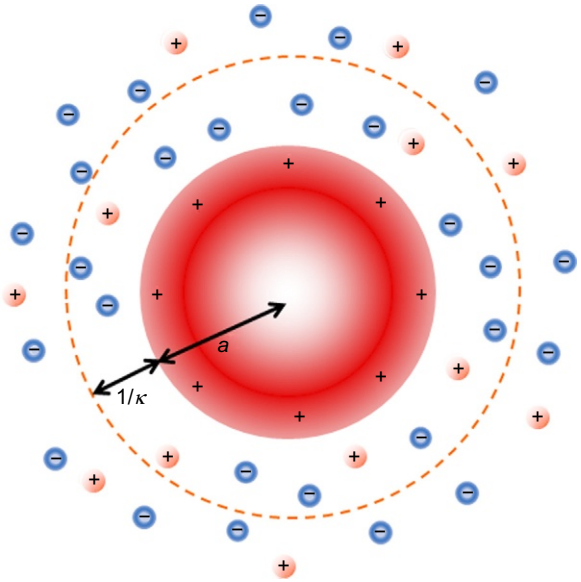

Fig. 2.1
Electrical double layer of thickness $1/\kappa$ (the Debye length) around a spherical charged particle.

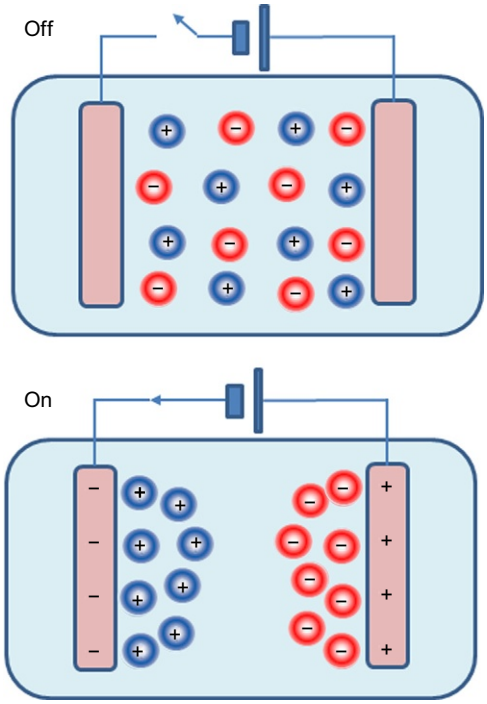

Fig. 2.2
Electrical double layer capacitor. An electrical double layer is formed around electrodes when a battery is connected to the electrodes but disappears when the battery is disconnected.

The present chapter starts with the Gouy-Chapman-Stern model [15–17] for an electrical double layer, which is the most widely used model for an electrical double layer (Section 2.2). The potential distribution in a Gouy-Chapman diffuse layer can be obtained by solving the Poisson-Boltzmann equation. After discussion of the general feature of electrical double layers around charged surfaces without surface structures in Sections 2.3 and 2.4, we consider the main topic of this chapter: electrical double layers around charged entities covered with surface layers of the order of nanometers, that is, nanolayer-coated surfaces, in Sections 2.5 and 2.6. We deal with surfaces coated with a nanolayer of porous material (Section 2.5) and that of polyelectrolytes (Section 2.6). Nanolayer-coated surfaces are of interest not only theoretically but also in applications, since in many cases electrodes in electrical double layer capacitors are covered with nanolayers. The effect of discreteness of charges in the surface nanolayer on an electrical double layer around the surface is then discussed in Section 2.7. Finally, in Section 2.8, we consider the modified Poisson-Boltzmann equation by taking into account the effects of finite ion size.

2.2 Gouy-Chapman-Stern Model for Electrical Double Layer

The most widely used model for an electrical double layer around a charged entity is the Gouy-Chapman-Stern model [15–17] (Fig. 2.3). In this model the electrical double layer consists of two layers, that is, an internal Stern layer, where the finite size of ions is taken into account, and a Gouy-Chapman diffuse layer, in which ions are treated as point-charges and move freely, forming a diffuse layer. The Stern layer has two planes, that is, the inner Helmholtz plane (IHP) and the outer Helmholtz plane (OHP), as shown in Fig. 2.3. The IHP is a plane on which some ions may specifically be adsorbed (specific adsorption), and it passes through the centers of the specifically adsorbed ions on the solid surface. The OHP, which passes through the centers of solvated ions at the distance of their closest approach to the solid surface, is the onset of the Gouy-Chapman diffuse layer.

Consider a planar wall surface in contact with an electrolyte solution and take an x-axis perpendicular to the surface with its origin 0 at the wall surface. The Gouy-Chapman-Stern model involves the values of electric potential on three planes, that is, (i) $\psi_o = \psi(0)$ on the wall surface at $x = 0$ (0-plane), (ii) $\psi_\beta = \psi(\beta)$ on the IHP at $x = \beta$ (the IHP potential), and (iii) $\psi_d = \psi(d)$ on the OHP at $x = d$ (the OHP potential). The OHP is the onset of the diffuse double layer. Let the values of the relative permittivity in the following three regions, (i) $0 < x < \beta$, (ii) $\beta < x < d$, and (iii) $x > d$ (the electrolyte solution), be ε_1, ε_2, and ε_r, respectively. We also denote the density of the wall charges on the 0-plane by σ_o and the density of the charges due to adsorption of ions on the IHP from the electrolyte solution phase by σ_β. The model taking into account the specific ion adsorption on the IHP is called the triple-layer model [18]. We denote the density of the total charges on and just outside the wall consisting of the charges on the 0- and β-planes by $\sigma = \sigma_o + \sigma_\beta$. We call σ the surface charge density of the wall.

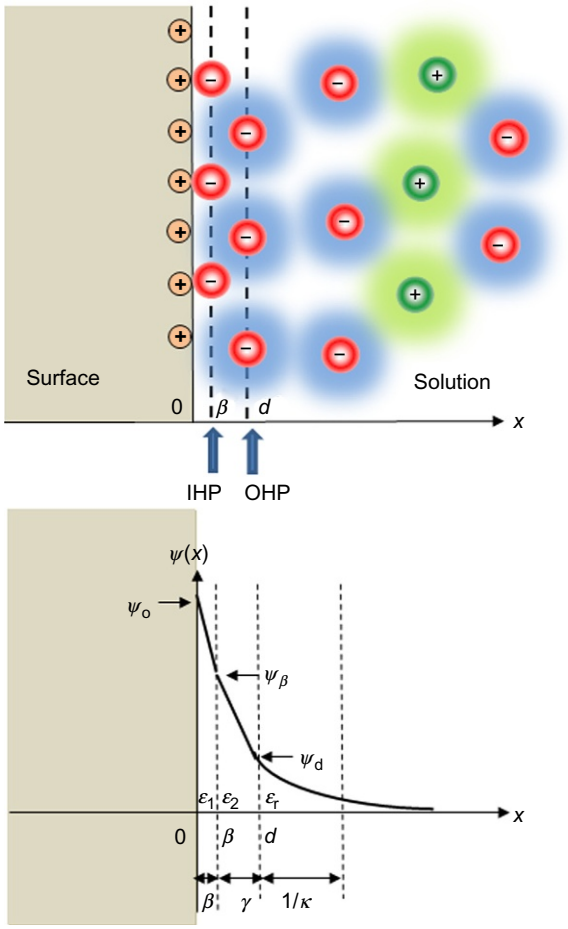

Fig. 2.3
Gouy-Chapman-Stern model for an electrical double layer. OHP is the outer Helmholtz plane and IHP is the inner Helmholtz plane.

The potential distribution $\psi(x)$ obeys the Laplace equation for the region between the 0-plane and the d-plane ($0 < x < d$) and the Poisson equation for the region $x > d$, namely:

$$\frac{d^2\psi}{dx^2} = 0, \quad 0 < x < d \tag{2.1}$$

$$\frac{d^2\psi}{dx^2} = -\frac{\rho_{el}(x)}{\varepsilon_r \varepsilon_0}, \quad x > d \tag{2.2}$$

where ε_o is the permittivity of a vacuum and $\rho_{el}(x)$ is the space charge density resulting from the electrolyte ions. The boundary conditions for Eqs. (2.1), (2.2) are

$$\psi(\beta^-) = \psi(\beta^+) = \psi_\beta \tag{2.3}$$

$$\psi(d^-) = \psi(d^+) = \psi_\mathrm{d} \tag{2.4}$$

$$\left.\frac{d\psi}{dx}\right|_{x=0^+} = -\frac{\sigma_o}{\varepsilon_1 \varepsilon_o} \tag{2.5}$$

$$\varepsilon_1 \left.\frac{d\psi}{dx}\right|_{x=\beta^-} - \varepsilon_2 \left.\frac{d\psi}{dx}\right|_{x=\beta^+} = \frac{\sigma_\beta}{\varepsilon_o} \tag{2.6}$$

$$\varepsilon_2 \left.\frac{d\psi}{dx}\right|_{x=d^-} - \varepsilon_\mathrm{r} \left.\frac{d\psi}{dx}\right|_{x=d^+} = 0 \tag{2.7}$$

$$\psi(x) \to 0 \quad \text{and} \quad \frac{d\psi}{dx} \to 0 \quad \text{as} \quad x \to \infty \tag{2.8}$$

Equation (2.5) implies that it is assumed that there is no electric field within the wall. By solving Eq. (2.1) subject to Eqs. (2.3), (2.4), we find that the potential distribution $\psi(x)$ for $0 < x < \beta$ and that for $\beta < x < d$ are given by

$$\psi(x) = \psi_\mathrm{o} + \frac{\psi_\beta - \psi_\mathrm{o}}{\beta} x, \quad 0 < x < \beta \tag{2.9}$$

$$\psi(x) = \psi_\beta + \frac{\psi_\mathrm{d} - \psi_\beta}{\gamma} (x - \beta), \quad \beta < x < d \tag{2.10}$$

with $\gamma = d - \beta$. Eqs. (2.9), (2.10) show a linear potential drop in the regions $0 < x < \beta$ and $\beta < x < d$. By substituting Eqs. (2.9), (2.10) into Eqs. (2.5), (2.6), we obtain the following relationships among ψ_o, ψ_β, and ψ_d:

$$\psi_\mathrm{o} - \psi_\beta = \frac{\sigma_\mathrm{o}}{C_1} \tag{2.11}$$

$$\psi_\beta - \psi_\mathrm{d} = \frac{\sigma_\mathrm{o} + \sigma_\beta}{C_2} \tag{2.12}$$

Here C_1 is the capacitance per unit area of the first capacitor formed by the 0- and β-planes, and C_2 is the capacitance per unit area of the second capacitor formed by the β- and d-planes. They are given by

$$C_1 = \frac{\varepsilon_1 \varepsilon_\mathrm{o}}{\beta} \tag{2.13}$$

$$C_2 = \frac{\varepsilon_2 \varepsilon_\mathrm{o}}{\gamma} \tag{2.14}$$

We obtain the total charge amount σ_d contained in the electrical double layer per unit area, which is given by

$$\sigma_{\mathrm{d}} = \int_{d}^{\infty} \rho_{\mathrm{el}}(x)dx \tag{2.15}$$

By substituting Eq. (2.2), that is, $\rho_{\mathrm{el}}(x) = -\varepsilon_{\mathrm{r}}\varepsilon_{\mathrm{o}}\left(d^2\psi/dx^2\right)$, into Eq. (2.15) and using the second equation of Eq. (2.8), we obtain

$$\sigma_{\mathrm{d}} = -\varepsilon_{\mathrm{r}}\varepsilon_{\mathrm{o}}\int_{d}^{\infty}\frac{d^2\psi}{dx^2}dx = \varepsilon_{\mathrm{r}}\varepsilon_{\mathrm{o}}\left.\frac{d\psi}{dx}\right|_{x=d^+} \tag{2.16}$$

From Eqs. (2.5)–(2.7), (2.11), (2.12), (2.16), we find

$$\sigma_{\mathrm{o}} + \sigma_{\beta} + \sigma_{\mathrm{d}} = 0 \quad \text{or} \quad \sigma + \sigma_{\mathrm{d}} = 0 \tag{2.17}$$

This agrees with the electroneutrality condition for the whole system (the charged wall plus the electrolyte solution). It is also to be noted that Eq. (2.16) can be rewritten, by using Eq. (2.17), as

$$\left.\frac{d\psi}{dx}\right|_{x=d^+} = -\frac{\sigma}{\varepsilon_{\mathrm{r}}\varepsilon_{o}} \tag{2.18}$$

This is equivalent to the boundary condition for a wall located at $x = d$ carrying a surface charge density $\sigma = \sigma_{\mathrm{o}} + \sigma_{\beta}$. We use Eq. (2.18) as the boundary condition for the electrical double layer potential $\psi(x)$ for the Gouy-Chapman diffuse layer in the region $x > d$.

2.3 Electrical Double Layer Around a Planar Surface

In the Gouy-Chapman-Stern model, the electric potential $\psi(x)$ in the Gouy-Chapman diffuse layer ($x > d$) can be obtained by solving the Poisson-Boltzmann equation, which assumes that electrolyte ions behave like point charges. Let the electrolyte be composed of N ionic mobile ions of valence z_i and bulk concentration (number density) n_i^{∞} ($i = 1, 2, \ldots, N$), where

$$\sum_{i=1}^{N} z_i n_i^{\infty} = 0 \tag{2.19}$$

Since electroneutrality holds in the bulk solution phase. The space charge density resulting from the electrolyte ions $\rho_{\mathrm{el}}(x)$ is given by

$$\rho_{\mathrm{el}}(x) = \sum_{i=1}^{N} z_i e n_i(x) \tag{2.20}$$

where $n_i(x)$ is the concentrations of ith ions at position x and e is the elementary electric charge. We assume that the ion distribution is given by the Boltzmann distribution:

$$n_i(x) = n_i^{\infty} \exp\left(-\frac{z_i e\psi(x)}{kT}\right) \tag{2.21}$$

where k is Boltzmann's constant and T is the absolute temperature. Eq. (2.21) can be derived as follows. The electrochemical potential $\mu_i(x)$ of ith ion at position x is given by

$$\mu_i(x) = \mu_i^{\circ} + z_i e\psi(x) + kT \ln(n_i(x)) \tag{2.22}$$

where μ_i° is a constant. At equilibrium, $\mu_i(x)$ takes the same value as that in the bulk solution phase, where $\psi(x) = 0$, namely,

$$\mu_i(\infty) = \mu_i^{\circ} + kT \ln n_i^{\infty} \tag{2.23}$$

By equating $\mu_i(x) = \mu_i(\infty)$, we obtain Eq. (2.23) and thus Eq. (2.20) becomes

$$\rho_{\mathrm{el}}(x) = \sum_{i=1}^{N} z_i en \exp\left(-\frac{z_i e\psi(x)}{kT}\right) 1, \quad x > d \tag{2.24}$$

then Eq. (2.2) as combined with Eq. (2.24) becomes the following Poisson-Boltzmann equation:

$$\frac{d^2\psi}{dx^2} = -\frac{1}{\varepsilon_{\mathrm{r}}\varepsilon_{\mathrm{o}}} \sum_{i=1}^{N} z_i en \exp\left(-\frac{z_i e\psi(x)}{kT}\right), \quad x > d \tag{2.25}$$

For the low potential case, Eq. (2.25) can be linearized into

$$\frac{d^2\psi}{dx^2} = \kappa^2\psi(x), \quad x > d \tag{2.26}$$

where

$$\kappa = \left(\frac{1}{\varepsilon_{\mathrm{r}}\varepsilon_o kT} \sum_{i=1}^{N} z_i^2 e^2 n_i^{\infty}\right)^{1/2} \tag{2.27}$$

is the Debye-Hückel parameter. This approximation is called the Debye-Hückel linearization approximation. Eq. (2.26) subject to Eqs. (2.4), (2.8) can be solved to give

$$\psi(x) = \psi_{\mathrm{d}} e^{-\kappa(x-d)}, \quad x > d \tag{2.28}$$

The reciprocal of κ (i.e., $1/\kappa$), which is called the Debye length, corresponds to the thickness of the Gouy-Chapman diffuse layer, since $\psi(x)$ decays over the distances of the order of $1/\kappa$. The value of $1/\kappa$ depends on the valences and concentrations of ions. Fig. 2.4 shows the Debye length calculated via Eq. (2.27) for various electrolyte solutions. It follows from Eqs. (2.5), (2.28) that the surface charge density σ/the OHP potential ψ_{d} relationship is given by

$$\sigma = \varepsilon_{\mathrm{r}}\varepsilon_{\mathrm{o}}\kappa\psi_{\mathrm{d}} \tag{2.29}$$

or

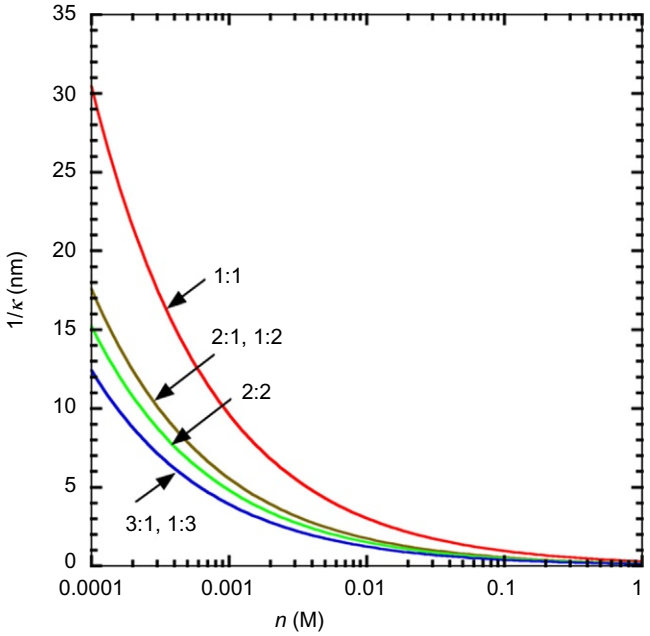

Fig. 2.4

The Debye length $1/\kappa$ for aqueous 1:1, 2:1 (or 1:2), 2:2, and 3:1 (or 1:3) electrolyte solutions as functions of electrolyte concentrations n (M) calculated at 298.15 K and $\varepsilon_r = 88.54$.

$$\psi_d = \frac{\sigma}{\varepsilon_r \varepsilon_o \kappa} \tag{2.30}$$

which gives the capacitance $C_d = \sigma/\psi_d$ of the Gouy-Chapman diffuse layer:

$$C_d = \varepsilon_r \varepsilon_o \kappa = \frac{\varepsilon_r \varepsilon_o}{\kappa^{-1}} \tag{2.31}$$

The capacitance C_d given by Eq. (2.31) is equivalent to the capacitance of a capacitor having the interelectrode distance equal to the Debye length $1/\kappa$. Also, in the absence of specific ion adsorption at the IHP ($\sigma_\beta = 0$ and thus $\sigma = \sigma_o$), it can be shown that the total capacitance of the electrical double layer $C = \sigma/\psi_o = \sigma_o/\psi_o$ is given by

$$\psi_o = \frac{\sigma}{C} \tag{2.32}$$

with

$$\frac{1}{C} = \frac{1}{C_1} + \frac{1}{C_2} + \frac{1}{C_d} \tag{2.33}$$

This means that the total electrical double layer capacitance C is given by C_1, C_2, and C_d connected in series.

Now we consider the case in which the wall surface is immersed in a z-z-type, symmetrical electrolyte solution of valence z and bulk concentration n. The Poisson-Boltzmann equation (2.25) reduces to

$$\frac{d^2\psi}{dx^2} = \frac{2zen}{\varepsilon_r\varepsilon_o}\sinh\left(\frac{ze\psi(x)}{kT}\right), \quad x > d \tag{2.34}$$

The nonlinear planar Poisson-Boltzmann equation (2.34) subject to Eq. (2.8) can be integrated by multiplying $d\psi/dx$ on both sides to give

$$\frac{d\psi}{dx} = -2\kappa\left(\frac{kT}{ze}\right)\sinh\left(\frac{ze\psi(x)}{2kT}\right), \quad x > d \tag{2.35}$$

Further integration of Eq. (2.35) yields

$$\psi(x) = \frac{kT}{ze}\ln\left[\frac{1+\gamma\exp(-\kappa(x-d))}{1-\gamma\exp(-\kappa(x-d))}\right], \quad x > d \tag{2.36}$$

with

$$\gamma = \tanh\left(\frac{ze\psi_d}{kT}\right) \tag{2.37}$$

and κ is the Debye-Hückel parameter of a z:z symmetrical electrolyte solution ($x > d$), defined by

$$\kappa = \left(\frac{2z^2ne^2}{\varepsilon_r\varepsilon_o kT}\right)^{1/2} \tag{2.38}$$

Note that the electrolyte concentration n in Eq. (2.38) is given in units of m^{-3}. If one uses the electrolyte concentration given in units of M, then C in Eq. (2.38) must be replaced by $1000\,N_A n$, where N_A is Avogadro's number. Fig. 2.5 shows some examples of the calculation of the electric potential $\psi(x)$ for an aqueous 1:1 monovalent electrolyte solution ($z = 1$) using Eq. (2.32) (solid lines) at 298.15 K and $\varepsilon_r = 78.55$ as a function of x-d measured from the OHP placed at $x = d$ for several values of the OHP potential ψ_d. Fig. 2.5 also gives the results obtained from the linearized Poisson-Boltzmann equation (2.28) as *dotted lines*, showing that the linearization approximation to the Poisson-Boltzmann equation always gives overestimation but the deviation becomes negligible for ψ_d lower than 50 mV. Fig. 2.6 shows an example of the calculation of the concentration of cations $n_+(x) = n\exp(-ze\psi(x)/kT)$ and that of anions $n_-(x) = n\exp(ze\psi(x)/kT)$ for an aqueous 1:1 monovalent electrolyte solution ($z = 1$, 298.15 K, and $\varepsilon_r = 78.55$) plotted as functions of the distance x-d measured from the OHP placed at $x = d$ at $C = 0.01$ M and $\psi_d = 50$ mV.

We can derive the relationship between the total surface charge density σ and the OHP potential ψ_d by evaluating the potential derivative $d\psi/dx$, which is given by Eq. (2.31), at $x = d$ and using Eq. (2.18), we obtain

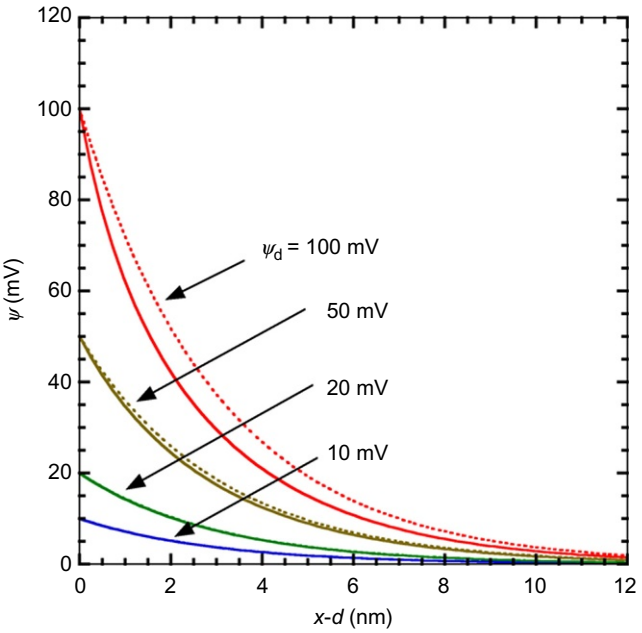

Fig. 2.5

Electric potential distribution $\psi(x)$ for an aqueous 1:1 monovalent electrolyte solution calculated using Eq. (2.36) (*solid lines*) at 298.15 K and $\varepsilon_r = 78.55$ as a function of x-d measured from the OHP at $x = d$ for several values of the OHP potential ψ_d. The *dotted lines* are the results obtained from the linearized Poisson-Boltzmann equation (2.28).

$$\sigma = \frac{2\varepsilon_r\varepsilon_o\kappa kT}{ze}\sinh\left(\frac{ze\psi_d}{2kT}\right) \tag{2.39}$$

or equivalently

$$\psi_d = \frac{2kT}{ze}\operatorname{arcsinh}\left(\frac{ze\sigma}{2\varepsilon_r\varepsilon_o\kappa kT}\right) \tag{2.40}$$

For the special case of low potentials ($|\psi_o| < 40$ mV for 1–1 electrolytes), Eqs. (2.39), (2.40) reduce to Eq. (2.29). Since Eqs. (2.35), (2.36) show that σ is not a linear function of ψ_d unlike Eqs. (2.30), (2.31), we derive the differential capacitance $C_d = d\sigma/d\psi_d$ with the result that

$$C_d = \varepsilon_r\varepsilon_o\kappa \cdot \cosh\left(\frac{ze\psi_d}{2kT}\right) \tag{2.41}$$

Eqs. (2.36), (2.39)–(2.41) apply for the planar solid surface in contact with a z-z symmetrical electrolyte solution. We now consider the potential distribution $\psi(x)$ and the σ/ψ_d relationship for the case where the planar wall is in contact with asymmetrical electrolyte solutions.

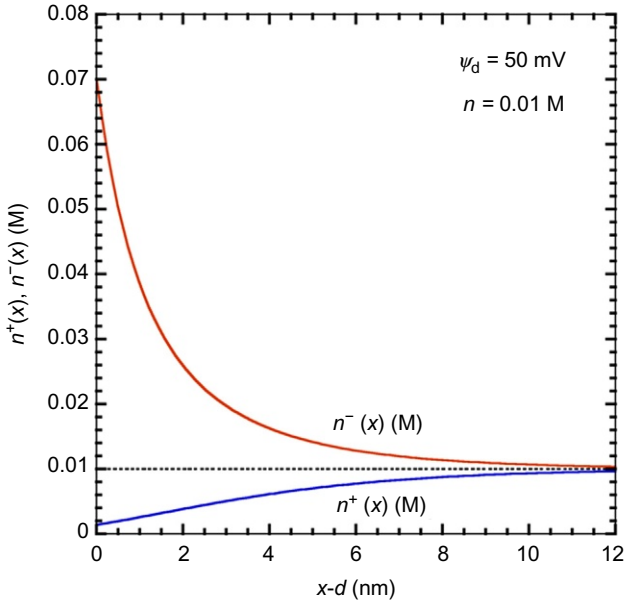

Fig. 2.6

The concentration of cations $n_+(x) = n\exp(-ze\psi(x)/kT)$ and that of anions $n_-(x) = n\exp(ze\psi(x)/kT)$ for an aqueous 1:1 monovalent electrolyte solution ($z = 1$, 298.15 K, and $\varepsilon_r = 78.55$) plotted as functions of the distance x-d measured from the OHP placed at $x = d$ at $n = 0.01$ M and $\psi_d = 50$ mV.

For 2-1 electrolytes, the Poisson-Boltzmann equation is given by

$$\frac{d^2\psi}{dx^2} = -\frac{en}{\varepsilon_r\varepsilon_o}\left[\exp\left(-\frac{2e\psi(x)}{kT}\right) - \exp\left(\frac{e\psi(x)}{kT}\right)\right] \tag{2.42}$$

which is solved to give the following expressions for the potential distribution $\psi(x)$, the relationship between the surface charge density σ and the OHP potential ψ_d, and the differential capacitance C_d:

$$\psi(x) = \frac{kT}{e}\ln\left[\frac{3}{2}\left\{\frac{1+(2/3)\gamma'\exp(-\kappa(x-d))}{1-(2/3)\gamma'\exp(-\kappa(x-d))}\right\}^2 - \frac{1}{2}\right], \quad x > d \tag{2.43}$$

$$\sigma = \frac{\varepsilon_r\varepsilon_o\kappa kT}{e}\left[1-\exp\left(-\frac{e\psi_d}{kT}\right)\right]\left[\frac{2}{3}\exp\left(\frac{e\psi_d}{kT}\right)+\frac{1}{3}\right]^{1/2} \tag{2.44}$$

$$C_d = \frac{\varepsilon_r\varepsilon_o\kappa}{3}\left[1+\exp\left(\frac{e\psi_d}{kT}\right)+\exp\left(-\frac{e\psi_d}{kT}\right)\right]\left[\frac{2}{3}\exp\left(\frac{e\psi_d}{kT}\right)+\frac{1}{3}\right]^{-1/2} \tag{2.45}$$

with

$$\gamma' = \frac{3}{2}\left\{\frac{\sqrt{2\exp(e\psi_d/kT)/3 + 1/3} - 1}{\sqrt{2\exp(e\psi_d/kT)/3 + 1/3} + 1}\right\} \tag{2.46}$$

$$\kappa = \left(\frac{6ne^2}{\varepsilon_r\varepsilon_o kT}\right)^{1/2} \tag{2.47}$$

In the case of a mixed solution of 1-1 electrolyte of concentration n_1 and 2-1 electrolyte of concentration n_2, we have

$$\frac{d^2\psi}{dx^2} = -\frac{e}{\varepsilon_r\varepsilon_o}\left[n_1\exp\left(-\frac{e\psi(x)}{kT}\right) + n_2\exp\left(-\frac{2e\psi(x)}{kT}\right) - (n_1 + n_2)\exp\left(\frac{e\psi(x)}{k_BT}\right)\right] \tag{2.48}$$

Eq. (2.48) yields

$$\psi(x) = \frac{k_BT}{e}\ln\left[\frac{1}{1-\eta/3}\left\{\frac{1 + (1-\eta/3)\gamma''\exp(-\kappa(x-d))}{1 - (1-\eta/3)\gamma''\exp(-\kappa(x-d))}\right\}^2 - \frac{\eta/3}{1-\eta/3}\right] \quad x > d \tag{2.49}$$

$$\sigma = \frac{\varepsilon_r\varepsilon_o\kappa k_BT}{e}\left[1 - \exp\left(-\frac{e\psi_d}{kT}\right)\right]\left[\left(1 - \frac{\eta}{3}\right)\exp\left(\frac{e\psi_d}{kT}\right) + \frac{\eta}{3}\right]^{1/2} \tag{2.50}$$

$$C_d = \frac{\varepsilon_r\varepsilon_o\kappa}{2}\left[\left(1 - \frac{\eta}{3}\right)\left\{1 + \exp\left(\frac{e\psi_d}{kT}\right)\right\} + \frac{2\eta}{3}\exp\left(-\frac{e\psi_d}{kT}\right)\right] \times \left[\left(1 - \frac{\eta}{3}\right)\exp\left(\frac{e\psi_d}{kT}\right) + \frac{\eta}{3}\right]^{-1/2} \tag{2.51}$$

where

$$\gamma'' = \frac{1}{(1-\eta/3)}\left\{\frac{\sqrt{(1-\eta/3)\exp(e\psi_d/kT) + \eta/3} - 1}{\sqrt{(1-\eta/3)\exp(e\psi_d/kT) + \eta/3} + 1}\right\} \tag{2.52}$$

$$\kappa = \left[\frac{2(n_1 + 3n_2)e^2}{\varepsilon_r\varepsilon_o kT}\right]^{1/2} \tag{2.53}$$

$$\eta = \frac{3n_2}{n_1 + n_2} \tag{2.54}$$

2.4 Electrical Double Layer Around Spherical and Cylindrical Surfaces

2.4.1 Spherical Surface

The Poisson-Boltzmann equation for a planar surface can be solved exactly. The spherical Poisson-Boltzmann equation, however, has not been solved analytically except when the Debye-Hückel linearization for small potentials is allowed. In this section we derive approximate analytic expressions for the potential distribution in the Gouy-Chapman diffuse

layer around the surface of a sphere of radius a and the surface charge density σ and the OHP potential ψ_d. Since the distance d between the sphere surface and the OHP is very small compared with sphere radius a, we may assume the OHP is located at the sphere surface.

Consider the potential distribution $\psi(r)$ around a spherical particle of radius a carrying a surface charge density σ immersed in a symmetrical electrolyte solution of valence z and bulk concentration n. We take a spherical polar coordinate with its origin 0 at the center of the particle (Fig. 2.7). The potential distribution $\psi(r)$ in the Gouy-Chapman diffuse layer obeys the spherical Poisson-Boltzmann equation for the region $r > a$,

$$\frac{d^2\psi}{dr^2} + \frac{2}{r}\frac{d\psi}{dr} = \frac{2zen}{\varepsilon_r\varepsilon_o}\sinh\left(\frac{ze\psi}{kT}\right), \quad r > a \tag{2.55}$$

subject to boundary conditions

$$\left.\frac{d\psi}{dr}\right|_{r=a^+} = -\frac{\sigma}{\varepsilon_r\varepsilon_o} \tag{2.56}$$

$$\psi(r) \to 0 \quad \text{and} \quad \frac{d\psi}{dr} \to 0 \quad \text{as} \quad r \to \infty \tag{2.57}$$

Loeb, Overbeek, and Wiersema [19] tabulated numerical computer solutions to the nonlinear spherical Poisson-Boltzmann equation (2.55). The following accurate analytic approximate expression for $\psi(r)$ has been derived [20,21]:

$$\psi(r) = \frac{2kT}{ze}\ln\left[\frac{(1+Bs)\left(1+\dfrac{Bs}{2\kappa a+1}\right)}{(1-Bs)\left(1-\dfrac{Bs}{2\kappa a+1}\right)}\right] \tag{2.58}$$

with

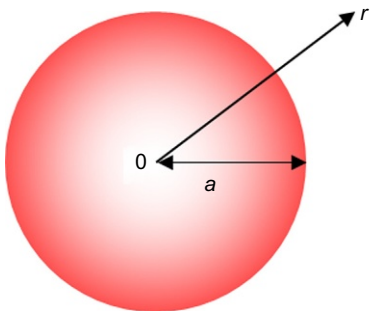

Fig. 2.7
A spherical particle of radius a.

$$s = \frac{a}{r}\exp(-\kappa(r-a)) \tag{2.59}$$

$$B = \frac{\left(\frac{2\kappa a+1}{\kappa a+1}\right)\tanh\left(\frac{ze\psi_d}{4kT}\right)}{1+\left\{1-\frac{2\kappa a+1}{(\kappa a+1)^2}\tanh^2\left(\frac{ze\psi_d}{4kT}\right)\right\}^{1/2}} \tag{2.60}$$

As for the σ/ψ_d relationship, the following first-order approximate expression derived [20,21] is

$$\sigma = \frac{2\varepsilon_r\varepsilon_o\kappa kT}{ze}\left[\sinh\left(\frac{ze\psi_d}{2kT}\right)+\frac{2}{\kappa a}\tanh\left(\frac{ze\psi_d}{2kT}\right)\right] \tag{2.61}$$

where κ is given by Eq. (2.38). The maximum error of Eq. (2.61) is about 20%. A more accurate σ/ψ_d relationship has been derived [20,21]. The result is

$$\sigma = \frac{2\varepsilon\varepsilon_o\kappa kT}{e}\sinh\left(\frac{e\psi_d}{2kT}\right)\times\left[1+\frac{1}{\kappa a}\frac{2}{\cosh^2(e\psi_d/4kT)}+\frac{1}{(\kappa a)^2}\frac{8\ln[\cosh(e\psi_d/4kT)]}{\sinh^2(e\psi_d/2kT)}\right]^{1/2} \tag{2.62}$$

which is the second-order σ/ψ_d relationship [20,21]. Eq. (2.62) is in excellent agreement with the exact computer results with the relative error $<1\%$ for $0.5 \le \kappa a \le \infty$.

The present approximation method can be applied also to the case of a sphere in a 2-1 symmetrical solution, yielding

$$\sigma = \frac{\varepsilon\varepsilon_o\kappa kT}{e}pq\left[1+\frac{2}{\kappa a}\frac{(3-p)q-3}{(pq)^2}\right] \tag{2.63}$$

as the first-order σ/ψ_d relationship and

$$\sigma = \frac{\varepsilon_r\varepsilon_o\kappa kT}{e}pq\left[1+\frac{4}{\kappa a}\frac{(3-p)q-3}{(pq)^2}+\frac{4}{(\kappa a)^2(pq)^2}\left\{6\ln\left(\frac{q+1}{2}\right)+\ln(1-p)\right\}\right]^{1/2} \tag{2.64}$$

as the second-order σ/ψ_d relationship, where κ is given by Eq. (2.47) and

$$p = 1-\exp(-e\psi_d/kT) \tag{2.65}$$

$$q = \left[\frac{2}{3}\exp\left(\frac{e\psi_d}{kT}\right)+\frac{1}{3}\right]^{1/2} \tag{2.66}$$

Exact numerical computer solution is also available in Ref. [19]. The relative error of Eq. (2.64) is found to be less than 1% for $0.5 \le \kappa a \le \infty$.

Similarly, for a sphere in a mixed solution of 1:1 electrolyte of concentration n_1 and 2:1 electrolyte of concentration n_2, in which case exact computer solutions are not available, the first-order σ_d/ψ_d relationship is given by

$$\sigma = -\frac{\varepsilon_r \varepsilon_o \kappa kT}{e}\left[pt + \frac{2}{\kappa a' pt}\left\{(3-p)t - 3 - \frac{3^{1/2}(1-\eta)}{2\eta^{1/2}} \times \ln\left(\frac{\left\{1+(\eta/3)^{1/2}\right\}\left\{t-(\eta/3)^{1/2}\right\}}{\left\{1-(\eta/3)^{1/2}\right\}\left\{t+(\eta/3)^{1/2}\right\}}\right)\right\}\right] \tag{2.67}$$

with

$$t = \left[\left(1-\frac{\eta}{3}\right)\exp\left(\frac{e\psi_d}{kT}\right) + \frac{\eta}{3}\right]^{1/2} \tag{2.68}$$

$$\eta = \frac{3n_2}{n_1 + 3n_2} \tag{2.69}$$

where κ is the Debye-Hückel parameter for a mixed solution of 2-1 and 1-1 electrolytes (Eq. 2.53) and p is given by Eq. (2.65).

For low potentials, Eq. (2.58) reduces to

$$\psi(r) = \psi_d \frac{a}{r} e^{-\kappa(r-a)} \tag{2.70}$$

and Eqs. (2.61)–(2.64), (2.67) all reduce to

$$\sigma = \varepsilon_r \varepsilon_o \kappa \psi_d \left(1 + \frac{1}{\kappa a}\right) \tag{2.71}$$

which holds irrespective of the type of electrolyte.

2.4.2 Cylindrical Surface

Now we consider an electrical double layer around a cylindrical particle of radius a carrying a surface charge density σ immersed in a symmetrical electrolyte solution of valence z and bulk concentration n (Fig. 2.8) [22].

$$\frac{d^2\psi}{dr^2} + \frac{1}{r}\frac{d\psi}{dr} = \frac{2zen}{\varepsilon_r \varepsilon_o}\sinh\left(\frac{ze\psi}{kT}\right), \quad r > a \tag{2.72}$$

The following approximate expressions for the potential distribution $y(r)$ have been derived [22]:

$$\psi(r) = \frac{2kT}{ze} \ln\left[\frac{(1+Dc)\left\{1+\left(\frac{1-\beta}{1+\beta}\right)Dc\right\}}{(1-Dc)\left\{1-\left(\frac{1-\beta}{1+\beta}\right)Dc\right\}}\right] \tag{2.73}$$

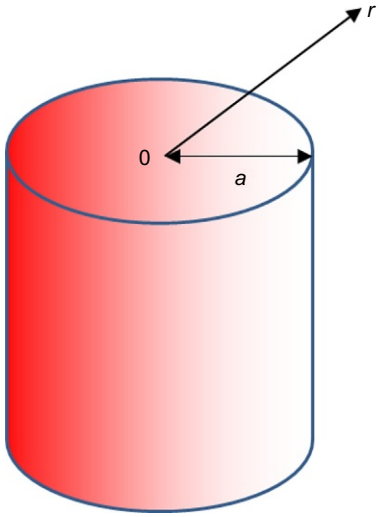

Fig. 2.8
A cylindrical particle of radius *a*.

with

$$D = \frac{(1+\beta)\tanh\left(\frac{ze\psi_o}{4kT}\right)}{1+\left\{1-(1-\beta^2)\tanh^2\left(\frac{ze\psi_o}{4kT}\right)\right\}^{1/2}} \tag{2.74}$$

$$\beta = \frac{K_0(\kappa a)}{K_1(\kappa a)} \tag{2.75}$$

where $K_n(z)$ is the modified Bessel function of the second kind of order n.

Approximate analytic expressions for the σ/ψ_d relationship have also been derived [22]. For a cylinder in a z:z electrolyte of concentration n,

$$\sigma = \frac{2\varepsilon_r\varepsilon_o\kappa kT}{ze}\sinh\left(\frac{ze\psi_o}{2kT}\right)\left[1+\left\{\left(\frac{K_1(\kappa a)}{K_0(\kappa a)}\right)^2-1\right\}\frac{1}{\cosh^2(ze\psi_d/4kT)}\right]^{1/2} \tag{2.76}$$

where κ is given by Eq. (2.38). For a spherical particle in a 2:1 electrolyte of concentration n,

$$\sigma = \frac{\varepsilon_r\varepsilon_o\kappa kT}{e}pq\left[1+2\left\{\left(\frac{K_1(\kappa a)}{K_0(\kappa a)}\right)^2-1\right\}\frac{(3-p)q-3}{(pq)^2}\right]^{1/2} \tag{2.77}$$

where κ, p, and q are, respectively, given by Eqs. (2.47), (2.65), (2.66). For a cylindrical particle in a mixed solution of 1:1 electrolyte of concentration n_1 and 2:1 electrolyte of concentration n_2,

$$\sigma = \frac{\varepsilon_r \varepsilon_o \kappa kT}{e} pt \left[1 + \frac{2}{(pt)^2} \left\{ \left(\frac{K_1(\kappa a)}{K_0(\kappa a)} \right)^2 - 1 \right\} \times \left\{ (3-p)t - 3 - \frac{3^{1/2}(1-\eta)}{2\eta^{1/2}} \ln \left(\frac{\left\{ 1 + (\eta/3)^{1/2} t - (\eta/3)^{1/2} \right\}}{\left\{ 1 - (\eta/3)^{1/2} t + (\eta/3)^{1/2} \right\}} \right) \right\} \right]^{1/2} \tag{2.78}$$

where κ, p, and t are, respectively, given by Eqs. (2.53), (2.65), (2.68).

For low potentials, Eq. (2.73) reduces to

$$\psi(r) = \psi_o \frac{K_0(\kappa r)}{K_0(\kappa a)} \tag{2.79}$$

and Eqs. (2.76)–(2.78) all reduce to

$$\sigma = \varepsilon_r \varepsilon_o \kappa \psi_d \frac{K_1(\kappa a)}{K_0(\kappa a)} \tag{2.80}$$

2.5 Electrical Double Layer Across a Nanolayer of Porous Material

In this section we consider the electric double layer potential distribution in a charged cylindrical narrow pore [23,24]. This problem is important especially in applications, since the large surface area of highly porous activated carbon electrodes is used for electrical double layer capacitors, in which a porous nanolayer is modeled as a sheet with an array of ordered cylindrical pores, as shown in Fig. 2.9 [25–27].

Consider a charged cylindrical narrow pore of radius a filled with an electrolyte solution (Fig. 2.10), which is connected to an external bulk symmetrical electrolyte solution of valence z and concentration n. We treat the case where the pore space can be considered to be an infinitely long cylinder so that end effects may be neglected. We take a radial cylindrical coordinate r measured from its origin 0 on the cylinder axis. We assume that the electric potential $\psi(r)$ obeys the cylindrical Poisson-Boltzmann equation, namely,

$$\frac{d^2\psi}{dr^2} + \frac{1}{r}\frac{d\psi}{dr} = \frac{2zen}{\varepsilon_r \varepsilon_o} \sinh\left(\frac{ze\psi}{kT} \right) \tag{2.81}$$

where ε_r is the relative permittivity of the electrolyte solution. Eq. (2.81) is subject to the following boundary conditions:

$$\psi(a) = \psi_d \tag{2.82}$$

$$\left. \frac{d\psi}{dr} \right|_{r=0} = 0 \tag{2.83}$$

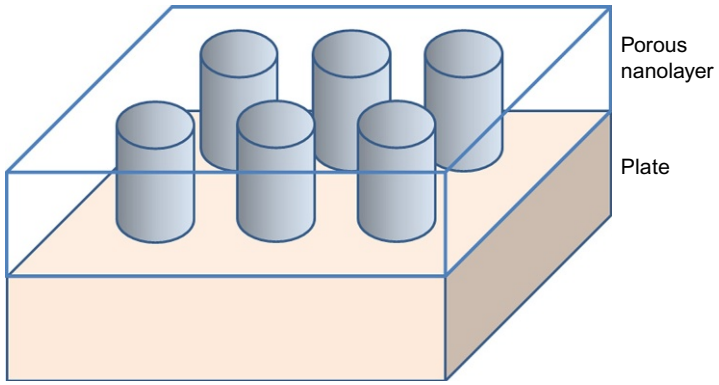

Fig. 2.9
A planar substrate covered with a nanolayer of porous material, which is modeled as a sheet with an array of ordered cylindrical pores.

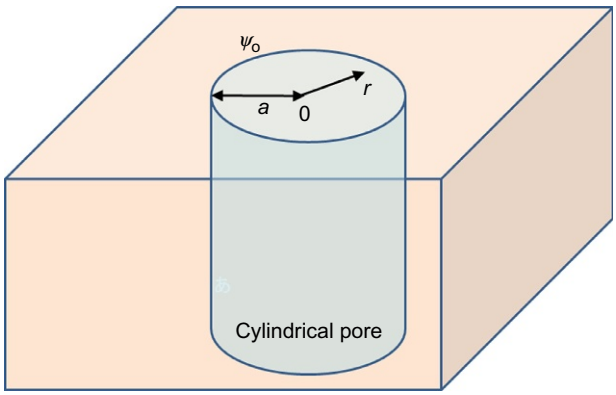

Fig. 2.10
Schematic representation of a cylindrical narrow pore of radius a carrying the OHP potential ψ_d filled with an electrolyte solution.

Here ψ_d is the pore OHP potential and Eq. (2.83) is derived from the symmetry of the system. The OHP potential ψ_d is further related to the pore surface charge density σ by

$$\left.\frac{d\psi}{dr}\right|_{r=a^-} = \frac{\sigma}{\varepsilon_r \varepsilon_o} \tag{2.84}$$

Here we have assumed that the OHP is located at the pore surface at $r = a$. If we introduce the scaled potential $y(r) = ze\psi(r)/kT$, then Eq. (2.81) becomes

$$\frac{d^2y}{dr^2} + \frac{1}{r}\frac{dy}{dr} = \kappa^2 \sinh y \tag{2.85}$$

where $\kappa = \sqrt{2z^2e^2n/\varepsilon_r\varepsilon_o kT}$ is the Debye-Hückel parameter. The potential distribution $y(r)$ in a cylindrical pore is given by the solution to the cylindrical Poisson-Boltzmann equation (2.85). An example of the numerical solution $y(r)$ for $y_d = 1$ and $\kappa a = 1$ is shown in Fig. 2.11.

Now in order to obtain an approximate analytic solution to Eq. (2.85), we put

$$y(r) = y_m + \Delta y(r) \tag{2.86}$$

where $y_m = y(0)$ is the scaled potential $y(0) = ze\psi(0)/kT$ at the cylinder axis, and we consider Δy to be the small quantity. This treatment holds good when the pore radius a is less than the Debye length $1/\kappa$, i.e., $\kappa a \leq 1$. Then on the right-hand side of Eq. (2.85) we have that

$$\sinh y = \sinh(y_m + \Delta y) \approx \sinh y_m + \cosh y_m \cdot \Delta y = \cosh y_m \cdot (\Delta y + \tanh y_m) \tag{2.87}$$

Thus Eq. (2.85) reduces to the following equation linearized with respect to Δy

$$\frac{d^2\Delta y}{dr^2} + \frac{1}{r}\frac{d\Delta y}{dr} = \kappa^2 \cosh y_m \cdot (\Delta y + \tanh y_m) \tag{2.88}$$

which can easily be solved subject to Eqs. (2.82), (2.83) so that we finally obtain

$$y(r) = y_o - (y_o - y_m + \tanh y_m) \cdot \left\{1 - \frac{I_0(\sqrt{\cosh y_m} \cdot \kappa r)}{I_0(\sqrt{\cosh y_m} \cdot \kappa a)}\right\} \tag{2.89}$$

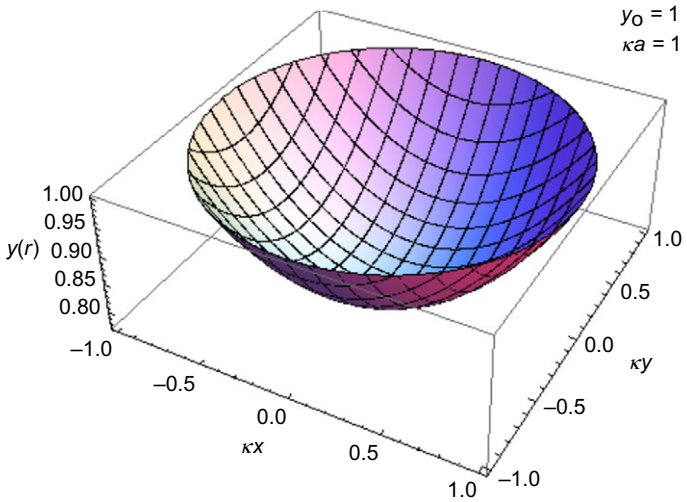

Fig. 2.11

Scaled electric potential distribution $y(r)$ in a cylindrical pore as a function of $\kappa r = \kappa\sqrt{x^2 + y^2}$ calculated for $y_d = 1$ and $\kappa a = 1$. *From Ref. H. Ohshima, A simple algorithm for the calculation of the electric double layer potential distribution in a charged cylindrical narrow pore, Colloid Polym. Sci. 294 (2016) 1871–1875.*

Here $I_0(z)$ is the zeroth-order modified Bessel function of the first kind. Eq. (2.91) involves an unknown quantity y_m. We obtain the value of y_m and thus the potential distribution $y(r)$ by iteration approximation. As the zero-order solution, we put

$$y_m^{(0)} = y_o \tag{2.90}$$

Then Eq. (2.89) gives

$$y^{(0)}(r) = y_o - \tanh y_o \cdot \left\{ 1 - \frac{I_0(\sqrt{\cosh y_o} \cdot \kappa r)}{I_0(\sqrt{\cosh y_o} \cdot \kappa a)} \right\} \tag{2.91}$$

Eq. (14) was first derived by Martynov and Avdeev [23].

The first-order solution is obtained by putting

$$y_m^{(1)} = y^{(0)}(0) = y_o - \tanh y_o \cdot \left\{ 1 - \frac{1}{I_0(\sqrt{\cosh y_o} \cdot \kappa a)} \right\} \tag{2.92}$$

and thus we have the first-order approximation for $y(r)$ from Eq. (2.89), namely,

$$y^{(1)}(r) = y_o - \left(y_o - y_m^{(1)} + \tanh y_m^{(1)} \right) \cdot \left\{ 1 - \frac{I_0\left(\sqrt{\cosh y_m^{(1)}} \cdot \kappa r \right)}{I_0\left(\sqrt{\cosh y_m^{(1)}} \cdot \kappa a \right)} \right\} \tag{2.93}$$

In a similar manner, higher-order approximate expressions $y_m^{(n)}$ and $y^{(n)}(r)$ for y_m and $y(r)$ can be derived. Fig. 2.12 show some example of the calculation of $y(r)$ on the basis of the zeroth-order approximation derived by Martynov and Avdeev [23] (Eq. 2.91) in comparison with the exact numerical results (given by filled circles). It is seen that the zeroth-order approximation is in excellent agreement with the exact results for $\kappa a = 0.1$.

One can also derive the zeroth-order and first-order approximations for the relationship between the surface charge density σ and the OHP potential ψ_d (or the scaled OHP potential $y_d = ze\psi_d/kT$) from Eqs. (2.91), (2.93), respectively, as combined with Eq. (2.94), namely,

$$\sigma^{(0)} = \frac{\varepsilon_r \varepsilon_o \kappa kT}{ze} \sqrt{\cosh y_o} \cdot \tanh y_o \cdot \frac{I_1(\sqrt{\cosh y_o} \cdot \kappa a)}{I_0(\sqrt{\cosh y_o} \cdot \kappa a)} \tag{2.94}$$

$$\sigma^{(1)} = \frac{\varepsilon_r \varepsilon_o \kappa kT}{ze} \sqrt{\cosh y_m^{(1)}} \cdot \left(y_o - y_m^{(1)} + \tanh y_m^{(1)} \right) \cdot \frac{I_1\left(\sqrt{\cosh y_m^{(1)}} \cdot \kappa a \right)}{I_0\left(\sqrt{\cosh y_m^{(1)}} \cdot \kappa a \right)} \tag{2.95}$$

where $I_1(z)$ is the second-order modified Bessel function of the first kind.

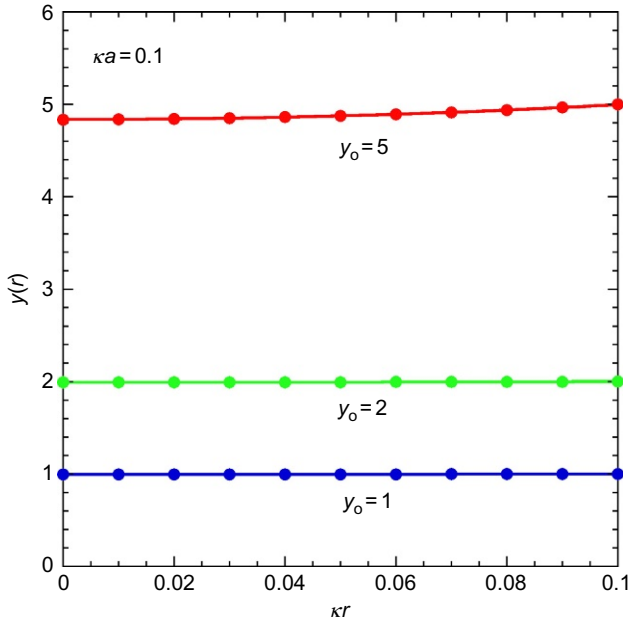

Fig. 2.12

Scaled electric potential distribution $y(r) = ze\psi(r)/kT$ as a function of κr calculated with the zeroth-order approximation (*solid lines*, Eq. (2.91), Martynov and Avdeev [23]) in comparison with the exact numerical solution (*filled circles*) to Eq. (2.81) calculated at $\kappa a = 0.1$ for several values of y_d. *From Ref. H. Ohshima, A simple algorithm for the calculation of the electric double layer potential distribution in a charged cylindrical narrow pore, Colloid Polym. Sci. 294 (2016) 1871–1875.*

For the low surface potential limit, Eqs. (2.91)–(2.93) reduce to

$$y(r) = y_o \cdot \frac{I_0(\kappa r)}{I_0(\kappa a)} \tag{2.96}$$

and Eqs. (2.94), (2.95) to

$$\sigma = \frac{\varepsilon_r \varepsilon_o \kappa kT}{ze} y_o \cdot \frac{I_1(\kappa a)}{I_0(\kappa a)} = \varepsilon_r \varepsilon_o \kappa \psi_o \cdot \frac{I_1(\kappa a)}{I_0(\kappa a)} \tag{2.97}$$

We can further derive the corresponding expressions for the differential electric double layer capacitance $C_d = d\sigma/d\psi_o$ (or $d\sigma/dy_o$) for a narrow cylindrical pore from Eqs. (2.94)–(2.95). The result for $d\sigma^{(0)}/dy_o$ is explicitly given here:

$$C_d = \varepsilon_r \varepsilon_o \kappa \left[\frac{1}{\cosh^{3/2} y_o} \cdot \frac{I_1(\sqrt{\cosh y_o} \cdot \kappa a)}{I_0(\sqrt{\cosh y_o} \cdot \kappa a)} + \frac{\kappa a}{2} \cdot \frac{\sinh^2 y_o}{\cosh y_o} \left\{ 1 - \left(\frac{I_1(\sqrt{\cosh y_o} \cdot \kappa a)}{I_0(\sqrt{\cosh y_o} \cdot \kappa a)} \right)^2 \right\} \right] \tag{2.98}$$

For the low potential case, Eq. (2.98) reduces to

$$C_{\mathrm{d}} = \varepsilon_{\mathrm{r}}\varepsilon_{\mathrm{o}}\kappa\frac{I_1(\kappa a)}{I_0(\kappa a)} \tag{2.99}$$

2.6 Electrical Double Layer Across a Nanolayer of Polyelectrolytes

In this section, we consider a charged planar plate covered with a surface nanolayer of polyelectrolytes. Polyelectrolyte-coated surfaces or particles are often called soft surfaces or particles, which can be a model for biocolloids and biointerfaces [9,11,28–49].

Consider a surface nanolayer (or, simply, a surface layer) of thickness d coating a planar hard plate in a symmetrical electrolyte solution of valence z and bulk concentration (number density) n (Fig. 2.13). We suppose that fully ionized groups of valence Z are distributed at a uniform density of N in the surface layer and the plate core surface is charged with a surface charge density σ. We take an x-axis perpendicular to the surface nanolayer with its origin $x=0$ at the boundary between the surface nanolayer and the surrounding electrolyte solution so that the surface nanolayer corresponds to the region $-d<x<0$ and the electrolyte solution to $x>0$ (Fig. 2.14).

The charge density $\rho_{\mathrm{el}}(x)$ resulting from the mobile charged ionic species is related to the electric potential $\psi(x)$ by the Poisson equation

$$\frac{d^2\psi}{dx^2} = -\frac{\rho_{\mathrm{el}}(x)}{\varepsilon_{\mathrm{r}}\varepsilon_{\mathrm{o}}}, \quad 0<x<+\infty \tag{2.100}$$

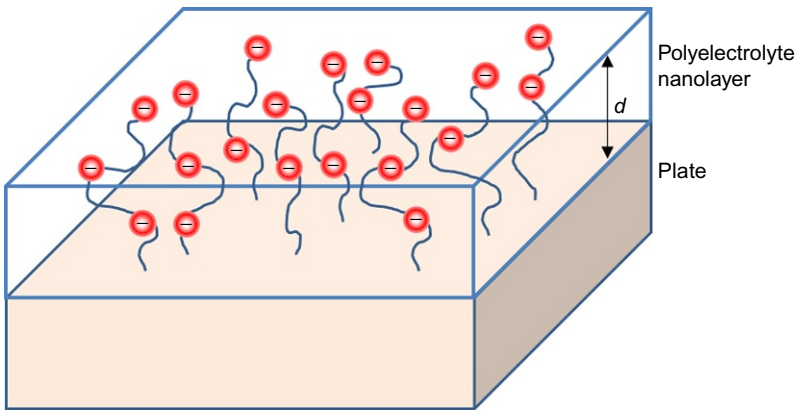

Fig. 2.13
A hard substrate covered with an ion-penetrable surface nanolayer of polyelectrolytes of thickness d.

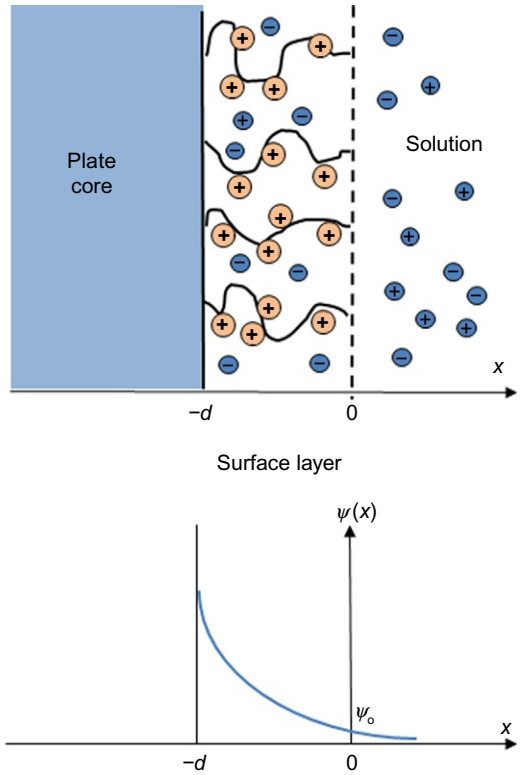

Fig. 2.14
Ion and potential distributions around a polyelectrolyte-coated plate. Potential distribution $\psi(x)$ across a surface layer of thickness d coating a solid surface.

$$\frac{d^2\psi}{dx^2} = -\frac{\rho_{\mathrm{el}}(x) + \rho_{\mathrm{fix}}}{\varepsilon_{\mathrm{r}}\varepsilon_{\mathrm{o}}}, \quad -d < x < 0 \tag{2.101}$$

with

$$\rho_{\mathrm{fix}} = ZeN \tag{2.102}$$

where ε_{r} is the relative permittivity of the solution. Here we have assumed that the relative permittivity in the region within the surface layer takes the same value as that in the bulk electrolyte solution phase. Note that the right-hand side of Eq. (2.101) contains the contribution of the fixed charges of density $\rho_{\mathrm{fix}} = ZeN$ in the polyelectrolyte layer. We assume that the distribution of electrolyte ions obeys Boltzmann's law. Then, the concentrations of cations, $n_+(x)$ and that of anions, $n_-(x)$ are given by

$$n_{\pm}(x) = n\exp\left(\mp\frac{ze\psi(x)}{kT}\right) \tag{2.103}$$

and thus

$$\rho_{el}(x) = ze\{n_+(x) - n_+(x)\} = 2zen \sinh\left(\frac{ze\psi}{kT}\right) \tag{2.104}$$

The potential $\psi(x)$ at position x in the regions $x > 0$ and $-d < x < 0$ thus satisfies the following Poisson-Boltzmann equations:

$$\frac{d^2\psi}{dx^2} = \frac{2zen}{\varepsilon_r\varepsilon_o} \sinh\left(\frac{ze\psi}{kT}\right), \quad x > 0 \tag{2.105}$$

$$\frac{d^2\psi}{dx^2} = \frac{2zen}{\varepsilon_r\varepsilon_o} \sinh\left(\frac{ze\psi}{kT}\right) - \frac{ZeN}{\varepsilon_r\varepsilon_o}, \quad -d < x < 0 \tag{2.106}$$

Eq. (2.105) is the usual Poisson-Boltzmann equation whereas Eq. (2.106) contains an additional term $ZeN/\varepsilon_r\varepsilon_o$, which arises from the fixed charges $\rho_{fix} = ZeN$ in the surface layer.

As will be shown, the Donnan potential in a polyelectrolyte nanolayer plays an important role in determining the potential distribution across the surface nanolayer [9,11]. Donnan potential ψ_{DON} is obtained by setting the right-hand side of Eq. (2.106) to zero,

$$\sinh\left(\frac{ze\psi_{DON}}{kT}\right) = \left(\frac{ZN}{2zn}\right) \tag{2.107}$$

or equivalently

$$\psi_{DON} = \left(\frac{kT}{ze}\right) \text{arc sinh}\left(\frac{ZN}{2zn}\right) = \left(\frac{kT}{ze}\right) \ln\left[\frac{ZN}{2zn} + \left\{\left(\frac{ZN}{2zn}\right)^2 + 1\right\}^{1/2}\right] \tag{2.108}$$

Note that the Donnan potential ψ_{DON} does not depend on ε_r. Eq. (2.108) can also be obtained by equating the electrochemical potentials of ions deep inside the surface layer and those in the bulk electrolyte solution phase. When $|ZN/zn| \ll 1$, Eq. (2.108) gives the following linearized Donnan potential:

$$\psi_{DON} = \frac{ZNkT}{2z^2ne} = \frac{ZeN}{\varepsilon_r\varepsilon_o\kappa^2} \tag{2.109}$$

Eq. (2.106) may be rewritten in terms of the Donnan potential ψ_{DON}, namely,

$$\frac{d^2\psi}{dx^2} = \frac{2zen}{\varepsilon_r\varepsilon_o}\left\{\sinh\left(\frac{ze\psi}{kT}\right) - \sinh\left(\frac{ze\psi_{DON}}{kT}\right)\right\}, \quad -d < x < 0 \tag{2.110}$$

Also, we term $\psi_o \equiv \psi(0)$ (which is the potential at the boundary between the surface layer and the surrounding electrolyte solution) the surface potential of the polyelectrolyte layer.

The boundary conditions at $x = -d$ and $x = 0$ are

$$\psi(-d^-) = \psi(-d^+) \tag{2.111}$$

$$\psi(-0^-) = \psi(-0^+) \tag{2.112}$$

$$\left.\frac{d\psi}{dx}\right|_{x=-d^+} = -\frac{\sigma}{\varepsilon_r \varepsilon_o} \tag{2.113}$$

$$\left.\frac{d\psi}{dx}\right|_{x=-0^-} = \left.\frac{d\psi}{dx}\right|_{x=-0^+} \tag{2.114}$$

$$\psi(x) \to 0 \quad \text{as } x \to \infty \tag{2.115}$$

$$\frac{d\psi}{dx} \to 0 \quad \text{as } x \to \infty \tag{2.116}$$

Eq. (2.113) corresponds to the situation in which the plate surface is charged with a surface charge density σ and the electric field within the plate can be neglected. The solution to Eqs. (2.105), (2.106) (or Eq. (2.110) subject to the boundary conditions (2.111)–(2.116) completely determines the potential $\psi(x)$ in the present system.

Fig. 2.15 shows some examples of the calculation of the potential distribution using Eqs. (2.105), (2.106) for several values of the scaled surface charge density $Q = ze\sigma/\varepsilon_r \varepsilon_o \kappa kT$ (where $\kappa = \sqrt{2z^2 e^2 n/\varepsilon_r \varepsilon_o kT}$ is the Debye-Hückel parameter) and the scaled Donnan potential $y_{DON} = ze\ \psi_{DON}/kT$.

For the simple case where $\psi(x)$ is low, Eqs. (2.105), (2.106) can be linearized to become

$$\frac{d^2\psi}{dx^2} = \kappa^2 \psi, \quad x > 0 \tag{2.117}$$

$$\frac{d^2\psi}{dx^2} = \kappa^2 \left(\psi - \frac{ZNkT}{2z^2 ne}\right) \quad -d < x < 0 \tag{2.118}$$

The solution to Eqs. (2.117) and (2.118) subject to Eqs. (2.111)–(2.116) is given by

$$\psi(x) = \frac{ZeN}{2\varepsilon_r \varepsilon_o \kappa^2}\left(1 - e^{-2\kappa d}\right) e^{-\kappa x}, \quad x > 0 \tag{2.119}$$

$$\psi(x) = \frac{ZeN}{\varepsilon_r \varepsilon_o \kappa^2}\left\{1 - \frac{e^{\kappa x} + e^{-\kappa(x+2d)}}{2}\right\}, \quad -d < x < 0 \tag{2.120}$$

The surface potential $\psi_o \equiv \psi(0)$ and the potential at the particle core, $\psi_c = \psi(-d)$ are given by

$$\psi_o = \frac{\sigma}{\varepsilon_r \varepsilon_o \kappa} e^{-\kappa d} + \frac{ZeN}{2\varepsilon_r \varepsilon_o \kappa^2}\left(1 - e^{-2\kappa d}\right) \tag{2.121}$$

$$\psi_c = \frac{\sigma}{\varepsilon_r \varepsilon_o \kappa} + \frac{ZeN}{\varepsilon_r \varepsilon_o \kappa^2}\left(1 - e^{-\kappa d}\right) \tag{2.122}$$

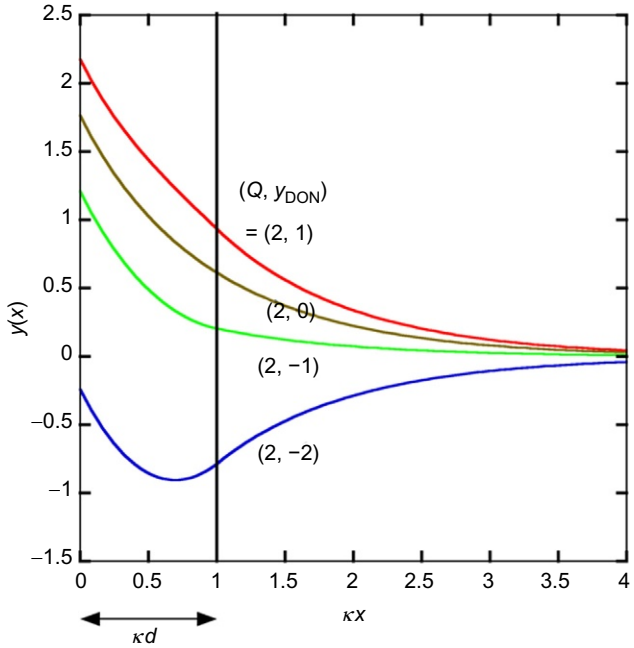

Fig. 2.15
Scaled potential distribution $y(x)$ across a polyelectrolyte nanolayer of thickness d as a function of scaled distance κx for several values of the scaled surface charge density $Q = ze\sigma/\varepsilon_r\varepsilon_o\kappa kT$ and the scaled Donnan potential $y_{DON} = ze\,\psi_{DON}/kT$.

Note that when $\kappa\, d \gg 1$, the surface potential ψ_o becomes half the Donnan potential:

$$\psi_o = \frac{1}{2}\psi_{DON} = \frac{ZeN}{2\varepsilon_r\varepsilon_o\kappa^2} \tag{2.123}$$

Consider the case where the plate core is uncharged and the thickness of the surface layer d is much larger than the Debye length $1/\kappa$. In this case the electric field $(d\psi/dx)$ and its derivative $(d^2\psi/dx^2)$ deep inside the surface layer become zero so that it follows from Eq. (2.110) that the potential deep inside the surface layer becomes the Donnan potential ψ_{DON}, given by Eq. (2.108). By integrating Eqs. (2.104), (2.110) once and equating them at $x = 0$ (Eq. 2.114), we obtain

$$\begin{aligned}\psi_o &= \psi_{DON} - \left(\frac{kT}{ze}\right)\tanh\left(\frac{ze\psi_{DON}}{2kT}\right) \\ &= \left(\frac{kT}{ze}\right)\left(\ln\left[\frac{ZN}{2zn} + \left\{\left(\frac{ZN}{2zn}\right)^2 + 1\right\}^{1/2}\right] + \frac{2zn}{ZN}\left[1 - \left\{\left(\frac{ZN}{2zn}\right)^2 + 1\right\}^{1/2}\right]\right)\end{aligned} \tag{2.124}$$

An approximate expression for the potential $\psi(x)$ at an arbitrary point in the surface layer can be obtained by expanding $y(x)$ around y_{DON}. If we put $\psi = \psi_{\mathrm{DON}} + \Delta\psi$ in Eq. (2.110) and linearize it with respect to $\Delta\psi$, then we obtain

$$\frac{d^2\psi}{dx^2} = \kappa_m^2(\psi - \psi_{\mathrm{DON}}) \tag{2.125}$$

with

$$\kappa_{\mathrm{m}} = \kappa\sqrt{\cosh\left(\frac{ze\psi_{\mathrm{DON}}}{kT}\right)} = \kappa\left[1 + \left(\frac{ZN}{2zn}\right)^2\right]^{1/4} \tag{2.126}$$

where κ_{m} may be interpreted as the effective Debye-Hückel parameter of the surface charge layer that involves the contribution of the fixed charges ZeN. Eq. (2.125) is solved to give

$$\psi(x) = \psi_{\mathrm{DON}} + (\psi_{\mathrm{o}} - \psi_{\mathrm{DON}})e^{-\kappa_{\mathrm{m}}|x|} \quad -d < x < 0 \tag{2.127}$$

For the external region outside the polyelectrolyte layer, the potential distribution $y(x)$ is given by Eq. (2.36), namely,

$$\psi(x) = \left(\frac{2kT}{ze}\right)\ln\left(\frac{1+\gamma e^{-\kappa x}}{1-\gamma e^{-\kappa x}}\right) \qquad x > 0 \tag{2.128}$$

with $\gamma = \tan h(ze\psi_{\mathrm{o}}/4kT)$. Fig. 2.16 shows some examples of the calculation of the potential distribution using Eqs. (2.126), (2.128) for three values of y_{DON}. It is seen that the potential $y(r)$ in the region deep inside the surface layer is practically equal to the Donnan potential.

2.7 Discrete Charge Effect

In the preceding section, the electric potential distribution has been derived via a continuum model in which fixed charges arising from ionized groups inside the surface layer are uniformly distributed with a smeared continuous volume charge density. The continuum approximation, however, becomes invalid when the distance between the point charges is much larger than the Debye length. A number of theoretical studies have been made on the discrete charge effects on the electrical properties of two-dimensional charged surfaces. Nelson and McQuarrie [50], in particular, considered a charged surface carrying a squared lattice of point charges and solved the two-dimensional linearized Poisson-Boltzmann equation for the potential distribution. They showed that the potential is given by a sum of the screened Coulomb potential produced by point charges distributed on the surface. In this section, on the basis of a three-dimensional lattice array of fixed point charges distributed inside the surface layer and the linearized Poisson-Boltzmann equation, we derive expressions for the potential in the regions inside and outside the surface layer [51,52].

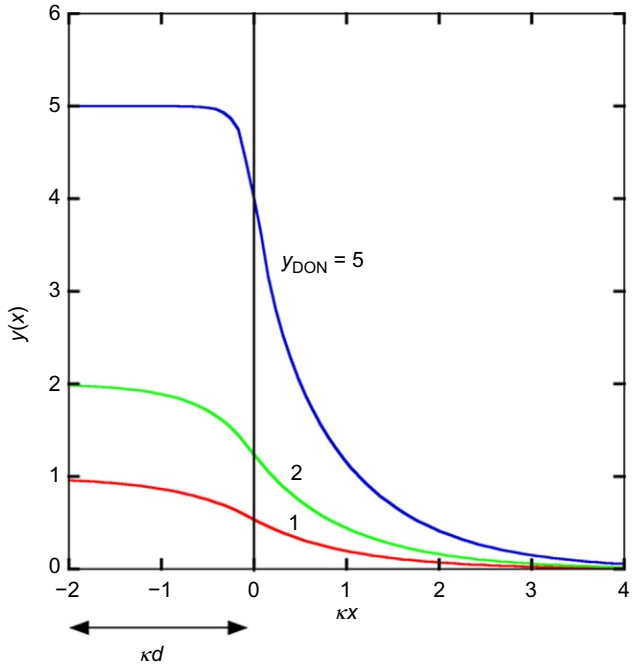

Fig. 2.16

Scaled potential distribution $y(x)$ across a polyelectrolyte nanolayer of thickness d coating an uncharged planar substrate ($\sigma = 0$) as a function of scaled distance κx for several values of the scaled Donnan potential $y_{DON} = ze\,\psi_{DON}/kT$ for the case where $d \gg 1/\kappa$.

We consider a platelike soft surface consisting of a hard planar substrate covered with an ion-penetrable surface layer of polyelectrolytes of thickness d in an aqueous electrolyte solution of relative permittivity ε_r and the Debye-Hückel parameter κ (Fig. 2.17). We treat the case where the surface layer carries fully ionized groups, giving rising to fixed charges distributed in the surface layer. We take x- and y-axes parallel to the plate surface and z-axis perpendicular to the plate surface with its origin 0 at the surface of the plate so that the region $0 < z < +\infty$ is the electrolyte solution and the region $-d < z \leq 0$ is the internal region of the surface layer (Fig. 2.17). We treat the case where the thickness d of the surface layer is much larger than the Debye length so that the surface layer can practically be considered to be infinitely thick. We also assume that the surface layer is penetrable to electrolyte ions as well as water molecules and that the relative permittivity ε_r takes the same value in the regions both outside and inside the surface layer. We treat the low potential case and employ the following linearized Poisson-Boltzmann equations for the electric potential $\psi(\boldsymbol{r})$ in the respective regions. Now consider the case where fixed charges are distributed within the surface layer ($-\infty < z \leq 0$) at a discrete density of $\rho(\boldsymbol{r})$, which is not uniform but a function of position $\boldsymbol{r}(x, y, z)$. Let us obtain the electric potential $\psi(\boldsymbol{r})$ at position $\boldsymbol{r}$ (relative to the bulk solution phase (where $\psi(\boldsymbol{r}) = 0$)), which

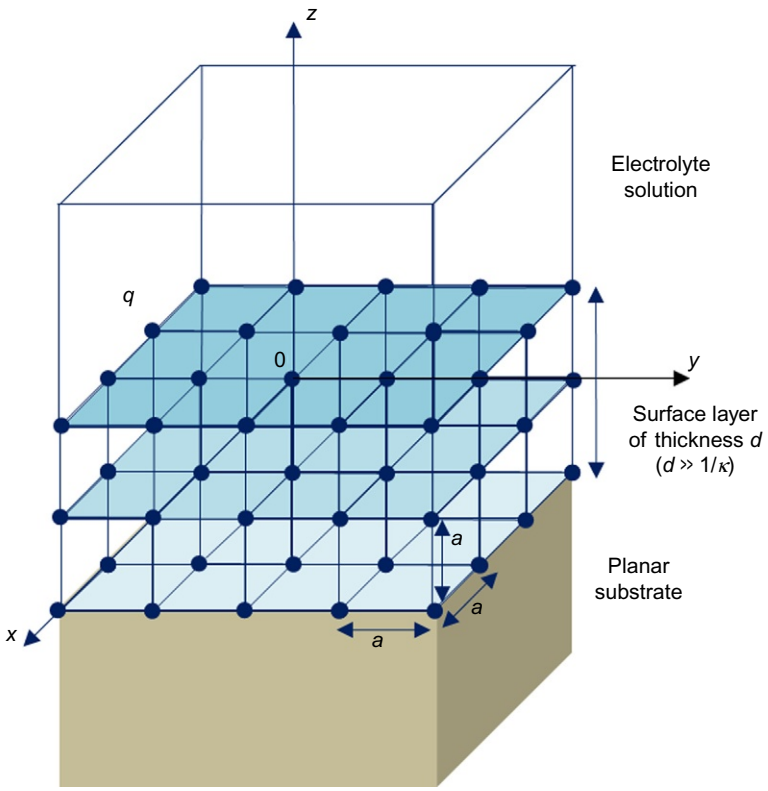

Fig. 2.17
Surface nanolayer consisting of a discrete cubic lattice of fixed point charges q with a spacing of a within a surface layer. *Reprinted with permission from H. Ohshima, Discrete charge effects on the Donnan potential and surface potential of a soft particle, Colloid Polym. Sci. 292 (2014) 749–756.*

depends not only on z but also on x and y. In this case, $\psi(\boldsymbol{r})$ satisfies the following three-dimensional linearized Poisson-Boltzmann equations:

$$\left(\frac{\partial^2}{\partial x^2}+\frac{\partial^2}{\partial y^2}+\frac{\partial^2}{\partial z^2}\right)\psi(\boldsymbol{r})=\kappa^2\psi(\boldsymbol{r})-\frac{\rho(\boldsymbol{r})}{\varepsilon_r\varepsilon_o},\quad -\infty<z\le 0 \tag{2.129}$$

$$\left(\frac{\partial^2}{\partial x^2}+\frac{\partial^2}{\partial y^2}+\frac{\partial^2}{\partial z^2}\right)\psi(\boldsymbol{r})=\kappa^2\psi(\boldsymbol{r}),\quad 0<z<+\infty \tag{2.130}$$

Eqs. (2.129), (2.130) are subject to the following boundary conditions:

$$\left.\frac{\partial\psi(\boldsymbol{r})}{\partial z}\right|_{z=0^-}=\left.\frac{\partial\psi(\boldsymbol{r})}{\partial z}\right|_{z=0^+},\quad \psi(\boldsymbol{r})|_{z=0^-}=\psi(\boldsymbol{r})|_{z=0^+} \tag{2.131}$$

$$\psi(\mathbf{r})\to 0,\quad \frac{\partial\psi(\boldsymbol{r})}{\partial z}\to 0\ \text{ as } z\to+\infty \tag{2.132}$$

$$\frac{\partial \psi(\boldsymbol{r})}{\partial z} \to 0 \quad \text{as } z \to -\infty \tag{2.133}$$

In order to solve Eqs. (2.129), (2.130) subject to Eqs. (2.131)–(2.133), we write $\psi(\boldsymbol{r})$ and $\rho(\boldsymbol{r})$ by their Fourier transforms,

$$\psi(\boldsymbol{r}) = \psi(\boldsymbol{s}, z) = \frac{1}{(2\pi)^2} \int \hat{\psi}(\boldsymbol{p}, z) \exp\left(i(\boldsymbol{p} \cdot \boldsymbol{s})\right) d\boldsymbol{p} \tag{2.134}$$

$$\rho(\boldsymbol{r}) = \rho(\boldsymbol{s}, z) = \frac{1}{(2\pi)^2} \int \hat{\rho}(\boldsymbol{p}, z) \exp\left(i(\boldsymbol{p} \cdot \boldsymbol{s})\right) d\boldsymbol{p} \tag{2.135}$$

where $\hat{\psi}(\boldsymbol{p}, z)$ and $\hat{\rho}(\boldsymbol{p}, z)$ are the Fourier coefficients, $\boldsymbol{s} = (x, y)$ and $\boldsymbol{p} = (p_x, p_y)$. We thus obtain

$$\hat{\psi}(\boldsymbol{p}, z) = \int \psi(\boldsymbol{s}, z) \exp\left(-i(\boldsymbol{p} \cdot \boldsymbol{s})\right) d\boldsymbol{s} \tag{2.136}$$

$$\hat{\rho}(\boldsymbol{p}, z) = \int \rho(\boldsymbol{s}, z) \exp\left(-i(\boldsymbol{p} \cdot \boldsymbol{s})\right) d\boldsymbol{s} \tag{2.137}$$

By solving Eqs. (2.129), (2.130) using the Fourier transforms, we finally obtain

$$\begin{aligned} \psi(\boldsymbol{r}) = \; & \frac{1}{2(2\pi)^2 \varepsilon_r \varepsilon_o} \left[\int \frac{1}{\sqrt{\kappa^2 + p^2}} \left\{ \int_{-\infty}^{z} \hat{\rho}(\boldsymbol{p}, z') \exp\left(+ \sqrt{\kappa^2 + p^2} \cdot z' \right) dz' \right\} \right. \\ & \times \exp\left(- \sqrt{\kappa^2 + p^2} \cdot z \right) \cdot \exp\left(i(\boldsymbol{p} \cdot \boldsymbol{s})\right) d\boldsymbol{p} \\ & + \left\{ \int_{z}^{0} \hat{\rho}(\boldsymbol{p}, z') \exp\left(- \sqrt{\kappa^2 + p^2} \cdot z' \right) dz' \right\} \\ & \left. \exp\left(+ \sqrt{\kappa^2 + p^2} \cdot z \right) \cdot \exp\left(i(\boldsymbol{p} \cdot \boldsymbol{s})\right) d\boldsymbol{p} \right], \quad -\infty < z \leq 0 \end{aligned} \tag{2.138}$$

$$\begin{aligned} \psi(\boldsymbol{r}) = \; & \frac{1}{2(2\pi)^2 \varepsilon_r \varepsilon_o} \int \frac{1}{\sqrt{\kappa^2 + p^2}} \left\{ \int_{-\infty}^{0} \hat{\rho}(\boldsymbol{p}, z') \exp\left(+ \sqrt{\kappa^2 + p^2} \cdot z' \right) dz' \right\} \cdot \\ & \exp\left(- \sqrt{\kappa^2 + p^2} \cdot z \right) \cdot \exp\left(i(\boldsymbol{p} \cdot \boldsymbol{s})\right) d\boldsymbol{p}, \quad 0 < z < \infty \end{aligned} \tag{2.139}$$

where

$$p = |\boldsymbol{p}| = \sqrt{p_x^2 + p_y^2} \tag{2.140}$$

Eqs. (2.138), (2.139) are the general expressions for the electric potential $\psi(\boldsymbol{r})$ at position $\boldsymbol{r}$ in the regions inside and outside the surface layer.

Now we deal with the case in which a surface layer consists of a cubic lattice of point charges q with spacing a (Fig. 2.17). The point charges are thus located at lattice point (la, ma, na), where m and n take both positive and negative integers and n takes only negative integers, since the

surface layer occupies the half space $-\infty < z \le 0$. The volume charge density $\rho(\boldsymbol{r})$ $(-\infty < z \le 0)$ is then expressed as

$$\rho(\boldsymbol{r}) = \rho(\boldsymbol{s}, z) = q \sum_{\substack{-\infty<l,m<\infty,\\ -\infty<n\le 0}} \delta(x-la)\delta(y-ma)\delta(z-na), \quad -\infty < z \le 0 \tag{2.141}$$

from which we have

$$\begin{aligned}\hat{\rho}(\boldsymbol{p}, z) &= q \int \sum_{\substack{-\infty<l,m<\infty,\\ -\infty<n\le 0}} \delta(x-la)\delta(y-ma)\delta(z-na)\exp\left(-i(\boldsymbol{p}\cdot\boldsymbol{s})\right)d\boldsymbol{s} \\ &= q \sum_{\substack{-\infty<l,m<\infty,\\ -\infty<n\le 0}} \exp\left(-i\left(p_x la + p_y ma\right)\right)\cdot\delta(z-na)\end{aligned} \tag{2.142}$$

Substituting Eq. (2.142) into Eqs. (2.138), (2.139), we have [51]

$$\psi(\boldsymbol{r}) = \frac{q}{4\pi\varepsilon_r\varepsilon_o} \sum_{\substack{-\infty<l,m<\infty,\\ -\infty<n\le 0}} \frac{\exp\left[-\kappa\sqrt{(x-la)^2+(y-ma)^2+(z-na)^2}\right]}{\sqrt{(x-la)^2+(y-ma)^2+(z-na)^2}} \quad -\infty < z < +\infty \tag{2.143}$$

Eq. (2.143) is the required expression for the potential distribution $\psi(\boldsymbol{r})$ for the case of cubic lattice of charges. The surface potential, which is a function of x and y, is given by the potential at $z = 0$, that is, $\psi(x, y, 0)$, which is a function of x and y, is given by

$$\psi(x, y, 0) = \frac{q}{4\pi\varepsilon_r\varepsilon_o} \sum_{\substack{-\infty<l,m<\infty,\\ -\infty<n\le 0}} \frac{\exp\left[-\kappa\sqrt{(x-la)^2+(y-ma)^2+(na)^2}\right]}{\sqrt{(x-la)^2+(y-ma)^2+(na)^2}} \tag{2.144}$$

It is seen that Eq. (2.143) is just a sum of screened Coulomb potentials produced by point charges located at the lattice points. The results of some calculations for the electric potential $\psi(\boldsymbol{r})$ are given in Figs. 2.18–2.20 [51]. Figs. 2.18 and 2.19 show a profile of electric potential $\psi(x, y, z)$ on the x-y plane at z $= -0.5$ nm and $z = -1$ nm in the region inside the surface layer (Fig. 2.18) and at $z = 0.5$ nm and $z = 1$ nm in the region outside the surface layer (Fig. 2.19) calculated via Eq. (2.143) using Mathematica. Here the surface layer has a cubic lattice of point charges $q = e = 1.6 \times 10^{-19}$ C with a spacing of $a = 2.5$ nm in an aqueous 1-1 electrolyte solution of bulk concentration 0.05 M at 25°C ($\varepsilon_r = 78.55$). It is seen that the potential exhibits peaks at positions closest to the lattice points.

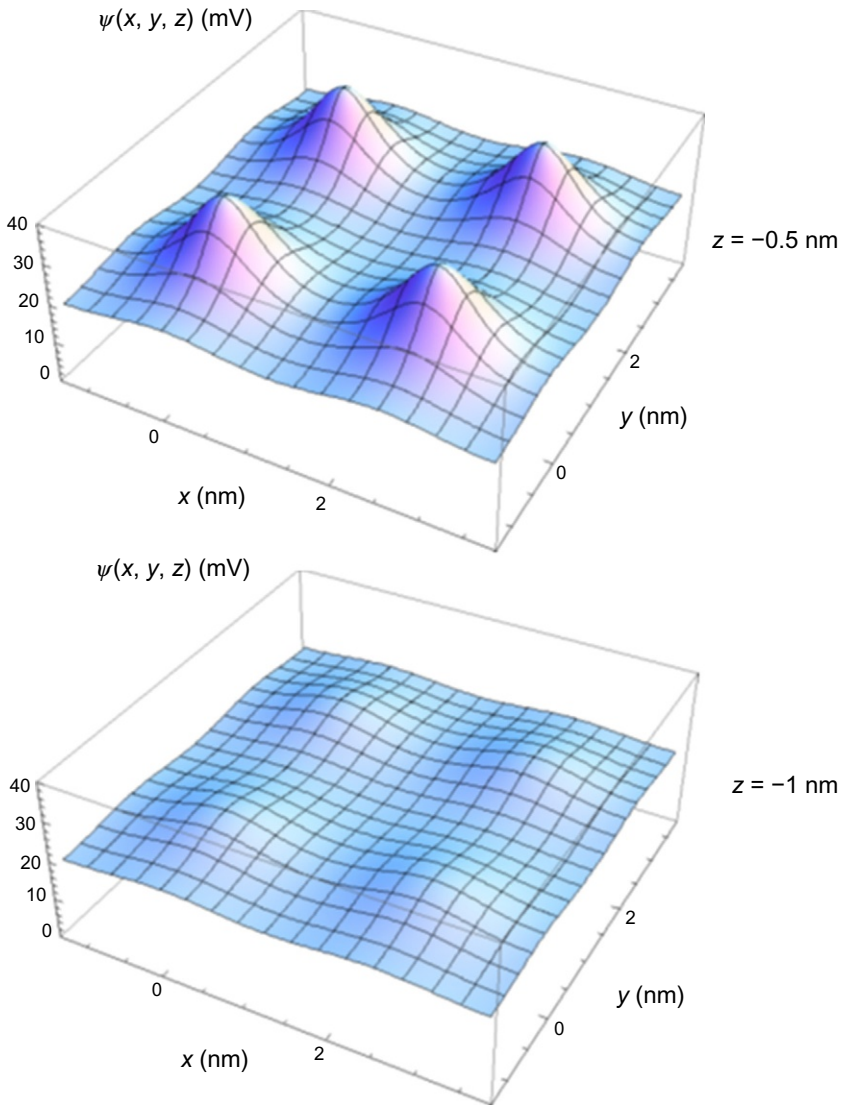

Fig. 2.18

Profile of electric potential $\psi(x, y, z)$ on the x-y plane at $z = -0.5$ nm and $z = -1$ nm inside the surface layer. The surface layer has a cubic lattice of point charges $q = e = 1.6 \times 10^{-19}$ C with a spacing of $a = 2.5$ nm in an aqueous 1-1 electrolyte solution of bulk concentration 0.05 M at 25°C ($\varepsilon_r = 78.55$).
Reprinted with permission from H. Ohshima, Discrete charge effects on the Donnan potential and surface potential of a soft particle, Colloid Polym. Sci. 292 (2014) 749–756.

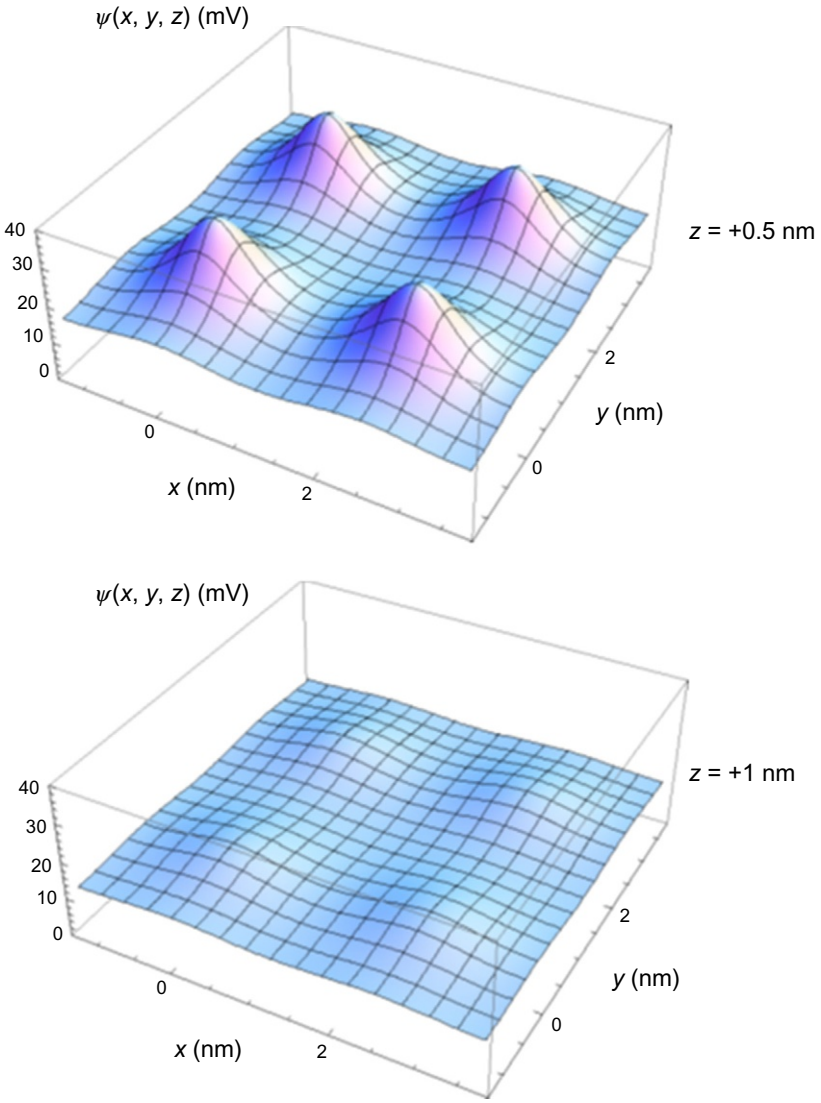

Fig. 2.19

Same as Fig. 2.18 except that $z = 0.5$ nm and $z = 1$ nm in the region outside the surface layer. *Reprinted with permission from H. Ohshima, Discrete charge effects on the Donnan potential and surface potential of a soft particle, Colloid Polym. Sci. 292 (2014) 749–756.*

Fig. 2.20 shows $\psi(x, y, z)/\psi_{DON}$ as a function of scaled distance κz calculated at $x = \kappa a/2$ and $y = \kappa a/2$ for several values of κa in comparison with the continuous mode (given by the *dotted line*). We see that $\psi(x, y, z)$ oscillates with a period of κa and the amplitude of the oscillation decreases with decreasing κa, and in the limit of $\kappa a \to 0$, the discrete charge model approaches the continuous charge model.

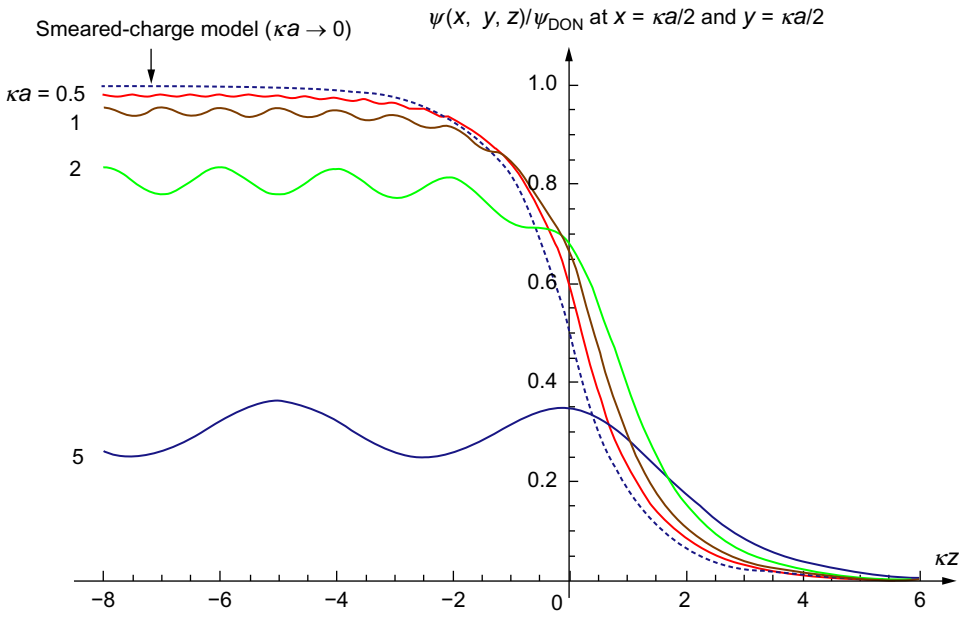

Fig. 2.20

Change in $\psi(x, y, z)/\psi_{\mathrm{DON}}$ along the z-direction at $x=\kappa a/2$ and $y=\kappa a/2$. *Reprinted with permission from H. Ohshima, Discrete charge effects on the Donnan potential and surface potential of a soft particle, Colloid Polym. Sci. 292 (2014) 749–756.*

It can be shown analytically on the basis of Eq. (2.143) that the discrete charge model approaches the continuous charge model in the limit of $\kappa a \to 0$. In this limit, the discrete sum with respect to l, m, and n in Eq. (2.143) can be replaced by a continuous integration. By introducing a smeared continuous charge density $\rho = q/a^3$, we consider the following potential deep inside the surface layer, which is shown to be equal to the Donnan potential:

$$\lim_{\substack{z\to-\infty \\ \kappa a\to 0}} \psi(\boldsymbol{r}) = \lim_{\substack{z\to-\infty \\ \kappa a\to 0}} \frac{q}{4\pi\varepsilon_{\mathrm{r}}\varepsilon_{\mathrm{o}}} \sum_{-\infty<l,m,n<\infty} \frac{\exp\left[-\kappa\sqrt{(x-la)^2+(y-ma)^2+(z-na)^2}\right]}{\sqrt{(x-la)^2+(y-ma)^2+(z-na)^2}} \tag{2.145}$$

Here the range of n, that is, $-\infty < n \le 0$ has approximately been extended to $-\infty < z < +\infty$, since we are treating the limiting case of $z \to -\infty$. We introduce $r = \sqrt{(x-la)^2+(y-ma)^2+(z-na)^2}$ and replace the discrete sum with a continuous integration

$$\sum_{-\infty<l,m,n<+\infty} \to \frac{1}{a^3}\int_0^\infty 4\pi r^2 dr \quad \text{as } ka \to 0 \tag{2.146}$$

then Eq. (2.145) becomes the Donnan potential,

$$\psi_{\mathrm{DON}} = \frac{\rho}{4\pi\varepsilon_{\mathrm{r}}\varepsilon_{\mathrm{o}}}\int_0^{\infty}\frac{e^{-\kappa r}}{r}4\pi r^2 dr = \frac{\rho}{\varepsilon_{\mathrm{r}}\varepsilon_{\mathrm{o}}\kappa^2} \tag{2.147}$$

which agrees with the result obtained by the continuous charge model (Eq. 2.109). We thus see that integration of the screened Coulomb potential over the entire space $-\infty < z < +\infty$ yields the Donnan potential. If the integration is made over a half-space $-\infty < z \le 0$, then the surface potential ψ_{o} is obtained and its value is half the Donnan potential, that is, $\psi_{\mathrm{o}} = \psi_{\mathrm{DON}}/2$, which agrees with the result of the continuum approximation (Eq. 2.123). The overall potential distribution in the limit of $\kappa a \to 0$ can also be derived in a similar manner. We introduce cylindrical coordinates: $s = \sqrt{(x-la)^2 + (y-ma)^2}$ and $z = na - z'$, and replace the discrete sum with a continuous integration

$$\sum_{\substack{-\infty<l,m<+\infty \\ -\infty<n\le 0}} \to \frac{1}{a^3}\int_{s=0}^{\infty}\int_{z'=-\infty}^{-z} 2\pi s\,ds\,dz' \quad \text{as } ka \to 0 \tag{2.148}$$

then Eq. (2.143) tends to

$$\psi(z) = \frac{\rho}{4\pi\varepsilon_{\mathrm{r}}\varepsilon_{\mathrm{o}}}\int_{s=0}^{\infty}\int_{z'=-\infty}^{-z}\frac{\exp\left[-\kappa\sqrt{s^2+z'^2}\right]}{\sqrt{s^2+z'^2}}2\pi s\,ds\,dz' = \begin{cases} \dfrac{\rho}{\varepsilon_{\mathrm{r}}\varepsilon_{\mathrm{o}}\kappa^2}\left(1-\dfrac{1}{2}e^{\kappa z}\right), & -\infty < z \le 0 \\ \dfrac{\rho}{2\varepsilon_{\mathrm{r}}\varepsilon_{\mathrm{o}}\kappa^2}e^{-\kappa z}, & 0 < z < +\infty \end{cases} \tag{2.149}$$

Eq. (2.149), which depends only on z, agrees with Eqs. (2.119), (2.120) for $d \gg 1/\kappa$.

2.8 Modified Poisson-Boltzmann Equation

The standard Poisson-Boltzmann equation for the electric potential distribution in the preceding sections assumes that ions behave like point charges and neglect the effects of ionic size. There are many theoretical studies on the modified Poisson-Boltzmann equation [53–59], which take into account the effect of ionic size by introducing the activity coefficients of electrolyte ions [53,60–62]. In the present section on the basis of the equation for the ionic activity coefficients given by Carnahan and Starling [61], which is the most accurate among existing theories, we present a simple algorithm for solving the modified Poisson-Boltzmann equation and derive a simple approximate analytic expression for the surface charge density/surface potential relationship for a planar charged surface [59].

Consider a charged planar wall surface in contact with a symmetrical electrolyte solution of valence z and bulk concentration (number density) n and take an x-axis perpendicular to the

wall surface with its origin 0 at the wall surface. We denote the surface potential and the surface charge density of the wall by $\psi_o = \psi(0)$ and σ, respectively. The potential distribution $\psi(x)$ obeys the Poisson equation for the region $x > 0$,

$$\frac{d^2\psi}{dx^2} = -\frac{\rho_{el}(x)}{\varepsilon_r \varepsilon_o} \tag{2.150}$$

Here ε_r is the relative permittivity of the electrolyte solution and $\rho_{el}(x)$ is the space charge density resulting from the electrolyte ions and is given by

$$\rho_{el}(x) = ze\{n_+(x) - n_-(x)\} \tag{2.151}$$

where $n_+(x)$ and $n_-(x)$ are, respectively, the concentrations of cations and anions at position x, and e is the elementary electric charge.

The standard Poisson-Boltzmann equation (2.150) assumes that electrolyte ions are pointlike charges. This assumption, however, becomes invalid especially in the region very close to a highly charged surface, where the concentration of counterions is very high. We must thus take into account steric interactions among ions of the finite size, by introducing ionic activity coefficient γ into Eq. (2.22) in the standard Poisson-Boltzmann approach. We assume that the activity coefficients of cations and anion have the same value γ. The electrochemical potential $\mu_+(x)$ of cations and that of anions $\mu_-(x)$ are thus given by

$$\mu_\pm(x) = \mu_\pm^o \pm ze\psi(x) + kT \ \ln[\gamma(x) n_\pm(x)] \tag{2.152}$$

which must take the same value as those in the bulk solution phase, where $\psi(x) = 0$,

$$\mu_\pm(\infty) = \mu_\pm^o + kT \ \ln(\gamma^\infty n) \tag{2.153}$$

where $\gamma^\infty = \gamma\ (\infty)$. By equating $\mu_\pm(x) = \mu_\pm(\infty)$, we obtain

$$n_\pm(x) = \frac{\gamma^\infty n}{\gamma(x)} \exp\left(\mp \frac{ze\psi(x)}{kT}\right) \tag{2.154}$$

so that Eq. (2.151) gives

$$\rho_{el}(x) = \frac{\gamma^\infty}{\gamma(x)} zen\left\{\exp\left(-\frac{ze\psi(x)}{kT}\right) - \exp\left(\frac{ze\psi(x)}{kT}\right)\right\} = -\frac{2\gamma^\infty}{\gamma(x)} zen \sinh\left(\frac{ze\psi(x)}{kT}\right) \tag{2.155}$$

Thus Eq. (2.150) becomes the following modified Poisson-Boltzmann equation:

$$\frac{d^2\psi}{dx^2} = \frac{2zen}{\varepsilon_r \varepsilon_o} \cdot \frac{\gamma^\infty}{\gamma(x)} \sinh\left(\frac{ze\psi(x)}{kT}\right) \tag{2.156}$$

which reduces to the standard Poisson-Boltzmann equation (2.34) when $\gamma\ (x) = 1$ and $\gamma^\infty = 1$.

We now assume that cations and anions have the same radius a. We introduce the volume fraction ϕ_+ of cations and that of anions ϕ_- at position x. Then we have

$$\phi_{\pm}(x) = \left(\frac{4}{3}\pi a^3\right) n_{\pm}(x) \tag{2.157}$$

The total ion volume fraction $\phi(x)$ at position x is thus given by

$$\phi(x) = \phi_{+}(x) + \phi_{-}(x) = \left(\frac{4}{3}\pi a^3\right)\{n_{+}(x) + n_{-}(x)\} \tag{2.158}$$

Let the total ion volume fraction in the bulk solution phase be $\phi_{\mathrm{B}} \equiv \phi(\infty)$. Then from Eq. (2.158) we obtain

$$\phi_{\mathrm{B}} = \left(\frac{4}{3}\pi a^3\right) \cdot 2n \tag{2.159}$$

so that Eq. (2.158) becomes

$$\phi(x) = \frac{\phi_{\mathrm{B}}\{n_{+}(x) + n_{-}(x)\}}{2n} \tag{2.160}$$

By substituting Eq. (2.154) into Eq. (2.160), we obtain

$$\phi(x) = \phi_{\mathrm{B}} \frac{\gamma^{\infty}}{\gamma(x)} \cosh\left(\frac{ze\psi(x)}{kT}\right) \tag{2.161}$$

By using Eq. (2.161), Eq. (2.156) can be rewritten as

$$\frac{d^2\psi}{dx^2} = \frac{2zen}{\varepsilon_{\mathrm{r}}\varepsilon_{\mathrm{o}}} \cdot \frac{\phi(x)}{\phi_{\mathrm{B}}} \tanh\left(\frac{ze\psi(x)}{kT}\right) \tag{2.162}$$

Now we employ the expressions for $\gamma(x)$ derived by Carnahan and Starling [62], namely,

$$\gamma(x) = \exp\left[\frac{\phi(x)\{8 - 9\phi(x) + 3\phi^2(x)\}}{\{1 - \phi(x)\}^3}\right], \quad \gamma^{\infty} = \exp\left[\frac{\phi_{\mathrm{B}}\left(8 - 9\phi_{\mathrm{B}} + 3\phi_{\mathrm{B}}^2\right)}{\left(1 - \phi_{\mathrm{B}}\right)^3}\right] \tag{2.163}$$

Then Eq. (2.161) becomes

$$\phi(x) = \phi_{\mathrm{B}} \exp\left[-\left(\frac{\phi(x)\{8 - 9\phi(x) + 3\phi^2(x)}{\{1 - \phi(x)\}^3} - \frac{\phi_{\mathrm{B}}(8 - 9\phi_{\mathrm{B}} + 3{\phi_{\mathrm{B}}}^2)}{\left(1 - \phi_{\mathrm{B}}\right)^3}\right)\right] \times \cosh\left(\frac{ze\psi(x)}{kT}\right) \tag{2.164}$$

which is an equation for $\phi(x)$ for given values of ϕ_{B} and $\psi(x)$.

The zeroth-order approximation in the limit of very small ϕ_{B}, we have from Eq. (2.164) by approximating the exponential factor to be unity,

$$\phi(x) = \phi_{\mathrm{B}} \cosh\left(\frac{ze\psi(x)}{kT}\right) \tag{2.165}$$

If we substitute Eq. (2.165) into Eq. (2.162), then the modified Poisson-Boltzmann equation (2.162) reduces back to the standard Poisson-Boltzmann equation (2.34). In order to obtain the first-order approximation for $\phi(x)$, we expand the exponential factor on the right-hand side of Eq. (2.164) in a power series of $\phi(x)$ and ϕ_B to give

$$\phi(x) = \phi_B \frac{(1+8\phi_B)\cosh(ze\psi(x)/kT)}{1+8\phi_B\cosh(ze\psi(x)/kT)} \tag{2.166}$$

By substituting Eq. (2.166) into Eq. (2.162), we obtain the following first-order approximation to the modified Poisson-Boltzmann equation:

$$\frac{d^2\psi}{dx^2} = \frac{2zen}{\varepsilon_r\varepsilon_o} \cdot \frac{\sinh\left(\frac{ze\psi(x)}{kT}\right)}{1+\left(\frac{16\phi_B}{1+8\phi_B}\right)\sinh^2\left(\frac{ze\psi(x)}{2kT}\right)} \tag{2.167}$$

By solving Eq. (2.167), we find that the relationship between the surface charge density σ and the surface potential ψ_o is given by

$$\sigma = \mathrm{sgn}(\psi_o)\frac{2\varepsilon_r\varepsilon_o\kappa kT}{ze} \cdot \sqrt{\frac{1+8\phi_B}{16\phi_B}} \cdot \sqrt{\ln\left[1+\left(\frac{16\phi_B}{1+8\phi_B}\right)\sinh^2\left(\frac{ze\psi_o}{2kT}\right)\right]} \tag{2.168}$$

or equivalently

$$\psi_o = \mathrm{sgn}(\sigma)\frac{2kT}{ze} \cdot \mathrm{arcsinh}\left(\sqrt{\frac{1+8\phi_B}{16\phi_B}\left\{\exp\left[\left(\frac{4\phi_B}{1+8\phi_B}\right)\left(\frac{ze\sigma}{\varepsilon_r\varepsilon_o\kappa kT}\right)^2\right]-1\right\}}\right) \tag{2.169}$$

and the potential distribution is given by

$$\kappa x = -\mathrm{sgn}(\psi_o)\sqrt{\frac{4\phi_B}{1+8\phi_B}}\int_{y_o}^{y} \frac{dy}{\sqrt{\ln\left[1+\left(\frac{16\phi_B}{1+8\phi_B}\right)\sinh^2\left(\frac{y}{2}\right)\right]}} \tag{2.170}$$

where $y_o = ze\psi_o/kT$ is the scaled surface potential. Eq. (2.170) gives the scaled potential distribution $y(x) = ze\psi(x)/kT$ as a function of the scaled distance κx.

In the limit of $\phi_B \to 0$, these results tend to the results obtained via the standard Poisson-Boltzmann equation. Fig. 2.21 shows an example of the calculation of the surface potential ψ_o via Eq. (2.169) as a function of the electrolyte concentration n (in units of M) in an aqueous monovalent electrolyte solution containing cations and anions of radius $a = 0.4$ nm ($z = 1$, $\varepsilon_r = 78.55$) for three values of the surface charge density σ ($\sigma = 0.01$, 0.02, and 0.05 C/m^2) at $T = 298.15$ K. The solid lines are the results obtained by the modified Poisson-Boltzmann

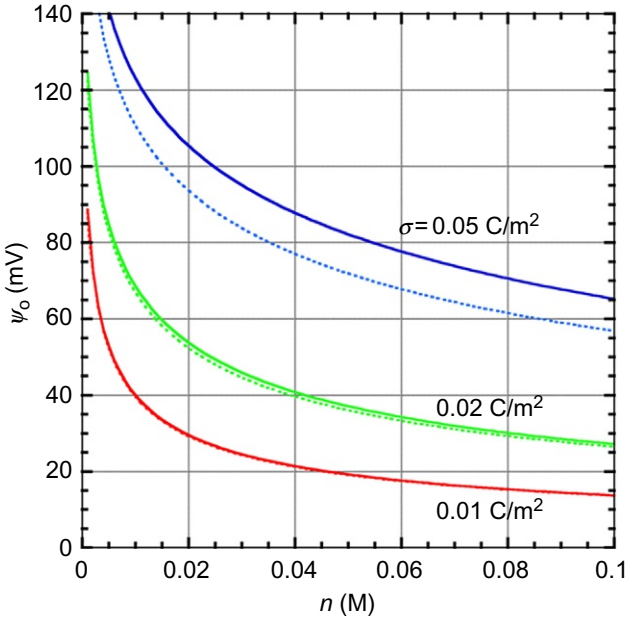

Fig. 2.21

Surface potential ψ_o of a charged planar surface in contact with an aqueous electrolyte solution. The *solid lines* are the results obtained via the modified Poisson-Boltzmann equation (Eq. 2.169), and the *dotted lines* are the results from the standard Poisson-Boltzmann equation (Eq. 2.40). Calculated for the surface charge density $\sigma = 0.01$, 0.02, and 0.04 C/m^2, the ionic radius $a = 0.4$ nm, $T = 298.15$ K, and $\varepsilon_r = 78.55$. *From H. Ohshima, An approximate analytic solution to the modified Poisson-Boltzmann equation. Effects of ionic size, Colloid Polym. Sci. 294 (2016) 2121–2125.*

equation (Eq. 2.169), and the dotted lines are those obtained by the standard Poisson-Boltzmann equation (Eq. 2.40). Fig. 2.21 shows how the effects of ionic size on the surface potential become appreciable for higher surface charge density and higher electrolyte concentrations. For $\sigma = 0.05$ C/m^2 and $n = 0.05$ M, for example, the modified Poisson-Boltzmann equation gives ca. $\psi_o = 82$ mV, while the standard Poisson-Boltzmann equation gives only ca. 72 mV, the difference being higher than 12%. The ionic size effect always gives rise to an increase in the surface potential ψ_o. This is because the ionic concentration becomes lower due to the ionic size effect, leading to a decrease in the ionic shielding effects so that the magnitude of ψ_o increases. If the surface charge density σ is low, on the other hand, then the ionic size effect becomes small. In order to see this more clearly, we expand ψ_o given by Eq. (2.169) in a power series of σ with the result that

$$\psi_o = \frac{\sigma}{\varepsilon_r \varepsilon_o \kappa} - \left(\frac{1}{24} - \frac{\phi_B}{1 + 8\phi_B}\right)\left(\frac{ze}{kT}\right)\left(\frac{\sigma}{\varepsilon_r \varepsilon_o \kappa}\right)^3 + O(\sigma^5) \tag{2.171}$$

We see that the first term on the right-hand side of Eq. (2.171) does not involve ϕ_B so that in the limit of $\sigma \to 0$, the ionic size effect vanishes. The ionic size effect appears only in terms of the second and higher orders of σ.

Finally, we present an approximate expression for the differential electric double layer capacitance $C_d = d\sigma/d\psi_o$:

$$C_d = \mathrm{sgn}(\psi_o)\varepsilon_r\varepsilon_o\kappa\sqrt{\frac{16\phi_B}{1+8\phi_B}}\cdot\frac{\sinh\left(\frac{ze\psi_o}{kT}\right)}{\sqrt{\ln\left[1+\left(\frac{16\phi_B}{1+8\phi_B}\right)\sinh^2\left(\frac{ze\psi_o}{2kT}\right)\right]}} \times\frac{1}{1+\left(\frac{16\phi_B}{1+8\phi_B}\right)\sinh^2\left(\frac{ze\psi_o}{2kT}\right)} \tag{2.172}$$

2.9 Conclusion

We have developed theories of electrical double layers at nanolayer interface. We started with the discussion on the general feature of the electrical double layer around charged surfaces. We then considered the electrical double layers across nanolayers coating hard substrates. As two important examples, we treated a nanolayer of porous materials and a monolayer of polyelectrolytes. In the latter case, the Donnan potential was shown to play an essential role in determining the electrical double layer across a polyelectrolyte layer. We then discussed the discrete charge effect on the Donnan potential in the polyelectrolyte layer. Finally, the modified Poisson-Boltzmann equation taking into account the ionic size effect was discussed.

References

[1] B.V. Derjaguin, L.D. Landau, Theory of the Stability of Strongly Charged Lyophobic Sols and of the Adhesion of Strongly Charged Particles in Solutions of Electrolytes, Acta Physicochim. USSR 14 (1941) 633–662.

[2] E.J.W. Verwey, J.T.G. Overbeek, Theory of the Stability of Lyophobic Colloids, Elsevier/Academic Press, Amsterdam, 1948.

[3] B.V. Derjaguin, Theory of Stability of Colloids and Thin Films, Consultants Bureau, New York, London, 1989.

[4] S.S. Dukhin, Non-equilibrium electric surface phenomena, Adv. Colloid Interface Sci. 44 (1993) 1–134.

[5] H. Ohshima, K. Furusawa (Eds.), Electrical Phenomena at Interfaces, Fundamentals, Measurements, and Applications, second ed., Dekker, New York, NY, 1998. revised and expanded.

[6] A.V. Delgado (Ed.), Electrokinetics and Electrophoresis, Dekker, New York, NY, 2000.

[7] J. Lyklema, Fundamentals of Interface and Colloid Science, Volume 2, Solid-Liquid Interfaces, Elsevier/Academic Press, Amsterdam, 2005.

[8] A. Spasic, J.-P. Hsu (Eds.), Finely Dispersed Particles. Micro-. Nano-, Atto-Engineering, CRC Press, Boca Raton, FL, 2005.

[9] H. Ohshima, Theory of Colloid and Interfacial Electric Phenomena, Elsevier/Academic Press, Amsterdam, 2006.

[10] T.F. Tadros (Ed.), Colloid Stability, The Role of Surface Forces—Part 1, Wiley-VCH, Weinheim, 2007.
[11] H. Ohshima, Biophysical Chemistry of Biointerfaces, John Wiley & Sons, Hoboken, NJ, 2010.
[12] J.N. Israelachvili, Intermolecular and Surface Forces, third ed., Academic Press, New York, NY, 2011.
[13] H. Ohshima (Ed.), Electrical Phenomena at Interfaces and Biointerfaces: Fundamentals and Applications in Nano-, Bio-, and Environmental Sciences, John Wiley & Sons, Hoboken, NJ, 2012.
[14] H. Ohshima, K. Makino (Eds.), Colloid and Interface Science in Pharmaceutical Research and Development, Elsevier/Academic Press, Amsterdam, 2006.
[15] G. Gouy, Sur la constitution de la charge électrique a la surface d'un électrolyte, Anniue Physique (Paris) 9 (1910) 457–468.
[16] D.L. Chapman, A contribution to the theory of electrocapillarity, Philos. Mag. 25 (1913) 475–481.
[17] O. Stern, Zur Theorie der Electrolytischen Doppelschicht, Z. Elektrochem. 30 (1924) 508–516.
[18] J. Lützenkirchen (Ed.), Surface Complexation Modelling, Elsevier/Academic Press, Amsterdam, 2006.
[19] A.L. Loeb, J.T.G. Overbeek, P.H. Wiersema, The Electrical Double Layer Around a Spherical Colloid Particle, MIT Press, Cambridge, MA, 1961.
[20] H. Ohshima, T.W. Healy, L.R. White, Accurate analytic expressions for the surface charge density/surface potential relationship and double-layer potential distribution for a spherical colloidal particle, J. Colloid Interface Sci. 90 (1982) 17–26.
[21] H. Ohshima, Surface charge density/surface potential relationship for a spherical colloidal particle in a solution of general electrolytes, J. Colloid Interface Sci. 171 (1995) 525–527.
[22] H. Ohshima, Surface charge density/surface potential relationship for a cylindrical particle in an electrolyte solution, J. Colloid Interface Sci. 200 (1998) 291–297.
[23] G.A. Martynov, S.M. Avdeev, Solution of the nonlinear Poisson-Boltzmann equation. 1. Outer and inner problems for a cylinder, Colloid J 44 (1983) 626–632. (Translated from Z. Kolloidn 44 (1982) 702–708).
[24] H. Ohshima, A simple algorithm for the calculation of the electric double layer potential distribution in a charged cylindrical narrow pore, Colloid Polym. Sci 294 (2016) 1871–1875.
[25] J. Varghese, H. Wang, L. Pilon, Simulating electric double layer capacitance of mesoporous electrodes with cylindrical pores, J. Electrochem. Soc. 158 (2011) A1106–A1114.
[26] H. Wang, L. Pilon, Accurate simulations of electric double layer capacitance of ultramicroelectrodes, J. Phys. Chem. 115 (2011) 16711–16719.
[27] D.A.B. Iozzo, M. Tong, G. Wu, E.P. Furlani, Numerical analysis of electric double layer capacitors with mesoporous electrodes: effects of electrode and electrolyte properties, J. Phys. Chem. 119 (2015) 25235–25242.
[28] H. Ohshima, Electrophoretic mobility of soft particles, J. Colloid Interface Sci. 163 (1994) 474–483.
[29] H. Ohshima, Electrophoresis of soft particles, Adv. Colloid Interface Sci. 62 (1995) (1995) 189–235.
[30] H. Ohshima, Electrophoretic mobility of soft particles, Colloids Surf. A Physicochem. Eng. Asp. 103 (1995) 249–255.
[31] H. Ohshima, On the general expression for the electrophoretic mobility of a soft particle, J. Colloid Interface Sci. 228 (2000) 190–193.
[32] R.J. Hill, D.A. Saville, W.B. Russel, Electrophoresis of spherical polymer-coated colloidal particles, J. Colloid Interface Sci. 258 (2003) 56–74.
[33] S.S. Dukhin, R. Zimmermann, C. Werner, Electrokinetic phenomena at grafted polyelectrolyte layers, J. Colloid Interface Sci. 286 (2005) 761–773.
[34] J.J. Lopez-Garcia, C. Grosse, J. Horno, Numerical calculation of the electrophoretic mobility of concentrated suspensions of soft particles, J. Colloid Interface Sci. 301 (2006) 651–659.
[35] J.F.L. Duval, H. Ohshima, Electrophoresis of diffuse soft particles, Langmuir 22 (2006) 3533–3546.
[36] H. Ohshima, Electrophoresis of soft particles: analytic approximations, Electrophoresis 27 (2006) 526–533.
[37] S.S. Dukhin, R. Zimmermann, C. Werner, Electrokinetic fingerprinting of grafted polyelectrolyte layers—a theoretical approach, Adv in Colloid Interface Sci 122 (2006) 93–105.
[38] H. Ohshima, Electrokinetics of soft particles, Colloid Polym. Sci. 285 (2007) 1411–1421.

[39] H. Ohshima, Theory of electrostatics and electrokinetics of soft particles, Sci Tech. Adv. Mater. 10 (2009) 063001–063013.
[40] S.S. Dukhin, R. Zimmermann, J.F.L. Duval, C. Werner, On the applicability of the Brinkman equation in soft surface electrokinetics, J. Colloid Interface Sci. 350 (2010) 1–4.
[41] H. Ohshima, Electrophoretic mobility of a highly charged soft particle: relaxation effect, Colloids Surf. A Physicochem. Eng. Asp. 376 (2011) 72–75.
[42] H. Ohshima, Electrical phenomena in a suspension of soft particles, Soft Matter 8 (2012) 3511–3514.
[43] H. Ohshima, Electrical phenomena of soft particles A soft step function model, J. Phys. Chem. A 116 (6473) (2012) 6480.
[44] H. Ohshima, Electrical phenomena of soft particles, Curr. Opinion Colloid Interface Sci. 18 (2013) 73–82.
[45] H. Ohshima, Electrophoretic mobility of soft particles A soft step function model, Colloids Surf. A Physicochem. Eng. Asp. 440 (2014) 151–154.
[46] M.H. Matin, H. Ohshima, Thermal transport characteristics of combined electroosmotic and pressure driven flow in soft nanofluidics, J. Colloid Interface Sci. 576 (2016) 167–176.
[47] R.P. Gopmandal, S. Bhattacharyya, M. Banerjee, H. Ohshima, Electrophoresis of diffuse soft particles with dielectric charged rigid core grafted with charge regulated inhomogeneous polymer segments, Colloids Surf. A Physicochem. Eng. Asp. 504 (2016) 116–125.
[48] R.P. Gopmandal, S. Bhattacharyya, H. Ohshima, Effect of core charge density on the electrophoresis of a soft particle coated with polyelectrolyte layer, Colloid Polym. Sci. 294 (2016) 727–733.
[49] K. Makino, H. Ohshima, Soft particle analysis of electrokinetics of biological cells and their model system, Sci. Technol. Adv. Mater. 12 (2011) 023001–023013.
[50] A.P. Nelson, D.A. McQuarrie, The effect of discrete charges on the electrical properties of a membrane. I, J. Theor. Biol. 55 (1975) 13.
[51] H. Ohshima, Discrete charge effects on the Donnan potential and surface potential of a soft particle, Colloid Polym. Sci. 292 (2014) 749–756.
[52] H. Ohshima, Discrete charge effects on the potential distribution in and around soft particles, J. Surface Sci. Technol. 31 (2015) 9–12.
[53] M.J. Sparnaay, Ion-size corrections of the Poisson-Boltzmann equation, J. Electroanal. Chem. 37 (1972) 65–70.
[54] P.W. Biesheuvel, M. van Soestbergen, Counterion volume effects in mixed electrical double layers, J. Colloid Interface Sci. 316 (2007) 490–499.
[55] J.J. Lopez-Garcia, J. Horno, C. Grosse, Poisson-Boltzmann description of the electrical double layer including ion size effects, Langmuir 27 (2011) 13970–13974.
[56] J.J. Lopez-Garcia, J. Horno, C. Grosse, Equilibrium properties of charged spherical colloidal particles suspended in aqueous electrolytes: finite ion size and effective ion permittivity effects, J. Colloid Interface Sci. 380 (2012) 213–221.
[57] B. Giera, N. Henson, E.M. Kober, M.S. Shell, T.M. Squires, Electric double-layer structure in primitive model electrolytes: comparing molecular dynamics with local-density approximations, Langmuir 31 (2015) 3553–3562.
[58] J.J. Lopez-Garcia, J. Horno, C. Grosse, Ion size effects on the dielectric and electrokinetic properties in aqueous colloidal suspensions, Curr. Opinion in Colloid Interface 24 (2016) 23–31.
[59] H. Ohshima, An approximate analytic solution to the modified Poisson-Boltzmann equation, Effects of ionic size, Colloid Polym. Sci 294 (2016) 2121–2125.
[60] J.J. Bikerman, Structure and capacity of electrical double layer, Philos. Mag. 33 (1942) (1942) 384.
[61] T.L. Hill, Statistical Thermodynamics, Addison-Westley, Reading, MA, 1962.
[62] N.F. Carnahan, K.E. Starling, Equation of state for nonattracting rigid spheres, J. Chem. Phys. 51 (635) (1969) 636.

CHAPTER 3

Scanning Probe Microscopy Techniques for Modern Nanomaterials

Masashi Kunitake[*,1], **Satoshi Watanabe**[*], **Akihiro Ohira**[†]

[*] *Kumamoto University, Kumamoto, Japan* [†] *National Institute of Advanced Industrial Science and Technology (AIST), Tsukuba, Japan*

[1] *Corresponding author*

3.1 Introduction

Scanning probe microscopy (SPM) has become an indispensable tool for visual understanding of the nanospace for development of modern materials research, especially for nanoscience. SPM is used to visualize solid surface structures with nanoscale resolution. All SPM techniques are based on tracing a surface with an atomically sharp needlelike probe controlled by a feedback loop with interaction monitoring between the probe and the surface. SPM skims the surface of an object while the distance (or interaction, such as the force or tunneling current) between the apex of the probe and the surface is kept constant by a feedback mechanism. From the traces of the tip probe, surface morphology images are created.

SPM techniques are classified by the difference in the physical quantity between the probe and the surface. Scanning tunneling microscopy (STM) is based on the tunneling current as the feedback. It was developed by Binnig and Rohrer in 1982, and it was the first SPM method [1]. Atomic force microscopy (AFM), which is also known as scanning force microscopy (SFM), is based on the force as the feedback. A large variety of AFM techniques and peripheral measuring modes have been developed, not only for simple surface morphological imaging but also for mapping of the surface properties, surface manipulation, surface processing, and so on. SPM techniques have been widely used to elucidate the structures of various surfaces, including metals, semiconductors, and organics (polymers), in air, in vacuum, and even in liquid. In this chapter, we introduce SPM techniques and their applications in modern nanomaterial chemistry.

Nanolayer Research. http://dx.doi.org/10.1016/B978-0-444-63739-0.00003-7

3.2 Submolecular Imaging of Two-Dimensional Supramolecular Systems by SPM

With the progress of semiconductor lithography technology, production of large-scale integration circuits based on sub-10-nm-scale patterning has become a reality. However, lithography is approaching its theoretical limit. Therefore, over the last two decades, construction of sophisticated supramolecular architectures by self-assembly has attracted considerable attention as a "bottom-up" approach starting from atoms or molecules [2,3]. Self-assembly based on supramolecular chemistry and in-space imaging by SPM has attracted considerable attention in the last two decades as bottom-up nanoscience [4,5]. Among the SPM techniques, STM is advantageous in terms of real atomic resolution, although it has the disadvantage that an electroconductive substrate is required to apply the bias while AFM does not have this limitation. However, it is also possible to observe a very thin insulating adlayer with a thickness less than the tunnel distance on a conductive substrate. STM can be used to visualize each atom and molecule on a conductive surface. Therefore, highly ordered molecular adlayers on atomically flat electroconductive substrates, such as single-crystal metals, semiconductors, and highly ordered pyrolytic graphite (HOPG), have been intensively investigated as visualizable two-dimensional (2D) supramolecular systems by STM.

In general, adlayer structures are strongly affected by adsorbate-substrate interactions, intermolecular interactions, and their balance. In the case where the adsorbate-substrate interactions are dominant, molecular adlayer structures have often been considered from the point of view of epitaxy in terms of the crystallographic match with the substrate lattice. Where the adsorbate-substrate interactions are relatively weak, adsorption is predominately governed by the thermodynamic equilibrium as a function of the surface concentration of molecules based on solution conditions, such as temperature and concentration. In this case, the molecules on the surface are relatively unrestrained by the surface, so isolated molecules on the surface can freely move to form a thermodynamically stable adlayer structure, as a result of 2D crystallization. Thermodynamic self-assembly can be explained by classical theories according to crystallization and colloidal chemistry. High-resolution STM images of various complicated 2D supramolecular systems produced by well-controlled self-assembly have been reported in air [6–8], under ultrahigh vacuum (UHV) [9–11], in nonpolar solutions, and in aqueous solutions under electrochemical potential control [12–18]. STM operation in an open gas condition is rare owing to high electric noise. In UHV systems, molecular adlayers are usually prepared by controlled sublimation and subsequent thermal annealing to induce self-assembly. The molecular dynamics on substrates is frequently described as a function of the temperature. Low-temperature STM is commonly used to observe isolated molecules because the motion of molecules is frozen at low temperatures.

In solution systems, the adlayers on solid-liquid interfaces are generally prepared by spontaneous adsorption from the solution phase, and STM imaging is performed at the solid-solution interface in the presence of sample molecules in the solution. Under appropriate

conditions, highly ordered molecular adlayers with supramolecular arrangements form as a thermodynamically stable phase. In situ STM imaging at the solid-liquid interface is a powerful tool because it allows not only static nanostructures but also dynamic molecular motion to be observed [19]. Observation of dynamic processes is crucial to understand the mechanism of self-assembly on surfaces. Ordering, breaking, Ostwald ripening, and order-disorder and order-order phase transitions of molecular arrays on surfaces have been successfully visualized as a function of the surface coverage by in situ STM [20]. Adjusting the thermodynamic self-assembly conditions can also be achieved by the management of the electrochemical potential because the adsorption strength is a function of the potential [21,22]. Potential control (at the millivolt scale) is advantageous for very delicate tunes of adsorption and the ordering equilibrium on the surface.

As typical examples of order-order phase transitions, highly ordered adlayer structures of the triangular building block molecules trimesic acid (TMA) [23] and 2,5,8-triamino-tri-*s*-triazine (melem) [24] have been independently reported. Two ordered phases, namely, a honeycomb network and a close-packed structure, were reversibly observed for both systems, as shown in Fig. 3.1. In the honeycomb network, TMA and melem molecules are connected to each other by hydrogen bonds. Increasing the surface coverage induces a transformation from a honeycomb network to a close-packed structure with much higher coverage by breaking intermolecular

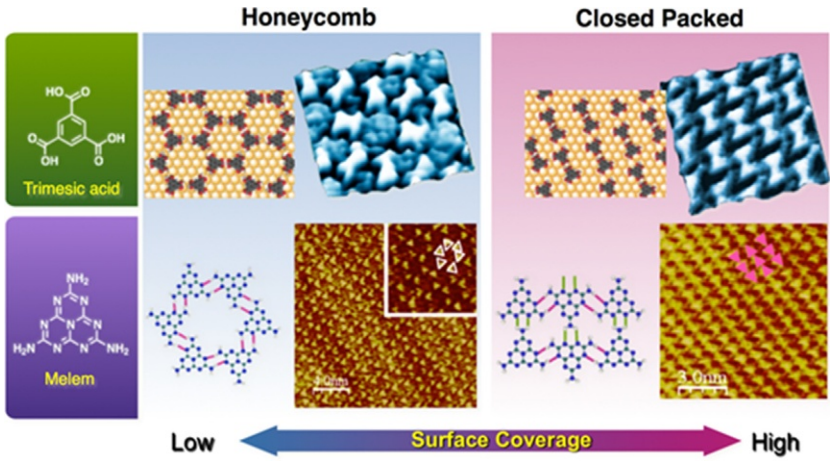

Fig. 3.1

High-resolution electrochemical STM images and the corresponding models of the honeycomb networks and close-packed ordered adlayers of trimesic acid and melem on Au(111) in aqueous solution. *Reprinted with permission from the references. Y. Ishikawa, A. Ohira, M. Sakata, C. Hirayama, M. Kunitake, A two-dimensional molecular network structure of trimesic acid prepared by adsorption-induced self-organization, Chem. Commun. (2002) 2652–2653. Copyright 2002 Royal Society of Chemistry. S. Uemura, M. Aono, T. Komatsu, M. Kunitake, Two-dimensional self-assembled structures of melamine and melem at the aqueous solution-Au(111) interface, Langmuir 27 (2011) 1336–1340. Copyright 2011 American Chemical Society.*

hydrogen bonds in the honeycomb network. Specific intermolecular interactions, such as hydrogen bonds, can overcome the loss of the thermodynamic energy owing to the low coverage. In addition, construction of diverse, multiple-component, supramolecular architectures has also been achieved. Different two-component self-assembled structures composed of melamine and melem have been formed on the Au(111) surface by varying the melamine and melem concentrations and the electrochemical potential [25].

3.3 On-Site STM Imaging of Covalently Bonded 2D Supramolecular Structures by Surface-Mediated Selective Polycondensation

Initially, sophisticated supramolecular structures were self-assembled by adjusting relatively weak noncovalent interactions, and they were mainly based on structural beauty rather than functionality. Construction of covalently bonded nanostructures on well-defined substrates has recently attracted attention because of the use of nanomaterials and nanodevices with the progress of bottom-up technology.

Most covalent self-assembly systems are prepared by a thermally initiated reaction on surfaces in UHV, such as thermally initiated C–C coupling [26–28], Ullmann coupling between aromatic halogen molecules [29–31], esterification between boronic acid and hydroxyl units [32,33], and azomethine (Schiff base) coupling between a primary amine and aldehyde units [34,35]. Among these systems, preparation of graphene nanoribbons (GNRs) on surfaces has attracted attention because GNRs have excellent thermal, electronic, and magnetic properties [36]. A variety of linear, zigzag, and branch-shaped GNRs have been constructed on surfaces under UHV by the appropriate selection of building blocks and controlled thermal reactions.

In covalently bonded molecular systems, it is difficult to avoid unfavorable disordered nanostructures because of the irreversibility of the coupling reactions. A dynamic reaction equilibrium for the coupling of building blocks is generally required to construct highly sophisticated ordered structures. Under UHV conditions, successful preparative strategies are kinetically controlled, thermally activated reactions performed at very low surface coverage of building blocks. Note that many covalent architecture systems have been constructed at high temperature in UHV, and the STM observations were performed at or below room temperature.

Reversible polycondensation reactions have been proposed to connect building blocks in extended frameworks as a soft solution process based on aromatic Schiff base (also known as imine or azomethine) coupling between aromatic primary amines and aromatic aldehydes [37–40]. The important concept of this methodology is the surface-selective polycondensation reaction even under solution conditions, wherein homogeneous solution reactions do not occur [41]. This has been achieved by carefully controlled conditions based on two major equilibria: adsorption-desorption and coupling-decoupling. The reaction equilibrium is then essentially controllable by tuning the solution pH. At higher pH values relative to the pK_a of the building

blocks bearing primary amino units, the reaction immediately proceeds at room temperature, frequently inducing sedimentation of an oligomeric product. However, protonation of the primary amino group at acidic pH values induces "breakdown" of the coupling. Therefore, the pH of the reaction solution is carefully selected for each system and is slightly acidic relative to the pK_a. Under such pH conditions, the surface reaction might proceed even though the reaction in a homogeneous solution might be restrictively inhibited. The reaction equilibrium on the surface is shifted onto a chemically inert and hydrophobic substrate surface.

Because of the high degree of reversibility and controllability of the reaction, pH-controlled Schiff-base coupling is useful in supramolecular chemistry as a dynamic reversible covalent coupling reaction with a high reaction equilibrium rate even at room temperature. The basic concept of the careful control of dynamic reversible reactions for thermodynamic equilibria can be generalized by the design and construction of various supramolecular systems through the use of a wide array of equilibrium coupling reactions. This soft solution process is not limited to a planar 2D surface and can be readily applied to arbitrary three-dimensional (3D) micro- and macrostructured objects. The combination of top-down lithography and the previously mentioned bottom-up assembly allows arbitrary patterned deposition to be performed by the strong surface selectivity of the reaction.

Various nanomesh structures have been constructed by combining 5,10,15,20-tetrakis-(4-aminophenyl)-21,23H-porphyrin (TAPP) and several linker molecules prepared by thermodynamic self-assembly as shown in Fig. 3.2. High-resolution STM imaging allows

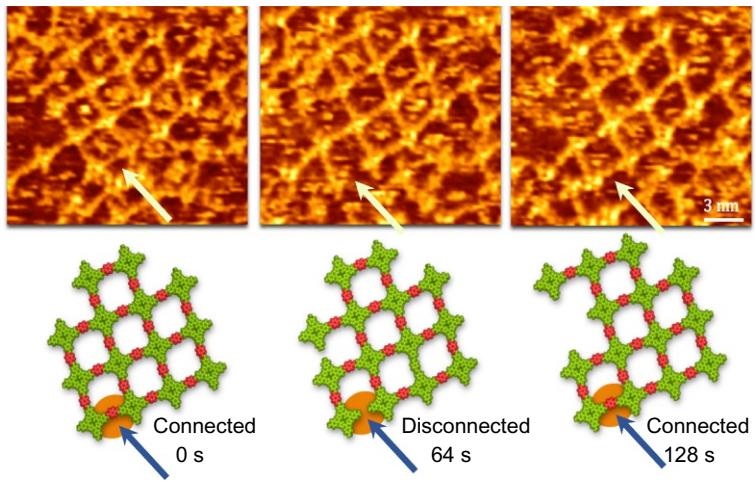

Fig. 3.2

Sequential in situ STM images of a TAPP-TPA(terephthalaldehyde) nanomesh of 2D π-conjugated supramacromolecular frameworks prepared by on-site successive polycondensation. *Reprinted with permission from the reference R. Tanoue, R. Higuchi, N. Enoki, Y. Miyasato, S. Uemura, N. Kimizuka, Thermodynamically controlled self-assembly of covalent nanoarchitectures in aqueous solution, ACS Nano 5 (2011) 3923–3929. Copyright 2011 American Chemical Society.*

discrimination of each building block molecule in the covalent porphyrin-based 2D mesh frameworks. Moreover, visualization of the molecular dynamics, such as bond formation, bond dissociation, the host-guest reaction, and the order-order phase transition, has been achieved by in situ real-space imaging. These observations clearly show the reversibility of the covalently bonded systems at the solid-liquid interface at a well-balanced equilibrium point. When the equilibrium slightly shifts toward the adsorption or coupling side under typically less acidic conditions, continuous lateral film growth on the substrate can be achieved by chemical liquid deposition (CLD). Various colorful π-conjugated films of very simple building blocks can be spontaneously formed by simple immersion in a solution. Furthermore, they frequently have unique surface morphologies; for example, vertical nanowalls were frequently observed [44]. In addition, a position selective reaction to form a high-symmetry product has also been achieved by surface-selective polycondensation [45].

In contrast to dry processes, such as molecular beam epitaxy, CLD based on surface-mediated selective polycondensation is a low-cost and ecofriendly soft solution process, because the reaction can essentially be performed in a beaker of water at room temperature. Construction of 2D and 3D macromolecular architectures that consist of functional building blocks on well-defined solid surfaces is a crucial milestone to bridge top-down and bottom-up nanotechnologies, and also to bridge supramolecular chemistry and nanomaterial science.

3.4 Surface Characterization of 2D Nanomaterials by AFM and KPFM

Even without real atomic resolution as in STM, AFM has been established as a popular research method to observe surface morphologies in material science because an electrically conducting substrate is not necessary. Here, we introduce several studies of nanofilm materials using AFM, especially studies beyond simple topological imaging.

Metal-organic frameworks (MOFs) [46–54], also known as porous coordination polymers [55–59], and covalent organic frameworks (COFs) have had a large impact in the field of materials science because of the possibility of designable crystalline porous frameworks with a wide range of applications. Moreover, surface-attached MOFs (SURMOFs) on well-defined substrates have been investigated for device applications, such as functional electrodes [60], sensors [61,62], and electronic devices [63–66]. Simple thermal equilibrium treatment in acetic acid vapor has been proposed as a straightforward method to produce large 2D nanosheets of crystalline coordination frameworks on HOPG [67]. An acetic acid vapor environment dramatically accelerates recombination of coordination bonds between metal ions and carboxylate ligands by decreasing the activation energy, as shown in Fig. 3.3.

AFM imaging is effective for evaluating SURMOFs in spite of the relatively low resolution. Generally, AFM imaging simultaneously gives a topographic image and a phase image. Phase imaging is extremely effective for surface mapping of the physical characteristics, such as the

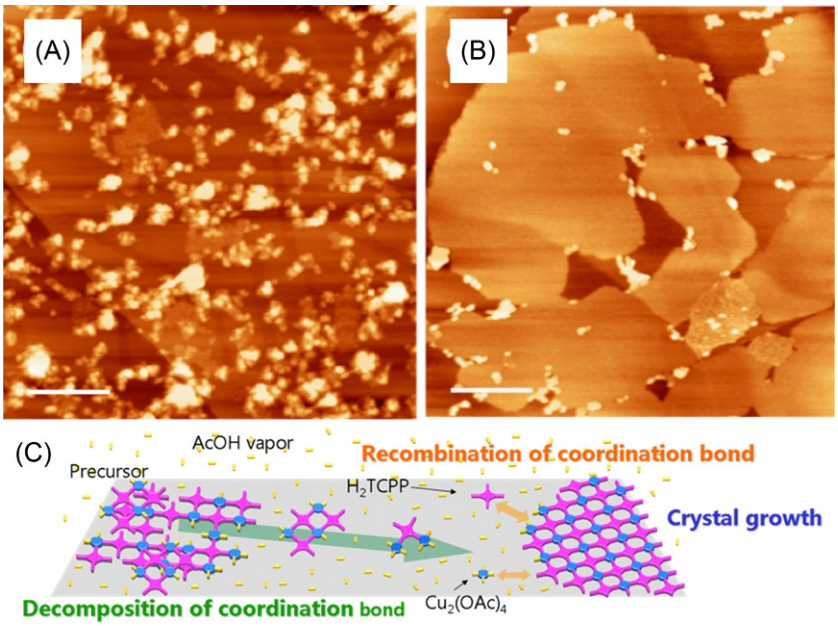

Fig. 3.3

AFM images of (A) the spin-coated precursor MOF before thermal treatment and (B) MOF nanosheets formed after thermal treatment in acetic acid vapor. (C) Schematic representation of 2D crystal growth of MOF nanosheets achieved by treatment in acetic acid vapor. Each scale bar represents 200 nm. *Reprinted with permission from the reference K. Sakata, S. Kashiyama, G. Matsuo, S. Uemura, N. Kimizuka, M. Kunitake, Growth of two-dimensional metal-organic framework nanosheet crystals on graphite substrates by thermal equilibrium treatment in acetic acid vapor, Chem. Nano Mater. 1 (2015) 259–263. Copyright 2015 Wiley.*

roughness, friction, adhesiveness, stiffness, and elasticity [68,69]. In the topographic image (Fig. 3.4a), the intact HOPG and MOF islands are not easy to distinguish. In contrast, in the phase AFM image (Fig. 4a′), the flat nanosheets are easily distinguishable from the uncoated HOPG regions by different contrast [70],

Precise phase imaging has been shown to be remarkably useful for analyzing the crystalline domains of SURMOF nanosheets. In the phase image (Fig. 3.4b′), multiple domains with different phase contrast are found even in regions that appear to be a single uniform nanosheet with homogeneous contrast in the topographic image (Fig. 4b). The phase contrast of the flat sheets without differences in the topographic thickness can be attributed to the differences in the crystal orientation of the 2D single crystalline domains in the nanosheets (Fig. 3.4c). The phase signal in tapping AFM imaging is very sensitive to the anisotropic angle between the AFM scan direction and the crystal orientation of the nanosheets. Similar visual discrimination of anisotropic domains in a single-crystal lamella of polyethylene has been reported using AFM with frictional force mode [71].

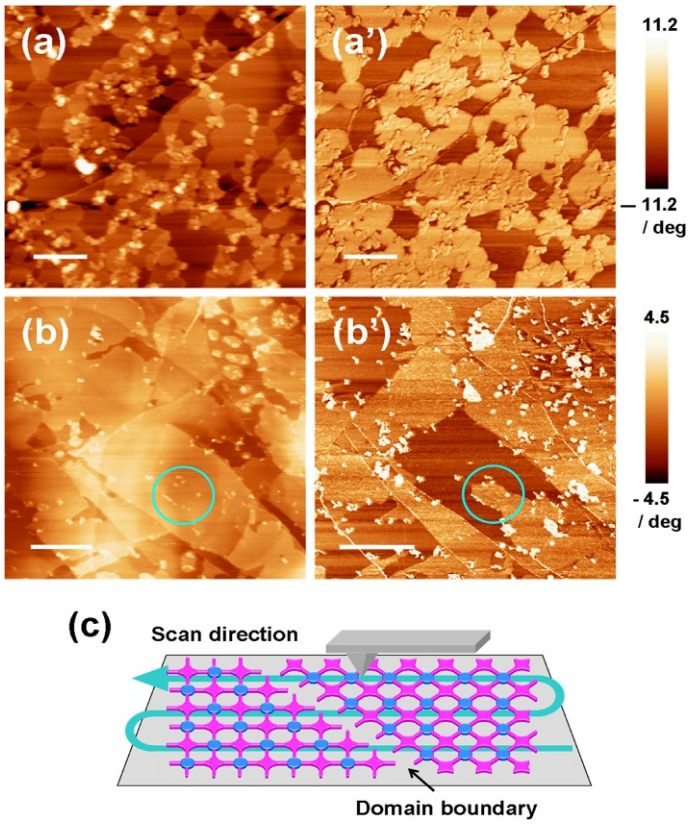

Fig. 3.4

Simultaneously recorded topographic (a and b) and phase (a′ and b′) images of the MOF nanosheets, and schematic representation of discrimination of crystalline domains in MOF nanosheets by phase imaging (c). The scale bars in (a and a′) and (b and b′) are 200 and 500 nm, respectively. *Reprinted with permission from the reference K. Sakata, S. Kashiyama, G. Matsuo, S. Uemura, N. Kimizuka, M. Kunitake, Growth of two-dimensional metal-organic framework nanosheet crystals on graphite substrates by thermal equilibrium treatment in acetic acid vapor, Chem. Nano Mater. 1 (2015) 259–263. Copyright 2015 Wiley.*

Stretched helical polymers with large molecular weight and high persistent length, such as DNA, are suitable samples to relatively easily visualize the real chain structures. Molecular nonwoven fabrics, which are helical polymer films with covalent crosslinking, have been assembled on substrates by the layer-by-layer techniques based on an alternate ester-amide exchange reaction between poly(γ-methyl-L-glutamate) (PMLG) and crosslinking agents, such as ethylene diamine. The secondary structures of the helical polymer are advantageous for construction of a covalently bonded, ultrathin nonwoven fabric consisting of single polymer strands based on regular growth of helical monolayers without excessive adsorption [72].

In the high-resolution AFM images as shown in Fig. 3.5B and C, the PMLG strings are scattered and partially connected to each other over the surface in a meshlike assembly. Frequently,

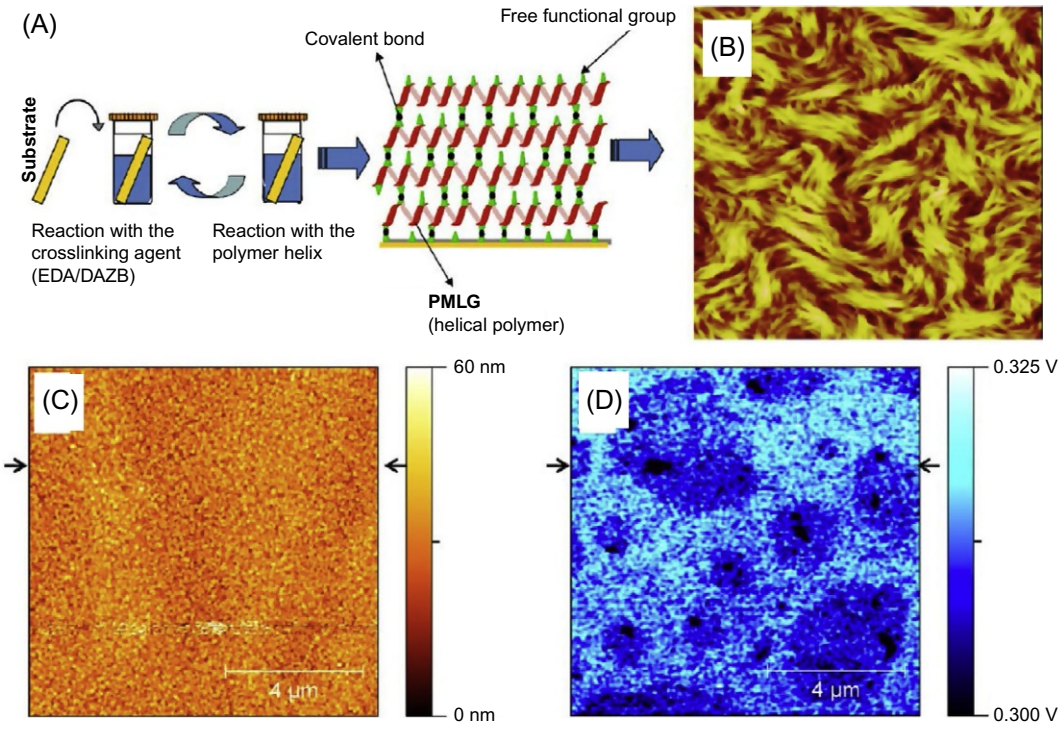

Fig. 3.5

(A) Schematic representation of alternate deposition of helical polymers. (B) Topographic AFM image of molecular nonwoven fabrics consisting of a 20 PMLG multilayer. (C) Topographic AFM and (D) surface potential images of 5 PMLG multilayers. *Reprinted with permission from the reference R. Higuchi, M. Hirano, M. Ashaduzzaman, N. Yilmaz, T. Sumino, D. Kodama, S. Chiba, S. Uemura, K. Nishiyama, A. Ohira, et al., Construction and characterization of "molecular nonwoven fabrics" consisting of crosslinked poly(γ-methyl-L-glutamate), Langmuir 29 (2013) 7478–7487. Copyright 2013 American Chemical Society.*

individual helical polymer chains can be clearly recognized on indium tin oxide (ITO) substrates. The height and width of the single PMLG chains are about 1.2 and 40 nm, respectively. Although the height is similar to the real diameter of α-helical PMLG (1.20 nm) [73,74], the width might reflect the radius of curvature of the AFM tip.

The PMLG nanofilms have been characterized by Kelvin probe force microscopy (KPFM), which is also known as surface potential microscopy, and the potential of KPFM as a technique for characterizing organic materials has been simultaneously evaluated. In principle, KPFM allows the work function of surfaces to be visualized. The work function is related to many surface phenomena, including the catalytic activity, reconstruction of surfaces, doping and band-bending of semiconductors, charge trapping in dielectrics, and corrosion. A KPFM image can be simultaneously collected with an AFM image at the same location. Comparison between

the topographic image and the corresponding KPFM image is useful to estimate the surface structure and properties. The principle of KPFM and its application to organic semiconductor systems will be discussed later.

A segregated bundle structure in PMLG nanofilms has also been observed in KPFM images shown in Fig. 3.5D, similar to topographic images. When the surface roughness is high, the structure in the KPFM image will be mainly reflected in the topographic features rather than the difference in the surface potential. Although it can be very difficult to eliminate topographic information from KPFM images, KPFM achieves imaging of defects based on differences in the surface potential.

Local surface potential mapping measured by KPFM is highly significant for organic materials. However, the reproducibility and reliability of KPFM images, especially in terms of the surface potential values, are not high because of contamination of the tip and difficulty in deconvolution of the topographic information. To avoid these problems, normalization of the tip before and after imaging has been proposed using standard samples of HOPG and well-cleaned ITO, which have standard surface potentials of -0.16 ± 0.01 and 0.00 ± 0.03 V, respectively [72].

3.5 Characterizations of Advanced Materials for Polymer Electrolyte Fuel Cells by SPM Techniques

More recently, the characterization of energy materials for fuel cells, solar cells, and batteries by using the SPM technique has been developed [75]. Here, we will give examples of SPM observations in polymer electrolyte fuel cell (PEFC) research, especially for advanced electrode materials and electrolytes, which are the key components for high performance of PEFCs [75].

In PEFCs, highly active platinum is used for the oxygen reduction reaction (ORR) [76]. There is great interest in understanding the effect of the size, form, including the index surface, and dispersibility of platinum particles loaded on carbon supports on the catalytic activity of the ORR [77]. To investigate the influence of the exposed surface of the platinum particles on the catalytic activity, an atomically flat single-crystal surface is frequently used as a model electrode for fundamental research [78]. Direct observation of the electrode surfaces and electrolyte adsorption under potential controlled conditions has been reported using electrochemical STM [78–80]. In particular, because the perfluorinated sulfonic acid ionomer is used for the polymer electrolyte membrane (PEM) in PEFCs, many studies have reported STM observation of specific adsorption of sulfuric acid anions [78,81–85].

Watanabe et al. investigated the relationship between not only different index surfaces of single-crystal platinum but also platinum-based nanoparticles with different surface texture and

the ORR activity by electrochemistry and STM observation in acid solution [76,86,87]. O'Hayre et al. reported that an AFM measurement system with a platinum-coated cantilever and a solid PEM, such as Nafion, under hydrogen flow conditions can be used to investigate the ORR characteristics in an environment that closely mimics PEFC operating conditions [88]. Hoshi et al. showed that the ORR activity of the high-index platinum surfaces is higher for steps than terraces using a combination of techniques, such as AFM observations, electrochemistry, and simulations [89–91]. Furthermore, they first succeeded in direct observation of the degradation behavior of platinum particles with different surface indexes under potential cycling in real time using high-speed AFM, as shown in Fig. 3.6 [91]. In Fig. 3.6, the detailed change of the shape of a single platinum particle has been clearly observed during potential cycling in acid solution.

Masuda et al. investigated the adsorption behavior of the perfluorinated sulfonic acid ionomer as an electrolyte on the platinum single-crystal (111) surfaces by a combination of in situ AFM, quartz crystal microbalance measurements, and surface-sensitive surface X-ray scattering coupled with electrochemistry [92]. They reported that the adsorption-desorption behavior of the ionomer significantly depends on the state of surface oxidation of platinum: The ionomer adsorbs on pure platinum surfaces but detaches from oxidized surfaces, as shown in Fig. 3.7. This result implies that the catalytic activity for ORR is governed by the adsorption state of the ionomer present in the vicinity of surfaces.

In recent years, alloy systems and core-shell catalysts that have relatively high catalytic activity to reduce the amount of platinum for practical use have been developed [93]. If SPM can analyze the electronic states of the interface between dissimilar metals, it is expected that the catalytic activity mechanism will become clear.

As previously mentioned, the PEM, which is one of the most important components of PEFCs, requires various characteristics, such as high proton conductivity with low humidity not only at high temperature but also in the subzero region, a high gas barrier, and mechanical and chemical stability [94–96]. Even though various types of PEMs based on perfluorinated and hydrocarbon-type sulfonic acid (perfluorosulfonic acid [PFSA]-type and hydrocarbon [HC]-type, respectively) PEMs have been developed, PFSA-type PEMs, such as Nafion, Aciplex, and Flemion, are still state-of-the-art because these membranes possess high mechanical, thermal, and chemical stability as well as high proton conductivity [94,95,97–100]. However, alternative HC-type membranes have recently become desirable in terms of their cost, environmentally friendly nature, and stability at high temperature [94,96]. As non-PFSA-type alternative membranes based on aromatic hydrocarbon polymers, sulphonated poly(ether ether ketone) (SPEEK), poly(ether sulfone) (SPES), poly(imide)s (SPI), polyphenylene (SPP), poly(phenylquinoxaline) (SPPQ), and polybenzimidazoles (PBI) doped with phospholic acid that possess superior heat-resistant and mechanical stability have been developed so far

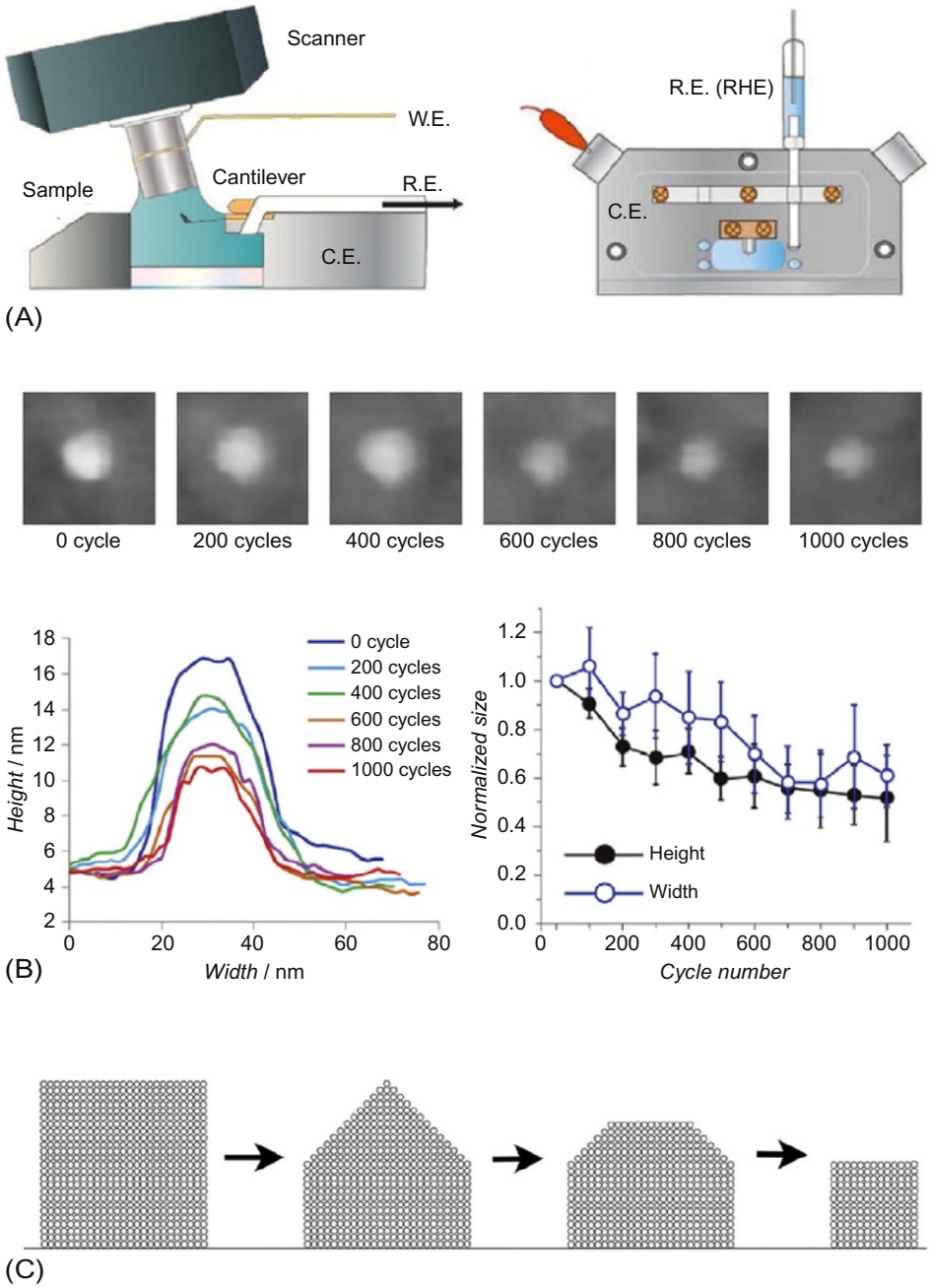

Fig. 3.6

(A) Schematic illustration of high-speed AFM cell ((left) side, (rigt) top view), (B) high-speed AFM images of cubic Pt nanoparticle in 0.1 M $HClO_4$ saturated air during potential cycles between 0.05 and 1.6 V (RHE) at a scanning rate of 2.0 V s^{-1}, cross-sections, height, and width normalized to the values before the potential cycles (imaged area: 70 nm × 70 nm), and (C) corresponding dissolution model of cubic Pt nanoparticle (side view) determined by high-speed AFM observation. *Reprinted with permission from the reference N. Hoshi, M. Nakamura, C. Yoshida, Y. Yamada, M. Kameyama, Y. Mizumoto, In situ high-speed AFM of shape-controlled Pt nanoparticles in electrochemical environments: structural effects on the dissolution mechanism, Electrochem. Commun. 72 (2016) 5–9. Copyright 2016 Elsevier.*

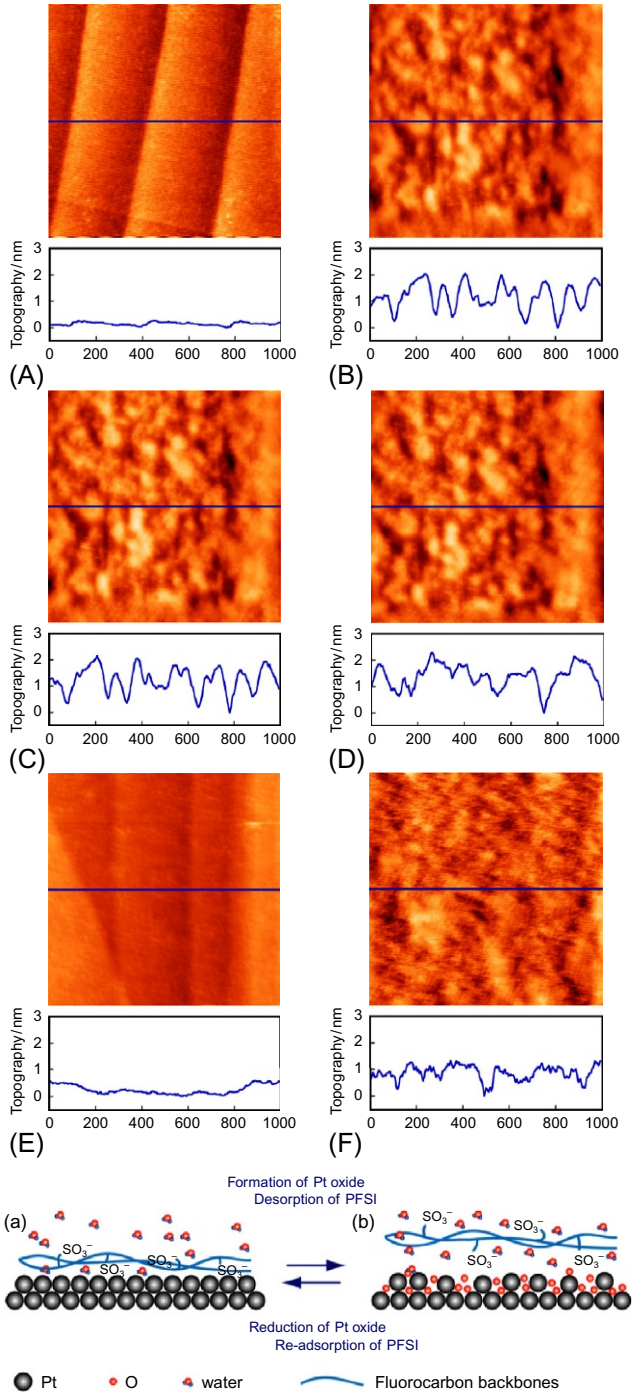

Fig. 3.7

Top: AFM images of the Pt(111) surface measured (A) without potential control in water and at (B) 0.1, (C) 0.6, (D) 0.8, (E) 1.2, and (F) 0.6 V in 12 meq/L Nafion solution. Bottom: Schematic illustrations of potential dependent adsorption behavior of PFSI on Pt electrode. *Reprinted with permission from the reference T. Masuda, F. Sonsudin, P.R. Singh, H. Naohara, K. Uosaki, Potential-dependent adsorption and desorption of perfluorosulfonated ionomer on a platinum electrode surface probed by electrochemical quartz crystal microbalance and atomic force microscopy, J. Phys. Chem. C 117 (2013) 15704–15709. Copyright 2013 American Chemical Society.*

[94,96,101–113]. Furthermore, development of building blocks that can be prepared by copolymerization with various types of sulfonated and nonsulfonated aromatic hydrocarbon monomers has advanced the potential application to PEFCs [114–119].

McGrath et al. first demonstrated that multiblock-type membranes composed of completely aromatic copolymers with a sulfonated poly(arylene ether) block part and a nonsulfonated poly(arylene ether) or poly(imide) block part show much better performance for proton conductivity at lower humidity than membranes composed of random copolymers [114–116]. The existence of phase-separated, hydrophilic-hydrophobic domains in the membrane, which provide the opportunity for the formation of large continuous water channels where protons are mobile, may result in the membrane exhibiting high proton conduction, especially at low humidity. Miyatake et al. reported that synthesized multiblock-type PEMs in which the sulfo groups are integrated with a hydrophilic block show good proton conductivity comparable with that of Nafion in the low relative humidity (RH) region [117].

Rikukawa et al. successfully synthesized diblock and triblock polyphenylene-based copolymers that are expected to have a high-order structure, such as a favorable cylindrical or lamellar structure for high proton conductivity, and they reported that the proton conductivities of these membranes are much higher than that of the homopolymer system even with much lower water content [119].

With the development of polymer synthesis, understanding the structural properties is necessary to develop high-performance PEMs, and elucidation of the relationship between the morphology and physical properties, such as the proton conductivity, gas permeability, and chemical/physical stability, is also required. In the case of PFSA-type PEMs, much information about the surface and bulk morphologies has been obtained [120], and the relationships among the morphology, proton conductivity, and gas permeability seem to be relatively clear. Although the recent progress in various analytical methods has accelerated elucidation of the structural properties, there is not as much structural information about HC-type PEMs as there is about PFSA-type PEMs. Because the characteristics of PEMs strongly depend on the water activity under PEFC operating conditions where water is constantly generated and ejected, it is important to investigate the dependence of the physical properties and functions on the water activity. The characteristics of PEMs, such as their proton conductivity and gas permeability, are evaluated under a controlled atmosphere. Therefore, to investigate the correlation between the structure and the physical properties, it is also necessary to analyze the structural changes under controlled conditions. TEM is mainly used for structural observation of PEM at the molecular level. However, there is a concern about unexpected structural deformation and change caused by the electron beam and staining with metal ions, in addition to the advanced techniques required for sample preparation. Furthermore, because TEM observations are generally performed in UHV conditions, it is difficult to confirm the structural changes of the PEM accompanied with the water content change. SPM allows direct visualization of not only

the conformation of the isolated polymer chain but also the intricate morphology of solid films with nanoscale resolution under various conditions, such as in vacuum and liquid even at high temperature. In particular, because SPM can generate an image that reflects the interaction between the membrane surface and the probe tip, the morphological features of the hydrophilic-hydrophobic region can be evaluated. This flexibility of the measurement conditions is a great advantage for PEM research because the proton conductivity, gas permeability, and viscoelastic properties of membranes depend on the water uptake, which is associated with the RH. There have been various unique and interesting reports of AFM observation of PFSA-type PEMs, such as the Nafion membrane [121–124].

McLean et al. used AFM to observe the phase-separated morphology of PEMs, and they successfully distinguished the crystalline and ionic domains at the surface of Nafion by precisely controlling the oscillation amplitude of the cantilever in phase mode [124]. These morphological features were supported by SAXS measurements. After this pioneering work, characterization of the membrane morphology of perfluorinated PEMs by SPM has rapidly progressed, and it has been established as a useful method for advancing PEM development. In addition to characterization of the phase-separated structure, direct imaging of active proton-conductive regions has also recently been reported using conductive AFM based on current detection (current mapping), which is usually performed in contact mode coupled with the electrochemical method [125].

Ohira et al. succeeded in simultaneous observation of proton conduction and the surface morphology of PEMs using AC mode, rather than contact mode, coupled with the electrochemical method [126–130]. Direct simultaneous imaging clearly revealed that the phase images have higher correlation with the current mapping images than with the topographies for Nafion. Furthermore, active proton paths were found to cluster into large proton-conductive regions during hydration. However, for SPEEK and SPES, only a relatively small and disperse proton path was observed, and it showed no significant change even with an increase in the water content. Moreover, a very poor relationship between the phase image and the current mapping image was obtained for SPEEK and SPES, in contrast to the case of Nafion. This difference in the structural change during hydration between PFSA- and HC-type membranes indicates that very careful interpretation of typical AFM images is required to determine the surface morphology (Fig. 3.8), and it is difficult to characterize morphological change only by AFM phase imaging.

There has been only one study of the correlation between the membrane surface morphology and the fuel cell performance using AFM coupled with electrochemistry. In that case, a series of hydrophilic-hydrophobic multiblock copolymers based on SPES with different block lengths was investigated. The results revealed a significant dependence of the hydrophilic/hydrophobic phase-separated structure on the block length. The conductive area ratio estimated from the current mapping image decreases as the block length increases in addition to the difference on

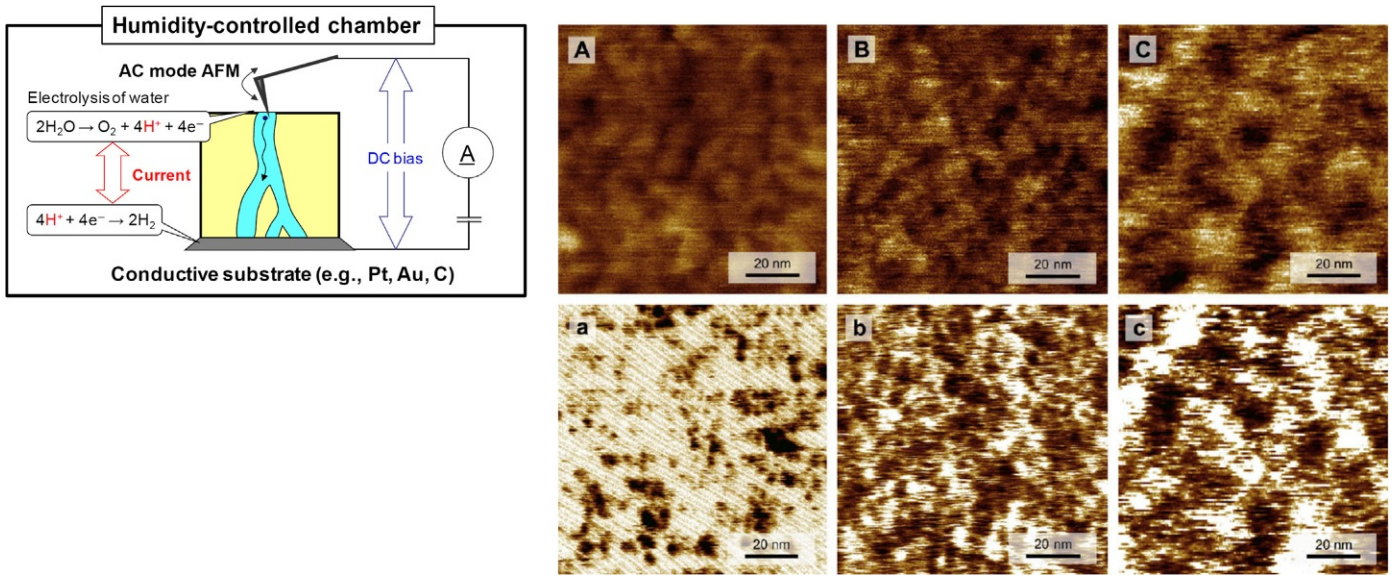

Fig. 3.8

Left: Schematic illustration of the principle of atomic force microscopy coupled with an electrochemical imaging technique. Right: AC-AFM images of (A, a) SPEEK, (B, b) SPES, and (C, c) Nafion N-115 at 90% RH. (A)–(C) are phase images (z-scale 20°), and (a)–(c) are corresponding current-mapping images (z-scale maximum 10 pA). The dark regions corresponding to the proton-conductive regions. Scan size is 100 nm × 100 nm. Scan rate was 5 Hz and the applied bias voltage was −1.5 V. *Left: Phys. Chem. Chem. Phys. 15 (2013) 11494–11500—Reproduced by permission of the PCCP Owner Societies. Right: Reprinted with permission from the reference N. Takimoto, L. Wu, A. Ohira, Y. Takeoka and M. Rikukawa, Hydration behavior of perfluorinated and hydrocarbon-type proton exchange membranes: relationship between morphology and proton conduction, Polymer 50 (2009) 534–540.*

the front and back side of the membrane, and it was found to be closely related to the cell resistance, which is one of the most important factors for the fuel cell performance (Fig. 3.9). The most important finding was that although a well-defined, phase-separated structure of

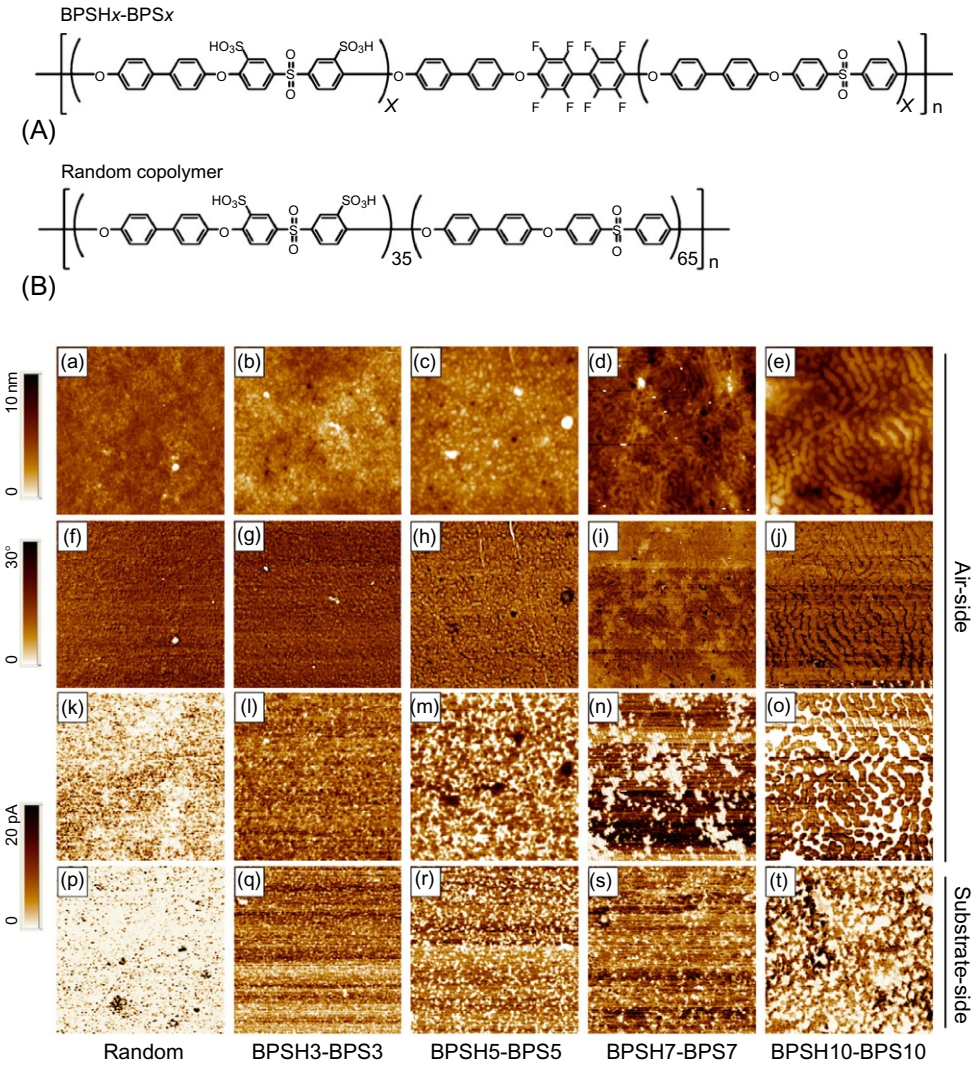

Fig. 3.9

Top: Chemical structures of multiblock and random copolymers based on SPES (A) BPSHx-BPSx and (B) random copolymers. Middle: AFM images of BPSHx-BPSx and random copolymer membranes at 22°C and 50% RH. (a–e) Topographic, (f–j) phase, and (k–t) proton conduction images. The scan box size was 1 μm × 1 μm and the bias voltage was −1.6 V. The conductive regions are the dark regions. *Reprinted with permission from reference N. Takimoto, S. Takamuku, M. Abe, A. Ohira, H.S. Lee, J.E. McGrath, Conductive area ratio of multiblock copolymer electrolyte membranes evaluated by E-AFM and its impact on fuel cell performance, J. Power Sources 194 (2009) 662–667. Copyright 2009 Elsevier.*

multiblock copolymers potentially improves the proton conductivity without any undesirable large water uptake or dimensional change by swelling, it sometimes affects the interfacial connection with the catalyst layer adversely, resulting in lower fuel cell performance. The knowledge obtained from this study indicates the importance of understanding the interfacial structure between membrane surface and catalyst layer, and the need for further improvement of the membrane morphology by optimizing both the casting conditions and the molecular design of the block sequences. These results also suggest that well-controlled microscopic morphologies, which can associate the proton path with a small amount of absorbed water, are crucial to improve the proton conductivity at low RH. Thus the observation technique that can directly visualize an active proton path is a powerful method for characterizing phase-separated structures.

Hara et al. constructed a new experimental system that mimics the reaction of the fuel cell to more quantitatively evaluate the fuel cell performance using current-mapping AFM, and they observed the proton-conductive region of PEMs formed from their synthesized multiblock copolymers [131] (Fig. 3.10). This method is expected to be a useful method for investigating the fuel cell performance as a membrane surface analysis technology that is taking into consideration the influence of the interface between the membrane and the catalyst layer.

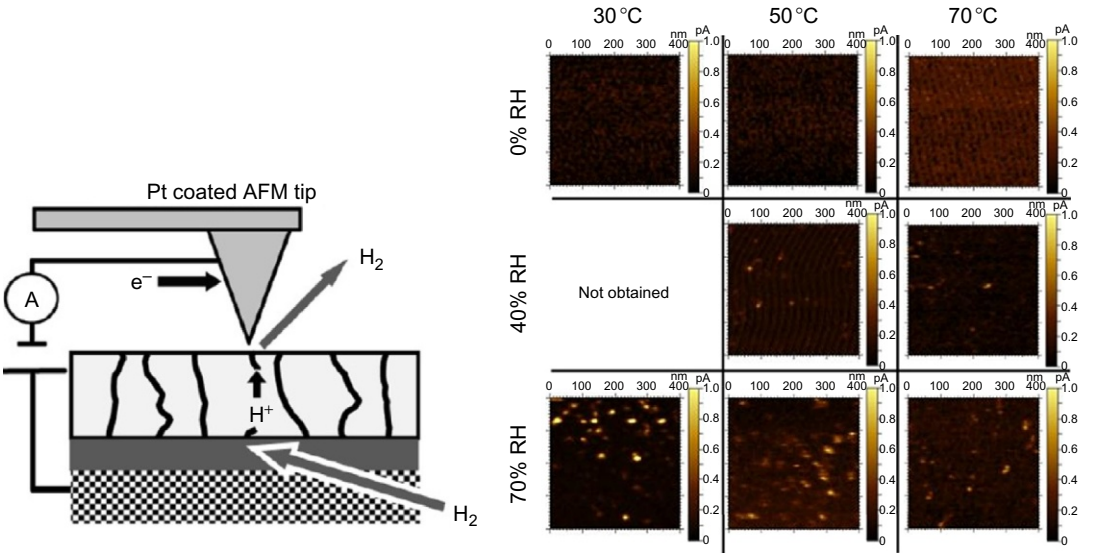

Fig. 3.10

Left: Schematic illustration of the principle of the current-sensing AFM measurement under hydrogen atmosphere. Right: Current sensing (CS)-AFM images of hydrocarbon-type multiblock copolymer (SPE-bl-1 membrane) at 30°C–70°C and 0%–70% RH under 5% H_2. Tip bias voltage = −0.6 V. The image at 40% RH and 30°C was not obtained due to experimental difficulty. *Reprinted with permission from the reference M. Hara, D. Hattori, J. Inukai, B. Bae, T. Hoshi, M. Hara, K. Miyatake and M. Watanabe, Imaging individual proton-conducting spots on sulfonated multiblock-copolymer membrane under controlled hydrogen atmosphere by current-sensing atomic force microscopy, J. Phys. Chem. B 117(2013) 3892–3899. Copyright 2013 American Chemical Society.*

Thus recent progress in the SPM technique enables understanding the structural-property relationship of the electrode materials and the PEM, which can contribute to further advances in materials for PEFC.

3.6 Recent Thin Film Organic and/or Inorganic Solar Cells

On the development of organic, inorganic, and organic/inorganic hybrid solar cells, SPM has attracted much attention for investigating the local morphology, work function, and photocurrent. Conventional analyzing techniques give photoelectric conversion efficiency calculated from the short-circuit photocurrent, open-circuit voltage, and fill factors in the current/voltage curves. To determine the work function and energy level of the highest occupied and lowest unoccupied molecular orbitals of semiconductor layers, Kelvin probe, UV photoelectron spectroscopy, UV-vis absorption spectroscopy are used. In the case of inorganic solar cells such as Si and compound solar cells, these techniques are sufficient to determine the photovoltaic characteristics because three-dimensional crystal structures can be formed over a wide range in the active layers of solar cells. However, in the case of organic solar cells, phase-separated and amorphous structures often form in the electron donor and electron accepter layers, which cause formation of the boundary of the crystal domains in each layers. These domain boundaries cause a decrease in the carrier mobilities, resulting in the low power conversion efficiencies as low as 0.97% in pn junctions [132] and Schottky organic solar cells [133] fabricated with small molecular organic semiconductors by dry processes.

To enhance the power conversion efficiencies of organic solar cells, the approaches of increases in electron donor and electron accepter phases have been developed as pin-type [134] and bulk heterojunction solar cells [135] by utilizing easy occurrence of phase separation of electron donors and electron acceptors at the micrometer or nanometer length scales in the active layer of organic solar cells, resulting in the enhancement of the power conversion efficiency by as much as 5%. The power conversion efficiency is determined by four parameters: (1) the photon absorption efficiency, (2) the transport efficiency of excitons to the electron donor and accepter interface, (3) the charge separation efficiency, and (4) the carrier collection efficiency. The strategy of phase-separation approaches is categorized in the improvement of (2) and (3). However, the random distribution of electron donor and acceptor domains in the active layer of the solar cells causes carrier traps at the surface of the electron donor or acceptor domains, which means decreases in (4) the carrier collection efficiency. For the necessity of adjusting these trade-off parameters, Günes et al. proposed ideal bulk heterojunction solar cells structures consisting of an active layer of periodically aligned electron donor and acceptor phases at a diffusion length of excitons of less than 50 nm, hole transport layers of donors, and electron transport layers of acceptors [136–138]. The morphology and electric properties at the nanometer length scale need to be known to discuss formation of such periodically aligned structures and their electric properties.

3.7 KPFM for Determination of the Work Function in Solar Cells

Varieties of AFM such as scanning capacitance microscopy (SCM), electric force microscopy (EFM), and scanning near-field optical microscopy (SNOM) are used to investigate the small photocurrent, carrier densities, and other semiconductor properties. In this section, we focus on conductive AFM and KPFM operated with conductive probes and lock-in amplifiers for determination of the local photovoltaic characteristics in solar cells. The details of the principles of conductive AFM and KPFM have been summarized in other reviews [139,140].

The name of Kelvin probe originates from the method developed by William Thomson (Lord Kelvin) to explain the formation of contact potential differences in metals [141]. The work function ϕ is the minimum energy required to remove an electron from the electronic ground state. In metals, ϕ can be described by the free-electron model [142], which defines the difference in the electron energy between the vacuum state and the Fermi energy (Fig. 3.11A). In the case of semiconductors or insulators, ϕ can be estimated by the energy difference between the vacuum level and the most loosely bound electron [143]. When two plates of a capacitor consisting of different materials are electrically connected (Fig. 3.11B), electrons will move from the lower work function material (ϕ_2) to the higher work function material (ϕ_1), generating opposite charges on the capacitor plates, which leads to the formation of contact potential difference (CPD). To detect the CPD, an external potential V_c is applied to force electrostatic force between the electrodes to zero, resulting in the externally applied potential being equal to the CPD (Fig. 3.11C). Normally, the work function of the reference plate (ϕ_1), such as Pr and Au, is known and the work function of the sample material can be determined by $\phi_2 = \phi_1 - qV_c$, where q is the elementary charge. Zisman improved the Kelvin probe technique by vibrating the reference plates [144]. This mechanical oscillation induces capacitance changes, leading to small alternating signals that can easily be detected even down to $\sim$1 mV [145–147]. The principle of KPFM is similar to the Kelvin probe technique, except that it is for investigating not electrical currents but electrostatic forces. An oscillating potential V_{ac} at frequency x is applied to the probe, and the probe displacement is detected at the same frequency as V_{ac} on photodiode detectors by a lock-in amplifier. The oscillation amplitude at frequency x is proportional to the surface potential difference between the probe and the sample surface. However, these electrostatic interactions will be essentially difficult to be quantified because of the complexity of the system dynamics and the shapes of the probe and the sample. To minimize the electrostatic interaction between the probe and the sample surface, an additional feedback loop of direct current (dc) offset voltage (V_{dc}) is applied to the probe (Fig. 3.8D). The total voltage between the probe and the sample can be expressed as

$$\Delta V = \Delta\varnothing - V_{dc} + V_{ac}\sin(\omega t) \tag{3.1}$$

where $\Delta\phi$ is the CPD, V_{dc} is the dc offset potential, and V_{ac} and x are the amplitude and frequency of the applied ac voltage, respectively. The potential energy U in the plate capacitors can be expressed as

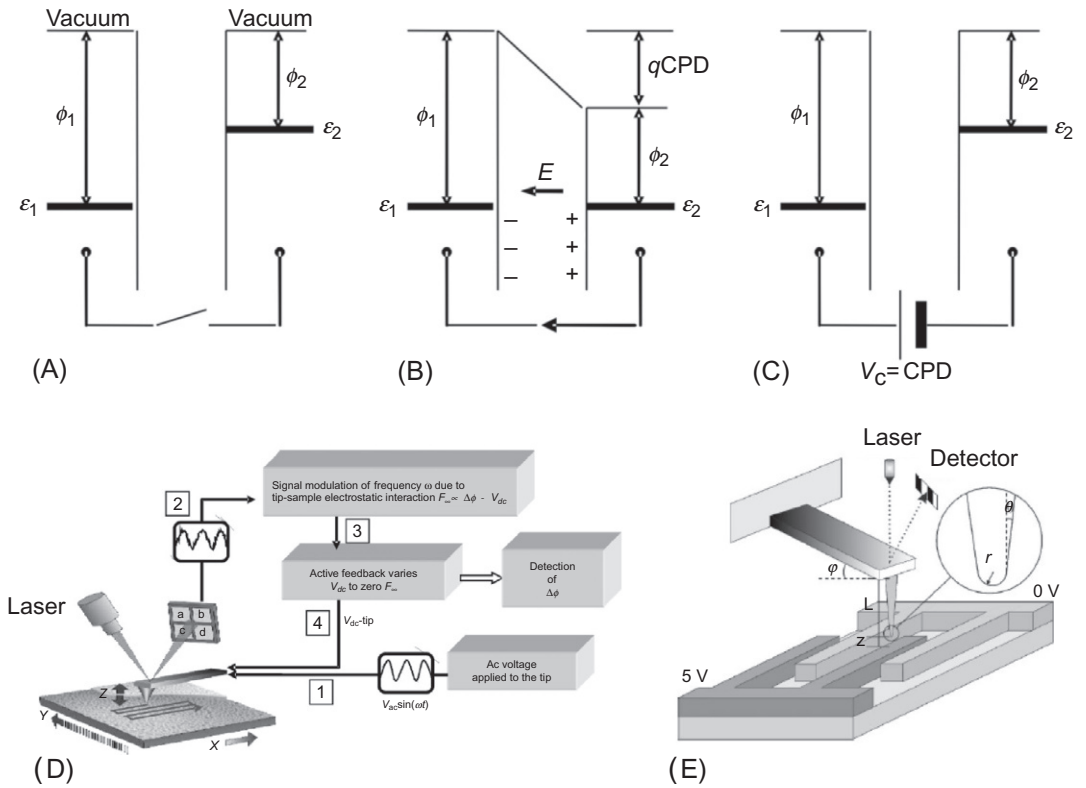

Fig. 3.11

Schematic diagram of KPFM. (A) Two different work function materials 1 and 2, where ϕ_1 and ϕ_2 correspond to the corresponding energy differences between the Fermi level ε and the vacuum level. (B) When the two materials are electrically connected, electrons move from 2 to 1 until the Fermi levels coincide, leading to appearance of a contact potential V_b. The presence of the charges in the two materials causes an electric field E. q is the electron charge and CPD is the contact potential difference. (C) The electric field is removed by applying an external potential V_{dc} that is equal to the CPD. Illustrations of the (D) KPFM setup and (E) morphological effect between conductive probes and rough surfaces. *Reprinted with permission from reference V. Palermo, M. Palma, P. Samori, Electronic characterization of organic thin films by kelvin probe force microscopy, Adv. Mater 18 (2) (2006) 145–164. Copyright 2006 Wiley.*

$$U = \frac{1}{2} C \Delta V^2 \tag{3.2}$$

where C is the capacitance between the probe and the sample. The electrostatic force is defined as the derivative of the energy with respect to the probe-sample distance z:

$$F = -\frac{\partial U}{\partial z} = -\frac{\partial C}{\partial z} \Delta V^2 = F_{dc} + F_{\omega} + F_{2\omega} \tag{3.3}$$

with components at the dc

$$F_{dc} = -\frac{1}{2}\frac{\partial C}{\partial z}\left[(\Delta\varnothing - V_{dc})^2 + \frac{\Delta V^2{}_{ac}}{2}\right] \tag{3.4}$$

and at frequencies ω and 2ω

$$F_{\omega} = -\frac{1}{2}\frac{\partial C}{\partial z}[(\Delta\varnothing - V_{dc})V_{ac}\sin(\omega t)] \tag{3.5}$$

$$F_{2\omega} = -\frac{1}{4}\frac{\partial C}{\partial z}\left[V_{ac}{}^2\cos(2\omega t)\right] \tag{3.6}$$

When the x component is zero, V_{dc} is equal to the work function difference $\Delta\phi$ between the probe and the sample surface (i.e., $V_{dc} = \Delta\phi$), allowing quantitative imaging of the CPD ($\Delta\phi$) by monitoring V_{dc}. KPFM uses the first harmonic component (F_x) to determine the local work function on the samples. The measurements can be performed using the frequency-modulation method. Two different KPFM modes are commonly used: noncontact mode and lift mode. In noncontact mode, the CPD and the topographical signals are simultaneously detected from two different oscillation frequencies. In lift mode, a first scan records the topography while a second scan operated at a large probe-surface distance gives the CPD. The probe shape often affects electrostatic interactions between the probe and the sample surface. Numerical simulations of the probe shapes have been performed to determine the influence on the KPFM resolution (Fig. 3.11E) [148,149].

3.8 Morphology and Work Function Distribution of Bulk Heterojunction Solar Cells

The morphology of bulk heterojunction organic solar cells has been investigated by AFM as well as transmittance microscopy [150–152]. To discuss the local work functions, Hoppe et al. reported surface potential measurements of poly[2-methoxy-5-(3′,7′-dimethyloctyloxy)-1,4-phenylenevinylene] (MDMO-PPV)/[6,6]-phenyl-C61-butyric acid methyl ester (PCBM) films [42,43]. Fig. 3.12 shows an AFM image, surface potential images, and schematic images of MDMO-PPV/PCBM films at a weight ratio of 1:4 with toluene and chlorobenzene. In the case of toluene, the fast evaporation leads to formation of small PCBM domains with sizes of several tens of nanometers. In the case of chlorobenzene, the slow evaporation leads to formation of larger PCBM domains with sizes of several hundreds of nanometers. The surface potentials are homogeneously distributed in the MDMO-PPV/PCBM films prepared with toluene, and with the PCBM domains in the MDMO-PPV/PCBM films prepared with chlorobenzene. The increase in the surface potential is because of a decrease in the work function of the sample, indicating that the domains consist of PCBM-rich films. The external quantum efficiency of the films prepared from toluene solution is higher than that of the chlorobenzene films. This can be explained by considering that the PCBM domains are completely covered with MDMO-PPV layers, which causes electron carrier traps. Chiesa et al. also reported surface potential images of

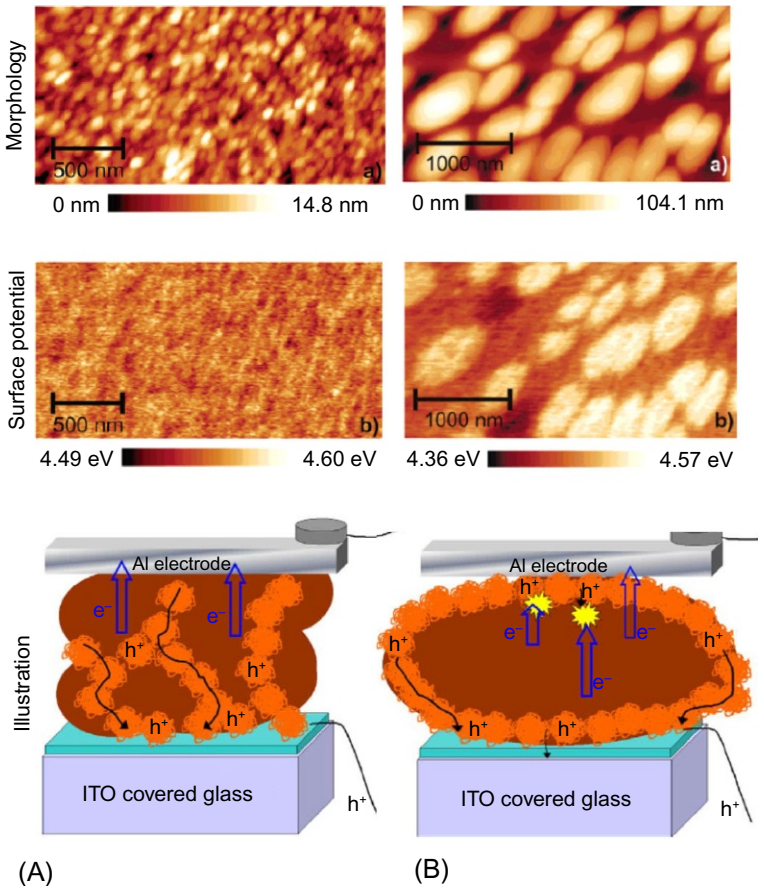

Fig. 3.12

Morphology, surface potential, and schematic images of MDMO-PPV/PCBM films prepared at a weight ratio of 1:4 with (A) toluene and (B) chlorobenzene in the dark [42,43]. Note that the work function in the *z*-range scales should be replaced by the surface potential because of a mistake in the original article. *Reprinted with permission from references H. Hoppe, T. Glatzel, M. Niggemann, A. Hinsch, M.C. Lux-Steiner, N.S. Sariciftci, Kelvin probe force microscopy study on conjugated polymer/fullerene bulk heterojunction organic solar cells, Nano Lett. 5(2) (2005) 269–274. H. Hoppe, T. Glatzel, M. Niggemann, W. Schwinger, F. Schaeffler, A. Hinsch, M.C. Lux-Steiner, N.S. Sariciftci, Efficiency limiting morphological factors of MDMO-PPV: PCBM plastic solar cells, Thin Solid Films 511–512 (2006) 587–592. Copyright 2005 American Chemical Society and copyright 2006 Elsevier, respectively.*

polyfluorene/PCBM diodes [153]. In this work, local work functions on a heterojunction morphology of the solar cells were observed, and the path of electron donors in the electron acceptor regions were visualized.

Watanabe et al. reported quantitative analysis of the electron donor and acceptor concentrations in the structured bulk heterojunctions photovoltaic devices of polyvinyl carbazole/PCBM films [154,155]. The surface relief gratings were fabricated by periodic photopolymerization of vinyl

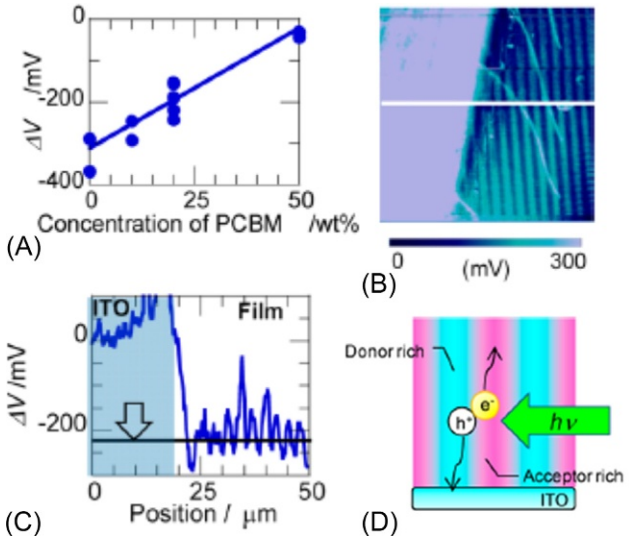

Fig. 3.13

(A) Calibration curve of the ITO-normalized surface potential plotted against the concentration of PCBM (from 0 to 50 wt%) in poly(*N*-vinylcarbazole)/PCBM, (B) surface potential image, and (C) profile of the surface relief gratings in poly(*N*-vinylcarbazole)/PCBM films (80/20 wt%). The black line in profile (C) is the ITO-normalized surface potential in the poly(*N*-vinylcarbazole)/PCBM films (80/20 wt%). (D) Illustration of the surface relief gratings of the poly(*N*-vinylcarbazole)/PCBM films. *Reprinted with permission from reference S. Watanabe, Y. Fukuchi, M. Fukasawa, T. Sassa, M. Uchiyama, T. Yamashita, M. Matsumoto, T. Aoyama, Electron donor and acceptor spatial distribution in structured bulk heterojunction photovoltaic devices induced by periodic photopolymerization, Langmuir 28 (28) (2012) 10305–10309. Copyright 2012 American Chemical Society.*

carbazole/PCBM films exposed to an interference pattern of two laser beams. Fig. 3.13A shows the surface potential of the films compared with that of ITO plotted against the concentration of PCBM in poly(*N*-vinylcarbazole)/PCBM films. The increase of the surface potential by increasing the PCBM concentration is due to higher work function of PCBM against poly(*N*-vinylcarbazole). Fig. 3.13B–D shows the surface potential, profile, and schematic images of the surface relief gratings in poly(*N*-vinylcarbazole) and PCBM films fabricated by periodic photopolymerization with exposure to the interference pattern of two laser beams. The surface potential increases and decreases in the photo-illuminated and unilluminated regions of the films, respectively, indicating formation of a PCBM concentration distribution along with the surface relief gratings. KFPM can obtain a resolution as small as several millivolts, meaning that the concentration of the electron donors and acceptors in the films can be determined at high resolution.

3.9 Local Photovoltaic Characteristics of Bulk Heterojunction Solar Cells

The local photocurrents of photovoltaic devices have been investigated with near-field excited light [156–160]. Ginger et al. reported time-resolved electrostatic force microscopy for observation of the generation rate of photocarriers, which is proportional to the photovoltaic

efficiency [161], and local photocurrent images of organic bulk heterojunction solar cells obtained by conductive AFM [162]. Fig. 3.14A–D shows an AFM image, a photocurrent image, the current-applied voltage curve, and schematic images of MDMO-PPV/PCBM films on an ITO substrate. A photocurrent response can be observed on the domains at a diameter of 100 nm. The important point is that the photocurrent is also distributed over micrometer length scale regions, indicating that there are large PCBM domains in the MDMO-PPV films, as shown in Fig. 3.14D. In the case of the PCBM domains near the surface of the films, the photocurrent responses increase because of smooth charge separation. Similar results have been obtained for bulk heterojunction organic solar cells consisting of tetrabenzoporphyrin and PCBM [163]. Hole-blocking layers have also been investigated by conductive AFM [164,165]. Kutes et al. successfully obtained the short circuit photocurrent, open-circuit voltages, and fill factor mapping of organic solar cells at several tens of nanometers length scales, meaning that nanoscale photocurrent conversion efficiency can be discussed [166].

KPFM is also a powerful method for characterizing organic solar cells under light illumination. The surface potential changes because of the generation of photocarriers in the films, which is proportional to the open-circuit voltage. This in situ KPFM also enables the photovoltaic characteristics of organic semiconductor films with low carrier mobilities to be determined

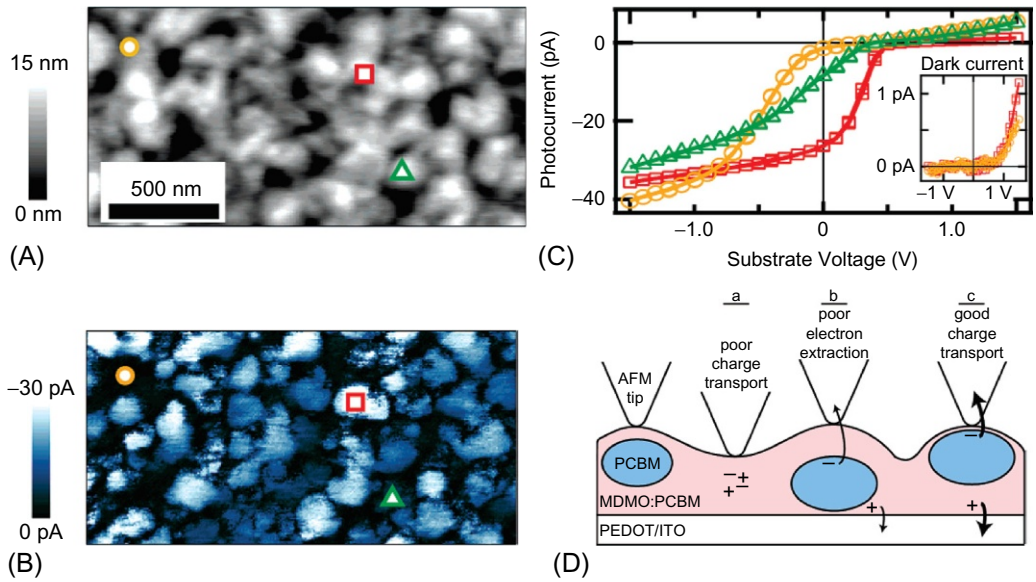

Fig. 3.14

(A) AFM image of MDMO-PPV:PCBM (20:80 wt%) films and (B) photocurrent map at an external bias of 0 V and an illumination intensity of 100 Wm^{-2} at 532 nm. (C) Local current voltages obtained at the three locations in (A) and (B). The inset shows the local current-voltage data without illumination. (D) Scheme of MDMO-PPV:PCBM (20:80 wt%) films under light illumination. *Reprinted with permission from reference D.C. Coffey, O.G. Reid, D.B. Rodovsky, G.P. Bartholomew, D.S. Ginger, Mapping local photocurrents in polymer/fullerene solar cells with photoconductive atomic force microscopy, Nano Lett. 7(3) (2007) 738–744. Copyright 2007 American Chemical Society.*

because of the high resolution of the surface potentials. In addition, the carrier traps can also be investigated by measuring the disappearance speeds of photocarriers after the light illumination is turned off. The in situ KPFM has been investigated in organic bulk heterojunction solar cells prepared with poly(3-hexylthiophene) (P3HT)/*N*,*N*′-bis(1-ethylpropyl)-3,4:9,10-perylenebis (dicarboximide) (PDI) and its derivatives [167,168].

Fig. 3.15 shows AFM and KPFM images of P3HT/PDI derivative films in the dark and under light illumination. The PDI derivatives formed 100-nm width nanofibers consisting of H aggregates in the P3HT matrix. Light illumination leads to a decrease in the surface potentials for all of the regions of the films, and also a decrease in the surface potential difference between the electron donor (P3HT) and acceptor (PDI) regions. The decrease in the average surface potential is because the hole carriers generated by light illumination migrating to the ITO substrates.

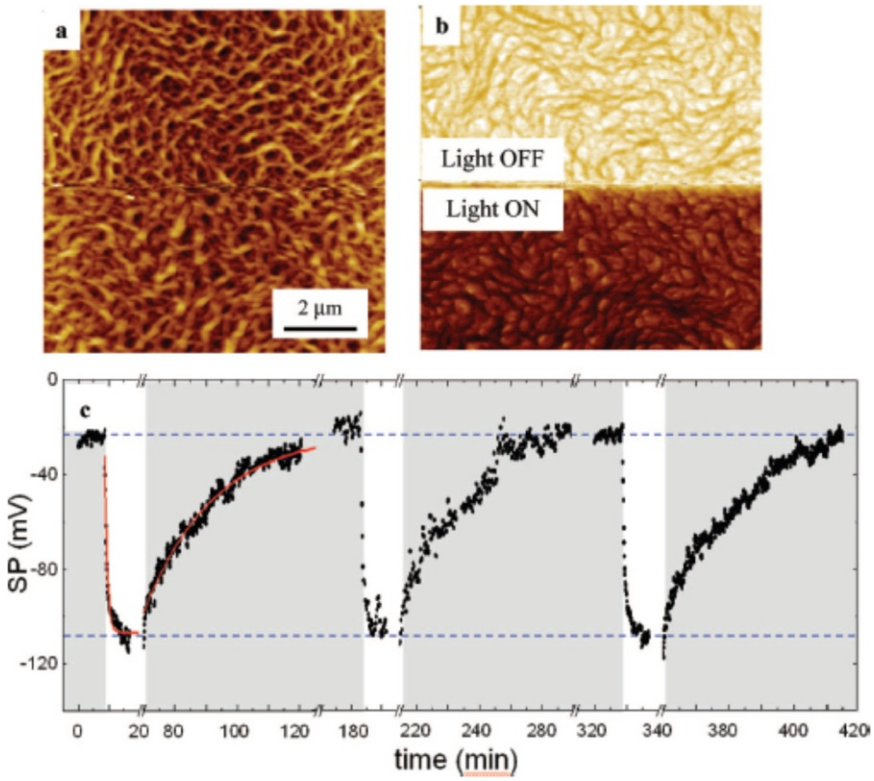

Fig. 3.15

(A) AFM and (B) KPFM images of a 60-nm-thick film of P3HT/PDI derivative films spin-coated on poly (3,4-ethylenedioxythiophene):poly(styrenesulfonate) films. The light was switched on during the AFM and KPFM measurements. (C) Surface potential plotted against elapsed time in dark (*gray region*) and under white light illumination at 60 mW cm^{-2} (*white region*). The red lines show the exponential curves of the charging and discharging processes. *Reprinted with permission from references A. Liscio, G. De Luca, F. Nolde, V. Palermo, K. Müllen, P. Samorí, Photovoltaic charge generation visualized at the nanoscale: a proof of principle, J. Am. Chem. Soc. 130 (3) (2008) 780–781. Copyright 2008 American Chemical Society.*

The decrease in the surface potentials of the PDI acceptors can be explained by migration of electron carriers to a PDI acceptor resulting in formation of stable PDI anions [169,170]. In the case of MDMO-PPV/PCBM films, the surface potential shift remains unchanged after light illumination is turned off, indicating carrier traps and low carrier mobilities. In situ KPFM mapping of nanostacked structures consisting of thiophene-fluorene-2,1,3-benzothiadiazole derivatives at the nanometer scale has been achieved by frequency-modulated-KPFM in UHV [171]. The action spectra in situ KPFM on the surface relief gratings in the bulk heterojunction photovoltaic devices under illumination at each wavelength were reported [172].

Fig. 3.16A and B shows the change of surface potential difference between the electron donor and acceptor moieties ΔV_d and the baseline shift of the surface potential ΔV_a under light

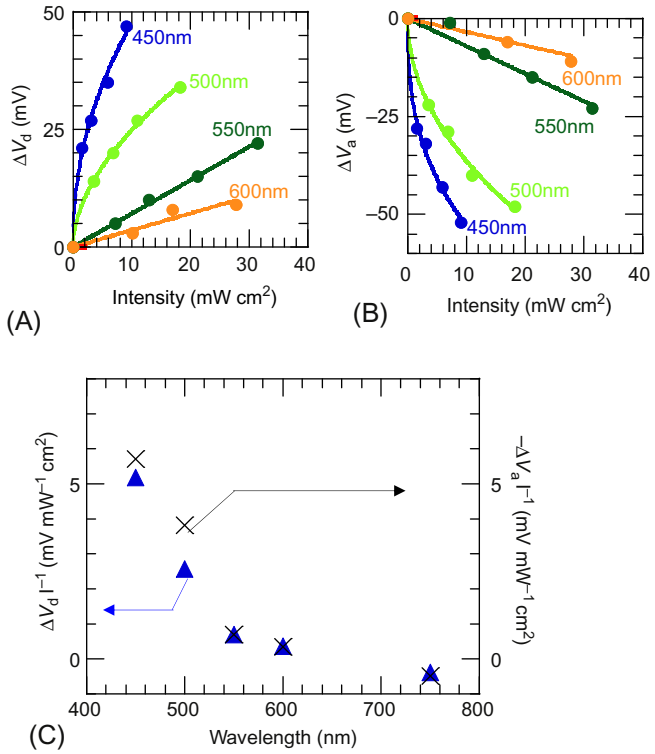

Fig. 3.16

(A) Surface potential difference of the surface relief gratings on polycarbazole/PCBM (80/20 wt%) between the donor- and accepter-rich regions ΔV_d and (B) the average surface potential difference between the baseline in the dark and under illumination ΔV_a plotted against the intensity of the incident light fitted with a sublinear function. (C) Surface potential action spectra of ΔV_d and ΔV_a normalized with respect to the light intensity. The KPFM probes were repeatedly scanned at the same line position of the samples. *Reprinted with permission from the reference S. Watanabe, Y. Fukuchi, M. Fukasawa, T. Sassa, A. Kimoto, Y. Tajima, M. Uchiyama, T. Yamashita, M. Matsumoto, T. Aoyama, In situ KPFM imaging of local photovoltaic characteristics of structured organic photovoltaic devices, ACS Appl. Mater. Interfaces 6 (3) (2014) 1481–1487. Copyright 2014 American Chemical Society.*

illumination plotted against the light intensity at each wavelength, respectively. The ΔV_d and ΔV_a values indicate migration of hole carriers to the ITO substrates and formation of PCBM anions, respectively. Fig. 3.16C shows the action spectra of ΔV_d and ΔV_a normalized by the light intensity. The action spectra are almost the same as the UV-vis absorption spectra of poly(*N*-vinylcarbazole) and PCBM films, indicating the surface potential changes originate from photovoltaic effects. These reports demonstrate that photocurrent AFM and in situ KPFM allow nanoscale mapping of the short circuit photocurrent, open-circuit voltages, fill factor, and phase-separated structures in organic bulk heterojunction solar cells.

3.10 Local Photovoltaic Inorganic and Organic/Inorganic Hybrid Solar Cells

Silicon [173] and compound semiconductors [174–176] solar cells have been investigated for local photovoltaic imaging with SFM. The work function changes and diffusion rate of carriers under light illumination have been determined by in situ KPFM and SCM [177–179]. Recently, inorganic/organic hybrid perovskite solar cells have attracted much attention because of their high power conversion efficiency [180–182]. Gao et al. reported photocurrent AFM observations for discussion of the local photovoltaic characteristics of perovskite solar cells [183].

Fig. 3.17 shows an AFM image, photocurrent images, and schematic images of the carrier mobilities on perovskite solar cells fabricated with variation in the experimental conditions for the TiO_2 layers, perovskite active layers, and capping layers. The AFM and photocurrent images indicate that the photocurrent on the grain boundary is lower than that on the surface of the particles. This can be explained by considering recombination of hole and electron carriers at the interface of the electrode and perovskite active layers. The high power conversion efficiency of the perovskite solar cells is because of the micrometer length scale of the diffusion length of the exciton in the perovskite active layers. Extremely long diffusion length of the exciton was proved by Weber et al. using photoconductive AFM [184].

3.11 Conclusions and Outlook

In this chapter, we have discussed the recent progress of SPM methods and their application to evaluate nanomaterials. The importance of SPM in materials science will continue to increase. Because it can overcome the limitation of the need for a conductive sample in STM, the real atomic resolution achieved by AFM is increasing the scope of applications. High-speed AFM systems above the ordinary video rate have also been developed while maintaining high resolution. This progress allows investigation of the atomic and molecular dynamic motions in materials. Moreover, on-site imaging and nanoscale mapping of the physical properties by SPM allows investigation of the behavior at the sites where the device is working or the reaction is in progress. Surface imaging methods based on modern SPM will pave the way for revolutionary innovation in nanomaterial science.

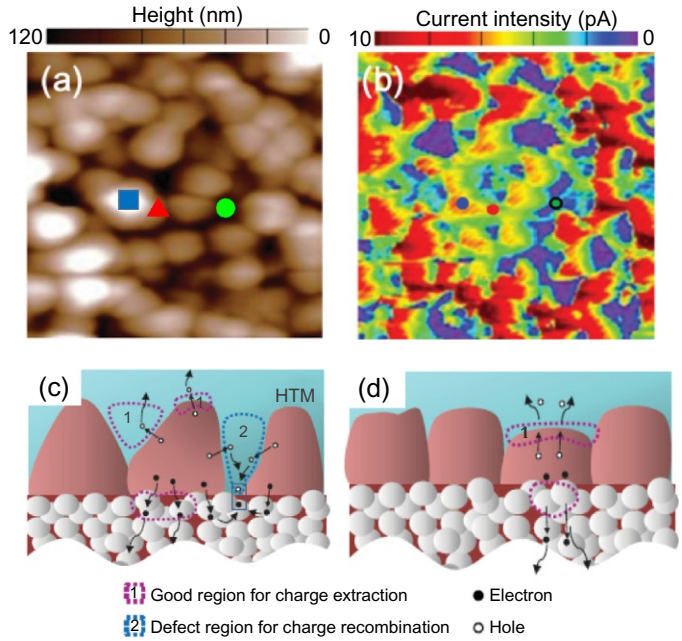

Fig. 3.17

(A) AFM and (B) current images of perovskite capping layers. Three colored dots (blue square, red triangle, and green circle) point the top interface and defects of the perovskite crystals. Schematic diagrams of charge extraction and recombination inside perovskite crystals with (C) rough and (D) packed structures. *Reprinted with permission from reference Z. Zhao, X. Chen, H. Wu, X. Wu, G. Cao, Probing the photovoltage and photocurrent in perovskite solar cells with nanoscale resolution. Adv. Funct. Mater. (2016) 3048–3058. Copyright 2016 Wiley.*

References

[1] G. Binnig, H. Rohrer, C. Gerber, E. Weibel, Tunneling through a controllable vacuum gap, Appl. Phys. Lett. 40 (1982) 178–180.
[2] J.-M. Lehn, Toward self-organization and complex matter, Science 295 (2002) 2400–2403.
[3] P. Samorì, F. Cacialli, Functional Supramolecular Architectures, Wiley-VCH, Weinheim, 2011.
[4] D. Bonifazi, S. Mohnani, A. Llanes-Pallas, Supramolecular chemistry at interfaces: molecular recognition on nanopatterned porous surfaces, Chem. Eur. J. 15 (2009) 7004–7025.
[5] J.A.A.W. Elemans, S.B. Lei, S. De Feyter, Molecular and supramolecular networks on surfaces: from two-dimensional crystal engineering to reactivity, Angew. Chem. Int. Ed. 48 (2009) 7298–7332.
[6] J.P. Rabe, Molecules at interfaces: STM in materials and life sciences, Ultramicroscopy 42–44 (1992) 41–54.
[7] C. Ludwig, B. Gompf, J. Petersen, R. Strohmaier, W. Eisenmenger, STM investigations of PTCDA and PTCDI on graphite and MoS2. A systematic study of epitaxy and STM image contrast, Z. Phys. B 93 (1994) 365–373.
[8] J. Teyssandier, N. Battaglini, M. Seydou, G. Anquetin, B. Diawara, X. Sun, F. Maurel, P. Lang, Elaboration of hydrogen-bonded 2D supramolecular assemblies on Au(111) from solutions: toward naphthalene tetracarboxylic diimide-melamine nanoporous networks, J. Phys. Chem. C 117 (2013) 8737–8745.

[9] P.S. Weiss, D.M. Eigler, Site dependence of the apparent shape of a molecule in scanning tunneling micoscope images: benzene on Pt{111}, Phys. Rev. Lett. 71 (1993) 3139–3142.
[10] S. Behler, H.P. Lang, S.H. Pan, Imaging C60 fullerite at 4.5 K by scanning tunneling microscopy, Z. Phys. B 91 (1993) 1–2.
[11] C.P. Huang, C.C. Su, M.-S. Ho, Intramolecular structures of C60 and C84 molecules on Si(111)-7 × 7 surfaces by scanning tunneling microscopy, Appl. Surf. Sci. 254 (2008) 7712–7717.
[12] H. Ohtani, R.J. Wilson, S. Chiang, C.M. Mate, Scanning tunneling microscopy observations of benzene molecules on the Rh(111)-(3 × 3) (C_6H_6+2CO) surface, Phys. Rev. Lett. 60 (1988) 2398–2401.
[13] V.M. Hallmark, S. Chiang, J.K. Brown, C. Wöll, Real-space imaging of the molecular organization of naphthalene on Pt(111), Phys. Rev. Lett. 66 (1991) 48–51.
[14] P.H. Lippel, R.J. Wilson, M.D. Miller, C. Wöll, S. Chiang, High-resolution imaging of copper-phthalocyanine by scanning-tunneling microscopy, Phys. Rev. Lett. 62 (1989) 171–174.
[15] G.A. Somorjai, Introduction to Surface Chemistry and Catalysis, first ed., John Wiley & Sons Inc, New York, NY, USA, 1994.
[16] R. Guckenberger, T. Hartmann, W. Wiegrabe, W. Baumeister, R. Wiesendanger, H. Guntherodt, J. Eds (Eds.), In: Scanning tunneling microscopy II, Springer-Verlag, New York, USA, 1991.
[17] S. Uemura, M. Sakata, C. Hirayama, M. Kunitake, Fullerene adlayers on various single-crystal metal surfaces prepared by transfer from L films, Langmuir 20 (2004) 9198–9201.
[18] H. Bertrand, R. Guillot, M.P. Teulade-Fichou, D. Fichou, Synthesis, properties, and remarkable 2D self-assembly at the liquid/solid interface of a series of triskele-shaped 5,11,17-triazatrinaphthylenes (TrisK), Chem. Eur. J. 19 (2013) 312–317.
[19] S. Uemura, R. Tanoue, N. Yilmaz, A. Ohira, M. Kunitake, Molecular dynamics in two-dimensional supramolecular systems observed by STM, Materials (Basel) 3 (2010) 4252–4276.
[20] M. Kunitake, U. Akiba, N. Batina, K. Itaya, Structures and dynamic processes of the formation of porphyrin adlayers on iodine-modified Au(111) in solution: in situ STM study, Langmuir 13 (1997) 1607–1615.
[21] A. Ohira, M. Sakata, I. Taniguchi, C. Hirayama, M. Kunitake, Comparison of nanotube structures constructed from α-, β- and γ-cyclodextrins by potential-controlled adsorption, J. Am. Chem. Soc. 125 (2003) 5057–5065.
[22] S. Yoshimoto, K. Itaya, Adsorption and assembly of ions and organic molecules at electrochemical interfaces: nanoscale aspects, Annu. Rev. Anal. Chem. 6 (2013) 213–235.
[23] Y. Ishikawa, A. Ohira, M. Sakata, C. Hirayama, M. Kunitake, A two-dimensional molecular network structure of trimesic acid prepared by adsorption-induced self-organization, Chem. Commun. (2002) 2652–2653.
[24] S. Uemura, M. Aono, T. Komatsu, M. Kunitake, Two-dimensional self-assembled structures of melamine and melem at the aqueous solution-Au(111) interface, Langmuir 27 (2011) 1336–1340.
[25] S. Uemura, M. Aono, K. Sakata, T. Komatsu, M. Kunitake, Thermodynamic control of 2D bicomponent porous networks of melamine and melem: diverse hydrogen-bonded networks, J. Phys. Chem. C 117 (2013) 24815–24821.
[26] L. Grill, M. Dyer, L. Lafferentz, M. Persson, M.V. Peters, S. Hecht, Nano-architectures by covalent assembly of molecular building blocks, Nat. Nanotechnol. 2 (2007) 687–691.
[27] M. Matena, T. Riehm, M. Stöhr, T.A. Jung, L.H. Gade, Transforming surface coordination polymers into covalent surface polymers: linked polycondensed aromatics through oligomerization of N-heterocyclic carbene intermediates, Angew. Chem. Int. Ed. 47 (2008) 2414–2417.
[28] M.I. Veld, P. Iavicoli, S. Haq, D.B. Amabilino, R. Raval, Unique intermolecular reaction of simple porphyrins at a metal surface gives covalent nanostructures, Chem. Commun. (2008) 1536–1538.
[29] M. Bieri, M. Treier, J. Cai, K. Ait-Mansour, P. Ruffieux, O. Groning, Porous graphenes: two-dimensional polymer synthesis with atomic precision, Chem. Commun. (2009) 6919–6921.
[30] R. Gutzler, H. Walch, G. Eder, S. Kloft, W.M. Heckl, M. Lackinger, Surface mediated synthesis of 2D covalent organic frameworks: 1,3,5-tris(4-bromophenyl)benzene on graphite(001), Cu(111), and Ag(110), Chem. Commun. (2009) 4456–4458.

[31] J.A. Lipton-Duffin, O. Ivasenko, D.F. Perepichka, F. Rosei, Synthesis of polyphenylene molecular wires by surface-confined polymerization, Small 5 (2009) 592–597.
[32] N.A.A. Zwaneveld, R. Pawlak, M. Abel, D. Catalin, D. Gigmes, D. Bertin, Organized formation of 2D extended covalent organic frameworks at surfaces, J. Am. Chem. Soc. 130 (2008) 6678–6679.
[33] R. Coratger, B. Calmettes, M. Abel, L. Porte, STM observations of the first polymerization steps between hexahydroxy-tri-phenylene and benzene-di-boronic acid molecules, Surf. Sci. 605 (2011) 831–837.
[34] S. Weigelt, C. Bombis, C. Busse, M.M. Knudsen, K.V. Gothelf, E. Lægsgaard, Molecular self-assembly from building blocks synthesized on a surface in ultrahigh vacuum: kinetic control and topo-chemical reactions, ACS Nano 2 (2008) 651–660.
[35] S. Weigelt, C. Busse, C. Bombis, M.M. Knudsen, K.V. Gothelf, E. Lægsgaard, Surface synthesis of 2D branched polymer nanostructures, Angew. Chem. Int. Ed. 47 (2008) 4406–4410.
[36] J. Cai, P. Ruffieux, R. Jaafar, M. Bieri, T. Braun, S. Blankenburg, Atomically precise bottom-up fabrication of graphene nanoribbons, Nature 466 (2010) 470–473.
[37] R. Tanoue, R. Higuchi, N. Enoki, Y. Miyasato, S. Uemura, N. Kimizuka, Thermodynamically controlled self-assembly of covalent nanoarchitectures in aqueous solution, ACS Nano 5 (2011) 3923–3929.
[38] R. Tanoue, R. Higuchi, K. Ikebe, S. Uemura, N. Kimizuka, A.Z. Stieg, In situ STM investigation of aromatic poly(azomethine) arrays constructed by "on-site" equilibrium polymerization, Langmuir 28 (2012) 13844–13851.
[39] R. Tanoue, R. Higuchi, K. Ikebe, S. Uemura, N. Kimizuka, A.Z. Stieg, Thermodynamic self-assembly of two-dimensional π-conjugated metal-porphyrin covalent organic frameworks by "on-site" equilibrium polymerization, J. Nanosci. Nanotechnol. 3 (2014) 2211–2216.
[40] R. Tanoue, R. Higuchi, K. Ikebe, S. Uemura, N. Kimizuka, A.Z. Stieg, J.K. Gimzewskid, M. Kunitake, Positional selectivity of reversible azomethine condensation reactions at solid/liquid interfaces leading to supramolecule formation, J. Electroanal. Chem. 716 (2014) 145–149.
[41] M. Kunitake, Y. Deguchi, K. Kawatana, O. Manabe, N. Nakashima, Interfacial buffer effect' of self-assembled monolayers of a carboxylic acid terminated alkanethiol on a gold electrode, J. Chem. Soc. Chem. Commun. (1994) 563–564.
[42] H. Hoppe, T. Glatzel, M. Niggemann, A. Hinsch, M.C. Lux-Steiner, N.S. Sariciftci, Kelvin probe force microscopy study on conjugated polymer/fullerene bulk heterojunction organic solar cells, Nano Lett. 5 (2) (2005) 269–274.
[43] H. Hoppe, T. Glatzel, M. Niggemann, W. Schwinger, F. Schaeffler, A. Hinsch, M.C. Lux-Steiner, N. S. Sariciftci, Efficiency limiting morphological factors of MDMO-PPV:PCBM plastic solar cells, Thin Solid Films 511–512 (2006) 587–592.
[44] R. Higuchi, R. Tanoue, K. Sakaguchi, K. Yanai, S. Uemura, M. Kunitake, Vertically standing nanowalls of pristine poly(azomethine) on a graphite by chemical liquid deposition, Polymer (Guildf) 54 (2013) 3452–3457.
[45] R. Tanoue, R. Higuchi, K. Ikebe, S. Uemura, N. Kimizuka, A.Z. Stieg, J.K. Gimzewski, M. Kunitake, Positional selectivity of reversible azomethine condensation reactions at solid/liquid interfaces leading to supramolecular formation, J. Electroanal. Chem. 716 (2014) 145–149.
[46] M. Eddaoudi, D.B. Moler, H. Li, B. Chen, T.M. Reineke, M. O'Keeffe, O.M. Yaghi, Modular chemistry: secondary building units as a basis for the design of highly porous and robust metal-organic carboxylate frameworks, Acc. Chem. Res. 34 (2001) 319–330.
[47] N.L. Rosi, J. Eckert, M. Eddaoudi, D.T. Vodak, J. Kim, M. O'Keeffe, O.M. Yaghi, Hydrogen storage in microporous metal-organic frameworks, Science 300 (2003) 1127–1129.
[48] O.M. Yaghi, M. O'Keeffe, N.W. Ockwig, H.K. Chae, M. Eddaoudi, J. Kim, Reticular synthesis and the design of new materials, Nature 423 (2003) 705–714.
[49] H. Deng, J.C. Doonan, H. Furukawa, R.B. Ferreira, J. Towne, C.B. Knobler, B. Wang, O.M. Yaghi, Multiple functional groups of varying ratios in metal-organic frameworks, Science 327 (2010) 846–850.
[50] J.V. Barth, G. Costantini, K. Kern, Engineering atomic and molecular nanostructures at surfaces, Nature 437 (2005) 671–679.

[51] O. Shekhah, H. Wang, T. Strunskus, P. Cyganik, D. Zacher, R. Fischer, C. Wçll, Layer-by-layer growth of oriented metal organic polymers on a functionalized organic surface, Langmuir 23 (2007) 7440–7442.
[52] N. Lin, S. Stepanow, M.V. Ruben, J. Barth, Surface-confined supramolecular coordination chemistry, Top. Curr. Chem. 287 (2009) 1–44.
[53] D. Grumelli, B. Wurster, S. Stepanow, K. Kern, Bio-inspired nanocatalysts for the oxygen reduction reaction, Nat. Commun. 4 (2013) 2904.
[54] S. Vijayaraghavan, D. Ecija, W. Auw•rter, S. Joshi, K. Seufert, M. Drach, D. Nieckarz, P. Szabelski, C. Aurisicchio, D. Bonifazi, et al., Supramolecular assembly of interfacial nanoporous networks with simultaneous expression of metal-organic and organic-bonding motifs, Chem. Eur. J. 19 (2013) 14143–14150.
[55] S. Noro, S. Kitagawa, M. Kondo, K. Seki, A new, methane adsorbent, porous coordination polymer, Angew. Chem. Int. Ed. 39 (2000) 2081–2084.
[56] S. Noro, S. Kitagawa, M. Kondo, K. Seki, [{CuSiF6(4,4′-bipyridin)2}*n*], ein neues methanadsorbierendes poröses koordinationspolymer, Angew. Chem. Int. Ed. 11 (2000) 2161–2164.
[57] R. Kitaura, S. Kitagawa, Y. Kubota, T. Kobayashi, C.K. Kindo, Y. Mita, A. Matsuo, M. Kobayashi, H. Chang, T.C. Ozawa, et al., Formation of a one-dimensional array of oxygen in a microporous metal-organic solid, Science 298 (2002) 2358–2361.
[58] S. Kitagawa, R. Kitaura, S. Noro, Functional porous coordination polymers, Angew. Chem. Int. Ed. 43 (2004) 2334–2375.
[59] R. Matsuda, R. Kitaura, S. Kitagawa, Y. Kubota, R.V. Belosludov, T. Ozawa, C. Kobayashi, H. Sakamoto, T. Chiba, M. Takata, et al., Highly controlled acetylene accommodation in a metal-organic microporous material, Nature 436 (2005) 238–241.
[60] A. Dragsser, O. Shekhah, O. Zybaylo, C. Shen, M. Buck, C.D. Wçll, Schlettwein. Redox mediation enabled by immobilised centres in the pores of a metal-organic framework grown by liquid phase epitaxy, Chem. Commun. 48 (2012) 663–665.
[61] G. Lu, J.T. Hupp, Metal-organic frameworks as sensors: a ZIF-8 based fabry-pérot device as a selective sensor for chemical vapors and gases, J. Am. Chem. Soc. 132 (2010) 7832–7833.
[62] J. Zhuang, D. Ar, X. Yu, J. Liu, A. Terfort, A solvent-free hot-pressing method for preparing metal-organic-framework coatings, Adv. Mater. 25 (2013) 4631–4635.
[63] A.A. Talin, A. Centrone, A.C. Ford, M.E. Foster, V. Stavila, P. Haney, R.A. Kinney, V. Szalai, F.E. Gabaly, H.P. Yoon, et al., Tunable electrical conductivity in metal-organic framework thin-film devices, Science 343 (2014) 66–69.
[64] E. Redel, Z. Wang, S. Walheim, J. Liu, H. Gliemann, C. Wçll, On the dielectric and optical properties of surface-anchored metal-organic frameworks: a study on epitaxially grown thin films, Appl. Phys. Lett. 103 (2013) 91903–91905.
[65] J.T. Joyce, F.R. Laffir, C. Silien, Layer-by-layer growth and photocurrent generation in metal-organic coordination films, J. Phys. Chem. C 117 (2013) 12502–12509.
[66] T. Kambe, R. Sakamoto, T. Kusamoto, T. Pal, N. Fukui, K. Hoshiko, T. Shimojima, Z. Wang, T. Hirahara, K. Ishizaka, et al., Redox control and high conductivity of nickel Bis(dithiolene) complex π-nanosheet: a potential organic two-dimensional topological insulator, J. Am. Chem. Soc. 136 (2014) 14357–14360.
[67] K. Sakata, S. Kashiyama, G. Matsuo, S. Uemura, N. Kimizuka, M. Kunitake, Growth of Two-dimensional metal-organic framework nanosheet crystals on graphite substrates by thermal equilibrium treatment in acetic acid vapor, Chem. Nano Mater. 1 (2015) 259–263.
[68] N.S. John, C. Scherb, M. Shçe-eÀ, M.W. Anderson, M.P. Attfield, T. Bein, Single layer growth of sub-micron metal-organic framework crystals observed by in situatomic force microscopy, Chem. Commun. (2009) 6294–6296.
[69] P. Cubillas, M.W. Anderson, M.P. Attfield, Influence of isomorphous substituting cobalt ions on the crystal growth of the MOF-5 framework determined by atomic force microscopy of growing core-shell crystals, Cryst. Growth Des. 13 (2013) 4526–4532.

[70] T. Kambe, R. Sakamoto, K. Hoshiko, K. Takada, M. Miyachi, J. Ryu, S. Sasaki, J. Kim, K. Nakazato, M. Takata, et al., π-conjugated nickel bis(dithiolene) complex nanosheet, J. Am. Chem. Soc. 135 (2013) 2462–2465.
[71] Y. Ryousho, S. Sasaki, T. Nagamura, A. Takahara, T. Kajiyama, Anisotropic-to-isotropic change in lateral force at the surface of single-crystal lamellae of high-density polyethylene during low-temperature annealing, Macromolecules 37 (2004) 5115–5117.
[72] R. Higuchi, M. Hirano, M. Ashaduzzaman, N. Yilmaz, T. Sumino, D. Kodama, S. Chiba, S. Uemura, K. Nishiyama, A. Ohira, et al., Construction and characterization of "molecular nonwoven fabrics" consisting of crosslinked poly(γ-methyl-L-glutamate)", Langmuir 29 (2013) 7478–7487.
[73] R.L. Shuler, W.A. Zisma, A study of films of poly(7-methyl-L-glutamate) adsorbed on water using wave damping and other methods, Macromolecules 5 (1972) 487–492.
[74] H.L. Yakel, An X-ray diffraction investigation of poly-ε- carbobenzoxy-L-lysine and a complex form of poly-γ-methyl-L-glutamate, Acta Crystallogr. 6 (1953) 724–727.
[75] D.A. Bonnell, S.V. Kalinin, Scanning Probe Microscopy for Energy Research, World Scientific Publishing, Singapore, 2013.
[76] M. Watanabe, A.D. Tryk, M. Wakisaka, H. Yano, H. Uchida, Overview of recent developments in oxygen reduction electrocatalysis, Electrochim. Acta 84 (2012) 187–201.
[77] R.B. Cuenya, Synthesis and catalytic properties of metal nanoparticles: size, shape, support, composition, and oxidation state effects, Thin Solid Films 518 (2010) 3127–3150.
[78] N.M. Marković, P.N. Ross Jr., Surface science studies of model fuel cell electrocatalysts, Surf. Sci. Rep. 45 (2002) 117–229.
[79] A. Foelske-Schmitz, A. Peitz, V.A. Guzenko, D. Weingarth, G.G. Scherer, A. Wokaun, R. Kötz, In situ electrochemical STM study of platinum nanodot arrays on highly oriented pyrolythic graphite prepared by electron beam lithography, Surf. Sci. 606 (2012) 1922–1933.
[80] J. Inukai, D.A. Tryk, T. Abe, M. Wakisaka, H. Uchida, M. Watanabe, Direct STM elucidation of the effects of atomic-level structure on Pt(111) electrodes for dissolved CO oxidation, J. Am. Chem. Soc. 135 (2013) 1476–1490.
[81] A.M. F, U. Stimming, R. Vogel, Anion adsorption from sulfuric acid solutions on Pt(111) single crystal electrodes, J. Electroanal. Chem. 428 (1997) 47–153.
[82] A. Funtikov, U. Linke, U. Stimming, A. Vogel, An in situ STM study of anion adsorption on Pt(111) from sulfuric acid solutions, Surf. Sci. 324 (1995) L343–L348.
[83] Y. Shingaya, H. Matsumoto, H. Ogasawara, M. Ito, In situ and ex situ IRAS, LEED and EC-STM studies of underpotentially deposited copper on a Pt(111) electrode in sulfuric acid solution: coadsorption of sulfate ion with copper, Surf. Sci. 335 (1995) 23–31.
[84] Y. Kuo, W. Liao, S. Yau, Effects of anions on the electrodeposition of cobalt on Pt(111) electrode, Langmuir 30 (2014) 13890–13897.
[85] O.M. Magnussen, Ordered anion adlayers on metal electrode surfaces, Chem. Rev. 102 (2002) 679–726.
[86] M. Wakisaka, S. Asizawa, H. Uchida, M. Watanabe, In situ STM observation of morphological changes of the Pt(111) electrode surface during potential cycling in 10 mM HF solution, Phys. Chem. Chem. Phys. 12 (2010) 4184–4190.
[87] J. Omura, H. Yano, M. Watanabe, H. Uchida, Electrochemical quartz crystal microbalance analysis of the oxygen reduction reaction on Pt-based electrodes. Part 1. Effect of adsorbed anions on the oxygen reduction activities of Pt in HF, $HClO_4$, and H_2SO_4 solutions, Langmuir 27 (2011) 6464–6470.
[88] O' Hayrea, F.B. Prinza, The air/platinum/nafion triple-phase boundary: characteristics, scaling, and implications for fuel cells, J. Electrochem. Soc. 151 (2004) A756–A762.
[89] Y. Onochi, N. Hoshi, Atomic force microscopy of the dissolution of cubic and tetrahedral Pt nanoparticles in electrochemical environments, J. Phys. Chem. C 116 (2012) 15134–15140.
[90] N. Hoshi, M. Nakamura, A. Hitotsuyanagi, Active site for the oxygen reduction reaction on the high index planes of Pt, Electrochim. Acta 112 (2013) 899–904.

[91] N. Hoshi, M. Nakamura, C. Yoshida, Y. Yamada, M. Kameyama, Y. Mizumoto, In situ high-speed AFM of shape-controlled Pt nanoparticles in electrochemical environments: structural effects on the dissolution mechanism, Electrochem. Commun. 72 (2016) 5–9.
[92] T. Masuda, F. Sonsudin, P.R. Singh, H. Naohara, K. Uosaki, Potential-dependent adsorption and desorption of perfluorosulfonated ionomer on a platinum electrode surface probed by electrochemical quartz crystal microbalance and atomic force microscopy, J. Phys. Chem. C 117 (2013) 15704–15709.
[93] J. Wu, H. Yang, Platinum-based oxygen reduction electrocatalysts, Acc. Chem. Res. 46 (2013) 1848–1857.
[94] H. Zhang, P.K. Shen, Recent development of polymer electrolyte membranes for fuel cells, Chem. Rev. 112 (2012) 2780–2832.
[95] K.A. Mauritz, R.B. Moore, State of understanding of Nafion, Chem. Rev. 104 (2004) 4535–4585.
[96] M.A. Hickner, H. Ghassemi, Y.S. Kim, B.R. Einsla, J.E. McGrath, Alternative polymer systems for proton exchange membranes, Chem. Rev. 104 (2004) 4587–4612.
[97] R. Souzy, B. Ameduri, Functional fluoropolymers for fuel cell membranes, Prog. Polym. Sci. 30 (2005) 644–687.
[98] V. Arcella, C. Troglia, A. Ghielmi, Hyflon ion membranes for fuel cells, Ind. Eng. Chem. Res. 44 (2005) 7646–7651.
[99] S. Banerjee, D.E. Curtin, Nafion® perfluorinated membranes in fuel cells, J. Fluor. Chem. 125 (2004) 1211–1216.
[100] N. Yoshida, T. Ishisaki, A. Watakabe, M. Yoshitake, Characterization of Flemion® membranes for PEFC, Electrochim. Acta 43 (1998) 3749–3754.
[101] A. Carbone, R. Pedicini, G. Portale, A.D. Longoc, L. Ilario, E. Passalacqua, Sulphonated poly(ether ether ketone) membranes for fuel cell application: thermal and structural characterisation, J. Power Sources 163 (2006) 18–26.
[102] H. Dai, R. Guan, C. Li, J. Liu, Development and characterization of sulfonated poly(ether sulfone) for proton exchange membrane materials, Solid State Ionics 178 (2007) 339–345.
[103] W.L. Harrison, M.A. Hickner, Y.S. Kim, M.J. E, Poly(arylene ether sulfone) copolymers and related systems from disulfonated monomer building blocks: synthesis, characterization, and performance—a topical review, Fuel cells 5 (2005) 201–212.
[104] R. Jiang, H.R. Kunz, J.M. Fenton, Investigation of membrane property and fuel cell behavior with sulfonated poly(ether ether ketone) electrolyte: temperature and relative humidity effects, J. Power Sources 150 (2005) 120–128.
[105] D.J. Jones, J. Rozière, K.D. Kreuer, On the development of proton conducting polymer membranes for hydrogen and methanol fuel cells, J. Memb. Sci. 185 (2001) 29–39.
[106] M.S. Kanga, Y.J. Choi, I.J. Choi, T.H. Yoon, S.H. Moon, Electrochemical characterization of sulfonated poly(arylene ether sulfone) (S-PES) cation-exchange membranes, J. Memb. Sci. 216 (2003) 39–53.
[107] K. Miyatake, Y. Chikashige, E. Higuchi, M. Watanabe, Tuned polymer electrolyte membranes based on aromatic polyethers for fuel cell applications, J. Am. Chem. Soc. 129 (2007) 3879–3887.
[108] N. Asano, M. Aoki, S. Suzuki, K. Miyatake, H. Uchida, M. Watanabe, Aliphatic/aromatic polyimide ionomers as a proton conductive membrane for fuel cell applications, J. Am. Chem. Soc. 128 (2006) 1762–1769.
[109] K. Miyatake, Y. Chikashige, M. Watanabe, Novel sulfonated poly(arylene ether): a proton conductive polymer electrolyte designed for fuel cells, Macromolecules 36 (2003) 9691–9693.
[110] J. Fang, X. Guo, S. Harada, T. Watari, K. Tanaka, H. Kita, K. Okamoto, Novel sulfonated polyimides as polyelectrolytes for fuel cell application. 1. Synthesis, proton conductivity, and water stability of polyimides from 4,4′-diaminodiphenyl ether-2,2′-disulfonic acid, Macromolecules 35 (2002) 9022–9028.
[111] S. Wu, Z. Qiu, S. Zhang, X. Yang, F. Yang, Z. Li, The direct synthesis of wholly aromatic poly(p-phenylene)s bearing sulfobenzoyl side groups as proton exchange membranes, Polymer (Guildf) 47 (2006) 6993–7000.
[112] H. Fujimoto, M.A. Hickner, C.J. Cornelius, D.A. Loy, Ionomeric poly(phenylene) prepared by Diels-Alder polymerization: synthesis and physical properties of a novel polyelectrolyte, Macromolecules 38 (2005) 5010.
[113] M. Rikukawa, K. Sanui, Proton-conducting polymer electrolyte membranes based on hydrocarbon polymers, Prog. Polym. Sci. 25 (2000) 1463–1502.

[114] H. Wang, A.S. Badami, A. Roy, J.E. McGrath, Multiblock copolymers of poly(2,5-benzophenone) and disulfonated poly(arylene ether sulfone) for proton-exchange membranes. I. Synthesis and characterization, J. Polym. Sci. A Polym. Chem. 45 (2007) 284–294.
[115] H.S. Lee, A.S. Badami, A. Roy, J.E. McGrath, You have full text access to this contentSegmented sulfonated poly(arylene ether sulfone)-B-polyimide copolymers for proton exchange membrane fuel cells. I. Copolymer synthesis and fundamental properties, J. Polym. Sci. A Polym. Chem. 45 (2007) 4879–4890.
[116] A. Roy, M.A. Hickner, X. Yu, Y. Li, T.E. Glass, J.E. McGrath, Influence of chemical composition and sequence length on the transport properties of proton exchange membranes, J. Polym. Sci. B Polym. Phys. 44 (2006) 2226–2239.
[117] B. Bae, T. Yoda, K. Miyatake, H. Uchida, M. Watanabe, Proton-conductive aromatic ionomers containing highly sulfonated blocks for high-temperature operable fuel cells, Angew. Chem. Int. Ed. 49 (2010) 317–320.
[118] Y.A. Elabd, M.A. Hickner, Block copolymers for fuel cells, Macromolecules 44 (2011) 1–11.
[119] K. Umezawa, T. Oshima, M. Yoshizawa-Fujita, Y. Takeoka, M. Rikukawa, Synthesis of hydrophilic-hydrophobic block copolymer ionomers based on polyphenylenes, ACS Macro Lett. 1 (2012) 969–972.
[120] K.D. Kreuer, S.J. Paddison, E. Spohr, M. Schuster, Transport in proton conductors for fuel-cell applications: simulations, elementary reactions, and phenomenology, Chem. Rev. 104 (2004) 4637–4678.
[121] J.R. O'Dea, S.K. Buratto, Phase imaging of proton exchange membranes under attractive and repulsive tip-sample interaction forces, J. Phys. Chem. B 115 (2011) 1014–1020.
[122] K. Umemura, T. Wang, M. Hara, R. Kuroda, O. Uchida, M. Nagai, Nanocharacterization and nanofabrication of a Nafion thin film in liquids by atomic force microscopy, Langmuir 22 (2006) 3306–3312.
[123] P.J. James, M. Antognozzi, J. Tamayo, T.J. McMaster, J.M. Newton, M.J. Miles, Interpretation of contrast in tapping mode AFM and shear force microscopy. A study of Nafion, Langmuir 17 (2001) 349–360.
[124] R.S. McLean, M. Doyle, B.B. Sauer, High-resolution imaging of ionic domains and crystal morphology in ionomers using AFM techniques, Macromolecules 33 (2000) 6541–6550.
[125] R. Hiesgen, I. Wehl, E. Aleksandrova, E. Roduner, A. Bauder, K.A. Friedrich, Nanoscale properties of polymer fuel cell materials—a selected review, Int. J. Energy Res. 34 (2010) 1223–1238.
[126] N. Takimoto, A. Ohira, Y. Takeoka, M. Rikukawa, Surface Morphology and Proton Conduction Imaging of Nafion Membrane, Chem. Lett. 37 (2008) 164–165.
[127] N. Takimoto, L. Wu, A. Ohira, Y. Takeoka, M. Rikukawa, Hydration behavior of perfluorinated and hydrocarbon-type proton exchange membranes: relationship between morphology and proton conduction, Polymer (Guildf) 50 (2009) 534–540.
[128] M.A. Barique, S. Seesukphronrarak, L. Wu, A. Ohira, A comparison between highly crystalline and low crystalline poly(phenylene sulfide) as polymer electrolyte membranes for fuel cells, J. Phys. Chem. B 115 (2011) 27–33.
[129] N. Takimoto, S. Takamuku, M. Abe, A. Ohira, H.S. Lee, J.E. McGrath, Conductive area ratio of multiblock copolymer electrolyte membranes evaluated by E-AFM and its impact on fuel cell performance, J. Power Sources 194 (2009) 662–667.
[130] A. Ohira, S. Kuroda, H.F.M. Mohamed, B. Tavernier, Effect of interface on surface morphology and proton conduction of polymer electrolyte thin films, Phys. Chem. Chem. Phys. 15 (2013) 11494–11500.
[131] M. Hara, D. Hattori, J. Inukai, B. Bae, T. Hoshi, M. Hara, K. Miyatake, M. Watanabe, Imaging individual proton-conducting spots on sulfonated multiblock-copolymer membrane under controlled hydrogen atmosphere by current-sensing atomic force microscopy, J. Phys. Chem. B 117 (2013) 3892–3899.
[132] C.W. Tang, Two-layer organic photovoltaic cell, Appl. Phys. Lett. 48 (1986) 183.
[133] A.K. Ghosh, T. Feng, Merocyanine organic solar cells, J. Appl. Phys. 49 (1978) 5982–5989.
[134] B. Maennig, J. Drechsel, D. Gebeyehu, P. Simon, F. Kozlowski, A. Werner, F. Li, S. Grundmann, S. Sonntag, M. Koch, et al., Organic P-I-N solar cells, Appl. Phys. A 79 (1) (2004) 1–14.
[135] G. Yu, J. Gao, J.C. Hummelen, F. Wudl, A.J. Heeger, Polymer photovoltaic cells - enhanced efficiencies Via a network of internal donor-acceptor heterojunctions, Science 270 (5243) (1995) 1789–1791.
[136] S. Günes, H. Neugebauer, N.S. Sariciftci, Conjugated polymer-based organic solar cells, Chem. Rev. 107 (4) (2007) 1324–1338.

[137] M.S. Kim, J.S. Kim, J.C. Cho, M. Shtein, L.J. Guo, J. Kim, Flexible conjugated polymer photovoltaic cells with controlled heterojunctions fabricated using nanoimprint lithography, Appl. Phys. Lett. 90 (2007) 123113.
[138] D.C. Olson, J. Piris, R.T. Collins, S.E. Shaheen, D.S. Ginley, Hybrid photovoltaic devices of polymer and ZnO nanofiber composites, Thin Solid Films 496 (1) (2006) 26–29.
[139] W. Melitz, J. Shen, A.C. Kummel, S. Lee, Kelvin probe force microscopy and its application, Surf. Sci. Rep. 66 (1) (2011) 1–27.
[140] V. Palermo, M. Palma, P. Samori, Electronic characterization of organic thin films by kelvin probe force microscopy, Adv. Mater. 18 (2) (2006) 145–164.
[141] L. Kelvin, No title, Philos. Mag. 46 (1898) 82.
[142] H.M. Rosenberg, The Solid State, Oxford, Clarendon, UK, 1975.
[143] M. Pruton, Introduction to Surface Physics, Oxford University Press, New York, 1994.
[144] W.A. Zisman, A new method of measuring contact potential differences in metals, Rev. Sci. Instrum. 3 (1932) 367.
[145] M. Nonnenmacher, M.P. O'Boyle, H.K. Wickramasinghe, Kelvin probe force microscopy, Appl. Phys. Lett. 58 (1991) 2921.
[146] L. Kronik, Y. Shapira, Surface photovoltage phenomena: theory, experiment, and applications, Surf. Sci. Rep. 37 (1) (1999) 1–206.
[147] D.K. Schroder, Surface voltage and surface photovoltage: history theory and applications, Meas. Sci. Technol. 12 (3) (2001) R16–R31.
[148] G. Koley, M.G. Spencer, H.R. Bhangale, Cantilever effects on the measurement of electrostatic potentials by scanning kelvin probe microscopy, Appl. Phys. Lett. 79 (2001) 545.
[149] O. Cherniavskaya, L. Chen, V. Weng, L. Yuditsky, L.E. Brus, Quantitative noncontact electrostatic force imaging of nanocrystal polarizability, J. Phys. Chem. B 107 (7) (2003) 1525–1531.
[150] S.E. Shaheen, C.J. Brabec, N.S. Sariciftci, F. Padinger, T. Fromherz, J.C. Hummelen, 2.5% efficient organic plastic solar cells, Appl. Phys. Lett. 78 (2001) 841.
[151] J.K.J. Van Duren, X. Yang, J. Loos, C.W.T. Bulle-Lieuwma, A.B. Sieval, J.C. Hummelen, R.A.J. Janssen, Relating the morphology of poly(p-phenylene vinylene)/methanofullerene blends to solar-cell performance, Adv. Funct. Mater. 14 (5) (2004) 425–434.
[152] T. Martens, J. D'Haen, T. Munters, Z. Beelen, L. Goris, J. Manca, M. D'Olieslaeger, D. Vanderzande, L. De Schepper, R. Andriessen, Disclosure of the nanostructure of MDMO-PPV:PCBM bulk hetero-junction organic solar cells by a combination of SPM and TEM, Synth. Met. 138 (1–2) (2003) 243–247.
[153] M. Chiesa, L. Bu, J. Kim, R. Shikler, R.H. Friend, Correlation between surface photovoltage and blend morphology, Nano Lett. 5 (2005) 559–563.
[154] S. Watanabe, Y. Fukuchi, M. Fukasawa, T. Sassa, M. Uchiyama, T. Yamashita, M. Matsumoto, T. Aoyama, Electron donor and acceptor spatial distribution in structured bulk heterojunction photovoltaic devices induced by periodic photopolymerization, Langmuir 28 (28) (2012) 10305–10309.
[155] S. Watanabe, T. Aoyama, Y. Fukuchi, T. Sassa, T. Yamashita, M. Matsumoto, T. Wada, KPFM observation for photo-assisted formation of donor-acceptor spatial distribution in organic photovoltaic devices, J. Photopolym. Sci. Technol. 22 (5) (2009) 571–574.
[156] J.D. McNeill, P.F. Barbara, NSOM investigation of carrier generation, recombination, and drift in a conjugated polymer, J. Phys. Chem. B 106 (18) (2002) 4632–4639.
[157] A. Cadby, R. Dean, A.M. Fox, R.A.L. Jones, D.G. Lidzey, Mapping the fluorescence decay lifetime of a conjugated polymer in a phase-separated blend using a scanning near-field optical microscope, Nano Lett. 5 (11) (2005) 2232–2237.
[158] R. Riehn, R. Stevenson, D. Richards, D.J. Kang, M. Blamire, A. Downes, F. Cacialli, Local probing of photocurrent and photoluminescence in a phase-separated conjugated-polymer blend by means of near-field excitation, Adv. Funct. Mater. 16 (4) (2006) 469–476.
[159] C.R. McNeill, H. Frohne, J.L. Holdsworth, P.C. Dastoor, Near-field scanning photocurrent measurements of polyfluorene blend devices: directly correlating morphology with current generation, Nano Lett. 4 (12) (2004) 2503–2507.

[160] J.A. DeAro, D. Moses, S.K. Buratto, Near-field photoconductivity of stretch-oriented poly(para-phenylene vinylene), Appl. Phys. Lett. 75 (1999) 3814.
[161] D.C. Coffey, D.S. Ginger, Time-resolved electrostatic force microscopy of polymer solar cells, Nat. Mater. 5 (2006) 735–740.
[162] D.C. Coffey, O.G. Reid, D.B. Rodovsky, G.P. Bartholomew, D.S. Ginger, Mapping local photocurrents in polymer/fullerene solar cells with photoconductive atomic force microscopy, Nano Lett. 7 (3) (2007) 738–744.
[163] M. Guide, X.D. Dang, T.Q. Nguyen, Nanoscale characterization of tetrabenzoporphyrin and fullerene-based solar cells by photoconductive atomic force microscopy, Adv. Mater. 23 (20) (2011) 2313–2319.
[164] L.S.C. Pingree, B.A. MacLeod, D.S. Ginger, The changing face of PEDOT : PSS films: substrate, bias, and processing effects on vertical charge transport, J. Phys. Chem. C 112 (2008) 7922–7927.
[165] M. Brumbach, P.A. Veneman, F.S. Matrikar, T. Schulmeyer, A. Simmonds, W. Xia, P. Lee, N.R. Armstrong, Surface composition and electrical and electrochemical properties of freshly deposited and acid-etched indium tin oxide electrodes, Langmuir 23 (22) (2007) 11089–11099.
[166] Y. Kutes, B.A. Aguirre, J.L. Bosse, J.L. Cruz-Campa, D. Zubia, B.D. Huey, Mapping photovoltaic performance with nanoscale resolution, Prog. Photovolt Res. Appl. 2016 (24) (2013) 315–325.
[167] A. Liscio, G. De Luca, F. Nolde, V. Palermo, K. Müllen, P. Samorì, Photovoltaic charge generation visualized at the nanoscale: a proof of principle, J. Am. Chem. Soc. 130 (3) (2008) 780–781.
[168] V. Palermo, M.B.J. Otten, A. Liscio, E. Schwartz, P.A.J. De Witte, M.A. Castriciano, M.M. Wienk, F. Nolde, G. De Luca, J.J.L.M. Cornelissen, et al., The relationship between nanoscale architecture and function in photovoltaic multichromophoric arrays as visualized by Kelvin probe force microscopy, J. Am. Chem. Soc. 130 (44) (2008) 14605–14614.
[169] K. Maturova, M. Kemerink, M.M. Wienk, D.S.H. Charrier, R.a.J. Janssen, K. Maturová, Scanning Kelvin probe microscopy on bulk heterojunction polymer blends, Adv. Funct. Mater. 19 (9) (2009) 1379–1386.
[170] E.J. Spadafora, R. Demadrille, B. Ratier, B. Grévin, Imaging the carrier photogeneration in nanoscale phase segregated organic heterojunctions by kelvin probe force microscopy, Nano Lett. 10 (9) (2010) 3337–3342.
[171] B. Grévin, P.-O. Schwartz, L. Biniek, M. Brinkmann, N. Leclerc, E. Zaborova, S. Méry, High-resolution noncontact AFM and Kelvin probe force microscopy investigations of self-assembled photovoltaic donor-acceptor dyads, Beilstein J. Nanotechnol. 7 (2016) 799–808.
[172] S. Watanabe, Y. Fukuchi, M. Fukasawa, T. Sassa, A. Kimoto, Y. Tajima, M. Uchiyama, T. Yamashita, M. Matsumoto, T. Aoyama, In situ KPFM imaging of local photovoltaic characteristics of structured organic photovoltaic devices, ACS Appl. Mater. Interfaces 6 (3) (2014) 1481–1487.
[173] A. Kikukawa, S. Hosaka, R. Imura, Silicon Pn junction imaging and characterizations using sensitivity enhanced Kelvin probe force microscopy, Appl. Phys. Lett. 66 (1995) 3510.
[174] M. Tanimoto, O. Vatel, Kelvin probe force microscopy for characterization of semiconductor devices and processes, J. Vac. Sci. Technol. B 14 (1996) 1547.
[175] R. Shikler, N. Fried, T. Meoded, Y. Rosenwaks, Measuring minority-carrier diffusion length using a kelvin probe force microscope, Phys. Rev. B 61 (2000) 11041.
[176] S. Sadewasser, T. Glatzel, S. Schuler, S. Nishiwaki, R. Kaigawa, M.C. Lux-Steiner, Kelvin probe force microscopy for the nano scale characterization of chalcopyrite solar cell materials and devices, Thin Solid Films 431–432 (3) (2003) 257–261.
[177] S.A. Galloway, P.R. Edwards, K. Durose, Characterisation of thin film CdS/CdTe solar cells using electron and optical beam induced current, Sol. Energy Mater. Sol. Cells 57 (1) (1999) 61–74.
[178] S. Smith, P. Zhang, T. Gessert, A. Mascarenhas, Near-field optical beam-induced currents in CdTe/CdSCdTe/CdS solar cells: direct measurement of enhanced photoresponse at grain boundaries, Appl. Phys. Lett. 85 (2004) 3854–3856.
[179] I. Visoly-Fisher, S.R. Cohen, A. Ruzin, D. Cahen, How polycrystalline devices can outperform single-crystal ones: thin film CdTe/CdS solar cells, Adv. Mater. 16 (11) (2004) 879–883.
[180] M.M. Lee, J. Teuscher, T. Miyasaka, T.N. Murakami, H.J. Snaith, Efficient hybrid solar cells based on meso superstructured organometal halide perovskites, Science 338 (2012) 643–647.
[181] J. Burschka, N. Pellet, S.-J. Moon, R. Humphry-Baker, P. Gao, M.K. Nazeeruddin, M. Grätzel, Sequential deposition as a route to high-performance perovskite-sensitized solar cells, Nature 499 (7458) (2013) 316–320.

[182] M. Liu, M.B. Johnston, H.J. Snaith, Efficient planar heterojunction perovskite solar cells by vapour deposition, Nature 501 (7467) (2013) 395–398.
[183] Z. Zhao, X. Chen, H. Wu, X. Wu, G. Cao, Probing the photovoltage and photocurrent in perovskite solar cells with nanoscale resolution, Adv. Funct. Mater. (2016) 3048–3058.
[184] V.W. Bergmann, Y. Guo, H. Tanaka, I.M. Hermes, D. Li, A. Klasen, S.A. Bretschneider, E. Nakamura, R. Berger, S.A.L. Weber, Local time-dependent charging in a perovskite solar cell, ACS Appl. Mater. Interfaces 8 (30) (2016) 19402–19409.

CHAPTER 4

Surface-Enhanced Spectroscopy for Surface Characterization

Masaki Ujihara[1], **Toyoko Imae**

National Taiwan University of Science and Technology, Taipei, Taiwan
[1]*Corresponding author*

4.1 Introduction

It has been known from the Roman era that gold and silver compounds can stain glass [1]. In the middle of 19th century, Faraday found the size dependency on the colorization of colloidal gold; however, he could not interpret this phenomenon [2]. Today, the colors of gold and silver nanoparticles are understood as the results of interaction between free electrons in the nanoparticles and the incident light, and the group motion of free electrons in the nanoparticles is named "localized surface plasmon" [3]. The behaviors of localized surface plasmon are being investigated within the fields of electronics and optics, and this is itself developing as a field of science and technology named plasmonics [4,5]. An important application of plasmonics is ultrasensitive spectroscopy. The localized surface plasmon can resonate with incident light and provide a strong electric field in the vicinity of metallic nanoparticles [3]. The intensified electric field can interact with surrounding materials, allowing the enhanced spectrum to be observed. Therefore, this interaction is called "surface-enhanced spectroscopy" [6]. This method is now applied in various spectroscopies, such as Raman spectroscopy [7,8], infrared (IR) absorption spectroscopy [9], and fluorescence spectroscopy [10]. In this chapter, we focus on these surface-enhanced spectroscopies.

Historically, a unique enhancing effect of a roughened silver surface in Raman spectroscopies was first reported in 1974 [11]. In this study, the silver surface was electrically treated to extend its surface area and to allow more adsorption than the plain surface. The Raman spectra obtained from the rough surface indicated strong Raman signals from pyridine molecules adsorbed on the silver surface. First, the enhanced Raman scattering was associated with an increased amount of adsorption, as the researcher intended. However, the intensity ratios of Raman scattering differed from those in bulk solution. This difference was attributed to the coordination of pyridine molecules onto the charged surfaces. In 1977, another mechanism of enhancement was proposed: the localized surface plasmon intensified the Raman scattering

Nanolayer Research. http://dx.doi.org/10.1016/B978-0-444-63739-0.00004-9

[12,13]. This mechanism was widely accepted, and since then, effective nanostructures have been designed to maximize the plasmonic effects. Some studies report the single-molecule measurement adsorbed on the silver nanoparticle, and in this case, the enhancement was higher than 10^{14} times [14,15]. The theory of surface-enhanced Raman spectroscopy has also been developed, and the extremely high enhancement can be explained as the two-fold resonances of the localized surface plasmon with light (resonances between excitation light-plasmon and plasmon-emission light) and the resonance with the adsorbed molecules [16,17].

As mentioned above, the surface-enhancing effect has also been examined for the other spectroscopies. For the IR absorption spectra, the enhancements are generally at the order of $\sim 10^3$ [9]. The IR light can't resonate with the localized surface plasmon well because their frequencies differ substantially, and the enhancement in the emission doesn't occur. However, IR absorption spectroscopy is intrinsically much more sensitive than Raman spectroscopy, so measurement of single-molecule level can be realized in surface-enhanced IR absorption spectroscopy (SEIRAS) using a specially designed antenna (a study reported the enhancing of 12,000) [18]. Fluorescence spectroscopy also enables observation at the single-molecule level for similar reasons [19]. However, the fluorescence on the nanoparticles can be quenched, which suggests energy transfers between the localized surface plasmon and the emission light. The idea of chemiluminescence enhancement by the metallic nanoparticles was suggested by this energy transfer mechanism, and has been applied to chemiluminescence analysis [20,21].

Thus, the "surface-enhanced" phenomenon using metallic nanostructures has developed beyond the field of spectroscopy. Today, enhancement caused by the interaction between the localized surface plasmon and light is applicable to the photoelectric devices [22] and photochemical reactors [23]. In this chapter, surface-enhancing nanostructures and physicochemical phenomena associated with them will be discussed, and practical technologies involved in surface-enhanced spectroscopies will be explained. Moreover, recent applications using the interaction between localized surface plasmon and light will be touched.

4.2 Types of Surface-Enhanced Spectroscopies

Surface-enhanced spectroscopies are based on two enhancing mechanisms: the intensification of an electric field by metallic nanostructures, and the charge transfer between the metal surface and the adsorbates. In this section, these mechanisms are explained.

When a metallic nanoparticle is exposed in an electromagnetic field (light), free electrons in the nanoparticle are oscillated by the external electric field as their collective motion (localized surface plasmon) (Fig. 4.1).

The polarization of nanoparticles can be described as in Eq. (4.1). The dielectric constant of metal depends on the nanoparticles' size and frequency (ω) (Eqs. 4.2, 4.3). Then, the dipole moment caused by the electromagnetic field (polariton) can be coupled with the localized

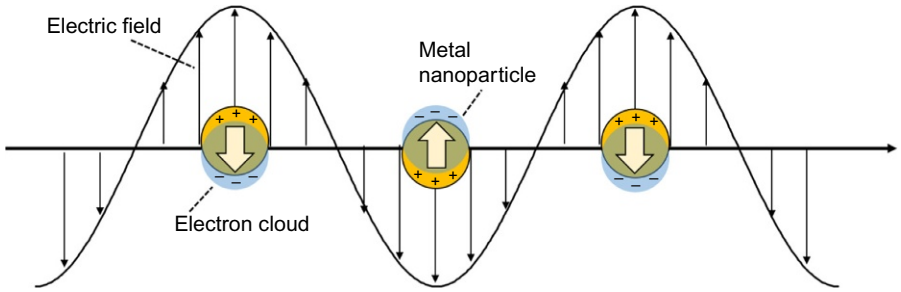

Fig. 4.1
A schematic of interaction between incident light and metal nanoparticles. *Arrows* in nanoparticles represent the polarization of nanoparticles.

surface plasmon as the localized plasmon polariton at a certain frequency to maximize polarization [1,24].

$$\alpha = \frac{4}{3}\pi abc \frac{\varepsilon - \varepsilon_m}{\varepsilon_m + L_i(\varepsilon - \varepsilon_m)} \tag{4.1}$$

α is the polarizability
a, b, and c are the radius of metal nanoparticle along principal axes
ε and ε_m are the dielectric constant of metal and surrounding medium, respectively
L_i is the geometrical depolarization factors, index i is principal axes and $\Sigma L_i = 1$

$$\omega_p{}^2 = Ne^2/\varepsilon_0 m_e \tag{4.2}$$

$$\varepsilon = 1 - \omega_p{}^2/\left(\omega^2 + i\gamma\omega\right) \tag{4.3}$$

ω_p is the plasmon velocity of bulk metal
N is the electron density
e is the elementary charge
ε_0 is the dielectric constant of vacuum space
m_e is the effective electron mass
γ is the relaxation frequency

The localized surface plasmon polariton is constrained in the nanoparticle, and its dispersion relation can't match with that of the light in the surrounding medium. Then, the electromagnetic field generated in the nanoparticle can't be propagative in the surrounding medium; the intensity of electromagnetic field decreases inversely with the triplet of distance from the particle center: $a^3/(a+d)^6$, where a is radius of the nanoparticle and d is the distance from surface of nanoparticle [3,25]. This means that the electric field is concentrated in the vicinity of the nanoparticle. Therefore, the adsorbed molecules on the nanoparticle can be strongly excited

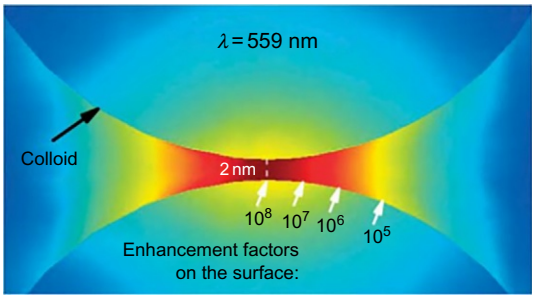

Fig. 4.2

A simulated image of hot-site generated in the gap of two gold nanoparticles and its enhancing effect in the gap of 2 nm [30]. *Modified from P.G. Etchegoin, E.C.L. Ru, A perspective on single molecule SERS: current status and future challenges, Phys. Chem. Chem. Phys. 10 (2008) 6079–6089. PCCP Owner.*

by the concentrated electric field on the nanoparticle. In this case, the enhancement in the electric field is at the order of 10 to 10^3 [26].

A set of two nanoparticles allows a polarization of the localized surface plasmon in their gap, as the two electrodes in a capacitor (Fig. 4.2).

The electric field is more concentrated in the gap, and the enhancement becomes stronger for the adsorbates in the gap. The electric field can be concentrated typically at an order of $10^{5–6}$, which differs by the distance between the nanoparticles, as their interaction decreases at longer distances [27]. This "nanodimer" is a basic structure for surface-enhanced spectroscopies [28–30], and arrangements of nanoparticles are important for surface-enhanced spectroscopy. Another structure contributing to the surface-enhanced spectroscopies is taper structures. The electric field concentrates at the tip of metallic nanostructures, in what is known as the "lightning-rod effect" [27,31–33]. The degree of concentration depends on the aspect ratio of the projections in nanostructures, and the adsorbates on the tips are strongly excited. These structures (nanogaps and tips) are called "hot sites" (or "hot spots") (Fig. 4.3) [27,34]. To prepare hot sites, the simplest method is to use agglomeration of nanoparticles. More precisely, the nanostructures can be designed by chemical and physical methods. These methods will be discussed in Section 4.3.

Raman spectroscopy is generally of low sensitivity: the scattering cross-section is $\sim 10^{-30}$ to 10^{-25} cm^2, and it is much smaller than that of fluorescence (from 10^{-16}) [14,35,36]. Therefore, surface-enhancement is especially important for Raman spectroscopy. According to the two-fold enhancing mechanism (Eq. 4.4) [16], the magnitude of enhancement (M) in Raman scattering is described by both excitation (factor of M_1) and emission (factor of M_2) processes via resonance with localized surface plasmon.

$$M(\lambda_L, \lambda) = \left|\frac{E^{loc}(\lambda_L)}{E^I(\lambda_L)}\right|^2 \times \left|\frac{E^{loc}(\lambda)}{E^I(\lambda)}\right|^2 = M_1(\lambda_L) M_2(\lambda) \tag{4.4}$$

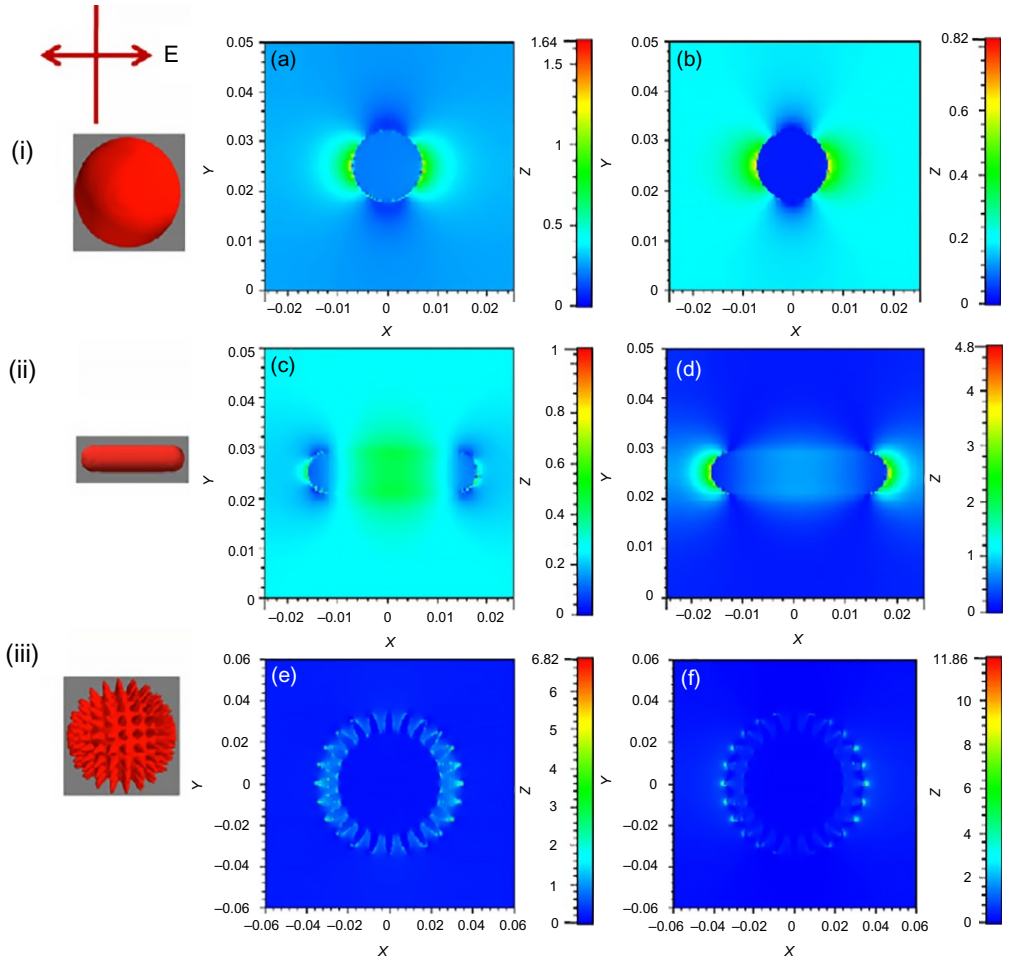

Fig. 4.3

3D FDTD simulations on the electromagnetic field distributions of gold ((i): (a), (b) spherical, (ii): (c), (d) nanorod, (iii): (e), (f) nanostar). Excitation wavelengths are 532 nm (a, c, e), and 785 nm (b, d, f) [34]. *Modified from M. Li, S.K. Cushing, J. Zhang, J. Lankford, Z.P. Aguilar, D. Ma, N. Wu, Shape-dependent surface-enhanced Raman scattering in gold–Raman-probe–silica sandwiched nanoparticles for biocompatible applications, Nanotechnology 23 (2012) 115501. Institute of Physics – Journals.*

M is the enhancing factor of electric field intensity
λ_L and λ are the wavelengths of excitation and emission, respectively
E^{loc} and E^{I} are the intensity of a local field and a far field, respectively

Moreover, the effective enhancement is achieved via the resonance of surface plasmon with both of lights (excitation and emission) and the molecular Raman band of adsorbed molecules [14,37–40]. This surface-enhanced resonance Raman scattering can lead to enhancement of

$\sim 10^{14}$, as demonstrated in the single-molecule measurement of rhodamine 6G adsorbed on silver nanoparticles [14,15]. To this ultrahigh enhancement, the contribution of concentrated electric field (electromagnetic effect) is estimated to be in the order of 10^8 to 10^{11}, and the additional effects of resonance (10^3 to 10^4) and charge transfer effects ($\sim 10^3$) can be considered [26,27].

For IR absorption spectroscopy, the contribution of resonance effects is relatively small, because of the mismatched frequencies between the excitation light and the localized surface plasmon. The enhancement in the IR absorption is instead induced by the polarization of metal nanostructures, which causes oscillation of dipole moments of adsorbed molecules [9]. That is, the metal nanostructure can absorb the light more than the molecules, and the molecules in hot spots are polarized much more strongly than in other locations. This polarization of molecules perturbs the dipole moment of metal nanostructures. Then, the IR absorption spectra are amplified. This mechanism is supported by the low dependency of wavelength on the enhancement. The enhancement can be caused by a thick film ($\sim$20 nm) which has metallic luster [41]. This low dependency could be preferable for IR absorption spectroscopy, which uses a wide range of incident light (700–4000 cm^{-1}, typically). Besides the electromagnetic effects, a charge transfer effect using a conducting polymer is also suggested. This effect can be useful to understand the charged-carrier transfers in materials [42].

In contrast, surface-enhanced fluorescence spectroscopy depends on the resonance of surface plasmon with light and molecular bands [19,25,43–47]. A concentrated electric field can improve the excitation probability of fluorescent molecules, and emission is also strengthened by metal nanoparticles: energy transfers from the excited molecules to the metallic nanoparticles allows an effective emission [43]. This emission is strongly polarized by the oriented film of gold nanorods, which suggests that the nanorods worked as an antenna to emit the light [19]. That is, there is a two-step enhancing mechanism as in Raman scattering [16,17]. However, the emission process has a bilateral character: enhancement and quenching [19,44]. The energy transferred from molecules to the metal nanoparticle can be emitted with certain efficiency. Therefore, enhancement in the emission process is positive when the quantum yield of the dye itself is lower than the luminous efficiency of the nanoparticle. Inversely, dye with higher quantum yield can suffer a loss of emission in the nonradiative process in the metallic nanoparticle [25,45]. Therefore, the fluorescence of molecular probes with low quantum yields but high usefulness in biological applications can be significantly enhanced using gold nanostructures [43,46].

The enhancing effect of an electric field in the vicinity of nanoparticle is inversely proportional to the cube of distance from the surface (d^{-3}) [1,3]. On the other hand, the energy transfer ratio sharply depends on the distance between the dye and the metallic surface (as an interaction between spherical particle and a molecule, distance (R) dependencies of $R^{-6} = a^6/(a+d)^6$ at large distances and d^{-4} for shorter distances, where a is radius of the nanoparticle) [25,47].

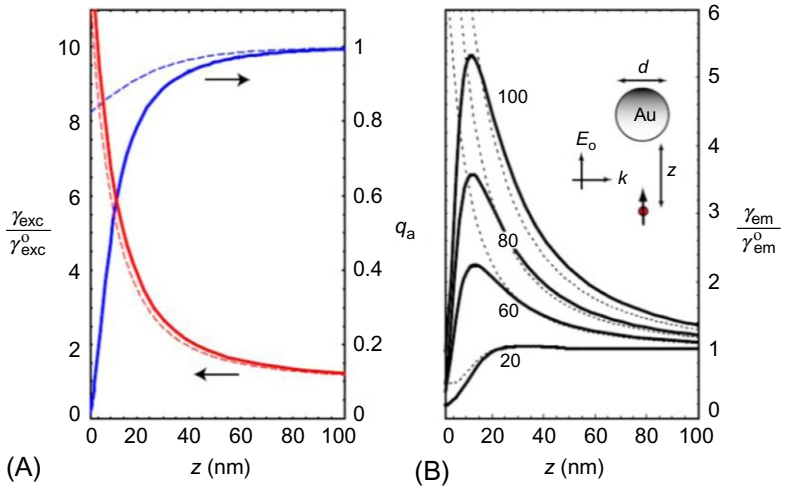

Fig. 4.4

(A) Quantum yield (q_a) and excitation rate ($\gamma_{exc}/\gamma^0_{exc}$) and (B) emission rate ($\gamma_{em}/\gamma^0_{em}$)at distances *Z*. The *solid curves* are obtained by MMP calculations (max. error 2%), whereas the *dashed curves* are from the dipole approximation, which fails for short distances. Particle diameter is *d* ((A) 80 nm (B) indicated in the *curves*) [25]. *Reproduced with permission from P. Anger, P. Bharadwaj, L. Novotny, Enhancement and quenching of single-molecule fluorescence, Phys. Rev. Lett. 96 (2006) 113002. American Physical Society.*

Then, there is an optimum distance at which to maximize fluorescence (Fig. 4.4). These behaviors were confirmed using proper spacers (e.g., DNA, silica shell, self-assembled monolayer (SAM), and polymer thin films) [48–53]. Moreover, as expected from the mechanism, quenching/emission is facilitated by overlapping the plasmon band and molecular band [54,55]. When the energy level of the plasmon band is lower than the emission band of molecule A and higher than the absorption band of molecule B, the metal nanoparticle can mediate the energy transfer from the molecule A (donor) to the molecule B (accepter) [56].

Enhancement of the emission process is supported by enhancement in chemiluminescence [20,21]. Typically, the emission from luminol reaction is enhanced by tens of times. In this case, matching between the plasmon absorption band and emission wavelength was effective for valid enhancement. As an application, the gold nanorods were chemically modified with an enzyme to catalyze the chemiluminescence reaction, and then the chemiluminescence was measured to quantify the target compound [21]. The enhancing mechanisms in the Raman, IR absorption, fluorescence, and chemiluminescence spectroscopies are summarized in Fig. 4.5.

Some studies report ultrasensitive analyses of monolayers using metallic nanoparticles in the UV-vis absorption spectra [57–61]. Although significant enhancement in the absorption spectra was observed (at the order of 10 times), these changes could overlap with a shift of the plasmon absorption band of metallic nanoparticles. As demonstrated in Eqs. (4.1)–(4.3), the plasmon

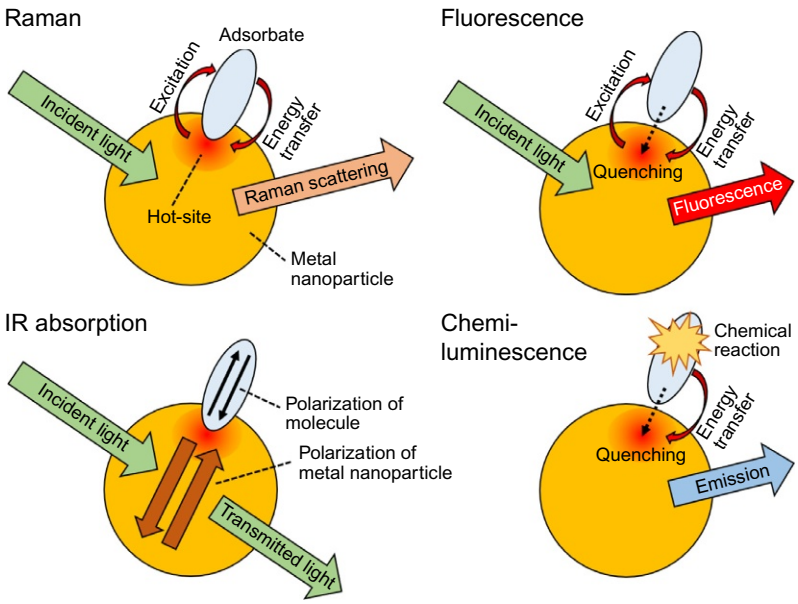

Fig. 4.5
Schematic of enhancing mechanisms in Raman, IR absorption, fluorescence, and chemiluminescence.

absorption band depends on the dielectric constant in the vicinity of nanoparticles. However, this behavior can be applied for ultrasensitive detection using a micro-tip of gold nanoparticles [57,58]. The color change of nanoparticles induced by the aggregation can be used in ultrasensitive detection, too [60]. The other ultrasensitive detection methods, such as extraordinary optical transmission using nanohole and nanoarray, have been reported [61]. However, these methods detect change in the dielectric constant in the vicinity of metallic nanostructures, not the molecular band itself. Therefore, these methods can be lumped into the same category as surface plasmon resonance (SPR) analysis [62], and should not be classified with surface-enhanced spectroscopies.

4.3 Metallic Nanostructures for Surface Enhanced Spectroscopies

Commonly, gold and silver are used for surface-enhanced spectroscopies. Compared to gold, silver has better plasmon resonance properties (sharper and stronger resonance) because of its high density of free electrons [63,64]. However, the silver nanostructures have a disadvantage in chemical stability [65]. To solve this issue, hybridization of silver with gold is reported; the core-shell structure of gold-silver nanoparticles produced nanoparticles with silver-like plasmonic properties and gold-like chemical stability [66,67]. Although aluminum can have a plasmon absorption band in the visible range and be used for optical devices [68], it is chemically too unstable, making it unsuitable for spectroscopies, which require close contact with specimens. Copper is also unstable in oxidative conditions and requires surface

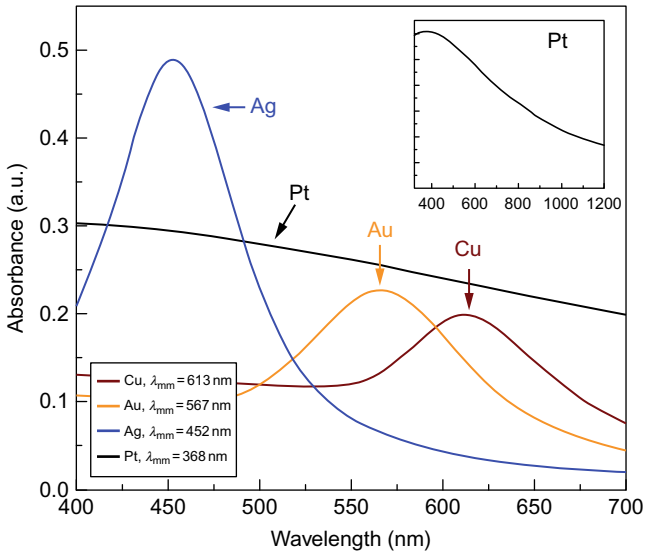

Fig. 4.6

UV-vis absorbance spectra of various metal nanoparticle arrays (nanoparticle diameter of 40 nm, and height of 30 nm.) The inset is extended spectrum of Pt [64]. *Reproduced with permission from D. Ok Shin, J.-R. Jeong, T. Hee Han, C. Min Koo, H.-J. Park, Y. Taik Lim, S. Ouk Kim, A plasmonic biosensor array by block copolymer lithography, J. Mater. Chem. 20 (2010) 7241–7247. The Royal Society of Chemistry.*

protection, although it is available for surface enhancing [69]. Platinum is chemically stable, but its complex permittivity has a large imaginary component, which dampens oscillation of localized surface plasmon [64]. The plasmon absorption spectra of these metals (Au, Ag, Cu, and Pt) are shown in Fig. 4.6.

However, the catalytic activity of platinum is attractive and valuable in various applications, so nanostructures of platinum may be preferable for surface-enhanced spectroscopies to trace chemical reactions on platinum catalysts [70]. To improve the enhancing effect, the core-shell structures can be used. In the core-shell structure, the charge transfer from the core metal (gold) to shell (platinum) improves the plasmonic properties of platinum [71,72]. Some common metals, such as iron and nickel, are also used as catalysts. For these cases, SEIRAS is preferable because of its low dependency on the resonance between the excitation wavelength and the localized surface plasmon [73].

The localized SPRs of gold and silver nanoparticles can be easily observed as the colors of their colloidal dispersions [1,2,74]: typically, the spherical nanoparticles of gold are red, and the spherical nanoparticles of silver are yellow. These colors are explained by the plasmon absorption bands, which satisfy $\varepsilon' = -2\varepsilon_m$ (Eq. 4.5).

$$A \propto \frac{\varepsilon_m^{\frac{3}{2}} a^3}{\lambda} \frac{\varepsilon''}{(\varepsilon' + 2\varepsilon_m)^2 + \varepsilon''^2} \tag{4.5}$$

A is the absorbance
a is the radius of nanoparticle (sphere)
ε' and ε'' are the real part and imaginary part of dielectric constants of nanoparticle, respectively

These colors change by the aggregation of nanoparticles: Their absorption bands red-shift and broaden by the interparticle interaction (Fig. 4.7) [28–30,75,76]. The hot site for surface-enhanced spectroscopies would be formed in the gaps between the nanoparticles by this interparticle interaction [27,28,34]. This change can also be used for other ultrasensitive analyses as mentioned in Section 4.2 [57,59]. The color is sensitive to the structure of nanoparticle. As the particle size increases, the band red-shifts, and then a new band corresponding to the quadrupolar excitation appears [77].

The crystal growth can result in polyhedral and plate-like structures, such as triangle shapes, and the additional band appears in the near-IR region as the Eq. (4.1) suggests [78,79]. The electric field is concentrated at the tips of the edges on nanoparticles, and relatively weak resonance modes appear at the sides [1,77,80]. Therefore, these polyhedral structures can be used for surface-enhanced spectroscopies, too [14,81,82]. Therefore, the nanoparticles for surface-enhanced spectroscopies can be designed by controlled particle growth. These

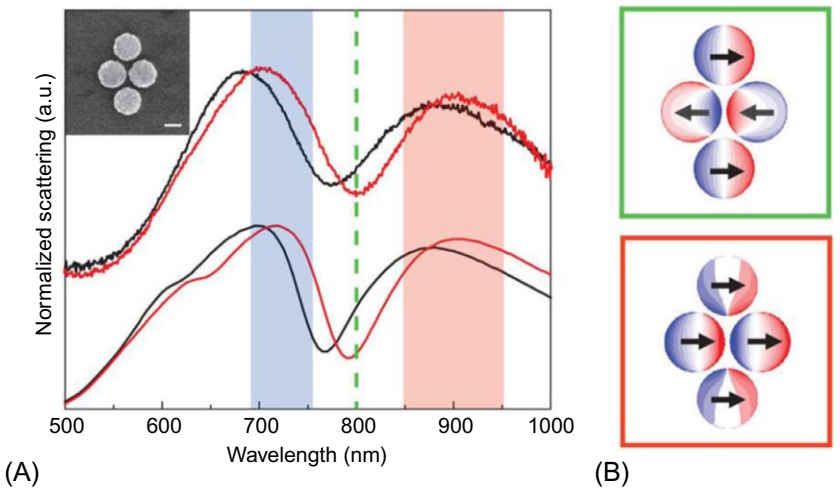

Fig. 4.7

(A) Experimental (top) and calculated (bottom) linear scattering spectra of a single quadrumer before (*left*) and after (*right*) adsorption of *p*-MA. *Dashed line*: the pump beam at 800 nm; *zone (850–950 nm)*: the Stokes scattering region; *zone (700–750 nm)*: the anti-Stokes scattering region. The inset is an SEM image of a gold quadrumer. (B) Schematic of polarization of the quadrumer at 800 nm pump (top) and 900 nm (bottom) [76]. *Modified from Y. Zhang, Y.-R. Zhen, O. Neumann, J.K. Day, P. Nordlander, N.J. Halas, Coherent anti-stokes Raman scattering with single-molecule sensitivity using a plasmonic Fano resonance, Nat. Commun. 5 (2014) 4424. Copyright 2014, Macmillan Publishers Ltd: Nature Communications.*

morphological changes are due to the differences in surface free energies of each facet. That is, octahedral and plate-like morphologies are formed to extent (111) planes of face-centered cubic lattices, while cubic nanoparticles can be covered with (100) planes [83,84]. Typically, these morphologies appear when the gold nanoparticles are synthesized with citrate as the protecting agent [85]. The protecting agents can adsorb on specific crystalline facets through selectivity [83,84]. Hexadecyltrimethylammonium bromide (CTAB) can preferably cap the (100) and (110) facet of a gold nanoparticle, and then the crystal grows on the (111) facet to be the nanorods under a mild reaction condition [86]. The aspect ratio of nanorods can be controlled via reaction condition, and then their localized surface plasmon bands can be tuned [86,87]. The nanorods have two sharp bands, which correspond to the dielectric constants in short and long axes (see Eq. 4.1). The band of longer wavelength is for the long axis, and it shifts to a longer wavelength as the aspect ratio of the nanorod becomes higher. The absorption in the long axis is stronger than that of short axis because of its higher dielectric constant [86,88]. These properties are preferable for the surface-enhanced spectroscopies: The sharp and strong bands can be tuned for the light sources and the molecular bands of target compounds to achieve resonance effects [3,14,16,17,19,37–40,43]. The hot site is formed at the edges of nanorods [1,34,80], and substrates for surface-enhanced spectroscopies have been designed with gold nanorods [21,88–91]. The vertical orientation of nanorods leads to higher enhancement than horizontal and random orientations [91].

Other types of nanoparticles have been designed and examined for surface-enhanced spectroscopies. The point is how to prepare sharp edges and tips on the surfaces of nanoparticles. Cubic and octahedral structures [92–94] can be formed by specific protecting agents [83], and they were used for surface-enhanced spectroscopies. Selective crystal growth [95,96] and etching [97], or the aggregation of seeds of nanoparticles [98,99] can result in complicated structures which have strong plasmonic effects. These structures are named based upon their resemblance to common items, such as flower-like nanoparticles (nanoflower) [100,101], nanostar [102–104], nanourchin [105], confeito-like nanoparticles [106,107], and so on [33,108–112]. To avoid any confusion in their applications, these structures should be organized according to the scientific meaning. Control of particle growth can result in a network of metallic nanostructures [113]. The surface plasmon would be concentrated also in the voids in network. The networks can be obtained by etching [114,115] and electrochemical deposition [116], and then the network can be used as plasmonic material.

More precisely, the tips and pores in ultrathin metallic films are prepared with templates. The metals can be formed with physical methods, such as lithography [117] and vapor deposition [118–123], and the electrochemical deposition [124]. These methods allow various structures, such as nanorods [118,119], spikes [120] arrays of triangles [121], cups [123], and pores [122,124]. These nanostructures provide strong surface-enhancing effects, and are formed using templates and masks independently from the crystal lattice of metals (Fig. 4.8). This high degree of structural design freedom is attractive for plasmonics.

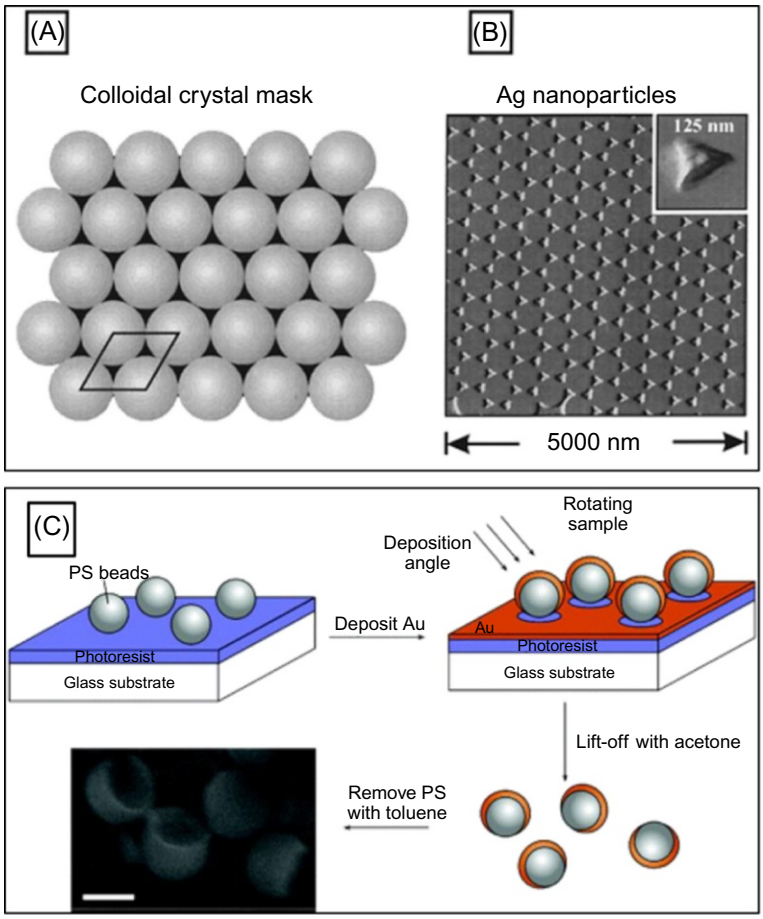

Fig. 4.8

Colloidal crystal masks (A) and silver nanoparticle arrays obtained (B). Fabrication procedure of gold nanocrescent moons using polystylene (PS) templates (C). The scale bar represents 200 nm [120,123]. *Modified from C.L. Haynes, R.P. Van Duyne, Nanosphere lithography: a versatile nanofabrication tool for studies of size-dependent nanoparticle optics, J. Phys. Chem. B. 105 (2001) 5599–5611; Y. Lu, G.L. Liu, J. Kim, Y.X. Mejia, L.P. Lee, nanophotonic crescent moon structures with sharp edge for ultrasensitive biomolecular detection by local electromagnetic field enhancement effect, Nano Lett. 5 (2005) 119–124. Copyright 2001 and 2005, American Chemical Society, respectively.*

To design metallic nanostructures for surface-enhanced spectroscopies, the finite-difference time-domain (FDTD) method is preferable to simulate electric field distributions in the vicinity of nanostructures [1,3,26–28,77,80]. Excitation energy is given to the surrounding molecules as the square of field intensity, providing enhanced optical responses [3,16,17,19,25–27,34,43–47]. Enhancement in the spectrum is also affected by other factors, such as resonance effects [3,14,16,17,37–40,43] and charge transfer effects [26,27].

Eventually, the enhancement is experimentally quantified by the enhancing factor (EF) as the ratio of intensity, which is normalized via concentration of target compound (Eq. 4.6).

$$\mathrm{EF} = \frac{I_{\mathrm{enhanced}}}{I_{\mathrm{control}}} \times \frac{C_{\mathrm{control}}}{C_{\mathrm{enhanced}}} \tag{4.6}$$

I_{enhanced} is the intensity of enhanced spectral band
I_{control} is the intensity of corresponding spectral band in the control system
C_{enhanced} is the concentration of the target compound in the enhancing system
C_{control} is the concentration of the target compound in the control system

However, it should be noted that the EF does not directly reflect the degree of enhancement in the excitation of specific molecules at the hot site. As the Eq. (4.6) suggests, the EF is corrected by the concentration of target compound applied to the system. Therefore, the EF indicates averaged enhancement in the whole system, and then the ratio of molecules properly located in the hot site versus their total amount can significantly change the EF. The adsorption behavior is influenced by surface conditions of metallic nanostructures and their interactions with the target compounds. A study suggested that the intrinsic EF could be 10^6 to 10^7 times higher than the apparent EF [14]. These issues will be discussed in the Sections 4.4 and 4.5.

The stability of metallic nanostructures should also be considered as a factor in enhancing phenomena. As the Gibbs-Thomson effect suggests, nanostructures are thermodynamically unstable. The melting points of nanoparticles significantly drop when particle sizes decrease to a single nanometer [125,126]. Light absorption by a nanostructure leads to the heat generation in media by several 10 degrees [127], and local temperature at the hot spots can rise high enough to deform the nanostructures during laser irradiation. It is reported that gold nanorods can be thermally deformed in dispersions to be short (even lower than 100°C), while they are stable to 600°C at a dry condition [128,129]. The surface-enhanced Raman scattering (SERS) measurements are carried out via laser irradiation on sample solutions, and then the thermal deformation of nanostructures can be caused. Several studies estimated the local temperature of molecules in the SERS measurements from the ratio of anti-Stokes and Stokes Raman scattering. They suggested that even weak laser irradiation (0.5 and 0.2 mW) significantly increased local temperature by several 10 degrees within seconds [130,131]. It is interesting that the temperatures fluctuate and differ according to the vibration mode, suggesting that the adsorption states of molecules vary according to the amount of irradiation [131]. This phenomenon is likely related to "blinking" of SERS, which is discussed later. As mentioned above, the structural changes in plasmonic materials can be easily observed as their color changes. Therefore, the substrate should be checked if the color didn't change during the measurement, and reproducibility of EF should be confirmed. The decreasing in intensity during a measurement is reported, and it is attributed to relaxation in the nanoarray [132].

4.4 Physicochemical Phenomenon of Materials in the Vicinity of Metal Nanostructures

The localized surface plasmon is affected by the surrounding medium, as indicated in Eqs. (4.1), (4.5): the plasmon band shifts as the dielectric constant of the matrix changes [78,133,134]. If the surface of a metallic nanostructure is oxidized or suffers other chemical modifications, materials on the metal surface can change the plasmonic properties [65,68,135]. SPR measurement is based on this phenomenon and can detect changes on the metallic surface as the angle shift of reflectance [62]. The adsorbed molecules on metallic nanostructures change plasmonic properties as well, making preparation methods for metallic nanostructures a factor for surface plasmon; the surface of nanostructures synthesized by the wet process are covered by protecting agents and solvent molecules [47,85,86].

The substrate also interacts with the nanostructures (Fig. 4.9). The nanoparticles are spread, adsorbed, and deposited on a dielectric substrate, and then the substrate is polarized by the localized surface plasmon [136]. This interaction provides hot sites in the gaps between the nanoparticles and the substrate, making a higher dielectric constant of the substrate material preferable for intensifying the electric field [137]. Not only molecules beneath the nanoparticles (sandwiched by the substrate), but also molecules adsorbed on substrate between nanoparticles can be excited by polarization of the substrate [138]. Polarization can propagate on the substrate and then couple with the other nanoparticles not irradiated by the incident light [139,140]. Therefore, it should be considered that molecules on the substrate in the light spot and nanoparticles out of the light spot can be excited and emit surface-enhanced light.

The substrate can be a metal. In this case, the coupling of surface plasmon between nanoparticles can compete with interaction with the substrate [141–143]. Proper distance between nanoparticles should be maintained to maximize the intensity of the electric field between the nanoparticle and substrate. The distance between the nanoparticle and the substrate can be easily and precisely controlled by coating layers, while the gaps between nanoparticles would be influenced by the nanoparticles' density.

Since the surface plasmon is localized in the nanostructure, the target molecules should be in the vicinity of the nanostructure. The relation between the adsorption state of a molecule and the enhancing effect has been investigated [14]. In this study, the molecule (rhodamine 6G) was diluted, and it was expected that about 80% of rhodamine 6G molecules adsorbed on the nanoparticles. Then, each nanoparticle carried an average of one molecule. The results suggested that the polarization of excitation light should match the orientation of the nanoparticle (nanorod) and the vibrational modes of the target molecule. The importance of the orientation of the molecule on the hot site is explained by the surface-selection rule [9,144,145]: the vertical components of vibrational modes are selectively excited due to the strong polarization of the electric field from the surface of the metal and the offsetting of the horizontal component of the dipole moment of molecule by the mirror-dipoles in the metal surface (Fig. 4.10).

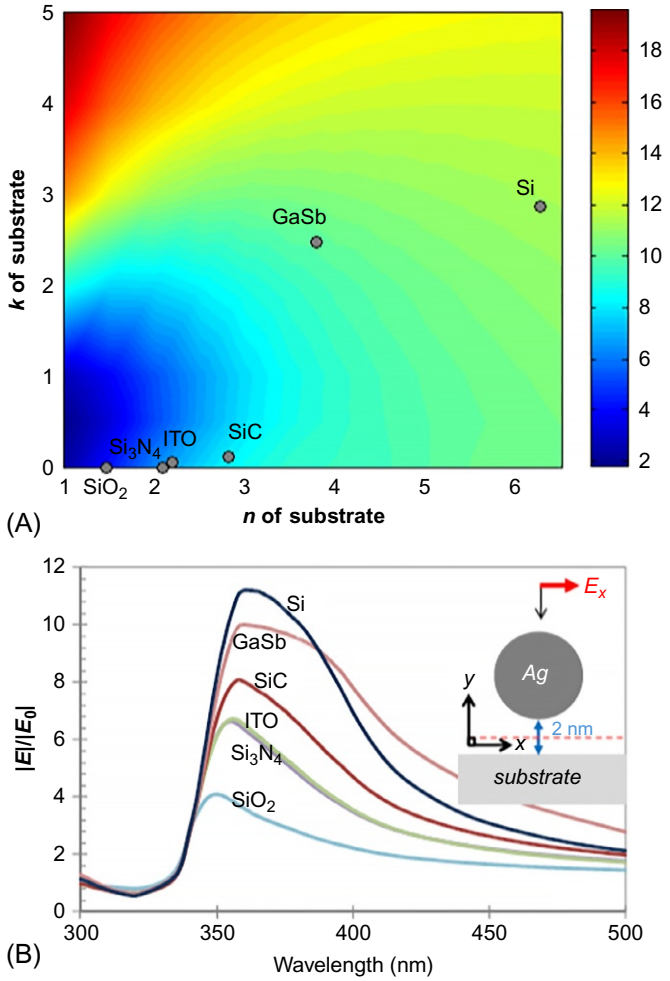

Fig. 4.9

(A) Maximum electric field $|E|/|E_0|$ in the gap (2 nm) between the Ag nanoparticle ($R=25$ nm) and substrates with various refractive indices (n: real part, k: imaginary part). (B) Spectra of the maximum electric field $|E|/|E_0|$ [137]. *Modified from T. Hutter, S.R. Elliott, S. Mahajan, Interaction of metallic nanoparticles with dielectric substrates: effect of optical constants, Nanotechnology 24 (2013) 035201. Institute of Physics - Journals.*

However, it should be noted that the "mirror-dipoles" theory is questioned for the SEIRAS, because the occurrence of mirror-dipoles is too sensitive to the distance from the surface [9]. This was also confirmed by the variation of spectra obtained from different particles, which corresponded to the difference in adsorption states [14]. Therefore, only limited molecules can be effectively excited in the hot site. In this study, it was estimated that only one out of 100 to 1000 particles was optically hot, and only one out of the 10^4 molecules could be effectively excited. The adsorption states change by time, too. The studies on the

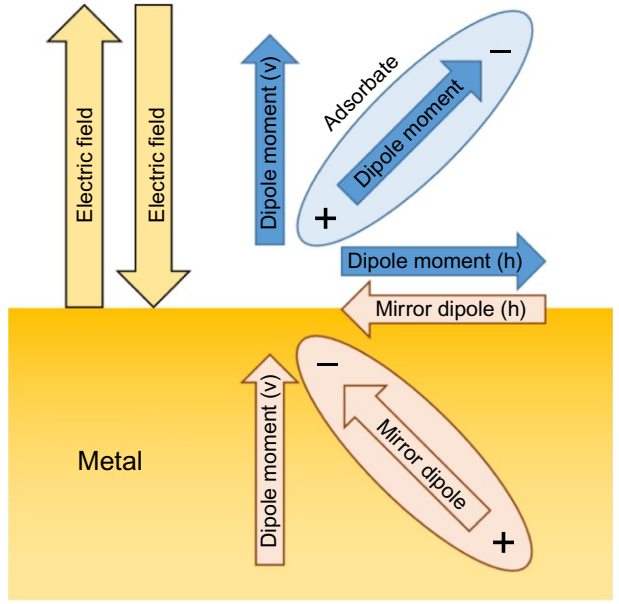

Fig. 4.10
A schematic of the "surface-selection rule." The electric dipole moment and its mirror dipole are divided into their vertical (v) and horizontal (h) components, respectively.

SERS at much diluted conditions report a "blinking" of SERS from the single particle [14,146]. The Raman scattering indicates a sudden on-off intermittency when the number of molecules adsorbed on one particle becomes lower than several tens. This blinking is attributed to the adsorption/desorption of the single molecule onto the hot-site [147], and is considered evidence of the single-molecular measurement [14,146]. Therefore, blinking can be inhibited by fixing the molecule onto the hot site [148] and cooling to 77 K to reduce thermal motion of the molecule [149]. The dynamic properties of molecules adsorbed on the surface would result in time-dependent spectrum changes, allowing adsorption behaviors and configuration changes in the adsorbed film (orientation of molecules) to be observed (Fig. 4.11) [150,151].

For effective enhancement, effective adsorption on the hot site is essential, and the co-existing ions can play an important role in improving the adsorption of specific molecules on the nanoparticles [39]. The silver nanoparticles strongly adsorb chloride ions on their surface, changing their surface charge to negative [14]. Thus, negatively charged silver nanoparticles can selectively adsorb cationic dyes on their surfaces through electrostatic interaction, improving the enhancing effect. The interaction of the metallic surface with the ions and functional groups differs from metal to metal, as does the binding site of molecules on the metallic nanostructures. Typically, rhodamine molecules can take rather vertical orientation toward the silver surface via their electrostatic interactions, while they form coordination bonds between their amino groups and the gold surface and flatly adsorb on the gold surface

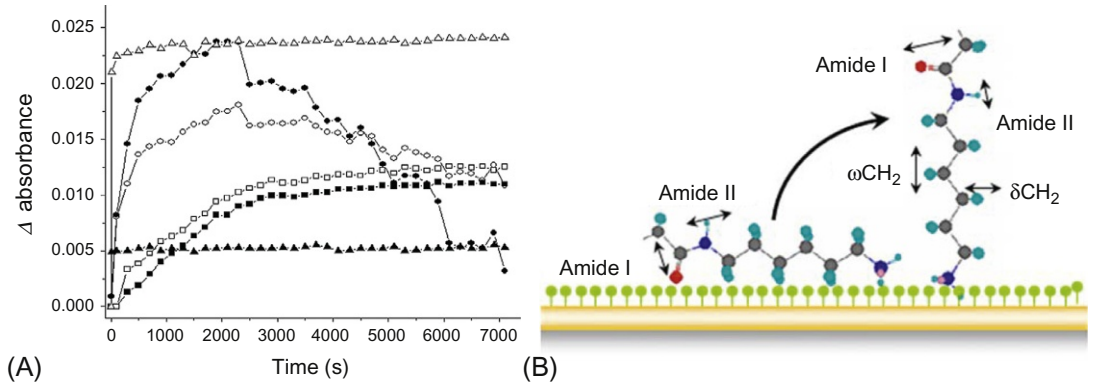

Fig. 4.11

(A) Adsorption time dependence of amide I (closed) and II (open) band intensities on ATR–SEIRAS of generation 2 (G2) and 3 (G3) aza-C6-PAMAM dendrimers. Marks: G2 on bare gold (*square*), G2 on MPA SAM (*circle*), and G3 on MPA SAM (*triangle*). (B) The schematic of change in the orientation of molecular parts [150]. *Modified from M. Ujihara, T. Imae, Adsorption behaviors of poly(amido amine) dendrimers with an azacrown core and long alkyl chain spacers on solid substrates, J. Colloid Interface Sci. 293 (2006) 333–341. Elsevier.*

(Fig. 4.12) [152,153]. Other functional groups such as carboxyl groups can also strongly interact with gold surfaces to control the orientation of molecules [154,155]. Thiols take different angles toward the gold and silver surfaces [156]. A porphyrin ring vertically adsorbs on the gold surface via ionic interaction, while the SAM of 4-pyridinethiol interacts with the central metal ion (Zn^{2+}) to allow horizontal adsorption [157,158].

The interaction between functional groups and metals are well studied on the adsorption of the thiols on gold surfaces, and it is widely applied for the surface modification of gold [159,160]. For the SERS, thiols are used as model compounds, and it was reported that different crystal planes of gold surface vary enhancing effects on the adsorbed thiols [161,162]. First, the thiol was adsorbed on the gold substrate to form the SAM, and then the gold nanoparticles were placed on the SAM. The hot site was formed in the gap between the substrate and the nanoparticle, and then the SERS from sandwiched SAM was measured (Fig. 4.13). It was reported that the SERS from the SAM formed on (111) plane was around four times stronger than that from SAM on (100) plane, and the ratios of band intensities in their spectra were different. This difference was attributed to the strong chemical effect (charge-transfer effect) on the (111) plane. Moreover, the importance of the interaction between sulfur atoms and gold atoms was confirmed via SERS measurement using the single-molecular junction of benzene-1,4-dithiol [163]. The sulfur atom can take three states of adsorption on the gold surface (top, bridge, and hollow: Fig. 4.14). The adsorption states were controlled by changing the distance of the nanogap, and the degree of coupling between the sulfur and gold atoms was measured by the current-voltage properties of the single-molecular junction. Then, the SERS of the dithiol linking the gold electrodes was measured in parallel. The results demonstrated that the

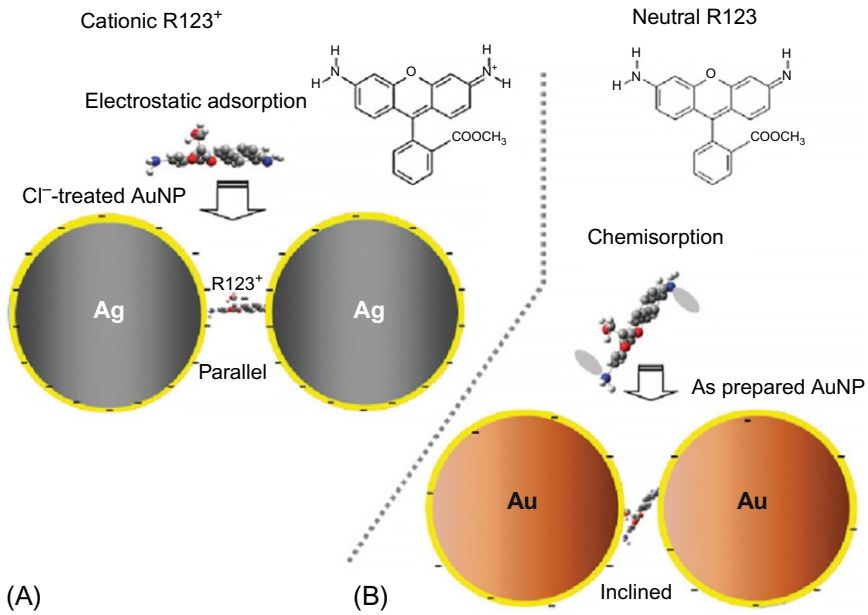

Fig. 4.12

Presumable adsorption structure of rhodamine 123 (R123) on flocculated silver nanoparticles and gold nanoparticles. (A) The cationic $R123^+$ adsorbed via an electrostatic interaction, while the neutral R123 formed a coordination bond via lone pair electrons of amino groups (B) [152]. *Modified from T. Yajima, Y. Yu, M. Futamata, Closely adjacent gold nanoparticles linked by chemisorption of neutral rhodamine 123 molecules providing enormous SERS intensity, Phys. Chem. Chem. Phys. 13 (2011) 12454–12462. PCCP Owner.*

SERS was measured only for the "bridge" state, which had the highest conductivity of the molecular junction. That is, the strong coupling between sulfur and gold atoms is required for the SERS.

As mentioned above, the difference in chemical interactions between the metallic surface and specific molecules results in selective capping on crystal facets, which can be used to control particle morphology [83,86]. This phenomenon can be applied to selective modification to immobilize the target molecule on the hot site (e.g., edges of nanorod). The details of surface modification will be introduced in the next section.

It should be considered that the conformation and the other characteristics of molecules adsorbed on the metallic nanostructures can be varied from those of molecules in bulk solutions. The adsorbed molecules could change their vibrational modes, and then the variety in Stokes shift in SERS (within several cm^{-1}) was observed as the results of adsorption by their different moieties in the molecule [14]. The strong interaction between the nanostructure and the target molecule can induce the orientation of the molecule on the surface [164,165]. This interaction increases the local concentration of molecules on the nanostructure's surface,

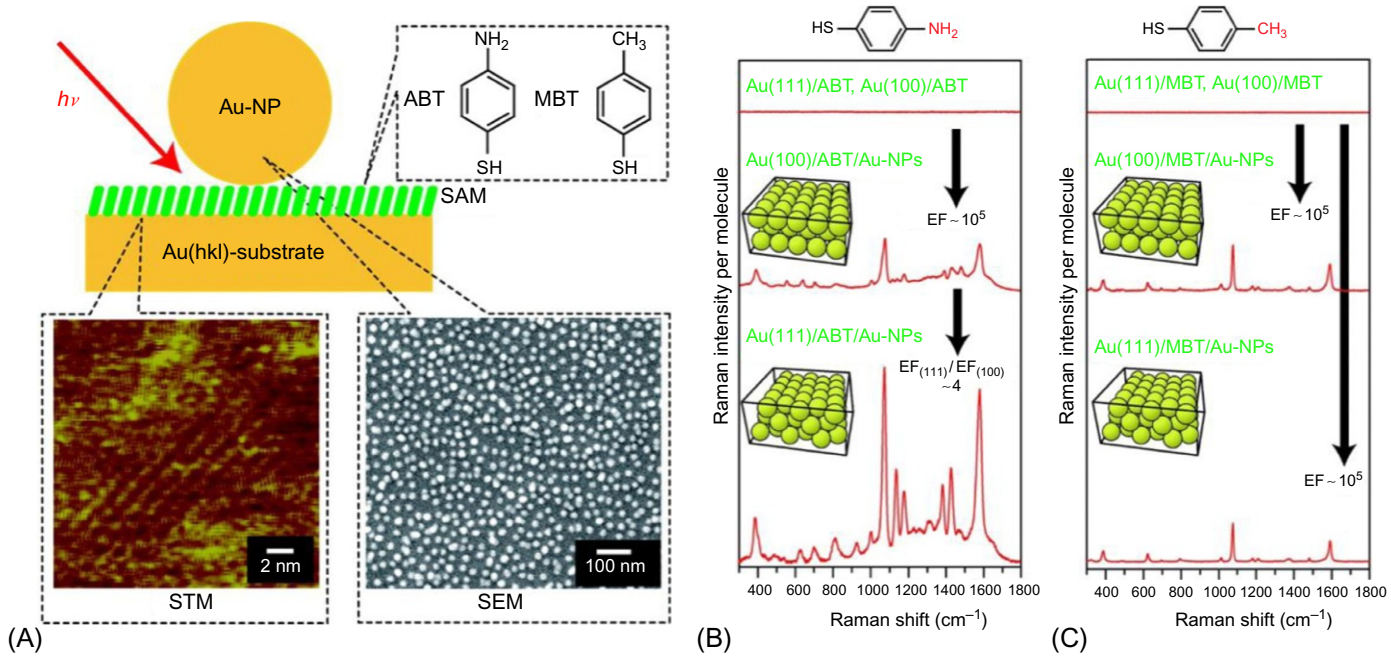

Fig. 4.13

(A) Schematic of gold nanoparticle-SAM-gold substrate hybrids and their morphologies (STM and SEM images). (B) and (C) Spectra of SERS obtained from the hybrids with different crystal planes [159]. *Modified from K. Ikeda, S. Suzuki, K. Uosaki, Crystal face dependent chemical effects in surface-enhanced raman scattering at atomically defined gold facets, Nano Lett. 11 (2011) 1716–1722, Copyright 2011, American Chemical Society.*

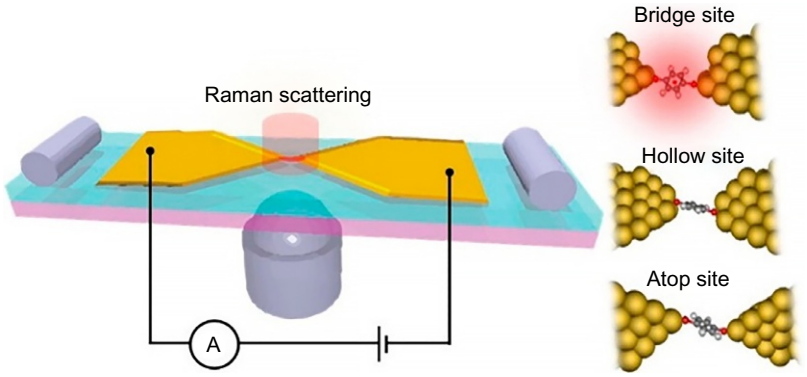

Fig. 4.14

A schematic of nanogap electrodes and the adsorption states of 4-benzothiol in it [161]. *Modified from S. Kaneko, D. Murai, S. Marqués-González, H. Nakamura, Y. Komoto, S. Fujii, T. Nishino, K. Ikeda, K. Tsukagoshi, M. Kiguchi, Site-selection in single-molecule junction for highly reproducible molecular electronics, J. Am. Chem. Soc. 138 (2016) 1294–1300. Copyright 2016, American Chemical Society.*

and the complicated nanostructures allow the molecules to take J-aggregates [16,166–168]. J-aggregates can be detected by the red-shift of fluorescence, which is measured with the SERS emission. This orientation can be facilitated more easily on the tips of nanostructures than in the gaps in aggregates of nanoparticles because of the spatial degrees of freedom on the tips and the crowdedness in the gaps.

Change in molecular conformation can be induced by mechanical stress, too. The tip-enhanced Raman spectroscopy [30,71,169,170] can be used to apply pressure on the target molecule by sandwiching it between the tip and the substrate, and the obtained spectra differed from both SERS and the bulk Raman spectrum [171,172].

4.5 Practical Methods for Surface-Enhanced Spectroscopies

Historically, the SERS was found on electrochemically roughened silver surfaces, and the aggregates of colloidal particles have been used to measure surface-enhanced spectra. Today, metallic nanostructures are designed and synthesized with some techniques. In this section, these techniques are introduced.

First, the metallic nanostructures can be formed using vapor deposition and sputtering methods. The obtained film on substrate has an island structure, which consists of aggregates of "pancake-like" nanoparticles [173]. Then, the gaps between the nanoparticles work as hot sites to enhance the optical responses of adsorbed molecules. This island structure of pancake-like nanoparticles can be flattened to a step-terrace structure with (111) plane through annealing [174]. Therefore, the thermal deformation of metallic ultrathin films should be considered to control their roughness [175]. The vapor deposition and sputtering methods can be applied to

templates to obtain patterned structures (see Fig. 4.8) [118–123]. These films demonstrate high surface-enhancement efficiency, as introduced in Section 4.3.

Metallic films can also be formed to sandwich the target molecule [176]. In this case, hot sites are formed between the two layers, and then the target molecules can be effectively trapped in the hot sites to provide strongly enhanced spectra. This sandwich structure can be prepared using a template, too; the SAM of target molecule was sandwiched by a bilayer of silver nanorods formed in the nano-pores of anodized alumina template, indicating much stronger SERS than the single nanorod did [177]. In this case, the nanorods were oriented well, as the pores arranged in alumina membrane, and then the excitation light was effectively coupled with the nanorods' localized surface plasmon.

Optical properties of the substrate for the vapor deposition/sputtering should be considered for the enhancing effect: the high dielectric constant of a substrate would improve its enhancing effect [136,137]. The methods of measurement (e.g., the transmission, reflection, or attenuated total reflection (ATR) method) can also be the issue. Especially for the SEIRAS, the Kretschmann configuration is preferably used (Fig. 4.15), because this ATR apparatus can be directly applied to in-situ observation and it allows the flow cell system for kinetics study [151].

Of course, the prism should be transparent to IR light, and Si and Ge should be used as the prism. This configuration has an issue to be solved: if the metallic film is too thick, the light and plasmonic effect can't penetrate the specimen, even if the upper surface is properly prepared to localize the surface plasmon. On the contrary, the too thin film can't provide enough hot sites. The optimum thickness was estimated to be around 20 nm, and this maximum condition was associated with the saturation of plasmon absorption in the UV-vis transmission spectra (Fig. 4.16) [41].

Thus, the thickness of metallic films should be ultrathin to maximize enhancement. The deposited film is just physically adsorbed on the substrate, and is then mechanically unstable. This metallic film can be easily removed from the substrate, and then should be carefully

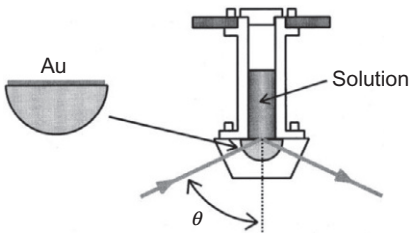

Fig. 4.15

A schematic of an ATR attachment for the SEIRAS measurement with the Kretschmann configuration. Angle θ indicates the incident angle of infrared light [151]. *Reproduced with permission from T. Imae, H. Torii, In situ investigation of molecular adsorption on au surface by surface-enhanced infrared absorption spectroscopy, J. Phys. Chem. B. 104 (2000) 9218–9224. Copyright 2000, American Chemical Society.*

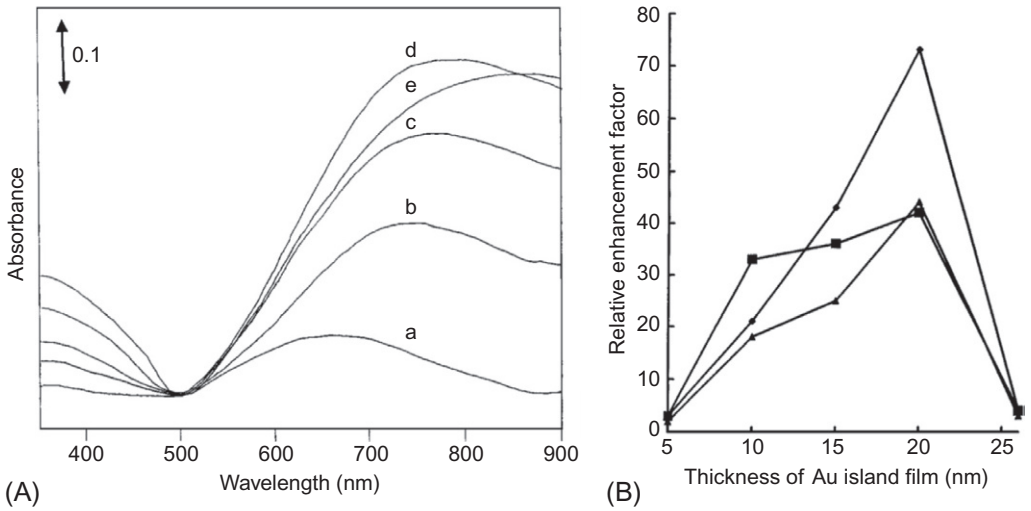

Fig. 4.16

(A) UV-vis spectra of gold vacuum-deposited films with thicknesses of (a) 5, (b) 10, (c) 15, (d) 20, and (e) 26 nm. (B) Plots of the relative enhancement factors for the bands at 1612, 1571, and 1472 cm^{-1}, respectively [41]. *Reproduced with permission from Z. Zhang, T. Imae, Study of surface-enhanced infrared spectroscopy, J. Colloid Interface Sci. 233 (2001) 99–106. Elsevier.*

handled. Often, the film would be exfoliated from the substrate in the flow cell during measurement, and its spectral intensity drops. To avoid this trouble, the SAM can be applied on the substrate: typically, dithiol and (3-aminopropyl)triethoxysilane are used to modify the substrates to immobilize gold nanoparticles [57,178–180]. This method allows the use of nonspherical nanoparticles synthesized via wet processes [83,86,92].

The other methods for preparation of metallic nanostructures on substrates are the Langmuir-Blodgett (LB) method and the Langmuir-Schaefer method [181–183]. Metallic nanoparticles, which were prepared via a wet process, are spread on a water subphase as their monolayer and then transferred onto the proper substrate. To use this method, the nanoparticles should be hydrophobized by SAMs and then dispersed in organic solvents such as chloroform and toluene. To improve homogeneity of the Langmuir film of nanoparticles, a drop of the dispersion medium (e.g., chloroform and toluene) can be spread before the application of nanoparticles on the water surface. The nanoparticles form domains or networks on the water surface because of their hydrophobic interactions, and their density can be controlled by the surface pressure (Fig. 4.17) [184].

In this case, the nanoparticles are fully covered by the SAM, and then the nanoparticles are arranged with a gap of few nm, which corresponds to the thickness of protecting SAMs (bilayer). Therefore, the plasmon absorption band of the film doesn't change significantly during the compression on the Langmuir trough, and its absorbance increases. On the other hand, the nanoparticles can be arranged by another process using the LB method: a monolayer

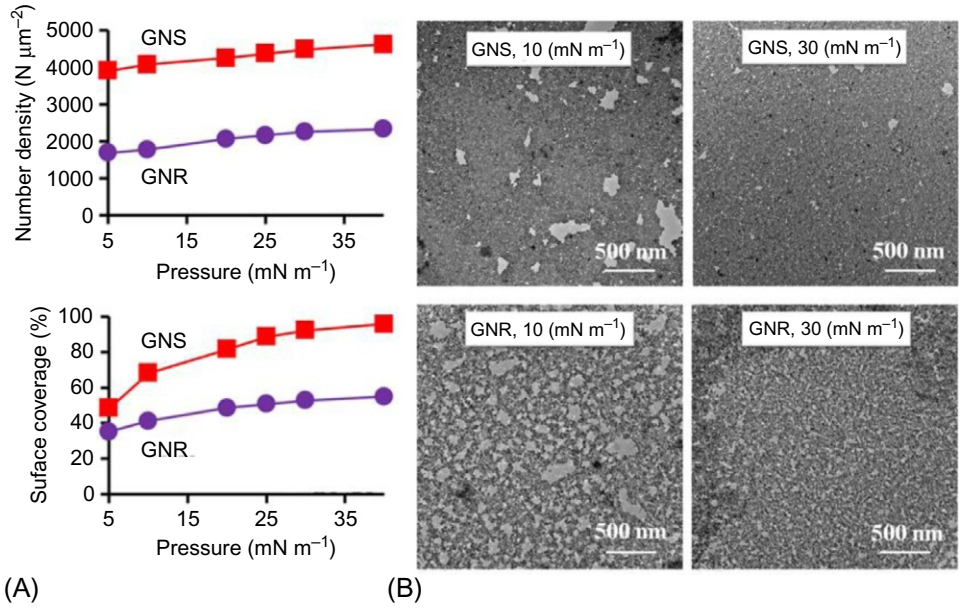

Fig. 4.17

(A) Number density and surface coverage of gold nanospheres (GNS) and nanorods (GNR) in LB films against surface pressure. (B) TEM images of LB films of GNS and GNR at surface pressures of 10 and 30 mN m^{-1} [182]. *Reproduced with permission from Y.-H. Wu, T. Imae and M. Ujihara, Surface enhanced plasmon effects by gold nanospheres and nanorods in Langmuir-Blodgett films, Colloids Surf. A (2017), doi.org/10.1016/j.colsurfa.2017.05.015. Elsevier.*

of amphiphilic molecule is spread on the dispersion of nanoparticles, and then the nanoparticles are adsorbed beneath the monolayer [185,186]. In this case, the hemispheres of nanoparticles are covered by amphiphiles, and the other hemisphere is exposed to the water phase [187]. Then, these Janus-type nano-composites have an amphiphilicity, and they distribute at the air-water interface in the balance of attractive (e.g., hydrophobic interaction and van der Waals' force) and repulsive (e.g., electrostatic interaction) forces. By the compression of Langmuir film, its plasmon absorption band changed from that of isolated nanoparticles to that of the aggregates [185]. The LB film of spherical nanoparticles can form a hexagonal lattice as the closest packing on the water subphase after compression (Fig. 4.18). The other nanostructures, such as nanorods, are difficult to take the closest packing (Fig. 4.17). Their anisotropy prevents them from rearrangement during film compression. The nanorods first form domains of raft-structures consisting of several nanorods on the water subphase because of their strong hydrophobic interaction between their side walls [187–189]. Then, the rafts aggregate to form networks with many voids. Therefore, the obtained films have rather low density.

From the viewpoint of enhancing effect, the orientation of nanorods in the LB film is important. The fully hydrophobized nanorods lie on the water surface when they spread. Therefore, the hot sites in their film are not effectively facing the target molecules, although the EF of LB film of

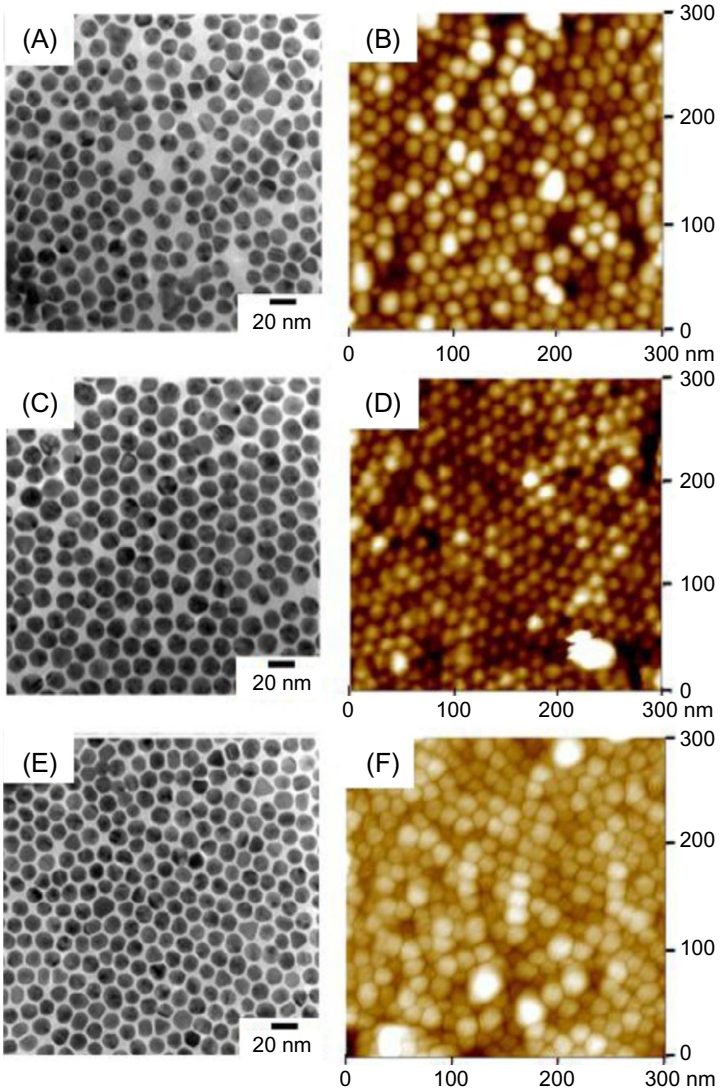

Fig. 4.18

TEM and AFM images of gold nanospheres in LB films on ultrathin carbon films (TEM) and Si substrates (AFM). TEM: (A) (C) (E). AFM: (B) (D) (F). Surface pressure (mN m^{-1}): (A) (B) 5, (C) (D) 20, (E) (F) 40 [182]. *Reproduced with permission from Y.-H. Wu, T. Imae and M. Ujihara, Surface enhanced plasmon effects by gold nanospheres and nanorods in Langmuir-Blodgett films, Colloids Surf. A (2017), doi.org/10.1016/j.colsurfa.2017.05.015. Elsevier.*

nanorods is significantly higher than that of spherical nanoparticles [187–189]. To improve the enhancing effect of films of anisotropic nanoparticles, their hot sites should be vertically arranged to face to the target molecules. The film of vertically-arranged nanorods can be prepared by drying the dispersion under controlled conditions [190]. When the nanorods

dispersed in chloroform slowly dry, they vertically adsorb on substrates. The importance of slow drying was also suggested in the case of the other nanorods [191]. On a patterned substrate (octadecylsilane/Si), a selective adsorption of vertically arranged nanorods was observed [192]: the nanorods are selectively accumulated on the octadecylsilane SAM. This suggests that the interactions between nanorods, substrates, and the dispersion medium play an important role in the aggregation at the liquid meniscus to form laminar aggregates. Obtained film of vertical nanorods demonstrates a higher enhancing effect than nanorod films with other orientations. A study reports that the enhancing effect of vertical nanorods is four times higher than that of randomly aggregated nanorods, and 1.6 times higher than the parallel nanorod (Fig. 4.19) [91].

The other nanostructures prepared using wet processes can be accumulated on substrates. To effectively use the hot sites of nanoparticles, they should be oriented to the target molecules, or symmetrically prepared to expose their hot-sites. A group of nanoparticles (flower-like, star-shaped, nano-urchin, confeito-like nanoparticles, etc.) have been designed in this strategy, and they demonstrated strong surface-enhancing effects [33,100–112]. However, these nanoparticles require specific protecting agents and messy processes. Recently, a simple method to prepare confeito-like gold nanoparticles was reported, and their strong enhancing effect was introduced [107]. In this preparation method, the protecting agent is not limited, and

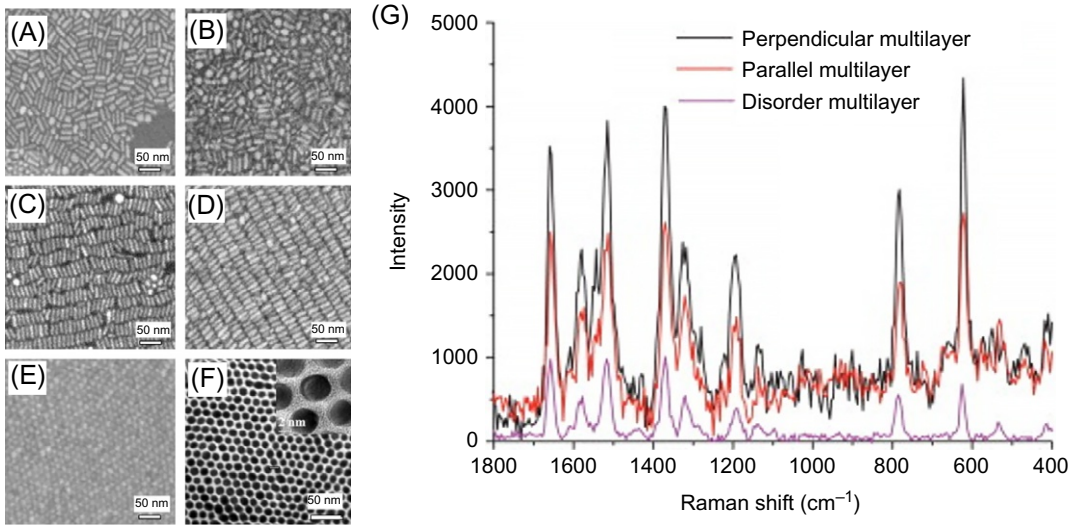

Fig. 4.19

(A)–(E) SEM images of LB films of gold nanorods in different arrangements. (F) TEM images of gold nanorods in perpendicular arrangement. The inset is a high-resolution image. (G) SERS spectra of rhodamine 6G adsorbed on gold nanorods array with different arrangements. Laser excitation wavelength was 532.3 nm [91]. *Modified from T. Imae, X. Zhang, Effect of Au nanorod assemblies on surface-enhanced Raman spectroscopy, J. Taiwan Inst. Chem. E. 45 (2014) 3081–3084. Elsevier.*

the reducing agent is hydrogen peroxide, which completely decomposes to water and oxygen. Therefore, the obtained nanoparticle can be easily used for further surface modification in various applications. The confeito-like nanoparticles indicate a significant enhancing effect even in dispersion [168], and they can be accumulated onto the patterned substrate to improve the enhancing effect as their amount increases [193].

The surface modification of nanostructures is important to capture target molecules on the hot sites, as mentioned above. The surfaces of nanoparticles adsorb the co-existing ions, which can change the adsorption behavior of the target molecules [14,39]. These ions can change the properties of nanoparticles by ambient conditions, such as pH, meaning the adsorption of the target could be controlled by the conditions. Typically, the citric acid covers the surface of gold nanoparticles when used as the protecting agent [85,193], and it can provide ionic interaction and hydrogen bonding to capture the target. This interaction would affect the orientation of adsorbed molecules, and it could be confirmed by the intensity ratio of the spectrum [168]. The carboxylic acid (target compound) was more strongly and more perpendicularly adsorbed on the surface.

However, the hot-sites on the nanoparticles are only small parts of the surface. The stronger enhancing effect is expected in the smaller part. Therefore, the most of target molecules are not effectively excited, and the intrinsic EF could be 10^6 to 10^7 times higher than the apparent EF, as mentioned above [14]. To estimate the adsorption behavior of the target molecules and the capacity of hot sites, the concentration dependency of the EFs should be checked. Based on Freundlich's equation (Eq. 4.7), the double logarithmic plot of EFs against concentration can be used [168,193].

$$\frac{x}{m} = KC_{\text{enhanced}}{}^{1/n} \tag{4.7}$$

x and m are the masses of adsorbate and adsorbent, respectively.
K and n are the empirical constants, which will be obtained from the data.

If it is assumed that the signal intensity of surface-enhanced spectrum is proportional to coverage of surface (x/m), the Eq. (4.7) is illustrated as the Eq. (4.8).

$$\text{EF} = AB\frac{{}^{x}\!/_{m}}{C_{\text{enhanced}}} \tag{4.8}$$

A is the a proportional constant of the intensity of surface-enhanced spectral band against x/m
B is the a constant representing the $C_{\text{control}}/I_{\text{control}}$.

Then, the Eqs. (4.7), (4.8) are merged to the Eq. (4.9) or (4.10).

$$\mathrm{EF} = ABKC_{\mathrm{enhanced}}{}^{\left(\frac{1}{n}-1\right)} \tag{4.9}$$

$$\log\ \mathrm{EF} = \left(\frac{1}{n}-1\right)\log\ C_{\mathrm{enhanced}} + \log\ ABK \tag{4.10}$$

Thus, the linearity of the double logarithmic plot of EFs against concentration suggests that the adsorption property of target molecules onto hot sites is constant. When the slope of plot is 0, the hot sites are open enough to allow the increasing of adsorption amount proportional to the concentration of target molecules. In contrast, the target molecules can't adsorb on the hot sites anymore if the slope is −1. The value intermediate between 0 and −1 implies that the hot sites are rather occupied, and then the target molecules can't adsorb onto the hot site effectively. It is likely they form multilayers. In a study comparing the EFs of dispersion and film of the confeito-like gold nanoparticles, dispersion was found to provide more hot sites and stronger EFs than the film did (Fig. 4.20) [168].

4.6 Recent Applications: Beyond the Spectroscopies

Surface-enhanced spectroscopies have been used as strong tools in biomedical fields. The minor components in the specimen are selectively adsorbed on the hot sites on the nanostructures, and the surface-enhanced spectra help the detection of the target molecules

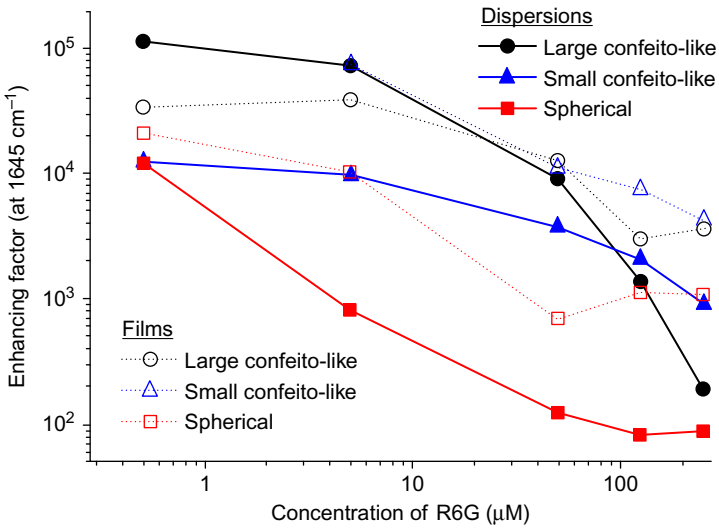

Fig. 4.20

Enhancing factors of SERS of rhodamine 6G mixed with the dispersions of gold nanoparticles (large confeito-like, small confeito-like, and spherical) and spread on their films. Laser excitation wavelength was 532.3 nm [166]. *Reproduced with permission from N.M. Dang, Surface plasmon resonance of confeito-like gold nanoparticles (Master's thesis), National Taiwan University of Science and Technology, Taipei, 2013. National Taiwan University of Science and Technology.*

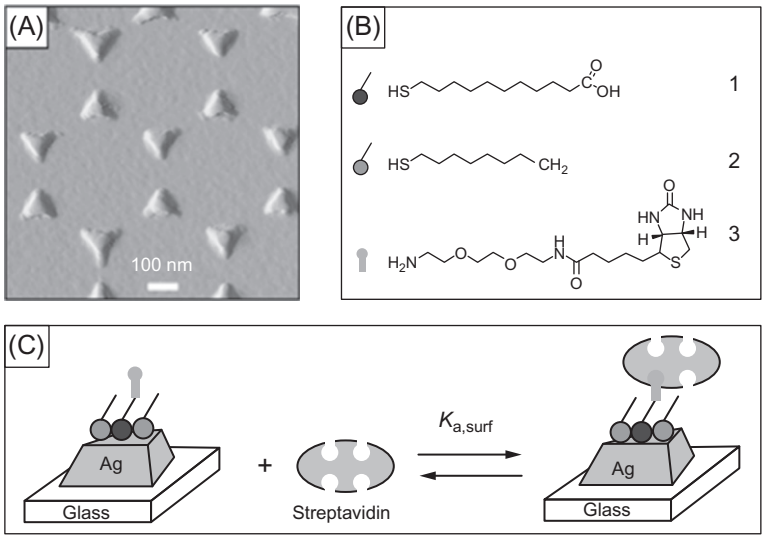

Fig. 4.21

(A) Tapping mode AFM image of the Ag nanoparticles deposited on a glass substrate. (B) Chemical modifiers applied on the Ag nanoparticles. A mixed monolayer of (1) 11-MUA and (2) 1-OT is covalently linked with (3) biotin via the esterification of the carboxyl groups of (1). (C) Schematic of streptavidin-biotinylated Ag nanoparticles on a glass substrate [194]. *Modified from A.J. Haes, R.P. Van Duyne, A nanoscale optical biosensor: sensitivity and selectivity of an approach based on the localized surface plasmon resonance spectroscopy of triangular silver nanoparticles, J. Am. Chem. Soc. 124 (2002) 10596–10604. Copyright 2002, American Chemical Society.*

[194,195]. In these cases, DNA, antibodies, and enzymes are preferable to achieve selective adsorption of the target biomolecules (Fig. 4.21). Using the surface-selection rule [9,144,145], the configuration of the adsorbed film and the orientation of functional groups in the target molecules can be estimated. The enhancement of spectra facilitates time-resolved spectrometry to interpret the mechanism of enzyme reaction; the mechanism of photosynthesis is energetically investigated using the SERS and SEIRAS [196–199].

While the SERS and SEIRAS can be performed on substrates with nanostructured metals, dispersions of nanoparticles can be used in biomedical research. Since metal nanoparticles strongly absorb or scatter light, they have been used as markers in tissue. Gold nanoparticles can be easily observed under dark-field microscopes [200]. These nanoparticles can provide a plasmonic effect to realize the multiphoton excitation of dyes on nanoparticles, and then the sensitivity and selectivity of fluorescent microscopy can be improved [201–204]. This improvement on the fluorescent microscopy can reveal the microenvironment in the living tissues. Moreover, the living cells adsorbing silver nanoparticles were observed by the SERS under microscope, and their local components (proteins) were analyzed (Fig. 4.22) [205–207]. This method is expected to be a strong tool to reveal biomaterials and their reaction mechanisms in situ.

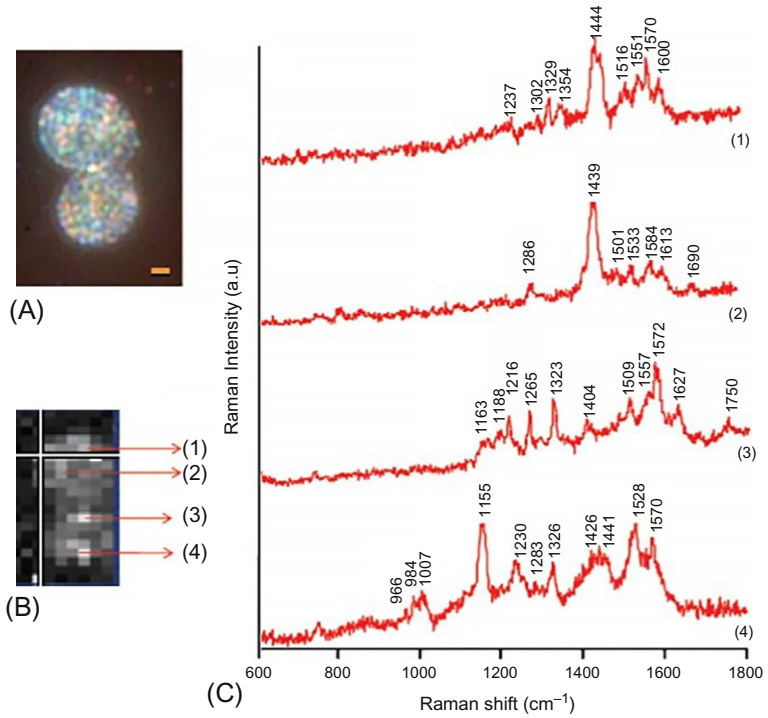

Fig. 4.22

(A) An optical microscopic image of a yeast cell with adsorbed Ag nanoparticles (*dark field*). The scale bar represents 1 μm. (B) Raman spectroscopic imaging of the yeast cell wall with adsorbed Ag nanoparticles. (C) Raman spectra obtained from positions (1) to (4) in (B) [206]. *Modified from A. Sujith, T. Itoh, H. Abe, K. Yoshida, M.S. Kiran, V. Biju, M. Ishikawa, Imaging the cell wall of living single yeast cells using surface-enhanced Raman spectroscopy, Anal. Bioanal. Chem. 394 (2009) 1803–1809. Springer.*

Even in the other research fields, applications for plasmonic behaviors are developing. For photoelectronic devices, enhancement of the electric field is used to improve the efficiency of LED and solar cells [22,208–211]. Metallic nanoparticles work as antennas to re-emit light at the interface in the LED. Nanoparticles can effectively absorb light and excite dyes and semiconductors in solar cells. This characteristic is desirable for dye-sensitized solar cells and organic solar cells, which have difficulties in the trade-off between the light absorption (the thicker, the better) and the electrical resistance (the thinner, the better). Metallic nanoparticles can provide the electron transfer pathway in the solar cell, and it can increase efficiency. While these solar cells use the surface-enhancing mechanism (excitation of dyes and semiconductors), some reports demonstrate direct energy generation. Metallic nanostructures absorb light and excite surface plasmon, and then the excited electrons (plasmon) transfer from the metal surface to other materials (typically, semiconductors) [212–219]. This electron transfer from the metals to the semiconductor is observed in the pairs

of gold/TiO_2, silver/TiO_2, and Cu/TiO_2. The nanostructures of silver and copper would be ionized by this electron transfer, and then their reactions would show as a change of their colors.

Thus, the plasmonic technology is now considered not only for passive applications (measurements and observation), but also for active ones; the microenvironment in the vicinity of metallic nanostructures can be changed by plasmonic effects. The photothermal effect is an application [220]. The electron-transfer results in reduction of H_2O on TiO_2 at the edges of gold nanorods (hot sites) [221]. The plasmon-induced redox reaction can be used for water-splitting and photosynthesis of ammonia and hydrocarbons with metal-semiconductor composites [221–225]. The photo-polymerization of monomers in nanogaps demonstrates selective polymerization via second-order harmonic generation [226]. Therefore, the active effects caused by plasmonic behaviors can be observed via in-situ surface-enhanced spectroscopies.

4.7 Conclusions

In this chapter, the basic concept of surface-enhanced spectroscopies, nanostructures for them, and physicochemical behaviors were introduced. Practical methods and new applications were presented, too. Recently, plasmonics have been rapidly developing, and understanding of the interactions between the light and materials has been expanded. Spectroscopies are direct methods for observing the interactions between light and materials, and their importance is increasing not only for applications, but also to provide new insight into the phenomena occurring at the interface of nanostructures.

References

[1] S.A. Maier, H.A. Atwater, Plasmonics: localization and guiding of electromagnetic energy in metal/dielectric structures, J. Appl. Phys. 98 (2005) 011101.
[2] M. Faraday, The Bakerian lecture: experimental relations of gold (and other metals) to light, Phil. Trans. R. Soc. 147 (1857) 145–181.
[3] K.A. Willets, R.P.V. Duyne, Localized surface plasmon resonance spectroscopy and sensing, Annu. Rev. Phys. Chem. 58 (2007) 267–297.
[4] S.A. Maier, M.L. Brongersma, P.G. Kik, S. Meltzer, A.A.G. Requicha, H.A. Atwater, Plasmonics—a route to nanoscale optical devices, Adv. Mater. 13 (2001) 1501–1505.
[5] E. Ozbay, Plasmonics: merging photonics and electronics at nanoscale dimensions, Science 311 (2006) 189–193.
[6] M. Moskovits, Surface-enhanced spectroscopy, Rev. Mod. Phys. 57 (1985) 783–826.
[7] M. Moskovits, Surface-enhanced Raman spectroscopy: a brief retrospective, J. Raman Spectrosc. 36 (2005) 485–496.
[8] P.L. Stiles, J.A. Dieringer, N.C. Shah, R.P.V. Duyne, Surface-enhanced Raman spectroscopy, Annu. Rev. Anal. Chem. 1 (2008) 601–626.
[9] M. Osawa, K.-I. Ataka, K. Yoshii, Y. Nishikawa, Surface-enhanced infrared spectroscopy: the origin of the absorption enhancement and band selection rule in the infrared spectra of molecules adsorbed on fine metal particles, Appl. Spectrosc. 47 (1993) 1497–1502.

[10] J.R. Lakowicz, K. Ray, M. Chowdhury, H. Szmacinski, Y. Fu, J. Zhang, K. Nowaczyk, Plasmon-controlled fluorescence: a new paradigm in fluorescence spectroscopy, Analyst 133 (2008) 1308–1346.
[11] M. Fleischmann, P.J. Hendra, A.J. McQuillan, Raman spectra of pyridine adsorbed at a silver electrode, Chem. Phys. Lett. 26 (1974) 163–166.
[12] D.L. Jeanmaire, R.P. Van Duyne, Surface raman spectroelectrochemistry, J. Electroanal. Chem. 84 (1977) 1–20.
[13] M.G. Albrecht, J.A. Creighton, Anomalously intense Raman spectra of pyridine at a silver electrode, J. Am. Chem. Soc. 99 (1977) 5215–5217.
[14] S. Nie, S.R. Emory, Probing single molecules and single nanoparticles by surface-enhanced Raman scattering, Science 275 (1997) 1102–1106.
[15] K. Kneipp, Y. Wang, H. Kneipp, L.T. Perelman, I. Itzkan, R.R. Dasari, M.S. Feld, Single molecule detection using surface-enhanced Raman scattering (SERS), Phys. Rev. Lett. 78 (1997) 1667–1670.
[16] K. Yoshida, T. Itoh, V. Biju, M. Ishikawa, Y. Ozaki, Experimental evaluation of the twofold electromagnetic enhancement theory of surface-enhanced resonance Raman scattering, Phys. Rev. B 79 (2009). 085419.
[17] H. Xu, E.J. Bjerneld, M. Käll, L. Börjesson, Spectroscopy of single hemoglobin molecules by surface enhanced Raman scattering, Phys. Rev. Lett. 83 (1999) 4357–4360.
[18] L.V. Brown, K. Zhao, N. King, H. Sobhani, P. Nordlander, N.J. Halas, Surface-enhanced infrared absorption using individual cross antennas tailored to chemical moieties, J. Am. Chem. Soc. 135 (2013) 3688–3695.
[19] T. Ming, H. Chen, R. Jiang, Q. Li, J. Wang, Plasmon-controlled fluorescence: beyond the intensity enhancement, J. Phys. Chem. Lett. 3 (2012) 191–202.
[20] M. Iranifam, Chemiluminescence reactions enhanced by silver nanoparticles and silver alloy nanoparticles: applications in analytical chemistry, TrAC, Trends Anal. Chem. 82 (2016) 126–142.
[21] S. Xu, Y. Liu, T. Wang, J. Li, Positive potential operation of a cathodic electrogenerated chemiluminescence immunosensor based on luminol and graphene for cancer biomarker detection, Anal. Chem. 83 (2011) 3817–3823.
[22] H.A. Atwater, A. Polman, Plasmonics for improved photovoltaic devices, Nat. Mater. 9 (2010) 205–213.
[23] W. Hou, S.B. Cronin, A review of surface plasmon resonance-enhanced photocatalysis, Adv. Funct. Mater. 23 (2013) 1612–1619.
[24] W.A. Murray, W.L. Barnes, Plasmonic materials, Adv. Mater. 19 (2007) 3771–3782.
[25] P. Anger, P. Bharadwaj, L. Novotny, Enhancement and quenching of single-molecule fluorescence, Phys. Rev. Lett. 96 (2006) 113002.
[26] W.E. Doering, S. Nie, Single-molecule and single-nanoparticle SERS: examining the roles of surface active sites and chemical enhancement, J. Phys. Chem. B 106 (2002) 311–317.
[27] H. Xu, J. Aizpurua, M. Käll, P. Apell, Electromagnetic contributions to single-molecule sensitivity in surface-enhanced Raman scattering, Phys. Rev. E 62 (2000) 4318–4324.
[28] P. Nordlander, C. Oubre, E. Prodan, K. Li, M.I. Stockman, Plasmon hybridization in nanoparticle dimers, Nano Lett. 4 (2004) 899–903.
[29] F. Nagasawa, M. Takase, H. Nabika, K. Murakoshi, Polarization characteristics of surface-enhanced Raman scattering from a small number of molecules at the gap of a metal nano-dimer, Chem. Commun. 47 (2011) 4514–4516.
[30] P.G. Etchegoin, E.C.L. Ru, A perspective on single molecule SERS: current status and future challenges, Phys. Chem. Chem. Phys. 10 (2008) 6079–6089.
[31] S. Berweger, J.M. Atkin, R.L. Olmon, M.B. Raschke, Adiabatic tip-plasmon focusing for nano-Raman spectroscopy, J. Phys. Chem. Lett. 1 (2010) 3427–3432.
[32] F. Hao, C.L. Nehl, J.H. Hafner, P. Nordlander, Plasmon resonances of a gold nanostar, Nano Lett. 7 (2007) 729–732.
[33] E. Hao, R.C. Bailey, G.C. Schatz, J.T. Hupp, S. Li, Synthesis and optical properties of "branched" gold nanocrystals, Nano Lett. 4 (2004) 327–330.

[34] M. Li, S.K. Cushing, J. Zhang, J. Lankford, Z.P. Aguilar, D. Ma, N. Wu, Shape-dependent surface-enhanced Raman scattering in gold–Raman-probe–silica sandwiched nanoparticles for biocompatible applications, Nanotechnology 23 (2012) 115501.
[35] K. Kneipp, H. Kneipp, H.G. Bohr, Single-molecule SERS spectroscopy, in: K. Kneipp, M. Moskovits, H. Kneipp (Eds.), Surface-Enhanced Raman Scattering, Springer, Berlin, Heidelberg, 2006, pp. 261–277.
[36] E.C. Le Ru, E. Blackie, M. Meyer, P.G. Etchegoin, Surface enhanced Raman scattering enhancement factors: a comprehensive study, J. Phys. Chem. C 111 (2007) 13794–13803.
[37] K. Kneipp, Y. Wang, R.R. Dasari, M.S. Feld, Approach to single molecule detection using surface-enhanced resonance Raman scattering (SERRS): a study using rhodamine 6G on colloidal silver, Appl. Spectrosc. 49 (1995) 780–784.
[38] G. McNay, D. Eustace, W.E. Smith, K. Faulds, D. Graham, Surface-enhanced Raman scattering (SERS) and surface-enhanced resonance raman scattering (SERRS): a review of applications, Appl. Spectrosc. 65 (2011) 825–837.
[39] P. Hildebrandt, M. Stockburger, Surface-enhanced resonance Raman spectroscopy of Rhodamine 6G adsorbed on colloidal silver, J. Phys. Chem. 88 (1984) 5935–5944.
[40] J.A. Dieringer, K.L. Wustholz, D.J. Masiello, J.P. Camden, S.L. Kleinman, G.C. Schatz, R.P. Van Duyne, Surface-enhanced Raman excitation spectroscopy of a single rhodamine 6G molecule, J. Am. Chem. Soc. 131 (2009) 849–854.
[41] Z. Zhang, T. Imae, Study of surface-enhanced infrared spectroscopy, J. Colloid Interface Sci. 233 (2001) 99–106.
[42] S. Ye, L. Fang, Y. Lu, Contribution of charge-transfer effect to surface-enhanced IR for Ag@PPy nanoparticles, Phys. Chem. Chem. Phys. 11 (2009) 2480–2484.
[43] F. Tam, G.P. Goodrich, B.R. Johnson, N.J. Halas, Plasmonic enhancement of molecular fluorescence, Nano Lett. 7 (2007) 496–501.
[44] E. Dulkeith, A.C. Morteani, T. Niedereichholz, T.A. Klar, J. Feldmann, S.A. Levi, F.C.J.M. van Veggel, D. N. Reinhoudt, M. Möller, D.I. Gittins, Fluorescence quenching of dye molecules near gold nanoparticles: radiative and nonradiative effects, Phys. Rev. Lett. 89 (2002) 203002.
[45] J.R. Lakowicz, Radiative decay engineering: biophysical and biomedical applications, Anal. Biochem. 298 (2001) 1–24.
[46] R. Bardhan, N.K. Grady, J.R. Cole, A. Joshi, N.J. Halas, Fluorescence enhancement by Au nanostructures: nanoshells and nanorods, ACS Nano 3 (2009) 744–752.
[47] R.S. Swathi, K.L. Sebastian, Resonance energy transfer from a fluorescent dye molecule to plasmon and electron-hole excitations of a metal nanoparticle, J. Chem. Phys. 126 (2007) 234701.
[48] G.P. Acuna, M. Bucher, I.H. Stein, C. Steinhauer, A. Kuzyk, P. Holzmeister, R. Schreiber, A. Moroz, F. D. Stefani, T. Liedl, F.C. Simmel, P. Tinnefeld, Distance dependence of single-fluorophore quenching by gold nanoparticles studied on DNA origami, ACS Nano 6 (2012) 3189–3195.
[49] E. Dulkeith, M. Ringler, T.A. Klar, J. Feldmann, A. Muñoz Javier, W.J. Parak, Gold nanoparticles quench fluorescence by phase induced radiative rate suppression, Nano Lett. 5 (2005) 585–589.
[50] N.S. Abadeer, M.R. Brennan, W.L. Wilson, C.J. Murphy, Distance and plasmon wavelength dependent fluorescence of molecules bound to silica-coated gold nanorods, ACS Nano 8 (2014) 8392–8406.
[51] K.W. Kittredge, M.A. Fox, J.K. Whitesell, Effect of alkyl chain length on the fluorescence of 9-alkylfluorenyl thiols as self-assembled monolayers on gold, J. Phys. Chem. B 105 (2001) 10594–10599.
[52] H. Imahori, Y. Kashiwagi, Y. Endo, T. Hanada, Y. Nishimura, I. Yamazaki, Y. Araki, O. Ito, S. Fukuzumi, Structure and photophysical properties of porphyrin-modified metal nanoclusters with different chain lengths, Langmuir 20 (2004) 73–81.
[53] G. Schneider, G. Decher, N. Nerambourg, R. Praho, M.H.V. Werts, M. Blanchard-Desce, Distance-dependent fluorescence quenching on gold nanoparticles ensheathed with layer-by-layer assembled polyelectrolytes, Nano Lett. 6 (2006) 530–536.
[54] W. Ni, T. Ambjörnsson, S.P. Apell, H. Chen, J. Wang, Observing plasmonic-molecular resonance coupling on single gold nanorods, Nano Lett. 10 (2010) 77–84.

[55] M. Ujihara, N.M. Dang, T. Imae, Fluorescence quenching of uranine on confeito-like Au nanoparticles, J. Nanosci. Nanotechnol. 14 (2014) 4906–4910.
[56] L. Zhao, T. Ming, L. Shao, H. Chen, J. Wang, Plasmon-controlled Förster resonance energy transfer, J. Phys. Chem. C 116 (2012) 8287–8296.
[57] N. Nath, A. Chilkoti, A colorimetric gold nanoparticle sensor to interrogate biomolecular interactions in real time on a surface, Anal. Chem. 74 (2002) 504–509.
[58] V.N. Rai, A.K. Srivastava, C. Mukherjee, S.K. Deb, Surface enhanced absorption and transmission from dye coated gold nanoparticles in thin films, Appl. Opt. 51 (2012) 2606–2615.
[59] T. Endo, K. Kerman, N. Nagatani, Y. Takamura, E. Tamiya, Label-free detection of peptide nucleic acid-DNA hybridization using localized surface plasmon resonance based optical biosensor, Anal. Chem. 77 (2005) 6976–6984.
[60] R. Elghanian, J.J. Storhoff, R.C. Mucic, R.L. Letsinger, C.A. Mirkin, Selective colorimetric detection of polynucleotides based on the distance-dependent optical properties of gold nanoparticles, Science 277 (1997) 1078–1081.
[61] R. Gordon, D. Sinton, K.L. Kavanagh, A.G. Brolo, A new generation of sensors based on extraordinary optical transmission, Acc. Chem. Res. 41 (2008) 1049–1057.
[62] J. Homola, Surface plasmon resonance sensors for detection of chemical and biological species, Chem. Rev. 108 (2008) 462–493.
[63] G.C. Schatz, R.P. Van Duyne, Electromagnetic mechanism of surface-enhanced spectroscopy. in: Handbook of Vibrational Spectroscopy, John Wiley & Sons, Hoboken, NJ, 2006. http://dx.doi.org/10.1002/0470027320.s0101.
[64] D. Ok Shin, J.-R. Jeong, T. Hee Han, C. Min Koo, H.-J. Park, Y. Taik Lim, S. Ouk Kim, A plasmonic biosensor array by block copolymer lithography, J. Mater. Chem. 20 (2010) 7241–7247.
[65] M. Erol, Y. Han, S.K. Stanley, C.M. Stafford, H. Du, S. Sukhishvili, SERS not to be taken for granted in the presence of oxygen, J. Am. Chem. Soc. 131 (2009) 7480–7481.
[66] P. Singh, N.T.B. Thuy, Y. Aoki, D. Mott, S. Maenosono, Intensification of surface enhanced Raman scattering of thiol-containing molecules using Ag@Au core@shell nanoparticles, J. Appl. Phys. 109 (2011). 094301.
[67] D.T.N. Anh, P. Singh, C. Shankar, D. Mott, S. Maenosono, Charge-transfer-induced suppression of galvanic replacement and synthesis of (Au@Ag)@Au double shell nanoparticles for highly uniform, robust and sensitive bioprobes, Appl. Phys. Lett. 99 (2011). 073107.
[68] M.W. Knight, N.S. King, L. Liu, H.O. Everitt, P. Nordlander, N.J. Halas, Aluminum for plasmonics, ACS Nano 8 (2014) 834–840.
[69] T. Ramani, K. Leon Prasanth, B. Sreedhar, Air stable colloidal copper nanoparticles: synthesis, characterization and their surface-enhanced Raman scattering properties, Phys. E. 77 (2016) 65–71.
[70] A. Miki, S. Ye, M. Osawa, Surface-enhanced IR absorption on platinum nanoparticles: an application to real-time monitoring of electrocatalytic reactions, Chem. Commun. (2002) 1500–1501.
[71] C. Zhang, B.-Q. Chen, Z.-Y. Li, Y. Xia, Y.-G. Chen, Surface plasmon resonance in bimetallic core–shell nanoparticles, J. Phys. Chem. C 119 (2015) 16836–16845.
[72] Z.-Q. Tian, B. Ren, J.-F. Li, Z.-L. Yang, Expanding generality of surface-enhanced Raman spectroscopy with borrowing SERS activity strategy, Chem. Commun. (2007) 3514–3534.
[73] Z.-Q. Tian, B. Ren, D.-Y. Wu, Surface-enhanced raman scattering: from noble to transition metals and from rough surfaces to ordered nanostructures, J. Phys. Chem. B 106 (2002) 9463–9483.
[74] J.J. Mock, M. Barbic, D.R. Smith, D.A. Schultz, S. Schultz, Shape effects in plasmon resonance of individual colloidal silver nanoparticles, J. Chem. Phys. 116 (2002) 6755–6759.
[75] S.K. Ghosh, T. Pal, Interparticle coupling effect on the surface plasmon resonance of gold nanoparticles: from theory to applications, Chem. Rev. 107 (2007) 4797–4862.
[76] Y. Zhang, Y.-R. Zhen, O. Neumann, J.K. Day, P. Nordlander, N.J. Halas, Coherent anti-Stokes Raman scattering with single-molecule sensitivity using a plasmonic Fano resonance, Nat. Commun. 5 (2014) 4424.

[77] K.L. Kelly, E. Coronado, L.L. Zhao, G.C. Schatz, The optical properties of metal nanoparticles: the influence of size, shape, and dielectric environment, J. Phys. Chem. B 107 (2003) 668–677.
[78] J.N. Anker, W.P. Hall, O. Lyandres, N.C. Shah, J. Zhao, R.P. Van Duyne, Biosensing with plasmonic nanosensors, Nat. Mater. 7 (2008) 442–453.
[79] X. Lu, M. Rycenga, S.E. Skrabalak, B. Wiley, Y. Xia, Chemical synthesis of novel plasmonic nanoparticles, Annu. Rev. Phys. Chem. 60 (2009) 167–192.
[80] E. Cubukcu, N. Yu, E.J. Smythe, L. Diehl, K.B. Crozier, F. Capasso, Plasmonic laser antennas and related devices, IEEE J. Sel. Top. Quantum Electron. 14 (2008) 1448–1461.
[81] V.S. Tiwari, T. Oleg, G.K. Darbha, W. Hardy, J.P. Singh, P.C. Ray, Non-resonance SERS effects of silver colloids with different shapes, Chem. Phys. Lett. 446 (2007) 77–82.
[82] J. Zeng, H. Jia, J. An, X. Han, W. Xu, B. Zhao, Y. Ozaki, Preparation and SERS study of triangular silver nanoparticle self-assembled films, J. Raman Spectrosc. 39 (2008) 1673–1678.
[83] A.R. Tao, S. Habas, P. Yang, Shape control of colloidal metal nanocrystals, Small 4 (2008) 310–325.
[84] D. Wang, T. Imae, Watching the transformation from au nanoparticles to microplates, Chem. Lett. 35 (2006) 1152–1153.
[85] X. Ji, X. Song, J. Li, Y. Bai, W. Yang, X. Peng, Size control of gold nanocrystals in citrate reduction: the third role of citrate, J. Am. Chem. Soc. 129 (2007) 13939–13948.
[86] J. Pérez-Juste, I. Pastoriza-Santos, L.M. Liz-Marzán, P. Mulvaney, Gold nanorods: synthesis, characterization and applications, Coord. Chem. Rev. 249 (2005) 1870–1901.
[87] A. Brioude, X.C. Jiang, M.P. Pileni, Optical properties of gold nanorods: DDA simulations supported by experiments, J. Phys. Chem. B 109 (2005) 13138–13142.
[88] X. Huang, S. Neretina, M.A. El-Sayed, Gold nanorods: from synthesis and properties to biological and biomedical applications, Adv. Mater. 21 (2009) 4880–4910.
[89] K.D. Alexander, K. Skinner, S. Zhang, H. Wei, R. Lopez, Tunable SERS in gold nanorod dimers through strain control on an elastomeric substrate, Nano Lett. 10 (2010) 4488–4493.
[90] B. Nikoobakht, M.A. El-Sayed, Surface-enhanced Raman scattering studies on aggregated gold nanorods, J. Phys. Chem. A 107 (2003) 3372–3378.
[91] T. Imae, X. Zhang, Effect of Au nanorod assemblies on surface-enhanced Raman spectroscopy, J. Taiwan Inst. Chem. Eng. 45 (2014) 3081–3084.
[92] Z. Zhu, H. Meng, W. Liu, X. Liu, J. Gong, X. Qiu, L. Jiang, D. Wang, Z. Tang, Superstructures and SERS properties of gold nanocrystals with different shapes, Angew. Chem. Int. Ed. 50 (2011) 1593–1596.
[93] J. Zhang, Y. Gao, R.A. Alvarez-Puebla, J.M. Buriak, H. Fenniri, Synthesis and SERS properties of nanocrystalline gold octahedra generated from thermal decomposition of HAuCl4 in block copolymers, Adv. Mater. 18 (2006) 3233–3237.
[94] C.J. Orendorff, A. Gole, T.K. Sau, C.J. Murphy, Surface-enhanced raman spectroscopy of self-assembled monolayers: sandwich architecture and nanoparticle shape dependence, Anal. Chem. 77 (2005) 3261–3266.
[95] T.K. Sau, A.L. Rogach, Nonspherical noble metal nanoparticles: colloid-chemical synthesis and morphology control, Adv. Mater. 22 (2010) 1781–1804.
[96] J.L. Burt, J.L. Elechiguerra, J. Reyes-Gasga, J. Martin Montejano-Carrizales, M. Jose-Yacaman, Beyond archimedean solids: star polyhedral gold nanocrystals, J. Cryst. Growth 285 (2005) 681–691.
[97] M.J. Mulvihill, X.Y. Ling, J. Henzie, P. Yang, Anisotropic etching of silver nanoparticles for plasmonic structures capable of single-particle SERS, J. Am. Chem. Soc. 132 (2010) 268–274.
[98] B.L. Sanchez-Gaytan, P. Swanglap, T.J. Lamkin, R.J. Hickey, Z. Fakhraai, S. Link, S.-J. Park, Spiky gold nanoshells: synthesis and enhanced scattering properties, J. Phys. Chem. C 116 (2012) 10318–10324.
[99] M. Zayats, R. Baron, I. Popov, I. Willner, Biocatalytic growth of Au nanoparticles: from mechanistic aspects to biosensors design, Nano Lett. 5 (2005) 21–25.
[100] J. Xie, Q. Zhang, J.Y. Lee, D.I.C. Wang, The synthesis of SERS-active gold nanoflower tags for in vivo applications, ACS Nano 2 (2008) 2473–2480.
[101] H. Liang, Z. Li, W. Wang, Y. Wu, H. Xu, Highly surface-roughened "flower-like" silver nanoparticles for extremely sensitive substrates of surface-enhanced Raman scattering, Adv. Mater. 21 (2009) 4614–4618.

[102] P.S. Kumar, I. Pastoriza-Santos, B. Rodríguez-González, F.J.G. de Abajo, L.M. Liz-Marzán, High-yield synthesis and optical response of gold nanostars, Nanotechnology 19 (2007). 015606.
[103] H. Yuan, C.G. Khoury, H. Hwang, C.M. Wilson, G.A. Grant, T. Vo-Dinh, Gold nanostars: surfactant-free synthesis, 3D modelling, and two-photon photoluminescence imaging, Nanotechnology 23 (2012). 075102.
[104] C.G. Khoury, T. Vo-Dinh, Gold nanostars for surface-enhanced raman scattering: synthesis, characterization and optimization, J. Phys. Chem. C 112 (2008) 18849–18859.
[105] Z. Liu, Z. Yang, B. Peng, C. Cao, C. Zhang, H. You, Q. Xiong, Z. Li, J. Fang, Highly sensitive, uniform, and reproducible surface-enhanced Raman spectroscopy from hollow Au-Ag Alloy nanourchins, Adv. Mater. 26 (2014) 2431–2439.
[106] J. Sharma, Y. Tai, T. Imae, Synthesis of confeito-like gold nanostructures by a solution phase galvanic reaction, J. Phys. Chem. C 112 (2008) 17033–17037.
[107] M. Ujihara, T. Imae, Versatile one-pot synthesis of confeito-like Au nanoparticles and their surface-enhanced Raman scattering effect, Colloids Surf. A 436 (2013) 380–385.
[108] X. Luo, T. Imae, Shape-controlled synthesis of gold nanoparticles under UV irradiation in the presence of poly(ethylene glycol), Curr. Nanosci. 3 (2007) 195–198.
[109] X. Luo, T. Imae, Photochemical synthesis of crown-shaped platinum nanoparticles using aggregates of G4-NH2 PAMAM dendrimer as templates, J. Mater. Chem. 17 (2007) 567–571.
[110] J. Sharma, Y. Tai, T. Imae, Biomodulation approach for gold nanoparticles: synthesis of anisotropic to luminescent particles, Chem. Asian. J. 5 (2010) 70–73.
[111] L. Wang, M. Imura, Y. Yamauchi, Tailored synthesis of various Au nanoarchitectures with branched shapes, CrystEngComm 14 (2012) 7594–7599.
[112] G.H. Jeong, Y.W. Lee, M. Kim, S.W. Han, High-yield synthesis of multi-branched gold nanoparticles and their surface-enhanced Raman scattering properties, J. Colloid Interface Sci. 329 (2009) 97–102.
[113] L. Pei, K. Mori, M. Adachi, Formation process of two-dimensional networked gold nanowires by citrate reduction of AuCl4- and the shape stabilization, Langmuir 20 (2004) 7837–7843.
[114] S.O. Kucheyev, J.R. Hayes, J. Biener, T. Huser, C.E. Talley, A.V. Hamza, Surface-enhanced Raman scattering on nanoporous Au, Appl. Phys. Lett. 89 (2006). 053102.
[115] L.H. Qian, X.Q. Yan, T. Fujita, A. Inoue, M.W. Chen, Surface enhanced Raman scattering of nanoporous gold: smaller pore sizes stronger enhancements, Appl. Phys. Lett. 90 (2007) 153120.
[116] C. Li, Ö. Dag, T.D. Dao, T. Nagao, Y. Sakamoto, T. Kimura, O. Terasaki, Y. Yamauchi, Electrochemical synthesis of mesoporous gold films toward mesospace-stimulated optical properties, Nat. Commun. 6 (2015) 6608.
[117] A.V. Whitney, B.D. Myers, R.P. Van Duyne, Sub-100 nm triangular nanopores fabricated with the reactive ion etching variant of nanosphere lithography and angle-resolved nanosphere lithography, Nano Lett. 4 (2004) 1507–1511.
[118] S. Shanmukh, L. Jones, J. Driskell, Y. Zhao, R. Dluhy, R.A. Tripp, Rapid and sensitive detection of respiratory virus molecular signatures using a silver nanorod array SERS substrate, Nano Lett. 6 (2006) 2630–2636.
[119] S.B. Chaney, S. Shanmukh, R.A. Dluhy, Y.-P. Zhao, Aligned silver nanorod arrays produce high sensitivity surface-enhanced Raman spectroscopy substrates, Appl. Phys. Lett. 87 (2005). 031908.
[120] C.L. Haynes, R.P. Van Duyne, Nanosphere lithography: a versatile nanofabrication tool for studies of size-dependent nanoparticle optics, J. Phys. Chem. B 105 (2001) 5599–5611.
[121] T.R. Jensen, M.D. Malinsky, C.L. Haynes, R.P. Van Duyne, Nanosphere lithography: tunable localized surface plasmon resonance spectra of silver nanoparticles, J. Phys. Chem. B 104 (2000) 10549–10556.
[122] D. Choi, Y. Choi, S. Hong, T. Kang, L.P. Lee, Self-organized hexagonal-nanopore SERS array, Small 6 (2010) 1741–1744.
[123] Y. Lu, G.L. Liu, J. Kim, Y.X. Mejia, L.P. Lee, Nanophotonic crescent moon structures with sharp edge for ultrasensitive biomolecular detection by local electromagnetic field enhancement effect, Nano Lett. 5 (2005) 119–124.

[124] J.J. Baumberg, T.A. Kelf, Y. Sugawara, S. Cintra, M.E. Abdelsalam, P.N. Bartlett, A.E. Russell, Angle-resolved surface-enhanced raman scattering on metallic nanostructured plasmonic crystals, Nano Lett. 5 (2005) 2262–2267.
[125] A. Moisala, A.G. Nasibulin, E.I. Kauppinen, The role of metal nanoparticles in the catalytic production of single-walled carbon nanotubes—a review, J. Phys. Condens. Matter 15 (2003) S3011.
[126] G. Schmid, B. Corain, Nanoparticulated gold: syntheses, structures, electronics, and reactivities, Eur. J. Inorg. Chem. 2003 (2003) 3081–3098.
[127] X. Xu, A. Meade, Y. Bayazitoglu, Numerical investigation of nanoparticle-assisted laser-induced interstitial thermotherapy toward tumor and cancer treatments, Lasers Med. Sci. 26 (2011) 213–222.
[128] M.B. Mohamed, K.Z. Ismail, S. Link, M.A. El-Sayed, Thermal reshaping of gold nanorods in micelles, J. Phys. Chem. B 102 (1998) 9370–9374.
[129] Z.L. Wang, M.B. Mohamed, S. Link, M.A. El-Sayed, Crystallographic facets and shapes of gold nanorods of different aspect ratios, Surf. Sci. 440 (1999) L809–L814.
[130] R.C. Maher, L.F. Cohen, E.C.L. Ru, P.G. Etchegoin, A study of local heating of molecules under surface enhanced Raman scattering (SERS) conditions using the anti-stokes/stokes ratio, Faraday Discuss. 132 (2006) 77–83.
[131] Y. Sawai, B. Takimoto, H. Nabika, K. Murakoshi, Anti-stokes/stokes ratio of surface-enhanced Raman scattering spectra observed at a metal nano-gap arrayed on a solid surface, Can. J. Anal. Sci. Spectrosc. 52 (2007) 142–149.
[132] K.W. Kho, Z.X. Shen, Z. Lei, F. Watt, K.C. Soo, M. Olivo, Investigation into a surface plasmon related heating effect in surface enhanced Raman Spectroscopy, Anal. Chem. 79 (2007) 8870–8882.
[133] F.H. Ho, Y.-H. Wu, M. Ujihara, T. Imae, A solution-based nano-plasmonic sensing technique by using gold nanorods, Analyst 137 (2012) 2545–2548.
[134] M. Duval Malinsky, K.L. Kelly, G.C. Schatz, R.P. Van Duyne, Nanosphere lithography: effect of substrate on the localized surface plasmon resonance spectrum of silver nanoparticles, J. Phys. Chem. B 105 (2001) 2343–2350.
[135] C. Langhammer, M. Schwind, B. Kasemo, I. Zorić, Localized surface plasmon resonances in aluminum nanodisks, Nano Lett. 8 (2008) 1461–1471.
[136] M.W. Knight, Y. Wu, J.B. Lassiter, P. Nordlander, N.J. Halas, Substrates matter: influence of an adjacent dielectric on an individual plasmonic nanoparticle, Nano Lett. 9 (2009) 2188–2192.
[137] T. Hutter, S.R. Elliott, S. Mahajan, Interaction of metallic nanoparticles with dielectric substrates: effect of optical constants, Nanotechnology 24 (2013). 035201.
[138] R.P. Van Duyne, J.P. Haushalter, Surface-enhanced Raman spectroscopy of adsorbates on semiconductor electrode surfaces: tris (bipyridine) ruthenium (II) adsorbed on silver-modified n-gallium arsenide (100), J. Phys. Chem. 87 (1983) 2999–3003.
[139] J.R. Krenn, J.C. Weeber, A. Dereux, E. Bourillot, J.P. Goudonnet, B. Schider, A. Leitner, F.R. Aussenegg, C. Girard, Direct observation of localized surface plasmon coupling, Phys. Rev. B 60 (1999) 5029.
[140] W. Khunsin, B. Brian, J. Dorfmüller, M. Esslinger, R. Vogelgesang, C. Etrich, C. Rockstuhl, A. Dmitriev, K. Kern, Long-distance indirect excitation of nanoplasmonic resonances, Nano Lett. 11 (2011) 2765–2769.
[141] J.F. Li, Y.F. Huang, Y. Ding, Z.L. Yang, S.B. Li, X.S. Zhou, F.R. Fan, W. Zhang, Z.Y. Zhou, D. Y. Wu, B. Ren, Z.L. Wang, Z.Q. Tian, Shell-isolated nanoparticle-enhanced Raman spectroscopy, Nature 464 (2010) 392–395.
[142] J. Lee, B. Hua, S. Park, M. Ha, Y. Lee, Z. Fan, H. Ko, Tailoring surface plasmons of high-density gold nanostar assemblies on metal films for surface-enhanced Raman spectroscopy, Nanoscale 6 (2014) 616–623.
[143] S.-Y. Ding, J. Yi, J.-F. Li, Z.-Q. Tian, A theoretical and experimental approach to shell-isolated nanoparticle-enhanced Raman spectroscopy of single-crystal electrodes, Surf. Sci. 631 (2015) 73–80.
[144] M. Moskovits, Surface selection rules, J. Chem. Phys. 77 (1998) 4408–4416.
[145] H.A. Pearce, N. Sheppard, Possible importance of a "metal-surface selection rule" in the interpretation of the infrared spectra of molecules adsorbed on particulate metals; infrared spectra from ethylene chemisorbed on silica-supported metal catalysts, Surf. Sci. 59 (1976) 205–217.

[146] K. Kneipp, H. Kneipp, I. Itzkan, R.R. Dasari, M.S. Feld, Ultrasensitive chemical analysis by Raman spectroscopy, Chem. Rev. 99 (1999) 2957–2976.
[147] E.C. Le Ru, M. Meyer, P.G. Etchegoin, Proof of single-molecule sensitivity in surface enhanced Raman scattering (SERS) by means of a two-analyte technique, J. Phys. Chem. B 110 (2006) 1944–1948.
[148] Z. Wang, L.J. Rothberg, Origins of blinking in single-molecule raman spectroscopy, J. Phys. Chem. B 109 (2005) 3387–3391.
[149] Y. Maruyama, M. Ishikawa, M. Futamata, Thermal activation of blinking in SERS signal, J. Phys. Chem. B 108 (2004) 673–678.
[150] M. Ujihara, T. Imae, Adsorption behaviors of poly(amido amine) dendrimers with an azacrown core and long alkyl chain spacers on solid substrates, J. Colloid Interface Sci. 293 (2006) 333–341.
[151] T. Imae, H. Torii, In situ investigation of molecular adsorption on Au surface by surface-enhanced infrared absorption spectroscopy, J. Phys. Chem. B 104 (2000) 9218–9224.
[152] T. Yajima, Y. Yu, M. Futamata, Closely adjacent gold nanoparticles linked by chemisorption of neutral rhodamine 123 molecules providing enormous SERS intensity, Phys. Chem. Chem. Phys. 13 (2011) 12454–12462.
[153] M. Futamata, Y. Yu, T. Yajima, Elucidation of electrostatic interaction between cationic dyes and Ag nanoparticles generating enormous SERS enhancement in aqueous solution, J. Phys. Chem. C 115 (2011) 5271–5279.
[154] M.A. Bryant, J.E. Pemberton, Surface Raman scattering of self-assembled monolayers formed from 1-alkanethiols: behavior of films at Au and comparison to films at Ag, J. Am. Chem. Soc. 113 (1991) 8284–8293.
[155] Zhang, T. Imae, Hydrogen-bonding stabilized self-assembled monolayer film of a functionalized diacid, protoporphyrin IX zinc(II), onto a gold surface, Nano Lett. 1 (2001) 241–243.
[156] Z. Zhang, T. Imae, H. Sato, A. Watanabe, Y. Ozaki, Surface-enhanced Raman scattering and surface-enhanced infrared absorption spectroscopic studies of a metalloporphyrin monolayer film formed on pyridine self-assembled monolayer-modified gold, Langmuir 17 (2001) 4564–4568.
[157] M.D. Porter, T.B. Bright, D.L. Allara, C.E.D. Chidsey, Spontaneously organized molecular assemblies. 4. Structural characterization of n-alkyl thiol monolayers on gold by optical ellipsometry, infrared spectroscopy, and electrochemistry, J. Am. Chem. Soc. 109 (1987) 3559–3568.
[158] M. Brust, M. Walker, D. Bethell, D.J. Schiffrin, R. Whyman, Synthesis of thiol-derivatised gold nanoparticles in a two-phase Liquid–Liquid system. J. Chem. Soc. Chem. Commun. (7) (1994) 801–802, http://dx.doi.org/10.1039/C39940000801.
[159] K. Ikeda, S. Suzuki, K. Uosaki, Crystal face dependent chemical effects in surface-enhanced raman scattering at atomically defined gold facets, Nano Lett. 11 (2011) 1716–1722.
[160] K. Ikeda, S. Suzuki, K. Uosaki, Enhancement of SERS background through charge transfer resonances on single crystal gold surfaces of various orientations, J. Am. Chem. Soc. 135 (2013) 17387–17392.
[161] S. Kaneko, D. Murai, S. Marqués-González, H. Nakamura, Y. Komoto, S. Fujii, T. Nishino, K. Ikeda, K. Tsukagoshi, M. Kiguchi, Site-selection in single-molecule junction for highly reproducible molecular electronics, J. Am. Chem. Soc. 138 (2016) 1294–1300.
[162] V. Martínez Martínez, F. López Arbeloa, J. Bañuelos Prieto, I. López Arbeloa, Characterization of rhodamine 6G aggregates intercalated in solid thin films of laponite clay. 2 fluorescence spectroscopy, J. Phys. Chem. B 109 (2005) 7443–7450.
[163] M.A. Noginov, M. Vondrova, S.N. Williams, M. Bahoura, V.I. Gavrilenko, S.M. Black, V.P. Drachev, V. M. Shalaev, A. Sykes, Spectroscopic studies of liquid solutions of R6G laser dye and Ag nanoparticle aggregates, J. Opt. A Pure Appl. Opt. 7 (2005) S219.
[164] Y. Kitahama, Y. Tanaka, T. Itoh, M. Ishikawa, Y. Ozaki, Identification of thiacyanine J-aggregates adsorbed on single silver nanoaggregates by surface-enhanced Raman scattering and emission spectroscopy, Bull. Chem. Soc. Jpn. 82 (2009) 1126–1132.
[165] J. Zhao, L. Jensen, J. Sung, S. Zou, G.C. Schatz, R.P. Van Duyne, Interaction of plasmon and molecular resonances for rhodamine 6G adsorbed on silver nanoparticles, J. Am. Chem. Soc. 129 (2007) 7647–7656.
[166] N.M. Dang, Surface plasmon resonance of confeito-like gold nanoparticles (Master's thesis), National Taiwan University of Science and Technology, Taipei, 2013.

[167] N. Hayazawa, Y. Inouye, Z. Sekkat, S. Kawata, Metallized tip amplification of near-field Raman scattering, Opt. Commun. 183 (2000) 333–336.
[168] Z.-C. Zeng, S.-C. Huang, D.-Y. Wu, L.-Y. Meng, M.-H. Li, T.-X. Huang, J.-H. Zhong, X. Wang, Z.-L. Yang, B. Ren, Electrochemical tip-enhanced Raman spectroscopy, J. Am. Chem. Soc. 137 (2015) 11928–11931.
[169] H. Watanabe, Y. Ishida, N. Hayazawa, Y. Inouye, S. Kawata, Tip-enhanced near-field Raman analysis of tip-pressurized adenine molecule, Phys. Rev. B 69 (2004) 155418.
[170] H. Watanabe, N. Hayazawa, Y. Inouye, S. Kawata, DFT vibrational calculations of rhodamine 6G adsorbed on silver: analysis of tip-enhanced raman spectroscopy, J. Phys. Chem. B 109 (2005) 5012–5020.
[171] J.A. DeRose, T. Thundat, L.A. Nagahara, S.M. Lindsay, Gold grown epitaxially on mica: conditions for large area flat faces, Surf. Sci. 256 (1991) 102–108.
[172] A. Serrano, O.R. de la Fuente, M.A. García, Extended and localized surface plasmons in annealed Au films on glass substrates, J. Appl. Phys. 108 (2010). 074303.
[173] S. Szunerits, V.G. Praig, M. Manesse, R. Boukherroub, Gold island films on indium tin oxide for localized surface plasmon sensing, Nanotechnology 19 (2008) 195712.
[174] Z. Zhang, T. Imae, Study of surface-enhanced infrared spectroscopy, J. Colloid Interface Sci. 233 (2001) 107–111.
[175] G.H. Gu, J.S. Suh, Enhancement at the junction of silver nanorods, Langmuir 24 (2008) 8934–8938.
[176] J. Zheng, Z. Zhu, H. Chen, Z. Liu, Nanopatterned assembling of colloidal gold nanoparticles on silicon, Langmuir 16 (2000) 4409–4412.
[177] M. Fan, A.G. Brolo, Self-assembled Au nanoparticles as substrates for surface-enhanced vibrational spectroscopy: optimization and electrochemical stability, ChemPhysChem 9 (2008) 1899–1907.
[178] H.X. He, H. Zhang, Q.G. Li, T. Zhu, S.F.Y. Li, Z.F. Liu, Fabrication of designed architectures of Au nanoparticles on solid substrate with printed self-assembled monolayers as templates, Langmuir 16 (2000) 3846–3851.
[179] V. Santhanam, J. Liu, R. Agarwal, R.P. Andres, Self-assembly of uniform monolayer arrays of nanoparticles, Langmuir 19 (2003) 7881–7887.
[180] B. Kim, S.L. Tripp, A. Wei, Self-organization of large gold nanoparticle arrays, J. Am. Chem. Soc. 123 (2001) 7955–7956.
[181] Y. Lu, G.L. Liu, L.P. Lee, High-density silver nanoparticle film with temperature-controllable interparticle spacing for a tunable surface enhanced Raman scattering substrate, Nano Lett. 5 (2005) 5–9.
[182] Y.-H. Wu, T. Imae, M. Ujihara, Surface enhanced plasmon effects by gold nanospheres and nanorods in Langmuir-Blodgett films. Colloids Surf. A (2017). http://dx.doi.org/10.1016/j.colsurfa.2017.05.015.
[183] M. Ujihara, J. Orbulescu, T. Imae, R.M. Leblanc, Film structures of poly(amido amine) dendrimers with an azacrown core and long alkyl chain spacers on water or Ag nanoparticle suspension, Langmuir 21 (2005) 6846–6854.
[184] M. Ujihara, K. Mitamura, N. Torikai, T. Imae, Fabrication of metal nanoparticle monolayers on amphiphilic poly(amido amine) dendrimer langmuir films, Langmuir 22 (2006) 3656–3661.
[185] F. Kim, S. Kwan, J. Akana, P. Yang, Langmuir-Blodgett nanorod assembly, J. Am. Chem. Soc. 123 (2001) 4360–4361.
[186] A. Tao, F. Kim, C. Hess, J. Goldberger, R. He, Y. Sun, Y. Xia, P. Yang, Langmuir-Blodgett silver nanowire monolayers for molecular sensing using surface-enhanced Raman spectroscopy, Nano Lett. 3 (2003) 1229–1233.
[187] M. Suzuki, Y. Niidome, N. Terasaki, K. Inoue, Y. Kuwahara, S. Yamada, Surface-enhanced nonresonance Raman scattering of rhodamine 6G molecules adsorbed on gold nanorod films, Jpn. J. Appl. Phys. 43 (2004) L554.
[188] K. Mitamura, T. Imae, N. Saito, O. Takai, Fabrication and self-assembly of hydrophobic gold nanorods, J. Phys. Chem. B 111 (2007). 8891–8898.
[189] J.L. Baker, A. Widmer-Cooper, M.F. Toney, P.L. Geissler, A.P. Alivisatos, Device-scale perpendicular alignment of colloidal nanorods, Nano Lett. 10 (2010) 195–201.

[190] X. Zhang, T. Imae, Perpendicular superlattice growth of hydrophobic gold nanorods on patterned silicon substrates via evaporation-induced self-assembling, J. Phys. Chem. C 113 (2009) 5947–5951.
[191] C.-C. Chang, T. Imae, L.-Y. Chen, M. Ujihara, Efficient surface enhanced Raman scattering on confeito-like gold nanoparticle-adsorbed self-assembled monolayers, Phys. Chem. Chem. Phys. 17 (2015) 32328–32334.
[192] J. Kimling, M. Maier, B. Okenve, V. Kotaidis, H. Ballot, A. Plech, Turkevich method for gold nanoparticle synthesis revisited, J. Phys. Chem. B 110 (2006) 15700–15707.
[193] M. Ujihara, N.M. Dang, C.-C. Chang, T. Imae, Surface-enhanced infrared absorption spectra of eicosanoic acid on confeito-like Au nanoparticle, J. Taiwan Inst. Chem. Eng. 45 (2014) 3085–3089.
[194] A.J. Haes, R.P. Van Duyne, A nanoscale optical biosensor: sensitivity and selectivity of an approach based on the localized surface plasmon resonance spectroscopy of triangular silver nanoparticles, J. Am. Chem. Soc. 124 (2002) 10596–10604.
[195] R. Picorel, R.E. Holt, T.M. Cotton, M. Seibert, Surface-enhanced resonance Raman scattering spectroscopy of bacterial photosynthetic membranes. The carotenoid of Rhodospirillum rubrum, J. Biol. Chem. 263 (1988) 4374–4380.
[196] M. Seibert, R. Picorel, J.H. Kim, T.M. Cotton, Surface-enhanced Raman scattering spectroscopy of photosynthetic membranes and complexes, Methods Enzymol. 213 (1992) 31–42.
[197] K. Saha, S.S. Agasti, C. Kim, X. Li, V.M. Rotello, Gold nanoparticles in chemical and biological sensing, Chem. Rev. 112 (2012) 2739–2779.
[198] K. Ataka, F. Giess, W. Knoll, R. Naumann, S. Haber-Pohlmeier, B. Richter, J. Heberle, Oriented attachment and membrane reconstitution of His-tagged cytochrome c oxidase to a gold electrode: in situ monitoring by surface-enhanced infrared absorption spectroscopy, J. Am. Chem. Soc. 126 (2004) 16199–16206.
[199] V. Nedelkovski, A. Schwaighofer, C.A. Wraight, C. Nowak, R.L.C. Naumann, Surface-enhanced infrared absorption spectroscopy (SEIRAS) of light-activated photosynthetic reaction centers from rhodobacter sphaeroides reconstituted in a biomimetic membrane system, J. Phys. Chem. C 117 (2013) 16357–16363.
[200] I.H. El-Sayed, X. Huang, M.A. El-Sayed, Surface plasmon resonance scattering and absorption of anti-EGFR antibody conjugated gold nanoparticles in cancer diagnostics: applications in oral cancer, Nano Lett. 5 (2005) 829–834.
[201] W. Denk, J.H. Strickler, W.W. Webb, Two-photon laser scanning fluorescence microscopy, Science 248 (1990) 73–76.
[202] H. Kano, S. Kawata, Two-photon-excited fluorescence enhanced by a surface plasmon, Opt. Lett. 21 (1996) 1848–1850.
[203] J. Kneipp, H. Kneipp, K. Kneipp, Two-photon vibrational spectroscopy for biosciences based on surface-enhanced hyper-Raman scattering, Proc. Natl. Acad. Sci. U. S. A. 103 (2006) 17149–17153.
[204] H. Wang, T.B. Huff, D.A. Zweifel, W. He, P.S. Low, A. Wei, J.-X. Cheng, In vitro and in vivo two-photon luminescence imaging of single gold nanorods, Proc. Natl. Acad. Sci. U. S. A. 102 (2005) 15752–15756.
[205] A. Sujith, T. Itoh, H. Abe, A.A. Anas, K. Yoshida, V. Biju, M. Ishikawa, Surface enhanced Raman scattering analyses of individual silver nanoaggregates on living single yeast cell wall, Appl. Phys. Lett. 92 (2008) 103901.
[206] A. Sujith, T. Itoh, H. Abe, K. Yoshida, M.S. Kiran, V. Biju, M. Ishikawa, Imaging the cell wall of living single yeast cells using surface-enhanced Raman spectroscopy, Anal. Bioanal. Chem. 394 (2009) 1803–1809.
[207] K. Kneipp, H. Kneipp, J. Kneipp, Surface-enhanced Raman scattering in local optical fields of silver and gold nanoaggregates-from single-molecule Raman spectroscopy to ultrasensitive probing in live cells, Acc. Chem. Res. 39 (2006) 443–450.
[208] D.-M. Yeh, C.-F. Huang, C.-Y. Chen, Y.-C. Lu, C.C. Yang, Localized surface plasmon-induced emission enhancement of a green light-emitting diode, Nanotechnology 19 (2008) 345201.
[209] C. Clavero, Plasmon-induced hot-electron generation at nanoparticle/metal-oxide interfaces for photovoltaic and photocatalytic devices, Nat. Photonics 8 (2014) 95–103.
[210] S. Pillai, K.R. Catchpole, T. Trupke, M.A. Green, Surface plasmon enhanced silicon solar cells, J. Appl. Phys. 101 (2007) 093105.

[211] L. Qiao, D. Wang, L. Zuo, Y. Ye, J. Qian, H. Chen, S. He, Localized surface plasmon resonance enhanced organic solar cell with gold nanospheres, Appl. Eng. 88 (2011) 848–852.
[212] S. Mukherjee, F. Libisch, N. Large, O. Neumann, L.V. Brown, J. Cheng, J.B. Lassiter, E. A. Carter, P. Nordlander, N.J. Halas, Hot electrons do the impossible: plasmon-induced dissociation of H2 on Au, Nano Lett. 13 (2013) 240–247.
[213] H. Nishi, T. Tatsuma, Oxidation ability of plasmon-induced charge separation evaluated on the basis of surface hydroxylation of gold nanoparticles, Angew. Chem. Int. Ed. 55 (2016) 10771–10775.
[214] T. Tatsuma, Y. Katagi, S. Watanabe, K. Akiyoshi, T. Kawawaki, H. Nishi, E. Kazuma, Direct output of electrical signals from LSPR sensors on the basis of plasmon-induced charge separation, Chem. Commun. 51 (2015) 6100–6103.
[215] Y. Tian, T. Tatsuma, Mechanisms and applications of plasmon-induced charge separation at TiO2 films loaded with gold nanoparticles, J. Am. Chem. Soc. 127 (2005) 7632–7637.
[216] E. Kazuma, N. Sakai, T. Tatsuma, Nanoimaging of localized plasmon-induced charge separation, Chem. Commun. 47 (2011) 5777–5779.
[217] Y. Ohko, T. Tatsuma, T. Fujii, K. Naoi, C. Niwa, Y. Kubota, A. Fujishima, Multicolour photochromism of TiO2 films loaded with silver nanoparticles, Nat. Mater. 2 (2003) 29–31.
[218] T. Yamaguchi, E. Kazuma, N. Sakai, T. Tatsuma, Photoelectrochemical responses from polymer-coated plasmonic copper nanoparticles on TiO2, Chem. Lett. 41 (2012) 1340–1342.
[219] I. Shown, M. Ujihara, T. Imae, Synthesis of β-cyclodextrin-modified water-dispersible Ag-TiO2 core–shell nanoparticles and their photocatalytic activity, J. Nanosci. Nanotechnol. 11 (2011) 3284–3290.
[220] X. Huang, P.K. Jain, I.H. El-Sayed, M.A. El-Sayed, Plasmonic photothermal therapy (PPTT) using gold nanoparticles, Lasers Med. Sci. 23 (2008) 217.
[221] S. Mubeen, J. Lee, N. Singh, S. Krämer, G.D. Stucky, M. Moskovits, An autonomous photosynthetic device in which all charge carriers derive from surface plasmons, Nat. Nanotechnol. 8 (2013) 247–251.
[222] K. Ueno, T. Oshikiri, H. Misawa, Plasmon-induced water splitting using metallic-nanoparticle-loaded photocatalysts and photoelectrodes, ChemPhysChem 17 (2016) 199–215.
[223] W. Hou, W.H. Hung, P. Pavaskar, A. Goeppert, M. Aykol, S.B. Cronin, Photocatalytic conversion of CO2 to hydrocarbon fuels via plasmon-enhanced absorption and metallic interband transitions, ACS Catal. 1 (2011) 929–936.
[224] B. Wu, D. Liu, S. Mubeen, T.T. Chuong, M. Moskovits, G.D. Stucky, Anisotropic growth of TiO2 onto gold nanorods for plasmon-enhanced hydrogen production from water reduction, J. Am. Chem. Soc. 138 (2016) 1114–1117.
[225] T. Oshikiri, K. Ueno, H. Misawa, Plasmon-induced ammonia synthesis through nitrogen photofixation with visible light irradiation, Angew. Chem. Int. Ed. 53 (2014) 9802–9805.
[226] K. Ueno, S. Juodkazis, T. Shibuya, Y. Yokota, V. Mizeikis, K. Sasaki, H. Misawa, Nanoparticle plasmon-assisted two-photon polymerization induced by incoherent excitation source, J. Am. Chem. Soc. 130 (2008) 6928–6929.

CHAPTER 5

Nanolayer Analysis by Neutron Reflectometry

Joseph A. Dura[1], Eric D. Rus, Paul A. Kienzle, Brian B. Maranville

NIST Center for Neutron Research, Gaithersburg, MD, United States
[1]*Corresponding author*

5.1 Introduction

Neutron reflectometry (NR) measures the nanometer-scaled structure of near-surface regions, interfaces, or thin films. Since many green chemistry phenomena involve surface and interface processes, this technique can provide valuable insights into the structures and phenomena that drive or result from these reactions. Specifically, specular neutron reflectometry measures a material property called the scattering length density (SLD) of the neutron or ρ_N (which is determined from the composition), as a function of depth relative to a surface or interface. Neutrons are particularly sensitive to light elements and can probe interfaces buried in samples, in contact with liquids, or deep within complex *in operando* sample environments. Therefore layered structures often found in green chemistry technologies, such as electrochemical, photoactive, or energy storage devices, can be characterized. This chapter describes the basis of the technique, concentrating on one of the most stringent, complicated, and comprehensive applications for which NR has been applied to green chemistry: *in operando* electrochemical measurements. Therefore this chapter focuses on the example of NR as applied to electrochemical systems for green energy storage.

The "contrast" that is observed with NR, i.e., the parameter that is described in the structural depth profile, is the scattering length density, $\rho_N(z)$, which is the sum over all the isotopes, i, of the bound coherent neutron scattering length, b_c (colloquially, the "neutron scattering power" of the nucleus) times the number density, N, of that isotope:

$$\rho_N(z) = \sum_i b_{c,i} N_i(z) \tag{5.1}$$

Here, the depth, z, dependence is specific to the specular geometry, which (as described in Section 5.2) averages over any variations of ρ_N in the plane parallel to the reflecting interface, but determines variations of ρ_N along the surface normal direction. In the z direction, specular

Nanolayer Research. http://dx.doi.org/10.1016/B978-0-444-63739-0.00005-0
2017 Published by Elsevier B.V.

reflectometry is sensitive to layers with thickness ranging from less than 1 nm depending on the system studied, up to roughly 0.5 μm, depending on the instrument resolution used. Since b_c values are known for all isotopes, a single measurement can determine composition in systems with two or fewer phases, or in binary alloys if the density versus composition is known. One of the main advantages of using neutron instead of X-ray or electron probes is that neutrons scatter from the nuclei, as opposed to scattering from the electrons in a material. First of all, this provides scattering lengths that are alternative and complementary to those probes (which have a low contrast for elements with low atomic number or neighboring elements). Also, because neutrons scatter from the nucleus, b_c can vary greatly for different isotopes of the same element, which can be used to determine the depth profile of the number density $N_i(z)$ by comparing the depth profiles determined from samples containing the two different isotopes. Furthermore, by labeling materials of interest with the isotope that has the highest contrast to surrounding materials one can highlight those features. Alternatively, an isotope abundance can be selected to match the contrast of one material to another (called "isotopic contrast matching"), thus eliminating scattering effects from those two materials in order to isolate the scattering from a third material. Finally, isotopic substitution can be used to label one of the reactants to determine the extent to which it contributes to the products that are incorporated into the sample.

Other unique advantages of neutron scattering are derived from the fact that neutrons are weakly interacting particles. Because of this, they are nondestructive, with no ionization or local heating, and can easily penetrate thick solid materials. This promotes both robust *in operando* and multimodal sample environments since the environment can be tailored to the other technique; for example, the neutron can be incident through infrared prisms. Neutrons can also probe the entire sample providing statistical ensemble averages of structures. Scattering from the nucleus eliminates the atomic form factor that must be applied to techniques that probe the electron cloud. With almost zero absorption, the scattering theory is simpler and quantitative, and in fact, the phase problem for diffraction can be solved, allowing inversion of the data if variable reference layers are employed.

Other neutron advantages are less applicable to green chemistry, but are mentioned here for completeness. Because neutrons also have a spin and magnetic moment, they scatter from, and thus are highly sensitive to, magnetism in materials. Polarized neutron reflectometry is thus able to determine the depth profile of both the vector magnetization and nuclear ρ_N. In addition, a magnetic layer can serve as the variable reference material required for phase inversion. Finally, because of their large mass, the energy of neutron is similar to that of vibrations, excitations, and diffusion in materials, and the neutron can exchange energy with these modes, in techniques (elastic or quasielastic scattering) collectively called neutron vibrational spectroscopy (NVS). NVS is complementary to IR or Raman spectroscopy and is especially sensitive to vibrational modes of H because of its large cross section. Because there are no dipole-selection rules for NVS, all vibrational modes are observable. NVS can also obtain the scattering direction in single crystals to obtain phonon dispersion curves, and the length scale of the excitations to help determine the physical mechanism of the vibrations or diffusion.

In specular NR measurements a ribbon-shaped beam of neutrons is directed onto the planar sample at a grazing incidence angle, θ, and the reflected intensity is measured as a function of the momentum transfer $\vec{Q}$, which has a magnitude:

$$Q = \frac{4\pi}{\lambda}\sin\theta \tag{5.2}$$

Diffraction of the neutron from the various interfaces in a material results in variations in the reflected intensity as a function of Q. For a pair of interfaces, i.e., a thin film, this results in an intensity oscillation with a period in Q that is inversely proportional to the thickness of the layer. Multiple layers in the sample produce a beating pattern. Generally, a continuously varying $\rho_N(z)$ can be accurately approximated by a series of thin layers with uniform ρ_N and distinct interfaces, from which the scattering can be determined. Least squares refinement or in some cases direct inversion is used to determine the $\rho_N(z)$ structure of the sample from the reflected intensity, $R(Q)$. Because specular NR requires very flat, smooth samples and averages in the plane, it is not possible to study surfaces, interfaces, or grain boundaries in three-dimensional samples, for example, between particles in agglomerations. Instead we study planar thin film layers made of the same materials as analogs to those grain boundaries or conformal coatings. These serve as idealized models of the real-world interfaces.

The many unique aspects of neutron reflectometry, primarily its proficiency for *in operando* sample environments, sensitivity to light elements, and isotopic control of contrast make it an excellent technique for studying electrochemical and other phenomena involving layered structures coatings and ordering at interfaces. Alone or in conjunction with complementary techniques, NR will continue to provide useful insights for green chemistry technologies.

5.2 Theory of Neutron Reflectometry

5.2.1 Introduction

The wavelike properties of a moving neutron can be used to measure distances, and the nuclear and magnetic interaction potentials to measure materials properties. Combining these properties with the geometry of a thin flat sample, we arrive at the concept of neutron reflectometry. The wavelength of the moving neutron depends on its velocity, through the de Broglie relationship (for nonrelativistic particles, wavelength $\lambda = \frac{h}{m_n v}$, where h is the Planck constant, m_n is the neutron mass, and v is the velocity). Neutrons with wavelengths close to the interatomic spacing are produced at research facilities in order to probe materials at the smallest scales.

There are two types of neutron sources for research in common use in the world today: reactor based and spallation sources. Reactor-based sources are centered around a nuclear fission

reactor, in which excess neutrons from the fission process are used, while in spallation sources a high-energy particle beam is focused onto a target, and neutrons are liberated from the nuclei of the target materials through kinetic energy. The particle beam in spallation sources is most often pulsed with time, so that a well-defined burst of neutrons is produced with each pulse, while reactor sources typically operate in a continuous mode where neutrons flow from the source at a nearly constant rate. Spallation sources have the advantage of having a band of wavelengths in each pulse (wavelength within a pulse is determined from the travel time to the detector, inversely proportional to the velocity), thus measuring a range of length scales simultaneously. Because accurate timing and predictable pulses are used, time-resolved probes of materials can be straightforward to set up at a spallation source. Continuous sources provide other optimizations; the time-averaged intensity at particular wavelengths of interest can be much higher than a spallation source, and instrument design can be simplified by not needing time-resolving hardware.

No matter which type of source it originated from, the interaction potential for a neutron with matter has two components:

1. The nuclear potential, which depends on the number of protons and neutrons in the nucleus of the atom with which the neutron is interacting. The nuclear potential varies in a nonmonotonic way with the atomic number of elements (and isotopes of those elements) in the periodic table [1]. Notably, many lighter elements have strong nuclear potentials (Be, B, C) while heavier elements sometimes are relatively weak scatterers (Co, In, Sm, W) and some are even negative (H, Li, Ti, Mn). A negative scattering length indicates an attractive force between the neutron and nucleus. Compare this to the scattering potential of X-rays with matter, which depends on the electron density of the material, and so X-ray scattering measurements are usually dominated by the heaviest elements present.
2. The magnetic field (B). Scattering only occurs from changes in the vector $\vec{B}$ as a function of z; further, Maxwell's equations applied to thin films dictate that the change in the z-component of B (B_z) along z must be zero, so that B_z is a constant through the film and magnetic NR is only sensitive to changes in the in-plane components B_x, B_y as a function of depth z. Any uniform field (e.g., the applied external magnetic field) does not contribute to the scattering, which arises only from the magnetic potentials due to the material itself, such as in ferromagnets or ferrimagnets, or in superconducting thin films which create magnetic discontinuities through the Meissner effect.

5.2.2 Specular Theory

The theory of specular scattering can only be completely solved for films that are uniform in-plane. In reality, the theory works quite well for samples that have relatively small contrast variations in-plane, or samples where this contrast has a much smaller length scale than the coherent extent of the neutron wavefunction during the interaction with the sample (e.g.,

interatomic variations in SLD in-plane, nanoscale porosity or domains, etc.) For most samples that can be described as layered thin films it works quite well; on the other hand, very strong in-plane contrast such as from a ruled grating on a surface [2] makes this analysis moot and computationally intense approximations are required.

If we go back to the de Broglie relationship mentioned earlier, we can write a wavefunction for the neutron: $\psi(z) = ce^{ikz} + de^{-ikz}$, where k is the wavevector along z, related to the momentum as $\hbar k = p_z = m_n v_z$ for nonrelativistic velocities v. The change in the momentum of the neutron due to the scattering is $\vec{Q} = \vec{k}_{out} - \vec{k}_{in}$, and Q is often used as the independent variable that is changed in a reflectometry experiment. On the actual instrument, Q is controlled through a combination of sample angle and incident wavelength, since $Q = \frac{4\pi}{\lambda}\sin\theta$ where λ is the wavelength and θ is the angle of incidence of the neutron on the sample. At a reactor source, the angle is typically varied for a fixed wavelength, while at a spallation source a spectrum of wavelengths is typically incident at just a few fixed angles.

The form of the wavefunction ψ given here has the correct wavelength as specified by de Broglie. The coefficients c and d correspond to the amplitudes of the forward- and backward-traveling waves. If we apply conservation of momentum, conservation of energy, and conservation of particle number at each of the boundaries between layers of the sample, we can write down a series of equations for the amplitude of the neutron wavefunction in each layer.

In the incident medium (the material through which the neutron travels to reach the first interface of the sample), we know that $c_0 = 1$ and $d_0 = r$, because the wave traveling toward the sample c is the incident flux which we normalize to 1, while the backward-traveling wave in the incident medium is the reflection that we measure, r. In every subsequent layer l there is a value of $\{c,d\}_l$ which can be determined by enforcing conservation of particle number across the boundary $\psi_l(Z_l) = \psi_{l+1}(Z_l)$ where Z_l is the interface between layers $l, l+1$, and also by enforcing conservation of momentum with the simultaneous equation $\frac{d}{dz}\psi_l(Z_l) = \frac{d}{dz}\psi_{l+1}(Z_l)$. Using conservation of energy, we can get an equation for k_l, the wavevector in the next layer, by keeping the sum of kinetic and potential energy the same:

$$E_0 = K.E. + P.E. = \frac{1}{2}m_n v_l^2 + \frac{\hbar^2}{2m_n}4\pi\rho_{n,l} = \frac{\hbar^2}{2m_n}\left(k_l^2 + 4\pi\rho_{n,l}\right) \tag{5.3}$$

where $\rho_n = \rho_N + \rho_M$ is the scattering length density for neutrons (the sum of nuclear and magnetic components).

So if we know the scattering length density of a layer, $\rho_{n,l}$ then

$$k_l = \sqrt{\left\{\frac{2m_N}{\hbar^2}\right\}E_0 - 4\pi\rho_{n,l}} \tag{5.4}$$

Note that this gives an imaginary value for k_l when the scattering potential in the material exceeds the incident energy $E_0 = \frac{\hbar^2}{2m_n} k_0^2 = \frac{\hbar^2}{2m_n}\frac{Q^2}{4}$. Then the wavefunction inside the layer is a decaying exponential rather than a plane wave, though the transmitted amplitude through the layer can still be large if the layer is thin compared to the decay length (quantum tunneling of the particle wavefunction!). If the layer with imaginary k is thick enough (such as the substrate), the transmission goes to zero and there is total external reflection. In this case the measured reflectivity R is 1: Every neutron that hits the sample is reflected. This happens for Q below the point we call the critical edge $Q_c^2 = 16\pi\rho_n$, which is where k_l in the high-SLD layer goes through zero (and then is imaginary).

The two boundary-value equations for ψ give two equations for the two unknowns c and d in the next layer, allowing us to calculate c_{l+1}, d_{l+1} based on the values c_l and d_l in the previous layer. Arranging these equations as a 2×2 matrix we get:

$$\begin{pmatrix} c \\ d \end{pmatrix}_{l+1} = \frac{1}{2k_{l+1}} \begin{pmatrix} (k_{l+1}+k_l)e^{-i(k_{l+1}-k_l)Z_l} & (k_{l+1}-k_l)e^{-i(k_{l+1}+k_l)Z_l} \\ (k_{l+1}-k_l)e^{+i(k_{l+1}+k_l)Z_l} & (k_{l+1}+k_l)e^{+i(k_{l+1}-k_l)Z_l} \end{pmatrix} \begin{pmatrix} c \\ d \end{pmatrix}_l \tag{5.5}$$

The off-diagonal matrix elements that connect the forward-traveling wave amplitudes c to the backward (reflected) wave amplitudes d are proportional to the difference in k between one layer and the next, which in turn depends on the difference in SLD at that interface. For large values of E_0 (high angle in a reflectometer), the difference in k at an interface becomes roughly linearly proportional to the difference in SLD, so that the amplitude of the high-angle reflectivity is a measure of the SLD contrast that caused it, while oscillations in the reflectivity are caused by interference between the reflected waves from interfaces at different depths. For a single layer, the reflections from the top and bottom of the layer will interfere destructively whenever $k_l \times (\Delta z)_l = \left(n + \frac{1}{2}\right)\pi$, so that the period of the oscillations (particularly at high Q) is roughly equal to $\Delta Q \approx \frac{2\pi}{\Delta z}$.

If we call the matrix above A_l (including the prefactor $1/2k_{l+1}$), we can write an equation that traverses all the layers as a product of the A_l, getting c_l and d_l in terms of the incident intensity 1 and reflected amplitude r (still unknown):

$$\begin{pmatrix} c \\ d \end{pmatrix}_L = \left[\prod_{l=L}^{0} (A_l)\right] \begin{pmatrix} c \\ d \end{pmatrix}_0 \tag{5.6}$$

Note that the product moves in reverse order through the indices l of the layers.

In the final layer (usually the sample substrate, if there is one, or the same material as the incident medium for a free-standing film), there is one more boundary condition: We can

identify the forward-traveling wave amplitude c_L as the transmission amplitude often called t, which is a measurable quantity like r, but also we know that for the experimental setup there is no backward-traveling wave (other neutron source) coming from that side, so that $d_L = 0$, where L is the total number of layers (including the incident and transmission media). Then we have two equations and we can solve for the two unknowns, t and r (where $\left[M = \prod_{l=L}^{0} A_l\right]$ as given previously)

$$\begin{pmatrix} t \\ 0 \end{pmatrix} = M \begin{pmatrix} 1 \\ r \end{pmatrix} \tag{5.7}$$

So

$$\begin{aligned} t &= M_{11} + M_{12} r \\ 0 &= M_{21} + M_{22} r \end{aligned} \tag{5.8}$$

Solving gives

$$\begin{aligned} r &= -\frac{M_{21}}{M_{22}} \\ t &= M_{11} - 1\frac{M_{12} M_{21}}{M_{22}} \end{aligned} \tag{5.9}$$

One can immediately see that for a single interface, this reduces to the familiar Fresnel reflectivity $r = (k_0 - k_1)/(k_0 + k_1)$.

Note that while the theory is derived for a series of slabs of constant ρ_n, any smooth depth profile for the SLD can be accurately approximated as a series of thin slabs. The thickness of the slabs can be made arbitrarily small without affecting the validity of the theory, although below a certain threshold (roughly calculated from the measured Q-range as $\frac{2\pi}{Q_{\max}}$) no accuracy in the model is gained by further reducing the thickness.

The amplitudes t and r here are complex numbers containing phase information. The measured quantities (reflectivity R and transmission T) are the square of the amplitudes $|r|^2$ and $|t|^2$, and all phase information is lost in the measurement.

5.2.3 Phase Recovery

For any scattering experiment such as reflectometry, the measured quantity (in this case, R) is a real number with no phase information, so the matrix equations that were described cannot be directly inverted to get a unique solution to the layer-by-layer scattering length density. There are some experimental tricks we can employ to recover that information, though. If we have perfect knowledge of the scattering length density of the media surrounding the sample of

interest, and we can vary that SLD, the mathematical constraints from this knowledge can be used to construct a series of equations where the phase is recovered. This technique is described in the literature [3].

The most commonly used methods of altering the media in a known way is to substitute pure D_2O for H_2O in a liquid reservoir that abuts the sample, or by flipping the magnetization of a magnetic underlayer, which changes the SLD by a known amount for a polarized neutron (polarized neutron techniques described elsewhere) [4]. The technique only works when there is no appreciable absorption in the sample, which makes it a more useful tool in neutron scattering than in X-ray scattering, where the absorption is much larger.

5.2.4 Isotope Substitution

Another useful strategy for extracting unambiguous real-space information from the scattering data is isotope substitution. One can achieve a targeted measurement of the density profile of a particular element by exchanging a particular atomic component of a material for a different isotope of the same element, in an otherwise identical structure. Then the difference in SLD (see Eq. (5.1)) as a function of depth, divided by the difference in $b_{c,i}$, is a direct measure of the distribution of that element. Because the exact location of this contrast in the SLD profile is unknown ahead of time, the data cannot be directly inverted with this strategy alone, but the two techniques (isotopic substitution and surround variation to achieve direct inversion) can be combined, of course.

5.2.5 Near-Specular Techniques

While the specular technique is an elegant solution for measuring uniform, flat samples, sometimes the sample of interest has some kind of in-plane structure, while still resembling mostly a thin-film structure. In this case, one must consider the scattering in more than just one dimension; unfortunately, there is no closed-form solution to the more general 3D scattering problem as there was for the 1D case given. Two near-surface scattering techniques in common use include:

1. GISANS, which is essentially SANS (small-angle neutron scattering) where the incident beam is at or below the critical angle of total external reflection, θ_c, for the sample. By small variation in the incident angle then, the user can tune the penetration depth of the evanescent probe wave that tunnels into the sample; through a series of measurements a depth-dependent, in-plane scattering picture can be built up. GISANS covers a Q-range in-plane that is similar to the out-of-plane direction.
2. Off-specular scattering, in which the instrument geometry is largely unchanged from the specular case, but the sample is tilted so that the momentum-transfer vector Q has a small in-plane component. Because of the very small angles of incidence involved, the range of Q_x (in-plane) that is covered is small but very good precision is achievable,

and long-range-ordered structures with repeat distances of hundreds of microns can be resolved [2]. While it is possible to measure with extremely high Q-resolution, the max Q_x that is attainable with reasonable scattering intensity is much smaller than specular Q_z-range.

5.3 Practical Aspects

Neutron reflectometry can provide precise and accurate structural information for features as small as subnanometer thickness under ideal conditions. However, in order to accurately achieve this level of precision, numerous practical aspects must be carefully attended to. These issues are addressed in this section, and range from sample preparation, sample environment (including electrochemical cell) construction, instrument use and data collection and reduction, to (not least importantly) selection and validation of models and data fitting. Best practices and the reasons behind them are presented, to provide the reader the basis to obtain useful NR results or when evaluating research to distinguish the accuracy of measurements.

5.3.1 Neutron Reflectometers

A basic understanding of a neutron reflectometer is necessary to both correctly and optimally collect data and to understand sample and cell design requirements. The specific design of neutron reflectometers differs slightly based on the type of instrument, for example, time-of-flight reflectometers at pulsed beam [5] or continuous beam spallation sources [6], monochromatic [7] or proposed polychromatic reflectometers (similar to polychromatic diffractometers [8]) at continuous beam, reactor-based sources. However, there are numerous similarities, and where differences exist there are typically analogs in the other techniques. Therefore, in the interest of brevity, to convey the concept of how a reflectometer works, the simplest form, a monochromatic reflectometer, will be described herein, with some of the more important differences with the other types pointed out.

Fig. 5.1 shows a typical monochromatic reflectometer with a horizontal scattering plane and thus a vertical sample surface, often called a vertical sample reflectometer (further details can be found in the literature [7]). For ease of discussion, the coordinate system is as shown with "z" in the vertical direction and "y", which rotates with the sample, along the bisector of the incident and reflected beams. A focusing monochromator is placed in a gap in the neutron guide to diffract a nearly monochromatic beam ($\Delta\lambda/\lambda = 0.015$) at a right angle from the guide for neutrons with a wavelength $\lambda = 0.4743$ nm; however, other angles and wavelengths can be used. A cryogenically cooled Be filter in the incident path removes neutrons with a wavelength under ~0.39 nm, particularly the λ/n higher orders that would otherwise also be diffracted by the monochromator into the beam direction. A vertical slit near the monochromator and another near the sample define a beam that is narrow and has small angular divergence in the horizontal plane (which is needed to provide high resolution for the incident angle, θ, and to control the

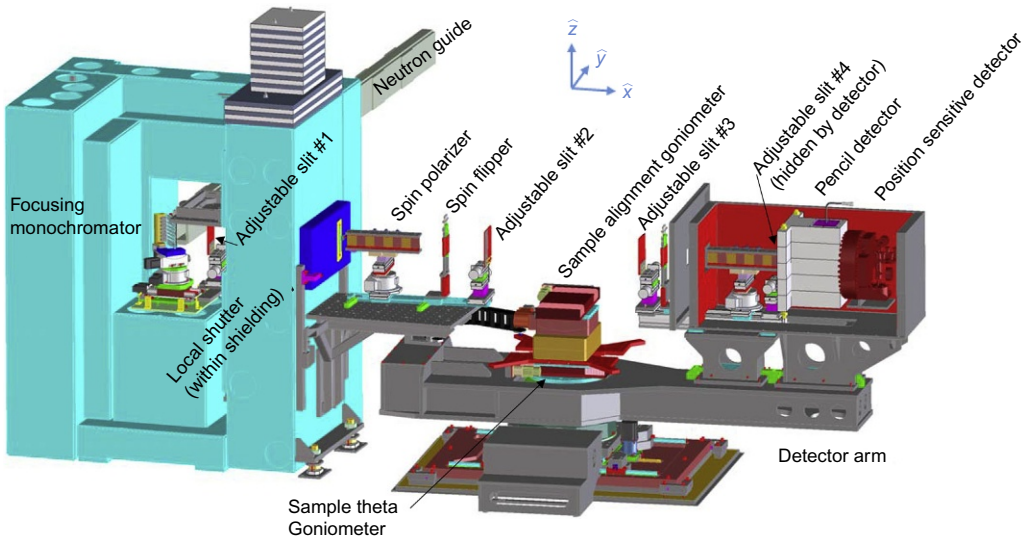

Fig. 5.1
Neutron reflectometer at a continuous source, with major components labeled. Axes are shown for ease of discussion.

area of the sample that is illuminated). The monochromator is curved to provide vertical focusing to allow a greater flux on the sample. An adjustable aperture is placed near the sample to better define the vertical extent of the beam. While the vertical focusing increases the beam divergence in this direction (relative to having a flat monochromator), this is orthogonal to theta, and therefore minimally increases the resolution along the specular direction. The only issue with a large vertical divergence is that it can integrate off specular scattering, if present, into the specular signal. Because the incident beam is fixed in space, the incident angle θ is set by rotating the sample on a goniometer, and similarly the reflected angle, D, is set by rotating the detector. For specular scattering $D = 2\theta$, both the θ and D axis must be concentric and vertical, and intercept the beam to an accuracy of a few tens of micrometers for typical reflectometers. A pair of slits, one just after the sample and the other just before the detector along the line between sample and detector, define the reflected beam and limit the acceptance to a region near the sample, to reduce the background signal. Each slit is composed of two blades of a neutron-absorbing material with an adjustable gap between them (called the slit width), but with a center point that is fixed to provide a stationary beam path and a fixed wavelength. Typically, a beam monitor is placed intercepting a portion of the incident beam at some point along its path and is used to normalize the incident intensity against variations in source flux over time. A cylindrical ^{3}He-type detector is typically used. This must be tall enough to intercept the diverging beam from the focusing monochromator. Alternatively, the detector slits can be removed and a position-sensitive detector can be installed to allow efficient measurements of off-specular scattering.

As a final note on neutron reflectometers, because acceptable neutron fluxes can only be achieved at specialized facilities (reactor or spallation sources) rather than lab-based neutron sources, NR experiments require travel to user facilities, of which there are currently 23 major ones throughout the world [9]. This in itself imposes additional constraints on experiment design. There is usually a significant lead time for proposals to be written, reviewed, and for beam time to be awarded and scheduled. There are limited opportunities for follow-on experiments or corrections. Therefore it is often helpful to precharacterize the samples to ensure that the structures are as desired and of sufficient quality, then to model the expected data to investigate the sensitivity of the measurements to the phenomena of interest. Most user facilities have instrument scientists to provide varying degrees of support from simply providing access through collaboration, which is a great advantage since it allows new users to learn a new technique while ensuring valid measurements.

5.3.2 Data Collection

The objective of an NR measurement is to accurately and precisely quantify the reflectivity, which is the specularly reflected intensity divided by the incident intensity as a function of incidence angle, which is often expressed as Q. To accurately determine the angle, sample alignment is crucial. The sample must be aligned to the common rotation axes of the sample and detector goniometers (to which the beam is already aligned) with precision to several micrometers. These axes must lie on and bisect the surface of the sample that is to be measured. The sample surface normal must also be aligned along the momentum transfer vector, $\vec{Q}$. Alignment begins with the detector placed in the incident, direct beam, and the sample is translated along y until the surface intersects the beam as indicated by a dip in intensity due to a reflection. Then θ is scanned and set to the value for the maximum transmitted beam. Finer alignment is achieved by setting the detector angle just below the critical edge of the sample to obtain total reflection, and adjusting θ, y, and χ (the rotation about the horizontal axis in the plane of the sample surface) to maximize the intensity of the reflected beam. This defines θ as half of the value of D that was used.

Data is typically collected with step scans where the sample angle, detector angle, and slit openings are driven to the desired values, and the reflected intensity is counted on the detector and monitor for a specified amount of time (or counts on the monitor or detector), then repeated for a range of theta values. Typically, the incident slits are increased linearly with θ to keep the beam footprint on the sample constant, to provide a constant $\Delta Q/Q$, and a flux that increases as Q^2, to partially offset the Q^{-4} dependence of R for reflectivity from a plane. The amount of time per point is also increased with Q to provide adequate counting statistics for the reduced reflectivity with increasing Q. However, at low angles where slit motor precision becomes a significant fraction of the slit opening, and at higher angles where the slit opening approaches the detector width, a fixed set of slit openings can be used. The specular condition is maintained

by setting the detector angle to twice the sample angle, and although this includes both specularly reflected neutrons and isotropically scattered neutrons as well as other sources of background, it is called the specular scan. For convenience, the Q-range of interest can be divided into a series of separate specular scans. In situations where the sample structure might change during the course of an experiment, this possibility should be checked by taking several series of specular data (over either the full or limited Q-range), retaining only those scans for which the reflectivity as a function of Q does not change. Measuring a sample that is changing over time could result in misinterpretation of the structure because the time average reflectivity curve does not correspond to the scattering from the time average structure. If the data were taken by scanning Q with time, the oscillations and Bragg peaks would shift with time, and each Q would correspond to a different structure, so that fitting the whole NR pattern would not correspond to any particular sample structure. For example, shifts in oscillation maxima due to a changing sample thickness could appear as a beating pattern in the oscillations, which in turn would be interpreted as a thin layer that does not exist in the sample. Even if all Q were measured simultaneously (as with time of flight reflectometers), changes in sample thickness would shift the phase of intensity oscillations, and time averaging especially at higher Q would broaden the oscillations, making the interfaces appear more diffuse than otherwise.

Since nonspecular scattering also occurs at the specular conditions, this and other sources of background must be accurately subtracted from the total intensity that was measured in the scan of the specular condition. This is achieved by offsetting either the sample or detector angle until the specular beam no longer enters the detector. Typically, this is done symmetrically on both sides of the specular condition (to account for possible gradients in the background intensity) and the average is used.

Finally, the incident intensity as a function of slit settings (and wavelength in polychromatic instruments) must be determined. This is typically done by taking a "slit scan" through the sample environments and incident media, but with the sample surface displaced from the beam, in which the detector is placed in the direct beam and the intensity is measured for the full range of slit settings used in the specular reflectivity measurement.

To determine R versus Q, the background is subtracted from the specular data, which is then divided by the slit scan. The counting statistics of these individual measurements are propagated through the reduction to provide uncertainty estimates for each data point. If fixed slits are maintained at low Q, the beam may be wider than the projection of the sample surface onto the plane perpendicular to the beam (YZ). This gives rise to a $\sin\theta$ (roughly linear) increase in intensity for the reflected intensity (proportional to the fraction of the beam intercepted by the sample, called the footprint) up until the point where either the sample fully intercepts the beam or where slits are opened in proportion to θ. A "footprint" correction can be applied if necessary. The sample is often not perfectly planar at the level of beam divergence, which can be on the order of 0.01 degree, either due to polishing errors, or warping due to film deposition,

other processing, stresses applied by the sample holder or cell. Therefore the reflected beam can be broadened by the sample. This will affect both the downstream slits openings needed to accept the full specular beam, and will round off the footprint profile, which can affect the choice of slit settings below the critical edge.

5.3.3 Data Fitting

Like diffraction, it is the intensity not amplitude that is measured in reflectivity, so the phase of the probe wave function is lost, and the data cannot be analytically inverted to determine the SLD profile that gives rise to the pattern in the reflected intensity. Instead, the SLD profile is usually determined by defining a model of the expected structure (typically a series of layers described by the complex SLD, the thickness, and amount of intermixing and profile shape at each interface), and adjusting the model parameters until the predicted reflectivity matches the data. Since most thin film samples consist entirely of intentionally placed layers, this approach is simple and direct; typically the parameters vary a limited amount from the expected values. However, in electrochemical systems, layers may be generated without a priori knowledge of their composition and structure, or in some cases without knowledge of even the number of distinct layer units. Therefore, in many of the systems of interest to this chapter, one does not even know what model will best describe the sample, and considerable effort must be employed to determine the appropriate model while at the same time determining the best fit parameters. In general, the model definition (in terms of fitting) includes not only the number of layers, but also the values of fixed parameters and the fitting ranges. Model selection in cases with an unknown structure is complicated by the fact that it is mathematically possible that two symmetry-related SLD profiles can result in exactly the same NR curve [10].

Several approaches can be applied to reduce the number of unknowns, both to provide accurate determination of the remaining parameters, and also to help determine the best model to describe the data. External probes can provide a great deal of complementary information. These can characterize the actual sample investigated with NR before and/or after the NR experiment to further define the initial and final states. Alternatively, samples can be prepared in the same manner and studied at each of the conditions also examined by NR, thus determining the model and restricting the parameter ranges to reflect sample-to-sample deviations. The most useful probes to help in model selection are those that also provide a depth profile, even if they lack the sensitivity or resolution of NR, for example X-ray reflectivity (XRR), Rutherford backscattering spectrometry (RBS), cross sectional electron microscopy, or sputter depth profiling coupled with compositional probes such as X-ray photoelectron spectroscopy (XPS), secondary ion mass spectrometry (SIMS), or secondary neutral mass spectrometry (SNMS).

There are several NR methods that can be applied to assist in model selection and fitting. If the initial sample consists of multiple layers, one can measure NR or XRR, at various stages of sample layer deposition to determine the layer parameters in simpler systems as the layers are added (though be aware that the underlayers can change over time depending on the deposition method). The inversion methods specific to neutron reflectometry (see Section 5.2.3) use information from a set of measurements with a reference layer set to different SLD values to directly invert the data. Reference layers can be a fluid reservoir, where fluid exchange controls the contrast, or a magnetic layer, where polarized neutron reflectometry provides different total SLD for the different polarizations. Simultaneously fitting the same pair of data sets will also resolve the symmetry issues, while allowing prior information from complementary measurements to constrain them [11]. Two samples that are prepared identically but with different isotopes for one component (isotopic substitution) can be used to determine the number density depth profile of that element, and to help verify that a correct model has been employed. Finally, if these methods are unavailable there are approaches that can be taken during fitting to determine the best model. For example, a series of models with different number of layers can be used to fit the data, and the Bayesian information criteria (BIC) can be applied to determine the best fit among varying models [12]. Models can be underdetermined, characterized by a relatively poor fit and high χ^2, or overdetermined as indicated by a low χ^2 and possibly strong correlations between parameters, but ultimately by a higher BIC than models with fewer parameters and similar SLD profiles [13]. Free-form modeling where the depth profile is described by a set of orthogonal basis functions has also been demonstrated [14]. Combined models, with structured layers for the well-defined parts of the structure and free-form sections where model composition is not well controlled, provide additional flexibility.

There are certain limitations on what can be determined from neutron reflectometry. Since the period of oscillation in Q space is inversely proportional to the thickness of a layer, a feature may be too thin to produce an observable oscillation in the data. Therefore, in general, a lower limit for observable feature size is approximately $2\pi/Q_{max}$, where Q_{max} is the largest Q for which the data has reasonably small error bars. In some cases, smaller features can be inferred from the data, for example if a certain contrast at an interface (which does not exist for the layers that are observable, being thicker than $2\pi/Q_{max}$) is required to fit an oscillation amplitude, but cannot be achieved by the SLD of the other adjacent layers due to known materials properties or the fitting. However, in these cases, extreme care must be used to demonstrate that such a contrast is actually required. Similarly, an upper limit on the thickness of a layer is set by the resolution of the instrument, $2\pi/Q_{min}$, where Q_{min} is the smallest oscillation period that is not obscured by instrumental broadening. Models must also be evaluated for realism; the SLD values determined by the fits must correspond to what is possible given the materials in the system. SLD values lower than what is expected for bulk materials can be explained by lower density or porosity. Interdiffusion from adjacent layers can explain SLD values either lower or greater than bulk, within reasonable limits dictated by mass balance.

When fitting, one must be diligent in evaluating whether the returned best fit is actually the global minimum in χ^2 or is merely a local minimum. Gradient descent approaches can easily get stuck in the nearest local minimum, but restarting the fit from numerous different initial conditions can increase the chances of finding the global minimum. The more robust but slower Monte Carlo approaches can ideally find the global minimum, and can also be used to determine a likelihood band for the model parameters, but even they have difficulty in distinguishing between different local minima with similar χ^2 See Section 5.4 for more details.

5.3.4 Sample Requirements

X-ray reflectometry and neutron reflectometry have similar sample requirements. First, samples must be very flat. Deviations from planarity, generically referred to as "warp" regardless of the cause, broaden the effective instrumental resolution by increasing the range of incident angles on the sample. Warp also increases the divergence of the reflected beam, requiring increased downstream slit width and thus decreasing signal-to-noise ratio. It also distorts the profile of the reflected intensity versus θ in the region before the sample intercepts the entire beam, making footprint corrections more difficult to apply, or alternatively decreasing the maximum initial beam width required to avoid these corrections.

Samples must also have smooth surfaces and interfaces (approximately less than 2 nm root mean square [RMS] or more depending on the system), since roughness increases the overall rate of decline in R versus Q, faster than the typical $R \sim Q^{-4}$ for smooth planar surfaces, thus decreasing signal to noise faster than otherwise. Interfacial roughness also decreases oscillation amplitude (by amounts that increase with Q), thus decreasing sensitivity to layers (or equivalently, in real space, distributing thinner layers over a larger depth range, thus averaging their distinct composition over larger regions and decreasing the ability to distinguish thin layers.)

Because of the relatively low fluxes of neutron sources, the sample area should be maximized (up to the limits of the beam size) to maximize the signal and minimize the time required for obtaining adequate counting statistics. However, film thickness must also be uniform across the film (typically $<2\%$ variation) since separate regions of the sample with various thicknesses each would produce different oscillation periods. These are measured simultaneously and incoherently averaged over, effectively broadening the oscillation and decreasing its amplitude increasingly with higher Q in a manner similar to the effects of interface roughness, for which it can be mistaken in the fits. On a smaller scale, in-plane inhomogeneities smaller than the projection of the neutron coherence length [2] onto the sample surface, $\sim 1\ \mu m/\sin\theta$, are averaged over. For larger inhomogeneities the measured intensity is an incoherent combination of the reflectivity from each component of the inhomogeneity. If the number of different lateral components is known, the data can still be analyzed, though with greater uncertainty. This requires a set of models of the depth profile for each lateral component of the inhomogeneity and a weighting parameter proportional to the relative area of that component. Except in the

simplest and most well-defined cases, this becomes unsolvable due to the large number of fitting parameters and the decrease in information content of the R versus Q due to averaging over multiple different NR curves.

Cells that contain a liquid reservoir typically require the neutrons to be incident through the substrate. At some angle the neutron beam will transition from being incident through a substrate edge to being incident through the back of the substrate. This should be avoided by using thick enough substrates (on the order of several mm) to avoid unnecessary scattering from the substrate edge and a change in incident angle due to a change in refraction of the beam. Electrochemical processing can induce stress in layers and materials, including adhesion layers, and processes must be chosen to avoid delamination. Surface oxides, even on the nanometer scale, that can develop upon exposure of the prepared thin film to the atmosphere, can drastically affect both the electrochemistry and the scattering, and must be taken into account. Relatively smooth films can be produced by sputtering; however, in some cases the ion energy can lead to interdiffusion, or penetration of the sputtered material through existing layers, such as the native oxide on Si [15].

While avoiding these pitfalls, the intentionally deposited thin films can be customized to provide advantages. The thickness of all layers and composition of the adjacent layers should be chosen to differ from the values of the layer expected from the electrochemical effect being tested, to avoid ambiguous interpretation of features in the NR data and to provide adequate contrast. In some cases, the underlying structures can be designed to actually enhance the sensitivity to those layers. Modeling the NR data produced by the potential underlying structures can be used to optimize the sensitivity to the phenomenon to be measured, and to demonstrate this sensitivity in proposals for beam time at neutron facilities.

5.3.5 *In Operando* Neutron Reflectometry/Electrochemical Cell Design Considerations

In operando/*in situ* NR-compatible electrochemical cells for battery materials have been described previously [13,16–21], and in other articles by the same groups. Since neutrons are weakly interacting due to their charge neutrality, they can readily penetrate single crystals, but are highly attenuated in amorphous materials and liquids (due to scattering from the liquid structure) and in particular from materials containing H (due to incoherent scattering). Therefore, all NR electrochemical cells operate in a back-reflection configuration, using a single crystal substrate (commonly silicon, quartz, or sapphire), which supports the working electrode (WE), as the incident medium. Refractive effects are avoided by directing the beam through the side of the substrate that is perpendicular to the sample surface. Thus the substrate itself must be sufficiently thick to accommodate the range of incident angles. This thickness is also useful in minimizing warp due to the stresses induced by sealing the cell. Additional thickness can be added by stacking another substrate of the same material behind the WE

substrate. However, the WE substrate should be thick enough that any reflection from its back surface occurs at adequately high angles that the reflectivity of the substrate is very weak. This reflection can be minimized by using unpolished surfaces and ensuring that there is no contamination, such as electrolyte, between the WE substrate and the additional backing plate. At the NIST Center for Neutron Research (NCNR), 5 mm-thick, 76.2 mm-diameter silicon substrates are typically used. With a 2.6 mm maximum beam width, this condition begins at $\theta =$ 5.55 degrees or $Q = 2.5\ \text{nm}^{-1}$, and no anomalies are observed there in either the specular or background scans.

The electrolyte reservoir can be sealed with a thin gasket or O-ring. In one commonly used cell type, referred to herein as "thin cells," the counter electrode (CE) is a film deposited onto a substrate similar to that used for the WE, and placed directly against the other side of the gasket [13,17–22] (see Fig. 5.2). The thickness and inner dimensions of the gasket thus define the electrolyte reservoir volume. Minimizing the volume is important for several reasons. First, large volumes increase the absolute amount of contaminants (such as water) even for small concentrations. For a cell containing 1 mL of solution, one monolayer of contamination would correspond to a solution contaminant concentration on the order of 10^{-5} mol/L. Also, deuterated solvents (which are very useful for controlling scattering length density contrast by mixing with natural isotopic abundance solvents, for measuring porosity, and for tagging reactants of interest) can be expensive, so minimizing both the reservoir volume and the volume required to fully exchange the fluid can be economically essential. The latter benefits from a

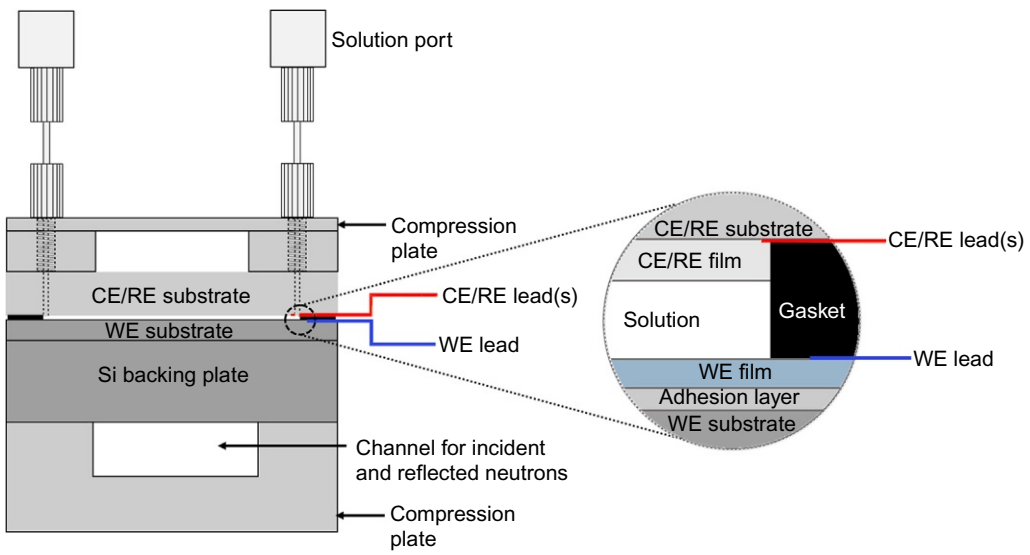

Fig. 5.2
Schematic cutaway view of an *in situ* NR electrochemical cell (not to scale), with magnified view to show greater detail.

uniform, nonturbulent, flow front in addition to the small reservoir volumes. Care must be taken, however, that the counter electrode does not contribute to the reflected signal, for example, by having a solution volume sufficiently thick to absorb or scatter the beam transmitted through the working electrode. Furthermore, the reservoir thickness should be greater than the projection of the longitudinal coherence length [2] of the neutron in that direction (~100 μm) so that any scattering that does occur is incoherent with the scattering from the working electrode. This must be balanced, however, with the desire to minimize the background scattering, which is achieved by both minimizing the thickness of the reservoir and by using deuterated solvents. Fortuitously, in the case of lithium ion measurements, a sufficiently thick lithium foil counter electrode will absorb most of the neutrons in the beam (though care must be taken in the disposal of the lithium, since ^{6}Li is converted to tritium by neutron absorption). In liquid cells without a lithium counter electrode, an unpolished side of a wafer is typically faced toward the reservoir, decreasing its reflectivity.

Thin cells have been made either with or without fluid inlets. In the latter case, the gasket is placed on top of one electrode, and solution added to the reservoir, then the second wafer is lowered onto this, taking care not to trap any bubbles. Alternatively, inlets can be provided via holes drilled through the counter electrode substrate. Tubing can then be sealed to the back side of the counter electrode substrate with O-rings, gaskets, or tube fittings such as those used for high-performance liquid chromatography (HPLC).

In another cell type, the reservoir is defined by a cavity within a structure that seals against the WE with the gasket or O-ring. Such "cavity cells" have been constructed from glass [17], polytetrafluoroethylene (PTFE) [16,23], and polyethylene [24]. The primary advantage of a larger cavity is that it allows a conventional reference electrode to be located within the reservoir between the WE and CE. It also facilitates incorporation of fluid inlets. The counter electrode can be a macroscopic sheet, wire, or gauze. Yonemura et al. employed a hybrid approach in which the cavity in an aluminum body was only 0.5 mm thick except for two ~5 mm-diameter inlet holes machined perpendicular to the WE surface, one that also housed a combination counter electrode/reference electrode [21].

The CE should have the same area as the WE to ensure uniform potential distribution, since nonuniform effects on the sample structure across its surface would incoherently contribute different reflectivity versus Q to the measured reflected intensity and prevent accurate modeling of the sample structure. Care must be taken that the CE reactions do not produce significant volumes of gas, as bubbles could become trapped in the gap. Not only would this lead to inhomogeneity in the electrochemical reactions at the working electrode, but the SLD of gas bubbles will most probably differ from the SLD of the solution, leading to lateral inhomogeneities of the sample. Furthermore, small bubbles would produce small angle scattering, leading to increased background. Also, given the long duration of NR measurements, species produced at the counter electrode have ample time to diffuse across the

gap and could potentially react at the working electrode. While a separator could slow this crossover, it would undesirably contribute to scattering at the working electrode/solution interface.

Platinum is commonly used as a counter electrode in aqueous media, and compensates charge passed at the working electrode either by oxidizing or reducing water. While platinum is quite stable, some soluble platinum species can form with the passage of current, and particularly under conditions where an oxide layer is repetitively formed and reduced [25]. For lithium ion measurements, lithium foil is most commonly used as the counter electrode. Lithium metal adheres fairly readily to glass and quartz, and to ground surfaces in particular, and counter electrodes can be prepared by pressing foil against the substrate with a roller.

A reference electrode (RE) can be incorporated in several ways. A conventional RE can be installed in the thick reservoir of a cavity cell. Alternatively, it can be installed in a "T" in one of the fluid inlets or can be placed in a dedicated cavity in the counter electrode substrate for a shorter path to the reservoir. A thin wire quasi/pseudoreference electrode can also be inserted directly into the reservoir, but these are potentially less accurate/reproducible than a conventional RE and more susceptible to drift since potential is not poised by a well-defined redox couple.

The type of reference should be chosen on a case-by-case basis, depending on compatibility with the system under consideration. The Ag/AgCl electrode is a convenient reference to use in aqueous media, but either the system must be tolerant of chloride contamination, or measures (e.g., use of a cation selective membrane) must be taken to prevent chloride from reaching the working electrode. Given the long time scales of NR measurements, there would be time for significant amounts of chloride to diffuse out of the reference. Chloride specifically adsorbs on metal electrodes, meaning it can adsorb in preference to other less strongly adsorbing species, even when present at far lower concentration. The reactivity of an electrode surface with adsorbed chloride may differ significantly from that of an electrode surface free from specifically adsorbing anions. There are other aqueous references, such as the saturated calomel electrode (SCE), Hg/Hg_2SO_4, Hg/HgO, and hydrogen electrodes (RHE, DHE, SHE/NHE), which are described in detail elsewhere [26].

One possible reference for nonaqueous measurements is the Ag/Ag^+ electrode [26]. For nonaqueous lithium ion electrolytes, a piece of metallic lithium can typically be used as a reference electrode. Very commonly, measurements in lithium ion electrolytes are carried out in a two-electrode configuration, with a single sheet of lithium serving as both the reference and counter electrode. Such two-electrode measurements are valid only so long as the polarization of the combined reference/counter electrode is minimal. While its placement is not ideal [27], one possible method of incorporating a lithium reference electrode is to adhere an additional piece of lithium to the counter electrode substrate in a location separate from the counter electrode (assuming the counter electrode substrate is an insulator).

The structure holding these components together should be electrically isolated from the working and counter electrodes and must be designed such that no additional material is placed in the direct and reflected beam paths in order to avoid background scattering and signal attenuation, respectively. An additional useful feature is to have a transparent component, either the counter electrode and its substrate (e.g., using a quartz substrate) in thin cells or a window in the cavity cells, to allow observation of the working electrode in case of bubble formation or delamination. It is important to confirm that all materials in contact with the electrolyte are chemically compatible. This includes the lining of inlet holes drilled in the CE substrate, all sealing materials, tubing for solution ports, and even adhesion layers under the working and counter electrodes, since those electrodes can become porous during an experiment. The material used to make electrical contact to the CE must either be stable within the potential range over which the CE polarizes, or must not come into contact with solution. Particular care must be taken that the current collector/lead used to make electrical contact to the WE is not in contact with the solution; otherwise the lead will contribute to the observed electrochemical behavior, producing ambiguous results. Due to the long times required for NR measurements, the cell should be tested before the experiment for similar amounts of time to determine if the structures are stable. Also, the WE should be checked after this test for delamination or in-plane nonuniformity.

In the case of cells containing lithium or other sensitive materials, assembly should be carried out in a glove box or dry room to protect the reactive components from atmospheric gases. Lithium will react with oxygen, nitrogen, and carbon dioxide. Additional protection can be added during the NR measurements by placing the cell in an enclosure with flowing inert gas. The material used for the neutron windows on this enclosure should be selected to minimize neutron absorption and scattering. Thin aluminum sheet functions adequately in this role.

5.4 Modern Data Analysis

As mentioned previously, it is typically not possible to invert reflectometry data, so we must fit the data to determine the SLD profile. Since we can exactly calculate the reflectivity from a given SLD profile as described in Section 5.2. we can adjust the parameters for the profile until we have the best fit to the data. We approach this from the Bayesian perspective, wherein we calculate the likelihood of seeing the measured data for a given set of parameters and adjust the parameters to maximize this likelihood. This approach allows us to incorporate prior information into the fitting process and to understand the uncertainty in the resulting fit parameters. In Section 5.4.1 we show that this approach is equivalent to traditional least squares and describe some practical algorithms for finding the maximum likelihood. In Section 5.4.2 we show how we can compute uncertainty on the fitted parameter values.

5.4.1 Maximum Likelihood Analysis

Consider what it means to perform a measurement. Given some control stimulus x, a system f characterized by parameters $\boldsymbol{b}$ produces response D. The purpose of the measurement is to infer the properties $\boldsymbol{b}$ from the response, i.e., given $D=f(x,\boldsymbol{b})$, determine $\boldsymbol{b}$. The measurement process is not perfect, with the measured response D only being known with some uncertainty, which can best be represented as probability distribution $P(D)$. There will be some information about the system from previous measurements, so $\boldsymbol{b}$ will have a prior probability $P(\boldsymbol{b})$. This is refined by the measurement to produce the posterior probability $P(\boldsymbol{b}\,|\,D)$, which is the probability of $\boldsymbol{b}$ updated by the information from the measurement D. (The control stimulus x also has uncertainty, but this is usually very small and can be ignored or incorporated into the model f.) Using the joint probability of two events A and B both occurring, $P(A,B)=P(A\,|\,B)P(B)=P(B\,|\,A)P(A)$, we can derive Bayes' rule for probabilistic inference. Applying this to the measurement question $P(D,\boldsymbol{b})$, we get

$$P(\boldsymbol{b}|\,D)=\frac{P(D|\,\boldsymbol{b})P(\boldsymbol{b})}{P(D)} \tag{5.10}$$

That is, if we can compute the probability of observing measured value D for system parameters $\boldsymbol{b}$, then we can combine that with prior information about $\boldsymbol{b}$ to refine our estimate of the probability of $\boldsymbol{b}$. The $P(D)$ term is a constant independent of $\boldsymbol{b}$, so we can form the maximum likelihood estimate using $\hat{\boldsymbol{b}}=\max_{\boldsymbol{b}}P(\boldsymbol{b}|\,D)=\max_{\boldsymbol{b}}P(D|\,\boldsymbol{b})P(\boldsymbol{b})$. Assuming normally distributed measurement uncertainty, $P(D\,|\,\boldsymbol{b})\propto e^{-\chi^2/2}$ where $\chi^2=\sum_i r_i^2(\boldsymbol{b})$ for weighted residual $r_i(\boldsymbol{b})=(f(x_i,\boldsymbol{b})-D_i)/\Delta D_i$, and no prior information so $P(\boldsymbol{b})$ is constant, then $-\ln P(\boldsymbol{b}\,|\,D)=\chi^2/2+C$ and traditional least squares optimization $\hat{\boldsymbol{b}}=\min_{\boldsymbol{b}}\chi^2$ determines the Bayesian maximum likelihood estimate.

The Levenberg-Marquardt (LM) algorithm [28] is a very efficient method for minimizing χ^2 in a nonlinear system. Using the $n\times m$ Jacobian matrix $\boldsymbol{J}$ with $J_{ij}=\dfrac{\partial r_i}{\partial b_j}$ for data point i and fitting parameter b_j, the LM algorithm updates an estimate $\boldsymbol{b}$ using

$$\boldsymbol{b}'=\boldsymbol{b}+\left(\boldsymbol{J}^T\boldsymbol{J}+\lambda\,\boldsymbol{diag}\left(\boldsymbol{J}^T\boldsymbol{J}\right)\right)^{-1}\boldsymbol{J}^T\boldsymbol{r}(\boldsymbol{b}) \tag{5.11}$$

The parameter λ controls the type of update step, ranging from the first-order gradient descent method for large λ to the second-order Gauss-Newton method for small λ. If the proposed step $\boldsymbol{b}'$ is an improvement with $\chi^{2'}<\chi^2$ then we are approaching the minimum, so favor the second-order method by decreasing λ, setting $\lambda\leftarrow\lambda/10$ for the next iteration and keep the improved point by setting $\boldsymbol{b}\leftarrow\boldsymbol{b}'$. If the step is worse, then reject it, leaving $\boldsymbol{b}$ unchanged and bias the next iteration toward the more robust first-order method by setting $\lambda\leftarrow 10\lambda$.

Because the LM algorithm only uses the gradient and curvature at the current point to determine the next point, it is a purely local optimizer and can fail on complex fit spaces. As layer thicknesses in reflectivity models change, the peaks and valleys of the reflectivity signal go in and out of phase with the data, leading to many widely separated local minima in χ^2, so LM is unlikely to find the global minimum from an arbitrary starting point. Since we cannot even be sure that we have the correct model to describe the system, we need robust optimizers, only using LM to perform quick fits at the beginning of the analysis and "finishing" fits at the end.

The LM algorithm, which requires that f be a sum of squares, is only useful for χ^2 minimization, and not for full Bayesian analysis with arbitrary prior information about the fitting parameters. Even simple bounds on a fit parameter, which corresponds to a uniform prior probability $P(b_k)$ for the parameter b_k within a range, is not supported by LM. More general Gauss-Newton and gradient descent optimizers such as Broyden-Fletcher-Goldfarb-Shanno (BFGS) can operate directly on the negative log likelihood function $-\ln P(\boldsymbol{b}\,|\,D)$ using numerical derivatives, but these are still local optimizers that suffer from the robustness issues of the LM algorithm. Also, care is needed when handling parameter bounds, since the derivative is not defined at the boundary. The Nelder-Mead simplex algorithm [29], while still a local optimizer, does not directly use the gradient and so is less drawn toward the nearest minimum and can handle more complex constraints but has slower convergence. Differential evolution (DE) is still more robust, using population-based search to traverse the parameter space $\boldsymbol{b}$ [30]. DE selects a pair of points $\boldsymbol{b}_i$ and $\boldsymbol{b}_j$ from the population, defines the difference vector $\delta\boldsymbol{b} = \boldsymbol{b}_i - \boldsymbol{b}_j$, projects this onto a random subspace by setting components to zero with probability CR (or "crossover ratio"), scales by a factor F near 1 and applies the resulting vector to a third point $\boldsymbol{b}_k$ producing

$$\boldsymbol{b}_k' = \boldsymbol{b}_k + F\delta\boldsymbol{b}_{\boldsymbol{CR}} \tag{5.12}$$

If the step is an improvement, so that $P(D\,|\,\boldsymbol{b}_k')P(\boldsymbol{b}_k') > P(D\,|\,\boldsymbol{b}_k)P(\boldsymbol{b}_k)$, then point k is updated using $\boldsymbol{b}_k \leftarrow \boldsymbol{b}_k'$. While still a "descent" algorithm in that it only accepts parameter sets that improve the likelihood, the population $\{\boldsymbol{b}_i \mid i = 1, \ldots, n\}$ tunes itself to the space $\boldsymbol{b}$, collecting in the minima. This works well for reflectivity problems, allowing DE to jump between the quasiregular minima in the probability density.

The most robust algorithms are not strictly descent algorithms, but are instead able to take steps to lower probability points in the parameter space. With many iterations they can take enough "bad" steps to climb out of a local minimum and drop into another one. Simulated annealing [31] uses the notion of temperature T, with the probability of taking the step from $\boldsymbol{b}_i$ to $\boldsymbol{b}_j$ as

$$\alpha_{ij} = \begin{cases} \dfrac{e^{-\Delta E}}{T}, & \Delta E > 0 \\ 1, & \Delta E \le 0 \end{cases} \tag{5.13}$$

The ΔE term is the log probability ratio

$$\Delta E = \ln \frac{\dfrac{P(D|\boldsymbol{b}_j)P(\boldsymbol{b}_j)}{P(D)}}{\dfrac{P(D|\boldsymbol{b}_i)P(\boldsymbol{b}_i)}{P(D)}} = \ln \frac{P(D|\boldsymbol{b}_j)P(\boldsymbol{b}_j)}{P(D|\boldsymbol{b}_i)P(\boldsymbol{b}_i)} \tag{5.14}$$

The selection of the test point $\boldsymbol{b}_j$ given the current point $\boldsymbol{b}_i$ must be random, selected from some "proposal distribution" q with $q_{ij} = P(\boldsymbol{b}_j|\boldsymbol{b}_i)$ giving the probability of selecting $\boldsymbol{b}_j$. This could be as simple as picking a random direction in the n-dimensional parameter space and stepping a random distance, $\boldsymbol{b}_j = \boldsymbol{b}_i + F\boldsymbol{b}/|\boldsymbol{b}|$ for random F and $\boldsymbol{b}$, or it could use an adaptive step such as the $F\delta\boldsymbol{b}_{\boldsymbol{CR}}$ update from DE. Simulated annealing also needs an "annealing schedule," which starts at high temperature allowing easy movement between minima, and then lowers with each iteration until the algorithm is strictly descending and converges to the local minimum. The annealing schedule may include temperature increases, allowing the algorithm to cycle between searching for the nearest minima and then allowing it to escape to nearby minima.

5.4.2 Uncertainty Analysis

Parameter uncertainty can be characterized by integrating over the posterior distribution $P(\boldsymbol{b}|D)$ using Markov chain Monte Carlo analysis (MCMC). Consider the sequence of points at each iteration of simulated annealing, including duplicates if the proposed point is rejected. When run at a constant temperature $T = 1$ with steps chosen from proposal distribution q which preserves the "detailed balance" condition $q_{ij}\alpha_{ij}\pi_i = q_{ji}\alpha_{ji}\pi_j$ [32], the sequence forms a Markov chain with the remarkable property that it will eventually reach a steady state wherein the elements $\boldsymbol{b}_i$ of the chain appear with probability π_i. That is, using $\pi_i = P(D|\boldsymbol{b}_i)P(\boldsymbol{b}_i)/P(D)$ the sequence $\boldsymbol{b}_1, \boldsymbol{b}_2, \ldots$ will be a "random draw" from the posterior distribution $P(\boldsymbol{b}|D)$. (Since $P(D)$ is constant it cancels when computing ΔE, so we only need $\pi_i \propto P(D|\boldsymbol{b}_i)P(\boldsymbol{b}_i)$.) With randomized DE as the proposal distribution, the resulting differential evolution adaptive metropolis (DREAM) algorithm [33] provides the framework for robust optimization with uncertainty analysis. Unlike many other MCMC algorithms, the DE proposal distribution is self-adaptive, so the DREAM algorithm can be applied to many different problems with very little parameter tuning.

Given the sequence of points generated by MCMC, we can use Monte Carlo integration with importance sampling to estimate a number of statistical properties of the fitted parameters. Importance sampling allows us to compute the integral $\int f(\boldsymbol{b})\pi(\boldsymbol{b})d\boldsymbol{b}$ by selecting points $\boldsymbol{b}_i$ from $\pi(\boldsymbol{b})$ and summing $f(\boldsymbol{b}_i)$ over all points. Since points from high-probability regions are more likely to appear in the sequence, those regions will contribute more to the sum,

implicitly weighting $f(\boldsymbol{b})$ by $\pi(\boldsymbol{b})$**.** More formally, given a random draw S from $x \in \mathbb{R}^n$ with probability $\pi(x)$,

$$S = \{x_i | \, i = 1 \ldots N\} \text{ with } P(x_i \in S) = \pi(x_i) \tag{5.15}$$

then

$$\hat{I} = \int_{\mathbb{R}^n} f(x)\pi(x)\, dx \approx \frac{1}{N}\sum\nolimits_i f(x_i) \tag{5.16}$$

with variance

$$\text{Var}\left(\hat{I}\right) \propto \frac{1}{N} \tag{5.17}$$

So if we have enough samples S from $P(\boldsymbol{b}\,|\,D)$ we can estimate the following to arbitrary precision:

- the expected value, or mean of parameter b_k as

$$b_k = \int_{\mathbb{R}} b_k P(b_k | \, D)\, db_k = \int_{\mathbb{R}^n} b_k P(\boldsymbol{b} | \, D)\, d\boldsymbol{b} \approx \frac{1}{N}\sum\nolimits_i b_k[i] \tag{5.18}$$

Here, $b_k[i]$ is the value of parameter k from point i in the set S. The resulting average is "marginalized" across the entire joint distribution $P(\boldsymbol{b}\,|\,D)$, including any correlations between the parameters that might favor some values of b_k over others.

- the variance of parameter b_k as

$$\sigma^2 = \int_{\mathbb{R}} b_k^2 P(b_k | \, D)\, db \, b_k^2 P(b_k | \, D) db_k - \mu^2 \approx \frac{1}{N}\sum\nolimits_i b_k[i]^2 - \mu^2 \tag{5.19}$$

Using estimated mean $\hat{\mu} = b_k$ instead of the true mean μ, the usual correction of $N/(N-1)$ is required to remove the bias in sample variance.

- the probability density histogram as a set of integrals plotted as a bar chart, with width 2Δ and probability $p(x)$ as

$$p(x) = \int_{x-\Delta}^{x+\Delta} P(b_k | \, D)\, db_k \approx \frac{1}{N}\sum\nolimits_{x-\Delta < b_k \leq x+\Delta} 1 \tag{5.20}$$

The 2D correlation histogram is similar, but uses pixels rather than bars.

- the $1-\alpha$ credible interval as (x_l, x_r) where

$$\int_{-\infty}^{x_l} P(b_k | \, D)\, db_k = \int_{x_r}^{\infty} P(b_k | \, D)\, db_k = \frac{\alpha}{2} \tag{5.21}$$

which can be estimated by $\left(b_k\left[\frac{N\alpha}{2}\right], b_k\left[N-\frac{N\alpha}{2}\right]\right)$ for sorted b_k. This extends to all quantiles q including the median $q=0.5$, which can be approximated using $b_k[Nq]$.

- the $1-\alpha$ shortest credible interval as (x_l, x_r) from

$$\min_{x_l<x_r} x_r - x_l \text{ such that } \int_{x_l}^{x_r} P(b_k|D)\, db_k = 1-\alpha \tag{5.22}$$

which can be estimated as $x_r - x_l = \min_i(b_k[N(1-\alpha)+i] - b_k[N\alpha+i])$ for sorted b_k. This estimate will be biased low and should only be used for large sample sizes.

- the maximum likelihood value $\hat{\boldsymbol{b}}$ as the value with the highest probability; the value $\min_i -\ln P(b_i|D)$ should be close to the maximum likelihood value, and is an excellent starting point for the Gauss-Newton algorithm to find the best fit. Note that the best fit is an accident of the measurement. If you were to repeat the experiment with an identical sample in the identical environment, you would measure slightly different $R(Q)$ and find a different maximum likelihood value, but the credible intervals should remain mostly unchanged.
- a random sample as a subset of S. Random samples can be useful for example to generate a set of typical scattering length density profiles from the fit and compute a 68% confidence band. The subset should be selected at random to avoid short distance correlations between points in the Markov chain.

The quality of the estimated values depends not only on the length of the Markov chain, but also on its quality. If the DREAM algorithm is stopped too soon, then the Markov chain may not have converged, and sample set will be skewed toward the initial guess. This will be visible as a gradual reduction in the average $P(\boldsymbol{b}|D)$ value with each generation. The points from this "burn-in" period cannot be used for subsequent analysis, and are thrown away. For particularly difficult problems, the DREAM algorithm may become stuck and show poor "mixing," so instead of well-behaved chains that quickly traverse the high-density regions of the posterior probability $P(\boldsymbol{b}|D)$, many consecutive samples on each chain will remain at the same value. Sometimes "thinning" the chain by only keeping 1 in 10 samples will help in this situation, but usually it requires constraints on the search space, such as limiting the fit range or reducing the number of fitted parameters.

The correlation histograms are particularly useful for understanding uncertainty in the model parameters. The ideal situation would show circular patterns for every pair of parameters, indicating that every parameter is independent of every other parameter. A correlation between parameters will appear as a diagonal on the parameter-parameter plot. With the reflectivity interference pattern highly dependent on the overall thickness, these can appear as a trade-off between the thickness of one layer with another. If there are many correlations, this can be a sign of an overly complex model, with the extra degrees of freedom trading among each other, and so the number of layers should be reduced. More complex correlations can appear,

especially with constraints between the parameters. Although rare in reflectivity modeling, multiple solutions will appear as disconnected blobs in the correlation plots. For example, in small angle scattering models with ρ_f and ρ_s as the SLD for the particle and the solvent respectively, the intensity $I(Q) = \Delta^2 V^2 F^2(Q)$ is proportional to the square of the contrast $\Delta = \rho_{N,f} - \rho_{N,s}$ so identical scattering will appear for $\rho_{N,f} = \rho_{N,s} + \Delta$ and $\rho_{N,f} = \rho_{N,s} - \Delta$. When fitting $\rho_{N,f}$ using DREAM with no prior probability restricting $\rho_f > \rho_s$, the returned fit will show equal probability for each solution. Similarly, when applied to a crystallography problem in which symmetries were not removed, DREAM was able to return the four equally probable solutions within the fit range [34]. The demonstrated ability of DREAM to return multiple widely separated minima in a multidimensional search space provides confidence that it is able to find the global minimum.

The Refl1D [35] software package from the NCNR includes support for the various optimization methods found in this section, including LM, BFGS, Nelder-Mead simplex, DE, and DREAM. MotoFit [36] from ANSTO provides LM and DE.

5.5 Current Examples

Neutron reflectometry has been applied to electrochemical systems for green energy including batteries, supercapacitors, and fuel cells. These energy conversion and storage technologies most often rely on light nuclei, i.e., hydrogen and lithium, to which neutrons are particularly sensitive relative to photon- and electron-based techniques. In studying these interfaces, NR has been used to detect the formation/presence of surface layers, to measure layer porosities, thickness changes, water (or solvent) uptake, and diffusion rates through layers. After an overall review of these applications, three specific examples will be presented to highlight in greater detail some of the techniques that make NR of particular value to studies of electrochemical energy storage and conversion.

5.5.1 General Review of Many Types of Green Energy Applications

5.5.1.1 Li-ion batteries

Lithium ion batteries achieve high energy densities by the use of anodes poised at extremely reducing potentials and cathodes poised at highly oxidizing potentials. The anode and sometimes the cathode potentials are poised outside the thermodynamic window of stability of the solvent and electrolyte [37,38]. Without the formation of a passivating layer, referred to as the solid electrolyte interface (or interphase) (SEI) [39], at the solid-liquid interface, continuous breakdown of the solution would occur, and the battery would rapidly fail. Major aims of

battery research are to improve the energy density, safety, and cycle life of Li-ion batteries, and the nature of the SEI plays an important role in all of these aspects.

The importance of understanding the SEI is evident in the gamut of techniques that have been used in characterizing it [38,40]. Characterization of the SEI is challenging as it is highly sensitive to the ambient atmosphere, and removing an SEI-coated electrode from a cell for ex situ measurements could alter it, as even trace levels of oxygen can oxidize these nanometer-scale films. Even if the electrode is kept in an inert atmosphere between being removed from the cell and being characterized, washing procedures could also alter the SEI, e.g., by removal of material or collapse of porosity [41]. Thus *in situ* measurements are of great value. Techniques including Fourier transform infrared (FTIR) spectroscopy, electrochemical quartz crystal microbalance, cantilever surface stress measurement, x-reflectometry [42,43], ellipsometry [44,45], scanned-probe techniques, and others have been used for *in situ* characterization. The SEI consists mostly of light element-containing compounds, to which neutrons show greater sensitivity/specificity than other probes. Neutron reflectometry is also sensitive to the nanometer-scale thickness of the SEI.

Several groups have recently used NR to characterize SEI formation on electrodes including titanium dioxide [46], copper [20], carbon [47], and silicon [24,48–52] as model anodes, and on lithium iron phosphate [23,53], lithium manganese nickel oxide [22], lithium manganese nickel oxide [22], and lithium cobalt oxide [54] cathodes.

5.5.1.1.1 Li-ion battery anodes

Anatase In the study of lithium intercalation in an anatase TiO_2 thin film, the nature of the phase boundary between lithium titanate and lithium anatase phases was investigated [46]. The phase front was found to be parallel with the surface throughout reduction and oxidation, with a model showing the titanium oxide layer splitting into two layers of differing SLD during reduction. This model was taken to support lithium ion diffusion across the anatase/lithium titanate phase boundary as the rate-limiting step. Another possible mechanism considered was for the phase transformation to proceed heterogeneously (e.g., propagating fastest along grain boundaries and then spreading out laterally from these boundaries). The layer model proposed for this mechanism showed the SLD of the titanium oxide layer changing homogeneously (since reflected neutrons would average out lateral inhomogeneity). This model was found to be a worse fit than that in which the oxide layer bifurcated, so the latter was preferred. Additionally, it was noted that there was an additional surface layer, interpreted to be an SEI, on an electrode that had been reduced and oxidized once. The oxidation and reduction of anatase proceeded at about +1.8 V *vs* Li/Li^+. This material could be considered a high-potential (safer) anode, or possibly as a low-potential cathode.

Copper Owejan et al. were the first to apply NR to systematically characterize the evolution of the SEI layer as a function of potential and number of cycles in an experiment specifically designed to emphasize the SEI [20]. Cu was chosen as a working electrode since it alloys essentially no Li, and thus all the changes to the NR could be associated with the evolving SEI layer and all the accumulated charge could be associated with the electrolyte breakdown. A 4 nm SEI was found to form after 10 potential cycles, and evolve in thickness, composition, and uniformity with depth as a function of the cell potential. This study will be described more fully as one of the three detailed examples to follow.

Carbon Carbon (graphite) is the anode used in commercial Li-ion cells at present. Preparation of model carbon electrodes presents a challenge because deposition of thin graphite films typically results in the graphitic planes parallel to the surface, rather than the more technologically interesting plane edges through which the Li intercalates. While other types of carbon can have significant capacity [55], SEI growth on these may differ from that on graphite. Kawaura et al. prepared amorphous carbon thin films on a titanium adhesion layer by magnetron sputtering [47]. Fitting of *in operando* NR data indicated a 21% expansion of the carbon layer and a decrease in its SLD when sweeping the electrode potential from open-circuit potential to 0 V vs. Li/Li^+, which was attributed to lithiation of the carbon. The model also included an interfacial layer, interpreted to be the SEI, which approximately doubled in thickness during the negative-going potential sweep. Inclusion of an interfacial layer in the model was needed even for fitting the data at open circuit. Based on the decrease in the SLD of the carbon layer, it was determined that about 25% of the total reduction charged passed went into SEI formation, though this calculation did not take into account the possibility of co-intercalation of ^1H–containing species (solvent molecules) along with lithium ions, as graphite may do [56,57].

Silicon Silicon is presently of interest as a high-capacity anode material (3580 mAh/g on a prelithiated basis for a $Li_{3.75}Si_1$ stoichiometry) and has been the focus of several NR studies [24,48–52]. Silicon undergoes a volume expansion of up to 300% upon lithiation [58], which is particularly demanding on the SEI, which must expand with the electrode or be broken to allow expansion of the electrode. The latter may allow for further SEI formation (and irreversible lithium sequestration) with the electrode surface reexposed to solution.

In an initial study, Jerliu et al. measured NR of an amorphous silicon thin film electrode at open circuit, and after each of three periods of galvanostatic reduction (lithiation) and two periods of oxidation (delithiation) [24]. No SEI/reaction layer formation was noted at open circuit. With reduction, the silicon layer thickness increased and its SLD decreased, as would be expected. During oxidation, the layer contracted, returning to the initial thickness to within error, and its SLD increased. The silicon film SLD did not return to a value as high as the original value, indicating some lithium remained in the layer. Interestingly, while an SEI was not detected after reduction, it was present after oxidation.

In a subsequent study, Jerliu et al. used NR to measure changes in this thickness of an amorphous silicon thin film at several points during electrochemical lithiation [48]. A more limited range of Q_z was used to shorten the data acquisition time to enable collection of more data sets. Fitting of the data showed the thickness did not change in the initial stages of lithiation, though no explanation was offered for this. At higher degrees of lithiation, a linear relation of thickness with degree of lithiation was shown, with a slope of about 0.8 (V/V_0)/stoichiometric equivalent of Li. This value was found to be consistent between 40 nm and 140 nm silicon films, and also between the first and second cycles. After the 40 nm electrode was reduced, it was reoxidized galvanostatically. Its thickness after oxidation was 60 nm, indicating the reduction process was chemically irreversible, and that some lithium remained in the film. The limited Q_z range made it impossible to discern whether any gradients in lithium concentration existed within the film, or whether an SEI was present.

An initial study by Veith et al. investigated the nonelectrochemical reaction of an amorphous Si surface with an electrolyte consisting of a $LiPF_6$ solution in a mixed dimethyl carbonate/ethylene carbonate solvent [49]. Measurements of the as-deposited sample in air indicated a 2.3 nm-thick surface layer attributed to a suboxide or contamination. The sample was then soaked in the electrolyte, washed in dimethyl carbonate, and finally assembled into a liquid cell in contact with deuterated cyclohexane. In this state the surface layer of 3.5 nm thickness appeared, consuming both the former 2.3 nm layer and 1.8 nm of the Si layer (which decreased from 76.5 to 74.7 nm in thickness). Also, fitting of NR data from the bare electrode showed a lower than theoretical SLD of the silicon film, suggesting that the film contained 5% void space, which was further substantiated by another measurement in which the film was immersed in deuterated cyclohexane.

In subsequent work Veith et al. measured NR of an amorphous silicon film electrode [51]. A 4.5 ± 0.5 nm SEI/reaction layer with a $(2.4 \pm 0.5) \times 10^{-4}$ nm^{-2} SLD formed at open circuit, accompanied by consumption of some of the silicon layer as this became thinner when placed in contact with the electrolyte (decreasing from 66.3 ± 0.1 nm in air to 59.3 ± 3 nm in solution at open circuit) [59]. The reaction layer was taken to be formed from the $LiPF_6$ rather than the solvents as its SLD was significantly lower than that of the deuterated solution (4.6×10^{-4} nm^{-2}). An initial process observed during galvanostatic reduction was assigned to the reduction of an impurity, possibly hydrofluoric acid, and resulted in an increase of the surface layer thickness to 17.5 ± 3.5 nm, with an SLD of $(4.7 \pm 0.3) \times 10^{-4}$ nm^{-2}, which is similar to that of the solvent. With further cycling, the SEI thickness was found to decrease with reduction and increase with oxidation, although both changes were within one standard error. Based on the fitted SEI SLD, it was concluded that the SEI had higher LiF content at low potentials and higher Li-C-O-F content at higher potentials.

Most recently the same group studied the behavior of a silicon thin film electrode in a solution consisting of a novel dimethyl perfluoroglutarate solvent and a bis(trifluoromethanesulfonyl)

imide electrolyte [41]. While this solution has significantly lower conductivity than typical Li-ion electrolytes, it could be prepared with higher purity than commercially available deuterated solvents, since it has a relatively high scattering length density and low incoherent scattering. Also, it may be stable to higher potentials than conventional carbonate solvent-based solutions, have lower flammability, and good SEI characteristics. No SEI/reaction layer was detected at open circuit, but a 14.4 ± 3.2 nm SEI with an SLD of $(4.5 \pm 0.1) \times 10^{-4}$ nm^{-2} (slightly below that of the electrolyte SLD of 4.78×10^{-4} nm^{-2}) formed upon reduction to +0.7 V vs. Li/Li^{+}. The SEI thickened to 26.6 ± 2.1 nm with an SLD of $(4.7 \pm 0.1) \times 10^{-4}$ nm^{-2} after reduction to +0.4 V. Further cycling of the electrode showed the SEI to contract during reduction and swell during oxidation. Ex situ XPS measurements on another electrode indicated the opposite: contraction of the SEI during oxidation and swelling during reduction. The discrepancy was attributed to loss of weakly bound species from the SEI upon removal from the cell and washing, highlighting the value of performing measurements *in situ*.

DeCaluwe et al. [50] used NR to study a thin film amorphous silicon electrode covered with an aluminum oxide protective layer. The protective layer acts as an artificial SEI providing ionic conductivity while being electronically insulating, thus preventing direct contact of the solution with the electrode and preventing SEI formation. This simplifies the system under study since the changes should then only be due to bulk transformation of the silicon layer and not changes to its surface. It was found that in the initial stages of lithiation, the silicon layer thickness did not increase significantly, though it did in later stages of lithiation (as seen in the earlier studies). The pore collapse and regrowth (PCRG) mechanism was proposed wherein expansion of the silicon layer first proceeded by isotropic expansion of the silicon to fill void space initially present in the layer. Once the void space was filled, the layer expanded anisotropically along the surface normal. When the electrode was reoxidized, the silicon layer first receded along the surface normal anisotropically, and then the void space regrew. Addition of an SEI layer to the model used to fit the data did not improve the quality of the fit, indicating the AlO_x layer was effective at preventing SEI formation.

A different approach taken recently by Seidlhofer et al. was to use a bulk sample consisting of a conductive (0.005 Ω cm) phosphorous-doped single crystal silicon <100> wafer as the electrode, rather than an amorphous thin film over an Li-blocking substrate [52]. At open circuit, a 2 nm-thick reaction layer with an SLD of 1.87×10^{-4} nm^{-2} was present on the surface over the native SiO_2. The wafer was subjected to two cycles of galvanostatic reduction and oxidation, while NR was measured between 0.07 nm^{-1} and 0.63 nm^{-1} at 5 min/pattern. Upon galvanostatically reducing the electrode, a layer of SLD lower than that of the solution, presumably due to enrichment of Li in the phase, formed over the native silicon oxide. With continued reduction, the Li-enriched layer and the native oxide were removed, and a decrease in the silicon SLD penetrating about 50 nm into the bulk was then noted. This lithiated layer consisted of a 20 nm-thick skin region of higher lithium content (with a calculated $Li_{2.5}Si$ stoichiometry), and a second region of lower lithium concentration ($Li_{0.1}Si$) extending beyond

this into the bulk. The limited depth to which the lithium penetrated into the bulk may be attributed to the build-up of stress limiting further lithiation. Some lithium remained in the bulk upon reoxidation of the electrode as was indicated by the presence of a 3 nm-thick layer with a 0.56×10^{-4} nm^{-2} SLD, corresponding to about $Li_{1.1}Si$. Additionally, a 3.6 nm-thick surface layer with a 1.99×10^{-4} nm^{-2} SLD, taken to be the SEI, formed during oxidation. The changes in the NR during the second cycle of galvanostatic reduction and oxidation were similar to those in the first cycle, again showing the formation of a more heavily lithiated skin layer and a more dilute lithiation region extending further into the bulk. The SEI that had formed during the first oxidation step was removed during the second reduction, though it formed again during the second oxidation.

The larger number of studies of the Si surface allows some trends to be observed. A surface layer/solid electrolyte interface was noted in some of these studies [24,41,49,51,52]. In one of the cases in which it was not observed, it could have been present but not detectable due to the limited range of Q_z measured [48], and in another case the presence of a protective layer over the silicon prevented SEI formation [50]. In the cases in which an SEI was detected, one group observed it to form during oxidation following an initial reduction [24,52], while another group observed it to form during the initial reduction [41,51]. It was suggested that the difference was possibly due to differing experimental conditions, e.g., the rate at which the electrochemical reaction was driven or the supporting electrolyte used. The formation of a reaction layer at open circuit was noted in some cases [49,52], which may be produced by a reaction between the solution and a preexisting oxide or contamination layer present on the as-prepared film. There is a general consensus that no expansion occurs for low Li concentration in amorphous Si, which, in the absence of contamination, can be explained by the PCRG mechanism [50].

In addition to these *in situ* electrochemical NR measurements, Hüger et al. studied lithium transport in silicon using a multilayer structure consisting of repeated $^{6}LiNbO_3$/Si/$^{natural}LiNbO_3$/Si units, [60,61] which showed superlattice peaks corresponding to the chemical, 2-layer Si/$LiNbO_3$ periodicity and also half-order peaks corresponding to the isotopic 4-layer $^{6}LiNbO_3$/$^{natural}LiNbO_3$ periodicity. Upon thermal annealing, lithium diffused between the $LiNbO_3$ layers through the silicon layers, resulting in the loss of the $^{6}LiNbO_3$/$^{natural}LiNbO_3$ half-order peaks. From these data, the diffusion coefficient of Li in silicon was determined to be $(1.0 \pm 0.6) \times 10^{-13}$ cm^2/s. These experiments will be elaborated on as one of the following detailed examples.

5.5.1.1.2 Li-ion battery cathodes

$LiFePO_4$ Cathodes were first investigated in 2010 by Hirayama et al. in a study of epitaxial pulsed laser deposition (PLD) deposited $LiFePO_4$ that utilized both XRR and NR [23,53]. The XRR of the initial sample in air indicated a 2.4 nm-thick contamination layer on the surface and showed no significant changes to the $LiFePO_4$ when again measured in air after cycling. XRR measurements in an electrochemical cell (after removing the electrolyte and contacting the

surface with a Kapton [62] window) showed effects of the window on the scattering and could not detect any significant changes to the sample. The NR was done *in operando* with Si incident and a thick electrolyte reservoir. The three oscillations seen in the NR data in air were severely suppressed upon adding the electrolyte.

$LiMn_2O_4$ The same group investigated the cathode material $LiMn_2O_4$ [21]. Here, fits to the NR data showed that the $LiMn_2O_4$ SLD increased and decreased with the delithiation and lithiation processes; however, the thickness of this cathode remained constant within the measurement uncertainty which was relatively large due to the low amplitude of the oscillations due to the large roughness in the sample.

$LiMn_{1.5}Ni_{0.5}O_4$ Browning et al. investigated $LiMn_{1.5}Ni_{0.5}O_4$ cathode film before and after adding electrolyte and after oxidation (delithiation) to 4.75 V [22]. Their data had much larger amplitude oscillations, corresponding to much sharper interfaces than the previous two studies, allowing them to confirm that the LMNO film became thinner and increased in SLD after oxidation. A 3.3 nm-thick surface layer was observed in the presence of the electrolyte, which remained the same thickness and SLD to within uncertainty upon reduction of the film. However, since the data obtained on this sample in air prior to insertion in electrolyte were not comprehensively fit to models that included the surface, it is not clear when it formed.

$LiCoO_2$ Most recently, NR was used to study the interface at $LiCoO_2$ thin films oriented with the (104) plane exposed to solution [54]. The as-prepared sample had an 0.9 nm surface layer of Li_2CO_3 or LiOH formed by the reaction with moisture and carbon dioxide in air. When it was brought into contact with the solution, the surface layer apparently became much thicker, 30.6 nm, and rougher, limiting the features in the NR.

The cathode studies may be classified into two groups, those which report a thick SEI ($LiFePO_4$, $LiMn_2O_4$, $LiCoO_2$), and one with a thinner SEI that does not change thickness with potential ($LiMn_{1.5}Ni_{0.5}O_2$). The larger roughness in the thicker cases increases the uncertainty of the information that can be obtained. No systematic studies have yet been done to determine if this is an intrinsic effect or due to differing experimental procedures by the different research groups.

5.5.1.2 Fuel cells—Nafion

In the area of fuel cells, NR has been used to investigate the interface between Nafion (the membrane used in polymer electrolyte membrane fuel cells) and several solids at varying degrees of ambient humidification [15,62–68]. Nafion is a copolymer consisting of a perfluorinated alkyl backbone and sulfonate-functionalized side-chains [69]. The latter make the polymer a cation-conducting membrane. The hydrophobic perfluorinated backbone domains and hydrophilic sulfonate groups phase segregate, with the latter forming a cation-conducting network of inverted micelles connected by channels [69]. The degree of hydration affects the structure and the ionic conductivity.

NR has been used to investigate the interaction of Nafion with various substrates, including silicon oxide [63], organosilicate glasses of varying degrees of hydrophilicity [67], Pt and Au thin films [15,63], and glassy carbon [64]. It was found that the interaction of sulfonate groups with hydrophilic substrates leads to the formation of lamellar structures with alternating hydrophilic and hydrophobic domains (alternating low and high SLD layers, respectively, with hydration) [12,63,65,67]. These layered structures persist even when the film is dehydrated. The use of contrast variation to determine the depth profile of the three separate phases—water, fluorocarbons, and sulfonate groups—will be presented as one of the detailed examples in the following. In contrast, only a single water-rich layer formed at Au and Pt surfaces.

A study using D_2O to hydrate Nafion films indicated a hydrated layer adjacent to the vapor interface and a hydrophobic (lower SLD) region adjacent to Pt on an as-prepared Pt film on a glassy carbon substrate [64]. For an electrochemically oxidized Pt film, there was instead a D_2O-rich Nafion layer at the interface with Pt and a water-poor layer adjacent to the vapor phase. For a Nafion film on glassy carbon, the data were fit with a three-layer model with hydrophilic (higher SLD) regions adjacent to the Nafion/carbon and Nafion/air interfaces.

5.5.1.3 Capacitor

There is one example of NR used to characterize a supercapacitor electrode. Vezvaie studied a thin film Co_3O_4 in 0.01 mol/L potassium hydroxide solution [70]. Initially, two measurements were made in air, one with air as the incident medium and the other in back-reflectivity mode with silicon as the incident medium. Measurements were then made in three different (electrolyte-free) H_2O/D_2O mixtures of differing SLD in an attempt to match the SLD of the Co_3O_4 layer. These measurements suggested the presence of a surface layer with an SLD slightly lower than that of the bulk, which was attributed to either contamination or possibly nanobubbles or orientationally constrained water molecules. The SLD of the cobalt oxide layer increased when brought into contact with (mostly deuterated) water, indicating a reaction (e.g., forming CoOOD or $Co(OD)_2$). No significant change occurred when the electrode was brought into contact with potassium hydroxide (KOH)-containing solution. When a potential of +1 V versus SCE was applied to the working electrode, the SLD of the Co_3O_4 increased and the surface layer was removed. The increase in the SLD during the potential hold at +1 V versus SCE suggests greater incorporation of deuterium into the film (e.g., through further CoOOD formation). When the electrode was released to open circuit again, the SLD of the Co_3O_4 layer returned to the original value in solution, and a surface layer of SLD slightly higher than the bulk Co_3O_4 and SLD-matched solution was present. These changes indicate a chemically reversible reaction in the Co_3O_4 film attributed to Co hydroxide and or oxyhydroxide, and a chemically irreversible reaction in the in the contamination layer. The data also indicate that the entire thickness of the film is altered in the electrochemical reaction, rather than only a surface layer being active.

5.5.1.4 Aqueous battery cathode

There is an example of NR used to study nickel hydroxide, an aqueous cathode material, *in situ* [71]. Nickel hydroxide/oxyhydroxide-based materials are the cathode used in nickel metal hydride and nickel cadmium cells. When nickel hydroxide is oxidized and reduced, charge balance is maintained in the material by insertion and removal of hydrogen ions. Water can also intercalate into nickel hydroxide films, particularly the disordered α/γ phases. The SLD of the film is thus expected to vary with oxidation state.

A nickel hydroxide electrode was prepared by electrochemical precipitation from an 0.1 M $Ni(NO_3)_2$ solution onto a gold film and then transferred to a 1 mol/L LiOH solution in D_2O for NR measurements. NR was measured at a fixed angle just above the critical angle while the potential was cycled. It is not possible to fit the NR data at a fixed angle for a monochromatic instrument, though simulations indicated that the reflectivity at this angle would vary in approximately a linear manner with the SLD of the nickel hydroxide film. The advantage of this data collection strategy is better time resolution, though it sacrifices the ability to fit the data to a model to determine a thickness/composition profile. The reflectivity had an approximately linear dependence on the amount of charge passed. This was attributed to expulsion of deuterium with oxidation, though Li^+ insertion was also considered a possibility (however, this is unlikely during oxidation). In one complete potential cycle, a net oxidative charge was passed (i.e., there was Coulombic inefficiency), and the reflectivity did not return to its original value. This was attributed at least in part to trapping of some nickel with an oxidation state greater than +2 in the film.

5.5.1.5 Nonenergy storage/conversion electrochemistry

A few publications study the growth of oxides on refractory metals in aqueous media including titanium [13,17] and zirconium [72]. Reductive hydrogen absorption was also studied in the latter case [72], as well as in another paper considering titanium [73]. The corrosion behavior of nickel has also been studied in mildly acidic chloride-containing aqueous media [74].

5.5.1.6 Redox active polymers

There are also several papers regarding redox active polymers, including electropolymerized conducting polymers [16,75–80] and polymers functionalized with redox-active groups [81–86]. One example is polyvinyl ferrocene (PVF) [84–86], which has been considered as a lithium ion battery electrode [35], among other possible uses. The electrochemical behavior of electroactive spin-cast PVF films was investigated in a series of NR measurements in aqueous sodium perchlorate solutions. The initial study considered equilibrated films at constant potentials with different concentrations of supporting electrolyte [84]. In subsequent studies, a novel technique that allowed NR to be measured under potentiodynamic conditions was used [85,86]. While the electrode potential was cycled, the NR data was sorted into bins spanning different segments of the potential sweep using a boxcar averaging technique on a TOF

instrument. The bins covered either 20 mV or 50 mV potential ranges [85,86]. This type of measurement requires a system that undergoes very little change with cycling.

A PVF film with a capacity of about 1.75 mC/cm^2 and about 37 nm thick in the reduced state was studied at 1 mV/s [86]. The film expanded upon oxidation and contracted upon reduction in approximately a linear manner with charge passed (~0.2 nm/mC). In the reduced state, the ferrocene groups of PVF are neutral, but become positively charged with oxidation. To maintain charge neutrality, anions enter the film. The anions may remain solvated to some degree when entering the film. Contrast variation measurements were made with D_2O and H_2O solutions, which allowed the degree of film solvation to be determined. In the reduced state, the film contained about 1 molecule of water per ferrocene group. Upon oxidation, this increased to about 4.5 water molecules per ferrocene group, with most of the change taking place during the passage of the first 25% of the oxidation capacity of the film. Based on the molar volume of water and the perchlorate ionic radius, the swelling of the film with oxidation was not as great as would be expected. This was taken to indicate that there was void space in the reduced state of the film that is inaccessible to water, possibly due to greater hydrophobicity.

Measurements were also carried out at 10 mV/s. In this case, there was found to be more solvent remaining in the film in the reduced state than with the slower measurement. The SLD profile varied less homogeneously with oxidation and reduction at this higher sweep rate, and this was taken to indicate the anion movement was slower than electron transport within the film. Also, the film lost some capacity with cycling at the higher sweep rate, and the decreased film thickness measured with NR suggested this may have been due to loss of some of some material from the film.

5.5.2 Examples

Three different examples are chosen to highlight several advantages of neutron reflectometry that can be applied to green energy systems. In the first, the use of *in operando* electrochemistry is demonstrated through clear characterization of changes in the structure and composition of the SEI layer as a function of potential within a cycle and with number of cycles. In the second example, a detailed depth profile of composition at the interface between Nafion, a polymer electrolyte, and a hydrophilic surface is obtained using isotope substitution of water. Finally, isotopic contrast variation is used to measure the tracer diffusivity of Li in Si.

5.5.2.1 *In operando neutron reflectometry measurement of the evolution of the solid electrolyte interphase in Li-ion batteries with potential and number of cycles*

Owejan et al. used *in operando* NR to systematically characterize the evolution of the SEI structure as a function of potential and number of potential cycles on an anode-approximating working electrode [20]. To enhance the sensitivity of the measurement to the SEI, a nonintercalating working electrode, Cu, was selected. This ensured that all the changes to the

NR would be associated with the evolving SEI layer, and not with changes (due to Li absorption) to the working electrode itself. Furthermore, the total charge passed could be associated with the electrolyte breakdown. Cu could also be made with sufficient smoothness to avoid averaging over a thin SEI that could potentially be as thin as a few nanometers by allowing useful measurements to $Q > 1.5\ \text{nm}^{-1}$. The electrolyte consisted of 1 mol/L $LiPF_6$ in a 1:2 (v/v) mixture of ethylene carbonate-d_4 and diethyl carbonate. The ethylene carbonate was fully deuterated to increase the SLD of the electrolyte and thus increase its contrast with and sensitivity to the SEI (which was expected to have a low SLD due to the presence of ^1H from the DEC and particularly Li). The deuterated solvent also has the added benefit of decreasing incoherent scattering, thus decreasing the background and allowing measurements to higher Q values.

NR data (Fig. 5.3), collected at each fixed potential, was initiated after the current had decayed. NR data was taken as several series of specular scans, which were compared to ensure that the sample structure did not change (to within measurement statistics) over time. Consecutive scans that did not vary from one another within statistical uncertainty were subsequently combined to reduce measurement uncertainty. Therefore the duration of the reflectivity data collection is not believed to affect the interface structure being studied. Throughout the experiment the current was recorded and the integrated charge at each test point was determined. Model selection was aided by a simultaneous fit of the initial two data sets; one with the sample at open circuit, and the other after 10 potential cycles to form an SEI layer. This simultaneous fit reduced the uncertainty in the model and more accurately determined the structure of the underlying layers including the Cu electrode and the Ti adhesion layer.

Detailed statistical methods were used to demonstrate the accuracy of the fits, including χ^2 values below 1.59, a Bayesian comparison of fits between models with and without the SEI layer included, and 68% confidence intervals determined from Monte Carlo fitting techniques reported for both the fitted parameters and the best fit-determined SLD profiles. These validate the accuracy to which the presence of the SEI layer is demonstrated and show sufficient sensitivity to how it differs at various potentials and number of cycles. The NR results were combined with *in operando* electrochemical measurements and careful postmortem measurements to provide a more detailed discussion of the structure of the SEI and an interpretation of the processes that occurred.

In particular, the NR measurements were first taken in the presence of electrolyte at open circuit, which revealed the presence of a 7 nm-thick layer, likely consisting of Cu carbonate and copper hydroxide. After 10 potential cycles, ending with a hold at 0.25 V vs. Li/Li^+, the initial layer was removed and a 4.0 nm SEI was observed (which is similar in thickness to the SEI observed in several other studies. The next NR data was taken while holding at 0.15 V after 10 more potential cycles. Here it was found that the SEI had grown to 4.5 nm and had a nearly identical SLD. Subsequently, the potential was ramped to sequential test points corresponding to oxidation and reduction peaks and other points determined from the voltammogram. These

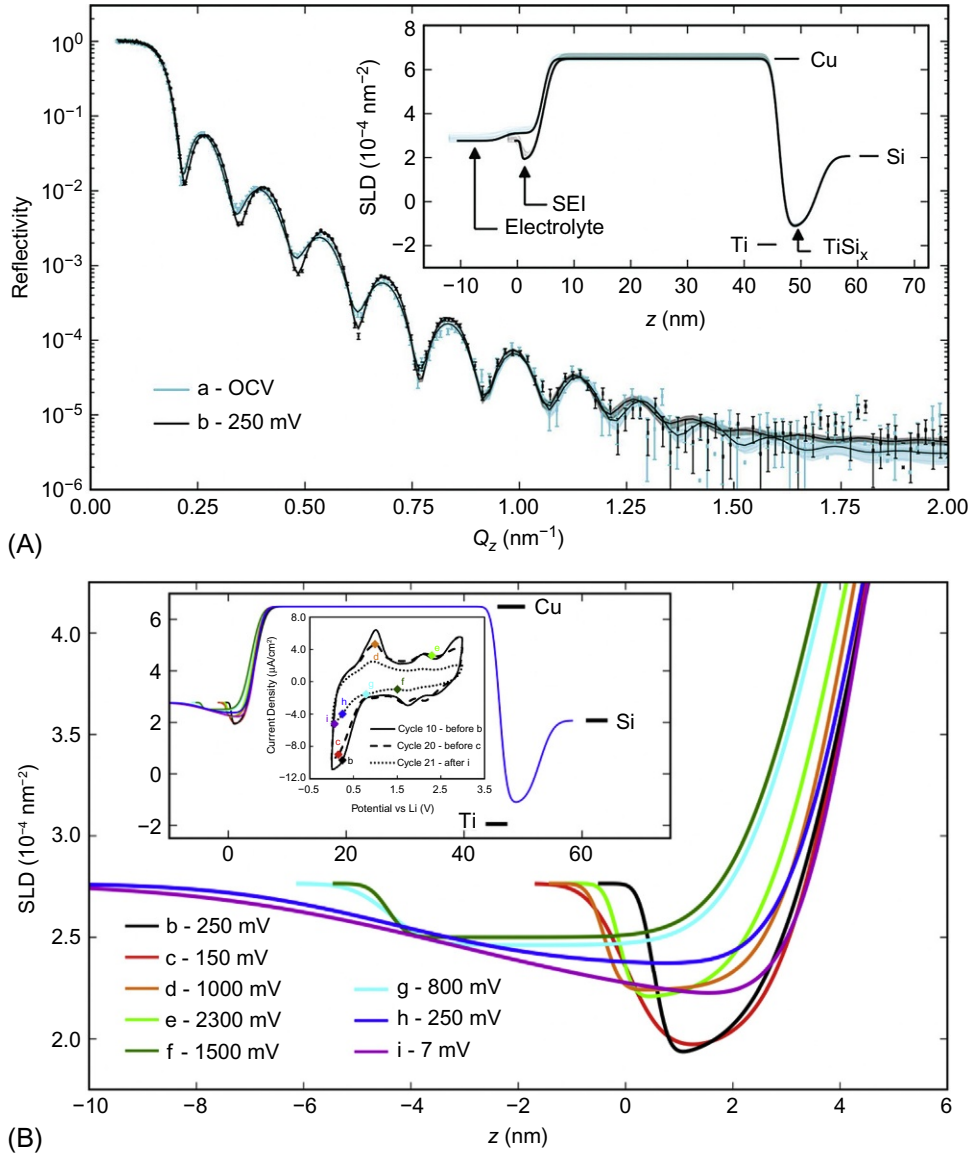

Fig. 5.3

(A) Neutron reflectivity of a thin-film copper electrode in a 1 mol/L $LiPF_6$ in ethylene carbonate-d_4 and diethyl carbonate (1:2 vol./vol.) solution at open circuit and then held at +0.25 V vs. Li/Li^+ after 10 potential cycles. The inset shows the SLD profiles determined by a simultaneous fit to the data. In both, the darker and lighter shaded bands represent the 68% and 95% confidence intervals, respectively. (B) Nested inset: cyclic voltammogram of the copper thin film electrode showing selected cycles at 10 mV/s. Test points b–i denote the locations of potentiostatic holds for NR measurements. (B) A portion of the SLD profile as a function of depth for the SEI deposited on Cu, showing the evolution of the thickness, SLD, and interface roughness with the potential at which the electrode was held indicated. Lines for b–i are the best individual fits, with several parameters kept constant at values determined from the simultaneous fit of the OCV and +0.25 V data (see text for details). The first inset shows the full SLD profile, with the fits coaligned on the Ti layer. *From J.E. Owejan, J.P. Owejan, S.C. DeCaluwe, J.A. Dura, Chem. Mater. 24 (11) (2012) 2133–2140.*

measurements revealed an SEI layer that became slightly thinner, and increased in SLD (lost Li atoms) as the potential was raised to the first oxidation process at 1 V, then became even thinner at 2.3 V, beyond a second oxidation process. Upon decreasing to 1.5 V, the SEI grew considerably in thickness with a much higher relative SLD as the potential dropped below the first reduction peak, presumably by adding material poor in Li at potentials where the electrolyte first became unstable. Lowering the potential to 0.8 V resulted in no significant change to the SEI as expected from the lack of features in the voltammogram in this range. Then, as the potential was sequentially lowered to 0.25 V, then 7 mV, the SEI increased in thickness and roughness with a lower SLD preferentially at the electrode side of the SEI, as presumably more Li was added. This final SEI was 8.9 nm thick but with a substantially increased surface roughness, perhaps due to the prolonged holds at intermediate potentials. Decreased amplitude of the features in the CV with SEI growth confirmed the passivating nature of the SEI. In addition, postmortem X-ray photoelectron spectroscopy (XPS) measurements established candidates for the composition of the final SEI. The volumes of each of these were adjusted to match both the SLD and thickness measured by NR at each test point. The charge associated with the formation of this suite was calculated for each test point. For earlier test points, roughly twice as much charge was measured compared to the amount needed to form the suite of molecules determined by the modeling. This ratio increased to a factor of 5 for later scans. This indicates that most of the species generated by reducing the electrolyte do not contribute to formation of the SEI (Fig. 5.3).

5.5.2.2 Detailed investigations of phase segregation in polymer electrolytes

Nafion has become the most widely used polymer electrolyte in PEM fuel cells because of its high proton conductivity, structural properties, and low permeability to fuel and oxygen. It is composed of a perfluoroethylene backbone with perfluorinated vinyl ether side chains that are terminated by sulfonic acid groups. When hydrated, the hydrophobic backbone phase-segregates from the water, with the sulfonic acid groups at the interface. In a fuel cell, H ions are transported through these interconnected ionic domains. However, the morphology of the ionic domains is poorly understood, with a variety of models that fit the small angle scattering data [69,87,88]. Recently cryo-TEM has indicated that the structure resembles an interconnected network of ribbonlike ionic domains [89]. In addition to the complex bulk structure, it was discovered [63] that while a single water-rich layer forms at the interface with metallic surfaces (e.g., Au and Pt) the ionic domains rearrange into a multilamellar structure near hydrophilic substrates, both the native oxide on Si in the original study and other hydrophilic materials, e.g., organosilicate glass [67]. These multilamellar structures may have relevance to the water retention effects of hydrophilic fillers [90,91] and to transport within the nanoscale Nafion coatings that surround the Pt nanoparticle catalyst and their carbon black supports in fuel cell catalyst layers. The spontaneous formation of these lamellae complicates the structural analysis since the number of layers in the sample must first be determined, as in the previous example and other green energy thin film systems.

DeCaluwe et al. sought to further characterize these lamellae in three ways [12]. Statistical methods were used to determine not only the best fit, but the best model (including the number of layers). Comparing the structure observed for samples with two very different thicknesses helped verify the model, by diminishing the possibility that the fit represented an incorrect symmetry-related model. Finally, isotopic substitution quantified the depth profile of the water content including lamellae, and also determined the SLD profile of the remaining material.

Two samples with Nafion content equivalent to thicknesses of 42 nm and 5 nm were prepared using standard spin coating techniques, annealed at 60°C to ensure bonding, and loaded into a custom-designed sample environment that would control temperature and relative humidity to within 0.2°C and 1.5%, respectively. Because of Nafion's slow uptake of water, repeated reflectivity scans were compared, and only data taken after the sample was verified to be at equilibrium water content was retained. Background scattering was measured and subtracted, for a useful Q range of 0–4.0 nm^{-1}.

The 42 nm sample was measured in a relative humidity, RH = 92% H_2O and, after drying, in RH = 0% (in Ar gas). A series of models, each with increasing number of independent lamellae, n, were fit to the data. The χ^2 values decreased with n, up to 6 and 3 layers for RH = 92% and 0% respectively, and were roughly constant for larger n, i.e., additional layers did not help the fit. Also the Bayesian information criteria (BIC) had a minimum for 6 and 3 layers, confirming that they were the statistically best models. As a further check, an additional model that could accommodate any number of layers with a fixed number of parameters within a single model was used to fit the data. This "damped oscillator model" implicitly supported the observed structure with composition variations of the lamellae decreasing from nearly pure water and pure Nafion near the interface toward an intermediate water volume fraction for the remainder of the film. The SLD of the water-rich layers (and separately the Nafion-rich layers) as a function of layer number were fit to exponential decay functions, as in a damped oscillator. Similarly, to allow for variations in the thickness of the Nafion-rich and water-rich layers, they were fit to functions that allowed a geometric increase or decrease with distance from the SiO_2 interface. The SLD of the layers were found to significantly vary from remainder of the film only for the first 6 and 3 lamellae in agreement with the independent layer series of models. Furthermore, the entire SLD profile of the best fit to this model was compared to the profile of the best independent lamellae model, and they were found to agree within the 1 sigma uncertainty bands, for both humidities. This confirms that these fits accurately describe the individual lamella thicknesses and compositions as well as the damped oscillator model of the composition variations.

The 5 nm sample, also measured in H_2O vapor at RH = 92%, had a lamellar structure very similar to that of the 42 nm sample. This indicated not only the lack of finite size and surface effects but also supported the accuracy of the measurement, model, and best fits. In addition, isotopic substitution of the H_2O for D_2O water was applied to analytically determine the depth

profile of the water volume fraction of the thin film. A simultaneous fit of these two data sets was used to provide more accurate SLD profiles for the two cases. By subtracting the two SLD profiles, the depth profile of the water volume fraction was derived, confirming that the SLD variations are due to water-rich lamellae and not simply density variations. In addition, the SLD depth profile of the remaining material was obtained. The variations in SLD of this profile indicated that the composition of this remaining material was not uniform. Assuming the bulk SLDs of the two components of Nafion, fluorocarbons and sulfonic acid, and maintaining the known stoichiometry to provide sensitivity for layers below the effective resolution of NR, a detailed nanoscaled depth profile of the phase segregation of the Nafion within the lamellar structure was determined (see Fig. 5.4). This structure includes -SO_3H side-chain terminal groups bonded to the SiO_2 substrate, with the attached side chains spanning across the first water-rich lamellae. The first Nafion-rich layer consists of hydrophobic fluorocarbon backbones expelled from the water-rich region, which in turn expel the additional layers of sulfonic acid groups to the next layer, which attracts water, thus establishing an alternating phase segregation between water-rich and water-poor lamellae, with -SO_3H groups lining the interfaces between.

Finally, to investigate the lamellar structure that is observed for a dried sample, its fitted SLD profile was compared to the SLD profile derived from the humidified sample by removing the water, which both increased the SLD and decreased the thickness of layers in proportion to the water volume fraction. These two profiles were very similar, having nearly the same layer thickness, but with fitted profile having smaller layer-to-layer SLD variations than the "water removed" model. Since the model retained the entire phase segregation of sulfonic acid and fluorocarbons seen when hydrated, the lower amplitude of SLD variations indicated partial but not complete interdiffusion of the fluorocarbon and sulfonic acid phases during the 1 h anneal at 60°C that was used to dry the sample.

This example highlights the utility of the quantitative nanoscale SLD depth profile obtained by NR when care is taken to establish the uniqueness of the model, the power of isotopic substitution to determine single component depth profile, and the ability to use an SLD depth profile to determine the depth profile of two known phases.

5.5.2.3 Studies of diffusion using isotopic labeled lithium

In two related papers, Hüger et al. used isotopically labeled Li to study its diffusion through Si thin films [60,61]. In this example the choice of the isotope not only controls the contrast, but also allows the investigation of diffusion in a material system under chemical equilibrium (after minor transients). The multilayer samples consisted of five repeats of four layers: Si, $^{6}LiNbO_3$ (92% ^{6}Li isotopic purity), Si, and $^{nat}LiNbO_3$ Si (where ^{nat}Li is $^{7}Li_{0.9}$ $^{6}Li_{0.1}$). These samples produce a large diffracted intensity in the Bragg peak arising from the 2-layer chemical periodicity due to large contrast between Si and either form of $LiNbO_3$. Additionally, due to the large isotopic difference in the scattering length for Li, there is also a large half-order peak

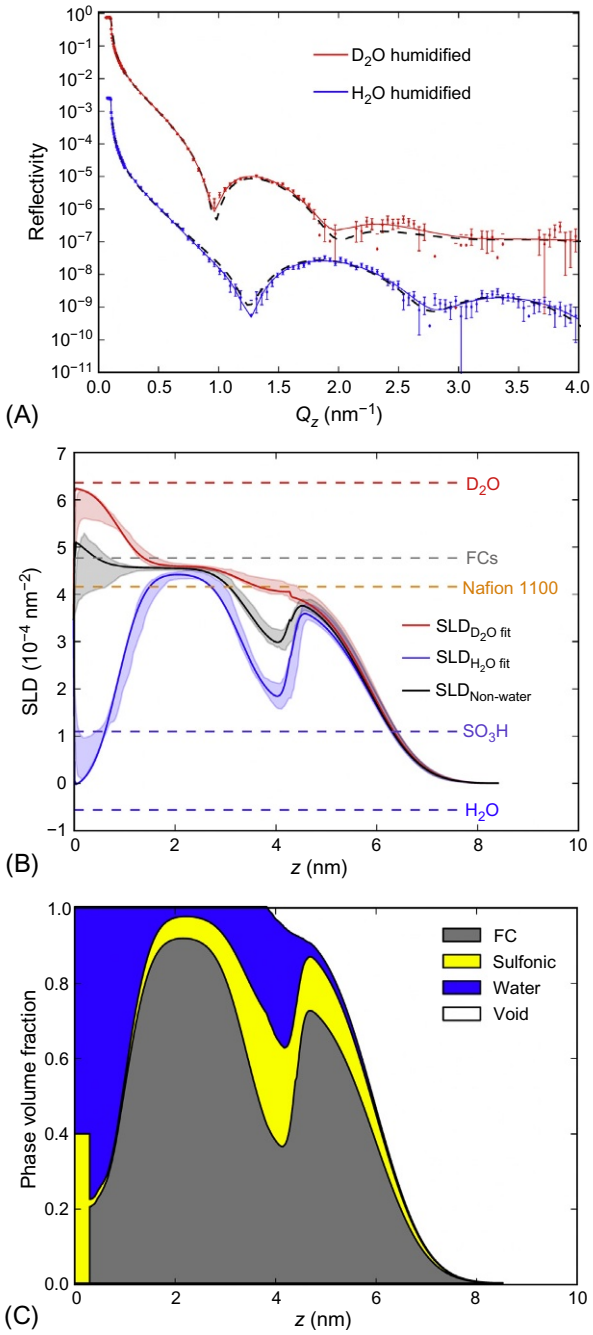

Fig. 5.4

(A) Neutron reflectometry data for a ~5 nm (dry thickness) Nafion film on Si, humidified in H_2O and D_2O vapor at RH = 92%. (B) SLD depth profiles from a simultaneous fit to the data, and the nonwater SLD profile *(black)* determined from the two SLD profiles. *Solid lines* show best fits and shaded regions show 68% confidence intervals. *Dashed horizontal lines* show known SLDs for constituent molecular groups. (C) The depth profile of the volume fractions of the four constituents of the sample (for the physical model). Here, Nafion bonds to the SiO_2 substrate via the -SO_3H side-chain terminal groups, with the side chains stretched across the water-rich first lamella. *From S.C. DeCaluwe, P.A. Kienzle, P. Bhargava, A.M. Baker, J.A. Dura, Soft Matter 10 (31) (2014) 5763–5776.*

corresponding to the 4-layer periodicity. As the sample is heated, the two isotopes are exchanged between the reservoirs of the two isotopes of Li, decreasing the isotopic dissimilarity of the two reservoirs and thus the half-order peak intensity, which is used to measure the diffusion constant. By moving Li between chemically equivalent full reservoirs, rather than from a full to an empty reservoir, this approach also eliminated the effects of variation in chemical stoichiometry, density, and unit volume (with its related degradation paths) on the structure that would have affected the transport properties and the interpretation of the SLD of the materials.

The multilayer samples were deposited by ion beam sputtering, and carefully precharacterized to determine the composition of interfacial layers that spontaneously formed. This ensured that the correct model was fit to the data and provided an accurate description of intervening layers through which Li must diffuse, which greatly improved the understanding of the transients that were observed during the approach to chemical equilibrium. Cross sectional scanning electron microscopy (SEM) images showed the distinct layer structure and Auger electron spectroscopy (AES) further identified a 2 to 3 nm-thick Li-Si-O interfacial layer. This was confirmed by Fourier transform infrared (FTIR) spectroscopy. The isotopic concentrations, as well as the Nb and Si composition modulations, were confirmed with secondary ion mass spectroscopy (SIMS) depth profiling.

In the first study, the intended thicknesses were 10 nm of Si and 15 nm of $LiNbO_3$, which, due to interfacial reactions upon deposition, formed 10.5 nm of Si surrounded by two 2.4 nm $Si_2Nb_2O_3$ interface layers, separated by 13.7 nm (12.5 nm) of $^{nat}LiNbO_3$ ($^6LiNbO_3$). NR data was collected out to a Q of $\sim 0.3\ nm^{-1}$, enough to observe both the half- and full-order Bragg peak. The sample was annealed at 225°C for 10 min, 45 min, 2 h, and 12 h and returned to room temperature after each anneal for measurement. For all measurements, the chemical Bragg peak had the same integrated intensity and height, indicating that the chemical modulation remained unaltered. After 10 min of annealing, the half- order peak was also the same as the initial condition, indicating that for this time period no isotopic intermixing had yet occurred (during which the intervening Si layers absorb a small amount of Li and the system approaches chemical equilibrium). Thereafter half-order peak intensity decreased monotonically.

The ^6Li and ^7Li concentrations in their respective reservoirs were determined by fitting the NR data. These concentrations versus time were fit to exponential decays, which determined the lag time to be $(9 \pm 2) \times 10^2$ s. The exponential decay constants were also determined, which yields the permeability, $P = (1.3 \pm 0.2) \times 10^{-17}\ cm^2/s$, which is the same for both isotopes. Using a solubility S from the literature, the tracer diffusivity was estimated to be $D_S = P/S \approx (6 \pm 2) \times 10^{-14}\ cm^2/s$.

The second experiment was enhanced by using the AMOR (apparatus for multioption reflectometry) reflectometer with the Selene option, which allows multiple incident angles to be measured simultaneously [92,93]. This provides much higher flux with a simultaneously

measured range of Q values. NR could be measured for a small, 2 mm × 10 mm sample in roughly 2 min out to $Q \approx 0.6\ \text{nm}^{-1}$, which was far enough to include the first two chemical Bragg peaks. Therefore the sample could be measured at the annealing temperature in real time for various snapshots of time ranging from 1 to 120 min. This *in situ* approach avoided the complications with accounting for diffusion during cooldown and reheating of the sample, and allowed for measurement on shorter time scales and with more test points. Background scattering with the multibeam approach was estimated by measuring an empty sample holder. The sample was similar to the one used in the first experiment, with five repetitions of the [$^{6}LiNbO_3$ (18 nm)/Si (9 nm)/$^{nat}LiNbO_3$ (18 nm)/Si (9 nm)] unit. Upon fitting it was determined that the thicknesses were Si (5 nm), with $Li_2Si_2O_5$ (1.8 nm), and $LiNbO_3$ (16.7 nm) for both isotopes of Li.

Again, only the half-order peak changed with annealing time. The rest of the reflectivity curve (including the critical edge, both chemical Bragg peaks, and the intensity between the Bragg peaks) remained the same, indicating that the chemical structure, including the interface widths, remained constant during the experiment, and that potential effects of sample warping with heating and prolonged annealing were not present in this case. This was corroborated by measurements at room temperature before and after annealing. The integrated intensity of the half-order peak, which is linearly proportional to contrast, or relative isotope abundance, was plotted as a function of time. The fraction of ^{6}Li/total Li in the reservoir that was initially ^{6}Li rich was determined by fitting the NR data. The time-dependence of this fraction was then fit to an exponential decay, yielding a permeability of $P = (2.8 \pm 0.3) \times 10^{-17}\ \text{cm}^2/\text{s}$, and a tracer diffusion coefficient of $D = (1.0 \pm 0.6) \times 10^{-13}\ \text{cm}^2/\text{s}$ at 240°C, which is in good agreement with the $D_S \approx (6 \pm 2) \times 10^{-14}\ \text{cm}^2/\text{s}$ at value obtained at 225°C in the first experiment.

While not discussed, the greater time resolution allowed better investigations of the time lag observed in the first experiment. While the first experiment included a 15-min lag, during which the isotopic ratio remained roughly constant, in the second experiment the greater time resolution showed that there was possibly a more rapid exponential decay to a plateau of approximately 82% ^{6}Li over the first roughly 15 min; however, this deviation from a single exponential decay (which was fit to the data) was within the error. It is possible that the higher temperature of the second experiment decreased the time lag disproportionally compared to the diffusion.

As mentioned in Section 5.3, measuring a sample that is changing over time could induce a misinterpretation of the structure in that the time average reflectivity curve may not correspond to the scattering from the time average structure. However, in this case two aspects of this experimental design minimize these effects. Because all Q were measured simultaneously rather than in series, the reflectivity curve does not have a Q versus time dependence, which can cause spurious layers to appear in fits. Furthermore, the chemical structure is shown to be

invariant after the transients occur, so the only effect is the intensity of the half-order peak. While averaging over time of an exponentially decaying intensity does not exactly give the intensity at the average time, it is a small effect for these short time integrations.

This third example demonstrates the power of isotope labeling made possible by the scattering lengths for neutron reflectometry. In addition, the ease of implementing *in situ* neutron sample environments and rapid data acquisition rates over a limited required Q range allows for measurements to be made in real time during annealing. Finally, by choosing a sample in which the chemical structure remained constant while only the isotopic concentrations varied allowed accurate measurements of the neutron reflectometry in a time-varying system. Combined, these approaches resulted in the precise determination of the tracer diffusion constant for Li in Si.

5.5.3 Summary

Numerous examples in the literature point out the usefulness of neutron reflectometry for studies of structures related to green energy applications. These examples benefit from the many advantages of neutron scattering, including the large variations in neutron scattering length for isotopes, particularly of H and Li, which are of interest to energy applications. This control of contrast enables self-diffusion studies and has been used to enhance contrast to layers of interest, for example the SEI, using proper selection of isotopes for components of the electrolyte. Also, contrast variation has been used to obtain precise depth profiles of a given phase, e.g., water volume fraction in polymer electrolytes. Moreover, robust and realistic *in operando* sample environments, such as electrochemical cells, are made possible by the large penetration lengths of neutrons to many materials. Studies successfully employing these have provided nanoscaled structural information for unperturbed structures, in their native environments at applied potentials. This not only removes the ambiguities caused by processing required for postmortem measurements but also provides access to nonequilibrium samples. For future studies of green energy systems neutron reflectometry can provide unique opportunities and perspectives.

5.6 Conclusions

Neutron reflectometry has been demonstrated to be a technique capable of providing unique benefits for studies related to nanolayer research in green chemistry. Proper application of this technique can be used to obtain accurate depth profiles with subnanometer precision under *in operando* condition of active material in their native environments. This chapter illuminated this less-known and underutilized technique by providing an introduction, practical guide, examples, and best practices; with the goal of bringing these opportunities to a larger audience. While there remain numerous opportunities to apply the demonstrated techniques to a greater

number of similar experiments, future enhancements to the technique will also allow a greater diversity of applications.

One of the largest future challenges will be to extend the Q-range of the measurements, so that smaller feature sizes can be discernible. Currently this is limited by the signal-to-noise ratio at higher Q where the reflectivity is low, rather than by the flux of the source. Signal to noise is dominated by isotropic scattering from the sample itself, predominantly liquid reservoirs, or absent this, from the substrate itself. Decreasing the noise will require some means to decrease the thickness of these components, or to distinguish and reject the isotropic scattering and retain the specular. The current method of isolating the specular intensity by subtracting the background (measured away from the specular conditions) is of limited value due to counting statistics. Inordinate time is required to achieve useful uncertainties as the difference between the specular reflection and background becomes small.

While extending the Q range may prove challenging, recent and planned developments are targeted toward much greater throughput, through shorter acquisition times and more effective data analysis. Several approaches have been reviewed [94], and new reflectometers such as AMOR with the Selene enhancement [6,92,93] and Candor apply multiple beams (and in the case of Candor also multiple wavelengths with a continuous source), to increase the effective flux on the sample, allowing for much quicker measurements. This greater throughput will not only allow more measurements to be made, but will also allow studies of kinetics on increasingly shorter time scales or studies of less stable samples, opening up additional possibilities for investigation. Advances in data fitting will allow the researcher to more quickly and efficiently determine the correct model corresponding to the sample structure, and thus decrease the time required to correctly fit the data, keeping up with the greater pace of data collection. Some data collection and fitting techniques (e.g., the expanded use of reference layers and model independent profiles) will also increase the ease of analysis and help provide unique solutions, thereby decreasing the level of experience required to ensure that the results accurately represent the structures that exist in the samples.

In addition, more sophisticated sample environments (e.g., automated fluid and sample changers, and more stable and easy to assemble electrochemical cells) will help researchers to better utilize the increases in throughput. Multimodal measurements (i.e., simultaneously performing a second type of measurement while taking NR data) is another advance that will increase the utility of neutron reflectometry. In particular, measurements capable of determining composition (crystallographic, molecular, and/or atomic) will best complement reflectometry where otherwise, the compositional information is limited to atomic concentrations.

These advances open up numerous new opportunities and applications for an expanding neutron reflectometry user community, as acquisition times get shorter, data fitting becomes easier, and complementary techniques enhance the applicability of the data to a greater diversity of scientific disciplines.

References

[1] V.F. Sears, Neutron News 3 (3) (1992) 26–37.
[2] C.F. Majkrzak, C. Metting, B.B. Maranville, J.A. Dura, S. Satija, T. Udovic, N.F. Berk, Phys. Rev. A 89 (3) (2014)033851.
[3] C.F. Majkrzak, N.F. Berk, Phys. Rev. B 52 (15) (1995) 10827–10830.
[4] M.R. Fitzsimmons, C.F. Majkrzak, Application of polarized neutron reflectometry to studies of artificially structured magnetic materials, in: Y. Zhu (Ed.), Modern Techniques for Characterizing Magnetic Materials, Springer US, Boston, MA, 2005, , pp. 107–155.
[5] M. Dubey, M.S. Jablin, P. Wang, M. Mocko, J. Majewski, Eur. Phys. J. Plus 126 (11) (2011) 110.
[6] J. Stahn, A. Glavic, Nuclear instruments and methods in physics research section A: accelerators, Spectrom. Detect. Assoc. Equip. 821 (2016) 44–54.
[7] J.A. Dura, D.J. Pierce, C.F. Majkrzak, N.C. Maliszewskyj, D.J. McGillivray, M. Lösche, K. V. O'Donovan, M. Mihailescu, U. Perez-Salas, D.L. Worcester, S.H. White, Rev. Sci. Instrum. 77 (7) (2006) 074301.
[8] J.M. Simmons, J.C. Cook, R.M. Ibberson, C.F. Majkrzak, D.A. Neumann, J. Appl. Crystallogr. 46 (5) (2013) 1347–1352.
[9] Neutron Sources. https://www.ncnr.nist.gov/nsources.html (accessed 14.11.16).
[10] C.F. Majkrzak, N.F. Berk, S. Krueger, J.A. Dura, M. Tarek, D. Tobias, V. Silin, C.W. Meuse, J. Woodward, A. L. Plant, Biophys. J. 79 (6) (2000) 3330–3340.
[11] B.J. Kirby, P.A. Kienzle, B.B. Maranville, N.F. Berk, J. Krycka, F. Heinrich, C.F. Majkrzak, Curr. Opin. Colloid Interface Sci. 17 (2012) 44–53.
[12] S.C. DeCaluwe, P.A. Kienzle, P. Bhargava, A.M. Baker, J.A. Dura, Soft Matter 10 (31) (2014) 5763–5776.
[13] D.G. Wiesler, C.F. Majkrzak, Phys. B Condens. Matter 198 (1) (1994) 181–186.
[14] N.F. Berk, C.F. Majkrzak, Phys. Rev. B 51 (1995) 11296–11309.
[15] V.S. Murthi, J. Dura, S. Satija, C. Majkrzak, ECS Trans. 16 (2) (2008) 1471–1485.
[16] Richardson, R. M.; Swann, M. J.; Hillman, A. R.; Roser, S. J., Faraday Discuss. 1992, 94 (0), 295–306.
[17] Z. Tun, J.J. Noël, D.W. Shoesmith, J. Electrochem. Soc. 146 (3) (1999) 988–994.
[18] Y. Lauw, T. Rodopoulos, M. Gross, A. Nelson, R. Gardner, M.D. Horne, Rev. Sci. Instrum. 81 (7) (2010). http://dx.doi.org/074101.
[19] H. Wang, R.G. Downing, J.A. Dura, D.S. Hussey, In situ neutron techniques for studying lithium ion batteries, in: Polymers for Energy Storage and Delivery: Polyelectrolytes for Batteries and Fuel Cells, Vol. 1096, American Chemical Society, 2012, , pp. 91–106.
[20] J.E. Owejan, J.P. Owejan, S.C. DeCaluwe, J.A. Dura, Chem. Mater. 24 (11) (2012) 2133–2140.
[21] M. Yonemura, M. Hirayama, K. Suzuki, R. Kanno, N. Torikai, N.L. Yamada, J. Phys. Conf. Ser. 502 (1) (2014) 012054.
[22] J.F. Browning, L. Baggetto, K.L. Jungjohann, Y. Wang, W.E. Tenhaeff, J.K. Keum, D.L. Wood, G. M. Veith, ACS Appl. Mater. Interfaces 6 (21) (2014) 18569–18576.
[23] M. Hirayama, M. Yonemura, K. Suzuki, N. Torikai, H. Smith, E. Watkinsand, J. Majewski, R. Kanno, Electrochemistry 78 (5) (2010) 413–415.
[24] B. Jerliu, L. Dorrer, E. Huger, G. Borchardt, R. Steitz, U. Geckle, V. Oberst, M. Bruns, O. Schneider, H. Schmidt, Phys. Chem. Chem. Phys. 15 (20) (2013) 7777–7784.
[25] A.A. Topalov, I. Katsounaros, M. Auinger, S. Cherevko, J.C. Meier, S.O. Klemm, K.J.J. Mayrhofer, Angew. Chem. Int. Ed. 51 (50) (2012) 12613–12615.
[26] C.G. Zoski, T.J. Smith, K.J. Stevenson (Eds.), Handbook of Electrochemistry, Elsevier, Amsterdam, 2007, pp. 73–110.
[27] M. Ender, A. Weber, I.-T. Ellen, J. Electrochem. Soc. 159 (2) (2011) A128–A136.
[28] D.W. Marquardt, J. Soc. Ind. Appl. Math. 11 (1963) 431–441.
[29] J.A. Nelder, R. Mead, Comput. J. 7 (1965) 308–313.
[30] R. Storn, K. Price, J. Glob. Optim. 11 (1997) 341–359.
[31] C.F. Laub, T.L. Kuhl, J. Chem. Phys. 125 (2006) 244702.

[32] W.K. Hastings, Biometrika 57 (1970) 97–109.
[33] J.A. Vrugt, C.J.F. Ter Braak, C.G.H. Diks, B.A. Robinson, J.M. Hyman, D. Higdon, Int. J. Nonlinear Sci. Numer. Simul. 10 (2009) 273–290.
[34] J.E. Lesniewski, S.M. Disseler, D.J. Quintana, P.A. Kienzle, W.D. Ratcliff, J. Appl. Crystallogr. 49 (6) (2016) 2201–2209.
[35] Kienzle, P. A.; Krycka, J.; Patel, N.; Sahin, I. Refl1D, 2011.
[36] A. Nelson, J. Appl. Crystallogr. 39 (2006) 273–276.
[37] J.B. Goodenough, Y. Kim, Chem. Mater. 22 (3) (2010) 587–603.
[38] M. Gauthier, T.J. Carney, A. Grimaud, L. Giordano, N. Pour, H.-H. Chang, D.P. Fenning, S. F. Lux, O. Paschos, C. Bauer, F. Maglia, S. Lupart, P. Lamp, Y. Shao-Horn, J. Phys. Chem. Lett. 6 (22) (2015) 4653–4672.
[39] E. Peled, J. Electrochem. Soc. 126 (12) (1979) 2047–2051.
[40] K. Xu, Chem. Rev. 114 (23) (2014) 11503–11618.
[41] T.M. Fears, M. Doucet, J.F. Browning, J.K.S. Baldwin, J.G. Winiarz, H. Kaiser, H. Taub, R.L. Sacci, G. M. Veith, Phys. Chem. Chem. Phys. 18 (20) (2016) 13927–13940.
[42] T.T. Fister, B.R. Long, A.A. Gewirth, B. Shi, L. Assoufid, S.S. Lee, P. Fenter, J. Phys. Chem. C 116 (42) (2012) 22341–22345.
[43] T.T. Fister, J. Esbenshade, X. Chen, B.R. Long, B. Shi, C.M. Schlepütz, A.A. Gewirth, M. J. Bedzyk, P. Fenter, Adv. Energy Mater. 4 (7) (2014) 1301494.
[44] M.A. McArthur, S. Trussler, J.R. Dahn, J. Electrochem. Soc. 159 (3) (2012) A198–A207.
[45] E.J. Dufek, ECS Electrochem. Lett. 3 (11) (2014) A108–A111.
[46] M. Wagemaker, R. van de Krol, A.A. van Well, Phys. B Condens. Matter 336 (1–2) (2003) 124–129.
[47] H. Kawaura, M. Harada, Y. Kondo, H. Kondo, Y. Suganuma, N. Takahashi, J. Sugiyama, Y. Seno, N. L. Yamada, ACS Appl. Mater. Interfaces 8 (15) (2016) 9540–9544.
[48] B. Jerliu, E. Hüger, L. Dörrer, B.K. Seidlhofer, R. Steitz, V. Oberst, U. Geckle, M. Bruns, H. Schmidt, J. Phys. Chem. C 118 (18) (2014) 9395–9399.
[49] G.M. Veith, L. Baggetto, R.L. Sacci, R.R. Unocic, W.E. Tenhaeff, J.F. Browning, Chem. Commun. 50 (23) (2014) 3081–3084.
[50] S.C. DeCaluwe, B.M. Dhar, L. Huang, Y. He, K. Yang, J.P. Owejan, Y. Zhao, A.A. Talin, J. A. Dura, H. Wang, Phys. Chem. Chem. Phys. 17 (17) (2015) 11301–11312.
[51] G.M. Veith, M. Doucet, J.K. Baldwin, R.L. Sacci, T.M. Fears, Y. Wang, J.F. Browning, J. Phys. Chem. C 119 (35) (2015) 20339–20349.
[52] B.-K. Seidlhofer, B. Jerliu, M. Trapp, E. Hüger, S. Risse, R. Cubitt, H. Schmidt, R. Steitz, M. Ballauff, ACS Nano 10 (8) (2016) 7458–7466.
[53] M. Hirayama, Electrochemistry 83 (9) (2015) 701–706.
[54] T. Minato, H. Kawaura, M. Hirayama, S. Taminato, K. Suzuki, N.L. Yamada, H. Sugaya, K. Yamamoto, K. Nakanishi, Y. Orikasa, H. Tanida, R. Kanno, H. Arai, Y. Uchimoto, Z. Ogumi, J. Phys. Chem. C 120 (2016) 20082–20088.
[55] J.R. Dahn, T. Zheng, Y. Liu, J.S. Xue, Science 270 (5236) (1995) 590–593.
[56] J.O. Besenhard, M. Winter, J. Yang, W. Biberacher, J. Power Sources 54 (2) (1995) 228–231.
[57] M.R. Wagner, J.H. Albering, K.C. Moeller, J.O. Besenhard, M. Winter, Electrochem. Commun. 7 (9) (2005) 947–952.
[58] L.Y. Beaulieu, T.D. Hatchard, A. Bonakdarpour, M.D. Fleischauer, J.R. Dahn, J. Electrochem. Soc. 150 (11) (2003) A1457–A1464.
[59] Throughout this chapter, unless otherwise noted, all uncertainties and error bars represent one standard error.
[60] E. Hüger, L. Dörrer, J. Rahn, T. Panzner, J. Stahn, G. Lilienkamp, H. Schmidt, Nano Lett. 13 (3) (2013) 1237–1244.
[61] E. Hüger, J. Stahn, H. Schmidt, J. Electrochem. Soc. 162 (13) (2015) A7104–A7109.
[62] Certain commercial equipment, instruments, or materials are identified in this paper to foster understanding. Such identification does not imply recommendation or endorsement by the National Institute of Standards and Technology, nor does it imply that the materials or equipment identified are necessarily the best available for the purpose.

[63] J.A. Dura, V.S. Murthi, M. Hartman, S.K. Satija, C.F. Majkrzak, Macromolecules 42 (13) (2009) 4769–4774.
[64] D.L. Wood, J. Chlistunoff, J. Majewski, R.L. Borup, J. Am. Chem. Soc. 131 (50) (2009) 18096–18104.
[65] S.A. Eastman, S. Kim, K.A. Page, B.W. Rowe, S. Kang, C.L. Soles, K.G. Yager, Macromolecules 45 (19) (2012) 7920–7930.
[66] S.A. Eastman, S. Kim, K.A. Page, B.W. Rowe, S. Kang, S.C. DeCaluwe, J.A. Dura, C.L. Soles, K. G. Yager, Macromolecules 46 (2) (2013) 571.
[67] S. Kim, J.A. Dura, K.A. Page, B.W. Rowe, K.G. Yager, H.-J. Lee, C.L. Soles, Macromolecules 46 (14) (2013) 5630–5637.
[68] W.P. Kalisvaart, H. Fritzsche, W. Mérida, Langmuir 31 (19) (2015) 5416–5422.
[69] K.A. Mauritz, R.B. Moore, Chem. Rev. 104 (10) (2004) 4535–4586.
[70] M. Vezvaie, P. Kalisvaart, H. Fritzsche, Z. Tun, D. Mitlin, J. Electrochem. Soc. 161 (5) (2014) A798–A802.
[71] P.M. Saville, M. Gonsalves, A.R. Hillman, R. Cubitt, J. Phys. Chem. B 101 (1) (1997) 1–4.
[72] J.J. Noël, D.W. Shoesmith, Z. Tun, J. Electrochem. Soc. 155 (8) (2008) C444–C454.
[73] M. Vezvaie, J.J. Noël, Z. Tun, D.W. Shoesmith, J. Electrochem. Soc. 160 (9) (2013) C414–C422.
[74] S. Singh, S. Basu, A.K. Poswal, R.B. Tokas, S.K. Ghosh, Corros. Sci. 51 (3) (2009) 575–580.
[75] S.J. Roser, R.M. Richardson, M.J. Swann, A.R. Hillman, J. Chem. Soc. Faraday Trans. 87 (17) (1991) 2863–2864.
[76] A.R. Hillman, P.M. Saville, A. Glidle, R.M. Richardson, S.J. Roser, M.J. Swann, J.R.P. Webster, J. Am. Chem. Soc. 120 (49) (1998) 12882–12890.
[77] A.R. Hillman, L. Bailey, A. Glidle, J.M. Cooper, N. Gadegaard, J.R.P. Webster, J. Electroanal. Chem. 532 (1–2) (2002) 269–276.
[78] A. Glidle, C.S. Hadyoon, N. Gadegaard, J.M. Cooper, A.R. Hillman, R.W. Wilson, K.S. Ryder, J.R. P. Webster, R. Cubitt, J. Phys. Chem. B 109 (30) (2005) 14335–14343.
[79] A. Glidle, A.R. Hillman, K.S. Ryder, E.L. Smith, J.M. Cooper, R. Dalgliesh, R. Cubitt, T. Geue, Electrochim. Acta 55 (2) (2009) 439–450.
[80] J.-P. Veder, R. De Marco, K. Patel, P. Si, E. Grygolowicz-Pawlak, M. James, M. T. Alam, M. Sohail, J. Lee, E. Pretsch, E. Bakker, Anal. Chem. 85 (21) (2013) 10495–10502.
[81] R.W. Wilson, R. Cubitt, A. Glidle, A.R. Hillman, P.M. Saville, J.G. Vos, J. Electrochem. Soc. 145 (5) (1998) 1454–1461.
[82] R.W. Wilson, L. Bailey, R. Cubitt, M. Gonsalves, A. Glidle, A. Robert Hillman, J.G. Vos, C. Hogan, J.R. P. Webster, Phys. Chem. Chem. Phys. 1 (5) (1999) 843–853.
[83] R.W. Wilson, R. Cubitt, A. Glidle, A.R. Hillman, P.M. Saville, J.G. Vos, Electrochim. Acta 44 (20) (1999) 3533–3548.
[84] A. Glidle, J. Cooper, A.R. Hillman, L. Bailey, A. Jackson, J.R.P. Webster, Langmuir 19 (2003) 7746–7753.
[85] J.M. Cooper, R. Cubitt, R.M. Dalgliesh, N. Gadegaard, A. Glidle, A.R. Hillman, R.J. Mortimer, K.S. Ryder, E. L. Smith, J. Am. Chem. Soc. 126 (47) (2004) 15362–15363.
[86] A. Glidle, A.R. Hillman, K.S. Ryder, E.L. Smith, J. Cooper, N. Gadegaard, J.R. P. Webster, R. Dalgliesh, R. Cubitt, Langmuir 25 (7) (2009) 4093–4103.
[87] H.G. Haubold, T. Vad, H. Jungbluth, P. Hiller, Electrochim. Acta 46 (10–11) (2001) 1559–1563.
[88] L. Rubatat, A.L. Rollet, G. Gebel, O. Diat, Macromolecules 35 (10) (2002) 4050–4055.
[89] F.I. Allen, L.R. Comolli, A. Kusoglu, M.A. Modestino, A.M. Minor, A.Z. Weber, ACS Macro Lett. 4 (1) (2015) 1–5.
[90] K.T. Adjemian, S.J. Lee, S. Srinivasan, J. Benziger, A.B. Bocarsly, J. Electrochem. Soc. 149 (3) (2002) A256–A261.
[91] I. Nicotera, T. Zhang, A. Bocarsly, S. Greenbaum, J. Electrochem. Soc. 154 (5) (2007) B466–B473.
[92] J. Stahn, T. Panzner, U. Filges, C. Marcelot, P. Böni, Nucl. Instr. Methods Phys. Res. A: Accel. Spectrom. Detect. Assoc. Equip. 634 (1, Supplement) (2011) S12–S16.
[93] J. Stahn, U. Filges, T. Panzner, Eur. Phys. J. Appl. Phys. 58 (1) (2012) 11001.
[94] F. Ott, A. Menelle, Eur. Phys. J. Spec. Topics 167 (1) (2009) 93–99.

CHAPTER 6

Interfacial Molecular Structure and Dynamics at Solid Surface Studied by Sum Frequency Generation Spectroscopy

Hidenori Noguchi, Kohei Uosaki[1]

National Institute for Materials Science, Tsukuba, Japan
[1] *Corresponding author*

6.1 Introduction

Many important processes such as electrochemical reactions, biological processes, and corrosion are taking place at solid/liquid interfaces. To precisely understand the mechanism of these processes at solid/liquid interfaces, information on structures of molecules at electrode/electrolyte interface including short-lived intermediates and solvent at the interface is essential. The determination of the interfacial structures of the intermediate and solvent is, however, difficult by conventional surface vibrational techniques because the number of molecules at the interfaces is far smaller than those of bulk molecules.

Recently, sum frequency generation (SFG) spectroscopy has been shown to be a very powerful technique for probing molecular structure at interface [1–6]. SFG is a second-order nonlinear optical (NLO) process, in which two photons of frequencies ω_1 and ω_2 generate one photon of sum frequency ($\omega_3 = \omega_1 + \omega_2$) [2]. The second-order NLO processes including SFG are prohibited in media with inversion symmetry under the electric dipole approximation and are allowed only at the interface between these media where the inversion symmetry is necessarily broken. By using visible light of fixed wavelength and tunable infrared (IR) light as two input light sources, SFG spectroscopy can be surface-sensitive vibrational spectroscopy as the SFG signal is resonantly enhanced when the energy of IR beam becomes equal to that of a vibrational state of surface species [2]. SFG spectroscopy is particularly useful to study the structure of water molecules, the most common solvent, at various interfaces where presence of much larger amount of bulk water than interfacial water makes the measurement of interfacial water by other vibrational techniques very difficult. Furthermore, SFG is free from the ambiguity

Nanolayer Research. http://dx.doi.org/10.1016/B978-0-444-63739-0.00006-2

associated with the choice of reference spectrum as required for linear spectroscopy applied to interfaces such as surface enhanced IR absorption spectroscopy (SEIRAS) [7] and surface enhanced Raman scattering (SERS) [8]. Furthermore, time-resolved vibrational spectroscopy based on SFG is possible because a short pulse laser is used. Thus SFG spectroscopy is an ideal technique for investigating the mechanism of interfacial processes at solid/liquid interfaces [6,9–12].

Here we describe the basic principle and detailed experimental arrangement of SFG spectroscopy and present several examples of SFG study at solid/liquid interfaces.

6.2 Sum Frequency Generation Spectroscopy

6.2.1 Brief Description of SFG

NLO phenomena that can be observed with static electric and magnetic fields such as the Pöckels and Faraday effects have been known since the 19th century. Frequency conversion such as second harmonic generation (SHG) and SFG requires intense optical fields, and its realization had to wait for the invention of the pulsed laser at the end of the 1950s. SHG was first observed by Franken et al. in a bulk of quartz crystal in 1961 [13]. The foundation of theory of NLO was laid by Bloembergen in the early 1960s [14]. The surface SHG was detected for the first time in 1974 from the surface of silver [15]. The first observation of surface SFG was in 1986 by Shen et al. for the coumarin dye on glass [16]. SFG spectroscopy has become extremely attractive for analysis of interface science, thanks to the recent development of tunable laser source.

SFG is one of the second-order NLO processes, in which two photons of frequencies ω_1 and ω_2 generate one photon of a sum frequency ($\omega_3 = \omega_1 + \omega_2$), as shown in Fig. 6.1.

The second-order NLO processes including SFG are strictly forbidden in media with inversion symmetry under the electric dipole approximation and are allowed only at the interface between these media where the inversion symmetry is necessarily broken. In the IR-visible SFG measurement, a visible laser beam (ω_{Vis}) and a tunable infrared laser beam (ω_{IR}) are overlapped at an interface, and the SFG signal is measured by scanning ω_{IR} while keeping ω_{Vis} constant.

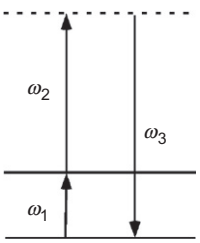

Fig. 6.1
Energetic scheme for SFG process.

The SFG intensity (I_{SFG}) is enhanced when ω_{IR} becomes equal to the vibration levels of the molecules at the interface. Thus one can obtain surface-specific vibrational spectra at an interface between two phases with inversion symmetry, which cannot be obtained using the traditional vibrational spectroscopy such as IR and Raman scattering.

In addition to the surface/interface selectivity, IR-visible SFG spectroscopy provides more attractive features since it is a coherent process: (1) Detection efficiency is very high because the angle of emission of SFG light is strictly determined by the momentum conservation of the two incident beams, together with the fact that SFG can be detected by a photomultiplier (PMT) or charge-coupled device (CCD), which are the most efficient light detectors, because the SFG beam is in visible region. (2) The polarization feature that NLO intrinsically provides enables us to obtain information about a conformational and lateral order of adsorbed molecules on a flat surface, which cannot be obtained by the traditional vibrational spectroscopy [17–20]. (3) A pump and SFG probe measurement can be used for an ultrafast dynamics study with a time resolution determined by the incident laser pulses [21–24]. (4) As a photon-in/photon-out method, SFG is applicable to essentially any system in as much as one side of the interface is optically transparent.

6.2.2 Origin of SFG Process

The induced dipole ($\vec{\mu}$) of a molecule placed in an electric field ($\vec{E}$) is given by

$$\vec{\mu} = \vec{\mu}^0 + \overleftrightarrow{\alpha}\,\vec{E} + \overleftrightarrow{\beta}\,\vec{E}\vec{E} + \overleftrightarrow{\gamma}\,\vec{E}\vec{E}\vec{E} + \cdots \tag{6.1}$$

$\overleftrightarrow{\alpha}$, $\overleftrightarrow{\beta}$, and $\overleftrightarrow{\gamma}$ are the linear polarizability, the first- and second-hyperpolarizabilities, respectively, and are represented by second-, third-, and fourth-rank tensor, respectively, and $\vec{\mu}^0$ is a static polarizability.

In condensed phases, it is more convenient to consider the dipole moment per unit volume or polarization ($\vec{P}$)

$$\begin{aligned}\vec{P} &= \vec{P}^{(0)} + \vec{P}^{(1)} + \vec{P}^{(2)} + \vec{P}^{(3)} + \cdots \\ &= \vec{P}^0 + \varepsilon_0\left(\overleftrightarrow{\chi}^{(1)}\vec{E} + \overleftrightarrow{\chi}^{(2)}\vec{E}\vec{E} + \overleftrightarrow{\chi}^{(3)}\vec{E}\vec{E}\vec{E} + \cdots\right)\end{aligned} \tag{6.2}$$

where $\overleftrightarrow{\chi}^{(1)}$, $\overleftrightarrow{\chi}^{(2)}$, and $\overleftrightarrow{\chi}^{(3)}$ are the first-, second, and third-ordered susceptibilities, respectively, and ε_0 is dielectric constant in vacuum. For a simple molecular material, the susceptibility depends on the number of molecules per unit volume, N, multiplied by molecular polarizability averaged over all orientation of molecules in the material.

$$\overleftrightarrow{\chi}^{(1)} = N\left\langle\overleftrightarrow{\alpha}\right\rangle/\varepsilon_0,\quad \overleftrightarrow{\chi}^{(2)} = N\left\langle\overleftrightarrow{\beta}\right\rangle/\varepsilon_0,\quad \overleftrightarrow{\chi}^{(3)} = N\left\langle\overleftrightarrow{\gamma}\right\rangle/\varepsilon_0 \tag{6.3}$$

where the brackets $< >$ denote the ensemble average of the molecular orientation. Since few materials have a static polarization, the first term in Eq. (6.2), $\vec{P}^{(0)}$, can be dropped.

$$\vec{P} = \varepsilon_0 \left(\overleftrightarrow{\chi}^{(1)} \vec{E} + \overleftrightarrow{\chi}^{(2)} \vec{E}\vec{E} + \overleftrightarrow{\chi}^{(3)} \vec{E}\vec{E}\vec{E} + \cdots \right) \tag{6.4}$$

When the electric field ($\vec{E}$) is weak, as it is in a nonlaser light source, the second and third terms can be neglected and polarization ($\vec{P}$) can be expressed as in the following, corresponding to a linear optics.

$$\vec{P} = \varepsilon_0 \overleftrightarrow{\chi}^{(1)} \vec{E} \tag{6.5}$$

When the electric field ($\vec{E}$) is strong, as in a laser light source, the second and third terms cannot be neglected and NLO processes take place. A remarkable consequence of the higher-order terms in Eq. (6.4) is that the frequency of the light can change. If we consider two electric fields with frequencies ω_1 and ω_2,

$$\vec{E}_1\left(\vec{r}, t\right) = \vec{E}_1\left(\vec{r}\right)\cos(\omega_1 t) \quad \vec{E}_2\left(\vec{r}, t\right) = \vec{E}_2\left(\vec{r}\right)\cos(\omega_2 t) \tag{6.6}$$

where $\vec{r}$ and t represent a position vector and time, respectively. The second-order polarization, $\vec{P}^{(2)}$, in a material in which $\overleftrightarrow{\chi}^{(2)}$ is nonzero is given by:

$$\begin{aligned} \vec{P}^{(2)} &= \varepsilon_0 \overleftrightarrow{\chi}^{(2)} \vec{E}_1 \vec{E}_2 \\ &= \varepsilon_0 \overleftrightarrow{\chi}^{(2)} \vec{E}_1\left(\vec{r}\right)\cos(\omega_1 t)\vec{E}_2\left(\vec{r}\right)\cos(\omega_2 t) \\ &= 1/2\varepsilon_0 \overleftrightarrow{\chi}^{(2)} \vec{E}_1\left(\vec{r}\right)\vec{E}_2\left(\vec{r}\right)\{\cos((\omega_1+\omega_2)t) + \cos((\omega_1-\omega_2)t)\} \end{aligned} \tag{6.7}$$

This shows that there are now oscillating dipoles at frequencies $(\omega_1+\omega_2)$ and $(\omega_1-\omega_2)$, which give rise to SFG and difference frequency generation (DFG), respectively. When $\omega_1 = \omega_2$, Eq. (6.7) becomes:

$$\vec{P}^{(2)} = 1/2\varepsilon_0 \overleftrightarrow{\chi}^{(2)} \vec{E}_1\left(\vec{r}\right)\vec{E}_2\left(\vec{r}\right)\{1 + \cos(2\omega_1 t)\} \tag{6.8}$$

The first term in the brackets represents a static electric field in the material, and the second term represents a dipole oscillating at 2ω, twice the frequency of the incident light. This is a process known as SHG.

6.2.3 SFG Spectroscopy

In SFG vibrational spectroscopy, ω_2 is usually fixed in the visible region and ω_1 is scanned in the infrared region. In the most widely used geometry, the two laser beams are incident in either counter- or collinear-propagating geometry and the reflected SF light (ω_{sum}) is detected. Let us consider the case where visible and infrared beams are incident from the medium 1 to the interface with the medium 2 as depicted in Fig. 6.2. The direction of emission is determined by conservation of momentum parallel to the surface.

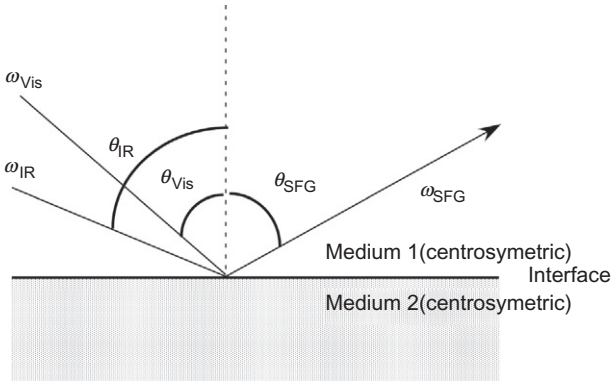

Fig. 6.2
Schematic drawing of optical arrangement of an SFG measurement.

$$\omega_{SFG} = \omega_{Vis} + \omega_{IR} \tag{6.9}$$

$$\omega_{SFG} \sin\theta_{SFG} = \omega_{Vis} \sin\theta_{Vis} + \omega_{IR} \sin\theta_{IR} \tag{6.10}$$

where θ_{SFG} is the emission angle of SFG light and θ_{Vis} and θ_{IR} are the incident angle of the visible and infrared light. Since the angles θ_{Vis}, θ_{IR}, and the frequency ω_{Vis} are constant in a given SFG measurement, θ_{SFG} can be expressed as a function of ω_{IR}.

$$\theta_{SFG}(\omega_{IR}) = \sin^{-1}\left\{\frac{\omega_{Vis}\sin\theta_{Vis} + \omega_{IR}\sin\theta_{IR}}{\omega_{Vis} + \omega_{IR}}\right\} \tag{6.11}$$

As shown in this equation, the angle of emission changes as ω_{IR} is scanned.

The intensity of emitted SF light (I_{SFG}) is expressed by the following equation [25],

$$I_{SFG} = \frac{8\pi^3 {\omega_{SFG}}^2 (\sec\theta_{SFG})^2}{\hbar c^3 \cdot n_1(\omega_{SFG}) \cdot n_1(\omega_{Vis}) \cdot n_1(\omega_{IR})} \left|\overleftrightarrow{F} : \overleftrightarrow{\chi}^{(2)}\right|^2 I_{Vis} I_{IR} A T \tag{6.12}$$

where I_{Vis} and I_{IR} are the intensities of incident visible and infrared lights, respectively; c is the speed of light in vacuum; A is an overlapping beam cross section at the sample; T is a pulse duration; and $n_1(\omega_i)$ is refractive index of the medium 1 at frequency ω_i and $\overleftrightarrow{F}$ is a Fresnel factor.

For a polar monolayer of molecules at an interface, the resonant $\overleftrightarrow{\chi}^{(2)}$ is typically $10^{-14} \sim 10^{-16}$ esu. If we take $\overleftrightarrow{\chi}^{(2)} \sim 10^{-15}$ esu, $I_{Vis} \sim 1$ mJ/pulse and $I_{IR} \sim 100$ μJ/pulse, $T \sim 25$ ps, $\omega_{Vis} = 5.64 \times 10^{14}$ s^{-1} (532 nm), $\omega_{IR} = 9.0 \times 10^{13}$ s^{-1} (3333 nm), $\omega_{SFG} = 6.55 \times 10^{14}$ s^{-1} (458.77 nm), A $\sim 10^{-3}$ cm^2, ω_{SFG} ~67 deg, Eq. (6.12) predicts a signal of 1.5×10^4 photon /pulse. Such signal can readily be detected by a PMT or CCD detector.

If neither ω_{Vis} nor ω_{SFG} is in resonance with an electric dipole transition in the material and only electric dipole transitions are considered, the hyperpolarizability, β_{lmn}, near a vibrational transition in a molecule is given by [25]

$$\beta_{lmn} = \frac{1}{2\hbar^2} \cdot \sum_s \left(\frac{\langle g|\mu_l|s\rangle\langle s|\mu_m|v\rangle}{\omega_{\mathrm{SFG}} - \omega_{sg}} - \frac{\langle g|\mu_m|s\rangle\langle s|\mu_l|v\rangle}{\omega_{\mathrm{Vis}} + \omega_{sg}} \right) \left(\frac{\langle v|\mu_n|g\rangle}{\omega_{\mathrm{IR}} - \omega_{vg} + i\Gamma} \right) + const. \tag{6.13}$$

where $|g>$ is the ground state, $|\nu>$ is the excited vibrational state, $|s>$ is any other state, Γ is the relaxation time of the excited vibrational state, const. is an off-resonant term, which can be considered as a constant and $\mu = er$ is the electric dipole operator. The first bracket is identified as a Raman transition dipole moment M_{lm}, and the term $<\nu|\mu_n|g>$ as an IR transition dipole moment μ_n^{vg}. If we substitute ω_{vg} to ω_0, Eq. (6.13) becomes:

$$\beta_{lmn} = \frac{1}{2\hbar^2} \cdot \frac{a_{lmn}}{\omega_{\mathrm{IR}} - \omega_0 - i\Gamma} + const. \tag{6.14}$$

where $a_{lmn} = M_{lm} \cdot \mu_n^{vg}$.

From this equation, it is clear that β_{lmn} takes the maximum value when the IR frequency is in resonance with the molecular vibration, that is, $\omega_{\mathrm{IR}} = \omega_0$, and only the molecular vibration that is both IR and Raman active is SFG active.

If we introduce $\overleftrightarrow{A} = N/\varepsilon_0 \left\langle \overleftrightarrow{a} \right\rangle$, a description of macroscopic resonant second-order susceptibility, $\overleftrightarrow{\chi}_R^{(2)}$, is given by

$$\overleftrightarrow{\chi}_R^{(2)} = \frac{1}{2\hbar^2} \frac{\overleftrightarrow{A}}{\omega_{\mathrm{IR}} - \omega_0 - i\Gamma} \tag{6.15}$$

The emitted SFG light is a sum of resonant contributions with n th vibrational states, $\overleftrightarrow{\chi}_{R,n}^{(2)}$ and nonresonant contributions, $\overleftrightarrow{\chi}_{\mathrm{NR}}^{(2)}$.

$$\overleftrightarrow{\chi}^{(2)} = \overleftrightarrow{\chi}_{\mathrm{NR}}^{(2)} + \sum_n \overleftrightarrow{\chi}_{R,n}^{(2)} = \overleftrightarrow{\chi}_{\mathrm{NR}}^{(2)} + \sum_n \frac{1}{2\hbar^2} \frac{\overleftrightarrow{A}_n}{\omega_{\mathrm{IR}} - \omega_n - i\Gamma_n} \tag{6.16}$$

Here, $\overleftrightarrow{\chi}_{\mathrm{NR}}^{(2)}$ is the sum of nonresonant contributions from molecules ($\overleftrightarrow{\chi}_{\mathrm{NR,mol}}$), substrate ($\overleftrightarrow{\chi}_{\mathrm{NR,sub}}$), and interaction between molecules and substrate ($\overleftrightarrow{\chi}_{\mathrm{NR},m-s}$).

$$\overleftrightarrow{\chi}_{\mathrm{NR}} = \overleftrightarrow{\chi}_{\mathrm{NR,mol}} + \chi_{\mathrm{NR,sub}} + \chi_{\mathrm{NR},m-s} \tag{6.17}$$

Combining Eqs. (6.12), (6.16), the SFG intensity can be written as:

$$I_{\mathrm{SFG}} \propto \left| \overleftrightarrow{\chi}_{\mathrm{eff,NR}}^{(2)} + \sum_n \frac{\overleftrightarrow{A}_{\mathrm{eff},n}}{\omega_{\mathrm{IR}} - \omega_n - i\Gamma_n} \right|^2 \tag{6.18}$$

where $\overleftrightarrow{\chi}_{\mathrm{eff,NR}}^{(2)} = \overleftrightarrow{F} : \overleftrightarrow{\chi}_{\mathrm{NR}}^{(2)}$ and $\overleftrightarrow{A}_{\mathrm{eff},n} = \overleftrightarrow{F} : \overleftrightarrow{A}_n$. This is the equation generally used to analyze an observed SFG spectrum.

6.2.4 Experimental Arrangement for SFG Measurements

6.2.4.1 Laser and detection systems

Picosecond (ps) and femtosecond (fs) laser systems are most often used for SFG spectroscopy. Ps SFG spectrometers cover a wide spectral scanning range (about 1000 cm^{-1} without realignment). The narrow band ps light pulses are tuned through the spectral region, while the SFG signal is generally collected for a few minutes for each wavenumber to gain reasonable signal-to-noise (S/N) ratios (the repetition rate for ps light pulses is usually in the order of 10–25 Hz). Detecting spectral regions of about 1000 cm^{-1} usually takes 10 min.

Broadband SFG (BB-SFG) spectroscopy is based on fs laser pulses (usually around 100 fs) covering a spectral range of about 200 cm^{-1}. The repetition rate of these systems is two orders of magnitude higher compared to ps systems (of the order of 1 kHz). This allows around 1000 acquisitions per second in a spectral range of about 200 cm^{-1}, with a reasonable S/N ratio in about 2–5 min. In an fs SFG spectrometer, a narrow band ps visible pulse is mixed at the interface with a broadband fs infrared pulse. The resulting broadband SFG signal is dispersed on a grating within a spectrometer and subsequently detected by a multichannel CCD detector.

Fig. 6.3 shows the schematic diagram of a picosecond SFG spectrometer used in this work. A passive mode-locked Nd:YAG laser system (EKSPLA, PL2143B) generates ~25 ps pulses of 1064 nm (fundamental), 532 nm (second harmonic generation: SHG), and 355 nm (third harmonic generation: THG) at a repetition rate of 10 Hz. The total output power was ca.33–5 mJ/pulse and typical pulse energy of 1064, 532, and 355 nm were 8, 8, and 6 mJ/pulse,

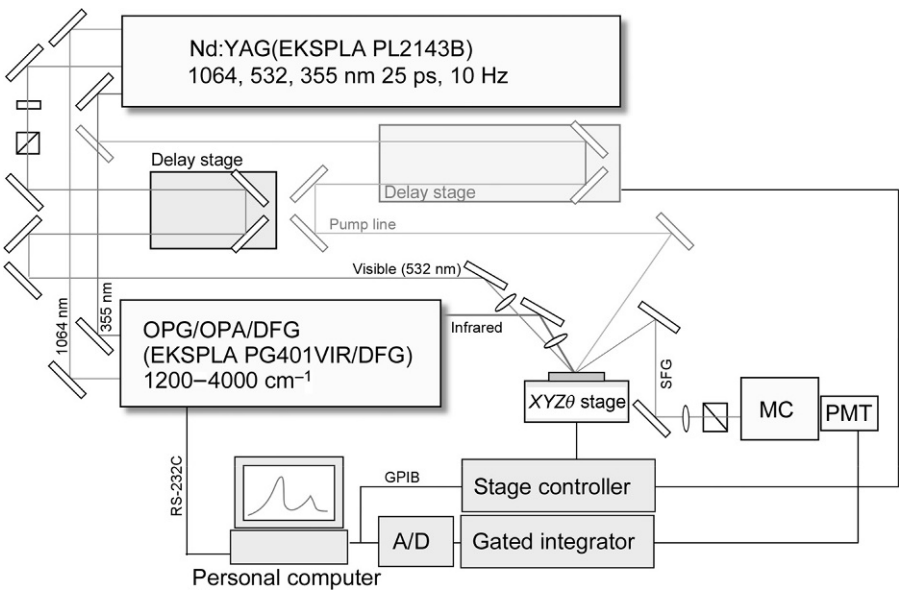

Fig. 6.3
Schematic drawing of picosecond SFG system.

respectively. The ratio of the harmonic generations can be adjusted to some extent by tuning the phase match angles of mixing crystals. Half of the SHG and 15% of the third harmonic generation (THG) were split and transferred to a pump line. The residual SHG was directed to a sample through a time-delay and used as the incident visible light for an SFG measurement. The power of the incident visible light can be adjusted by a combination of a half wave plate and a Gran-Taylor prism, and the polarization can be changed by an additional half wave plate. The 85% of THG output (ca.5 mJ/pulse) was used to pump an optical parametric generation and amplification (OPG/OPA) (EKSPLA,PG401VIR/DFG) system, containing a lithium triborate (LBO) crystal and double gratings. The output from the optical parametric generation/optical parametric amplification (OPG/OPA) was mixed with the 1064-nm laser output in a nonlinear crystal, Ag_2GaS_2, to generate a tunable infrared output from 2.3 to 8.5 μm by the DFG process. The power of the incident infrared light can be roughly adjusted by tuning a total power of the laser and the ratio of the harmonic generator. The polarization of the IR beam can be changed by exchanging the mirror sets, which contains 3 and 4 mirrors. The line-width of the tunable infrared output was $\sim 6\ cm^{-1}$ determined by the double grating setup in the OPA path.

The "visible" output from the laser and tunable infrared output from the DFG were incident and overlapped at the sample surface with angles of 70 and 50 degrees, respectively. Either 532 nm or 1064 nm laser output was used as the "visible" light in the SFG measurement. A BK7 lens ($f = 600$) and a ZnSe lens ($f = 50$) were used to focus the visible and IR beam, respectively. The position of the ZnSe lens was controlled by an *XY* stage to perform the spatial overlapping of the two incident beams. The beam spot of the "visible" and infrared lights had an elliptical shape with a dimension of ca.$2.5 \times 0.9\ mm^2$ and $0.3 \times 0.2\ mm^2$, respectively. The SFG signal was separated from the reflected visible and IR lights by passing through irises and a monochromator (Oriel Instruments, MS257) and was detected by a photomultiplier tube (PMT: Hamamatsu, R630-10 or R3896) with a gated electronic system (Stanford Research System). When the 532-nm visible light was used, two holographic Super Notch filters (Kaiser Optical System, INC, HSPF-532-1.0) were placed in front of the monochromator to further reduce scattered visible light.

All SFG spectra were obtained by averaging 50–400 pulses per data point and were normalized against the intensity of the visible and infrared inputs, which were simultaneously monitored by a power meter (Oriel instruments, Model 70833 and 70811) and Si photodiode, respectively.

6.2.4.2 Spectroscopic cells

6.2.4.2.1 Spectroelectrochemical cell

Fig. 6.4 shows spectroelectrochemical cells used in electrochemical SFG measurements. An Ag/AgCl (saturated NaCl) and a Pt wire were used as a reference electrode and a counter electrode, respectively. The electrolyte solution was deaerated by bubbling high-purity Ar gas

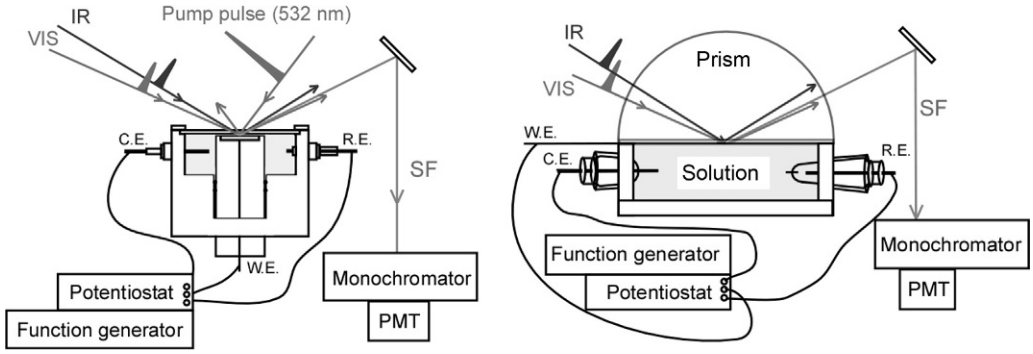

Fig. 6.4
Spectroelectrochemical cells for electrochemical SFG measurements.

(99.999%) for at least 30 min prior to the electrochemical measurements. The electrode potential was controlled with a potentiostat. The electrode potential, current, and SFG signal were recorded by using a personal computer through an analog-to-digital (AD) converter.

After the introduction of the working electrode to the spectroelectrochemical cell, continuous potential cycling was performed to obtain the clean surface before each electrochemical SFG experiment until the cyclic voltammogram (CV) became that of a clean electrode.

When single or polycrystalline disk electrodes are used as a working electrode, the electrode must be gently pushed against the CaF_2 window of the spectroelectrochemical cell to achieve a thin layer (ca.5 μm) configuration so that strong absorption of the IR beam by the electrolyte solution is avoided. Thin metal electrode deposited on a hemispherical prism can also be used as a working electrode. Strong absorption of the IR beam by the electrolyte solution can be more easily avoided in this configuration.

6.2.4.2.2 Flow cell

In situ SFG measurements were carried out in the internal reflection geometry to avoid the strong absorption of IR incident beam by water. Since SFG signal from the quartz disk/water interface is very weak if a flat quartz disk is used as a window due to the very large reflection loss of the incident beams at air/quartz interface and the small Fresnel factors at the quartz/water interface, a hemicylindrical prism, where higher enhancement of the sensitivity is expected, was used for the in situ SFG measurements. The flat face of the quartz prism was in contact with electrolyte solution, and the infrared and visible beams were incident from the quartz prism side and were overlapped at the quartz/electrolyte solution interface. The incident angle of the visible light was about 70 degrees, which is near the critical angle of the total reflection (Θ_c) of quartz/water (72 degrees), so that a strong surface field can be obtained. The incident angle of the infrared light was set at 50 degrees, which is far from Θ_c, so that a large change in the Fresnel factor can be avoided when the IR frequency is scanned over the OH stretching vibration region.

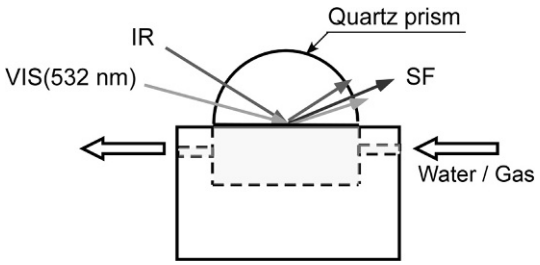

Fig. 6.5
A flow cell for SFG measurements.

A flow cell made of polychlorofluoroethylene, which is schematically shown in Fig. 6.5, was used for gas or liquid to be changed during SFG measurements. Electrolyte solution was introduced into the flow cell by the pressure of the pure argon gas so that the solution could be exchanged without being exposed to the atmosphere, and the optical alignment and the sample position were not affected when solution was exchanged.

6.3 Structure of Organic Monolayer Studied by SFG

Construction of molecular layers on solid surfaces is one of the most important subjects not only for fundamental science but also for a wide range of applications such as wetting control, corrosion inhibition, and molecular and bioelectronic devices and is one of the essential key techniques for the development of nanotechnology and nanoscience. A self-assembly (SA) technique in solution has been extensively employed to construct organic layers because a molecularly ordered structure can be very easily prepared without expensive equipment, which is essential for the organic layer formation in an ultrahigh vacuum [26].

The most studied SA system is the self-assembled monolayers (SAMs) of alkanethiols on various metals, especially on gold [26,27], and SAMs with a wide variety of functionalities have been constructed [28,29]. The formation process and the structure of the thiol SAMs on gold have been investigated in detail by various techniques including IR spectroscopy [30,31], a quartz crystal microbalance (QCM) [32,33], and a scanning tunneling microscope (STM) [34–36]. Guyot-Sionnest and Shen first obtained the vibrational SFG spectra in the CH stretching region of the Langmuir film of pentadecanoic acid (PDA) on water surface and demonstrated that vibrational SFG spectroscopy is effective for the investigation of an organic monolayer as shown in Fig. 6.6 [37].

Since then, a number of papers concerning the structure of the Langmuir-Blodgett (LB) film and SAM have been published by many research groups. SFG spectra of a long chain alkyl monolayer has a unique property such that the methylene bands, which are the dominant feature in an IR spectrum, are not seen and only the methyl bands are active when the monolayer is fully packed because the methylene groups in the alkyl chain of the *all-trans* configuration have

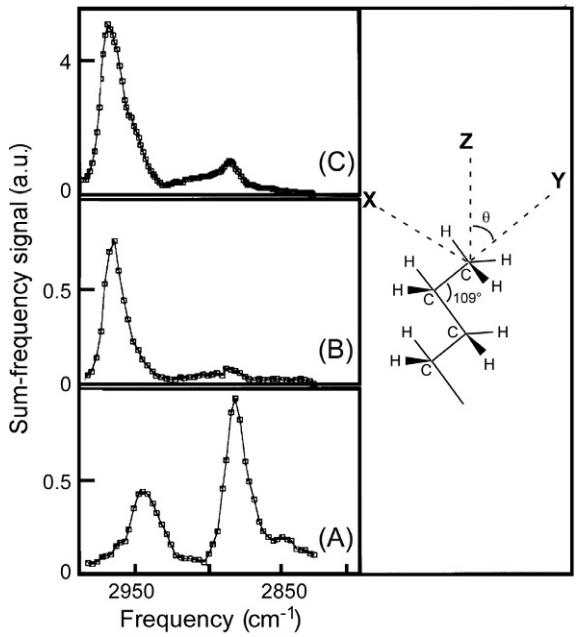

Fig. 6.6

SFG spectra of PDA at full monolayer coverage with various (IR) polarization combinations: (A) s visible, p IR; (B) p visible, s IR; (C) p visible, p IR. The lines simply connect the experimental data points (squares). Inset: coordinate axes chosen for the methyl group. *Reprinted with permission from P. Guyotsionnest, J.H. Hunt, Y.R. Shen, Phys. Rev. Lett. 59 (1987) 1597–1600.*

inversion symmetry and SFG signal of the methylene modes are canceled out. In another way, one can consider the SFG spectrum of alkyl monolayer to be an indicator of the *all-trans* configuration, that is, conformational order of the alkyl chain, when the SFG spectrum shows no methylene bands. For another feature, one can evaluate the orientation angle of a terminal group such as the methyl group from the ratio of the SFG intensities of the symmetric/asymmetric stretching modes in an SFG spectrum or of the SFG intensities of a stretching mode in different polarization combinations [17,18]. Furthermore, SFG provides information about the lateral order of adsorbed molecules on a flat surface. Over the last decade, several groups have reported the two-dimensional anisotropy of rubbed polymer films [38] and multilayered LB films [39] based on azimuthal dependent SFG measurements. However, only a few cases were reported for such anisotropy of a SAM [40,41].

6.3.1 Evidence for Epitaxial Arrangement and High Conformational Order of an Organic Monolayer on Si(111) by SFG Spectroscopy

To construct ordered molecular layers with various functionalities on a semiconductor surface will become important as far as technological applications are concerned. Although several attempts have been made to use GaAs [42–44] and InP [45] as a substrate, silicon should be the

most important semiconductor substrate for organic layer formation at present because of possible applications for molecular and biomolecular devices in conjunction with the advanced silicon technology. There are two major methods to form an organic layer on silicon. One is via the Si—O—Si bond using silane coupling reactions on a preoxidized Si surface. The other is via the direct Si—C bond either on a reconstructed Si(100) surface or on a hydrogen-terminated Si surface using thermal [46–48], photochemical [49], or electrochemical [50] reactions or reactions with radical initiators [50,51]. The latter method is more attractive because (1) the Si—C bond is expected to be more resistant to hydrolysis than the Si—O—Si bond, (2) a higher structural order is expected because an organic molecule directly bonds to the Si atom of the single crystalline surface, and (3) the thickness control of the oxide is difficult in the former method. Both gas phase [52,53] and liquid phase [46–51] reactions have been used to form organic layers via the Si—C bond, but the latter is more useful for practical applications because the former requires expensive ultrahigh vacuum (UHV) equipment to prepare and maintain the reconstructed, clean Si surface.

Here, we measured the SFG spectra of the C18 monolayer on a hydrogen-terminated Si(111) surface at various azimuthal angles and confirmed that the monolayer is in a nearly *all-trans*, that is, highly ordered, conformation as well as in threefold lateral symmetry, that is, epitaxial arrangement of the monolayer with the Si(111) substrate [54]. The SFG spectra were quantitatively analyzed, and lateral alignment with respect to the Si substrate and the tilt angle of the terminal methyl group were estimated.

6.3.1.1 Theoretical basis

We define the axis systems as depicted in Fig. 6.7. In the laboratory-fixed axis system ($I, J, K = X, Y, Z$), the Z-axis is surface normal and the X–Z plane is the incident plane of the visible and infrared beams. In the surface-fixed axis system ($i, j, k = x, y, z$), the x-axis is set in the $[2\bar{1}\,\bar{1}]$

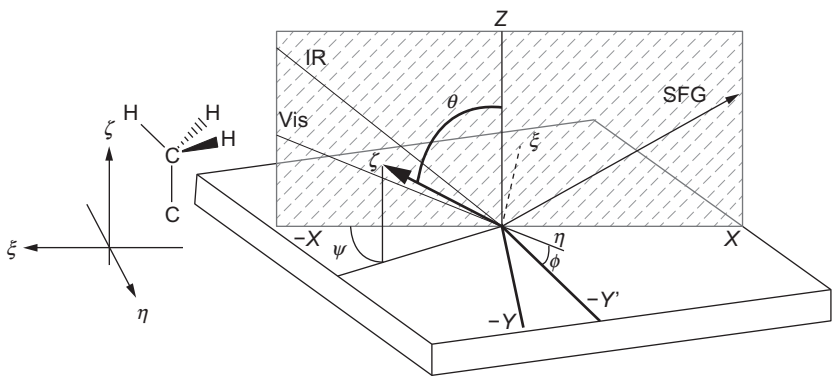

Fig. 6.7

Schematic drawing of the definition of the laboratory-, surface-, and molecular-fixed axis systems, The γ was defined as the angle between the $[2\bar{1}\,\bar{1}]$ direction of the Si(111) substrate and the plane of incidence. *Reprinted with permission from S. Nihonyanagi, D. Miyamoto, S. Idojiri, K. Uosaki, J. Am. Chem. Soc. 126 (2004) 7034–7040.*

direction of the Si(111) surface and the z-axis coincides with the Z-axis. The angle between the X–Z and the x–z planes is represented by γ. In the molecular-fixed axis system (p, q, $r = \xi$, η, ζ), the ζ-axis is taken to coincide with C_3 symmetry axis of a methyl (CH_3) group and the ξ–η plane is one of the C—C—H planes of the CH_3 group. The θ, ψ and φ are defined as angles between the z- and ζ-axes, the projection of the ζ-axis on the surface and the x-axis, and y'- and η-axes, respectively.

A resonant molecular hyperpolarizability near the nth vibrational state in the molecular fixed coordinates ($\beta_{pqr,n}$) is expressed as

$$\beta_{pqr,n} = \frac{a_{pqr,n}}{\omega_{\mathrm{IR}} - \omega_n + i\Gamma_n} \tag{6.19}$$

where $a_{pqr,n}$ is the product of a Raman polarization tensor ($\alpha_{pq,n}$) and vibrational transition dipole moment ($\mu_{r,n}$) with $<g|$ being ground state and $<v|$ being nth vibrational state [55]:

$$a_{pqr,n} = \langle g|\alpha_{pq}|v\rangle\langle v|\mu_r|g\rangle \tag{6.20}$$

Here, the relation between $\overleftrightarrow{A}_{\mathrm{eff},n}$ and $a_{pqr,n}$ is given by:

$$\overleftrightarrow{A}_{\mathrm{eff},n} = N\sum_{I,J,K} F_{IJK}\langle a_{IJK,n}\rangle = N\sum_{I,J,K} F_{IJK}\langle u_{IJK,pqr}a_{pqr,n}\rangle \tag{6.21}$$

where N and $u_{IJK,pqr}$ represent the total number of the surface molecules and a transformation coefficient, explicit expression of which is presented in Ref. [18]. The brackets $\langle\rangle$ denote the ensemble average. F_{IJK} is a combination of Fresnel factors and is represented as [56]:

$$F_{IJK} = \hat{e}_I(\omega_{\mathrm{SFG}})L_I(\omega_{\mathrm{SFG}}) \times \hat{e}_J(\omega_{\mathrm{Vis}})L_J(\omega_{\mathrm{Vis}}) \times \hat{e}_K(\omega_{\mathrm{IR}})L_K(\omega_{\mathrm{IR}}) \tag{6.22}$$

where $L_I(\omega_{\mathrm{SFG}})$, $L_J(\omega_{\mathrm{Vis}})$ and $L_K(\omega_{\mathrm{IR}})$ are the Fresnel factors for the SFG, visible, and IR beams, respectively, and $\hat{e}_I(\omega_{\mathrm{SFG}})$, $\hat{e}_J(\omega_{\mathrm{Vis}})$, and $\hat{e}_K(\omega_{\mathrm{IR}})$ are the unit polarization vectors for the SFG, visible, and IR beams, respectively. For the *ppp* polarization combination, $\overleftrightarrow{A}_{\mathrm{eff},n}$ is given by:

$$\begin{aligned}\overleftrightarrow{A}_{\mathrm{eff},n} = N\{&F_{ZZZ}\langle a_{ZZZ}\rangle - F_{XXZ}\langle a_{XXZ}\rangle - F_{XZX}\langle a_{XZX}\rangle + F_{ZXX}\langle a_{ZXX}\rangle \\ &+ F_{ZXZ}\langle a_{ZXZ}\rangle - F_{XZZ}\langle a_{XZZ}\rangle + F_{ZZX}\langle a_{ZZX}\rangle - F_{XXX}\langle a_{XXX}\rangle\}\end{aligned} \tag{6.23}$$

6.3.1.2 Determination of the molecular orientation by SFG

Fig. 6.8 shows an SFG spectrum in the CH stretching frequency region of a Si(111)-C18 monolayer at $\gamma = 0$. The open circles and solid line represent the experimentally observed SFG signals and a fitted curve using Eq. (6.18), respectively. The spectrum very much resembles the previously reported SFG spectra of the octadecyltrichlorosilane (OTS) monolayer on a fused quartz substrate with *ppp* polarization [1]. The three peaks observed at 2878, 2945, and 2962 cm^{-1} can be assigned to the CH symmetric vibration (r^+), Fermi resonance between r^+ and

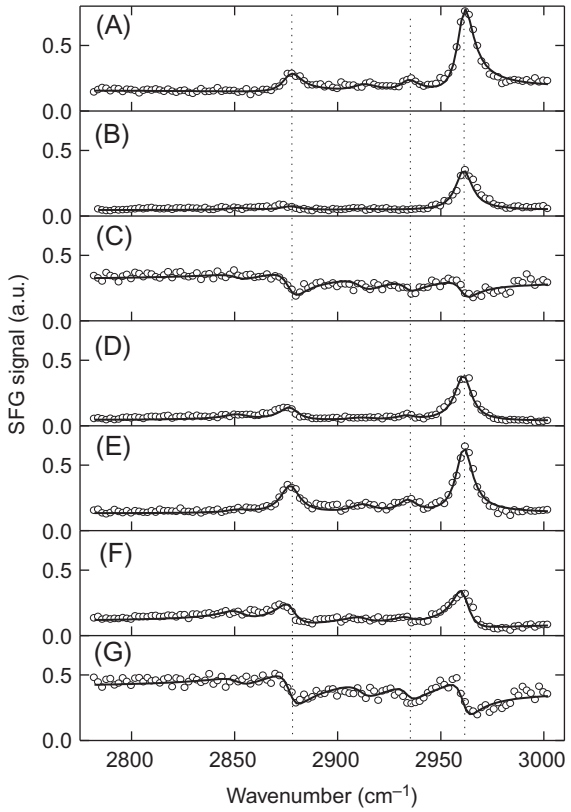

Fig. 6.8

The SFG spectra of an Si(111)-C18 monolayer obtained at various azimuthal angles (circle) with the fitted curves to Eq. (6.18) (solid line): (A) 0, (B) 30, (C) 60, (D) 90, (E) 120, (F) 150, and (G) 180 degrees. *Reprinted with permission from S. Nihonyanagi, D. Miyamoto, S. Idojiri, K. Uosaki, J. Am. Chem. Soc. 126 (2004) 7034–7040.*

the CH bending overtone, and the CH asymmetric vibration (r^-), respectively, of the terminal methyl (CH_3) group. Two peaks due to the CH symmetric stretching (d^+) at 2850 cm^{-1} and asymmetric stretching (d^-) at 2917 cm^{-1} of the methylene (CH_2) group are very weak compared to those of the CH_3 group. These results indicate that the octadecyl chain in the monolayer is essentially in an *all-trans* conformation. In this conformation, only the terminal CH_3 group, which is in noncentrosymmetry, contributes to the SFG spectrum because CH_2 groups are approximately in inversion symmetry and are, therefore, almost SFG inactive. Thus the formation of a highly organized octadecyl monolayer with a very low gauche density on the Si(111) surface [47] is confirmed.

One of the advantages of SFG spectroscopy compared to infrared absorption spectroscopy (IRAS) is the ability to determine the lateral symmetry based on the azimuthal angle dependence of the SFG spectra, that is, rotation anisotropy of the SFG spectra. Fig. 6.9 shows the azimuthal angle dependencies of the SFG intensity, that is, rotation anisotropy, at

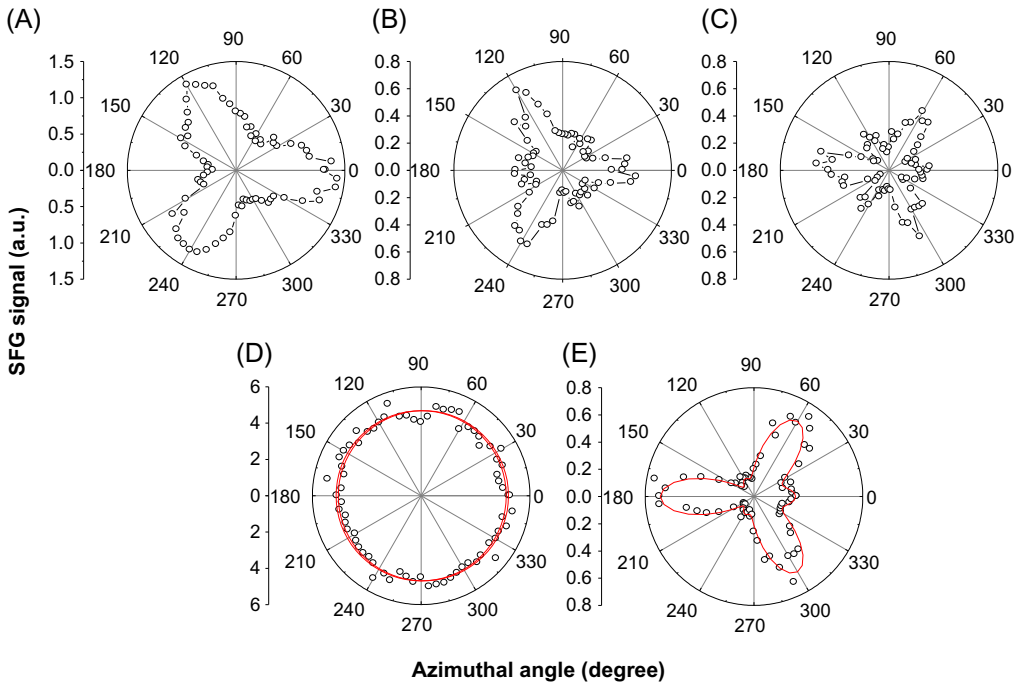

Fig. 6.9

Rotation anisotropy of the SFG intensity of the Si(111)-C18 monolayer at (A) 2962 cm^{-1}, (B) 2878 cm^{-1}, and (C) 2800 cm^{-1} and of Si(111)-H at (D) 2083 cm^{-1}, and (E) 2120 cm^{-1} as a function of the azimuthal angle. *Reprinted with permission from S. Nihonyanagi, D. Miyamoto, S. Idojiri, K. Uosaki, J. Am. Chem. Soc. 126 (2004) 7034–7040.*

(a) 2962 cm^{-1} for r^-, (b) 2878 cm^{-1} for r^+, and (c) 2800 cm^{-1} where no peak was observed. Threefold patterns were observed for the peaks at 2962 and 2878 cm^{-1}, suggesting the existence of lateral symmetry in the monolayer assembly. A threefold pattern was also observed at 2800 cm^{-1} where no peak corresponding to the monolayer exists and only the nonresonant component contributes to the SFG spectrum.

Because the SFG intensity of a hydrogen-terminated Si(111) at 2083 cm^{-1} corresponding to the Si—H vibration, whose symmetry axis is perpendicular to the surface, is essentially independent of the azimuthal angle (Fig. 6.9D) despite the fact that the SFG signal at 2120 cm^{-1} corresponding to the nonresonant response from the silicon substrate produces a threefold symmetry pattern (Fig. 6.9E), it is reasonable to conclude that the observed SFG anisotropy originated not from the anisotropy of the binding site but from the anisotropy of the orientation of the tilted alkyl chains.

To quantitatively discuss the symmetry of the methyl group, it is essential to study the azimuthal angle dependence of the effective amplitude of the CH signal. Fig. 6.8 shows the SFG spectra at various azimuthal angles with the fitted curves (solid line) to Eq. (6.18). It is clear that the shape and position of the resonant peaks as well as the nonresonant background level

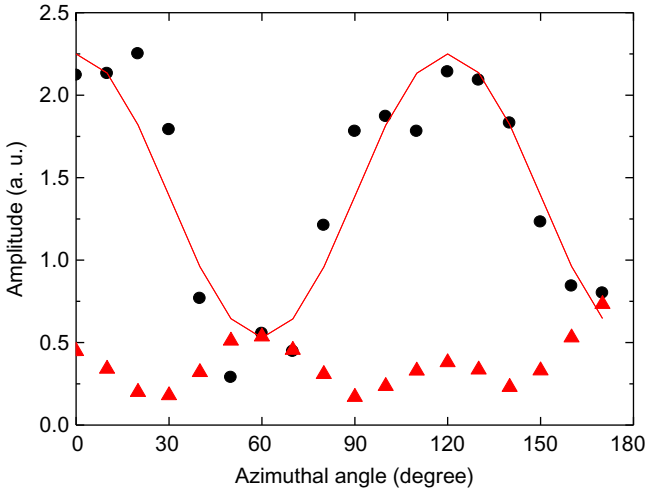

Fig. 6.10

Plots of $\overleftrightarrow{A}_{\text{eff},r^-}$ (circle) and $\chi^{(2)}_{\text{NR}}$ (triangle) determined by the fitting of the SFG spectra shown in Fig. 6.9 against the azimuthal angle. The solid line shows the fitted curve to Eq. (6.29). *Reprinted with permission from S. Nihonyanagi, D. Miyamoto, S. Idojiri, K. Uosaki, J. Am. Chem. Soc. 126 (2004) 7034–7040.*

strongly depended on the azimuthal angle. Thus the nonresonant contribution should be separated from the SFG spectra using Eq. (6.18). The amplitudes of the r^- mode (A_{eff,r^-}) and nonresonant contribution ($\chi^{(2)}_{\text{NR}}$) were determined by fitting to Eq. (6.18) and are plotted against the azimuthal angle as shown in Fig. 6.10. A threefold symmetry of the r^- mode is clearly demonstrated. $\chi^{(2)}_{\text{NR}}$ also shows threefold symmetry, but the phase angle is different from that of the r^- mode.

If we assume C_{3v} symmetry for the methyl group, the nonvanishing components of the amplitude of the molecular hyperpolarizability, $a_{pqr,n}$, for the r^- mode of the methyl group are [42]

$$a_{\zeta\xi\xi} = a_{\zeta\eta\eta}, \quad a_{\xi\zeta\xi} = a_{\eta\zeta\eta} \tag{6.24}$$

$$a_{\xi\xi\xi} = -a_{\eta\eta\xi} = -a_{\xi\eta\eta} = -a_{\eta\xi\eta} \tag{6.25}$$

where the subscript r^- is dropped for simplicity. Since the experiments were carried out at room temperature, free rotation of the methyl group is expected, and the components in Eq. (6.25) should be zero [18]. Moreover, since the Raman tensor components $\alpha_{\zeta\xi}$ and $\alpha_{\xi\zeta}$ are equal [17], $a_{\zeta\xi\xi}$ and $a_{\xi\zeta\xi}$ should also be equal according to Eq. (6.18) [57]. The nonvanishing a_{pqr} components for the r^- mode are then:

$$a_{\xi\zeta\xi} = a_{\eta\zeta\eta} = a_{\zeta\xi\xi} = a_{\zeta\eta\eta} \tag{6.26}$$

If the orientation of the tilted alkyl chain has C_{3v} symmetry, the nonvanishing components in the laboratory-fixed axis system, a_{IJK}, related to the r^- mode can be written as follows under the free rotation of the terminal methyl group [18].

$$a_{ZZZ} = 2a_{\zeta\xi\xi}\left(\cos\theta - \cos^3\theta\right), \quad a_{XXZ} = -a_{\zeta\xi\xi}\left(\cos\theta - \cos^3\theta\right),$$
$$a_{ZXX} = a_{XZX} = a_{\zeta\xi\xi}\cos^3\theta, \quad a_{XXX} = -\frac{a_{\zeta\xi\xi}}{2}\sin^3\theta \times \cos\{3(\gamma+\psi)\} \tag{6.27}$$

Since θ_{SFG} and θ_{Vis} are almost equal and the refractive indices of silicon at the SFG and visible wavelengths are not much different, the Fresnel factors F_{ZXX} and F_{XZX} are approximately the same, and therefore the third and the fourth terms in Eq. (6.23) are canceled out. Eq. (6.23) can then be rewritten as

$$A_{\mathrm{eff},r^-} = 2a_{\zeta\xi\xi}\left(\langle\cos\theta\rangle - \left\langle\cos^3\theta\right\rangle\right)NF_{ZZZ} + a_{\zeta\xi\xi}\left(\langle\cos\theta\rangle - \left\langle\cos^3\theta\right\rangle\right)NF_{XXZ} + \frac{a_{\zeta\xi\xi}}{2}NF_{XXX}\left\langle\sin^3\theta\right\rangle \times \langle\cos\{3(\gamma+\psi)\}\rangle \tag{6.28}$$

If we assume a delta function for the distribution of ψ, that is, the distribution being negligible, and introduce parameters U for the first and second (isotropic) terms and V for (anisotropic) in $\frac{a_{\zeta\xi\xi}}{2}NF_{XXX}\sin^3\theta$ the third term in Eq. (6.28), Eq. (6.28) can be written as:

$$A_{\mathrm{eff},r^-} = U + V\cos\{3(\gamma+\psi)\} \tag{6.29}$$

The experimental results were well reproduced by Eq. (6.29) with the angle offset $\Psi = 0$. Thus we can conclude that the terminal methyl groups in the octadecyl monolayer aligned in the particular directions of $\Psi = 0$, 120, and 240 degrees with respect to the in-plane orientation, resulting in C_{3v} symmetry. A possible lateral arrangement that has C_{3v} symmetry is illustrated in Fig. 6.11. In the present model, the octadecyl chains tilt toward either $[\bar{2}11]$, $[1\bar{2}1]$, and $[11\bar{2}]$ direction in each domain, forming C_{3v} symmetry as a result.

In most cases, the tilt angles of the terminal methyl groups of the alkyl monolayer on a metal and quartz and of the polymer side chain have been estimated by many researchers by comparing the SFG intensities of the r^+ mode with the *ssp* and *sps* polarization combinations or those of the r^+ and r^- modes with the *ssp* polarization combination [20,55,58]. The calculation

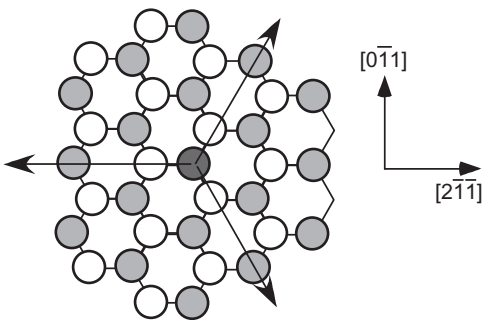

Fig. 6.11

A schematic model of the lateral arrangement of the alkyl chain with gray and white balls denoting the silicon atoms of the top and the second top layers, respectively. Arrows denote the dipole moment of the methyl group. *Reprinted with permission from S. Nihonyanagi, D. Miyamoto, S. Idojiri, K. Uosaki, J. Am. Chem. Soc. 126 (2004) 7034–7040.*

of tilt angle of the methyl group can also be carried out by comparing the value of the anisotropic term to the isotropic term in Eq. (6.29). This calculation has an advantage because the value of the ratio of the susceptibility tensors ($a_{\zeta\xi\xi,r^-}/a_{\xi\xi\zeta,r^+}a_{\xi\xi\zeta,r^+}/a_{\zeta\zeta\zeta,r^+}$), which is necessary to compare the SFG intensities for the r^+ and r^- modes [20,55,59], is not required.

By combining Eqs. (6.28), (6.29), the ratio between U and V is given as

$$\frac{U}{V}=\frac{2\left(\langle\cos\theta\rangle-\left\langle\cos^3\theta\right\rangle\right)(2F_{ZZZ}+F_{XXZ})}{F_{XXX}\langle\sin^3\theta\rangle} \tag{6.30}$$

The ensemble average of the tilt angle of the terminal methyl group is expressed as follows by assuming a Gaussian distribution [55],

$$\begin{aligned}\langle\cos^m\theta\rangle&=\int_{-1}^{1}\cos^m\theta\cdot f(\cos\theta)d(\cos\theta)\langle\sin^m\theta\rangle\\&=\int_{-1}^{1}\sin^m\theta\cdot f(\sin\theta)d(\sin\theta),\\f(\theta)&=C\exp\left[-\frac{(\theta-\theta_0)^2}{2\sigma_\theta^2}\right]\end{aligned} \tag{6.31}$$

where C, θ_0, and σ are the normalization constant, the center angle, and the root-mean square width of the distribution, respectively. The validity of the Gaussian distribution has been discussed by Wang et al. [60]. Fresnel factors F_{ZZZ}, F_{XXZ}, and F_{XXX} are estimated to be 0.17, 0.041, and 0.031, respectively, using refractive indices of silicon that are $n(\omega_{\mathrm{SFG}})=4.55+0.134i$, $n(\omega_{\mathrm{Vis}})=4.14+0.045i$, $n(\omega_{\mathrm{IR}})=3.42+2.0\times10^{-7}i$, [61], with the assumption that the refractive index of the interface is that of the monolayer, that is, $n'=1.42$. The ratio U/V is then plotted against the tilt angle of the methyl group (θ) as shown in Fig. 6.12.

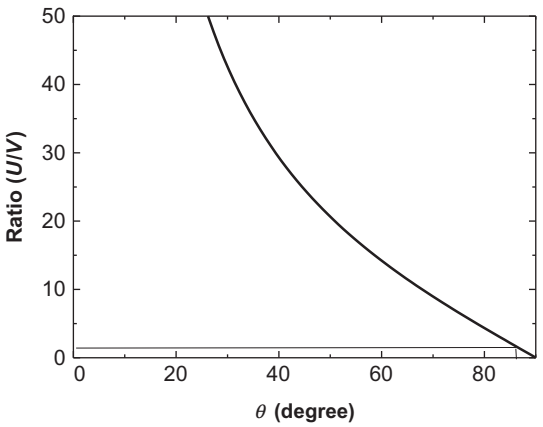

Fig. 6.12

The plot of the ratio (U/V) versus the tilt angle of the methyl group (θ). The bars show the experimental value obtained from Fig. 6.10. *Reprinted with permission from S. Nihonyanagi, D. Miyamoto, S. Idojiri, K. Uosaki, J. Am. Chem. Soc. 126 (2004) 7034–7040.*

Since the experimentally determined value of U/V is ~ 2, the angle θ is determined to be about 85 degrees, assuming $\sigma = 0$; that is, the distribution is neglected. Even in the case of $\sigma = 10$ and $\sigma = 20$, θ is still about 85 degrees. The corresponding tilt angle of the alkyl chain is ca.50 degrees, which is in qualitative agreement with the previously reported value of ca.45 degrees estimated from the IR and X-ray reflectivity [46] as well as the theoretical calculations [62,63].

It was found that the monolayer was epitaxially arranged with the Si(111) substrate with C_{3v} anisotropy, and the alkyl chains tilt toward the $[\bar{2}11]$ directions. The tilt angle of the methyl group was estimated to be about 85 degrees, which correspond to ca.50 degrees of the tilt angle of the alkyl chain. The possible orientation model is depicted in Fig. 6.13.

6.3.2 Interfacial Molecular Structures of Polyelectrolyte Brush in Contact with Dry Nitrogen, Water Vapor Studied by SFG Spectroscopy

Polyelectrolyte is one of the most important materials in many fields including biological systems and materials science. For examples, nucleic acids, one of the key materials in biological system, are polyelectrolytes with phosphate backbone. Polyelectrolytes are used for

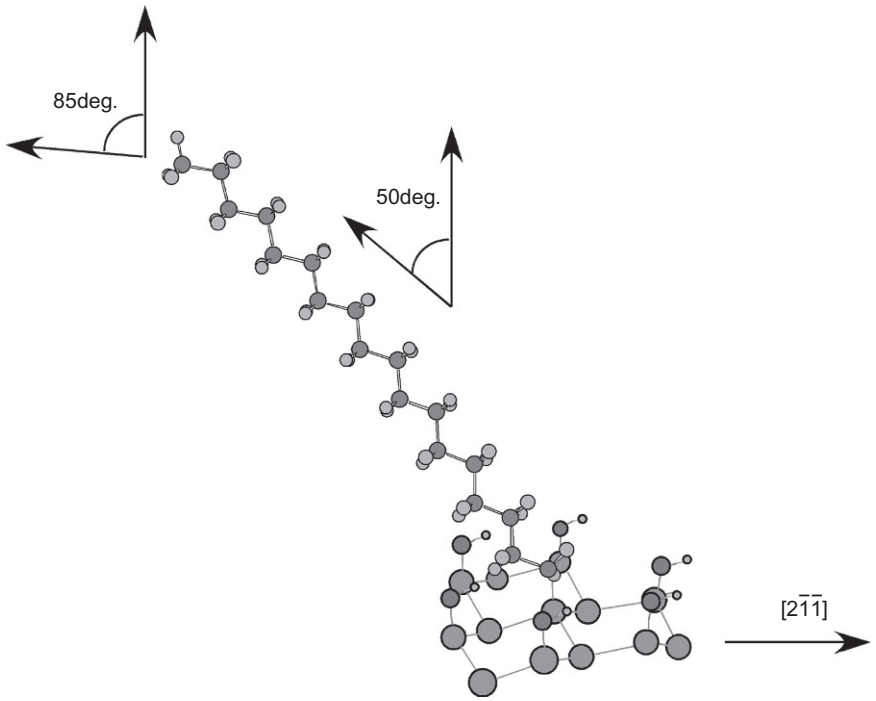

Fig. 6.13

The model of the possible orientation of the octadecyl chain. The alkyl chain is essentially in the all-trans conformation and epitaxially arranged being tilted toward the $[\bar{2}11]$ directions. The tilt angle of the methyl group is estimated to be about 85 degrees with respect to the surface normal. *Reprinted with permission from S. Nihonyanagi, D. Miyamoto, S. Idojiri, K. Uosaki, J. Am. Chem. Soc. 126 (2004) 7034–7040.*

polymeric drugs [64], antibacterial coatings [65] by protecting the surfaces of prostheses organs or catheters from adhesion of proteins, improvement of the stability of colloids [66–68], and the formation of multilayers of nanoparticles [69–71]. It is also a very important component of polymer electrolyte membrane (PEM) fuel cell. As polyelectrolyte has hydrophilic and hydrophobic components, an interaction between polyelectrolyte and water plays a crucial role in controlling the structure and functions of various materials. One of the most important examples is a folding/unfolding process of a protein.

A polymer, which is grafted on a solid substrate, is called "polymer brush" and in the case of polyelectrolyte, it is called "polyelectrolyte brush." The polyelectrolyte brush has recently attracted much attention because of its wide variety of possible applications [72,73]. It is also considered to be a model system of a biological membrane. To understand the function of polyelectrolyte in general and polyelectrolyte brush in particular, it is essential to know molecular structures of polyelectrolyte surfaces under various environments. However, only bulk structures of polyelectrolytes have been investigated [74–76], and almost no study on surface structure is available [77].

SFG spectroscopy is a useful technique for investigating the structure of polymer brush in contact with various environments including liquid water, and we apply it to poly(4-vinyl-N-n-alkylpyridinium)bromide (alkyl = ethyl, hexyl and dodecyl) polyelectrolyte brushes formed on a quartz surface, which have been reported to have an antibacterial function [78]. It was found that the conformational order of alkyl chains is very strongly affected by environment. Alkyl chains are in relatively high conformational order in dry nitrogen, gauche defects are introduced to alkyl chains upon contact with water vapor, and alkyl chains became totally disordered in liquid water. Structures of interfacial water of the brushes in contact with water vapor and liquid water were also investigated. Structural change was reversible and fast when the environment was changed between dry nitrogen and water vapor. Effects of chain length and ionic strength on the structure of water were also studied.

Fig. 6.14 shows the SFG spectra in the CH stretching region of (A) C2-PVP, (B) C6-PVP, (C) C12-PVP covered quartz prism in contact with dry nitrogen. For a comparison, the result of quartz prism modified by OTS monolayer is also shown in Fig. 6.14D. Open circles and solid lines represent experimental data points and fitting curves for Eq. (6.18), respectively. Several peaks were observed. Two peaks at 2862 and 2916 cm^{-1} were attributed to be due to CH symmetric stretching (d^+) and asymmetric stretching (d^-), respectively, of methylene (CH_2) group. Three peaks at 2880, 2941, and 2968 cm^{-1} were assigned to CH symmetric stretching (r^+), Fermi resonance between r^+ and CH bending overtone (FR), and CH asymmetric stretching (r^-), respectively, of methyl (CH_3) group. A broad peak observed at around 3040 cm^{-1} was assigned to overlapped aromatic CH stretching vibrations of the pyridinium ring (ring CH).

The SFG spectrum of C6-PVP (Fig. 6.14B) is similar to that of OTS (Fig. 6.14D), and the peaks corresponding to CH_2 groups were very weak. As mentioned previously, SFG is inhibited

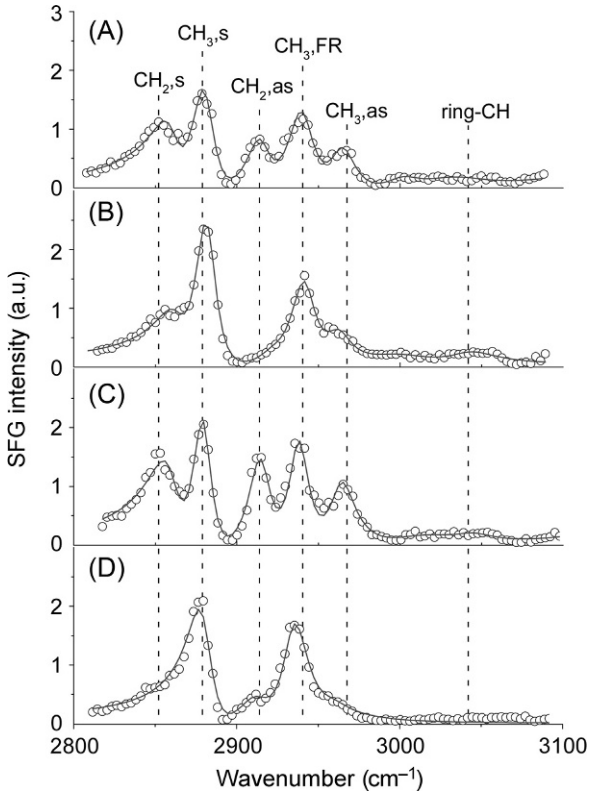

Fig. 6.14
SFG spectra in the CH stretching region of (A) C2-PVP, (B) C6-PVP, (C) C12-PVP, and (D) OTS covered quartz prism in dry nitrogen.

in the centrosymmetric media. It is well known that no methylene peak is observed at OTS-modified surface [79,80] when OTS is in *all-trans* conformation where CH_2 group is in inversion symmetry and is, therefore, SFG inactive [80]. Thus it can be concluded that hexyl side chain of the C6-PVP polymer brush is also mainly in *all-trans* conformation without gauche defect where only terminal CH_3 group is in noncentrosymmetry and contributes to the SFG spectrum.

Fig. 6.15 shows a series of SFG spectra of C6-PVP obtained sequentially in (A) dry nitrogen, (B) water vapor saturated nitrogen, (C) dry nitrogen after the removal of water vapor, (D) liquid water, and (E) dry nitrogen after the removal of water. The peaks due to CH_2 groups, which were very weak in dry nitrogen (Figs. 6.14C and 6.15A), were clearly observed when the brush was in contact with water vapor saturated nitrogen (Fig. 6.15B), indicating that a higher degree of gauche defects was introduced in the hexyl side chain with water vapor [81].

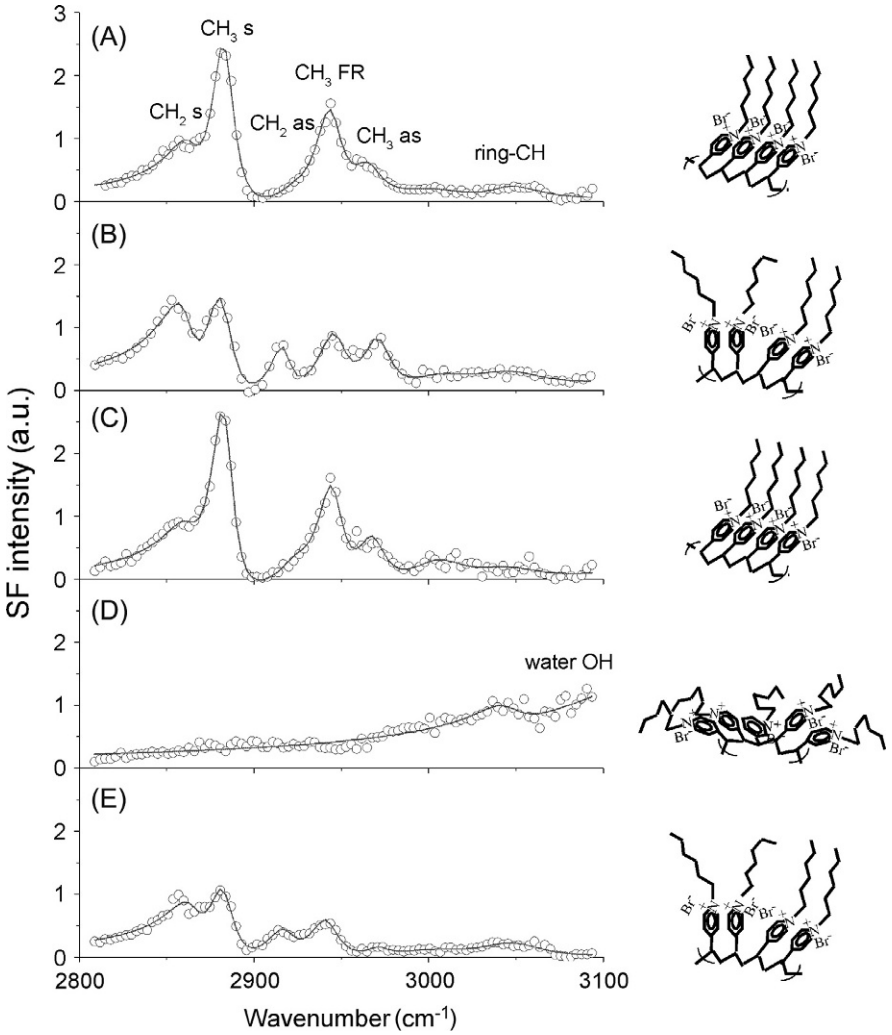

Fig. 6.15

SFG spectra of C6-PVP in the CH stretching region in (A) dry nitrogen, (B) water vapor-saturated nitrogen, (C) dry nitrogen after the removal of water vapor, (D) liquid water, and (E) dry nitrogen after the removal of water. Conformational structures of C6-PVP are schematically shown at the right hand side of each spectrum.

The tilt angle of the methyl group can be calculated from the intensity ratio of r^-/r^+ based on the procedure proposed by Hirose and his colleague [17,57]. By assuming an azimuthally isotropic interface, the ratio of the vibrational intensities of r^+ and r^- can be approximated by

$$\left|\frac{A(r^-)}{A(r^+)}\right| = \left|\frac{\beta_{caa}}{\beta_{aac}} \times \frac{-2(\cos\theta - \cos^3\theta)}{(1+r)\cos\theta - (1-r)\cos^3\theta}\right| \tag{6.32}$$

where θ is the angle between the main axis of the methyl group and the surface normal, β_{caa} and β_{aac} are the nonzero components of second-order hyperpolarizability β, and r is the ratio of β_{ccc}/β_{aac}. The values of β_{caa}/β_{aac} and r are 0.25 and 4.21, respectively [17]. Tilt angles of methyl group with respect to surface normal of C2-, C6-, and C12-PVP polymer brushes deduced from Eq. (6.32) in dry nitrogen are 43, 34, and 51 degrees, respectively.

6.4 Interfacial Water Structure Studied by SFG

Interfacial water molecules play prominent roles in many physical, chemical, and biological processes. Although many theoretical studies on the structure of water molecules at various interfaces are available, most of the experimental investigations on water structure have been carried out mainly in the vapor or bulk aqueous phase due to the lack of an experimental probe for interfacial study. Over the past decades, many spectroscopic techniques such as SERS, SEIRAS, and X-ray diffraction have been used to investigate the interfacial water structure. However, these techniques have limitations with respect to their surface selectivity applicable samples. Due to the high surface specificity based on second-order nonlinear spectroscopy, SFG spectroscopy has been widely employed to study the interfacial water at various interfaces.

6.4.1 SFG Study on Potential-Dependent Structure of Water at Pt Electrode/Electrolyte Solution Interface

Here, we demonstrate the usefulness of SFG spectroscopy in the study of water structure at electrode/electrolyte solution interfaces by showing the potential-dependent SFG spectra in OH stretching vibration region at a Pt thin film electrode/0.1M $HClO_4$ solution interface in internal reflection mode.

Fig. 6.16 shows a typical CV of a thin Pt film electrode in 0.1 M $HClO_4$ solution. The hydrogen waves in the potential range between −250 and ca.50 mV were observed, and surface oxidation and reduction peaks were observed in positive potential region (>600 mV). This result confirmed that the conductivity of the Pt thin film was good enough to be used as an electrode.

Fig. 6.17 shows SFG spectra in OH stretching region (2800–3800 cm^{-1}) obtained at the Pt electrode in 0.1 M $HClO_4$ solution at various potentials. Two broad peaks were observed at ca.3200 and 3400 cm^{-1}. The peaks around at 3200 and at 3400 cm^{-1} have been assigned to the vibration of OH oscillators of three coordinated hydrogen bonded water—that is, less ordered "liquid-like" water—molecules and that of the four coordinated hydrogen bonded water—that is, highly ordered "ice-like" water—molecules, respectively, based on the IR study of water clusters [82]. Thus the intensity ratio between these two peaks can be considered as an index of the order of the interfacial water [81,83]. Our previous work showed that the SFG spectra of Au

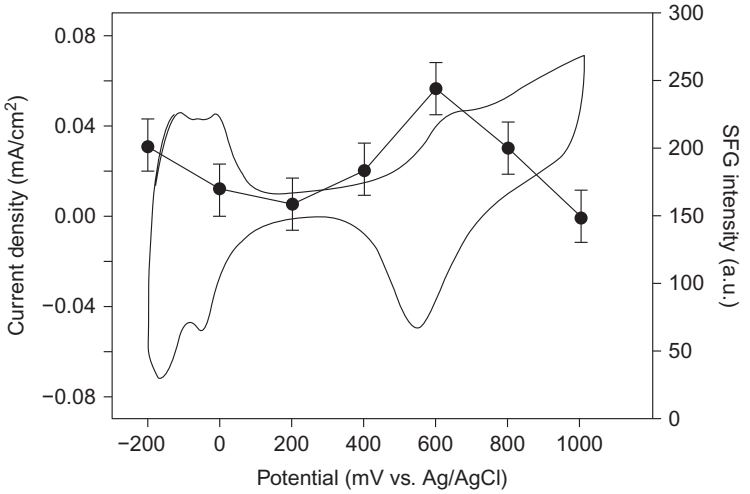

Fig. 6.16

CV obtained with a sweep rate of 50 mV/s (solid line) and potential dependence of integrated SFG intensity in OH stretching region (•) of a Pt thin film electrode in 0.1-M $HClO_4$ solution.

thin film/0.05 M H_2SO_4 solution interface were dominated by the peak corresponding to the "liquid-like" water at all potentials we investigated [84]. Thus water seems to be more highly oriented at the Pt electrode than at the Au electrode [9,85].

While the shape of the SFG spectra did not change significantly with potential, the intensity depended on potential. To clarify the potential dependencies of the SFG intensity, the integral intensities of SFG spectra between 2800 to 3800 cm^{-1} of the Pt electrode taken from Fig. 6.17 were plotted against electrode potential as shown also in Fig. 6.16. Parabolic behavior of SFG intensity was observed between −200 and 600 mV with a minimum around 200 mV, which is close to the potential of zero charge, pzc, of Pt electrode in $HClO_4$ solution [86], although the value of the pzc of Pt electrode is still debated [87].

Previously, we have proposed that SFG intensity due to interfacial water at quartz/water interfaces reflects the number of oriented water molecules within the electric double layer and in turn the double layer thickness based on the pH dependence of the SFG intensity [88] and a linear relation between the SFG intensity and $(\text{ionic strength})^{-1/2}$ [89]. In the case of Pt/electrolyte solution interface, the drop of the potential profile at the vicinity of electrode becomes precipitous as the electrode becomes more highly charged. Thus the ordered water layer at the vicinity of the electrode surface becomes thinner as the electrode is more highly charged. Since the number of ordered water molecules becomes smaller, the SFG intensity should become weaker at the potentials away from the pzc. This is contrary to the experimental result.

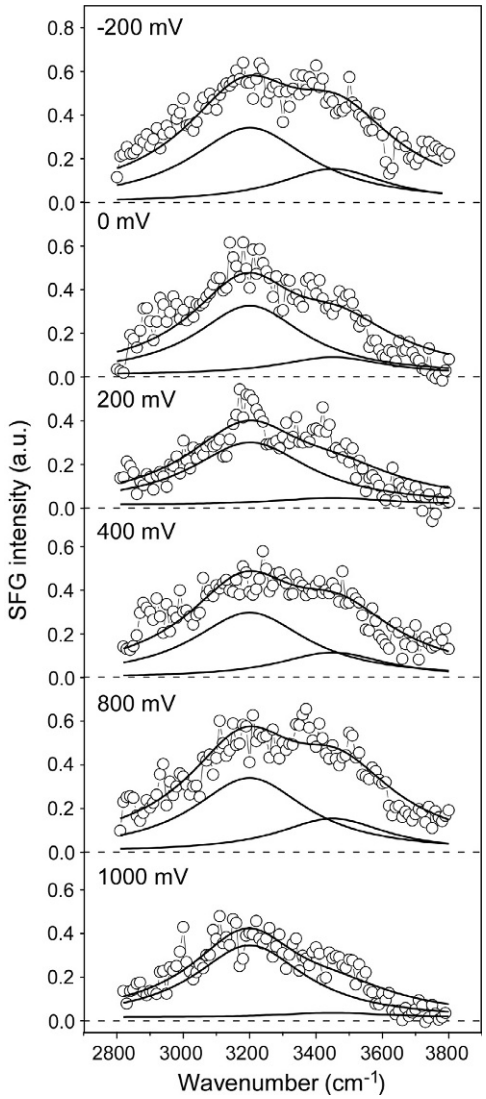

Fig. 6.17

SFG spectra in OH stretching region at a Pt electrode at each potential in 0.1 M $HClO_4$ solution.

When the electrolyte concentration is relatively high, potential dependence of the double layer thickness is low, and the potential dependence of the fraction of oriented water predominantly determines that of the SFG intensity. Since the polarization of IR in the present experiment is "p", water orienting in normal to the surface is effectively detected by SFG. Water molecules are expected to be lying parallel to the surface around the pzc and reorient from "oxygen-up" to "oxygen-down" as the surface charge of electrode surface changes from negative to positive as far as no specific adsorption of ions take place. IR study [90,91] as well as computer simulation

[92,93] also suggest that water molecules at the metal electrode surface have an oxygen-up and oxygen-down orientation on negatively and positively charged surfaces, respectively, on average.

For fixed nonresonant $\chi^{(2)}_{NR}$ sign, when the dipole moment of a molecule rotates by 180 degrees, the relative phase between the resonant and nonresonant part of the signal changes also by 180 degrees [19]. Thus, by analyzing the relative phase difference between $\chi^{(2)}_{NR}$ and $\chi^{(2)}_{R}$, the potential-dependent orientation of water molecules on Pt electrode surface can be determined.

Fig. 6.18 shows the potential dependence of relative phase difference between $\chi^{(2)}_{NR}$ and $\chi^{(2)}_{R}$. Relative phase was changed by ca.180 degrees at 200 mV, which is close to the pzc for Pt electrode in $HClO_4$ electrolyte solution [86]. This orientation change is most probably associated with a change in sign of the charge at Pt surface. This clearly demonstrates that the orientation of water dipoles flip by 180 degrees at the *pzc*.

SFG intensity in OH stretching region decreased as potential became more positive where Pt oxide was formed as shown in Fig. 6.17. There are several possibilities for this decrease. One is the disruption of well-ordered hydrogen bonded network structure of water molecules at a roughened Pt electrode surface compared to atomically flat surface since it is well known that the atomically flat surfaces of Pt were roughened by surface oxide formation [94]. The other possibility is the electric effect. Since Pt oxide is like an insulating thin film [95], additional potential drop takes occurred within the Pt oxide layer, resulting in a smaller electric field within the double layer. Furthermore, surface charge should also be affected by the oxide formation.

In conclusion, electrochemical SFG measurements showed that the SFG spectra in OH stretching region (2800–3800 cm^{-1}) at the Pt electrode in 0.1 M $HClO_4$ solution showed two broad peaks at

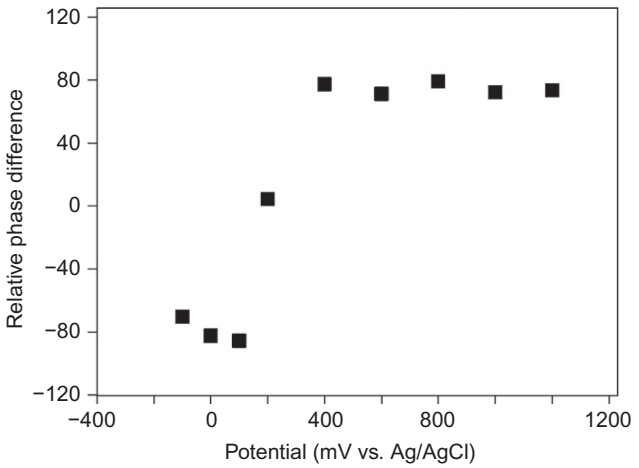

Fig. 6.18
Potential dependence of relative phase difference between $\chi^{(2)}_{NR}$ and $\chi^{(2)}_{R}$.

ca.3200 and 3400 cm^{-1}, which are assigned to the vibration of OH oscillators of three coordinated hydrogen bonded water (i.e., less ordered "liquid-like" water) molecules and that of the four coordinated hydrogen bonded water (i.e., highly ordered "ice-like" water) molecules, respectively, in contrast to the Au thin film/0.05 M H_2SO_4 solution interface where the spectra were dominated by the peak corresponding to the "liquid-like" water at all potentials, showing that water molecules are more highly oriented at the Pt electrode than at the Au electrode. The SFG intensity of OH stretching region of interfacial water at Pt/electrolyte solution interface exhibits a strong dependence on electrode potential. Parabolic behavior of SFG intensity was observed between −200 and 600 mV with a minimum around 200 mV, which is close to the pzc for Pt electrode in $HClO_4$ electrolyte solution. In the Pt oxide formation region (more positive than 600 mV), SFG intensity due to interfacial water decreased.

6.4.2 Humidity-Dependent Structure of Surface Water on Perfluorosulfonated Ionomer Thin Film Studied by SFG

Proton exchange membrane fuel cell (PEMFC), which electrochemically converts the chemical energy of a fuel, for example, hydrogen, directly into electrical energy, is one of the most promising energy conversion systems for the near future due to their high efficiency, high power density, and environmental benignity [96,97]. Considerable research efforts have been focused on improving the efficiency and stability of the PEMFC [96,97]. Water management is one of the most critical and widely studied issues in the PEMFC research [98,99], since the performance of a PEMFC is strongly dependent on the proton conductivity of the membrane.

Nafion is a perfluorosulfonated ionomer, which contains a fluorocarbon backbone with pendant side chains terminated with sulfonate groups and the most commonly used PEM [100]. The hydrophilic domain of Nafion, which is formed by the presence of sulfonate group, facilitates the uptake and transport of water, cation, and other polar solvents [101,102]. Proton conductivity is strongly dependent not only on temperature [103] but also on water content within the membrane. Thus understanding of the hydration behavior of Nafion membrane is not only a subject of chemical interest but also of great importance for the development of PEMFC.

Many studies on water structure in the Nafion membrane have been carried out by using IR [104,105], nuclear magnetic resonance (NMR) [106,107], neutron scattering [108], thermogravimetric analysis (TGA) [109], and impedance measurements [103]. However, all these experiments deal with the water "within" the Nafion membranes. Since electrochemical reactions take place at Nafion/electrode interfaces, molecular-level understanding of water structure at Nafion membrane surface is very important particularly when the reaction mechanisms at anode and cathode reactions in the PEMFC are considered. Humidity control is also another important issue for operating PEMFC, while excess water will result in electrode flooding, which may result in the decrease of cell performance [98,99].

Here, the structure of water at Nafion thin film surface was examined under various relative humidity (RH) by using SFG spectroscopy. It was found that water structure at Nafion thin film surface drastically changed depending on the RH. When Nafion thin film was exposed to low value of RH (<61%), a peak centered around 3600 cm^{-1} was dominant in the SFG spectra. With the increase of RH, both broad peaks centered around 3200–3300 cm^{-1} and a narrow peak at 3740 cm^{-1} increased. These results suggest that two different types of water exit on Nafion thin film surface, one at sulfonate site and the other at fluorocarbon site.

Fig. 6.19 shows SFG spectra in the OH stretching region of water molecules obtained at Nafion thin film surface measured at different RH.

Under dry Ar gas flow (RH = 0%), a very weak broad peak centered around 3300 cm^{-1} was observed (Fig. 6.19A). This peak should be originated from the water molecules, which are physisorbed on Nafion surface during the surface cleaning process. This broad peak disappeared when Nafion surface was exposed to a dry Ar gas for a long time. SFG peaks centered ca.3720 cm^{-1} (peak A), and ca.3600 cm^{-1} (peak B) appeared when water vapor was introduced into the cell (Fig. 6.19B–E). The position of peak A is close to that corresponding to the "dangling bond" or "free OH bond" of water molecules, observed at the vapor/water interface [110]. This "free OH bond" peak is usually observed when water molecules are in a

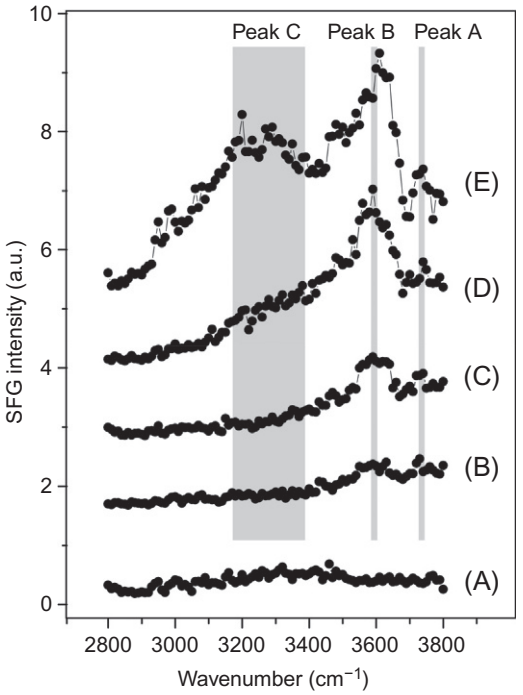

Fig. 6.19

SFG spectrum of OH stretching region of water at Nafion thin film/water vapor interface under various RH conditions: (A) 0%, (B) 17%, (C) 40%, (D) 61%, and (E) 100%.

hydrophobic environment [88,111]. The wavenumber of peak B is at slightly lower than the "free OH bond" peak. Falk and coworkers reported Fourier transform infrared (FTIR) studies for the water in Nafion membrane and showed two peaks in OH stretching region at ca.3700 and 3530 cm^{-1} [104]. They studied the Nafion membrane in various cationic forms, they assigned the higher wavenumber peak to the structure of water molecules forming hydrogen bonds between sulfonate in the proton channel, and low wavenumber peak as water molecules exposed to fluorocarbon environment [104]. Based on their assignments, we can conclude that peak B is originated from the water molecules at the proton channel surface.

When RH was increased to 61%, another new broad peak centered ca.3300 cm^{-1} (peak C) was observed. The intensity of this peak increased accompanied with a red shift as RH was increased and finally reached to ca.3200 cm^{-1} at RH = 100% (Fig. 6.19D and E). A shift of SFG peak in OH stretching region toward lower wavenumber indicates a structuring of hydrogen bonding network among water molecules. It is well known that the SFG spectrum of ice surface will give a broad OH stretching peak at around this low wavenumber region [112]. Such ordering of water molecules has also been observed at OTS/water interface [88]. The highly hydrophobic nature of surface should be the most important origin for the ordering of water molecules at the surface.

Fig. 6.20 shows the schematic model of Nafion/water vapor interface depending on RH. At low RH, most of the water molecules at Nafion surface exist in the proton channel, that is, sulfonate site to form a hydrogen bond between sulfonate sites. When the RH was increased, water started to adsorb also at the fluorocarbon site of Nafion surface, which has hydrophobic properties, and began to structure a hydrogen bond network among water molecules.

In conclusion, RH dependence of structure of water at Nafion thin film surface was studied for the first time by using SFG spectroscopy. It was demonstrated that two different types of water,

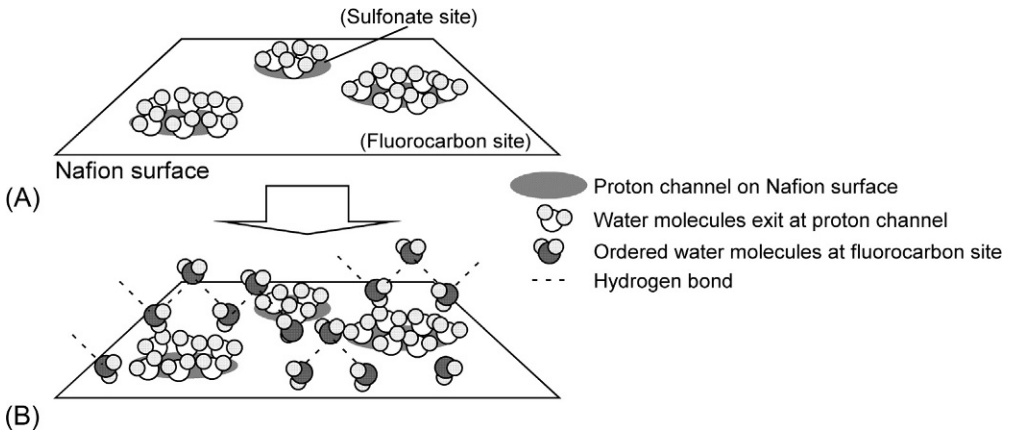

Fig. 6.20

A model of Nafion/water vapor interface depending on RH: (A) low RH and (B) high RH.

one at sulfonate site and the other at fluorocarbon site, exist at Nafion thin film surface, and its structure strongly depends on the RH.

6.5 Surface Dynamic of Surface Molecules Studied by SFG

Ultrafast dynamics studies dealing with short-lived reaction intermediates and vibrational relaxation are important for understanding the physical property of molecules and chemical reactions. SFG is almost the only technique that provides both a surface specificity and a high time resolution limited by pulse widths of an incident laser beam. Hydrogen on silicon is well studied by near IR pump/SFG probe technique due to its relatively long lifetime with respect to that of adsorbates on metal. The lifetime of the H-Si(111) stretch vibration (T_1) as well as its dephasing time (T_2) were determined to be 800 ps [113] and 13 ps [114], respectively. The vibrational relaxations of cyanide at the metal/electrolyte interface were also investigated. The lifetime of CN^- stretching mode was determined to be around 20 ps [115,116].

Ultrafast dynamics of adsorbates on catalyst surfaces have also been investigated by near infrared (NIR) pump/SFG probe technique in ultrahigh vacuum system. Domen and coworkers have investigated the thermal decomposition reaction of formate and succeeded in identifying the intermediate [117].

Subpicosecond time resolution can be achieved when a broadband (or multiplex) SFG is employed as a probe without lowering the spectral resolution. Bonn et al. investigated the CO stretching vibration of carbon monoxide adsorbed on a single crystal Ru(001) surface during fs NIR excitation leading to desorption (Fig. 6.21) [118].

Here we would like to discuss the photoinduced surface dynamics of adsorbed CO in electrochemical system.

6.5.1 Photoinduced Surface Dynamics of CO Adsorbed on a Platinum Electrode

The dynamics of interactions between molecules and a surface such as vibrational excitations, energy exchange, and relaxation are of fundamental importance in surface science [119,120]. The time scale of these processes is in the pico- to femtosecond regime. Recent development of short pulse laser techniques has enabled direct observation of ultrafast surface dynamics not only to identify the surface species but also to probe the transient species generated by the pump pulse in real time [121,122]. Although most of the SFG studies so far have been concerned with static structure of molecules at interfaces, a more important contribution of SFG spectroscopy should be its high time resolution, and time-resolved SFG (TR-SFG) is expected to be one of the most powerful methods for observing and identifying transient states of surface adsorbates [115,123–125].

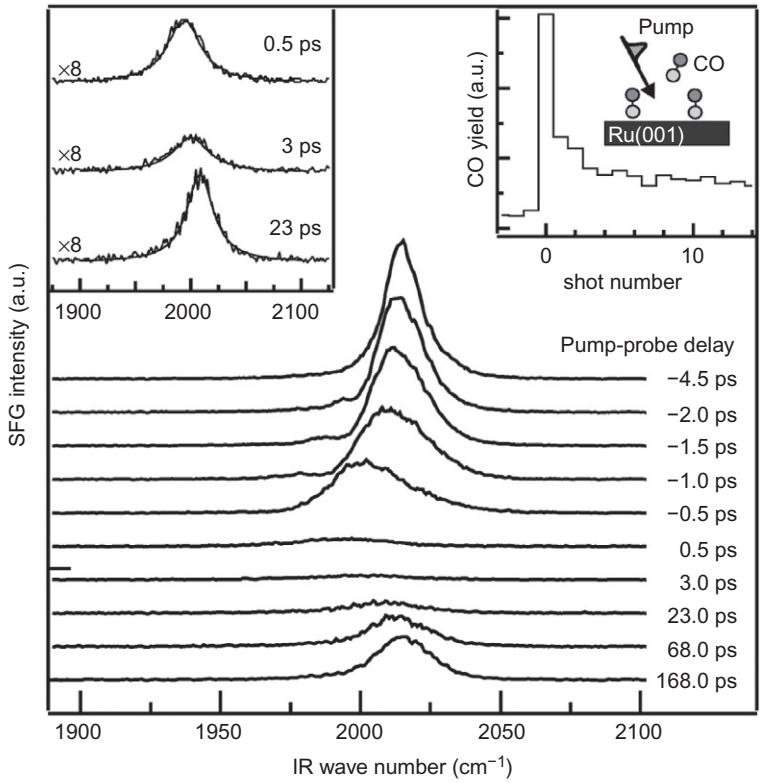

Fig. 6.21

Transient SFG spectra of the C—O stretch vibration while desorption is occurring for delay times indicated in the graph (absorbed pump fluence: 55 J/m^2). Lorentzian fits to data in the left inset are shown as dashed lines. Right inset: Depletion curve demonstrating CO desorption under these excitation conditions. At laser shot number 1, the shutter opens and the surface is irradiated. The CO yield decreases rapidly after the first shot, indicating a ~50% desorption probability for the first pulse. *Reprinted permission from M. Bonn et al., Phys. Rev. Lett. 84 (2000) 4653–4652.*

Adsorbed CO on a metal surface is one of the simplest adsorbates and has attracted significant interest within the community of fundamental surface science, catalysis, and electrochemistry. An understanding of the oxidation mechanism of adsorbed CO is important to design and develop electrocatalysts for fuel cells [126–129], and the surface dynamics of adsorbed CO on electrode surfaces in electrolyte solutions should, therefore, be very important to be investigated.

TR-SFG seems to be an ideal tool to study the surface dynamics of adsorbed CO at solid/liquid interfaces. Although there are several reports of TR-SFG study on an electrode, they are only of investigations of vibrational relaxation lifetime by IR excitation [115,123,130].

In the present study, we investigated the SFG response of CO adsorbed on a Pt electrode surface in an electrolyte solution upon irradiation of intense visible pulses in the time resolution of ca.20 ps.

Fig. 6.22 shows CVs of the Pt electrode in 0.1 M $HClO_4$ solution with and without (inset) 0.1 M HCHO. They are in good agreement with the results reported before [131]. The hydrogen waves in the potential range between −250 and ca.50 mV (inset) were suppressed in the solution containing HCHO, indicating the existence of a CO adlayer on the Pt electrode surface [129].

SFG measurements were carried out in the potential range between 0 and 300 mV, where the presence of adsorbed CO was expected, after a CO adlayer was formed at 0 V. Fig. 6.23 shows SFG spectra of the Pt electrode in 0.1 M $HClO_4$ solution containing 0.1 M HCHO at various potentials. A peak centered at ca.2055 cm^{-1} was observed in agreement with results of previous studies by IR spectroscopy [132], and was assigned to the stretching vibration of CO (ν_{CO}) adsorbed on a one-fold coordinated (atop) site of the Pt surface. As the potential became more positive, the peak position of this band shifted to a higher wavenumber by approximately 33 cm^{-1}/V up to 200 mV (Fig. 6.22 inset), which also agrees with the previous IR results [132]. This shift has often been referred to as electrochemical Stark tuning. Intensity decrease and red shift of the SFG peak were observed at 300 mV, indicating the loss of adsorbed CO as a result of CO oxidation. When the potential was made more positive, the SFG peak was not observed any more (data not shown), indicating complete loss of the adsorbed CO from the Pt surface. The CO oxidation threshold potential observed by SFG in the present experiments was c.200 mV more negative than that expected from the CV (Fig. 6.23). Similar discrepancy between the CO

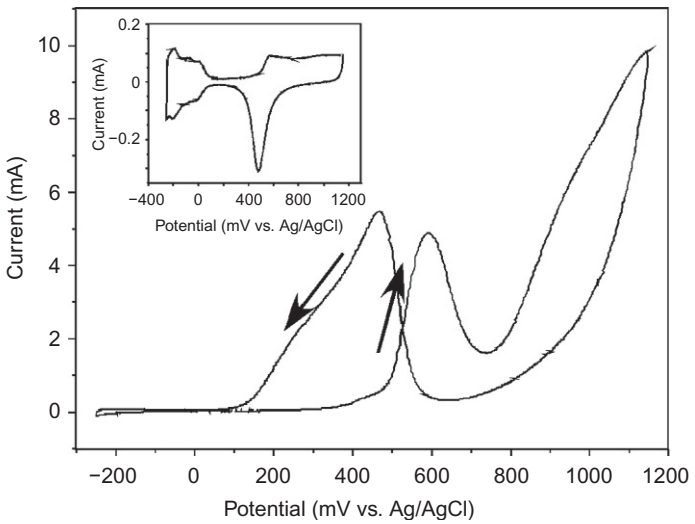

Fig. 6.22

CVs of a Pt-poly electrode in 0.1 M $HClO_4$ with and without (inset) 0.1 M HCHO with sweep rate of 20 mV/s.

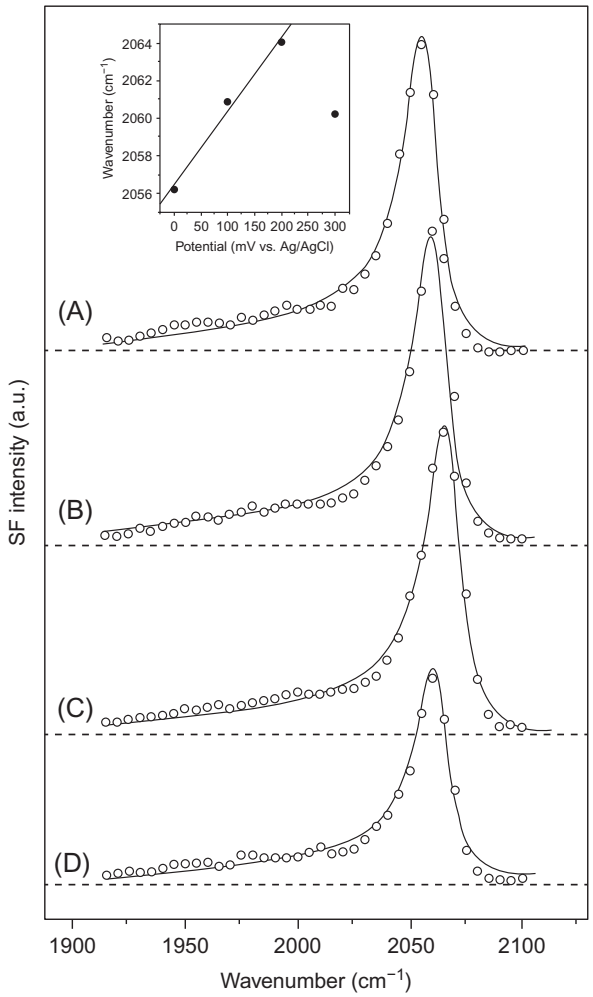

Fig. 6.23

SFG spectra of the Pt surface in a solution of 0.1 M HCHO in 0.1 M $HClO_4$ at (A) 0, (B) 100, (C) 200, and (D) 300 mV.

oxidation potential in CV and the potential of the disappearance of SFG signal was previously reported [133,134]. The difference in the data acquisition time (SFG: 20–60 min for a spectrum at a given potential, CV: typically less than 1 min) is considered to be the origin of this discrepancy.

Fig. 6.24 shows the temporal profile of the intensity change in the SFG signal at the peak of ν_{CO} mode (2055 cm^{-1}) at 0 mV induced by visible pump pulse irradiation. The solid line is the least-squares fit using a convolution of Gaussian function for the laser profile (FWHM = 20 ps)

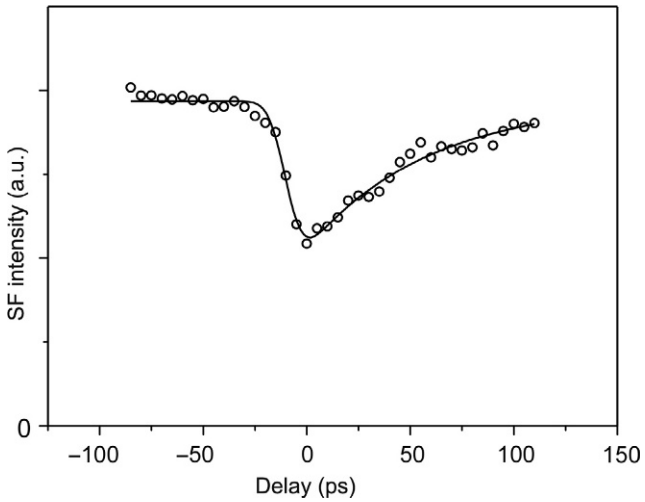

Fig. 6.24
Temporal profile of SFG signal intensity at 2055 cm^{-1} at potential of 0 mV. The solid line is the results of a least-squares fitting.

and a single exponential function for the recovery profile. The SFG signal fell into a minimum within ca.100 ps and recovered to the initial value. There was a linear correlation between the pump fluence and the intensity decrease induced by the pump pulse, and no intensity change was observed when the pump fluence was less than that of the SFG probe (532 nm) pulse.

Fig. 6.25 shows TR-SFG spectra at the delay times of −80, 0, and 70 ps. The spectrum observed at −80 ps, that is, 80 ps before pumping, is the same as those observed without pumping (Fig. 6.23), indicating that the irradiation-induced changes in the spectra were restored during the 0.1s interval of pump pulse repetition (10 Hz). When the delay time was 0 ps, maximum change in spectral features was observed. The height of the SFG peak at 2055 cm^{-1} was decreased, the peak position was slightly shifted to a lower wavenumber, and the peak was broadened. The values of FWHM derived from the fits are ca.20 and 25 cm^{-1} at −80 ps and 0 ps delay, respectively.

At 0 ps, in addition to the changes of the peak at 2055 cm^{-1}, a new peak appeared at around 1980 cm^{-1}. One possible origin of the new peak is $\nu = 1 \rightarrow 2$ transition (hot band) of stretching vibration of CO adsorbed on the Pt surface. Due to a vibrational anharmonicity, a hot band will give rise to a new peak in a lower wavenumber region than the fundamental peak ($\nu = 0 \rightarrow 1$). The frequency shift from the initial CO stretching band to the new broad peak observed in the present study was, however, ca.88 cm^{-1}, which is much larger than the previously reported value for CO on a Pt surface (ca.30 cm^{-1}) [118] and in gas phase (ca.27 cm^{-1}) [135]. Thus it is unlikely that the new peak is due to excitation of the hot band generated by pump pulses. Another possible reason for the appearance of the new peak is the transient site migration of CO on the Pt surface. It has been reported that CO adsorbed on a multibonded [136] or asymmetric

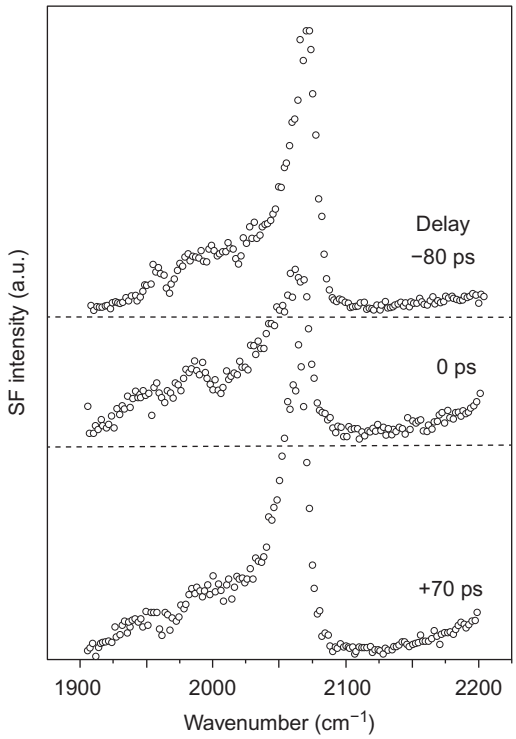

Fig. 6.25
TR-SFG spectra in the CO stretching region at delay times of −80, 0, and 70 ps.

bridge site [137] gives a peak at ca.1980 cm^{-1}, which is in agreement with the position of the transiently observed peak in the present study. Thus it is reasonable to assume that the decrease of the peak at 2055 cm^{-1} and the appearance of the new peak at 1980 cm^{-1} were caused by reversible site migration of CO on the Pt surface from the on-top site to a multibonded or asymmetric bridge site induced by intense pump pulse irradiation.

The low-frequency shift and the broadening of the CO spectra at 0 ps suggest that the low-frequency modes of adsorbed CO, that is, stretching, frustrated rotation, and frustrated translation modes of Pt-CO, were thermally excited by pump pulses as reported by Bonn et al. [118]. Thus, it is concluded that the transient site migration of adsorbed CO on the Pt electrode surface was caused by a transient rise in the surface temperature of Pt induced by pump pulses.

In conclusion, TR-SFG measurements at a Pt electrode/electrolyte interface covered with a CO monolayer excited by the irradiation of picosecond visible pulses showed that the population of on-top CO instantly decreased accompanied by an increase in multibonded CO due to the transient temperature jump at the surface, and the initial state was recovered within 100 ps, showing the transient reversible migration of CO molecules on the Pt surface under electrochemical conditions as schematically shown in Fig. 6.26.

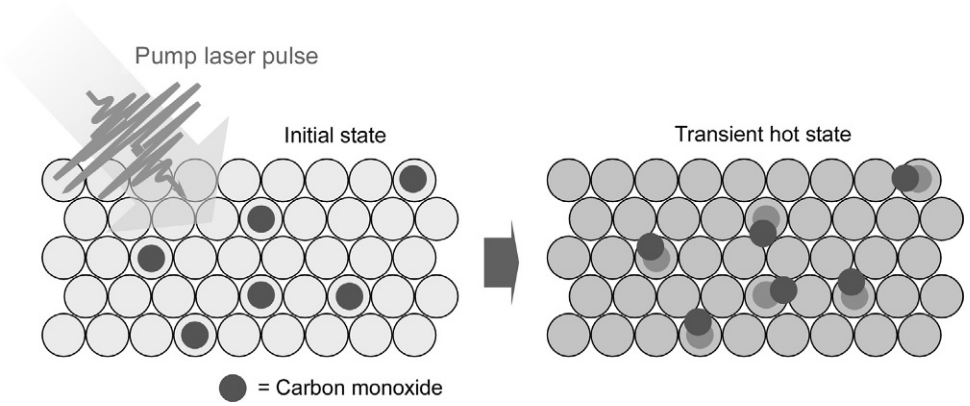

Fig. 6.26
Transient CO migration induced by intense pump pulse irradiation.

6.6 General Conclusion

SFG is a nonlinear, second-order optical technique that provides information about surfaces and interfaces. It is applicable to many interfaces accessible by light and is commonly used to obtain IR vibrational spectra of molecules at an interface.

Unlike the conventional UHV surface probe technique, SFG can be used under ambient conditions at air/liquid, air/solid, solid/liquid, and liquid/liquid interfaces. Although SFG can determine the molecular structure and orientation of adsorbates on the surface, it is more important to identify the structure of water molecules at solid/liquid interfaces, which are impossible to carry out in UHV condition.

Thus SFG spectroscopy receives a lot of attention from the medical community seeking a better understanding of biocompatible polymers. Performance of biocompatible materials depends on surface and interface properties that include wettability, friction, lubricity, adhesion. Because these properties, in turn, depend on molecular structure at the material surface, SFG spectroscopy may be the best tool for process control of biomedical surfaces.

Acknowledgment

This work was also carried out by Dr. S. Nihonyanagi, R. Yamamoto, T. Okada, and Dr. K. Taneda. Dr. S. Yang is acknowledged for proof reading.

References

[1] Y.R. Shen, Nature 337 (1989) 519–525.
[2] C.D. Bain, J. Chem. Soc.-Faraday Trans. 91 (1995) 1281–1296.
[3] F. Vidal, A. Tadjeddine, Rep. Prog. Phys. 68 (2005) 1095–1127.

[4] G.L. Richmond, Chem. Rev. 102 (2002) 2693–2724.
[5] S. Gopalakrishnan, D.F. Liu, H.C. Allen, M. Kuo, M.J. Shultz, Chem. Rev. 106 (2006) 1155–1175.
[6] H. Arnolds, M. Bonn, Surf. Sci. Rep. 65 (2010) 45–66.
[7] M. Osawa, Bull. Chem. Soc. Jpn. 70 (1997) 2861–2880.
[8] M.J. Weaver, J. Raman Spectrosc. 33 (2002) 309–317.
[9] H. Noguchi, T. Okada, K. Uosaki, Electrochim. Acta 53 (2008) 6841–6844.
[10] B. Bozzini, B. Busson, A. Gayral, C. Humbert, C. Mele, C. Six, A. Tadjeddine, Molecules 17 (2012) 7722–7736.
[11] K. Uosaki, H. Noguchi, R. Yamamoto, S. Nihonyanagi, J. Am. Chem. Soc. 132 (2010) 17271–17276.
[12] H. Noguchi, M. Hiroshi, T. Tominaga, J.P. Gong, Y. Osada, K. Uosaki, Phys. Chem. Chem. Phys. 10 (2008) 4987–4993.
[13] M. Bass, A.E. Hill, P.A. Franken, C.W. Peters, G. Weinreich, Phys. Rev. Lett. 18 (1962).
[14] N. Bolembergen, Nonlinear Optics, W. A. Benjamin Inc., New York, 1965.
[15] H.J. Simon, D.E. Mitchell, J.G. Watson, Phys. Rev. Lett. 33 (1974) 1531–1534.
[16] X.D. Zhu, H. Suhr, Y.R. Shen, Phys. Rev. B 35 (1987) 3047–3050.
[17] C. Hirose, N. Akamatsu, K. Domen, J. Chem. Phys. 96 (1992) 997–1004.
[18] C. Hirose, N. Akamatsu, K. Domen, Appl. Spectrosc. 46 (1992) 1051–1072.
[19] R.N. Ward, P.B. Davies, C.D. Bain, J. Phys. Chem. 97 (1993) 7141–7143.
[20] G.R. Bell, C.D. Bain, R.N. Ward, J. Chem. Soc.-Faraday Trans. 92 (1996) 515–523.
[21] H. Noguchi, T. Okada, K. Uosaki, J. Phys. Chem. B 110 (2006) 15055–15058.
[22] K. Domen, A. Bandara, J. Kubota, K. Onda, A. Wada, S.S. Kano, C. Hirose, Surf. Sci. 427–428 (1999) 349–357.
[23] C.L. Anfuso, A.M. Ricks, W. Rodriguez-Cordoba, T.Q. Lian, J. Phys. Chem. C 116 (2012) 26377–26384.
[24] J.A. Carter, Z.H. Wang, D.D. Dlott, Acc. Chem. Res. 42 (2009) 1343–1351.
[25] T.F. Heintz, Second-order nonlinear optical effects at surfaces and interfaces, in: H.E. Ponath, G.I. Stegeman (Eds.), Nonlinear Electromagnetic Phenomena, vol. 29, Elsevier, Amsterdam, 1991.
[26] A. Ulman, An Introduction to Ultra-thin Organic Films from Langmuir-Blodgett to Self-assembly, Academic Press, San Diego, 1991.
[27] A. Ulman, Chem. Rev. 96 (1996) 1533–1554.
[28] C.E.D. Chidsey, Science 251 (1991) 919–922.
[29] K. Uosaki, T. Kondo, X.Q. Zhang, M. Yanagida, J. Am. Chem. Soc. 119 (1997) 8367–8368.
[30] S. Ye, Y. Sato, K. Uosaki, Langmuir 13 (1997) 3157–3161.
[31] M.D. Porter, T.B. Bright, D.L. Allara, C.E.D. Chidsey, J. Am. Chem. Soc. 109 (1987) 3559–3568.
[32] K. Shimazu, I. Yagi, Y. Sato, K. Uosaki, Langmuir 8 (1992) 1385–1387.
[33] D.S. Karpovich, G.J. Blanchard, Langmuir 10 (1994) 3315–3322.
[34] R. Yamada, K. Uosaki, Langmuir 13 (1997) 5218–5221.
[35] H. Wano, K. Uosaki, Langmuir 17 (2001) 8224–8228.
[36] G.E. Poirier, Chem. Rev. 97 (1997) 1117–1127.
[37] P. Guyotsionnest, J.H. Hunt, Y.R. Shen, Phys. Rev. Lett. 59 (1987) 1597–1600.
[38] X. Wei, X.W. Zhuang, S.C. Hong, T. Goto, Y.R. Shen, Phys. Rev. Lett. 82 (1999) 4256–4259.
[39] M. Oh-e, A.I. Lvovsky, X. Wei, Y.R. Shen, J. Chem. Phys. 113 (2000) 8827–8832.
[40] N. Akamatsu, K. Domen, C. Hirose, J. Phys. Chem. 97 (1993) 10070–10075.
[41] M.S. Yeganeh, S.M. Dougal, R.S. Polizzotti, P. Rabinowitz, Thin Solid Films 270 (1995) 226–229.
[42] T. Baum, S. Ye, K. Uosaki, Langmuir 15 (1999) 8577–8579.
[43] C.W. Sheen, J.X. Shi, J. Martensson, A.N. Parikh, D.L. Allara, J. Am. Chem. Soc. 114 (1992) 1514–1515.
[44] S. Ye, G.F. Li, H. Noda, K. Uosaki, M. Osawa, Surf. Sci. 529 (2003) 163–170.
[45] Y. Gu, Z. Lin, R.A. Butera, V.S. Smentkowski, D.H. Waldeck, Langmuir 11 (1995) 1849–1851.
[46] M.R. Linford, P. Fenter, P.M. Eisenberger, C.E.D. Chidsey, J. Am. Chem. Soc. 117 (1995) 3145–3155.
[47] M.E. Quayum, T. Kondo, S. Nihonyanagi, D. Miyamoto, K. Uosaki, Chem. Lett. (2002) 208–209.
[48] H.Z. Yu, S. Morin, D.D.M. Wayner, P. Allongue, C.H. de Villeneuve, J. Phys. Chem. B 104 (2000) 11157–11161.

[49] J. Terry, M.R. Linford, C. Wigren, R.Y. Cao, P. Pianetta, C.E.D. Chidsey, Appl. Phys. Lett. 71 (1997) 1056–1058.
[50] A. Fidelis, F. Ozanam, J.N. Chazalviel, Surf. Sci. 444 (2000) L7–L10.
[51] A. Bansal, N.S. Lewis, J. Phys. Chem. B 102 (1998) 4058–4060.
[52] M.J. Bozack, W.J. Choyke, L. Muehlhoff, J.T. Yates, Surf. Sci. 176 (1986) 547–566.
[53] G.P. Lopinski, D.D.M. Wayner, R.A. Wolkow, Nature 406 (2000) 48–51.
[54] S. Nihonyanagi, D. Miyamoto, S. Idojiri, K. Uosaki, J. Am. Chem. Soc. 126 (2004) 7034–7040.
[55] C. Hirose, H. Yamamoto, N. Akamatsu, K. Domen, J. Phys. Chem. 97 (1993) 10064–10069.
[56] M. Oh-e, D. Kim, Y.R. Shen, J. Chem. Phys. 115 (2001) 5582–5588.
[57] N. Watanabe, H. Yamamoto, A. Wada, K. Domen, C. Hirose, T. Ohtake, N. Mino, Spectrochim. Acta A-Mol. Biomol. Spectrosc. 50 (1994) 1529–1537.
[58] J. Wang, C.Y. Chen, S.M. Buck, Z. Chen, J. Phys. Chem. B 105 (2001) 12118–12125.
[59] K.S. Gautam, A.D. Schwab, A. Dhinojwala, D. Zhang, S.M. Dougal, M.S. Yeganeh, Phys. Rev. Lett. 85 (2000) 3854–3857.
[60] J. Wang, Z. Paszti, M.A. Even, Z. Chen, J. Am. Chem. Soc. 124 (2002) 7016–7023.
[61] E.D. Palik, Handbook of Optical Constants of Solids, first ed., Academic Press Inc., Orlando, 1985.
[62] A.B. Sieval, B. van den Hout, H. Zuilhof, E.J.R. Sudholter, Langmuir 17 (2001) 2172–2181.
[63] L.Z. Zhang, K. Wesley, S.Y. Jiang, Langmuir 17 (2001) 6275–6281.
[64] L.G. Donaruma, R.M. Ottenbrite, V. Otto, Anionic Polymeric Drugs. Polymers in Biology and Medicine, vol.1; John Wiley & Sons, Inc., New York, 1980.
[65] R. Rajaraman, D.E. Rounds, S.P.S. Yen, A. Rembaum, Effects of ionenes on normal and transformed cells, in: A. Rembaum, E. Selegny (Eds.), Polyelectrolyte and Their Applications Volume 2 of the series Charged & Reactive Polymers. Springer, Boston, 1975, pp. 163–195.
[66] P. Pincus, Macromolecules 24 (1991) 2912–2919.
[67] H.J. Taunton, C. Toprakcioglu, L.J. Fetters, J. Klein, Macromolecules 23 (1990) 571–580.
[68] S.S. Patel, M. Tirrell, Annu. Rev. Phys. Chem. 40 (1989) 597–635.
[69] G. Decher, J.B. Schlenoff, Multilayer Thin Films: Sequential Assembly of Nanocomposite Materials, Wiley-VHC, Weinheim, 2003.
[70] J.W. Ostrander, A.A. Mamedov, N.A. Kotov, J. Am. Chem. Soc. 123 (2001) 1101–1110.
[71] K. Uosaki, T. Kondo, M. Okamura, W.B. Song, Faraday Discuss. 121 (2002) 373–389.
[72] M.L. Bruening, D.M. Dotzauer, P. Jain, L. Ouyang, G.L. Baker, Langmuir 24 (2008) 7663–7673.
[73] Y. Tran, P. Auroy, J. Am. Chem. Soc. 123 (2001) 3644–3654.
[74] M.J.R. Presa, L.M. Gassa, O. Azzaroni, C.A. Gervasi, Anal. Chem. 81 (2009) 7936–7943.
[75] Z.L. Liu, J.X. Liu, H.Y. Hu, B. Yu, M. Chen, F. Zhou, Phys. Chem. Chem. Phys. 10 (2008) 7180–7185.
[76] C. Schneider, A. Jusufi, R. Farina, F. Li, P. Pincus, M. Tirrell, M. Ballauff, Langmuir 24 (2008) 10612–10615.
[77] P.J.N. Kett, M.T.L. Casford, A.Y. Yang, T.J. Lane, M.S. Johal, P.B. Davies, J. Phys. Chem. B 113 (2009) 1559–1568.
[78] J.C. Tiller, S.B. Lee, K. Lewis, A.M. Klibanov, Biotechnol. Bioeng. 79 (2002) 465–471.
[79] P. Guyotsionnest, R. Superfine, J.H. Hunt, Y.R. Shen, Chem. Phys. Lett. 144 (1988) 1–5.
[80] A.S. Lagutchev, K.J. Song, J.Y. Huang, P.K. Yang, T.J. Chuang, Chem. Phys. 226 (1998) 337–349.
[81] Q. Du, E. Freysz, Y.R. Shen, Phys. Rev. Lett. 72 (1994) 238–241.
[82] U. Buck, F. Huisken, Chem. Rev. 100 (2000) 3863–3890.
[83] Q. Du, E. Freysz, Y.R. Shen, Science 264 (1994) 826–828.
[84] S. Nihonyanagi, Y. Shen, K. Uosaki, L. Dreesen, C. Humbert, P. Thiry, A. Peremans, Surf. Sci. 573 (2004) 11–16.
[85] H. Noguchi, T. Okada, K. Uosaki, Faraday Discuss. 140 (2008) 125–137.
[86] A. Cuesta, Surf. Sci. 572 (2004) 11–22.
[87] U.W. Hamm, D. Kramer, R.S. Zhai, D.M. Kolb, J. Electroanal. Chem. 414 (1996) 85–89.
[88] S. Ye, S. Nihonyanagi, K. Uosaki, Phys. Chem. Chem. Phys. 3 (2001) 3463–3469.
[89] S. Nihonyanagi, S. Ye, K. Uosaki, Electrochim. Acta 46 (2001) 3057–3061.
[90] K. Ataka, M. Osawa, Langmuir 14 (1998) 951–959.
[91] M. Osawa, M. Tsushima, H. Mogami, G. Samjeske, A. Yamakata, J. Phys. Chem. C 112 (2008) 4248–4256.

[92] G. Nagy, K. Heinzinger, J. Electroanal. Chem. 327 (1992) 25–30.
[93] R. Akiyama, F. Hirata, J. Chem. Phys. 108 (1998) 4904–4911.
[94] K. Sashikata, N. Furuya, K. Itaya, J. Vac. Sci. Technol. B 9 (1991) 457–464.
[95] A. Damjanovic, V.I. Birss, D.S. Boudreaux, J. Electrochem. Soc. 138 (1991) 2549–2555.
[96] K.V. Kordesch, G.R. Simader, Chem. Rev. 95 (1995) 191–207.
[97] M. Winter, R.J. Brodd, Chem. Rev. 104 (2004) 4245–4269.
[98] C.Y. Wang, Chem. Rev. 104 (2004) 4727–4765.
[99] K.D. Kreuer, Solid State Ionics 97 (1997) 1–15.
[100] K.A. Mauritz, R.B. Moore, Chem. Rev. 104 (2004) 4535–4585.
[101] P.W. Majsztrik, M.B. Satterfield, A.B. Bocarsly, J.B. Benziger, J. Membr. Sci. 301 (2007) 93–106.
[102] T.A. Zawodzinski, C. Derouin, S. Radzinski, R.J. Sherman, V.T. Smith, T. E. Springer, S. Gottesfeld, J. Electrochem. Soc. 140 (1993) 1041–1047.
[103] K. Uosaki, K. Okazaki, H. Kita, J. Electroanal. Chem. 287 (1990) 163–169.
[104] M. Falk, Can. J. Chem. 58 (1980) 1495–1501.
[105] R. Basnayake, W. Wever, C. Korzeniewski, Electrochim. Acta 53 (2007) 1259–1264.
[106] R.S. Chen, J.P. Jayakody, S.G. Greenbaum, Y.S. Pak, G. Xu, M.G. Mclin, J.J. Fontanella, J. Electrochem. Soc. 140 (1993) 889–895.
[107] K.W. Feindel, S.H. Bergens, R.E. Wasylishen, Phys. Chem. Chem. Phys. 9 (2007) 1850–1857.
[108] F. Xu, O. Diat, G. Gebel, A. Morin, J. Electrochem. Soc. 154 (2007) B1389–B1398.
[109] Y.Q. Wang, Y. Kawano, S.R. Aubuchon, R.A. Palmer, Macromolecules 36 (2003) 1138–1146.
[110] Q. Du, R. Superfine, E. Freysz, Y.R. Shen, Phys. Rev. Lett. 70 (1993) 2313–2316.
[111] K. Uosaki, T. Yano, S. Nihonyanagi, J. Phys. Chem. B 108 (2004) 19086–19088.
[112] X. Wei, P.B. Miranda, C. Zhang, Y.R. Shen, Phys. Rev. B 66 (2002).
[113] P. Guyotsionnest, P. Dumas, Y.J. Chabal, G.S. Higashi, Phys. Rev. Lett. 64 (1990) 2156–2159.
[114] P. Guyotsionnest, Phys. Rev. Lett. 66 (1991) 1489–1492.
[115] C. Matranga, P. Guyot-Sionnest, J. Chem. Phys. 112 (2000) 7615–7621.
[116] C. Matranga, B.L. Wehrenberg, P. Guyot-Sionnest, J. Phys. Chem. B 106 (2002) 8172–8175.
[117] A. Bandara, J. Kubota, K. Onda, A. Wada, S.S. Kano, K. Domen, C. Hirose, J. Phys. Chem. B 102 (1998) 5951–5954.
[118] M. Bonn, C. Hess, S. Frank, J.H. Miners, B.N.J. Person, M. Wolf, G. Ertl, Phys. Rev. Lett. 84 (2000) 4653–4656.
[119] H.L. Dai, W. Ho, Laser Spectroscopy and Photochemistry on Metal Surfaces, World Scientific, Singapore, 1995.
[120] H.G. Rubahn, Laser Applications in Surface Science and Technology, John Wiley & Sons, New York, 1999.
[121] H. Noguchi, E. Yoda, N. Ishizawa, J.N. Kondo, A. Wada, H. Kobayashi, K. Domen, J. Phys. Chem. B 109 (2005) 17217–17223.
[122] A. Yamakata, T. Uchida, J. Kubota, M. Osawa, J. Phys. Chem. B 110 (2006) 6423–6427.
[123] M.E. Schmidt, P. GuyotSionnest, Abstr. Pap. Am. Chem. Soc. 212 (1996) 25.
[124] M. Bonn, C. Hess, S. Funk, J.H. Miners, B.N.J. Persson, M. Wolf, G. Ertl, Phys. Rev. Lett. 84 (2000) 4653–4656.
[125] H. Noguchi, T. Okada, K. Onda, S.S. Kano, A. Wada, K. Domen, Surf. Sci. 528 (2003) 183–188.
[126] E.A. Batista, G.R.P. Malpass, A.J. Motheo, T. Iwasita, J. Electroanal. Chem. 571 (2004) 273–282.
[127] T. Yajima, H. Uchida, M. Watanabe, J. Phys. Chem. B 108 (2004) 2654–2659.
[128] A. Miki, S. Ye, T. Senzaki, M. Osawa, J. Electroanal. Chem. 563 (2004) 23–31.
[129] S. Nakabayashi, N. Sugiyama, I. Yagi, K. Uosaki, Chem. Phys. 205 (1996) 269–275.
[130] A. Peremans, A. Tadjeddine, P. GuyotSionnest, Chem. Phys. Lett. 247 (1995) 243–248.
[131] C.F. Mai, C.H. Shue, Y.C. Yang, L.Y.O. Yang, S.L. Yau, K. Itaya, Langmuir 21 (2005) 4964–4970.
[132] K. Nishimura, R. Ohnishi, K. Kunimatsu, M. Enyo, J. Electroanal. Chem. 258 (1989) 219–225.
[133] F. Dederichs, K.A. Friedrich, W. Daum, J. Phys. Chem. B 104 (2000) 6626–6632.
[134] G.Q. Lu, A. Lagutchev, D.D. Dlott, A. Wieckowski, Surf. Sci. 585 (2005) 3–16.
[135] P. Jakob, B.N.J. Persson, J. Chem. Phys. 109 (1998) 8641–8651.
[136] A. Peremans, A. Tadjeddine, J. Electroanal. Chem. 395 (1995) 313–316.
[137] S. Watanabe, J. Inukai, M. Ito, Surf. Sci. 293 (1993) 1–9.

This page intentionally left blank

CHAPTER 7

Nanolayer Analysis by X-Ray Absorption Fine Structure Spectroscopy

Toshiaki Ohta

Ritsumeikan University, Kusatsu, Japan

7.1 Fundamental Aspects of XAFS

Atomic absorption spectroscopy at energies near and above the core-level binding energies of the atom is called X-ray absorption spectroscopy (XAS). Specifically, in chemistry, it is called XAFS (X-ray absorption fine structure) because of spectral fine structures that reflect on chemical state and local atomic structure of a specified atomic species. X-ray absorption is associated with the probability of electronic transitions from a core level to empty orbitals and continuum states. In general, X-ray absorption transition probability $\sigma_{i\to f}$ is expressed by Fermi's golden rule with the dipole approximation, the same as UV-visible absorption spectra [1].

$$\sigma_{i\to f} \propto \left| \int \varphi_f \, \vec{e} \cdot \vec{r} \, \varphi_i d\tau \right|^2 \tag{7.1}$$

where φ_i, φ_f are wave functions of initial and final states, respectively. $\vec{e}$ is the X-ray polarization vector and $\vec{r}$ is the position vector. Unlike UV-visible spectra, φ_i is a core orbital, highly localized around the atomic nucleus. As a result, the atomic selection rule, $l \to l \pm 1$ (l is the orbital quantum number), holds for XAFS with a good approximation. This means that transitions $s \to p$, and $p \to s, d$ are only allowed. Eq. (7.1) tells us also that the transition probability is the largest when the transition moment is aligned to the electric polarization vector.[1]

As shown in Fig. 7.1, XAFS spectrum shows a sharp rise at the core electron binding energy and decay with fine structures. XAFS is expediently divided into two energy regions: X-ray absorption near edge structure (XANES) and extended X-ray absorption fine structure

[1] XANES is also called, **NEXAFS** (Near edge XAFS), especially for organic molecules in the soft X-ray region. In this chapter, we use XAFS instead of XAS, and XANES instead of NEXAFS.

Nanolayer Research. http://dx.doi.org/10.1016/B978-0-444-63739-0.00007-4

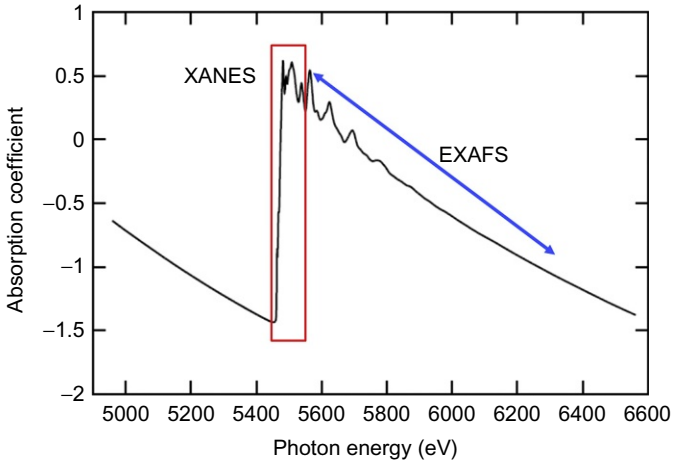

Fig. 7.1
V *K*-XAFS spectrum of vanadium foil [2].

(EXAFS). They have the same physical origin, but the information obtained is different from each other. Here, the basic aspects of XANES and EXAFS are briefly described.

7.1.1 XANES

XANES spectra correspond to the electronic transitions from a core orbital to empty orbitals below the ionization threshold and continuum states above that by 30–50 eV. As a typical example, Si *K*-XANES spectra of several Si compounds are shown in Fig. 7.2, where spectral profiles change dramatically depending on the nearest neighbor atoms. This clearly demonstrates that XANES spectra reflect the local environment around an X-ray absorbing atom.

K-edge XANES spectra are the most typical ones, which are associated with the transition from 1*s* orbital to *np* orbitals due to the dipole selection rule. Since 1*s* orbital is highly localized, the spectral profile should reflect directly on the unoccupied partial density of states (PDOS). This is true for the case of a metal, since the core hole is well screened by free electrons, while that of an insulator reflects fairly distorted PDOS due to the core hole Coulomb attraction. The absorption edge is defined as the ionization threshold to continuum states. Metals give a broadband starting from the ionization threshold, while insulators or semiconductors give sharp peak(s) below the threshold and broadband above the threshold. Fig. 7.3 shows S *K*-XANES spectra of several sulfur compounds [3]. The peak energy shifts to higher energy with the oxidation state. Each spectrum also has a specific profile depending on its functional group, which is useful information for identifying a compound.

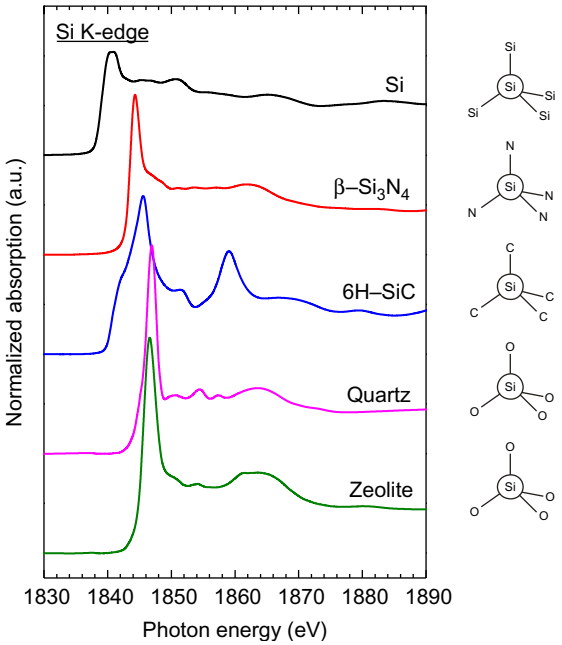

Fig. 7.2

Si *K*-XANES spectra of several Si containing materials. Spectral profile changes depending primarily on the nearest neighbor atoms [2].

XANES is also sensitive to the coordination symmetry. For the octahedral coordination with O_h symmetry, there is no mixing between 3d and 4p orbitals, while the mixing occurs for the tetrahedral coordination with T_d symmetry, and also for the case of symmetry breaking of O_h by distortion. Fig. 7.4A shows V *K*-XANES spectra of several vanadium oxides with different coordination symmetries. No pre-edge peak appears for VO with O_h symmetry, but the pre-edge peak gains its intensity with the extent of distortion. V_2O_5 has a square pyramidal structure, and the strong mixing of 3*d* and 4*p* orbitals exhibits a sharp pre-edge peak [4]. Fig. 7.4B shows the energy shift with oxidation state. Note that the slope changes depending on the absorption features. It is due to the fact that energies of the pre-edge features do not directly correspond to the oxidation state because both the energies of initial and final states are affected by the chemical state [4].

K-edge XANES spectra of organic molecules have been extensively studied and used for characterization of organic functional materials, following the pioneering work by J. Stöhr, who referred to them as NEXAFS [5]. Typical spectral profile consists of sharp π^* peak(s), if the molecule has unsaturated bonds, and broad σ^* band(s), whose energies are almost the same for the same functional group. A typical example is shown in Fig. 7.5 [6], which exhibits C *K*-XANES spectral change in the process of polyimide formation as a function of annealing time. The spectra clearly show how starting materials change their structures and finally form polyimide film.

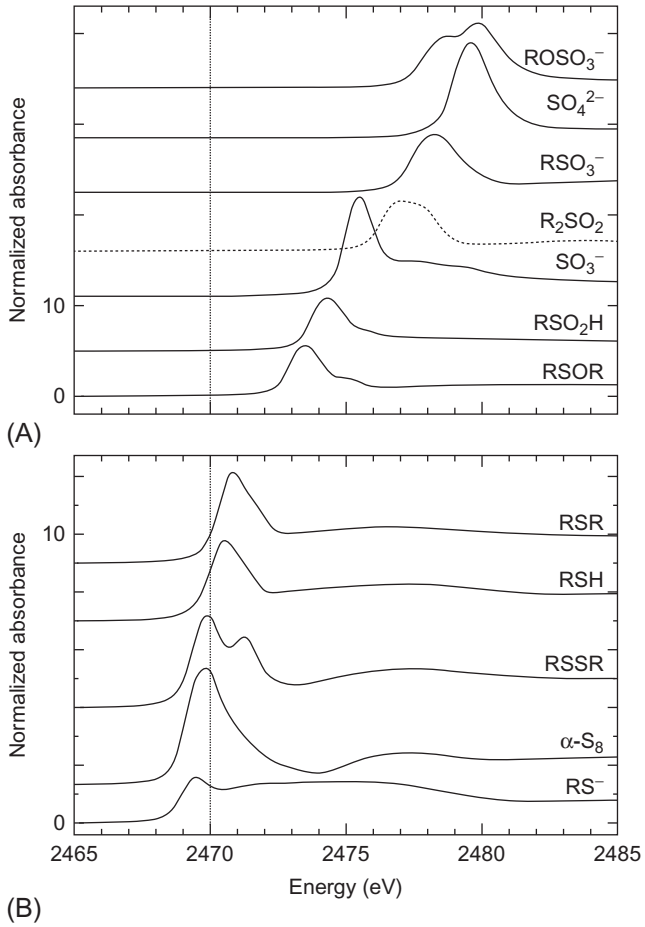

Fig. 7.3

S *K*-XANES spectra of several S containing compounds, where R denotes alkyl group. Sulfur has a valence from −2 to +6 and the peak shifts with the oxidation state [3]. *Copyright © 2001, American Chemical Society.*

If sample molecules are aligned to a specific direction, its *K*-edge XANES spectrum exhibits distinct polarization dependence. As described in the previous section, the peak intensity can be expressed by the Fermi's golden rule. When we focus on the molecular orientation, Eq. (7.1) can be rewritten as Eq. (7.2),

$$I \propto \left| \vec{e} \cdot \int \varphi_p \vec{r} \varphi_{1s} d\tau \right|^2 = \cos^2\delta \cdot M_{1s\to p}^2 \tag{7.2}$$

where $M_{1s\to p}$ is the transition matrix element from $1s$ to np orbital and δ is the angle between the electric vector of the incident X-ray and the transition moment for a specific peak. The intensity attains to the maximum when the $\boldsymbol{E}$-vector is parallel to the transition moment ($\delta = 0$). Since π^*

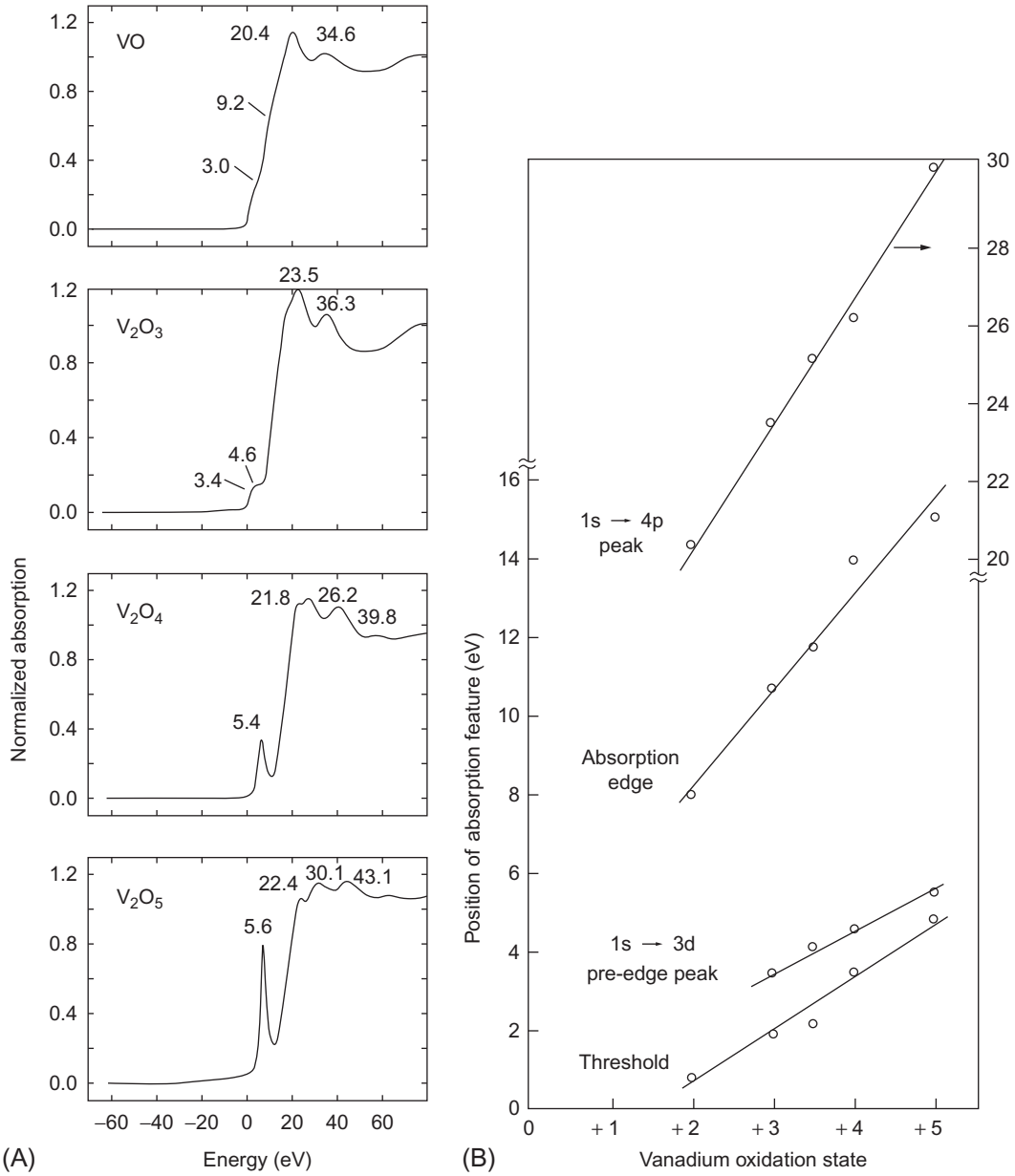

Fig. 7.4

(A) V *K*-XANES spectra of several vanadium oxides. (B) Energy shifts of several peaks and absorption edge as a function of the oxidation state [4]. *Copyright © 1984, American Physical Society.*

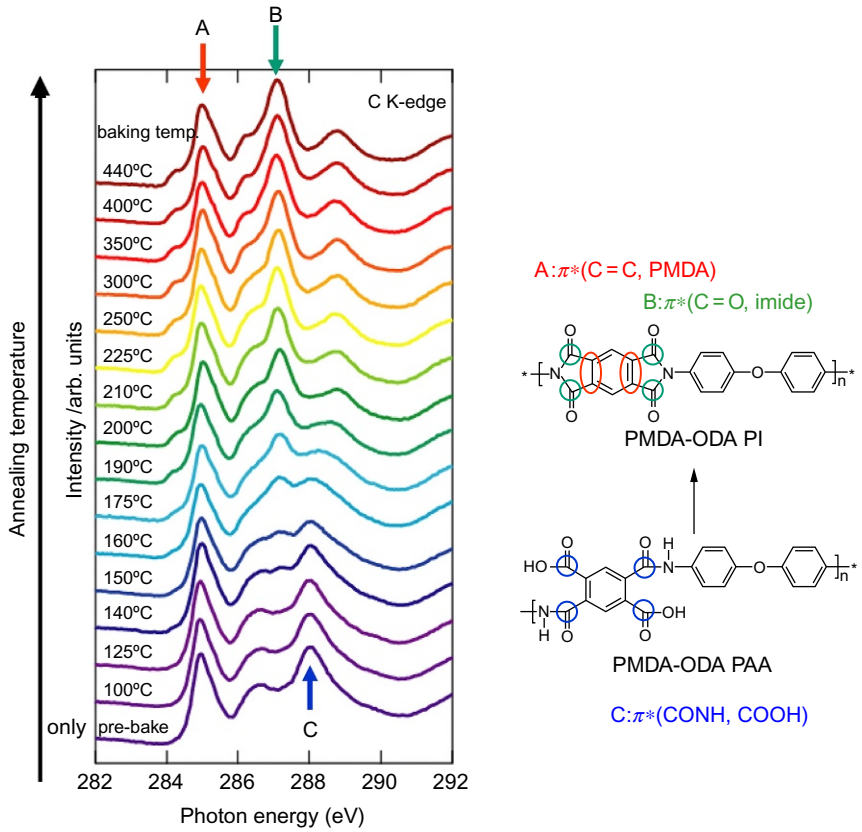

Fig. 7.5

Thermal annealing of PMDA (pyromellitic dianhydride)-ODA (oxidianiline) PAA (polyamic acid) to synthesize PI (polyimide) film monitored by C *K*-XANES spectral change. Arrows indicate the assigned functional groups in the polymer.

and σ^* transitions have the transition moments perpendicular and parallel to the chemical bond, respectively, the polarization dependence of the spectra gives the information of the orientation of the molecular axis if the specific peak can be assigned. A typical example is shown in Fig. 7.6 for C *K*-XANES of a single crystalline graphite [7].

In general, σ^* resonance is observed as a broadband. In the molecular orbital scheme, it is a transition to an antibonding orbital, and its energy becomes higher as the corresponding bond distance is shorter. In the scattering scheme, the resonance takes place when half of the de Broglie wavelength of the ejected electron is coincident with the atomic distance. In both schemes, the energy of the σ^* resonance is related to the interatomic distance. Empirical relations for several atomic pairs were obtained from experimental σ^* resonance energies, which are useful for the rough estimation of interatomic distances. Fig. 7.7 shows C *K*-XANES

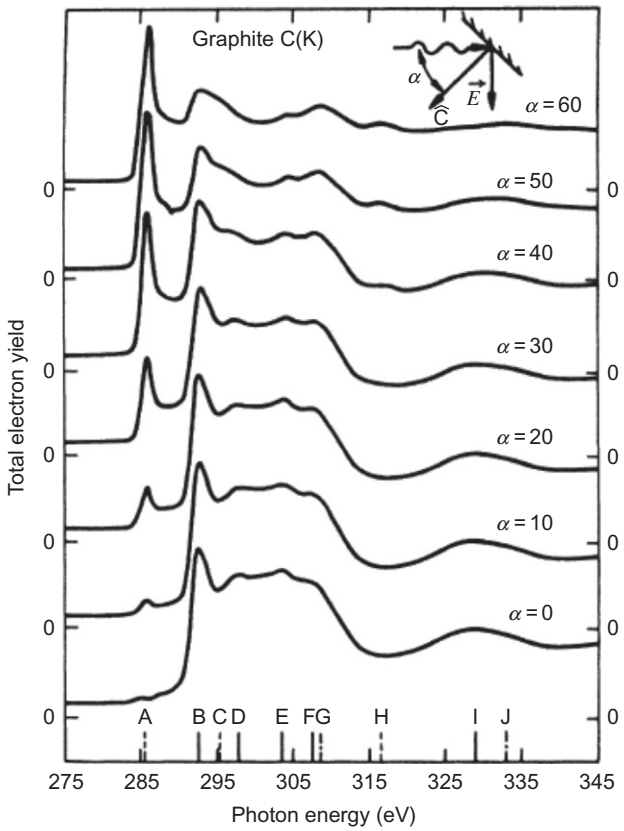

Fig. 7.6

C *K*-XANES spectra of single crystal graphite at various incidence angles α between the surface normal and the electric vector of X-rays [7]. Lines at the bottom are assigned transitions for π symmetry (dashed lines) and for σ symmetry (solid lines). *Copyright © 1986, American Physical Society.*

of acetylene, ethylene, and ethane, which indicates how the σ^* resonance shifts to lower energy with elongation of the C—C bond-length.

For the study of the electronic, magnetic, and geometric structures of transition metals and their compounds, *L*-edge XAFS can be effectively used, where $2p$ electron is excited to unfilled d orbitals. The created $2p^5$ core hole has an orbital angular momentum $L = 1$, which is coupled with the spin angular momentum $S = 1/2$ to produce $J = 3/2$ and $J = 1/2$ final states. These states are observed as lower energy $L_{2/3}$-edge and higher energy $L_{1/2}$-edge peaks. When we consider the electronic structures of the final states, $2p^5$ and $3d^{n+1}$, there are many possible configurations depending on the number of d electrons and spin states [9]. Accordingly, $L_{2,3}$-edge spectra are much more complicated than *K*-edge spectra, but they provide a wealth of information. Fig. 7.8 shows simulated spectral profiles of $L_{2,3}$-edge XANES [10]. Note that the

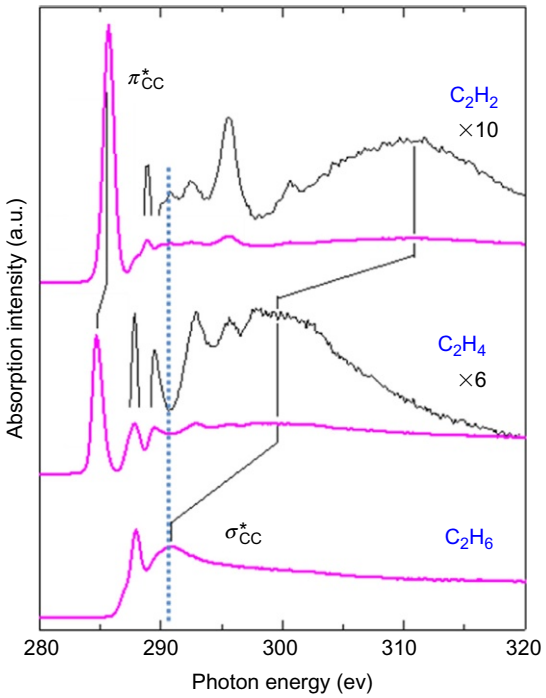

Fig. 7.7

C *K*-XANES spectra of acetylene, ethylene, and ethane. The C–C bond distances are 1.203, 1.337, and 1.533 Å for acetylene, ethylene, and ethane, respectively. In contrast, corresponding σ^* resonances are 312, 300, and 291 eV [8]. *Copyright © 2005, Elsevier B.V.*

profiles of high spin and low spin states are significantly different from each other. These spin structures cannot be observed in K-edge XAFS.

Circularly polarized X-ray is the electromagnetic wave propagating with rotating electric field and interacts with the angular momenta of atoms. Thus the circularly polarized X-ray absorption additionally requires a new selection rule, $\Delta m = \pm 1$ for magnetic quantum number m: $\Delta m = +1$ for right and $\Delta m = -1$ for left circularly polarized X-rays. If a metal or its compound is ferromagnetic, there exists an imbalance in empty spin-up and spin-down states. Accordingly, we can observe circular dichroism for a ferromagnetic sample, since the transition probability from the p state to the unfilled d states excited by the right circularly polarized X-ray is different from that excited by the left circularly polarized X-ray. This is called XMCD (X-ray magnetic circular dichroism), which is a very effective tool for studying magnetic properties of ferromagnetic materials [11,12]. It has several advantages, such as being element-specific and surface sensitive by adopting the electron yield mode as described later. It also provides unique information about spin orientation from the sign of XMCD signal, and separate orbital and spin moments from "magnetic sum rules" [13–15].

Fig. 7.9 schematically shows the origin of XMCD.

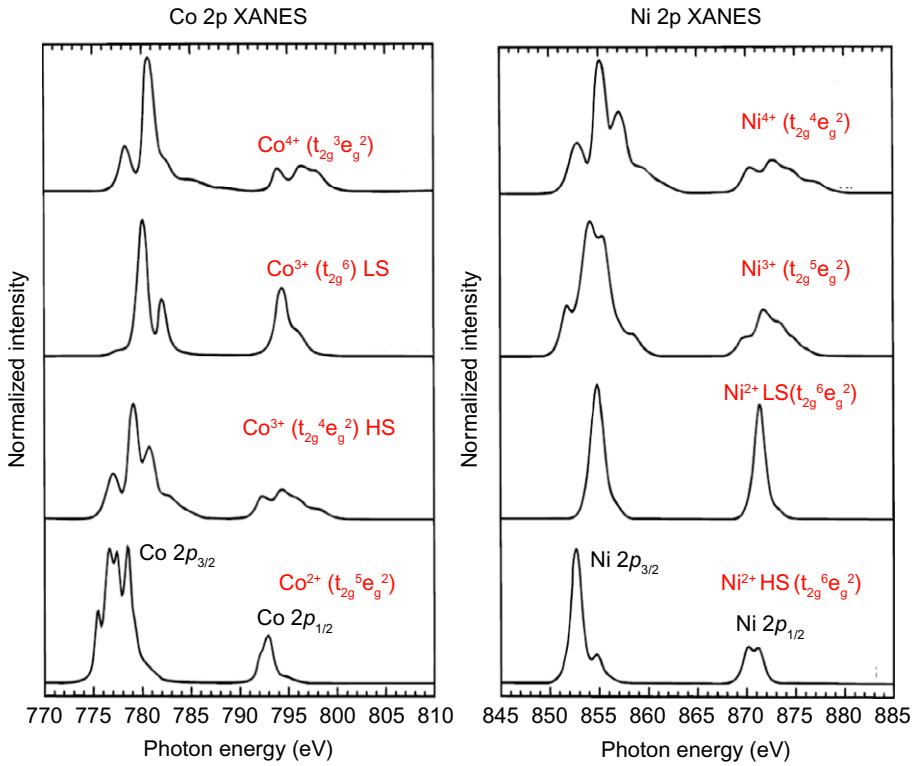

Fig. 7.8

Co and Ni *L*-XANES calculated spectra for Co and Ni compounds with different ionic charges. HS and LS indicate high and low spin Co and Ni ions, respectively [10]. *Copyright © 2000, reproduced by permission of the Electrochemical Society.*

7.1.2 EXAFS

It has been known since the 1930s that X-ray absorption spectrum exhibits fine structures extending up to 1000 eV from the ionization threshold, but has been neglected as a physical phenomenon until the 1970s.

In the early 1970s, Lytle, Stern, and Sayers developed a new analytical approach based on the scattering theory to interpret the fine structures [16–18]. They called this method EXAFS and demonstrated that the local structure around an X-ray absorbing atom can be obtained as a radial distribution function by using Fourier transformation of the fine structures. Their EXAFS theory has stimulated both theoreticians and experimentalists in the world, who contributed to the improvements of the analytical methods and experimental developments [19–21].

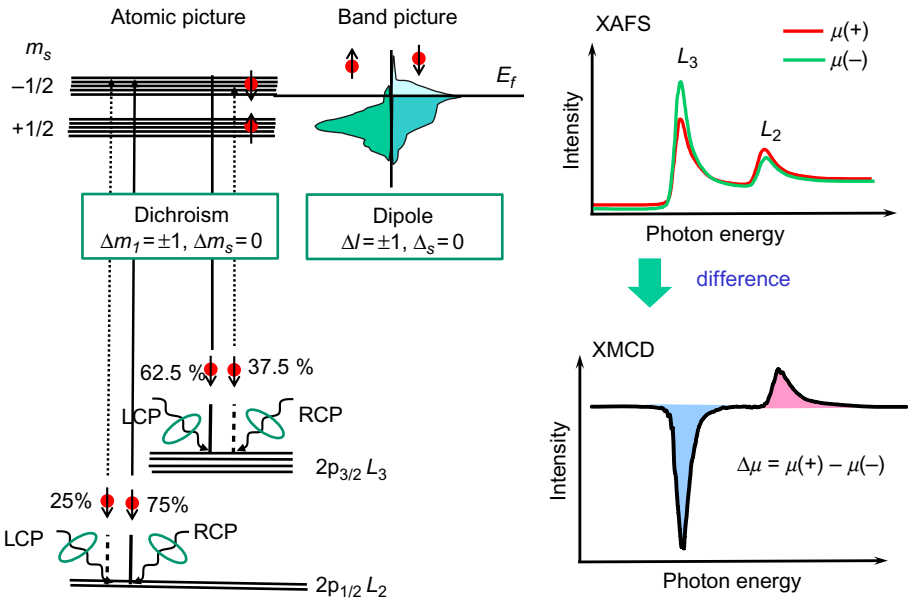

Fig. 7.9

Left: Schematic illustration of the origin of XMCD by the simple two-step dichroism model. In the first step, circularly polarized photons are absorbed by the spin-orbit split 2*p* core shell, leading to the excitation of spin-polarized electrons. In the second step, spin-polarized electrons are selectively analyzed by the spin imbalanced valence shell. Right: *L*-XANES spectra excited by right and left circularly polarized photons. By subtracting $\mu(-)$ from $\mu(+)$, XMCD spectrum can be obtained.

The X-ray absorption coefficient μ is proportional to the photoionization cross section as expressed in Eq. (7.1). Here, the oscillatory part is extracted and expressed as a function of wave vector, $k\left(=\sqrt{2m(E-E_0)}/\hbar\right)$, as follows,

$$\chi(k) = \frac{\mu(k) - \mu_0(k)}{\mu_0(k)} = \frac{1}{k}\sum_j A_j(k)\sin\left[2kR_j + \phi_j(k)\right] \tag{7.3}$$

where $E - E_0$ is the kinetic energy of the ejected photoelectron. $\mu_0(k)$ is an atomic absorption coefficient. R_j, $\phi_j(k)$ are the distance from the X-ray absorbing atom to the *j*th coordinated atom(s) and the phase shift. The amplitude function for the *j*th coordination, $A_j(k)$ is expressed as follows,

$$A_j(k) = S_0^2 \frac{N_j^*}{R_j^2}\left|f_j(k)\right|\exp\left(-2\sigma^2 R_j{}^2\right) \tag{7.4}$$

where S_0^2 is a reduction factor taking account of multiple excitations that do not contribute EXAFS oscillation. $f_j(k)$ is a backscattering amplitude, which is larger and decays slowly with k

in case of heavy atoms, smaller and decays rapidly with k in case of light atoms. An exponential term is introduced to take into account thermal and static disorders. σ^2 is called the Debye-Waller factor, which expresses the mean square relative displacement. N_j* is called the effective coordination number, which is expressed as follows for K-edge EXAFS:

$$N_j^* = 3\sum_{i=1}^{N_j} \cos^2\theta_i \tag{7.5}$$

where θ_i is the angle between the position vector $\boldsymbol{R}_i$ and X-ray electric vector **e** for a randomly oriented sample, $N_j^* = N_j$. But for an oriented sample, N_j* changes depending on the polarization angle, which gives information about the orientation of a bond.

Eq. (7.3) shows that the EXAFS function $\chi(k)$ is a sum of sine functions, indicating that Fourier transformation of Eq. (7.3) gives a radial distribution function with peaks at $R_j + \phi_j$. In principle, we can determine the distance R_j, since the phase shift, ϕ_j values can be theoretically obtained quite reliably. However, it is not straightforward for real samples composed of surrounding atoms with various distances. In general, the part of a specific bond is extracted with the Fourier-filtering technique and is transformed back to the k-space, which shows a simple sinusoidal EXAFS function by a single scattering atom. The analytical process is schematically shown in Fig. 7.10.

The scattering atom can be easily estimated from the envelope profile. The bond distance R_j, coordination number N_j*, and Debye-Waller factor σ_j^2 can be determined by the least square fitting of the EXAFS function. The software packages for EXAFS analysis have been well developed, and even beginners of EXAFS can analyze EXAFS spectra by using them. However, one should be careful to check whether the results obtained are chemically reasonable.

7.2 Experimental Development of XAFS

7.2.1 Electron Yield and Fluorescent Yield Methods

XAFS spectra can be measured for every element on the periodic table, regardless of the sample's state; gas, liquid, and/or solid. They can also be applied for noncrystalline and disordered materials. However, XAFS is inherently not surface sensitive because X-rays fairly penetrate in matter. For application of XAFS to the structure analysis of nanolayers, special techniques are required, which have been dramatically developed by the advent of synchrotron radiation. It is an ideal light source of XAFS due to its unique properties: highly intense photon density, wide energy range from infrared to X-rays, highly directed beam like laser, variable polarization, pulsed structure, etc.

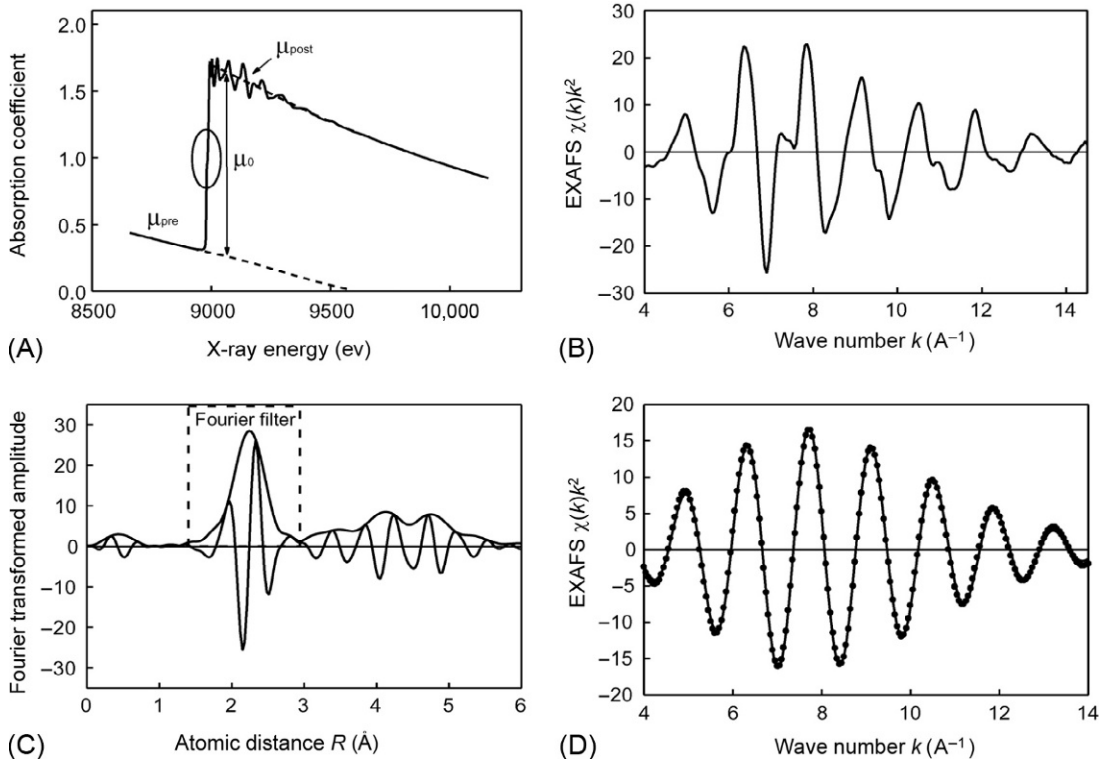

Fig. 7.10

Analytical process of an EXAFS spectrum [22]. (A) Experimentally measured Ni *K*-XAFS spectrum $\mu(E)$ from a Ni foil, from which pre-edge, and post-edge smooth functions, μ_{pre}, μ_{post} are estimated. E_0 is also determined, typically as the energy of the maximum derivative of $\mu(E)$. (B) EXAFS oscillations $\chi(E)$ is extracted from (A) by using μ_{pre}, μ_{post} and rescaled to $\chi(k)$ as a function of wave number, $k\left(=\sqrt{2m(E-E_0)}/\hbar\right)$. Sometimes, $\chi(k)$ is multiplied by k^n to emphasize the high k region. (C) Fourier transformation of the EXAFS function $\chi(k)$, which corresponds to the radial distribution function. (D) Back Fourier transformed spectrum from the first peak filtered out in (C). Dots are experimental plots and solid line is a curve-fitting from the structure parameters, R, σ^2, N^*, etc.

X-ray absorption causes photoelectron ejection, and core holes created as a result are quickly filled by electrons in upper levels. Energies gained by transitions from an upper level to a core orbital are compensated for either radiatively with fluorescent X-ray emission or nonradiatively with Auger electron emission. Nonradiative decay rate dominates for the lower Z elements than Zn for K-shell absorption and for almost all elements for L-shell absorption.

Photoelectrons and Auger electrons from the X-ray absorbing atom in the bulk collides with surrounding atoms elastically and/or inelastically, and only those reaching surface can come out from the surface. Electrons interact with solid much stronger than photons; thus most

electrons lose energies by inelastic collisions and only part of the electrons near the surface can escape.

Auger electron yield (AEY) and partial electron yield (*PEY*) which collect only electrons with higher kinetic energy, are surface-sensitive detection modes. On the other hand, total electron yield (TEY), which collects all electrons including secondary electrons, is less surface sensitive because most electrons are secondary electrons coming out after inelastic collisions. Typical photoelectron distribution curve and the kinetic energy dependence of the electron escape depth [23,24] are shown in Fig. 7.11. For the AEY mode, we need an electron energy analyzer to collect Auger electrons with a specific kinetic energy, while for the PEY mode, we adopt a simple assembly of the electron detection system composed of an MCP (microchannel plate) and a retarding grid, which rejects secondary electrons.

Consider the Auger yield in more detail. The number of electrons emitted from a layer dz in depth z in the sample can be expressed as Eq. (7.6), when X-rays with energy E impinge on a sample surface with the incident angle θ and electrons are emitted into vacuum. A schematic layout is given in Fig. 7.12.

$$dI_e(E,z) \propto I_0(E)\exp\left[-\mu_{\text{tot}}(E)\frac{z}{\sin\theta}\right]\mu_x(E)\varepsilon_e\exp\left[-\frac{z}{\lambda(E_k)}\right]dz \tag{7.6}$$

where $\mu_{\text{tot}}(E), \mu_x(E)$ are the absorption coefficients of the sample and of the element x at the X-ray energy E, respectively. $\lambda(E_k)$ is the escape depth of electrons with kinetic energy E_k and ε_e is the Auger probability. Eq. (7.6) indicates how incident photons $I_0(E)$ are lost in the

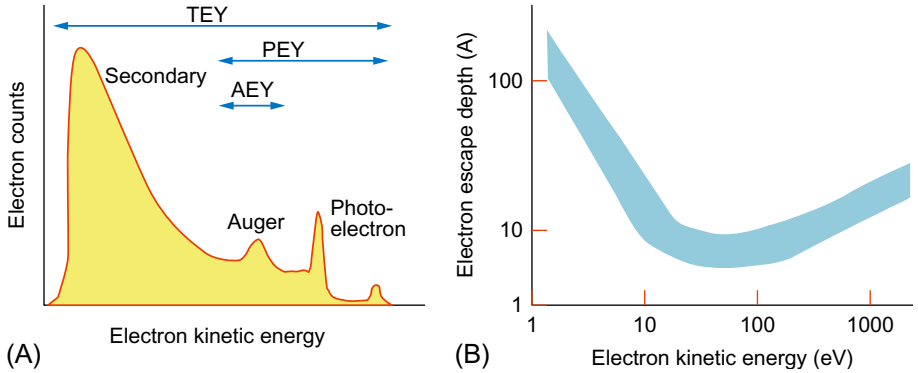

Fig. 7.11

(A) Typical photoelectron energy distribution curve, composing of photoelectron peaks, Auger bands, and secondary electron feature. Double-headed arrows indicate the energy regions for three electron yield modes. (B) Electron escape depth in solids as a function of electron kinetic energy. Depending on the density of solid, it has variability as shown by shaded area.

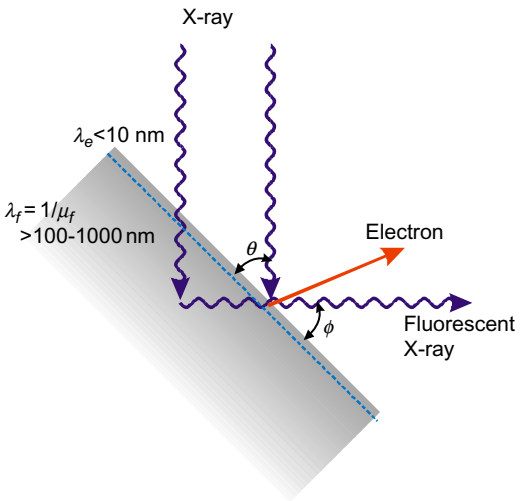

Fig. 7.12
Experimental layout of the electron and X-ray fluorescence yield modes. λ_e is the electron escape depth, depending on the kinetic energy, as shown in Fig. 7.11B. λ_f is the X-ray penetration depth, which is an inverse of X-ray absorption coefficient.

process of reaching an atom x (the first exponential term), and how ejected electrons from the atom x are lost in the process of reaching the surface (the last exponential term).

By integrating Eq. (7.6) along z from sample surface to infinity, we obtain the following relation.

$$I_e(E) \propto I_0(E)\mu_X(E)\varepsilon_e(E) \cdot \frac{1}{\mu_{\text{tot}}(E) + \dfrac{\sin\theta}{\lambda(E_k)}} \propto \mu_X(E) \tag{7.7}$$

Since the penetration depth of X-rays, $1/\mu_{\text{tot}}(E)$, is much longer than the electron escape depth, $\lambda(E_k)$, the second term of the denominator is dominant, which is independent of the X-ray energy. As a result, electron yield $I_e(E)$ turns out to be proportional to the absorption coefficient of the element x, $\mu_x(E)$.

Thus the electron yield is a simple and straightforward technique to get the surface-sensitive absorption spectra.

On the other hand, let's consider the fluorescence yield mode detecting the fluorescent X-rays of the energy E_f. This mode is called PFY (partial fluorescence yield), in contrast with the TFY (total fluorescence yield), which collects all the fluorescent emission. For the PFY mode, the number of fluorescent X-rays can also be expressed with an equation similar to Eq. (7.6), as follows,

$$dI_f(E,z) \propto I_0(E)\exp\left[-\mu_{\text{tot}}(E)\frac{z}{\sin\theta}\right]\mu_x(E)\varepsilon_e\exp\left[-\mu_{\text{tot}}(E_f)\frac{z}{\sin\varphi}\right]dz \tag{7.8}$$

where we define the direction of fluorescent X-rays from the surface plane, ϕ, as shown in Fig. 7.12. By integrating the equation along x, the following equation is obtained.

$$I_f(E) \propto I_0(E)\varepsilon_X(E)\cdot\frac{\mu_X(E)}{\mu_{tot}(E)+\mu_{tot}(E_f)\dfrac{\sin\theta}{\sin\phi}} \tag{7.9}$$

Here, $\mu_{\text{tot}}(E)(=\mu_x(E)+\mu_{\text{others}}(E))$ is comparable with $\mu_{\text{tot}}(E_f)$. Since E_f is constant, $\mu_{\text{tot}}(E_f)$ is constant, while $\mu_{\text{tot}}(E)$ changes with E. However, if the element x is very dilute $(\mu_x(E) << \mu_{\text{others}}(E))$, $I_f(E)$ is nearly proportional to $\mu_x(E)$, since $\mu_{\text{others}}(E)$ does not change around the absorption edge of the element x. Furthermore, if one sets the experimental layout with the normal incidence and glancing emission ($\sin\theta/\sin\phi \gg 1$), the constant second term is dominant in the denominator, prevailing over $\mu_{\text{tot}}(E)$. Consequently, $I_f(E)$ is again nearly proportional to $\mu_x(E)$.

Otherwise, the fluorescence yield is not proportional to $\mu_x(E)$, but is deformed by the so-called self-absorption effect [25,26].

Recently, another way of overcoming the self-absorption effect was proposed especially for metal oxide samples [27]. This is the way to monitor not the fluorescence from the element x, but that from oxygen, which appears as a negative signal, and to take the inverse of the signal.

This process can be expressed as the following equation.

$$I(E) \propto I_0(E)\varepsilon_X(E)\cdot\frac{\mu_O(E)}{\mu_{\text{tot}}(E)+\mu_O(E_f)\dfrac{\sin\theta}{\sin\phi}} \tag{7.10}$$

where $\mu_O(E)$ and $\mu_O(E_f)$ are the absorption coefficient of oxygen at the energy E around the absorption edge of the element x and at the energy E_f of O Kα.

By taking the inverse of Eq. (7.9),

$$\frac{I_0(E)}{I(E)} \propto \frac{\mu_{\text{tot}}(E)+\mu_O(E_f)\dfrac{\sin\theta}{\sin\phi}}{\varepsilon_X(E)\cdot\mu_O(E)} = A(\mu_{\text{tot}}(E)+B) \tag{7.11}$$

where A and B are constants. If the sample contains sufficient amount of element x, $I_0(E)/I(E)$ is proportional to the absorption coefficient of the element x. This method is called IPFY (inverse partial fluorescence yield) mode and can be effectively applied for L-edge XANES spectral measurements of 3*d* metal oxide samples. A typical example is shown in Fig. 7.13.

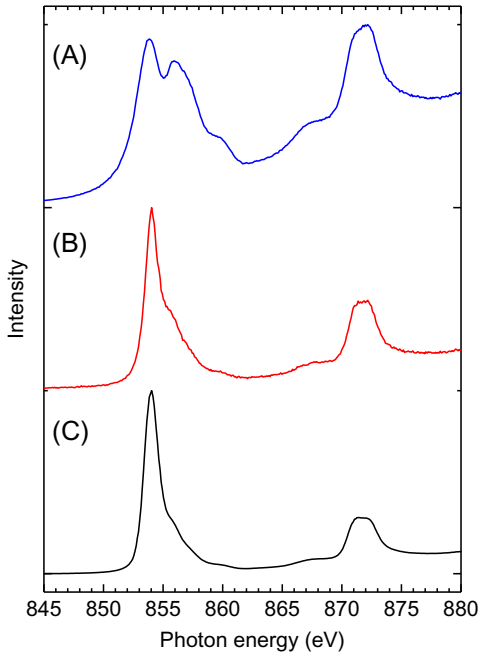

Fig. 7.13

Ni *L*-edge XANES spectra of NiO taken by (A) PFY, (B) IPFY, and (C) TEY modes. TEY mode gives a nearly correct spectrum, while the spectrum by PFY mode is significantly deformed by the self-absorption effect. This is fairly recovered by IPFY, in which Ni *L*-XANES spectrum is taken with O *Kα* emission [2].

7.2.2 Depth-Resolved XAFS for Nanolayers

The PEY, TEY, and FY modes are quite common for XAFS experiments in the soft X-ray region, in which the penetration depth of X-rays is relatively short. Typically it is about 1000 Å at $h\nu = 1$ keV. Simultaneous use of these three modes provides a useful depth profiling method. The PEY mode is generally performed by the set of a retarding grid and an MCP. It works successfully in the low-energy, soft X-ray region below 1000 eV, but it does not provide a surface-sensitive PEY spectrum above 1000 eV with the conventional setup due to mixing of FY spectra. A special setup to avoid FY spectra is necessary. One example is shown in Fig. 7.14A [28], which almost completely suppresses the mixing of FY spectra in the higher energy region above 1000 eV. A demonstrative example is shown for a silicon crystal covered with silicon oxide in Fig. 7.14B, where the surface-sensitive PEY gives exclusively a spectrum of SiO_2, while PFY with SDD (silicon drift detector) gives that of bulk Si, and TEY with a leak current gives a spectrum intermediate between Si and SiO_2.

Another application is characterization of multiwall carbon nanotube (MWCNT) grown by the surface decomposition of SiC [29], as shown in Fig. 7.15. The TEY mode spectra exhibit a

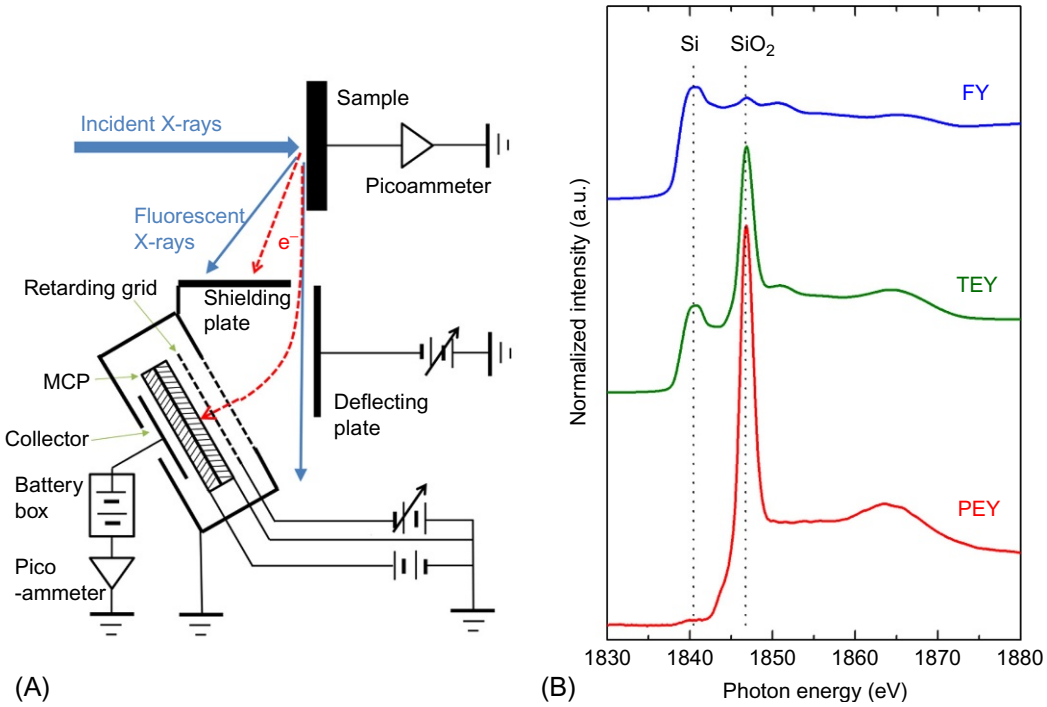

Fig. 7.14

(A) Experimental setup for the PEY mode for high-energy, soft X-ray XAFS, in which only electrons come into the MCP. (B) Si *K*-XANES spectra of an Si crystal covered by 8-nm-thick oxide, taken with FY, TEY, and PEY modes [28].

distinct polarization dependence, indicating that the MWCNT array stands upright. In contrast, the PEY mode with retarding voltage of 240 V gives almost no polarization dependence. This is due to the fact that the top of the MWCNT is covered by carbon nanocap, composed of hemispherical graphene sheets (see inset of Fig. 7.15A), and that their angular dependence should be small.

Order parameter (OP), defined as $(I\perp - I_{\parallel})/(I\perp + I_{\parallel})$, was determined to be 0.38, which is much higher than that of CNT grown by the CVD (chemical vapor deposition) method (0.08–0.145). Thus the polarization dependence of C *K*-XAFS revealed that the MWCNT grown from SiC is highly oriented.

Quantitative depth analysis can be performed by measuring the emission angle dependence of Auger electrons. Since the electron escape depth λ_e of Auger electrons is constant, electrons emitted in the glancing angle come out only from surface, but those in the normal direction come both from surface and bulk. Fig. 7.16A illustrates how the probing depth changes depending on the emitting direction. The probing depth is expressed as $\lambda_e \times \sin\theta$, where θ is the emitting angle with respect to the surface plane. More precisely, the relation between θ and λ_e is

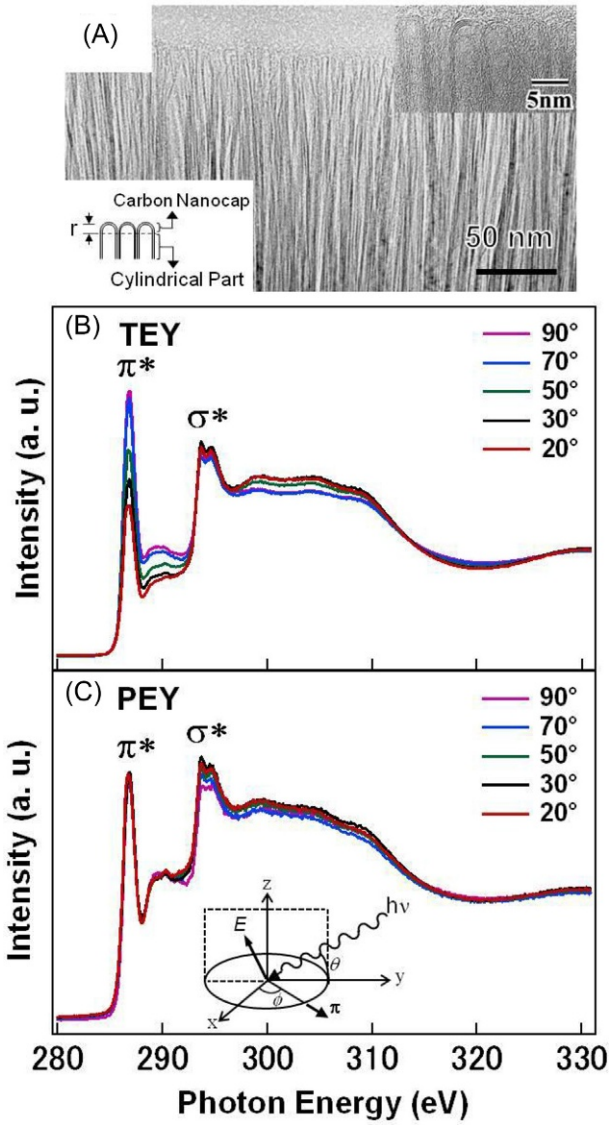

Fig. 7.15

(A) Cross-sectional TEM image of the CNTs. The upper inset shows a close-up image of the top of the CNTs, and the lower inset shows their schematics. (B) TEY and (C) PEY C *K*-edge NEXAFS spectra of the CNTs grown by the surface decomposition of the SiC obtained at different incidence angles. The inset in (C) shows the incident geometry of the vector orbitals for vertical CNTs (axis along *z*) on the sample surface (parallel to the *x*–*y* plane) with respect to the incident X-ray beam ($h\nu$) (in the *y*–*z* plane) and the electric field vector *E*, which remained perpendicular to the incident X-ray beam. The incidence angle,θ, is defined as the angle between the X-ray beam and the sample surface [29].

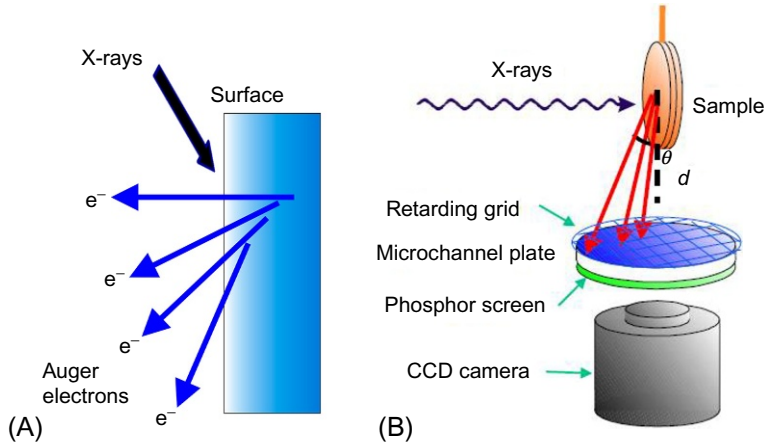

Fig. 7.16

Schematic drawing of (A) the principle of depth-resolved analysis and (B) the experimental layout. The emitted Auger electrons with various θ are simultaneously collected with an imaging type detector consisting of an MCP, phosphor screen, and a CCD camera. Note that a retarding voltage should be applied between the sample and detector to avoid secondary electrons.

experimentally determined by fitting the thickness dependence of the edge jump for a bilayer system. Thus, in principle, we can obtain layer by layer XAFS spectra from the analysis of angular dependence of the Auger electrons by using the experimental setup, as shown in Fig. 7.16B [30,31].

A typical example is an application to surface magnetic layers [31–34]. Magnetic thin films exhibit interesting phenomena depending on the thickness. Understanding the magnetic properties at surface and interface is important in developing actual magnetic materials. By using circularly polarized X-rays as an incident light and measuring XAFS spectra of a sample magnetized with one and another direction, we can obtain XMCD spectra. Furthermore, combining this with the depth-resolved technique, we can get information of magnetic properties of surface and interface layers.

Fig. 7.17 shows a series of Fe $L_{2,3}$ XMCD spectra of 3 ML thick and 7 ML thick Fe on Cu(100) samples as a function of effective escape depth. XMCD spectra were taken at the remnant magnetization at 130 K with the normal incidence. Observation of significant XMCD spectra for both cases indicates the perpendicular magnetization. However, the probing depth dependence is different from each other. For 3 ML Fe/Cu(100), XMCD profile is almost the same irrespective of the escape depth, while for 7 ML/Fe/Cu(100), the amplitude decreases as λ_e increases. These results suggest that Fe is uniformly magnetized for 3 ML Fe case, but the inner layer is nonmagnetized by increasing the Fe layer. Detailed magnetic structure can be analyzed by simulation. We can consider each spectrum as a sum of contributions from several

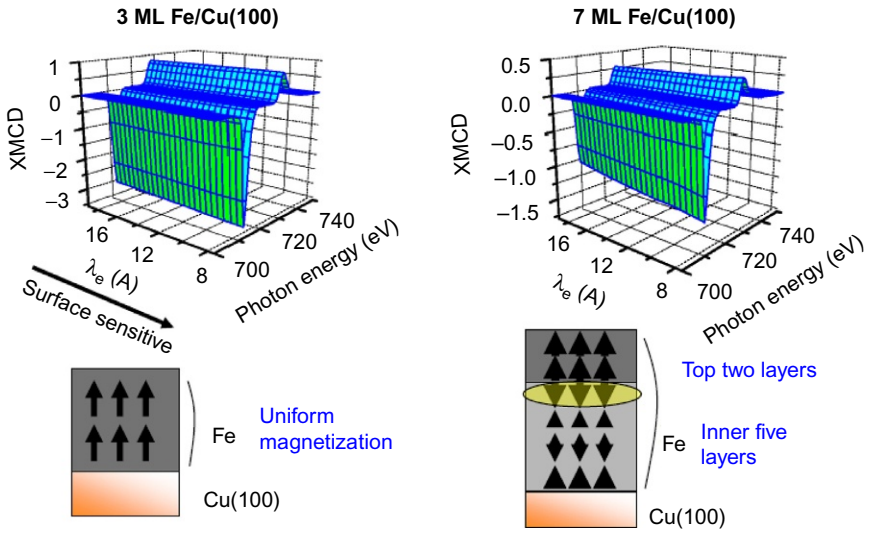

Fig. 7.17
Fe *L*-edge XMCD spectra from 3 ML and 7 ML thick Fe/Cu(100) films taken with various probing depths together with the corresponding magnetic structure models.

layers. It has been revealed that for 7 ML Fe/Cu(100), the top two layers are perpendicularly magnetized, but the inner layers are in the spin density wave (SDW) state antiferromagnetically coupled with the top layer.

Compared with soft X-ray, hard X-ray above 4 keV is highly penetrating in solid, and the transmission mode is generally adopted for absorption spectroscopy. Thus, to obtain XAFS information of surface and interface, measurement at glancing angles is often used.

The refraction index n of X-rays is expressed as follows.

$$n = 1 - \delta - i\beta, \quad \delta = \frac{r_e \lambda^2}{2\pi} N, \quad \beta = \frac{\lambda \mu}{4\pi} \tag{7.12}$$

where r_e is the classical electron radius, λ is X-ray wavelength, and N is electron density of the material. Since δ and β are of the order of 10^{-4}–10^{-6}, n is very close to 1, but less than 1. Accordingly, when one makes the incident angle of X-rays smaller and smaller on a flat sample surface, total external reflection suddenly occurs at the critical angle, θ_c. defined in Eq. (7.13).

$$\theta_c = \sqrt{2\delta} = \sqrt{\frac{r_e}{\pi}} \cdot \sqrt{N} \cdot \lambda \tag{7.13}$$

Eq. (7.13) means that the critical angle is smaller as the X-ray energy is higher and the atomic number of the material is smaller. In the total reflection condition, X-rays do not penetrate into bulk, but propagate along the surface as an evanescent wave in the surface region of 2–3 nm.

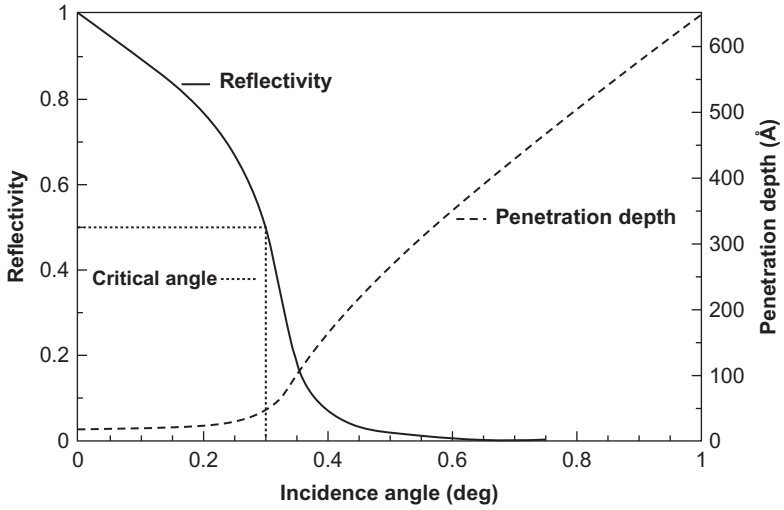

Fig. 7.18

X-ray incidence angle dependence of the reflectivity and penetration depth of Cu at an X-ray energy of 8 keV. Critical angle at 9 keV is about 0.3 degree (5.1 mrad) [35]. *Copyright © 2007, American Institute of Physics.*

When the incident angle becomes larger than θ_c, the reflectivity suddenly drops and the penetration depth increases. Such behavior is shown in Fig. 7.18 for Cu metal at an X-ray energy of 9 keV.

Using the Fresnel equation, reflectivity R can be expressed by optical constants, δ, β and the incidence angle θ [36].

$$R = \frac{h - (\theta/\theta_c)[2(h-1)]^{1/2}}{h + (\theta/\theta_c)[2(h-1)]^{1/2}}, \quad h = \left(\frac{\theta}{\theta_c}\right)^2 + \left\{\left[\left(\frac{\theta}{\theta_c}\right)^2 - 1\right]^2 + \left(\frac{\beta}{\delta}\right)^2\right\}^{1/2} \tag{7.14}$$

Eq. (7.14) indicates that reflectivity contains information of δ and β, which are also related to each other through Kramers-Kronig relation. Although it is not straightforward to extract EXAFS function from reflectivity $R(E)$, several methods have been proposed [37–39]. Below the critical angle, $\theta < \theta_c$, $R(E)$ spectrum exclusively comes from the evanescent wave, propagating parallel to the surface and the absorption coefficient μ can be approximated by the following relation.

$$\mu \approx \frac{1 - R(E)}{1 + R(E)} \tag{7.15}$$

The method to measure $R(E)$ is called "**ReflEXAFS**," which is a useful technique to obtain the structural information of surface and buried interface. A typical experimental setup is shown in Fig. 7.19.

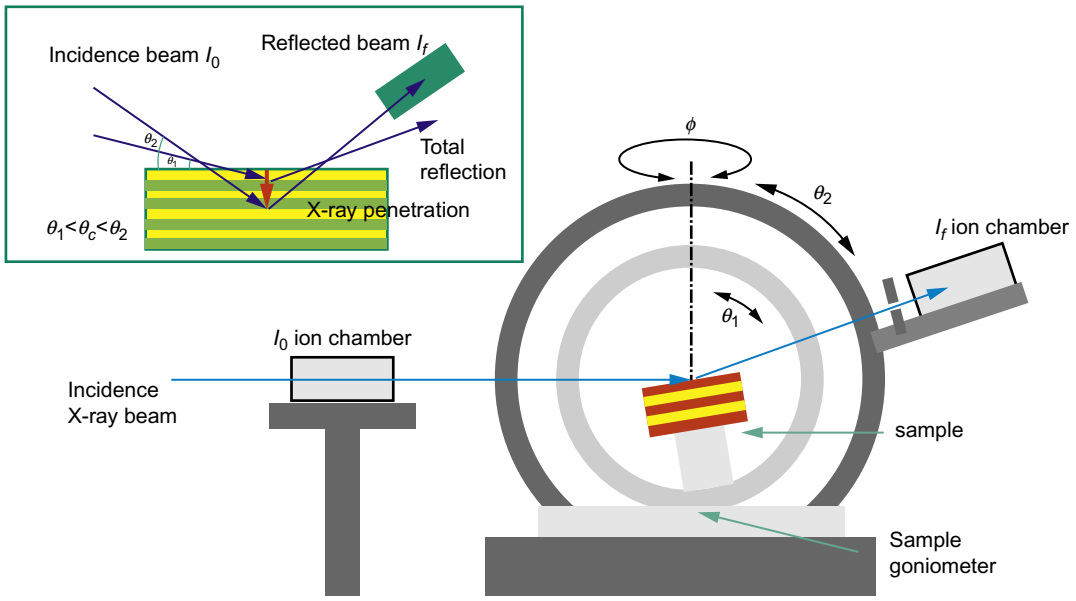

Fig. 7.19

Experimental setup of the three circle reflectometer for ReflEXAFS experiments constructed in ESRF [35]. Enlarged view of the sample position is shown in upper left inset.

In the experimental setup shown in Fig. 7.19, it is also possible to measure fluorescent X-rays emitted from surface, simultaneously with reflectivity, by setting a detector either on the top or the side of the sample.

Heald et al. demonstrated the usefulness of grazing-angle XAFS method to study surface and interface structures by using a model sample of 1000 Å thick, Al deposited Cu substrate [40]. Cu-Al alloy is formed in between Cu and Al layers, whose structure could be determined by grazing incidence XAFS. Fig. 7.20A shows theoretical reflectivity of a bilayer system of 1000 Å thick Al on a Cu substrate as well as those of pure Cu and Al surfaces. The reflectivity experimentally obtained well-reproduced the calculated one. Since Al is a lighter element than Cu, its critical angle is smaller. Note that strong interference oscillations are observed between the critical angles of Al and Cu, whose structure contains information concerning the thickness of Al overlayer.

Cu *K*-EXAFS spectra are shown in Fig. 7.20B for the fixed incidence angle (uncorrected) and the adjusted angle (angle corrected) cases. Since the incident X-ray energy scan is consistent with the incident angle scan, the critical angle is changed, which results in a distortion of the EXAFS spectrum.

This problem can be overcome by adjusting the incidence angle so as to synchronize with the scanning energy. Combining X-ray reflectivity (XRR) and grazing incidence X-ray absorption

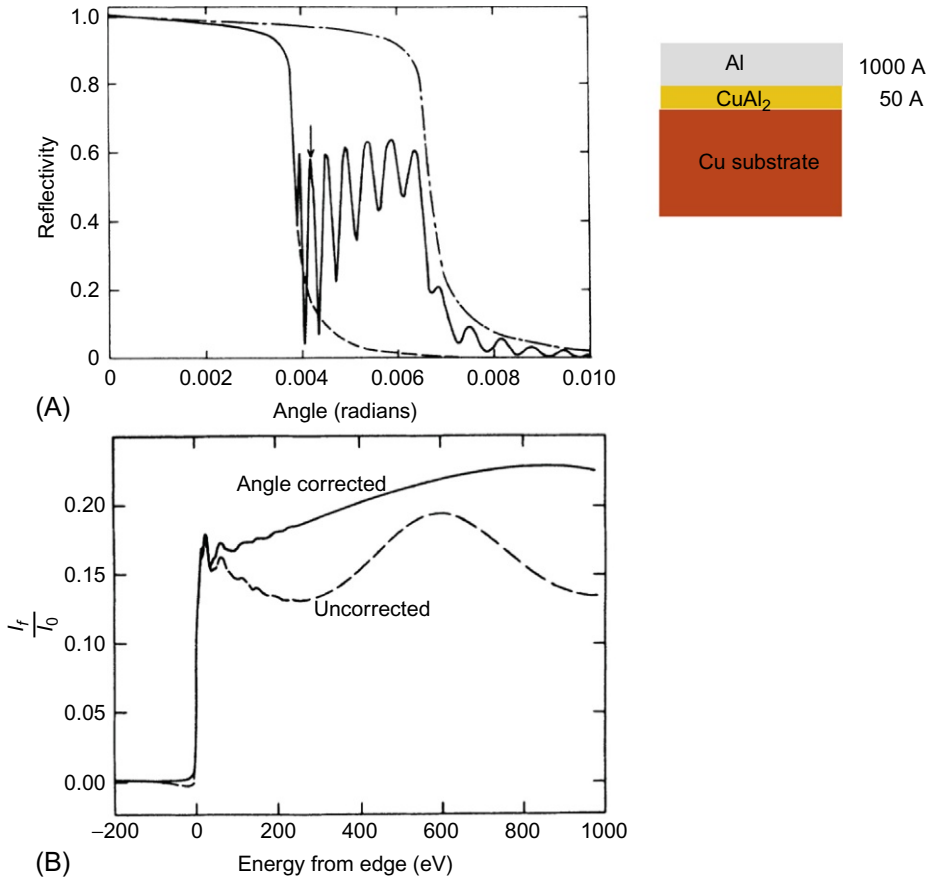

Fig. 7.20

(A) Calculated reflectivities of pure Al (dashed line), pure Cu (dotted-dashed line), and 1000 Å of Al on Cu (solid line at 8.6 keV). (B) Cu *K*-edge EXAFS spectrum taken at 4.0 mrad incident angle by the fluorescence yield mode for uncorrected spectrum, while the corrected spectrum was taken by scanning angle and energy simultaneously [40]. *Copyright © 1988, American Physical Society.*

(GI-XAFS) measurements is a useful technique for studying surface and interface. Several works have been done for nanolayer systems [41,42].

For the fluorescence yield XAFS experiment, it is essential to suppress the background X-rays as much as possible. For linearly polarized X-rays, the scattering cross section is not isotropic but has a certain angular dependence, which is minimized when the detector is set parallel to the incident X-ray *E* vector. Accordingly, in the case of *s*-polarization arrangement, the fluorescence detector should be set in plane with the sample surface and perpendicular to the beam direction, while the detector should be set vertical to the sample plane and perpendicular to the beam direction for the *p*-polarization arrangement, as shown in Fig. 7.21. Both

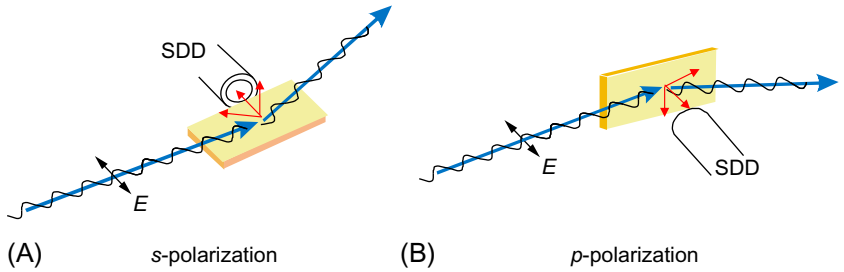

Fig. 7.21

Experimental layout for the grazing incidence XAFS with fluorescence yield mode for (A) *s*-polarization and (B) *p*-polarization arrangements. SDD (silicon drift detector) is used as a favorite detector for X-rays with energy resolution of about 50 eV at 500 eV.

arrangements are used case by case, but *s*-polarization is superior to *p*-polarization with respect of surface sensitivity. In case of the soft X-ray XAFS experiment, *p*-polarization is popular, and the detector is set not in plane like Fig. 7.21B, but out of plane, underneath the sample. This arrangement avoids scattering X-rays and enhances the surface sensitivity [5].

Recent advancement of a 2D X-ray detector has enabled us to develop a new type of depth-resolved XAFS. In the arrangement of Fig. 7.21A, one can set a 2D detector, PILATUS instead of SDD. The PILATUS is a space-resolved detector, composed of a number of pixels. Fluorescence X-rays emitted in normal direction are originated both from surface and bulk, while those emitted in the grazing direction are predominantly from surface. Situation is similar to the depth-resolved XMCD using Auger electrons described earlier, but X-rays penetrate in solid much deeper than electrons and the present depth-resolving technique using PILATUS gives deeper information from the surface.

Takamatsu et al. studied the local structure of an $LiCoO_2$ thin film at the solid electrode/electrolyte solution interface by the depth-resolved XAFS, as shown in Fig. 7.22 [43,44]. They designed a unique He gas filled spectroelectrochemical cell. During the charge process, the cathode was immersed in the electrolyte solution with Li metal as a counter electrode, and a constant voltage was applied by a potentiostat to charge the electrode. For each XAFS experiment, the cathode was pulled up from the electrolyte and was irradiated by the grazing incident SR beam coming through a Be window. Fluorescent X-rays were detected by a 2D pixel array detector, PILATUS 100 K, located 0.45 m apart from the sample. XAFS spectra were taken after soaking in the electrolyte, before charging (3.2 V vs. Li/Li+), charged to 4.2 V and overcharged to 4.4 V.

Fig. 7.23A and B shows Co K-edge depth-resolved XAFS spectra of the $LiCoO_2$ film after soaking and before charging and their Fourier transformations. From the bulk to the interface, the edge shifts toward lower energy, indicating the surface Co was reduced just by soaking. In

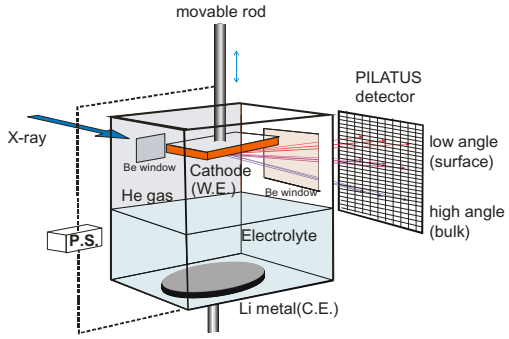

Fig. 7.22

Schematic illustration of the depth-resolved XAFS experiment. Emitted fluorescent X-rays are detected by the PILATUS detector which is located perpendicular to the incident X-ray beam direction. Positions at lower angles detect X-rays emitted from surface, while those at higher angles detect X-rays emitted both from bulk and surface.

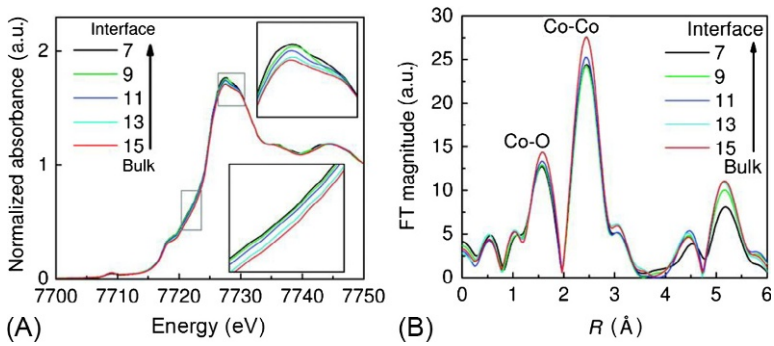

Fig. 7.23

Depth-resolved Co K-XAFS spectra of the $LiCoO_2$ electrode film at each channel of PILATUS detecting around the interface before charging. (A) XANES and (B) Fourier-transformed spectra of the k^3-weighted EXAFS oscillations [43]. *Copyright © 2011, American Chemical Society.*

the Fourier spectra, the first peak at 1.5 Å is associated with the Co—O bond. Its peak height decreases with decreasing channel number, keeping the bond distance the same, indicating that the Debye-Waller factor of the surface Co—O bond is more increased than the bulk ones. By charging to 4.2 V, the edge shifts to higher energy, and by overcharging to 4.4 V, the Co—O distance decreases and the DW factor increases significantly toward the surface (not shown). These structural and chemical changes of bulk and surface are useful information for secondary batteries.

Recently, the usefulness of combination of grazing emission XRF (X-ray fluorescence) and grazing emission XAFS with fluorescence yield mode is emphasized by applying the same setup to the study of surface oxidation of an Fe layer on Si and Ge, as shown in Fig. 7.24 [45]

7.2.3 Time-Resolved XAFS for Nanolayers

The use of intense and energy-continuous synchrotron radiation as the light source for XAFS spectroscopy dramatically shortens the data acquisition time. However, in the conventional method, spectra are taken point by point by scanning the photon energy step by step. It takes 5–10 min for XANES spectrum and 20–30 min for EXAFS spectrum. To shorten the acquisition time, the quick scan method (QXAFS) has been developed [46], where the photon energy is scanned continuously with a detector kept open. This method saves the loss of time in step scan and reduces the data acquisition time by 1/2 or 1/3. To shorten the time further, the dispersive XAFS (**DXAFS**) method was invented by Matsushita and Phizackerly [47], which can get a spectrum with one shot by using an energy dispersive method. The schematic drawing of this method is shown in Fig. 7.25. Synchrotron radiation is an X-ray nearly parallel white beam. By using a cylindrically bent Si crystal, X-rays are polychromatized and focused at a sample, and the transmitted X-rays are dispersed and detected by a position-sensitive detector located at the downstream of the sample. Recent advancement of synchrotron light source has made it possible to get XAFS spectra within 1 ms by using this DXAFS method. A number of DXAFS studies have been reported for tracing chemical reactions [48].

However, this is the transmission mode probing bulk of a sample. To apply XAFS to nanolayers, a surface-sensitive method is necessary.

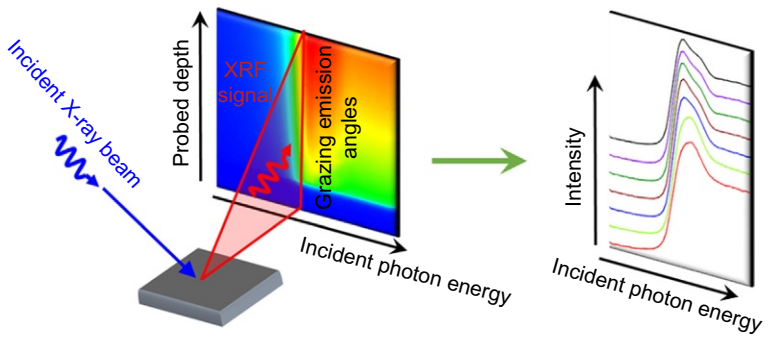

Fig. 7.24

Illustrative figure of grazing emission XRF and XAFS with fluorescence mode. In the 2D detector, abscissa corresponds to the incident photon energy and ordinate to the probing depth. By scanning the incident photon energy, one can get the depth profiled XAFS spectra [45]. *Copyright © 2015, American Chemical Society.*

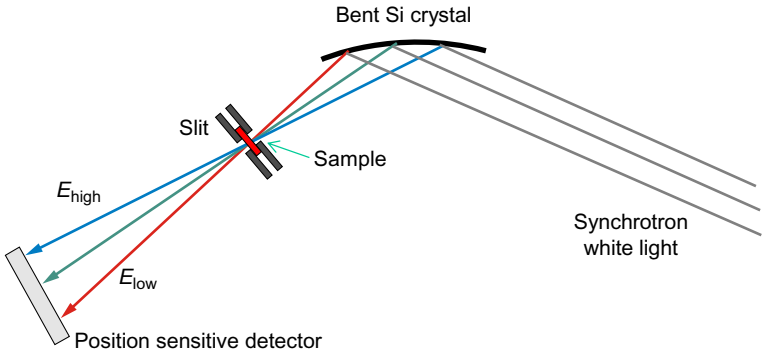

Fig. 7.25

Schematic view of DXAFS optics. Parallel white X-ray beam hits a bent crystal. Since the crystal is circularly bent, the incident angle changes point by point and as a result, diffracted X-ray energy changes point by point. These polychromatic X-rays are focused at a sample position and dispersed again.

Amemiya et al. have developed an energy dispersive XAFS method for soft X-ray region, applicable to nanolayer surface [49]. This method makes use of the Hettrick-type optics beamline with a varied-line-spacing grating and a micro ESCA with a position-sensitive electron analyzer. A schematic diagram of the system is shown in Fig. 7.26. In general, this beamline is used as a monochromator by narrowing the exit slit, but by fully opening the exit slit, it works also as a polychromator covering a certain energy range. Since the dispersed

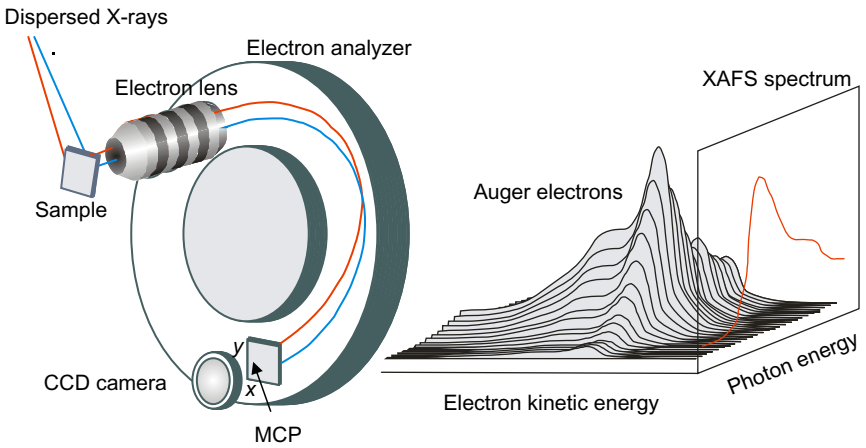

x: photon energy

y: electron kinetic energy

Fig. 7.26

Schematic diagram of an energy dispersive XAFS method in the soft-X-ray region. Energy dispersed photons irradiate the sample. Auger electrons emitted from a position generate Auger spectrum on a position of *x* axis of the MCP by using a micro-ESCA.

polychromatic X-rays are spread vertically, they are rotated by 90 degrees with a plane mirror and irradiate a sample surface with the X-ray energy spread along the horizontal axis. With X-ray absorption, Auger electrons are emitted from each position and collected separately with a micro ESCA system. A 2D image of Auger electrons can be obtained at once on an MCP, whose horizontal (x) and vertical (y) axes correspond to the position on the sample surface (that is, photon energy) and the electron kinetic energy, respectively.

Electrons are accelerated by MCP, keeping their positions and irradiating the phosphor screen, whose 2D image is taken by a CCD camera. By summing all the Auger electrons along the y (electron kinetic energy) axis, we can get the XAFS spectrum with the AEY mode with one shot. Since one makes use of all photons diffracted by grating at the same time, more than 100 times higher gain can be expected. It is easy to switch back to the conventional mode by narrowing the exit slit. However, it should be noted that there are some limitations for this system. The sample is assumed to be uniform, and the energy width is limited to ~20 eV at C K-edge region and 30 eV at O K-edge region. With this system, the spectral acquisition for the XANES region is less than 10 s even for submonolayer adsorbates.

As a typical application, this method was applied to the study of CO oxidation on Pt(111). This is one of the simplest surface reactions, well known since 1920, but practically important as automobile catalysts for exhaust gases. It has been established that atomic O adsorbed on a Pt(111) surface reacts only with adsorbed CO to form gaseous CO_2. Several reaction mechanisms have been proposed, but the dispersive XAFS is suitable for real-time monitoring of surface reactions and elucidation of the mechanisms via kinetic analyses. Fig. 7.27 (left) shows how O K-XANES spectra change by CO exposure on the O pre-adsorbed Pt (111) surface [50]. Intensities of atomic O and CO π^* peaks of each spectrum were converted to the coverages θ_O and θ_{CO}, which are plotted as the time evolution in Fig. 7.27 (right (A)). This figure shows that a fast reaction occurs at first, followed by a slow reaction process, as shown in Fig. 7.27B. According to the detailed analysis, the latter process was found to obey the half-order kinetics, suggesting that reaction occurs at O island peripheries. On the other hand, the former part can be interpreted as the reaction of disordered or isolated O atoms. The reaction mechanism was elucidated by using the dispersive XAFS method.

7.2.4 Space-Resolved XAFS for Nanolayers

XAFS measurement with wide X-ray beam size gives averaged structural information of the irradiated area, even though the sample is nonuniform. The impetus to pinpoint structural information of materials has prompted development of the space-resolved XAFS, in other words, micro-XAFS. This has been achieved thanks to the combination of high-brilliant synchrotron radiation and the advanced X-ray focusing optics and detectors.

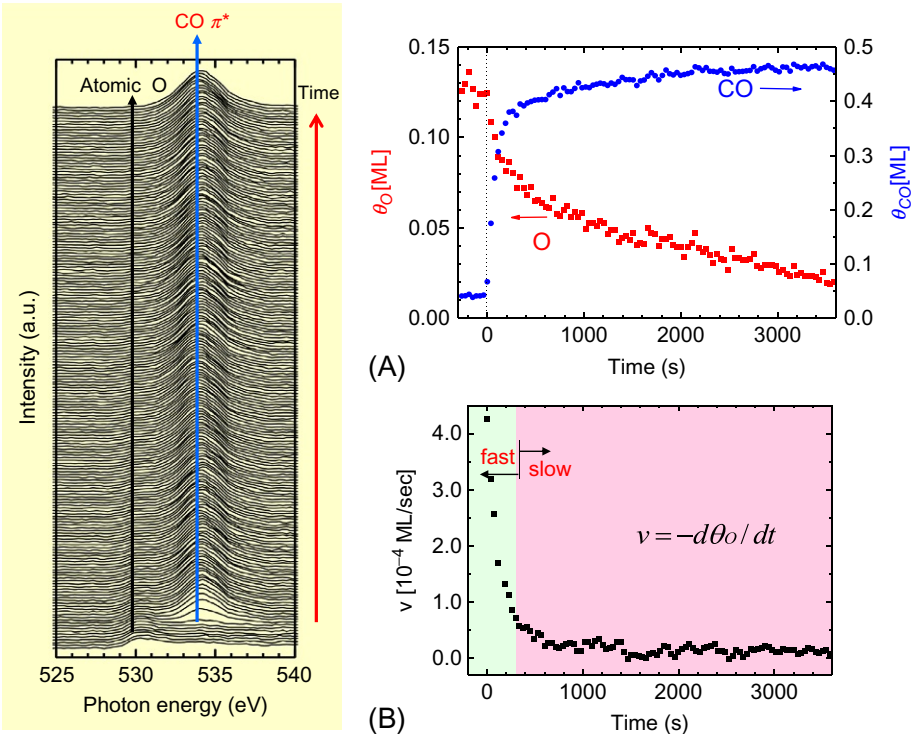

Fig. 7.27

Left: O *K*-XAFS of O pre-adsorbed Pt(111) during CO titration (1×10^{-8} Torr) at 240 K. It took 30 s to get each spectrum. Right (A) Time evolution of θ_O and θ_{CO}, and (B) Reaction rate as a function of time, which exhibits fast and slow processes.

Space-resolved XAFS is a technique for obtaining element-specific images of materials, or to obtain XAFS spectra of micron-order spots. These microscopes can generally be divided into three types:

(a) A monochromatic X-ray beam is focused either by an FZP (Fresnel zone plate) or by a KB (Kirkpatrick-Baez) mirror set to a sample on a stage that can move in *x*- and *y*-directions so as to raster-scan a whole area. Transmitted X-rays and emitted fluorescent X-rays are detected by an X-ray detector, and electrons (photoelectron, Auger electron, and secondary electrons) are detected by a channeltron or MCP. By scanning the incident X-rays with fixed sample stage, one can obtain micro XAFS spectrum of a specified element at a certain point. By scanning the sample stage at an incident X-ray energy tuned to the absorption edge of a specified element, one can obtain a spatial distribution of the element. Although this system is time-consuming, it provides plenty of information about a sample. This system is called STXM (scanning transmission X-ray microscopy) especially for the case of recording transmitted X-rays.

(b) A monochromatic or polychromatic X-ray beam is focused by a condenser FZP at a sample position, and the diverging beam is further focused by an objective FZP onto a CCD camera. A magnified image is taken the same way as with an optical microscope. The advantage of this system is to get the image of an element without scanning the stage by subtracting the image taken by the X-ray energy below the absorption edge of the element from that above the edge.

(c) Grazing incident monochromatic X-rays irradiate a sample. Photoelectrons emitted from different regions of the sample are imaged on a phosphor screen through electron microscopy optics with a magnified scale. By scanning the incident X-ray energy, one can get a series of images, from which a pinpoint view of the XAFS spectrum at each point can be obtained. Recent development of the electron lens system, this system provides images with a spatial resolution of 10 nm, which is much smaller than the X-ray focusing system. This system is called **XPEEM** (X-ray photoelectron emission microscopy) and is widely used for micro XPS and XAFS experiments. These three microscopy systems are schematically shown in Fig. 7.28.

Recently, a number of studies using micro-XAFS and imaging XAFS have been reported. Here we focus on the application to graphene. Graphene is a single layer of graphite, first prepared and studied in detail by Novoselov, Geim, and their group in 2004 [51]. Graphene exhibits interesting electronic properties and is promising for future applications, especially in nanoelectronics. Extensive studies have been performed both theoretically and experimentally to clarify these unique properties. XAFS is a powerful tool for characterizing graphene. Pacile et al. reported XAFS studies combined with XPEEM [52,53]. They prepared samples by micromechanical cleavage of HOPG (highly oriented pyrolytic graphite) on SiO_2 substrates. Fig. 7.29 shows OM (optical microscope) and XPEEM images collected at the peak of C *K*-edge (285.5 eV). Brighter parts indicate thicker layers and by the contrast of PEEM image, the number of layers can be easily discriminated.

Fig. 7.30A shows C- *K* spectra of single layer to four layers of graphene with two polarizations, E_1 and E_2 (perpendicular and parallel to the surface plane, respectively). Distinct polarization dependence exhibits flat lying structure of graphene, but a significant π^* peak appears in the spectra of E_2 polarization, indicating the possibility of distortion, corrugation, and/or roughness of SiO_2 substrate. Fig. 7.30B shows a zoom in of the π^* peak of a single layer graphene with E_2 polarization. Two distinct peaks appear below and above the main π^* peak. The authors assigned the lower peak to the van Hove singularity of the unoccupied π electronic states, and the higher peak to the analog of interlayer state of graphite. However, the possibility of residual COOH and CH species cannot be ruled out.

Schultz et al. also studied graphene sheets using STXM, C *K*-XAFS in conjunction with density functional theory calculations [54]. They prepared the samples with the CVD method using Ar,

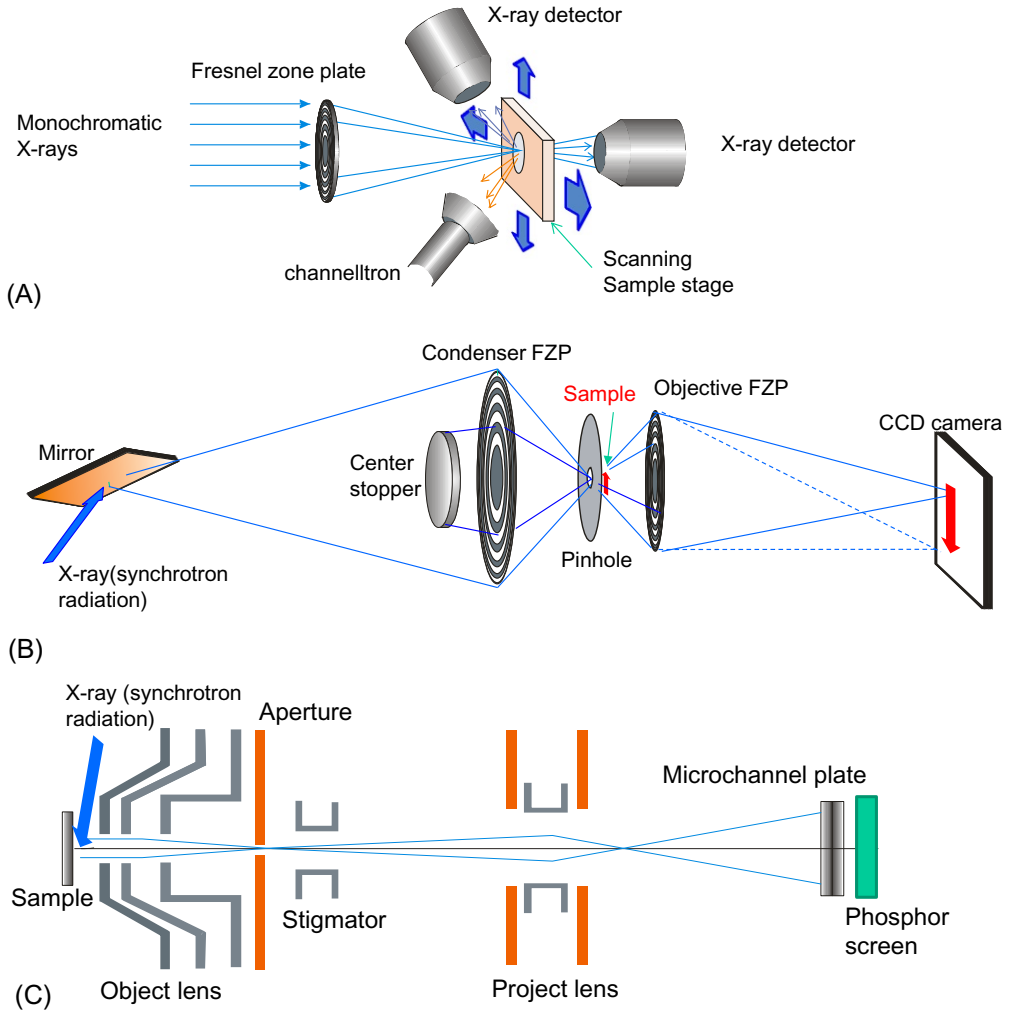

Fig. 7.28

Three types of typical space-resolved XAFS techniques: (A) X-ray beam focusing type (STXM), (B) imaging type using FZPs, and (C) electron imaging type (XPEEM).

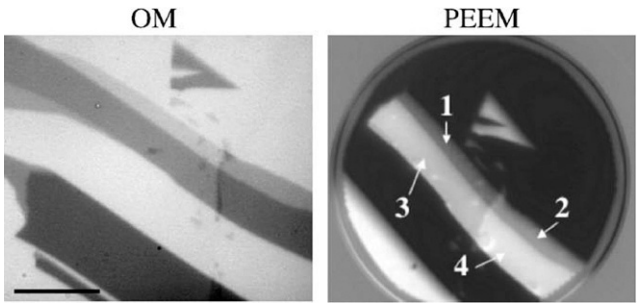

Fig. 7.29

Optical microscope and XPEEM images of graphene on SiO_2 [53]. In the PEEM image, the brighter part is thicker and the distinct difference of contrast indicates the difference of number of layers.

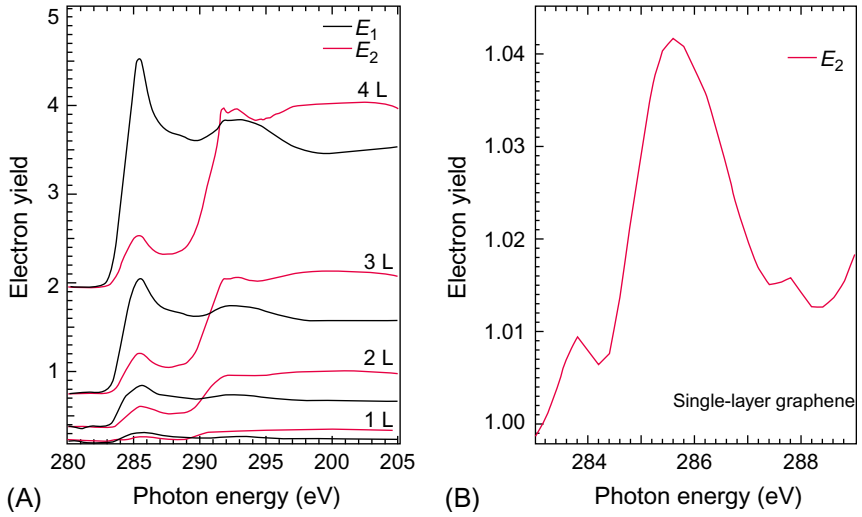

Fig. 7.30

(A) C *K*-edge XAFS spectra from 1 to 4 L graphene flakes with E_1 and E_2 polarizations. (B) Zoom in of the single layer graphene with E_2 polarization [53]. *Copyright © 2009, Elsevier B.V.*

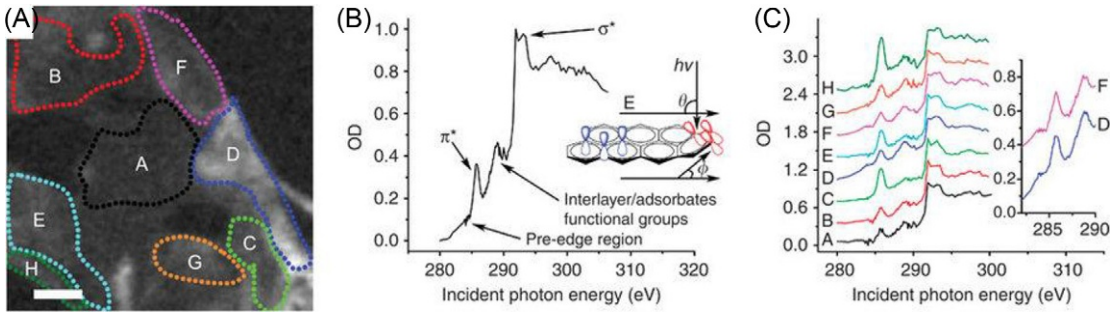

Fig. 7.31

(A) STXM mapping of the CVD grown single layer graphene on Cu. White scale bar is 1 μm. (B) Integrated C *K*-XAFS of entire image in (A). (C) Isolated C *K*-XAFS spectrum of each region displayed in (A). The pre-edge feature is clearly observed in spectra D and F shown in the inset [54]. *Copyright © 2011, Nature Publishing Group.*

H_2, and CH_4 at 1000°C. Fig. 7.31 shows an STXM image of a CVD grown graphene sheet and C *K*-XAFS spectra from individual regions. The domain *A* corresponds to a single layer graphene, and brighter domains to multiply folded layers.

As the STXM image was taken by polarized X-rays at normal incidence, the *E* vector is parallel to the graphene basal plane, suppressing π^* peak intensity. Appearance of the π^* peak can be correlated to electronic corrugations or roughness of graphene flakes. Interestingly,

the π^* peak intensity changes domain by domain. Peaks below and above the π^* peak are more clearly observed than the previous paper, especially in domains F and D. With the aid of DFT calculations, they assigned the pre-edge peak to dopant-induced states, as it has also been observed for graphite intercalated with $FeCl_3$. As for the higher energy peak, they found it disappeared by annealing and ascribed this to the COO- and CH-related carbon contaminations.

As has been described, graphene has unique electronic properties, such as linear band dispersion and high carrier mobility. Thus graphene is a promising optoelectronic device for the next generation. Recently, Fukidome et al. [55] assembled an actual graphene transistor, in which bilayer graphene and Ni thin films worked as a channel and metal electrode, respectively. SiO_2 thin film on a Si substrate worked as a capacitor. They obtained μ-XAFS spectra of the graphene foil by a PEEM with the AEY mode. The negative gate bias (V_g) was applied step by step, which caused hole-doping to graphene. C *K*-edge XAFS spectral change was monitored. Although detailed analyses have not been done yet, it should be emphasized that the μ-XAFS using PEEM can be effectively applied to real nanodevices.

For the 3D imaging of a specific element in a sample, X-ray computed tomography (XCT) is a well-known method in which the sample is rotated about an axis perpendicular to the incident X-ray beam with energies both below and above the absorption edge of the element. By using the angiography technique, a 3D image of the element is computationally reconstructed. This is used for bulk imaging, suitable for rod-shape sample. On the other hand, for a layer sample, X-ray computed laminography (XCL) is a useful technique, in which a sample is inclined and the rotation axis of a sample is not fixed at 90 degrees with respect to the X-ray beam.

This XCL can be easily combined with XAFS by measuring images, scanning the incident beam energy. It is rather time consuming, and only applicable in the hard X-ray region, but contains full of information about spatial distribution of a chemical state of a specific element. Saida et al. applied the XCL-XAFS technique to visualize a cathode catalyst layer in a polymer electrolyte fuel cell [56].

They prepared a membrane electrode assembly (MEA) for fuel cell, composed of 50 wt% Pt/C cathode layer, polymer electrolyte, 50 wt% Pd/C anode layer. They studied how the degradation affects the distribution of Pt catalyst by monitoring Pt L_3 edge XAFS-XCL. They found the degradation caused Pt nanoparticle aggregation. XAFS-XCL is a promising technique for visualizing heterogeneous structural information in MEAs.

7.3 Selected Applications to Green Chemistry

Proton-exchange-membrane fuel cells (PEMFC) are known to be an environment friendly device to convert chemical energy to electrical energy. When hydrogen is used as the fuel, the

combustion product is only water. Thus PEMFC should be used to solve environmental and energy problems. However, Pt and Pt alloys, currently used as the most efficient cathode materials, are very expensive and the cost of the cell hampers wide application. Many efforts have been directed at finding alternative materials for PEMFC cathode, and several candidates have been reported, such as metal carbides, transition metal chalcogenides, and biological mimics. Here, two promising materials are introduced, in which the XAFS method was effectively used for their characterization.

(1) Co-based pyrolyzed porphyrins

Porphyrin is regarded as an active site of biological mimics, although porphyrin itself does not work under various PH and temperature conditions. The materials obtained by pyrolyzing carbon-supported porphyrin precursors were found to be a possible candidate that is stable in PEMFC conditions [57]. However, the preparation of the materials, including pyrolysis, is a complicated procedure, which results in ambiguity of the active site. Ziegelbauer et al. studied the Co-based pyrolyzed porphyrins by using XPS, Co *K*- and *L*-edge XAFS [58]. They prepared samples by pyrolyzing silica supported Co-porphyrins under N_2 gas flow at 600°C, 700°C, and 800°C, and peeling off from the silica template by KOH washing and drying in air. Obtained samples were porous pyropolymer of balled-up graphite planes, as confirmed by transmission electron microscope (TEM). Electrochemical test using rotating ring disk electrode indicated the rank of the performance as 700°C > 600°C > 800°C.

Fig. 7.32 shows in situ Co *K*-edge XANES of three kinds of samples with reference Co(II)OEP (octaethyl porphinato) and Co metal foil.

Co(II)OEP, a model compound before pyrolysis, has a square planar structure and exhibits sharp pre-edge peak. Pyropolymer samples show similar profiles to that of Co(II) OEP, but loss of the pre-edge peak indicates the breaking of square planar structure. As shown in the right figure, by increasing the anode potential, the peak suddenly gains intensity at 0.80 V. This might be associated with oxygen adsorption. Co *K*-edge EXAFS analysis (figures not shown) revealed that the coordination numbers $N_{\mathrm{Co-N}}$ were 3.1, 2.8, 1.4 for 600°C, 700°C, and 800°C pyropolymers, respectively. This indicates that three Co–N bonds remain at 600°C and 700°C, one or two bonds remain at 800°C.

However, EXAFS provides bulk-averaging information, and the conventional analysis is of limited use for such heterogeneous pyropolymers. Thus they adopted the $\Delta\mu$ technique of XANES analysis [59], a subtraction method to extract the changed structures and oxygen adsorption sites. Here, the $\Delta\mu$ spectra were generated by the following relationship:

$$\Delta\mu = \mu(V) - \mu(0.30\,V)$$

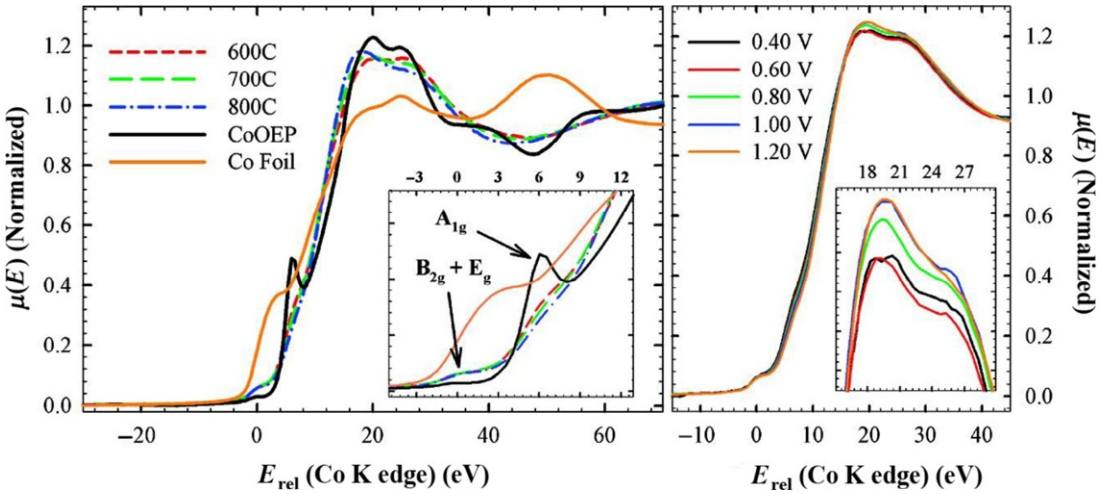

Fig. 7.32

In situ Co *K*-edge (7709 eV) XANES spectra of the pyropolymer electrocatalyst in 1.0 M $HClO_4$. Left: 0.40 V versus RHE with Co referenced [58]. Right: XANES spectra of pyropolymer (700°C) with several anodic potentials. *Copyright © 2008, American Physical Society.*

where the spectrum at 0.30 V was the reference spectrum of an adsorbate free structure. To interpret the $\Delta\mu$ spectra with different anode potentials, theoretical XANES spectra were calculated for several model structures by using the FEFF8 program package. Then the calculated spectra were subjected to the same difference process by the following relationship.

$$\Delta\mu = \mu(\mathrm{Co-N}_x\mathrm{-O_{ads}}) - \mu(\mathrm{Co-N}_x)$$

Fig. 7.33 are the experimental $\Delta\mu$ spectra for three pyrolyzed samples. For all the samples, a large minimum peak appears in the range 0–12 eV above the edge, suggesting the breaking of the square planar structure with increase of applied potential. In the energy range 12–40 eV, doubly split maxima is observed for 600°C, and a sharp decaying maximum for 800°C, and a mixed profile for 700°C pyropolymer samples. On the other hand, theoretical $\Delta\mu$ spectra are shown in Fig. 7.34 for three model structures. This clearly indicates that the axial adsorption gives double maxima, while planar adsorption gives a single maximum. Comparison between experimental and theoretical $\Delta\mu$ spectra clearly indicates that pyrolysis remove nitrogen from the plane of the $Co–N_4$ center, resulting in O_{ads} in a planar geometry.

The usual cathode half reaction in the fuel cell, oxygen reduction reaction (ORR), is

$$O_2 + 4H + 4e^- \rightarrow 2H_2O$$

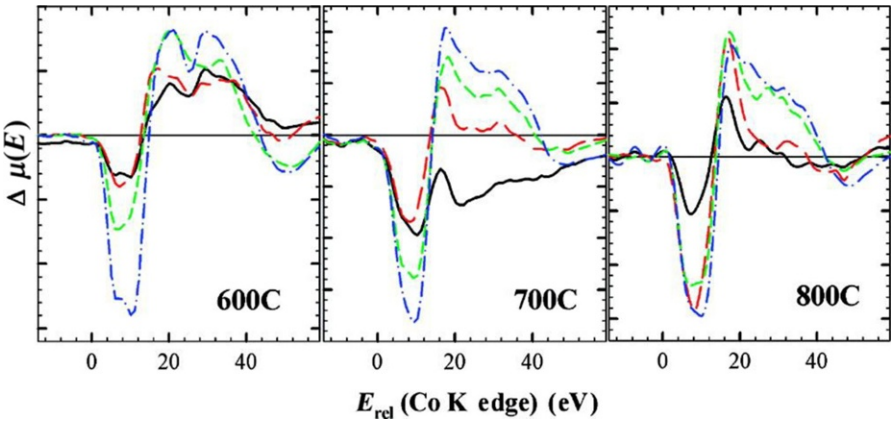

Fig. 7.33

The experimental $\Delta\mu = \mu(V) - \mu$ (0.30 V) spectra of Co *K*-edge spectra for the pyrolyzed pyropolymers: 0.50 V (solid), 0.60 V (long dash), 0.70 V (short dash), and 0.80 V (dash-dot). Data was collected in situ (anodic scans). *Copyright © 2008, American Physical Society.*

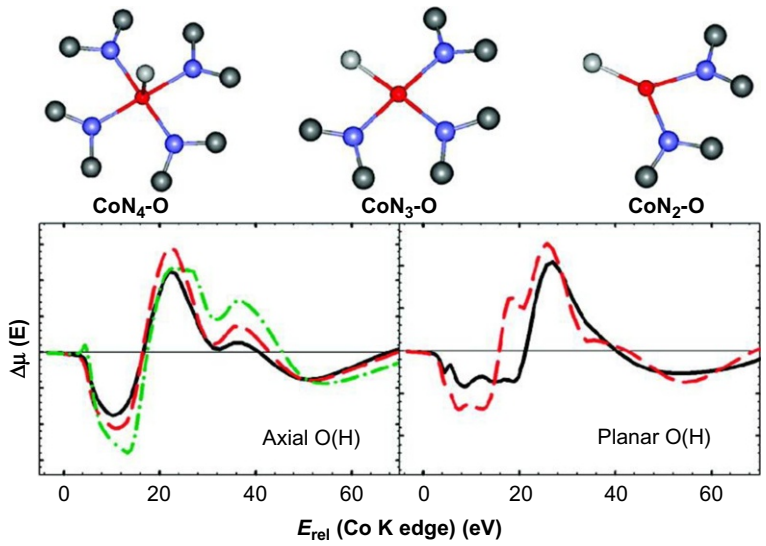

Fig. 7.34

Top: representative model structures for calculating the theoretical $\Delta\mu$ spectra by using the FEFF program code: (left) O_{axial} on Co-N_4, (center) O_{planar} on Co-N_3, (right) O_{planar} on Co-N_2. Bottom: theoretical $\Delta\mu = \mu(Co - N_x - O_{ads}) - \mu(Co - N_x)$ spectra obtained by FEFF8 calculations [58]. *Copyright © 2008, American Physical Society.*

However, another ORR with oxygen is possible: $O_2 + 2H^+ + 2e^- \rightarrow H_2O_2$.
This side reaction lowers the performance of the catalyst. The peroxide yield of the 800°C pyropolymer was found to be noticeably higher than for the other two samples. This $\Delta\mu$ result suggests that the O_{ads} in a planar geometry enhances the side reaction forming peroxide. These results demonstrate the usefulness of the $\Delta\mu$ method, which removes bulk information from standard XAFS spectra and allows for direct spectroscopic probing of adsorbates on an electrocatalyst surface in operando conditions.

(2) Nitrogen-doped carbon alloys
Recently, carbon-based materials doped with nitrogen or boron have attracted much attention due to their relatively high ORR (oxygen reduction reaction) activities [60]. However, there is still debate about which functional group is an active site.

Niwa et al. [61] prepared nitrogen-containing carbon materials with three kinds of methods and studied the ORR activities and N *K*-XAFS spectra for these samples and tried to correlate between the active site for ORR and the functional group. Samples prepared were (1) CoPc-ph-900, prepared by heating Co-phthalocyanine and N-containing polymers and acid washing to remove Co, (2) AO50 and AO90, prepared by amino-oxidation of carbon black and ammonia, and (3) N1 and N2, prepared by polymerizing melamine and furfuryl alcohol and carbonizing them by heating. The ORR activity was in the order of CoPc-ph-900 > N2 > AO50, in which surface composition ratio N/C, studied by hard X-ray PES, was N2 (2.1%) > AO050 (1.4%) > CoPh-ph-900 (0.8%).

N *K*-XAFS spectra from these samples are shown in Fig. 7.35. In the π^* state region, there are three characteristic peaks, A1, A2, and A3, which are assigned to pyrrole-type, pyridine-type, and graphite type nitrogen, respectively, with the aid of theoretical calculations. These assignments were further confirmed by DFT calculations [61a].

The sample CoPh-ph-900 has the highest ORR activity among three kinds of samples, even though the nitrogen content was relatively low. This suggests that the nitrogen site of CoPh-ph-900, graphite-type might be an active site for ORR. They proposed that the effective doping with graphite-like nitrogen is a practical guideline for the synthesis of active carbon alloy catalysts.

7.4 Future Prospects of XAFS

XAFS is the most fundamental technique for the monitoring of local electronic and atomic structures of specific elements in a material. It is applicable to any state of a sample, gases, liquids, bulk, and surface of solids, and has been applied to wide varieties of systems. Thanks to the development of the synchrotron light source and the detector system, the XAFS technique has been evolving with respect to the resolutions of energy, time, and space.

Space resolution is important for monitoring heterogeneous practical samples. It has been greatly improved by the advent of a highly brilliant synchrotron source and the technical

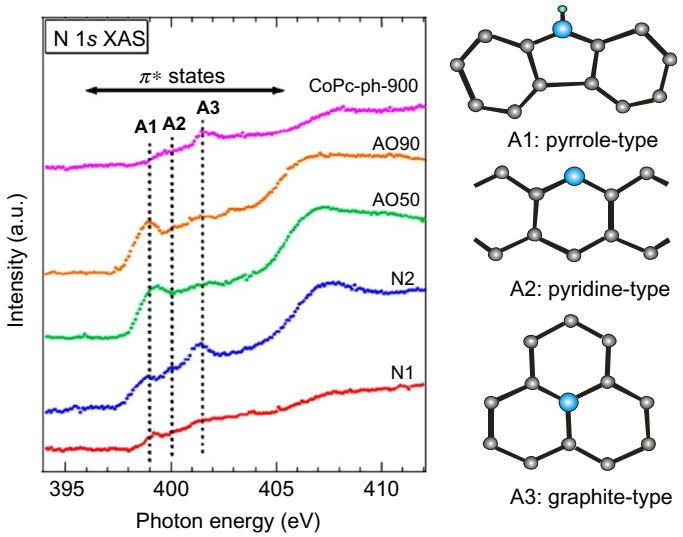

Fig. 7.35

N *K*-XAFS of π^* region from N-doped carbon materials. Peaks A1, A2, and A3 are associated to the pyrrole-type, pyridine-type, and graphite-type nitrogen, respectively [61]. *Copyright © 2009, Elsevier B.V.*

innovation to fabricate extremely smooth mirrors [62]. Now, the X-ray beam can be focused to the size of diffraction limit at a sample position with Kirkpatrick-Baez optics at SPring-8 (about 100 nm at the photon energy of 10 keV). Spatial resolution of the XPEEM method is also improved by reinforcing the aberration correction and has reached to about 10 nm. XPEEM is especially useful for nonhomogeneous nanolayer surface analysis.

Time resolution has been dramatically improved by adopting the DXAFS method, and is limited by the data acquisition speed. DXAFS spectra can be obtained within 1 ms for XANES and 5 ms for EXAFS at SPring-8 [48]. The recent advent of XFEL with 100% coherency has made it possible to get XANES spectra by subnanoseconds resolution by making use of its femotoseconds pulse structure [63]. Another aspect is XAFS measurements under various environments, such as high pressure, high or low temperature, and under operating conditions. Operando experiments of XAFS for secondary batteries and fuel cells have been strongly demanded to monitor in situ phenomena under a specific environment. Operando XAFS is rather easy for hard X-rays, but is difficult for soft X-rays due to the low penetration depth. Several challenges have been met by fabricating a specially designed electrochemical cell [64].

Green chemistry is one of the innovative scientific fields aiming at development of alternative sustainable technologies. The subjects to be clarified are getting more and more complicated. XAFS is a powerful tool of characterization, but provides only limited information about

short-range structures of specific elements. Combining with X-ray diffraction (XRD) and/or pair distribution function (PDF) analysis, which give long-range structural information, one can perform more detailed analysis [65]. Theoretical simulations are also quite helpful for interpreting complicated XAFS spectra. Now it is indispensable to combine these techniques to get the whole view of the targeted systems [66].

References

[1] W. Heitler, The Quantum Theory of Radiation, Clarendon Press, Oxford, 1954.
[2] XAFS Database of the SR Center, Ritsumeikan University.
[3] I.J. Pickering, G.N. George, E.Y. Yu, D.C. Brune, C. Tuschak, J. Overmann, J.T. Beatty, R.C. Prince, Analysis of sulfur biochemistry of sulfur bacteria using X-ray absorption spectroscopy, Biochemistry 40 (2001) 8138.
[4] J. Wong, F.W. Lytle, R.P. Messmer, D.H. Maylotte, X-edge absorption spectra of selected vanadium compounds, Phys. Rev. B 30 (1984) 5596.
[5] J. Stöhr, NEXAFS Spectroscopy, Springer, Berlin, 1991.
[6] H. Oji, K. Nishiyama, J. Ichikawa, Y. Kawakami, Y. Hamada, T. Okamoto, K. Ogawa, N. Namba, T. Tominaga, S. Kimura, Thermal imidization of PMDA-ODA polyimide studied by NEXAFS spectroscopy, Memoires of the SR Center, vol. 8, Ritsumeikan University, 2006, 187.
[7] R.A. Rosenberg, P.J. Love, V. Rehn, Polarization-dependent C(K) near-edge X-ray absorption fine structure of graphite, Phys. Rev. B 33 (1986) 4034.
[8] F. Matsui, H.W. Yeom, A. Imanishi, K. Isawa, I. Matsuda, T. Ohta, Adsorption of acetylene and ethylene on the Si(001) 2×1 surface studied by NEXAFS and UPS, Surf. Sci. (1998) L413.
[9] F. de Groot, Multiplet effects in X-ray spectroscopy, Coord. Chem. Rev. 249 (2005) 31.
[10] L.A. Montoro, M. Abbate, J.M. Rosolen, Electronic structure of transition metal ions in deintercalated and reintercalated $LiCo_{0.5}Ni_{0.5}O_2$, J. Electrochem. Soc. 147 (2000) 1651.
[11] G. Schütz, W. Wagner, W. Wilhelm, P. Kienle, R. Zeller, R. Frahm, G. Materlik, Absorption of circularly polarized X-rays in iron, Phys. Rev. Lett. 58 (1987) 737.
[12] C.T. Chen, F. Sette, Y. Ma, S. Modesti, Soft X-ray magnetic circular dichroism at the $L_{2,3}$ edges of nickel, Phys. Rev. B 42 (1990) R7262.
[13] B.T. Thole, P. Carra, F. Sette, G. van der Laan, X-ray circular dichroism as a probe of orbital magnetization, Phys. Rev. Lett. 68 (1992) 1943.
[14] P. Carra, B.T. Thole, M. Altarelli, X. Wang, X-ray circular dichroism and local magnetic fields, Phys. Rev. Lett. 70 (1993) 694–697.
[15] J. Stöhr, Y. Wu, X-ray magnetic circular dichroism: basic concepts and theory for 3d transition metal atoms, in: A.S. Schlachter, F.J. Wuilleumier (Eds.), New Directions in Research With Third Generation Soft X-Ray Synchrotron Radiation Sources, Kluwer Academic Pub, 1992, p. 221.
[16] E.A. Stern, Theory of the extended X-ray-absorption fine structure, Phys. Rev. B 10 (1974) 3027.
[17] F.W. Lytle, D.E. Sayers, E.A. Stern, Extended X-ray absorption fine structure technique. II. Experimental practice and selected results, Phys. Rev. B 11 (1975) 4825.
[18] E.A. Stern, D.E. Sayers, F.W. Lytle, Extended X-ray absorption fine structure technique. III. Determination of physical parameters, Phys. Rev. B 11 (1975) 4836.
[19] B.M. Kincaid, P. Eisenberger, Synchrotron radiation studies of the K-edge photoabsorption spectra of Kr, Br_2, and $GeCl_4$: a comparison of theory and experiment, Phys. Rev. Lett. 34 (1975) 1361.
[20] P.A. Lee, P.H. Citrin, P. Eisenberger, B.M. Kincaid, Extended X-ray absorption fine structure—its strengths limitations as a structural tool, Rev. Mod. Phys. 53 (1981) 769.
[21] D.C. Korningsberger, R. Prins (Eds.), X-Ray Absorption, Principles, Applications, Techniques of EXAFS, SEXAFS, and XANES, John Wiley & Sons, New York, 1988.
[22] T. Ohta, X-Ray Absorption Spectroscopy; XAFS and its Applications, in: IPC Publ. Co., Tokyo, 2002 (in Japanese).

[23] I. Lindau, W.E. Spicer, The probing depth in photoemission and Auger-electron spectroscopy, J. Electron. Spectrosc. 3 (1974) 409.
[24] C.J. Powell, Attenuation lengths of low-energy electrons in solids, Sur. Sci. 44 (1974) 29.
[25] J. Jaklevic, A.J. Kirby, M.P. Klein, A.S. Robertson, G.S. Brown, P. Eisenberger, Fluorescence detection of EXAFS: sensitivity enhancement for dilute species and thin films, Solid State Commun. 23 (1977) 679.
[26] L. Tröger, D. Arvanitis, K. Baberschke, H. Michaelis, U. Grimm, E. Zschrech, Full correction of the self-absorption in soft-fluorescence extended X-ray absorption fine structure, Phys. Rev. B 46 (1992) 3283.
[27] A.J. Acker, T.Z. Reier, H. Wadati Reier, Y.-J. Kim, H. Zhang, D.G. Hawthorn, Bulk sensitive X-ray absorption spectroscopy free of self-absorption effects, Phys. Rev. B 83 (2011) 081106.
[28] M. Ogawa, T. Yaji, K. Nakanishi, T. Ohta, Development of a partial electron yield detector for surface sensitive analysis in the high-energy soft X-ray absorption fine structure spectroscopy, Adv. X-ray Chem. Anal. Jpn. 47 (2016) 311.
[29] T. Maruyama, Y. Ishiguro, S. Nartitsuka, W. Norimatsu, M. Kusunoki, K. Amemiya, H. Ishii, T. Ohta, Near-edge X-ray absorption fine structure study of vertically aligned carbon nanotubes grown by the surface decomposition of SiC, Jpn. J. Appl. Phys. 51 (2012) 055102.
[30] K. Amemiya, S. Kitagawa, D. Matsumura, T. Yokoyama, T. Ohta, Development of a depth-resolved X-ray magnetic circular dichroism: application to Fe/Cu(100) ultrathin films, J. Phys. Condensed Mat. 15 (2003) S561.
[31] K. Amemiya, S. Kitagawa, D. Matsumura, H. Abe, T. Yokoyama, T. Ohta, Direct observation of magnetic depth profiles of thin Fe films on Cu(100) and Ni/Cu(100) with the depth-resolved X-ray magnetic circular dichroism, Appl. Phys. Lett. 84 (2004) 936.
[32] K. Amemiya, M. Sakamaki, NiO-like single layer formed on a Ni/Cu(001) thin film revealed by the depth-resolved X-ray absorption spectroscopy, Appl. Phys. Lett. 98 (2011) 012501.
[33] K. Amemiya, M. Sakamaki, M. Mizusawa, M. Takeda, Twisted magnetic structure in ferromagnetic Ni ultrathin film induced by magnetic anisotropy interaction with antiferromagnetic FeMn, Phys. Rev. B 89 (2014) 054404.
[34] O. Endo, M. Nakamura, K. Amemiya, Depth-dependent C K-NEXAFS spectra for self-assembled monolayers of 4-methylbenzenethiol and 4-ethylbenzenethiol on Au(111), J. Electron. Spectrosc. Relat. Phenom. 187 (2013) 72.
[35] V. López-Flores, S. Ansell, D.T. Bowron, S. Díaz-Moreno, S. Ramos, A. Muñoz-Páez, Optimized end station and operating protocols for reflection extended x-ray absorption fine structure (ReflEXAFS) investigations of surface structure at the European Synchrotron Radiation Facility beamline BM29, Rev. Sci. Instrum. 78 (2007) 013109.
[36] L.G. Parratt, Surface studies of solids by total reflection of X-rays, Phys. Rev. 95 (1954) 359.
[37] R. Barchewitz, M. Cremonse-Visicato, G. Onori, X-ray photoabsorption of solods by specular reflection, J. Phys. C 11 (1978) 4439.
[38] G. Martens, P. Rabe, The extended X-ray absorption fine structure by the reflectivity at the K-edge of Cu, J. Phys. C 14 (1981) 1523.
[39] S. Pizzini, K.J. Roberts, G.N. Greaves, N. Harris, P. Moore, E. Pantos, R.J. Oldman, Instrumentation for glancing angle X-ray absorption spectroscopy at the synchrotron radiation source, Rev. Sci. Instrum. 60 (1989) 2525.
[40] S.M. Heald, H. Chen, J.M. Tranquada, Glancing-angle extended X-ray absorption fine structure and reflectivity studies of interfacial regions, Phys. Rev. B 38 (1988) 1016.
[41] B. Pollakowski, P. Hoffmann, M. Kosinova, O. Baake, V. Trunova, R. Unterumsberger, W. Ensinger, B. Beckhoff, Nondestructive and nonpreparative chemical nanometrology of internal material interfaces at tunable high information depths, Anal. Chem. 85 (2013) 193.
[42] B. Pollakowski, B. Beckhoff, Nondestructive speciation depth profiling of complex TiO_x nanolayer structures by grazing incidence X-ray fluorescence analysis and near edge X-ray absorption fine structure spectroscopy, Anal. Chem. 87 (2015) 7705.

[43] D. Takamatsu, T. Nakatsutsumi, S. Mori, Y. Orikasa, M. Moi, H. Yamashige, K. Sato, T. Fujimoto, Y. Takanashi, H. Murayama, M. Oishi, H. Tanida, T. Uruga, H. Arai, Y. Uchimoto, Z. Ogumi, Nanoscale observation of the electronic and local structures of $LiCoO_2$ thin film by depth-resolved X-ray absorption spectroscopy, J. Phys. Chem. Lett. 2 (2011) 2511.

[44] D. Takamatsu, Y. Koyama, Y. Orikasa, S. Mori, T. Nakatsutsumi, T. Hirano, H. Tanida, H. Arai, Y. Uchimoto, Z. Ogumi, First in situ observation of the $LiCoO_2$ electrode/electrolyte interface by total-reflection X-ray absorption spectroscopy, Angew. Chem. 51 (2012) 11597.

[45] Y. Kayser, J. Sa, J. Szlachetko, Depth-resolved X-ray absorption spectroscopy by means of grazing emission X-ray fluorescence, Anal. Chem. 87 (2015) 10815.

[46] R. Frahm, Quick scanning EXAFS: first experiments, Nucl. Instrum. Methods A 270 (1988) 578.

[47] T. Matsushita, R.P. Phizackerly, A fast X-ray absorption spectrometer for use with synchrotron radiation, Jpn. J. Appl. Phys. 20 (1981) 2223.

[48] M. Tada, S. Murata, T. Asaoka, K. Hiroshima, K. Okumura, H. Tanida, T. Uruga, H. Nakanishi, S. Matsumoto, Y. Inada, M. Nomura, Y. Iwasawa, In situ time-resolved dynamic surface events on the Pt/C cathode in a fuel cell under operando conditions, Angew. Chem. Int. Ed. 46 (2007) 4310.

[49] K. Amemiya, H. Kondoh, A. Nambu, M. Iwasaki, I. Nakai, Y. Yokoyama, T. Ohta, Energy dispersive near edge X-ray absorption fine structure in the soft X-ray region: a new technique to investigate surface reactions, Jpn. J. Appl. Phys. 40 (2001) L718.

[50] I. Nakai, H. Kondoh, K. Amemiya, M. Nagasaka, A. Nambu, T. Ohta, Reaction-path switching induced by spatial-distribution change of reactants: CO oxidation on Pt(111), J. Chem. Phys. 121 (2004) 5035.

[51] K.S. Novoselov, A.K. Geim, S.V. Morozov, D. Jiang, Y. Zhang, S.V. Dubonos, I.V. Grigorieva, A.A. Firsov, Electric field effect in atomically thin carbon films, Science 306 (2004) 666.

[52] D. Pacilé, M. Papagno, A.F. Rodríguez, M. Grioni, L. Papagno, Ç.Ö. Girit, J.C. Meyer, G.E. Begtrup, A. Zettl, Near-edge X-ray absorption fine-structure investigation of graphene, Phys. Rev. Lett. 101 (2008) 066806.

[53] M. Papagno, A.F. Rodríguez, Ç.Ö. Girit, J.C. Meyer, A. Zettl, D. Pacilé, Polarization dependent C K near-edge X-ray absorption fine-structure of graphene, Chem. Phys. Lett. 475 (2009) 269.

[54] B.J. Schultz, C.J. Patridge, V. Lee, C. Jaye, P.S. Lysaght, C. Smith, J. Barnett, D.A. Fischer, D. Prendergast, S. Banerjee, Imaging local electronic corrugation and doped regions in graphene, Nat. Commun. 2 (2011) 372.

[55] H. Fukidome, M. Kotsugi, K. Nagashio, R. Sato, T. Ohkochi, T. Itoh, A. Toriumi, M. Suemitsu, T. Kinoshita, Orbital specific tunability of many—body effects in bilayer graphene by gate bias and metal contact, Sci. Rep. 4 (2014) 3713.

[56] T. Saida, O. Sekizawa, N. Ishuguro, M. Hoshno, K. Uesugi, T. Uruga, S. Ohikoshi, T. Yokoyama, M. Tada, 4D visualization of a cathode catalyst layer in a polymer electrolyte fuel cell by 3D laminography-XAFS, Angew. Chem. Int. Ed. 51 (2012) 10311.

[57] B. Wang, Recent development of non-platinum catalysts for oxygen reduction reaction, J. Power Sources 152 (2005) 1.

[58] J.M. Ziegelbauer, T.S. Olson, S. Pylypenko, F.A. lamgir, C. Jaye, P. Atanassov, S. Mukerjie, Diret spectroscopic observation of the structural origin of peroxide generation from Co-based pyrolyzed porphyrins for ORR applications, J. Phys. Chem. C 112 (2008) 8839.

[59] M. Teliska, W.E. O'Grady, D.E. Ramaker, Determination of H adsorption sites on Pt/C electrodes in $HClO_4$ from Pt L_{23} X-ray absorption spectroscopy, J. Phys. Chem. B 108 (2004) 2333.

[60] S. Maldonado, K.J. Stevenson, Direct preparation of carbon nanofiber electrodes via pyrolysis of iron (II) phthalocyanine: electrocatalytic aspects for oxygen reduction, J. Phys. Chem. B 108 (2004) 11375.

[61] H. Niwa, K. Horiba, Y. Harada, M. Oshima, T. Ikeda, K. Terakura, J. Ozaki, S. Miyata, X-ray absorption analysis of nitrogen contribution to oxygen reduction reaction in carbon alloy cathode catalysts for polymer electrolyte fuel cells, J. Power Sources 187 (2009) 93.

[61a] T. Shiros, D. Nordlund, L. Palova, D. Prezzi, L. Zhao, K.S. Kim, U. Wurstbauer, C. Gutierrez, D. Delongchamp, C. Jaye, D. Fischer, H. Ogasawara, L.G.M. Pettersson, D.R. Reichman, P. Kim, M. S. Hybertsen, A.N. Pasupathy, Connecting dopant bond type with electronic structure in N-doped graphene, Nano Lett. 12 (2012) 4025.

[62] S. Matsuyama, H. Nakamori, T. Goto, T. Kimura, K.P. Khakurel, Y. Kohmura, Y. Sano, M. Yabashi, T. Ishikawa, Y. Nishino, K. Yamauchi, Nearly diffraction-limited X-ray focusing with variable-numerical-aperture focusing optical system based on four deformable mirror, Sci. Rep. 6 (2016) 24801.
[63] Y. Ogi, Y. Obara, T. Katayama, Y.-I. Suzuki, S.Y. Liu, N.C.-M. Bartlett, N. Kurahashi, S. Karashima, T. Togashi, Y. Inubushi, K. Ogawa, S. Owada, M. Rubešová, M. Yabashi, K. Misawa, P. Slavíček, T. Suzuki, Ultraviolet photochemical reaction of $[Fe(III)(C_2O_4)_3]^{3-}$ in aqueous solutions studied by femtosecond time-resolved X-ray absorption spectroscopy using an X-ray free electron laser, Struct. Dyn. 2 (2015) 034901.
[64] K. Nakanishi, D. Kato, H. Arai, H. Tanida, T. Mori, Y. Orikasa, Y. Uchimoto, T. Ohta, Z. Ogumi, Novel spectro-electrochemical cell for in situ/operando observation of common composite electrode with liquid electrolyte by X-ray absorption spectroscopy in the tender X-ray region, Rev. Sci. Instrum. 85 (2014) 084103 (2014).
[65] K. Tokuda, T. Kawaguchi, K. Fukuda, T. Ichitsubo, E. Matsubara, Retardation and acceleration of phase separation evaluated from observation of imbalance between structure and valence on $LiFePO_4/FePO_4$ electrode, Appl. Phys. Lett. Mater. 2 (2014). 070701.
[66] Y. Iwasawa, K. Asakura, M. Tada (Eds.), XAFS Techniques for Catalysts, Nanomaterials, and Surfaces, Springer, 2016.

CHAPTER 8

Nanolayer Analysis by Photoelectron Spectroscopy

Masaharu Oshima

The University of Tokyo, Tokyo, Japan

8.1 Principle of Photoelectron Spectroscopy

Photoelectron spectroscopy (PES), or photoemission spectroscopy, is one of the most important and useful techniques for investigating electronic and chemical states in solids, especially in nanolayers because of its high-energy resolution and surface sensitivity [1–5]. The physics behind PES is an application of the photoelectric effect. Through photoelectric ionization by irradiating samples with X-rays, vacuum ultraviolet (VUV) or ultraviolet (UV) light, the energies of the emitted photoelectrons are characteristic of their original electronic and chemical states. Therefore PES is one of the most sensitive and accurate techniques for measuring the energies and shapes of electronic states and molecular orbitals. X-ray photoelectron spectroscopy (XPS) was developed by Kai Siegbahn in 1957 and is used to study the energy levels of atomic core electrons, mainly in solids. Siegbahn referred to the technique as electron spectroscopy for chemical analysis (ESCA), since chemical structure can be determined by analyzing the core levels with small chemical shifts depending on the chemical environment of the atom. Siegbahn was awarded the Nobel Prize in Physics in 1981.

Since photoelectrons can escape only from the surface region ranging from a monolayer or nanolayer to several tens of nanometers, depending on incident photon energy and sample materials, only the surface layer or nanolayers can be analyzed, as shown in Fig. 8.1. [6]. Therefore clean ultrahigh vacuum (UHV) condition is strongly required. The emitted photoelectrons are energy analyzed, resulting in a spectrum of electron intensity as a function of the measured kinetic energy. The kinetic energy values E_k can be converted into binding energy values E_B by using the equation: $E_k = h\nu - E_B - \phi$. Here, $h\nu$ is the energy of incident photons, and ϕ is the work function. Synchrotron radiation source is the most promising light because of its brightness, cleanness, variation of energy, directionality, linear and circular polarizability, and pulse character [6–8]. Taking advantage of these characteristics, ultrahigh energy resolution analysis, surface and bulk sensitive analysis, nanospace analysis, magnetic property

Nanolayer Research. http://dx.doi.org/10.1016/B978-0-444-63739-0.00008-6

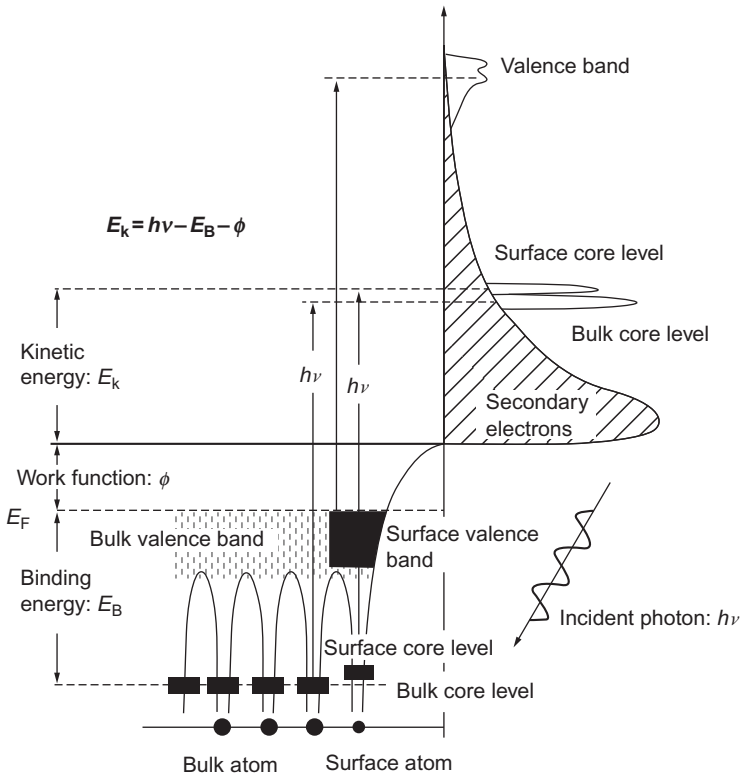

Fig. 8.1
Principle of photoelectron spectroscopy.

or spin-resolved analysis, and time-resolved analysis become possible. The binding energies of the measured electrons are characteristic of the chemical structure and molecular bonding of the material.

PES uses monochromatic sources of radiation. The photon is absorbed by an atom in a molecule or solid, resulting in the emission of an inner shell electron. In ultraviolet photoelectron spectroscopy (UPS), the photon interacts with valence levels of the molecule or solid, leading to ionization by removal of one of these valence electrons.

Although there are many different designs of electron energy analyzer, the most commonly used analyzer for high-energy resolution analysis is a concentric hemispherical analyzer, which uses an electric field between two hemispherical surfaces to disperse the electrons depending on their kinetic energy. Every element has its characteristic core levels with binding energy associated with each core atomic orbital. The presence of peaks at particular energies therefore indicates the existence of a specific element in the sample. Since the intensity of the peaks is related to the concentration of the element within the probed region, the technique provides a quantitative analysis of the surface composition. In order to precisely discriminate chemical

states with different oxidation states or chemical environments, high-energy resolution is required. Since the intrinsic width of the initial energy level and the lifetime of the final state are limited, only two factors can be improved. One is the line-width or energy-width of the incident radiation. The other is the resolving power of the electron-energy analyzer. Since the directionality or brightness of synchrotron radiation light from third-generation storage rings is much higher than the conventional X-ray and VUV sources, very high-energy resolution X-rays or VUV ranging from several tens meV to less than 1 meV strongly depending on photon energy can be obtained. Furthermore, thanks to the rapid progress of electron analyzer with large orbital radius (such as 200 mm) of hemispherical analyzer, total energy resolution of PES is reaching less than 1 meV, depending on photon energy.

The degree of surface sensitivity of PES can be controlled by collecting photoelectrons emitted at different emission angles to the surface plane by changing the incident photon energy. Fig. 8.2 exhibits Si 2*p* core level spectrum from the clean Si(100) surface with 2×1 reconstruction by incident photon energy of 130 eV, which is a very surface sensitive condition, resulting in a relatively large amount of surface state peaks such as S, SS, and S′ originating from surface atoms or surface core levels schematically shown in Fig. 8.1. [9] This approach can be used to perform nondestructive analysis of the variation of surface composition with depth. Furthermore, in-depth profiles can be obtained by means of maximum entropy method (MEM) or least square method from angle-resolved photoelectron spectroscopy (ARPES) intensity distribution. Thus the adsorption of relatively simple molecules on metals can be

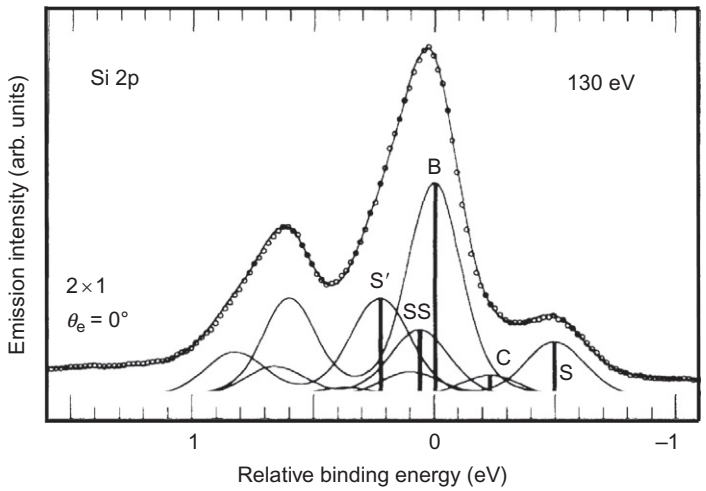

Fig. 8.2

Si 2p photoelectron spectrum from clean Si (100) surface with 2×1 reconstruction measured with synchrotron radiation at the photon energy of 130 eV. *Reprinted from E. Landemark, C.J. Karlsson, Y.C. Chao, R.I.G. Uhrberg, Core-level spectroscopy of the clean Si(001) surface: charge transfer within asymmetric dimers of the 2×1 and $c(4 \times 2)$ reconstructions, Phys. Rev. Lett. 69 (1992) 1588, with the permission of The American Physical Society.*

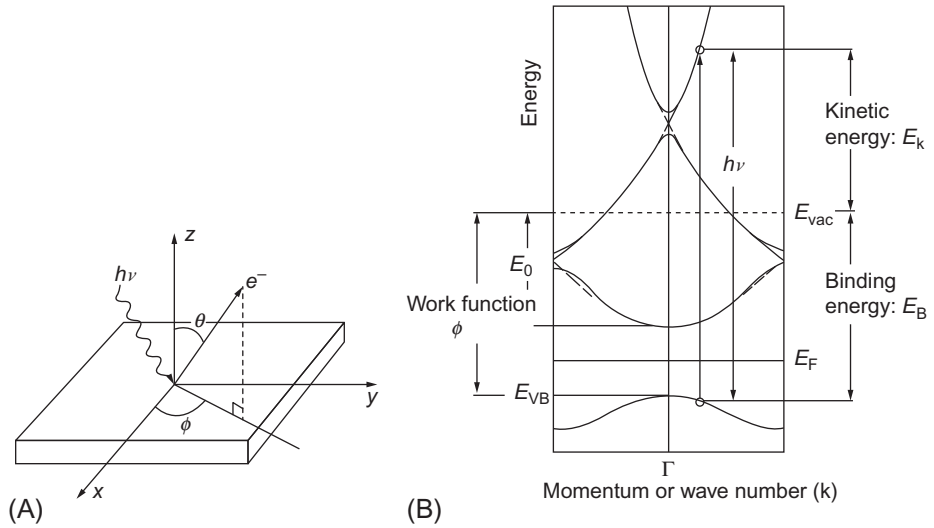

Fig. 8.3

Angle-resolved photoelectron spectroscopy: (A) geometry of photoemission angle and (B) energy band diagram as a function of momentum or wavenumber of electrons in solids.

analyzed by surface-sensitivity-dependent photoelectron spectra in comparison with the calculated molecular orbitals of the adsorbed species.

Furthermore, this ARPES method can provide us with detailed electronic structures of solids such as semiconductors, metals, superconductors, and two-dimensional unique materials that are typical nanolayers, which are the complete band structure mapped out in *k*-space. Fig. 8.3 shows the principle of ARPES, where the component of electron momentum in the plane of the sample should be conserved, resulting in energy band diagram as a function of wavenumber (*k*), as shown in Fig. 8.3B.

Thus PES is a very powerful technique for investigating electronic and chemical structures of various nanolayers and devices for green chemistry. In order to make sustainable society or low carbon society, we have to solve several problems such as energy problems and natural resource problems using green chemistry. As shown in Fig. 8.4, we classified energy problems into three categories: (1) power generation materials/devices such as fuel cells, solar cells, thermoelectric devices, and water-splitting photocatalysts for hydrogen generation, (2) energy efficient materials/devices such as low-voltage Si metal oxide semiconductor field-effect transistors (MOSFETs), graphene FETs (GFETs), organic FETs, resistance random access memories (ReRAMs), magnetic or spintronic materials/devices, and (3) energy storage materials/devices such as lithium (or sodium) ion batteries (LIB) and redox flow batteries. Since most of them utilize nanomaterials such as nanolayers, nanotubes/nanofibers, and nanoparticles for better performance, more advanced analytical methods to characterize electronic and chemical structures of these nanostructures are strongly demanded.

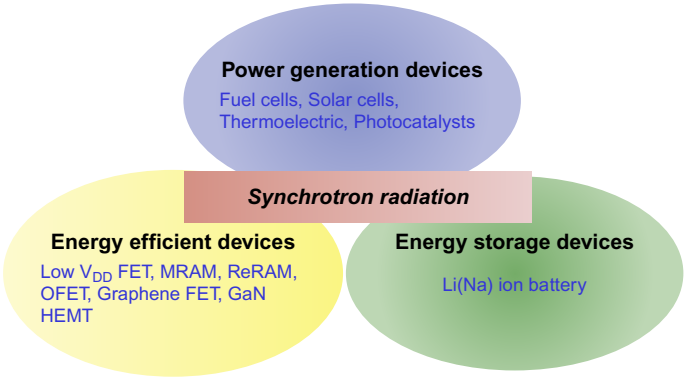

Fig. 8.4
Three categories of energy materials and devices analyzed by synchrotron radiation.

8.2 Highly Energy-Resolved PES for Chemical and Electronic Analysis

Taking advantage of highly bright synchrotron radiation with excellent directionality and high flux together with highly energy-resolved electron analyzer, extremely high energy resolution photoelectron spectroscopy (HRPES) in the VUV region, the soft X-ray (SX) region and the hard X-ray (HX) region, is now available at various third-generation storage rings in the world. Details in very high-resolution PES including PES below 1 meV energy resolution are reviewed in a book by Huefner [10], and most of them are related to basic physics in condensed matter. Therefore this chapter mainly focuses on more practical electronic and chemical properties in nanolayers with reasonably high-energy resolution for green chemistry.

One of the most important examples for HRPES may be the electronic structure of high T_c (critical temperature) oxide superconductors, which are expected to be applied to superconducting cable for electric transmitter with less energy loss, energy storage with superconductor magnets (SMES), and magnetic levitation (maglev) train with superconducting magnets. In order to develop higher T_c and J_c (critical current density) superconducting magnets, electronic structure of superconductors should be precisely investigated. In the VUV region, Ding et al. [11] reported high-energy resolution PES results on $Bi_2Sr_2CaCu_2O_8$ single crystals with the *Tc* of 87 K. They performed ARPES with the energy resolution of 18.8 meV (full width at half maximum, FWHM) at the sample temperature of 13 K. As shown in Fig. 8.5 (labeled 17) corresponding to near the $\overline{M}$ point, superconducting gap Δ_k is opened by 34 meV, while along the Γ-Y direction (labeled 12) no gap is opened. Based on various valence band spectra along the Fermi surface (FS), they concluded that superconducting gap in $Bi_2Sr_2CaCu_2O_8$ single crystal is consistent with anisotropic s-wave gap.

In the SX region, electronic structures of interfacial nanolayers can be probed because of longer escape depth of photoelectrons than the VUV region. One example is the unique metallic interfacial layer at the heterointerface between the band insulators $LaAlO_3$ and $SrTiO_3$, which

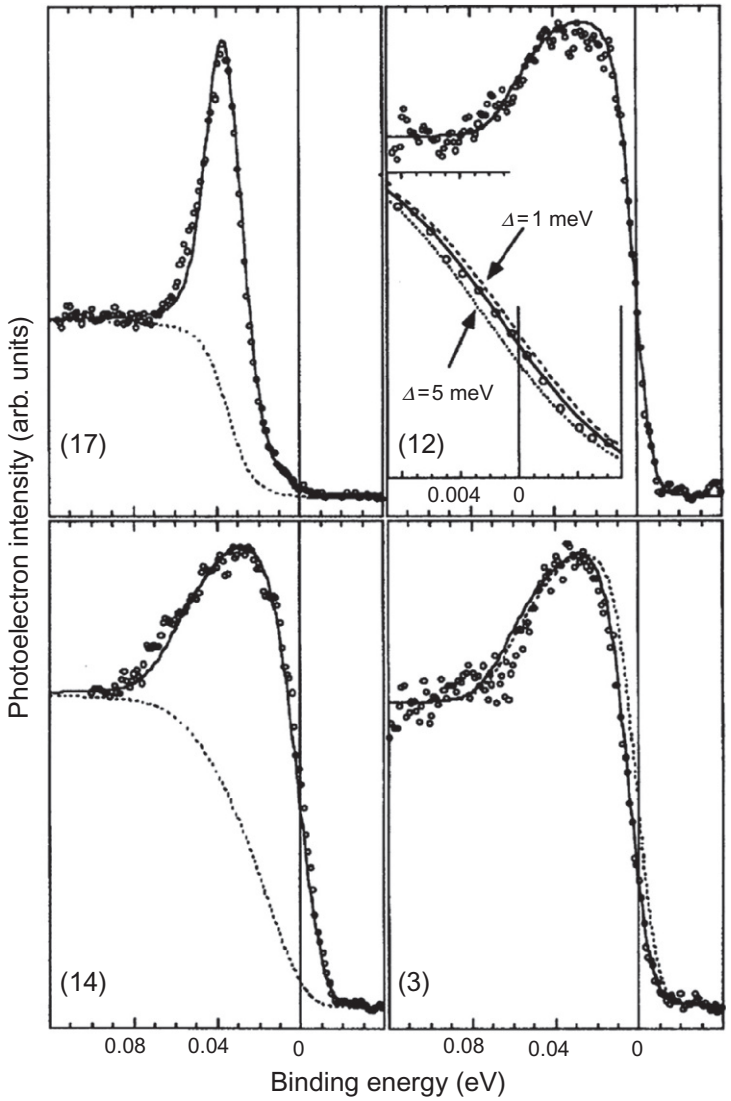

Fig. 8.5

High-resolution photoelectron spectra of valence band measured at different *k* points by ARPES for $Bi_2Sr_2CaCu_2O_8$ oxide superconductor. *Reprinted from H. Ding, J.C. Campuzano, A. Bellman, T. Yokoya, M.R. Norman, T. Takahashi, H. Katayama-Yoshida, T. Mochiku, K. Kadowaki, G. Jennings, Momentum dependence of the superconducting gap in $Bi_2Sr_2CaCu_2O_8$, Phys. Rev. Lett. 74 (1995) 2784–2787, with the permission of The American Physical Society.*

was discovered by Ohtomo et al. [12] This unique metallic interface can be applied to a switching device controlled by electric field through the third electrode, that is, a gate in FET. Then, Yoshimatsu et al. [13] investigated this unique interfacial metallic state and its origin by high energy resolution *in situ* PES of laser molecular beam epitaxy (MBE) grown $LaAlO_3$ thin

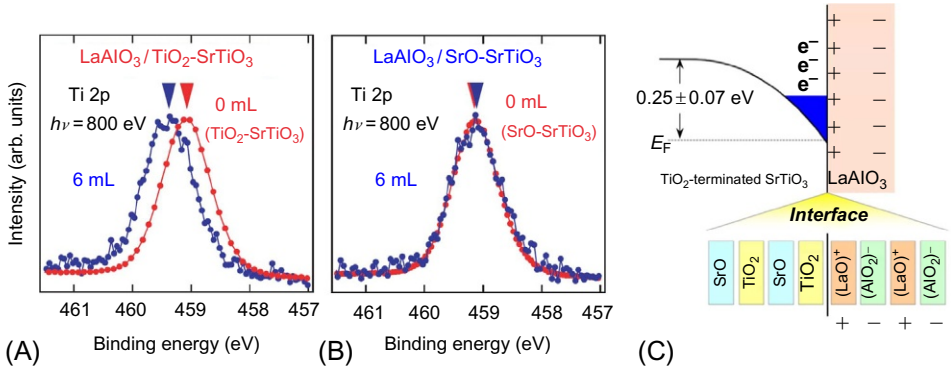

Fig. 8.6

Band bending features of $SrTiO_3$ layers for metallic and insulating $LaAlO_3/SrTiO_3$ interfaces: (A) Ti 2*p* core-level spectra of the TiO_2-terminated $SrTiO_3$ and the metallic $LaAlO_3/TiO_2$-$SrTiO_3$ interface. (B) Ti 2*p* spectra of the SrO-terminated $SrTiO_3$ and the insulating $LaAlO_3/SrO$-$SrTiO_3$ interface. (C) A band bending model for the $LaAlO_3/TiO_2$-$SrTiO_3$ interface. *Reproduced from K. Yoshimatsu, R. Yasuhara, H. Kumigashira, M. Oshima, Origin of metallic states at the heterointerface between the band insulators LaAlO3 and SrTiO3, Phys. Rev. Lett. 101 (2008) 026802, with the permission of The American Physical Society.*

films on $SrTiO_3$ substrates. As shown in Fig. 8.6A, Ti 2*p* peak is shifted toward higher binding energy for the metallic $LaAlO_3/TiO_2$-terminated $SrTiO_3$ interface, while almost no peak shift is observed for the insulating $LaAlO_3$/SrO-terminated $SrTiO_3$ interface (B). Plots of the energy shift of the Ti 2*p* core-level peaks for metallic and insulating $LaAlO_3/SrTiO_3$ interfaces as a function of the $LaAlO_3$ overlayer thickness suggested the formation of a notched structure on the $SrTiO_3$ side due to downward band bending at the metallic $LaAlO_3/TiO_2$-terminated $SrTiO_3$ interface, as shown in Fig 8.6C. In contrast, this structure is not observed at the insulating $LaAlO_3$/SrO-terminated $SrTiO_3$ interface. These results indicate that the metallic states originate not from the charge transfer through the interface on a short-range scale but from the accumulation of carriers on a long-range scale.

On the other hand, Yajima et al. [14] demonstrated the tuning behavior of the band alignment in perovskite metal-semiconductor heterojunctions over a broad range of 1.7 eV by the insertion of positive $(LaO)^+$ charge or negative $(AlO_2)^-$ charge at the $SrRuO_3$/Nb-doped $SrTiO_3$ interfaces, and the resultant dipole formed by the induced screening charge. They found that the interface dipole between the ionic charge and the induced screening charge decreases or increases the Schottky barrier height (SBH) with maintaining the relationship: $SBH = \phi - \chi + \Delta$, where ϕ is work function of $SrRuO_3$, χ is electron affinity of Nb:$SrTiO_3$ and Δ is interface dipole. They claim that this approach can be broadly applied to the cases where decoupling the band alignment from the constituent work functions and electron affinities can enhance device functionality. Thus new functional devices with nanolayers for green chemistry can be developed based on these electronic structures precisely analyzed by *in situ* SX PES.

Regarding energy storage devices, LIBs have attracted great attention nowadays because of their superior performance for storage of green energy generated by solar cells, wind-power generation, geothermal power generation, biomass generation, and so on. However, there remain several problems to be solved in order to improve the battery properties such as gravimetric energy density (Wh/kg) and gravimetric power density (W/kg).

Since LIB cathode materials usually contain 3*d* transition metal (TM) such as Co, Mn, Fe, and Ni, resonant photoelectron spectroscopy (RPES) using high-resolution SXs is a useful technique to selectively enhance 3*d* component compared to O 2*p* component in valence band spectra. Horiba et al. [15] attempted to utilize this TM 2*p*-3*d* resonant photoemission technique to clarify changes in the electronic structures under charging and discharging conditions, namely delithiation from and lithiation into cathode materials. This change corresponds to oxidation and reduction, namely hole doping and electron doping into 3*d* orbitals. Therefore they measured Fe partial density of states (DOS) of $LiFePO_4$, and its related compounds such as $Li_2FeP_2O_7$, $Li_2Fe_{1-x}Mn_xP_2O_7$ and $Na_2Fe_{1-x}Mn_xP_2O_7$ by resonant photoemission whose principle is schematically shown in Fig. 8.7A, where Fe 3*d* states in valence band are selectively enhanced through Fano resonance. They have succeeded in extracting the Fe^{2+} partial DOS and have found the systematic shift toward higher binding energy and broadening of Fe 3*d* t_{2g} down-spin states accompanying with the Mn substitution into Fe site, as shown in Fig. 8.7B. The peak shift of the Fe 3*d* t_{2g} down-spin states from 1.9 to 2.4 eV of binding energy is well matched to the change of Fe^{3+}/Fe^{2+} redox potential from 3.5 to 4.0 V for $x=0$ to 0.75, suggesting that the origin of high Fe^{3+}/Fe^{2+} redox potential in

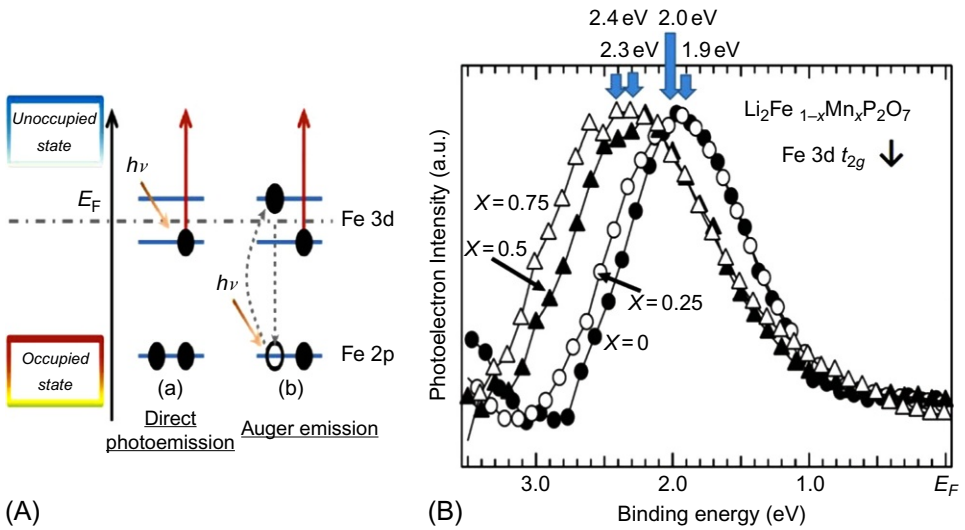

Fig. 8.7

(A) Schematic of resonant photoemission. (B) Extracted Fe 3*d* t_{2g} down-spin states obtained by subtracting the contribution from the other states from the RPES spectra for $Li_2Fe_{1-x}Mn_xP_2O_7$.

$Li_2Fe_{1-x}Mn_xP_2O_7$ is the shift of the Fe 3*d* t_{2g} down-spin states to the higher binding energy with Mn substitution. Thus cell voltages can be predicted by measuring the Fe 3d t_{2g} down-spin states in cathode materials.

Regarding energy-efficient devices, Si LSI (large scale integrated circuit) has been achieving continuous progress of four times in every 3 years following the Moore's law, contributing to green technology for sustainable society. In Si CMOS (complementary metal oxide semiconductor) technology, one of the most important processes is reportedly the formation process of gate stack structure consisting of metal gate layers, high-*k* (dielectric constant) gate insulator films, and Si substrates. So far, cross-sectional transmission electron microscope (TEM) has been used to analyze the gate stack structure. However, precise chemical and electronic information of gate stack nanolayers cannot be obtained by TEM. Toyoda et al. [16] developed a high-energy resolution in-depth profiling technique using MEM analysis of angle-resolved photoelectron spectra where in-depth information and chemical bonding information are contained.

Photoelectron intensity $F(s)$ can be expressed by the Laplace transformation, that is, the integral of $f(t)$ times the attenuation function of photoelectron: $\exp(-st)$, as follows:

$$F(s) = \int_0^\infty f(t)\exp(-st)dt \tag{8.1}$$

$$s = 1/\lambda\cos\theta,$$

where $f(t)$ is the real in-depth profile of atomic concentration as a function of depth or thickness (t), s is an angle factor, λ is escape depth or inelastic mean free path (IMFP) of photoelectron, and θ is take-off angle of photoelectron. Therefore $f(t)$ can be obtained by the inverse Laplace transformation. Toyoda et al. succeeded in obtaining in-depth profiles for a metal gate TiN/high-*k* gate stack structure of La_2O_3/HfSiO/SiO_2 on an Si substrate using backside ARPES, as shown in Fig. 8.8. They also discussed the annealing effects of gate stack nanolayer structure. In-depth profiles before and after annealing clearly show that La atoms diffuse through the HfSiO layer and reach interfacial SiO_2 layers by rapid thermal annealing. Peak shift of Si 2*p* core-level spectra by about 0.3 eV suggests that there are changes in the band discontinuity at the high-k/SiO_2 interface, which is well related to the V_{th} shift (0.3 V) based on the interface dipole model. Thus HRPES can correlate the electronic states with device performance in addition to in-depth profiling in nanolayers.

In the HX region, PES with much higher energy resolution than the conventional XPS with monochromatized Al K α X-rays [17] was realized using a combination of from Si (444) to Si (777) channel cut monochromator and Si (111) double crystal monochromator, and a high-sensitivity hemispherical electron analyzer [18]. Taking advantage of much deeper probing depth than 10 nm, various green chemistry materials and devices have been analyzed without any surface-cleaning procedures. The details will be described in Section 8.7).

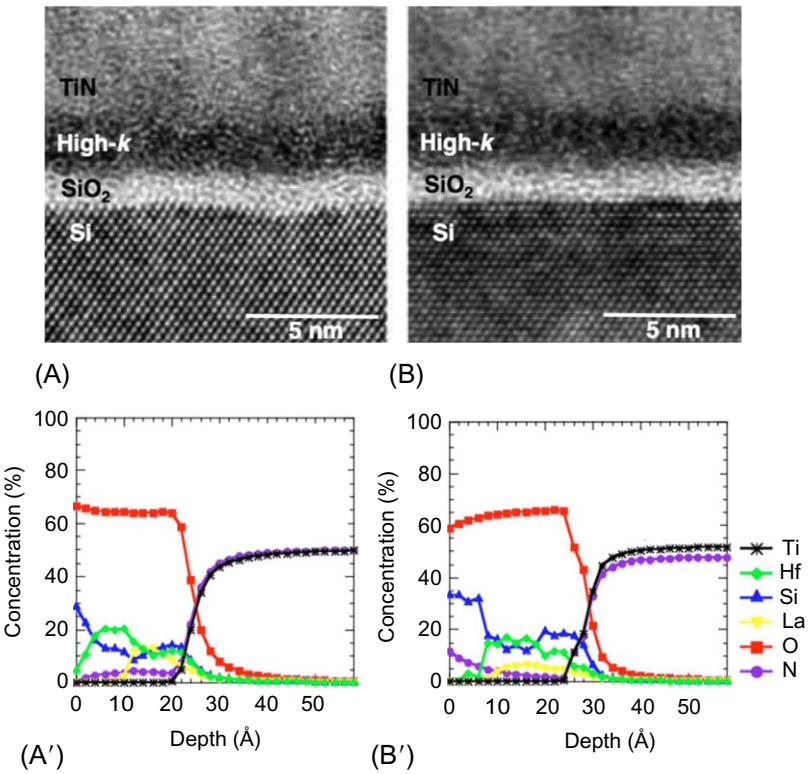

Fig. 8.8

Cross-sectional TEM images of the as-grown (A) and annealed (B) samples of a metal gate TiN/high-k gate stack nanolayer structure of La_2O_3/HfSiO/SiO_2 on an Si substrate. In-depth profiles for as-grown (A′) and annealed (B′) samples are obtained from the angle-resolved core-level intensity as a function of photoelectron take-off angle. *Reproduced from S. Toyoda, H. Kamada, T. Tanimura, H. Kumigashira, M. Oshima, T. Ohtsuka, Y. Hata, M. Niwa, Annealing effects of in-depth profile and band discontinuity in TiN/LaO/HfSiO/SiO_2/Si gate stack structure studied by angle-resolved photoemission spectroscopy from backside, Appl. Phys. Lett. 96 (2010) 042905, with the permission of AIP Publishing.*

8.3 ARPES for Band Structure of Nanolayers

ARPES is one of the most important methods to directly analyze the distribution of the electrons or the DOS in valence band in the momentum-energy space of solids, especially nanolayers. Detailed information on band dispersion and FS can be obtained by ARPES. Although conventional ARPES with VUV light can provide us with band structure in the surface region because of the short probing depth of photoelectrons within a few nanometers from surface, recent rapid progress in much brighter SX beam, and an angle-resolved electron analyzer with much higher angle resolution down to 0.1 degrees has enabled SX-ARPES, resulting in band dispersion in the deeper region, that is, more intrinsic bulk electronic properties undisturbed by surface effect.

Since photon momentum in the VUV and SX regions, which is relatively small compared to electron momentum, can be usually neglected, the component of electron momentum in the plane of the sample is conserved for the samples with smooth surface. Then the following equation can be given

$$\hbar k_{\mathrm{i}\parallel} = \hbar k_{\mathrm{f}\parallel} = \sqrt{2mE_f}\sin\theta \tag{8.2}$$

where $\hbar k_{\mathrm{f}}$ and $\hbar k_{\mathrm{i}}$ are the momentum of the outgoing electron and the initial momentum of the electron, respectively, and E_{f} is the energy of the final state. On the other hand, the normal component of electron momentum $k_{\mathrm{i}\perp}$ can be expressed by the following equation by assuming that the final in-crystal states are free-electron-like,

$$k_{\mathrm{i}\perp} = \frac{1}{\hbar}\sqrt{2m\left(E_{\mathrm{f}}\cos^2\theta + V_0\right)} \tag{8.3}$$

where V_0 is an inner potential denoting the band depth from vacuum including work function. In order to determine the dispersion relation between the binding energy, E_{B}, and the wave vector k_{i} of the photoelectron parallel to or perpendicular to the surface, as shown in Fig. 8.3, these equations for energy and momentum should be solved.

So far, ARPES had been applied to electronic structure analysis of cleavable layered materials such as graphite, black phosphor, and MoS_2. Since most of the technically and scientifically important materials are three-dimensional, ARPES was not significantly contributing to green chemistry, namely practical and industrial applications. However, since most of high Tc superconductors are layered materials that can be easily cleaved in UHV, yielding flat and smooth surface suitable for ARPES, various kinds of cuprate superconductors have been analyzed by ARPES so far. Ding et al. [19] succeeded in obtaining band mapping by high-resolution ARPES, and revealed spectroscopic evidence for a pseudogap (a suppression of spectral weight) in the normal state above T_{c} of underdoped high-T_{c} superconductors $Bi_2Sr_2CaCu_2O_{8+\delta}$ (Bi2212). They used 19 or 22 eV of photon energy with an energy resolution of 22 or 27 meV, respectively.

For terahertz wireless telecommunication applications of ultrahigh-speed FETs, graphene has exhibited great application potential as the host material for next-generation electronic devices because of its extremely high carrier mobility. However, despite its intriguing properties, the lack of an energy gap in its electronic spectra is a critically weak point for device applications. Zhou et al. [20] reported electronic structure for graphene determined with ARPES in order to open a gap in graphene's electronic spectra. They used epitaxial strain from SiC substrates and succeeded in obtaining a gap of 0.26 eV, as revealed by ARPES band mapping in Fig. 8.9. This gap decreases as the sample thickness increases and eventually approaches zero when the number of layers exceeds four. They also revealed that the origin of this gap is the breaking of sublattice symmetry owing to the graphene-substrate interaction. Their results with ARPES suggest a promising direction for bandgap engineering of graphene.

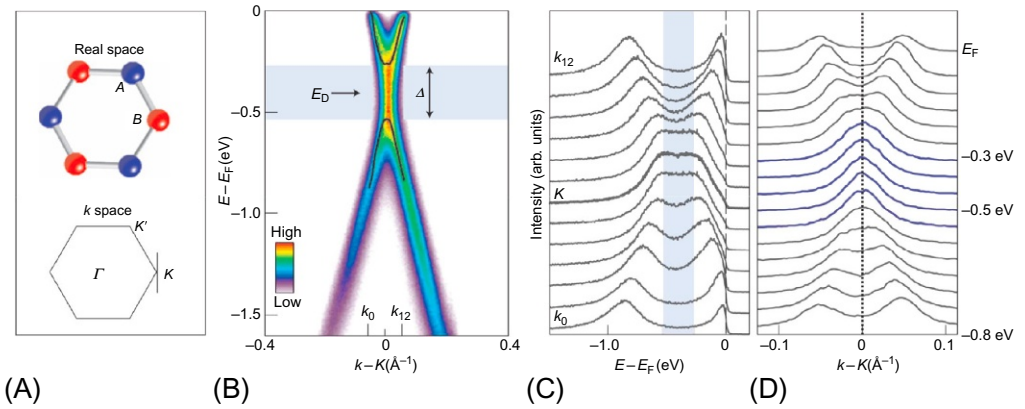

Fig. 8.9

Observation of the gap opening in single-layer graphene at the K point. (A) Structure of graphene in the real and momentum space. (B) ARPES intensity map taken along the black line in the inset of (A). (C) Energy dispersion curves (EDCs) taken near the *K* point from k_0 to k_{12} as indicated at the bottom of (B). (D) Momentum dispersion curves (MDCs) from E_F to −0.8 eV. *Reprinted from S.Y. Zhou, G.H. Gweon, A.V. Fedorov, P.N. First, W.A. de Heer, D.H. Lee, F.Guinea, A.H. Castro Neto, A. Lanzar, Substrate-induced bandgap opening in epitaxial graphene, Nat. Mater. 6 (2007) 770–775, with the permission of Macmillan Publishers Ltd: Nature Materials, advance online publication, 9 September 2007; doi:10.1038/nmat20.*

In order to widely apply ARPES to band dispersion analysis of three-dimensional materials, Horiba et al. [21] developed an *in situ* ARPES system combined with laser MBE system. Chikamatsu et al. [22] reported ARPES band mapping of $La_{1-x}Sr_xMnO_3$ (LSMO) showing a colossal magnetoresistance behavior that can be applied for switching devices. They observed changes in the electronic structure across the filling-control metal-insulator transition by means of *in situ* ARPES of epitaxial thin films. The FS gradually disappears near the MI transition by transferring spectral weight from the coherent band near the Fermi level E_F to the lower Hubbard band, as shown in Fig. 8.10 (upper panel), whereas a pseudogap behavior also exists in the ARPES spectra in the close vicinity of E_F for metallic LSMO. These results indicate that the spectral weight transfer derived from strong electron-electron interaction dominates the gap formation in LSMO associated with the filling-control MI transition, as schematically shown in Fig. 8.10 (lower panel).

Another interesting application of this *in situ* MBE-ARPES system is the first discovery of the quantum confinement of strongly correlated electrons in artificial structures grown by laser MBE, providing a platform for studying the behavior of correlated Fermi-liquid states in low dimensions. Yoshimatsu et al. [23] reported the creation and control of two-dimensional electron-liquid states in ultrathin films of $SrVO_3$ grown on Nb:$SrTiO_3$ substrates, which are artificial oxide structures that can be varied in thickness by single monolayers. As shown in Fig. 8.11, ARPES results for the $SrVO_3$/Nb:$SrTiO_3$ samples with quite low lattice mismatch clearly exhibit metallic quantum well states that can be appropriately described by the

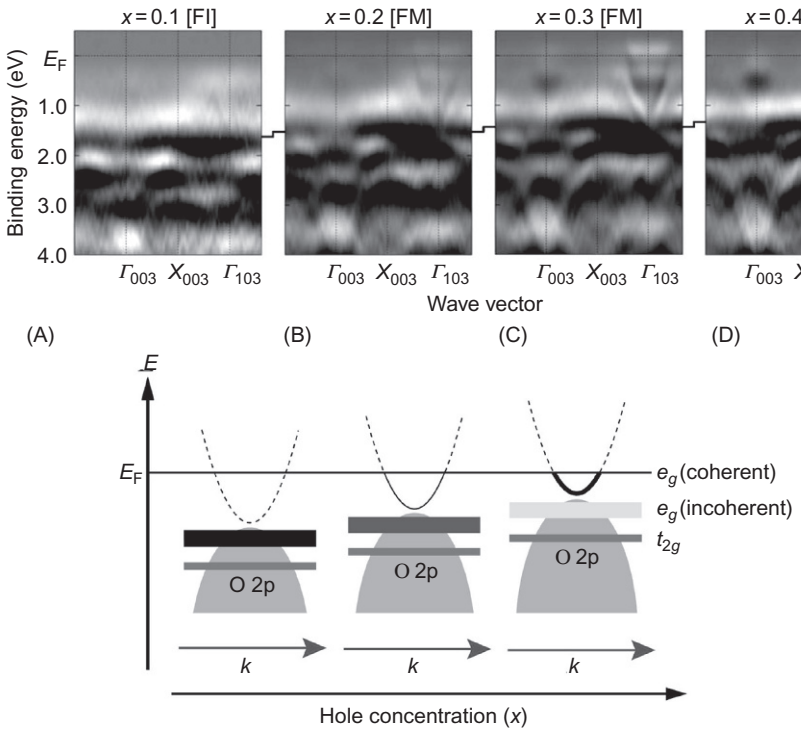

Fig. 8.10

Experimental band structure of the $La_{1-x}Sr_xMnO_3$ thin films along the Γ-X direction [x = (A) 0.1, (B) 0.2, (C) 0.3, and (D) 0.4] obtained from the ARPES measurements (upper pane). *Dark parts* correspond to energy bands. *Solid lines* represent the chemical potential shift determined by angle-integrated PES studies. Lower panel shows a schematic illustration for the composition dependence of the electronic structure of $La_{1-x}Sr_xMnO_3$. *Reprinted from A. Chikamatsu, H. Wadati, H. Kumigashira, M. Oshima, A. Fujimori, M. Lippmaa, K. Ono, M. Kawasaki, H. Koinuma, Gradual disappearance of the fermi surface near the metal-insulator transition in $La_{1-x}Sr_xMnO_3$, Phys. Rev. B Rapid Commun. 76 (2007) 201103(R),* © *2007, with the permission of The American Physical Society.*

well-known phase-shift quantization rule. The observed quantum well states in $SrVO_3$ ultrathin films show distinctive orbital-selective quantization originating from the anisotropic orbital character of the V 3*d* states and unusual band renormalization of the subbands near the Fermi level. These results suggest complex interactions in the quantum well.

For more practically applied materials, Ueoka et al. [24] reported ARPES results for low-power dissipation thin film transistor (TFT) InGaZnO (IGZO) materials for liquid crystal display. The electronic structures of amorphous IGZO film on SiO_2 layers before and after annealing were observed by constant, final state, angle-resolved X-ray photoelectron spectroscopy (CFS-XPS) and X-ray adsorption near-edge structure spectroscopy (XANES) using a two-dimensional, display-type, spherical mirror analyzer (DIANA: DIsplay-type, spherical mirror ANAlyzer Fig. 8.12A), with which Matsui et al. [25] succeeded in three-dimensional band mapping of graphite. Angle-resolved CFS-XPS using SXs reveals the in-depth change of the electronic state in

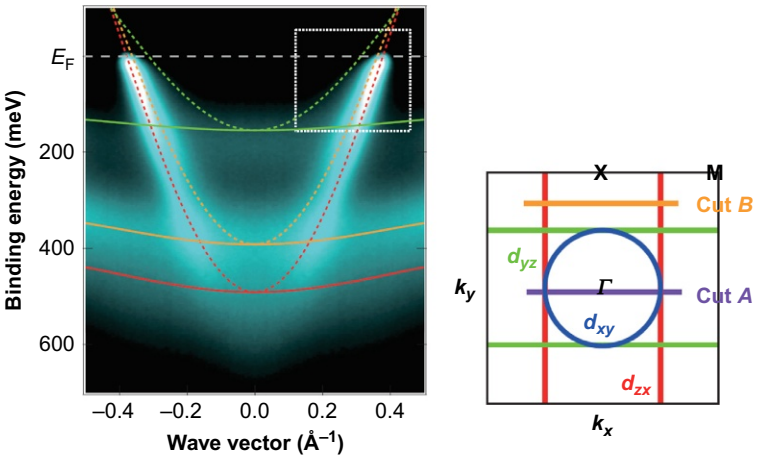

Fig. 8.11

Orbital-selective quantization of V 3*d* states in $SrVO_3$ ultrathin films. Intensity plots of ARPES spectra for 8-ML $SrVO_3$ ultrathin films for cut A. The *dashed and solid lines* represent the fitted curves to the dispersion for the d_{zx} and d_{yz} quantization states, respectively. *Red*, *orange*, and *green lines* which are parabolic lines located at about 500 meV, 400 meV and 150 meV, respectively at the Γ point correspond to states with $n = 1$, 2, and 3, respectively, indicating that both d_{zx} and d_{yz} orbitals show quantized states confined in the ultrathin $SrVO_3$ layers. *Reproduced from K. Yoshimatsu, K. Horiba, H. Kumigashira, T. Yoshida, A. Fujimori, M. Oshima, Metallic quantum well states in artificial structures of strongly correlated oxide, Science 333 (2011) 319–322, with the permission of the American Association for the Advancement of Science.*

the a-IGZO bulk rather than at the a-IGZO/SiO_2 interface, as shown in Fig. 8.12B and C. The tail states representing conduction band edge states in a-IGZO effectively decrease by high-pressure water vapor annealing (HPV). Combined with XANES results indicating an increase in the number of tail states upon atmospheric annealing (AT), they concluded that the increase in the number of tail states is well correlated with the decrease of the channel mobility. Thus ARPES can be applied to even amorphous materials for electron devices, although band dispersion cannot be obtained for amorphous materials.

Thus ARPES can provide us with very valuable information of electronic structure in solids including cleavable layered materials, MBE-grown thin films, and amorphous semiconductors. However, *in situ* ARPES of MBE-grown samples limits the applications, especially industrial applications which strongly require rapid analysis and ex situ analysis of home laboratory-made real samples with device quality using specialized fabrication apparatuses. In this viewpoint, Kobayashi et al. [26] successfully demonstrated a potential for band mapping by ex situ SX ARPES of single crystal samples using the capping layer technique with amorphous layers. They measured band dispersion of a GaAs thin film protected by an amorphous As layer with thickness exceeding the typical probing depths of VUV light up to 100 eV. Increasing the probing depth by increasing photon energy into the SX region such as several hundred eV clearly exposes the bulk band dispersion of the GaAs underlayer without any surface treatment.

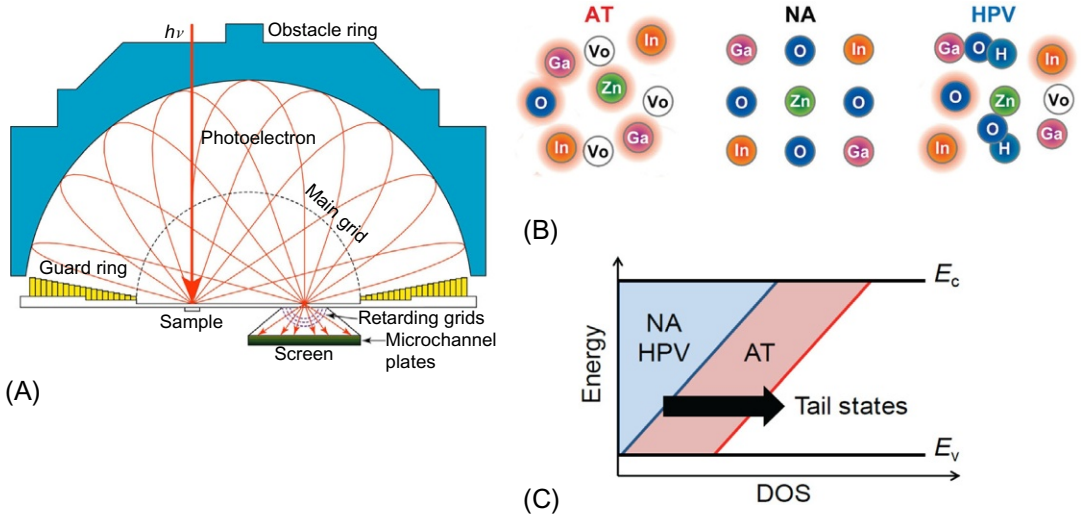

Fig. 8.12

(A) Pattern diagram of display-type spherical mirror analyzer. (B) Diagrammatic illustration of (A) electronic structure of a-IGZO bulk region after AT, before annealing (NA), and after high-pressure water vapor annealing (HPV), and (C) density of states in band gap. *Reproduced from Y. Ueoka, Y. Ishikawa, N. Maejima, F. Matsui, H. Matsui, H. Yamazaki, S. Urakawa, M. Horita, H. Daimon, Y. Uraoka, Analysis of electronic structure of amorphous InGaZnO/SiO_2 interface by angle-resolved X-ray photoelectron spectroscopy, J. Appl. Phys. 114 (2013) 163713, with the permission of AIP Publishing.*

Fig. 8.13A–E shows valence-band dispersion of the GaAs thin film. This ex situ SX-ARPES enables access to the three-dimensional band dispersion of buried underlayer through an amorphous overlayer. This technique would open up a new possibility of analyzing momentum-resolved electronic structure of protected thin-film heterostructures.

8.4 Spin-Resolved Photoelectron Spectroscopy

Magnetic materials have been utilized for large-scale data storage or spintronic device systems such as nonvolatile magnetic random access memory (MRAM) and magnetic disk or hard disk drive (HDD) system using magnetic nanolayers, and very strong magnets for electrical generators and electric motors applications. In order to improve magnetic properties of these materials, magnetic properties should be precisely analyzed for the bulk, nanolayers, surfaces, and interfaces. Spin-resolved photoelectron spectroscopy (SR-PES) is one of the most promising techniques for analyzing spin-polarized photoelectrons due to ferromagnetic exchange splitting in the spin states of the valence band of a ferromagnet. The spin-dependent many electron effects induced by the photoelectron excitation can also be analyzed.

SR-PES and ARPES provides “complete” information on an electronic state of a material, that is, “energy, momentum, and spin.” However, the detection of photoelectrons with spin- and angle-resolutions has been a challenging issue due to the extremely low count rate at a spin

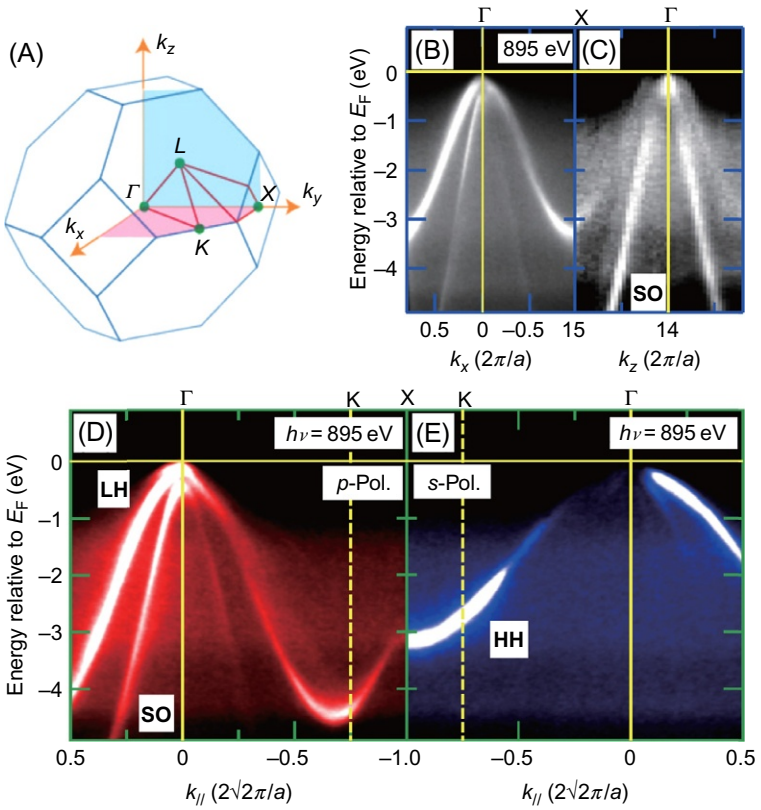

Fig. 8.13

Valence-band dispersion of the GaAs thin film. (A) Brillouin zone (BZ). (B) and (C) energy (E)-momentum plots of the *C-X-C* symmetric line along the surface-perpendicular k_x and surface-normal k_z momenta, respectively. SO denotes the split-off band of GaAs. (D) and (E) *E-k*(parallel) plots of the *C-K-X* symmetric line taken with *p*- and *s*-polarizations, respectively. The *dashed vertical lines* are the BZ boundary at the *K* point. LH and HH denote the light-hole and heavy-hole bands, respectively. *Reproduced from M. Kobayashi, I. Muneta, T. Schmitt, L. Patthey, S. Ohya, M. Tanaka, M. Oshima, V.N. Strocov, Digging up bulk band dispersion buried under a passivation layer, Appl. Phys. Lett. 101 (2012) 202103, with the permission of AIP Publishing.*

detector. So far a Mott-type spin polarimeter with the principle of spin-orbit interaction had been used for SR-PES from the 1970s to the 1990s. The most famous SR-PES experiment was done on Fe(100) by Gudat's group [27]. By spin- and angle-resolved photoemission with synchrotron radiation, the electronic structure of Fe(100) was tested between room temperature and the Curie temperature *Tc* for photon energies in the range 20–70 eV. However, the efficiency of the spin polarimeter was so low that SR-PES experiments were forced to be done with poor energy resolution (200–300 meV) and poor angle resolution (± several degrees) even using synchrotron radiation. So, great efforts have been devoted to develop more efficient spin polarimeters.

Recently, a new spin- and angle-resolved photoemission spectrometer was developed adopting the very-low-energy-electron-diffraction (VLEED)-type spin polarimeter with the principle of spin-exchange interaction operating at 6–20 V [28]. While the figure of merit (FOM) for Mott-type spin polarimeter is around 10^{-4}, that for this VLEED-type spin polarimeter is as high as 10^{-3} to 10^{-2}. The Fe(001)p(1×1)-O film grown on MgO(001) crystal for the VLEED target yields significantly high spin-resolving power, the effective Sherman function of 0.40 ± 0.02, with long lifetime and stability. Bertacco et al. [29,30] realized approximately 100 times higher efficiency than that of conventional Mott-type spin polarimeter with the FOM of about 0.019. Thanks to this high efficiency, high-energy resolution can be realized. The simplified ways of target preparation and revitalization make the VLEED spin polarimeter much more convenient and feasible for the spin-polarized PES.

TM dichalcogenides have recently attracted renewed attention because of the remarkable electronic and physical properties of two-dimensional materials such as graphene and topological insulators. The behavior of electrons and holes in a crystal lattice is a fundamental quantum phenomenon, accounting for a rich variety of material properties. One example is the anomalous bulk properties of semimetallic WTe_2. Das et al. [31] reported angle- and spin-resolved photoemission spectroscopy of WTe_2 single crystals, where they revealed the role of W and Te atoms in the formation of the band structure and identified the interplay of charge, spin, and orbital degrees of freedom. They found that at $k_x = -0.25\ \text{A}^{-1}$ and $k_y = 0\ \text{A}^{-1}$ the down-spin spectrum has a larger peak at 0.6 eV and the up-spin spectrum has a larger peak at 0.2 eV, whereas at $k_x = 0.25\ \text{A}^{-1}$ and $k_y = 0\ \text{A}^{-1}$ the up-spin spectrum has a dominating peak at 0.6 eV and the down-spin spectrum has a dominating peak at 0.2 eV, supporting time-reversal effect. Based on first-principles calculations and high-resolution surface topography, the existence of a layer-dependent behavior was observed.

Another interesting feature on the surfaces of three-dimensional topological insulators is $TlBiSe_2$ showing an in-gap Dirac point, where the upper and lower parts of the Dirac-cone surface state are both utilized. Although investigations of the surface transport properties of this material are limited due to the lack of bulk insulating characteristics, Kuroda et al. [32] reported a realization of the bulk insulating property by tuning the composition of $Tl_{1-x}Bi_{1+x}Se_{2-\delta}$ without introducing guest atoms. Fig. 8.14A shows spin-resolved energy dispersive curves (EDCs) along K-Γ-K at various emission angles. As shown in Fig. 8.14B and C, experimental spin polarization taken after subtraction of constant background clearly reveals the spin-helical surface Dirac cone with reversed spin helicity at the Dirac point. Thus SR-PES can provide useful information on exotic topological phenomena on the surface.

One of the important practical applications of magnetic materials is magnetic head or spin valve for HDD and spin transfer torque (STT) MRAM based on the identical principle of magnetic tunneling junction (MTJ). The tunneling probability between both magnetic electrode materials sandwiching an insulating nanolayer (about 1 nm thick) is expressed by $2P_tP_b/(1 - P_tP_b)$,

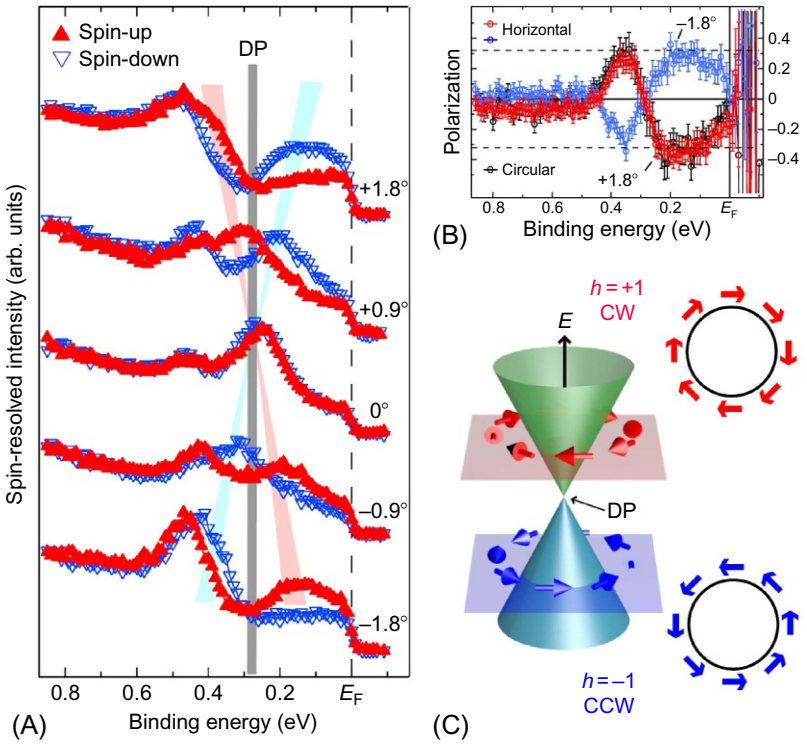

Fig. 8.14

(A) Spin resolved EDCs along *K-Γ-K* at the emission angle from -1.8 to +1.8 degrees. Spin-up and spin-down spectra are plotted with closed upright (*filled*) and inverted (*open*) triangles. (B) Experimental spin polarization taken after subtraction of constant background. (C) Schematic picture of the spin-helical surface Dirac cone with reversed spin helicity at the Dirac point. *Reprinted from K. Kuroda, G. Eguchi, K. Shirai, M. Shiraishi, Mao Ye, K. Miyamoto, T. Okuda, S. Ueda, M. Arita, H. Namatame, M. Taniguchi, Y. Ueda, A. Kimura, Tunable spin current due to bulk insulating property in the topological insulator Tl1-xBi1+xSe2-δ, Phys. Rev. B 91 (2015) 205306, with the permission of The American Physical Society.*

where P_t and P_b are spin polarization of top and bottom electrodes, respectively. Therefore, in order to develop better performance MTJ, ferromagnetic materials (thin films) with the spin polarization of unity, which is called "half-metal," should be developed. Half-metallic materials are characterized by the coexistence of metallic behavior for one electron spin (majority spin) and insulating behavior for the other (minority spin), resulting in completely spin polarized DOS at or near the Fermi level, and the conductivity is dominated by these metallic single-spin charge carriers. Park et al. [33] reported spin-resolved photoemission measurements of a ferromagnetic manganese perovskite, $La_{0.7}Sr_{0.3}MnO_3$, showing the half-metallic nature well below the Curie temperature. For the majority spin, the photoemission spectrum clearly shows a metallic Fermi cut-off, whereas for the minority spin, it shows an insulating gap with disappearance of spectral weight at approximately 0.6 eV binding energy, as shown in Fig. 8.15.

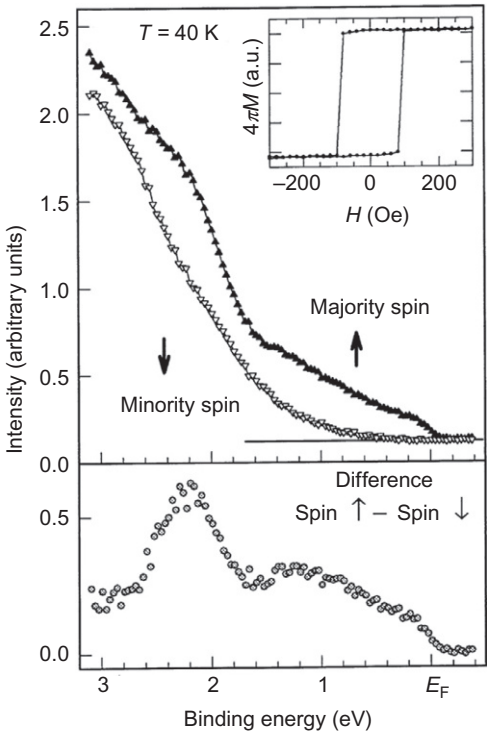

Fig. 8.15

Spin-resolved photoemission spectra of a thin film of $La_{0.7}Sr_{0.3}MnO_3$ near the Fermi energy (E_F). Measurements were done at 40 K. The photon energy and the experimental resolution were set at $h\nu = 40$ eV, and $\Delta E = 0.2$ eV, respectively. *Reprinted from J.H. Park, E. Vescovo, H.J. Kim, C. Kwon, R. Ramesh, T. Venkatesan, Direct evidence for a half-metallic ferromagnet Nature 392 (1998) 794, with the permission of Macmillan Publishers Ltd: Nature, advance online publication, 23 April 1998.*

Thus, SR-PES would become a more inevitable tool to characterize spintronic materials and devices for green chemistry.

8.5 Time-Resolved Photoelectron Spectroscopy for Transient Phenomena or Surface Dynamics

In order to develop more advanced devices with higher efficiency and faster operation for green chemistry, electronic structure in terms of dynamics or time-dependence should be analyzed for MOSFET, solar cells, photocatalysts, magnetic materials, strongly correlated electron materials, and low-dimensional materials like graphene in addition to static electronic structure revealed by ARPES and so on. Fig. 8.16 shows various chemical and physical phenomena on different time scales [34]. Elementary phenomena such as electron-electron (e-e) interactions, electron-coherent phonon (e-cph) coupling, and electron-phonon (e-ph) coupling occur mostly

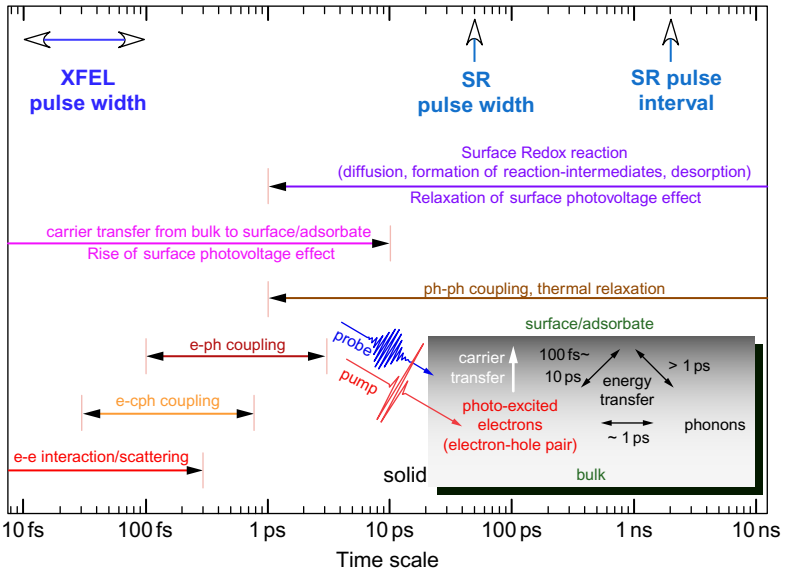

Fig. 8.16

Various chemical and physical phenomena and their time scale. Typical time scale of XFEL and SR light sources are also given for comparison. *Reprinted from S. Yamamoto, I. Matsuda, Time-resolved photoelectron spectroscopies using synchrotron radiation: past, present, and future J. Phys. Soc. Jpn. 82 (2013) 021003, © 2013. http://dx.doi.org/10.7566/JPSJ.82.021003, with the permission of Physical Society of Japan.*

on ultrafast time scales (typically less than picoseconds [1 ps = 10^{-12} s]). So, ultrafast time-resolved spectroscopy is strongly required to directly monitor these ultrafast processes. The dynamics in chemical reactions such as bond-breaking and bond-forming take place typically on a time scale of femtoseconds (1 fs = 10^{-15} s). However, other elementary processes of reaction such as surface diffusion, formation of reaction intermediates, and desorption occur on time scales longer than picoseconds.

A pump-probe spectroscopy is one of the most important methods for investigating dynamics of electronic structure, where a femtosecond infrared laser pulse excites the sample to create electron-hole pairs and a subsequent UV or SX pulse beam can probe the transient electronic structure after a time delay Δt. Time-resolved photoelectron spectroscopy (trPES) adds femtosecond time-resolution to conventional PES. Furthermore, by time- and angle-resolved photoelectron spectroscopy (trARPES) elementary scattering processes in complex materials can be directly analyzed or converted into the electronic band structure as a function of energy and electron momentum.

Most synchrotron radiation rings provide SR pulses with a pulse width in the range of 30–70 ps and repetition rates of 500 or 1.25 MHz depending on the storage ring operation mode. For pump-probe spectroscopy, an IR or visible light laser system synchronized to the SR storage ring is used. An optical delay line and an electronic delay are utilized to control the time delay between laser and SR pulses, as shown in Fig. 8.17 [35].

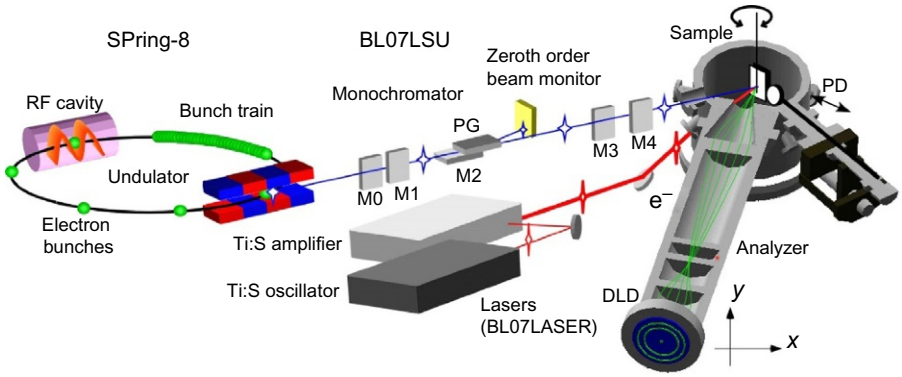

Fig. 8.17

Time-resolved photoelectron spectroscopy system at BL07LSU in SPring-8. *Reproduced from S. Yamamoto, I. Matsuda, Time-resolved photoelectron spectroscopies using synchrotron radiation: past, present, and future, Rev. Sci. Instrum. 83 (2012) 023109, with the permission of AIP Publishing.*

Ozawa et al. [36] reported trPES results on photocatalytic TiO_2 surfaces, where photocatalytic activity is determined by the transport property of photoexcited carriers from the bulk to the surface of photocatalysts. Because the carrier dynamics are influenced by a space charge layer (SCL) in the subsurface region, an understanding of the effect of the potential barrier of the SCL on the carrier behavior is essential. They measured the relaxation time of the photoexcited carriers on single-crystal anatase and rutile TiO_2 surfaces by trPES, as shown in Fig. 8.18. They found that carrier recombination is strongly influenced by the surface barrier height V_s* of the SCL. The carrier lifetime is determined to be 180 ± 100 ns on rutile (110), whose barrier height for the hole transport is 0.4 eV, whereas the lifetime on anatase (001) which has the surface barrier of 0.2 eV is 50 ± 30 ns. The analysis within the thermionic emission model, however, reveals that the carrier lifetime is longer on anatase if the barrier-height difference is <0.15 eV, even though the barrier is higher on the rutile surface than on anatase. The present study demonstrates that the photoexcited carrier lifetime can be tuned from subnanoseconds to microseconds by changing the surface barrier height. Such band engineering is applicable to design not only photocatalysts with higher activity but also photovoltaics with improved conversion efficiency.

For developing very fast FET for terahertz devices or many next-generation electronic devices, graphene has attracted great attention because of its large electron mobility around 200,000 cm^2/Vs. However, there is still much debate over how the electronic properties of graphene behave on ultrashort time scales. Gilbertson et al. [37] succeeded in the first direct measurement of carrier distribution dynamics in monolayer graphene after ultrafast photoexcitation. They obtained the evolving quantum distributions of the electrons and holes by trPES on an ultrashort 500 fs time scale, as shown in Fig. 8.19. For delays closer to time zero

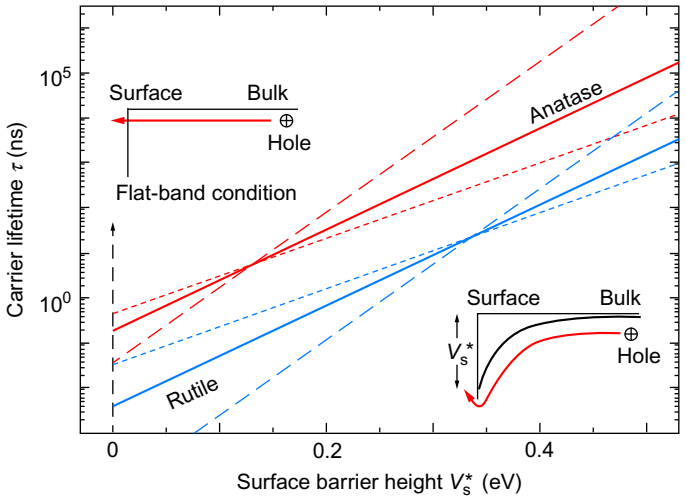

Fig. 8.18

Change in the carrier lifetimes τ on the anatase (001) and rutile (110) surfaces as a function of the surface barrier height for the hole transport V_s^*. *Solid lines* are the results of $\eta = 1.5$, *while dashed and dotted lines* are obtained with $\eta = 1.0$ and 2.0, respectively. *Reprinted from K. Ozawa, M. Emori, S. Yamamoto, R. Yukawa, S. Yamamoto, R. Hobara, K. Fujikawa, H. Sakama, I. Matsuda, Electron-hole recombination time at TiO2 single-crystal surfaces: influence of surface band bending, J. Phys. Chem. Lett. 5 (2014) 1953, with the permission of American Chemical Society.*

(a), the fitting cannot be accomplished without the inclusion of a nonzero chemical potential. At later delays (b), the chemical potential can be zero and still achieve fitting. The values of T and μ for several delay values are plotted in Fig. 8.19C. The shape of $T(t)$ is similar to results of the two-temperature model, whereas $\mu(t)$ could not be measured in previous experiments.

The chemical potentials assigned to the excess carrier distributions rapidly decrease, and after $\sim$1 ps they are equal to zero, indicating the complete crossover to a state described by the T^* model with electron and hole distributions in chemical and elevated temperature equilibrium.

For LSI devices, charge carrier dynamics are important especially at the gate insulator SiO_2-Si interface. Bröcker et al. [38] measured time-resolved Si 2*p* core level photoelectron spectra for a thermally grown 1.5-nm-thick SiO_2/Si(100) interface. Upon excitation of electron hole pairs in the surface-near region by picosecond laser pulses, the dynamics of the charge carrier recombination has been determined by time-resolved Si 2*p* core level photoemission via the time-dependent surface photovoltage, as shown in Fig. 8.20A. Fig. 8.20B shows a potential scheme for the surface of a p-doped semiconductor. Bröcker et al. found a nonexponential decay of the surface photovoltage on a time scale from picoseconds to 800 ns and a logarithmic dependence on laser intensity, which can be well described by a quasiequilibrium model based on charge carrier dynamics governed by thermionic emission.

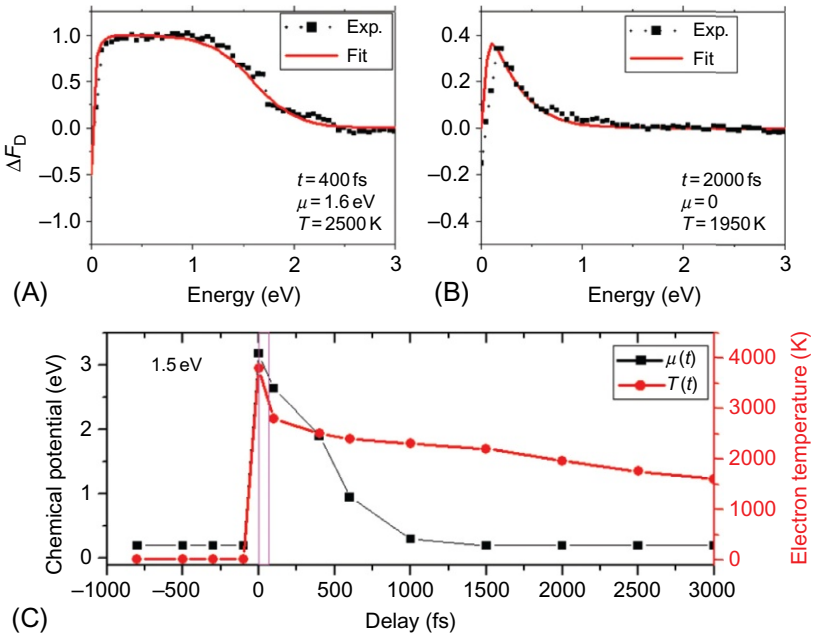

Fig. 8.19

Fitting of the experimental data (*black squares*) with ΔF_D (*red line; light gray line in print version*) for a 1.5 eV pump pulse at delays of (A) $t = 400$ fs and (B) $t = 2000$ fs. In (C), *red solid circles* (*light gray solid circles* in print version) are for $T(t)$, and *black solid squares* for $\mu(t)$. *Reprinted from S. Gilbertson, G.L. Dakovski, T. Durakiewicz, J.X. Zhu, K.M. Dani, A.D. Mohite, A. Dattelbaum, G. Rodriguez, Tracing ultrafast separation and coalescence of carrier distributions in graphene with time-resolved photoemission, J. Phys. Chem. Lett. 3 (2012) 64–68, with the permission of American Chemical Society*

Topological insulators including topological superconductors have attracted great attention because of their unique properties and potential applications to ultrafast quantum computers. Sobota et al. [39] reported time-resolved electronic structure of topological insulator, characterizing the occupied and unoccupied electronic structure of the topological insulator Bi_2Se_3 by one-photon and two-photon angle-resolved photoemission spectroscopy and slab band structure calculations. They revealed a second, unoccupied Dirac surface state with similar electronic structure and physical origin to the well-known topological surface state. This state is energetically located at 1.5 eV above the conduction band, which permits it to be directly excited by the output of a Ti:sapphire laser. This discovery demonstrates the feasibility of direct ultrafast optical coupling to a topologically protected, spin-textured surface state.

Schmitt et al. [40] used femtosecond trARPES to optically pump and probe $TbTe_3$. It is important to investigate microscopic cooperative effects that lead to instabilities with macroscopic impacts like phase transitions through self-coordination and collectivity. By driving a transient charge density wave melting, they observed excited collective vibrations in

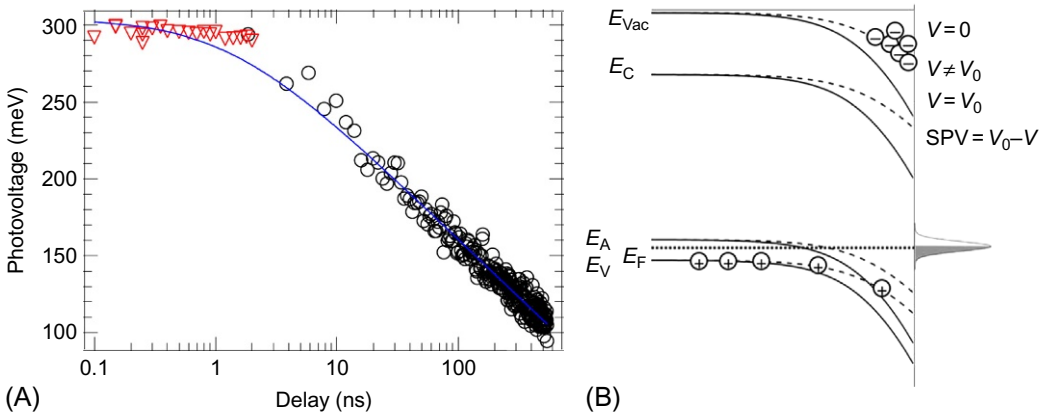

Fig. 8.20

(A) Time-resolved surface photovoltage for thermally grown SiO_2/Si(100) upon laser excitation on a logarithmic time scale. (B) Potential scheme for the surface of a p-doped semiconductor. The *solid lines* are for SPV = 0 and the *dashed lines* are for SPV not equal to 0. *Reprinted from D. Bröcker, T. Gießel, W. Widdra, Charge carrier dynamics at the SiO2/Si(100) surface: a time-resolved photoemission study with combined laser and synchrotron radiation, Chem. Phys. 299 (2004) 247, with the permission of Elsevier B.V.*

$TbTe_3$ through their time-, frequency-, and momentum-dependent influence on the electronic structure or FS, as shown in Fig. 8.21. They identified the role of the observed collective vibration in the transition and to document the transition in real time.

Thus trPES can provide us with deep insight into transient phenomena or dynamics that should be correlated with performance of green chemistry materials and devices.

8.6 Spatially Resolved PES for Green NanoMaterials and NanoDevices

With the rapid progress in nanotechnology and nanoscience, the demands for nanoscopic analyses of chemical, electronic, and magnetic properties, namely nanoscale imaging, are becoming stronger. In the field of catalysis, surface chemical reaction on a single particle of catalyst with the size of several tens of nm is a key issue to be analyzed for developing new catalysts with higher performance. In LSI devices, the gate channel is nowadays in the order of around 10 nm, and nanoscale electronic structure analysis is needed. For nonvolatile STT-MRAM, the cutting-edge devices with a diameter of about 10 nm are being developed, where magnetic imaging with the spatial resolution of a few nm is strongly required.

For that purpose, spatially resolved PES or imaging has been developed mainly in two ways, as shown in Fig. 8.22. One is to use focused X-rays or VUV beam by reflection mirrors like a Kirkpatrick-Baez (KB) mirror system and a Wolter mirror system, or by a diffraction lens like the Fresnel zone plate (FZP). Although the mirror system has a great advantage over FZP in terms of photon flux and fixed focal length regardless of photon energy, the focused beam size

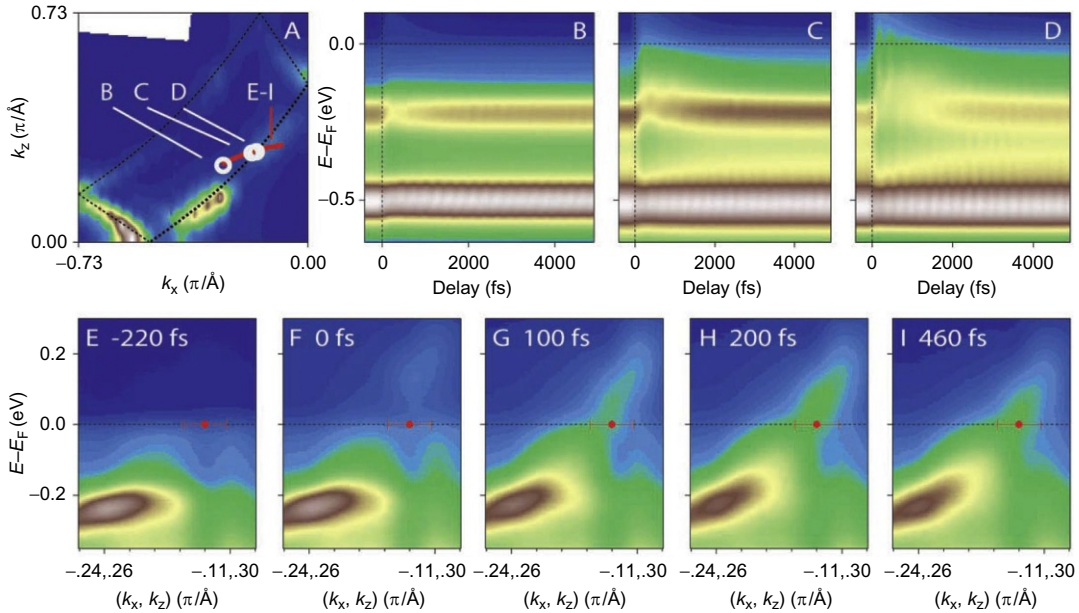

Fig. 8.21

(A) Detail of the FS plot with indicated positions (*white circles*) of time-resolved data shown in (B) to (D) for fixed *k* as a function of time delay. Indicated cut position (*red line; light gray line in print version denoted below "E-I"*) of photoelectron intensity is shown as a function of energy, and position [(E) to (I)] for a momentum scan is shown as a function of time delays. With time evolution from 0 fs (F) to 460 fs (I), the tail part in the *E-k* diagram is approaching the Fermi level. All data were collected at 100 K and $F = 2$ mJ/cm^2. k_F is marked in (E) to (I). *Reprinted from F. Schmitt, P.S. Kirchmann, U. Bovensiepen, R.G. Moore, L. Rettig, M. Krenz, J.H. Chu, N. Ru, L. Perfetti, D.H. Lu, M. Wolf, I.R. Fisher, Z.X. Shen, Effect of the amplitude mode and the transient melting of the charge density wave on the electronic structure of $TbTe_3$, Science 321 (2008) 1649, with the permission of the American Association for the Advancement of Science.*

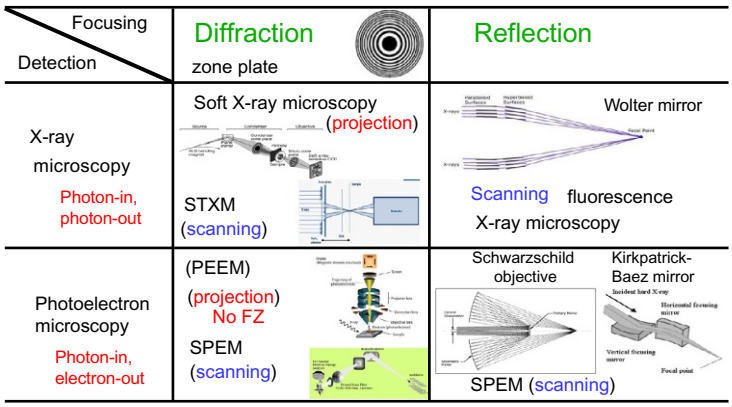

Fig. 8.22

Classification- of X-ray microscopy and photoelectron microscopy with diffraction and reflection methods.

is around 1 μm at present. In contrast, FZP can provide us with the focused beam of <100 nm. The other is to focus photoelectrons emitted from samples irradiated with unfocused SR beam with the size of several tens of μm by means of electron lens system. So, the former imaging is a kind of scanning electron microscope, while the latter one is a kind of TEM.

In order to meet these requests from industry, Horiba et al. [41] developed a 3D-nano-ESCA system for nondestructive observation of the three-dimensional spatially resolved electronic structure of solids. For focusing the X-rays, a FZP with a diameter of 200 μm and an outermost zone width of 35 nm is used. In order to obtain the angular dependence of the photoelectron spectra for the depth-profile analysis without rotating the sample, an angle-resolved electron analyzer with an acceptance angle of 60 degrees as a high-resolution angle-resolved electron spectrometer was used. From the results of the line-scan profiles of the FET poly-Si/high-k gate patterns, a total spatial resolution was determined to be better than 70 nm.

Regarding energy-efficient devices, Horiba et al. [42] applied the 3D-nano-ESCA system to reveal the change in the electronic structure of an Ni nanowire ReRAM device during resistance-switching operations using scanning photoelectron microscopy techniques in order to clarify the mechanism of resistance-switching phenomena. The disappearance of DOS at the Fermi level (E_F) in a high-resistance state and recovery of a finite DOS at E_F in a low-resistance state are directly observed, as shown in Fig. 8.23, indicating that the Ni

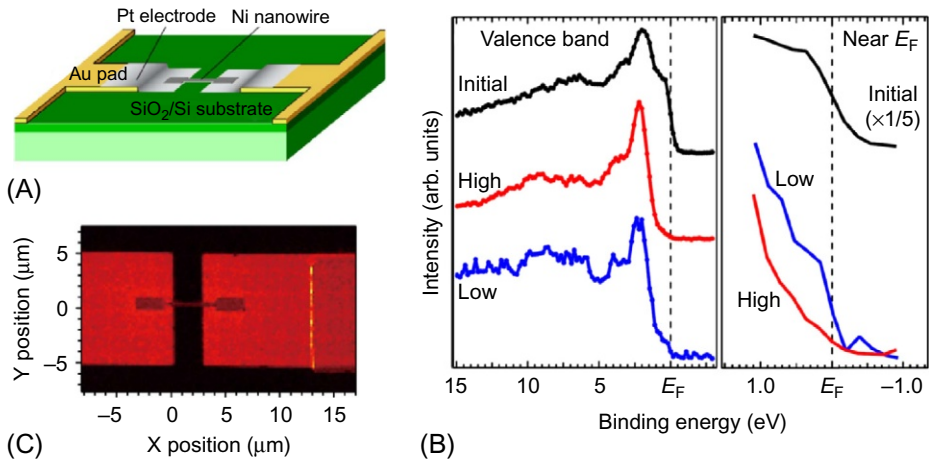

Fig. 8.23

(A) Schematic illustration of an Ni nanowire device. (B) Valence band PES spectra of Ni nanowire at the initial stage, high resistance, and low resistance states. (C) Photoelectron intensity mapping of the Ni nanowire device in the energy region of the Pt 4*f* core levels, including the Ni 3*p* core levels. *Reproduced from K. Horiba, K. Fujiwara, N. Nagamura, S. Toyoda, H. Kumigashira, M. Oshima, H. Takagi, Observation of rebirth of metallic paths during resistance switching of metal nanowire, Appl. Phys. Lett. 103 (2013) 193114, with the permission of AIP Publishing.*

nanowire is fully oxidized after switching to the high-resistance state and that Ni-metal conductive paths in the oxidized nanowire are recovered in the low-resistance state. Thus local electronic structure revealed by the 3D-nano-ESCA system has been well correlated with nanodevice operation mechanism.

Regarding nanospectroscopy of ReRAM, Yasuhara et al. [43] revealed the spatial distribution of chemical states in resistance-switching devices with a planar-type Pt/CuO/Pt structure by photoemission electron microscopy (PEEM) with the spatial resolution of <100 nm. It has been found from the pinpoint XAS spectra at the Cu L_3 edge that the change in resistance occurring by the application of the first voltage is caused by the formation of a reduction path, in other words, a Cu_2O or metallic Cu bridge through the CuO channel between the Pt electrodes, as shown in Fig. 8.24. A detailed analysis of various bridges suggests that Joule-heat-assisted reduction induced by the current flowing through the device may play an important role in the formation of the conductive reduction path. However, since the direct observation of conducting path formation could not be achieved, much higher spatial resolution such as 10 nm or less might be necessary.

Regarding magnetic memory applications of unique meteorite materials for energy-efficient devices, Kotsugi et al. [44] elucidated the relationship between the Widmanstaetten structure and the magnetic properties by means of PEEM combined with X-ray magnetic circular

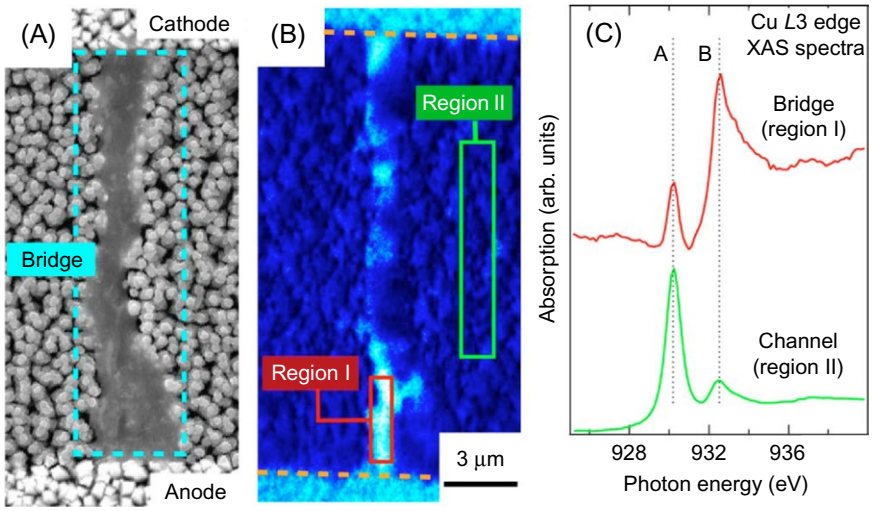

Fig. 8.24

(A) SEM image of the planar-type Pt/CuO/Pt device after the forming process, (B) chemical PEEM image at the same region as the SEM image, and (C) XAS spectra recorded inside (region I) and outside (region II) the bridge structure near the Cu L_3 absorption edge. *Reproduced from R. Yasuhara, K. Fujiwara, K. Horiba, H. Kumigashira, M. Oshima, H. Takagi, Inhomogeneous chemical states in resistance-switching devices with a planar-type Pt/CuO/Pt structure, Appl. Phys. Lett. 95 (2009) 012110, with the permission of AIP Publishing.*

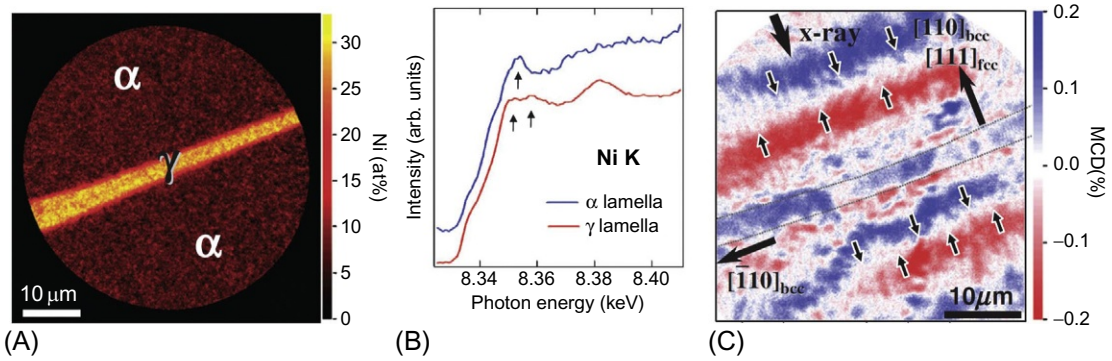

Fig. 8.25

Characterization of Widmanstaetten structure. (A) Ni distribution in boundary region between α and thin γ lamellae observed by PEEM. (B) XAFS spectrum at Ni K edge probed for each lamella. (C) Magnetic domain structure for the same region as (A). *Reprinted from M. Kotsugi, T. Wakita, T. Taniuchi, K. Ono, M. Suzuki, N. Kawamura, M. Takagaki, T. Nakamura, M. Taniguchi, K. Kobayashi, M. Oshima, N. Ishimatsu, H. Maruyama, Novel magnetic domain structure in iron meteorite induced by the presence of $L1_0$-FeNi, Appl. Phys. Express 3 (2010) 013001, with the permission of The Japan Society of Applied Physics.*

dichroic (XMCD). They used Gibeon iron meteorite, which is one of the typical iron meteorites showing a clear Widmanstaetten structure. Fig. 8.25A shows a PEEM Ni distribution in the boundary region between α (bcc) and thin γ (fcc) lamellae. As shown in Fig. 8.25B, X-ray absorption fine structure (XAFS) structures for α and thin γ lamellae are slightly different. Ni concentration profile drastically changes at the interface between α and thin γ lamellae. XMCD image in Fig. 8.25C reveals a unique magnetic domain structure, showing the "head-on" magnetic coupling over the interface between the α and γ lamellae. This kind of a magnetic domain structure is known to be unfavorable in any synthetic Fe-Ni alloys. However, micromagnetics simulation suggests that the formation of magnetic domains is induced by the $L1_0$-type FeNi (tetrataenite) phase with a large uniaxial magnetic anisotropy energy (K_u) of 1.3×10^7 erg/cc segregated at the boundary in the Widmanstaetten structure. Based on this unique magnetic structure, $L1_0$-type FeNi thin films or nanolayers showing high K_u with about 7×10^6 erg/cc have been developed for next-generation magnetic recording [45].

Graphene exhibits unusual electronic properties, caused by a linear band structure near the Dirac point. This band structure is determined by the stacking sequence in graphene multilayers. Fukidome et al. [46] reported electronic structure of graphene layers on 3C-SiC (111) and 3C-SiC(100) thin films grown on a 3D microfabricated Si(100) substrate (3D-GOS (graphene on silicon)) by 3D-nano-ESCA [40]. Si(111) microfacets as well as major Si(100) microterraces were fabricated by anisotropic etching. They have found that tuning of the interface between the graphene and the 3C-SiC microfacets enables microscopic control of stacking and ultimately of the band structure of 3D-GOS, as shown in Fig. 8.26. Peak B component in C 1*s* observed for graphene on the 3C-SiC(111) microfacet can be well correlated with the interfacial amorphous layer in the cross sectional (X)-TEM image for the

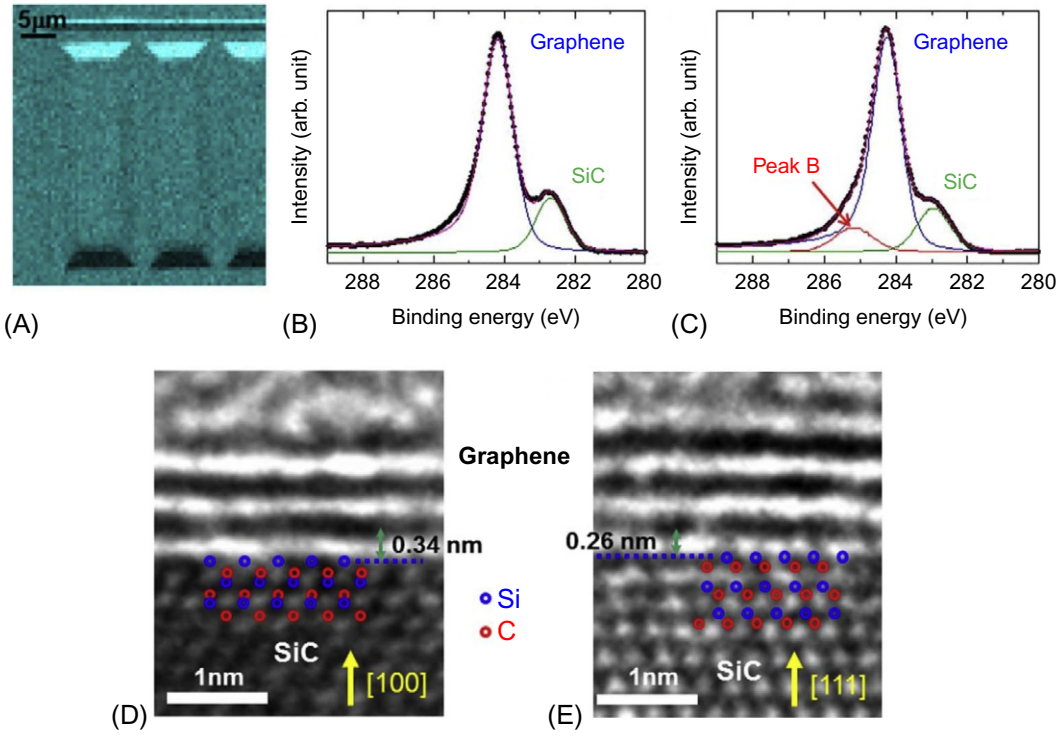

Fig. 8.26

(A) Intensity mapping of the 3D-GOS by using C 1*s* core-level photoelectrons at the binding energy of 284 eV. (B) Pinpoint C 1*s* core-level spectrum of graphene on the 3C-SiC(100) microterrace. (C) Pinpoint C 1*s* core-level spectrum of graphene on the 3C-SiC(111) microfacet. (D) X-TEM image of the interface between graphene and the 3C-SiC(100) microterrace. (E) X-TEM image of the interface between graphene and the 3C-SiC(111) microfacet. *Reproduced from H. Fukidome, T. Ide. Y. Kawai, T. Shinohara, N. Nagamura, K.Horiba, M. Kotsugi, T. Ohkochi, T. Kinoshita, H. Kumigashira, M. Oshima, M. Suemitsu, Microscopically-tuned band structure of epitaxial graphene through interface and stacking variations using Si substrate microfabrication, Sci. Rep. 4 (2014) 5173, with the permission of Nature Publishing Group.*

graphene/3C-SiC(111) microfacet interface. Thus pinpoint electronic state analysis would be very useful in opening up new possibilities of graphene in electronic or photonic devices.

Nagamura et al. [47] analyzed local electronic states and potential distribution at the metal electrode/graphene interface in GFET using 3D nano-ESCA. They have succeeded in detecting a charge transfer region at the graphene/metal-electrode interface, extending over 500 nm with the energy difference of 60 meV, as shown in Fig. 8.27. The C 1*s* sp^2 component binding energy profile at the Ni-graphene interface can be well fitted by calculated curve based on the screening potential using density-functional theory within the Thomas-Fermi approximation. Moreover, a nondestructive depth profiling by ARPES reveals the chemical properties, especially of O 1*s* component at the graphene/SiO_2/Si substrate interface, suggesting that the

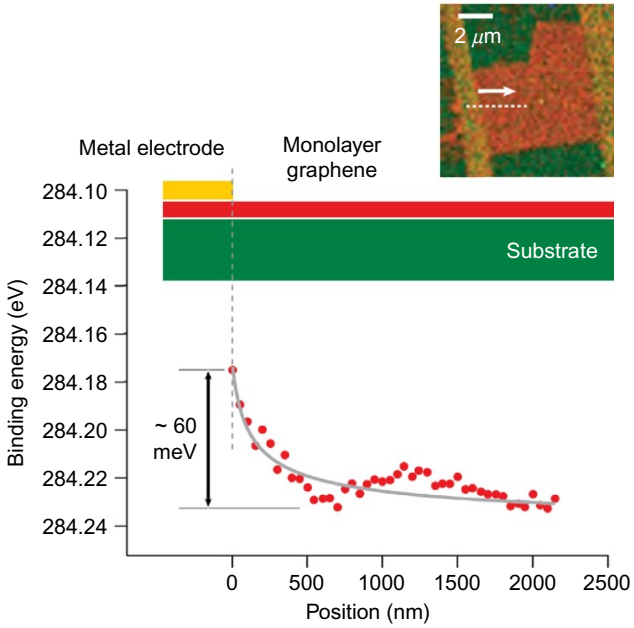

Fig. 8.27

Line profile for the binding energy peak position of the graphene component (sp^2) taken along the dashed white line shown in the inset mapping image. *Dots* indicate the results of peak fitting compared with the calculated curve based on the screening potential using density-functional theory. *Reproduced from N. Nagamura, K. Horiba, A. Toyoda, S. Kurosumi, T. Shinohara, M. Oshima, H. Fukidome, M. Suemitsu, K. Nagashio, A. Toriumi, Direct observation of charge transfer region at interfaces in graphene devices, Appl. Phys. Lett. 102 (2013) 241604, with the permission of AIP Publishing.*

Si—OH bonds of silanol group or water molecules existing between graphene and SiO_2 are attributed to the cause of this charge transfer phenomenon.

In order to realize local band structure analysis of functional materials such as graphene films with polycrystalline character by ARPES, Avila et al. [48] developed a high-resolution angle and lateral resolved photoelectron spectroscopy (nano-ARPES) system in SOLEIL. They studied one-atom-thick graphene films on thin copper foils synthesized by chemical vapor deposition. Moreover, by mapping grain by grain the electronic dynamics of this unique Dirac system, they have found that the single-grain gap-size is 80% smaller than the multigrain gap recently reported by classical ARPES. Such nanoscale electronic structure analysis could lead to the fabrication of one-atom-thick graphene films, which are robust in the Dirac relativistic-like electronic spectrum as a function of the size, shape, and orientation of the single-crystal pristine grains in the graphene films.

Johansson et al. [49] also reported detailed nano-ARPES band mappings of individual graphene grains, clearly showing that multilayer C-face graphene exhibits multiple *p*-bands.

The area shown is 35×50 μm^2, and the photon energy used was 100 eV. The band dispersions obtained close to the K-point moreover clearly indicate Bernal (AB) stacking within the grains comparing to theoretical band dispersion calculated in the framework of the density functional method. Thus a similar interaction between graphene layers on C-face and Si-face SiC was found.

8.7 Hard XPS for Bulk and Interface Analysis

Although PES is a powerful tool to investigate the electronic properties of solids, its usefulness is limited by the surface sensitivity, or the short probing depth such as a few nanometers for conventional X-ray photoemission spectroscopy with Al Kα and Mg Kα sources. It is well known that surface electronic structure is significantly different from the bulk for some group of materials such as strongly correlated materials. Small variations in the local environment strongly affect the orbitals that form the narrow bands and influence the properties of the electrons near the Fermi level. Furthermore, almost all practically important systems are buried interfaces such as metal/semiconductor (Schottky contact) interfaces, semiconductor heterojunctions, and liquid/solid interfaces.

In terms of the probing depth much larger than conventional XPS, hard X-ray photoelectron spectroscopy (HAXPES) is a very promising technique to probe deeper region from the surface to attain volume sensitivity in excess of 10 nm by analyzing photoelectrons in the 6–10 keV range of kinetic energy. Analyzing high kinetic energy (KE) electrons with a reasonably high energy resolution is the key issue for successful HAXPES experiments. While the KE is a key factor to define the probing depth which also depends on the electron density in samples, it is the total resolution that determines the energy scale of the finest details. In order to extract useful bulk information from the analysis of the valence band, spectra should be recorded with an energy resolution about 200 meV or below [50].

For high energy-resolution HAXPES, the incident X-rays are usually monochromatized with the combination of Si (111) double crystal and Si (444) or (555) channel-cut monochromators. In order to remove the nondipole effects, the analyzer was fixed at the parallel direction of X-ray polarization. The electron spectrometer commonly used is a hemispherical deflector analyzer with transmission lens, electronics, and 2D detector system designed and optimized to the purpose of high energy high-resolution photoemission experiments. The interest of HAXPES relies on the improved bulk sensitivity of the technique. An appropriate parameter that estimates the probing depth is the IMFP or the effective attenuation length λ. Under the assumption of negligible elastic scattering, λ is the thickness of a layer that reduces its intensity to $1/e$. The value of λ depends on the kinetic energy of the electrons and also on the material, as shown in Fig. 8.28.

In HAXPES, a total energy resolution of 239 meV at about 8 keV of photon energy was evaluated by Au Fermi edge at room temperature, as shown in Fig. 8.29. The IMFP (λ) of Pt was

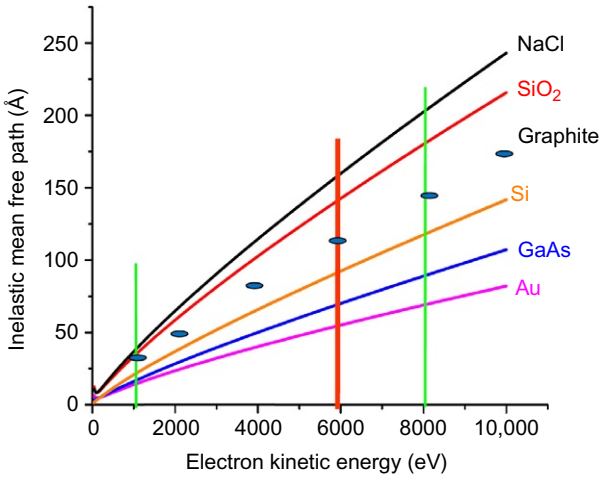

Fig. 8.28
Inelastic mean free path (IMFP) as a function of electron kinetic energy for HAXPES.

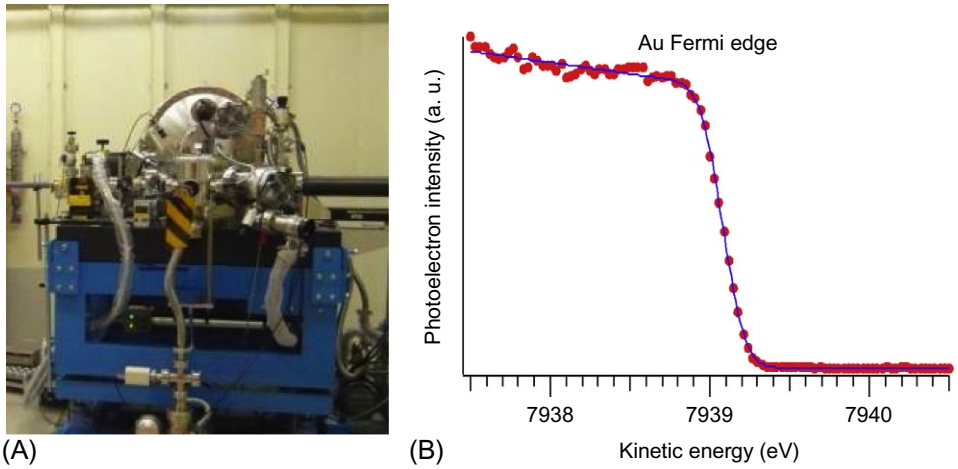

Fig. 8.29
Photo of HAXPES apparatus at BL46XU in SPring-8 (A) and total energy resolution determined by measuring valence band of Au (B).

approximately 6 nm (with the electron kinetic energy around Fermi level, 7939 eV). In contrast, a total energy resolution of about 150 meV was obtained at about 6 keV of photon energy.

Regarding power generation devices, polymer electrolyte fuel cells (PEFC) have attracted a lot of interests because of their clean technology emitting less amount of carbon dioxide as global warming gas. However, the high costs and the scarcity of platinum necessary especially for

cathode catalysts have obstructed the commercialization of PEFCs. Therefore, ORR (oxygen reduction reaction) catalysts without Pt should be developed. Niwa et al. [51] investigated electronic structure of non-Pt cathode catalysts for PEFC by HAXPES, which is a useful technique to probe not just surface properties, but bulk chemical and electronic properties. They analyzed various types of N-containing carbon-based cathode catalysts for PEFC, as shown in Fig. 8.30A and B. N 1*s* spectra of the carbon-based cathode catalysts can be decomposed into four components identified as pyridine-like, pyrrole- or cyanide-like, graphite-like, and oxide nitrogen. Samples showing high oxygen reduction reaction activity in terms of oxygen reduction potential contain high concentration of graphite-like nitrogen. Based on these results,

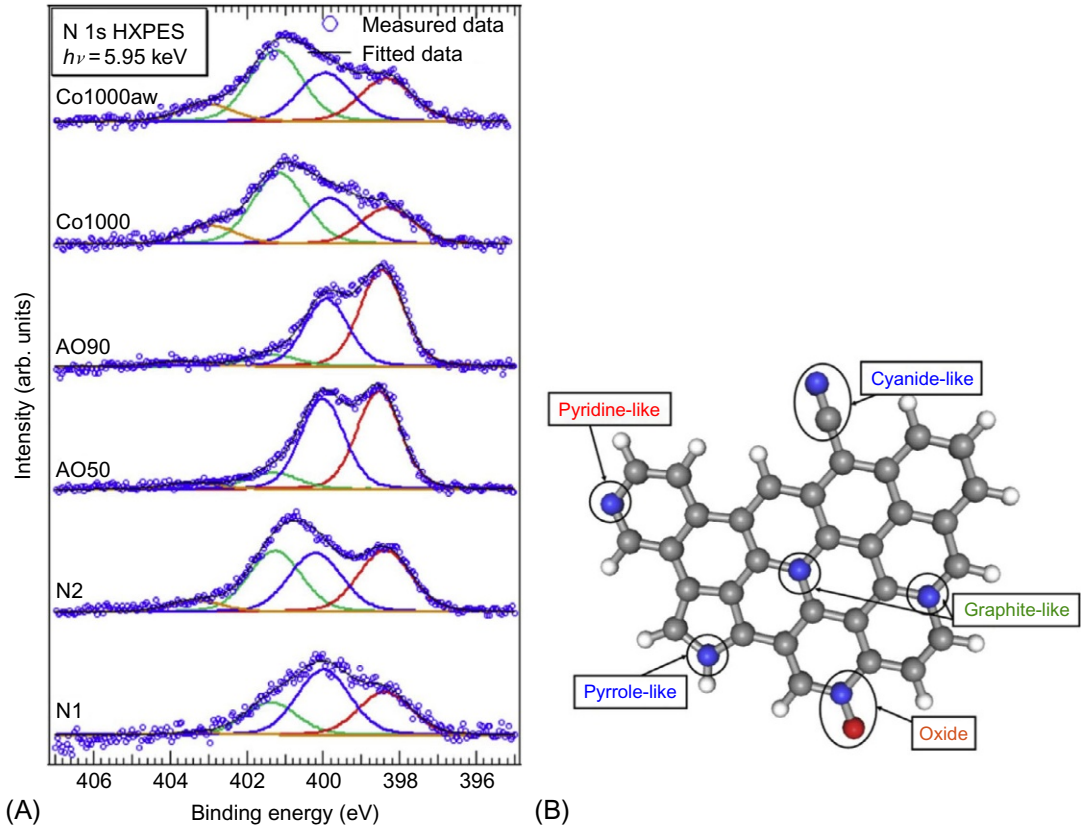

Fig. 8.30

N1*s* HXPES spectra (A) of the carbon-related catalysts and schematic of various nitrogen components corresponding to deconvoluted components in N 1*s* spectra (B). Each spectrum is fitted with Voigt functions followed by background subtraction with the Shirley method. *Reprinted from H. Niwa, M. Kobayashi, K. Horiba, Y. Harada, M. Oshima, K. Terakura, T. Ikeda, Y. Koshigoe, J. Ozaki, S. Miyata, S. Ueda, Y. Yamashita, H. Yoshikawa, K. Kobayashi, Electronic structure analysis of carbon alloy cathode catalysts for polymer electrolyte fuel cells by hard X-ray photoemission spectroscopy, J. Power Sources 196 (2011) 1006–1011, with the permission of Elsevier B.V.*

the oxygen reduction reaction activity of the carbon-based cathode catalysts can be improved by increasing concentration of graphite-like nitrogen in a developed sp^2 carbon network, which is also confirmed by first principles calculation showing the importance of graphitic N at the zigzag edge [52]. Thus, electronic structure of powder samples revealed by HAXPES is well correlated with electrochemical activity.

So far, various kinds of energy-efficient devices, such as ReRAM, IGZO (In-Ga-Zn-O) FET, Schottly diodes and so on have been analyzed as they are in the form of device structures by HAXPES, because no surface-cleaning procedures are required for analyzing bulk and interface electronic properties to correlate with electrical or device properties.

Regarding ReRAM applications, Wei et al. [53] developed highly reliable TaO_x ReRAM, where the memory cell shows stable pulse switching with endurance over 10^9 cycles and sufficient retention exceeding 10 years at 85°C. TaO_x exhibits stable high and low resistance states based on the redox reaction mechanism. To clarify the redox reaction mechanism, a large area test vehicle containing 100 cells with an area of $5 \times 20\ \mu m^2$ per each cell was fabricated, and the top electrode was thinned to 10 nm for HAXPES. With this nondestructive experiment technique, they succeeded in observing the Ta 4*d* bands at the deeply buried interface between anode electrode and TaO_x thin film. As shown in Fig. 8.31, the ratio of $TaO_{2-\beta}/Ta_2O_{5-\delta}$

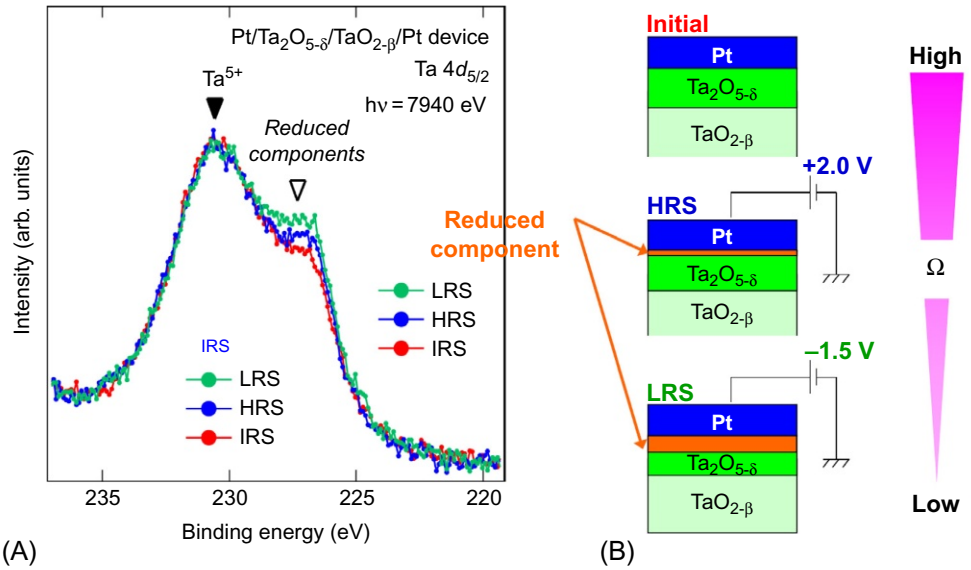

Fig. 8.31

(A) HAXPES Ta 4*d* photoelectron spectra for low resistance state (LRS) and high resistance state (HRS) of Pt/TaOx/Pt ReRAM structure, which shows that the $TaO_{2-\beta}$ component decreases at HRS. (B) Schematic redox reaction mechanism for ReRAM where O^{2-} ions are attracted or expelled by applying positive or negative bias to the top electrode, resulting in increase or decrease of insulating $Ta_2O_{5-\delta}$, respectively.

increases from HRS to LRS, indicating that the $Ta_2O_{5-\delta}$ component of HRS is reduced to the $TaO_{2-\beta}$ component of LRS. These results suggest the redox reaction mechanism for ReRAM.

Regarding valence band feature analysis using HAXPES, Horiba et al. [54] developed a special technique using core-level spectroscopy. Using HAXPES with the photon energy of 5.95 keV, they studied the intrinsic electronic structure of $La_{1-x}Sr_xMnO_3$ (LSMO) thin films, which have a possibility of switching devices and magnetic RAM taking advantage of half-metallicity. Comparison of Mn 2*p* core-levels with soft XPS with the photon energy of 1000 eV, a clear additional well-screened feature is observed only in practically more useful or convenient HAXPES. This feature shows a noticeable increase with decreasing temperature for the ferromagnetic metal compositions, indicating that the origin of this feature is strongly related to the ferromagnetic metal phase of LSMO thin films.

Nomura et al. [55] investigated the electronic states in amorphous IGZO films with high carrier concentrations with different Hall mobilities by optical absorption and HAXPES especially to examine the annealing effects of IGZO films. All HAXPES spectra showed clear Fermi edge structures and extra subgap density of states (DOS), as shown in Fig. 8.32. Subgap DOS greater than 10^{20} cm^{-3} near valence band maxima (VBM), which may be the origin for tail-like structures observed in the optical spectra, can also provide the explanation for why IGZO TFTs show hard saturation in off-states and are difficult to operate in an inversion p-channel mode. The group also performed the angle-resolved HAXPES and found that the density of defect states was increased toward the film surface. Thus, defect states of semiconductors can be precisely analyzed by HAXPES.

Interface potential profiles are very important in investigating metal/semiconductor contacts, in other words, Schottly contacts. Minohara et al. [56] investigated interfacial potential distribution by angle-resolved HAXPES to reveal the Schottly contact mechanism for $SrRuO_3$/Nb:STO heterojunction. They reported on the potential profiling in depth for promising oxide heterojunctions: $La_{0.6}Sr_{0.4}MnO_3$ (LSMO)/Nb-doped $SrTiO_3$ (Nb:STO) having different interfacial terminating layer and $SrRuO_3$/Nb:STO heterojunctions. The precise depth-profiling analysis of LSMO/TiO_2-Nb:STO interfaces with —$La_{0.6}Sr_{0.4}O/TiO_2/SrO$— structure reveals the existence of a certain thin depletion layer of 1–2 nm with an abrupt potential drop near the interface, as shown in Fig. 8.33. In contrast, the ideal depletion layer is formed for other interfaces with a —$SrO/TiO_2/SrO$— terminating layer. These results suggest that the adjacency of TiO_2 layer with $La_{0.6}Sr_{0.4}O$ donor layers at the interface is responsible for the formation of the thin depletion layer near the interface.

Regarding energy storage devices, LIBs are one of the most promising devices. Silicon, especially silicon nanoparticle, is a very good candidate for the next generation of negative electrodes for LIB, due to its high rechargeable capacity. An important issue for the implementation of silicon is the control of the chemical reactivity at the electrode/electrolyte interface upon cycling. Philippe et al. [57] reported improved performances of Li//Si cells by

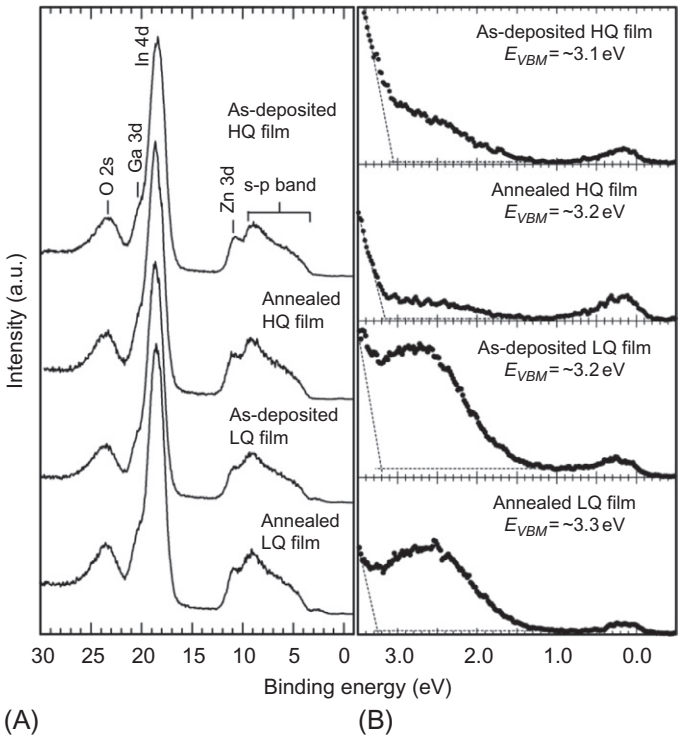

Fig. 8.32

HAXPES spectra for low-quality (LQ) films with lower mobility and high-quality (HQ) films with higher mobility. (A) VB spectra for the a-IGZO films. (B) A magnified view around the bandgap. Intensities are normalized with the *s-p* band observed in (A). *Reprinted from K. Nomura, T. Kamiya, H. Yanagi, E. Ikenaga, K. Yang, K. Kobayashi, M. Hirano, H. Hosono, Subgap states in transparent amorphous oxide semiconductor, In–Ga–Zn–O, observed by bulk sensitive X-ray photoelectron spectroscopy, Appl. Phys. Lett. 92 (2008) 202117, with the permission of AIP Publishing.*

using the new salt lithium bis(fluorosulfonyl)imide (LiFSI) with respect to $LiPF_6$. The interfacial chemistry after long-term cycling was investigated by both SX and hard XPS with different probing depths. They have revealed that LiFSI salts effectively prevent the fluorination process of the silicon particles surface or the formation of SiO_xF_y compounds upon long-term cycling, as shown in Fig. 8.34, resulting in preservation of the favorable interactions between the binder and the active material surface. It is suggested that the reduction products deposited at the surface of the electrode may act as a passivation layer that prevents further reduction of the salt and preserves the electrochemical performances of the battery.

Yabuuchi et al. [58] have demonstrated that the sodium polyacrylate (PANa) binder efficiently improves the electrode performance of graphite/silicon composite in the bis(trifluoromethylsulfonyl)amide (TFSA)-based pure ionic liquid (IL), achieving the reversible cycling with capacity of 1000 mAh g^{-1} using the graphite/Si-PANa composite electrode. In order to reveal the role of the PANa layer in preventing the decomposition

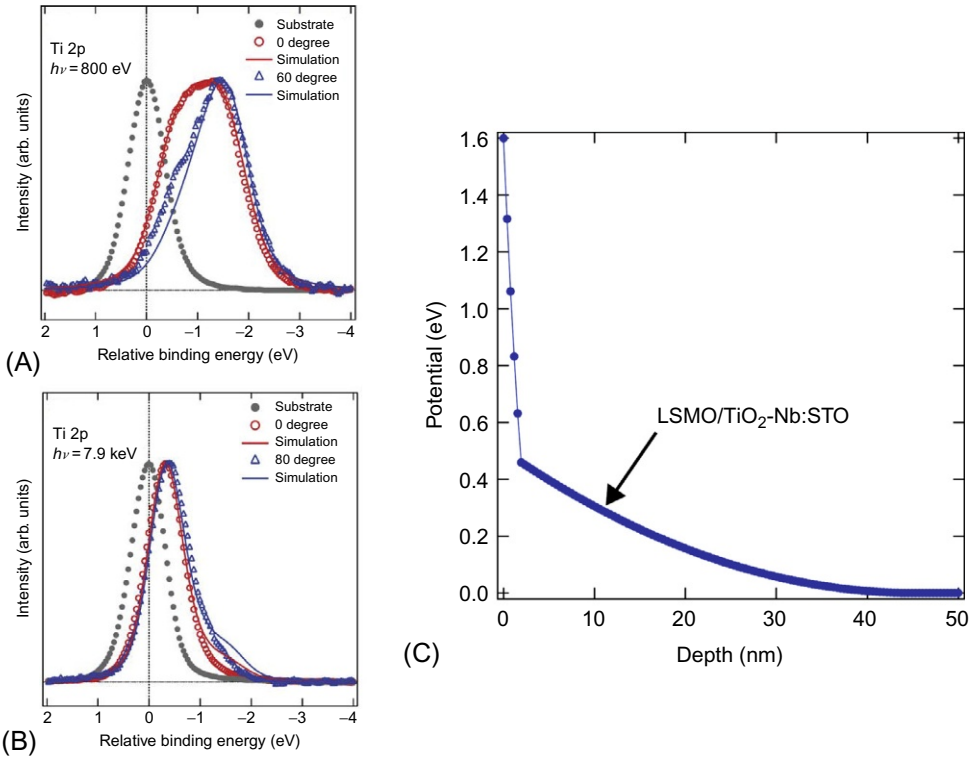

Fig. 8.33

The Ti 2*p* core-level spectra of buried Nb:STO substrate for LSMO/TiO_2-Nb:STO obtained by (A) SX-PES and (B) HAX-PES measurements. *Open circles* and *triangles* correspond to the normal emission and higher angle emission data, respectively. *Filled circles* correspond to the Ti 2*p* core-level spectra of bare Nb:STO substrate. (C) Simulated potential profile in depth for LSMO/TiO_2-Nb:STO. *Reprinted from M. Minohara, K. Horiba, H. Kumigashira, E. Ikenaga, M. Oshima, Potential profiling in depth for perovskite oxide heterojunctions using photoemission spectroscopy, Phys. Rev. B 85 (2012) 165108, with the permission of The American Physical Society.*

of IL during electrochemical cycling, they carried out SXPES and HAXPES experiments. The contribution from the carbon materials at 284.6 eV (—C—H, —C—C—) is clearly visible in HAXPES spectra of the PANa composite. Two components are observed in the Si 1*s* spectra; a sharp peak from Si^0 at 1839.5 eV and a broad peak from native oxide of Si surface in the state of Si^{4+} located at 5–6 eV higher than Si^0 are observed. Uniform distribution of the active materials in the PANa electrode results in much better local electric conduction to nanometer-sized Si particles than the polyvinylidene difluoride (PVdF) electrode. Thus they elucidated the reasons for the PANa composite showing much higher initial capacity by HAXPES.

Thus HAXPES is playing an important role in analyzing various green chemistry materials and devices in terms of bulk or interfacial properties that are intrinsic or essential to be correlated with

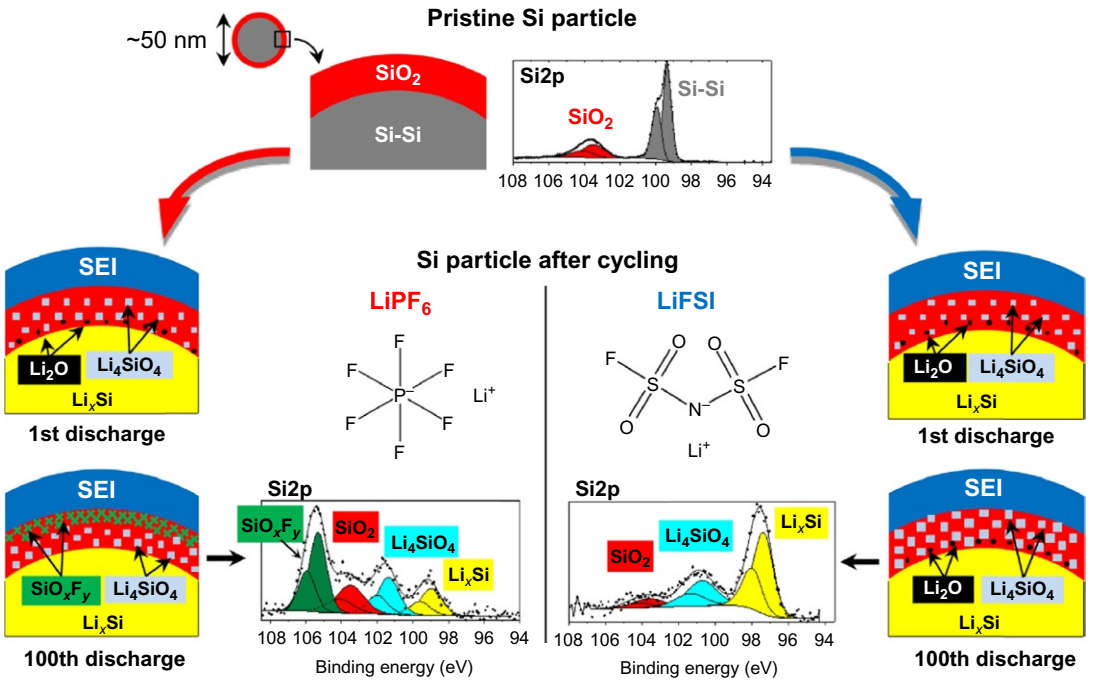

Fig. 8.34

Schematic comparison of the mechanisms occurring at the surface of a silicon nanoparticle upon cycling of an Li//Si cell using either $LiPF_6$ or LiFSI salts. *Reprinted from B. Philippe, R. Dedryvère, M. Gorgoi, H. Rensmo, D. Gonbeau, K. Edstroem, Improved performances of nanosilicon electrodes using the salt LiFSI: a photoelectron spectroscopy study, J. Am. Chem. Soc. 135 (2013) 9829, with the permission of American Chemical Society.*

functionalities. Taking advantage of these characteristics, various projects toward *operando* HAXPES analyses of real catalysts and electronic devices in collaboration with industry are ongoing.

8.8 In Situ and Operando PES During Green Chemical Reactions and Green Device Operation

It is well known that electronic structures of functional materials and devices under device operation such as (1) crystal growth at high temperature, (2) catalytic surface reaction at ambient pressure (AP), (3) electrochemical reaction in liquid phase with biasing, and (4) electron devices with/without strain under biasing are quite different from those at room temperature in UHV without biasing. So, in order to improve the performance of green chemistry and green devices, *operando* analyses are strongly required.

Regarding *operando* crystal growth analysis, various electron beam, X-ray, and infrared techniques have been developed and utilized so far, including RHEED (reflection high energy

electron diffraction) during MBE, surface X-ray diffraction during MOVPE (metalorganic vapor phase epitaxy) and electrochemical deposition, XFAS during MBE, and RDS (reflectance difference spectroscopy) during MOVPE. However, it was difficult to take photoelectron spectra during crystal growth, because UHV is required for PES.

Maeda et al. [59] developed a differential pumping system-combined MBE chamber directly connected to photoelectron analyzer, and analyzed GaSb(001) surfaces during an Sb desorption process at substrate-temperature-dependent growth conditions by measuring core-level photoelectron spectra in real time. The time dependence of the Ga 3*d* intensity revealed that Sb desorption from GaSb(001) can be explained by two competing processes with fast and slow time constants. By analyzing the Sb 4*d* and Ga 3*d* spectra at various stages during Sb desorption at the growth temperature, it is found that Sb atoms occupy different sites in the top layer of Sb double layers, which can be correlated well with fast and slow time constants.

Enta et al. [60] also developed a real-time monitoring system of Si epitaxial growth during MOVPE by PES, and found that the photoelectron intensities from the surface states on Si(100) periodically oscillate during Si growth at 500°C of substrate temperature by gas source MBE with a Si_2H_6 gas. For clarifying the origin of the oscillation in more detail, they measured angle-resolved UPS for both Si(100)2×1 and 1×2 clean surfaces, and found that the photoelectron intensity oscillations on Si(100) arise from the difference in the surface band dispersions of surface states between the 2×1 and the 1×2 clean surfaces.

Regarding *operando* catalytic reaction analysis, Rotermund et al. [61] performed a pioneering study on oscillation of oxidation and reduction of CO-adsorbed Pt(110) surface by controlling O_2 pressure by means of PEEM, although it was not an ambient pressure experiment. The catalytic oxidation of CO on Pt(110) showed oscillatory kinetics and spatiotemporal pattern formation, as shown in the PEEM images in Fig. 8.35. These patterns consist of solitary waves with bell-shaped profiles that propagate with a constant velocity of about 3 μm/s along the crystallographic [0 0 1] axis of the surface. Although these contrasts reflect just work function (ϕ) change from O-adsorbed dark areas with larger ϕ to CO-adsorbed gray areas with smaller ϕ, this technique would be a more powerful tool by combining with changeable photon energy for element imaging with separated chemical states and circularly polarized SXs for magnetic domain imaging.

As an example of catalytic surface reaction at ambient pressure, Nemšák et al. [62] reported combining ambient-pressure (AP) XPS and standing-wave photoemission for a model system of NaOH and CsOH in an ∼1-nm-thick hydrated layer on α-FeO (haematite), as shown in Fig. 8.36A. Fig. 8.36B and C shows an O 1*s* spectrum and the rocking curves derived from the four components, respectively. Thus, by the unique combination at ambient pressure, the in-depth profiles of chemical compositions and states focusing on narrow interfacial regions of a few to several nm even at the liquid/solid interface can be determined with sub-nm accuracy, as shown in Fig. 8.36D.

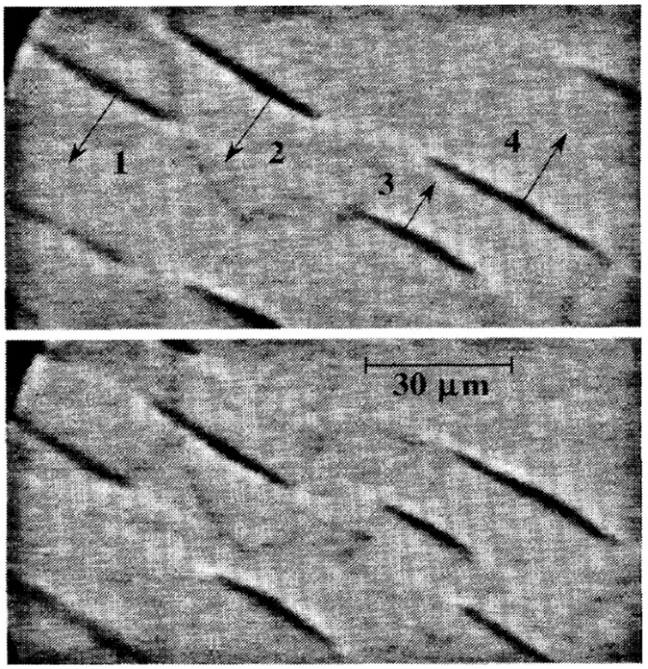

Fig. 8.35

PEEM images of catalytic CO oxidation on a Pt(110) surface, taken with an interval of 3 s. The dark objects are regions with enhanced O_{ad} coverage moving along the indicated directions with constant velocity. *Reprinted from H.H. Rotermund, S. Jakubith, A. von Oertzen, G. Ertl, Solitons in a surface reaction, Phys. Rev. Lett. 66 (1991) 3083, with the permission of The American Physical Society*

Regarding *operando* electrochemical reaction analysis, Zhang et al. [63] carried out *operando* spectroscopy to probe oxidation states of all exposed surfaces in operational solid oxide electrochemical cells at 750°C in 1 mbar reactant gases H_2 and H_2O using a combination of AP XPS and CeO_{2-x}/YSZ/Pt single-chamber cells. Ce 3*d* spectra shown in Fig. 8.37 suggest that the mixed ionic/electronic conducting CeO_{2-x} electrodes undergo Ce^{3+}/Ce^{4+} oxidation-reduction changes with applied bias. The simultaneous measurements of local surface Ce oxidation states and electric potentials reveal that the active ceria regions during H_2 electrooxidation and H_2O electrolysis are located in the 150 μm region from the current collectors. It is suggested from the persistence of the Ce^{3+}/Ce^{4+} shifts in the active region that the surface reaction kinetics and lateral electron transport on the thin ceria electrodes are co-limiting processes. Thus, *operando* AP PES reveals local surface potentials and the relative shift of Ce oxidation state out of equilibrium in this region.

As the second example for *operando* electrochemical reaction analysis, Casalongue et al. [64] performed ambient pressure PES of PEFC by directly probing the correlation between the adsorbed species on the surface and the electrochemical potential, as shown in Fig. 8.38. SX *operando* PES experiments were carried out using the incident photon energy of 670 eV under

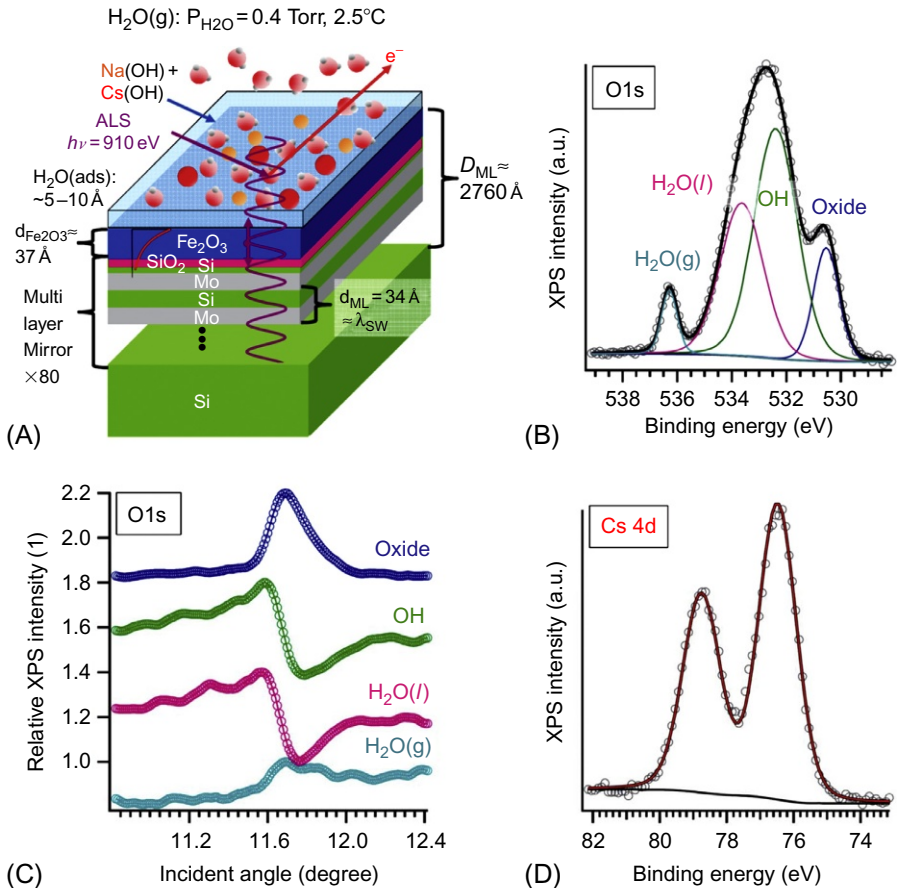

Fig. 8.36

(A) The sample configuration, with some relevant dimensions noted. (B) An O 1*s* spectrum, resolved into four components by peak fitting. (C) The rocking curves derived from the four components of (B). (D) Concentration distribution of all components on Fe_2O_3 film determined from relative XPS intensity rocking curves. *Reprinted from S. Nemšák, A. Shavorskiy, O. Karslioglu, I. Zegkinoglou, A. Rattanachata, C.S. Conlon, A. Keqi, P.K. Greene, E.C. Burks, F. Salmassi, E.M. Gullikson, S.-H. Yang, K. Liu, H. Bluhm, C.S. Fadley, Concentration and chemical-state profiles at heterogeneous interfaces with sub-nm accuracy from standing-wave ambient -pressure photoemission, Nat. Commun. 5 (2014) 5441, with the permission of Mucmillan Publishers Limited.*

600 Torr of humidified forming gas at the anode and varying O_2 pressures at the cathode, as schematically illustrated in Fig. 8.38A. Fig. 8.38B shows O 1*s* spectra consisting of many components such as multilayer H_2O, H_2O(ad), H_2O—OH, OH—O H_2O—OH, and OH—O. It should be noted that nonhydrated hydroxyl was the dominant surface species near the open-circuit potential. Together with density functional theory calculations, they found that the removal of hydration could enhance the reactivity of oxygen species, suggesting the importance of controlling the hydration of hydroxyl near the triple phase boundary for designing more

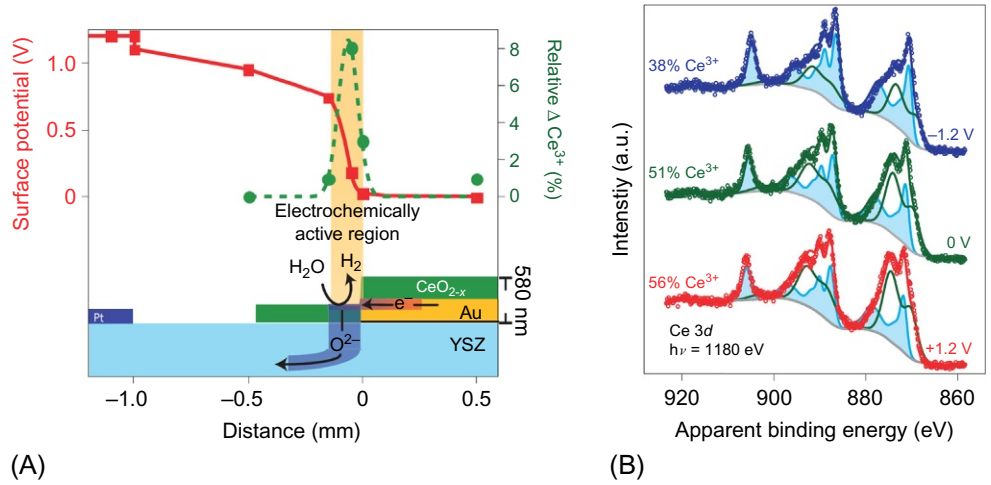

Fig. 8.37

(A) Distribution of electrochemical activity and relative increase of Ce^{3+} as a function of distance on the 250-nm-thick ceria anode on the Au thin film. (B) The Ce 3*d* spectrum changes based on % Ce^{3+} in the probed area for the 50-nm-thick ceria cell under different applied biases. *Reprinted from C. Zhang, M.E. Grass, A.H. McDaniel, S.C. DeCaluwe4, F. El Gabaly, Z. Liu, K.F. McCarty, R.L. Farrow, M.A. Linne, Z. Hussain, G.S. Jackson, H. Bluhm, B.W. Eichhorn, Measuring fundamental properties in operating solid oxide electrochemical cells by using in situ X-ray photoelectron spectroscopy, Nat. Mater. 9 (2010) 944, with the permission of Mucmillan Publishers Limited.*

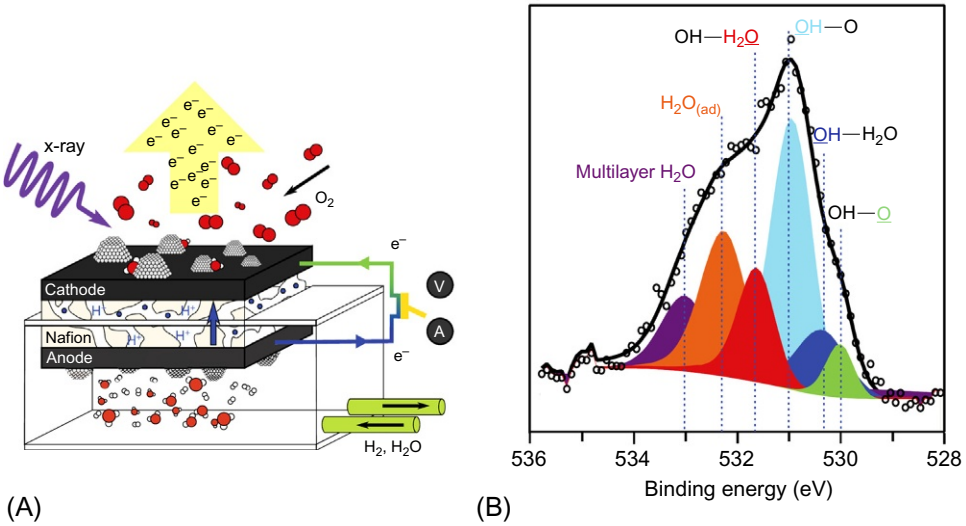

Fig. 8.38

(A) Schematic drawing of a PEM fuel cell set-up for APPES investigations. The cathode side of the electrochemical cell with a Nafion membrane coated on both sides with a mixture of Nafion and carbon-supported Pt nanoparticles was exposed to the APXPS gas cell connected to an external voltmeter or galvanometer. (B) Peak-fitted O 1*s* XPS spectrum in 0.8 Torr oxygen obtained for an operating (closed circuit) fuel cell cathode. *Reprinted from H.S. Casalongue, S. Kaya, V. Viswanathan, D.J. Miller, D. Friebel, H.A. Hansen, J.K. Nørskov, A. Nilsson, H.Ogasawara, Direct observation of the oxygenated species during oxygen reduction on a platinum fuel cell cathode, Nat. Commun. 4 (2014) 2817, with the permission of Mucmillan Publishers Limited.*

active fuel cell cathodes. Based on such fundamental understanding of surface reactions on fuel cell cathodes, various attempts including the use of IL (ionic liquid)-impregnated nanoporous PtNi catalysts to avoid the degradation due to water adsorption are being conducted for much higher electrochemical performance.

The third example for *operando* electrochemistry analysis is *operando* electrochemical PES system utilizing a microcell with an ultrathin Si membrane, reported by Masuda et al. [65] In this system, HXs from an SR source can penetrate into the Si membrane surface exposed to the solution, and photoemission measurements at solid/liquid interfaces under potential control are possible. They investigated the process of potential-induced Si oxide growth in water. Effect of potential and time on the thickness of Si and Si oxide layers was quantitatively determined at subnanometer resolution. This technique would shed light on the future trend of *operando* electrochemical PES for lithium ion battery and PEFC.

Regarding *operando* electron device analysis, Nagamura et al. [66] reported a chemical potential shift in an organic field effect transistor (OFET) during device operation revealed by SX *operando* nanospectroscopy analysis with the 3D-nano-ESCA system with a sample holder. Electrical properties of OFETs fabricated using ultrathin 3 mL single-crystalline C10-DNBDT-NW films on SiO_2/Si substrates with a backgate electrode and top source/drain Au electrodes were measured during *operando* photoemission experiments. Then, line profiles of C 1*s* binding energy under biasing at the backgate and drain electrodes were measured, as shown in Fig. 8.39A. Photon energy was 1000 eV. When applying −30 V to the backgate, C 1s core level shift of about 0.1 eV was observed, which can be attributed to a chemical potential shift corresponding to band bending of organic thin film in FET by the field effect. As shown in Fig. 8.39B, it is found that the logarithmic value of drain current is proportional to the measured chemical potential shift following Boltzmann distribution, suggesting successful p-type doping. Furthermore, they succeeded in measuring potential profiles in the channel region from the source electrode to the drain electrode, which can be well fitted with the calculated potential profile based on the gradual channel approximation with the assumed threshold voltage of OFET.

Fukidome et al. [67] measured GFET during biasing to the gate. Although graphene is a promising material for next-generation devices owing to its excellent electronic properties, graphene devices have not exhibited the high performance expected. *Operando* photoelectron nanospectroscopy is needed to observe electronic states under device operation conditions. So, they have achieved pinpoint *operando* core-level photoelectron nanospectroscopy of a channel of GFET. As shown in Fig. 8.40A, the graphene's binding energy (E_B) of C 1*s* is shifted toward lower E_B upon negative gate biasing. This shift corresponds to the lowering of Fermi level in graphene channel below the Dirac point (Fig. 8.40B), suggesting p-type doping due to the field effect. As shown in Fig. 8.40C, the direct relationship between C 1*s* E_B and gate voltage is well reproduced by a simulation assuming linear band dispersion. Thus *operando* nanospectroscopy will bridge the gap between electronic properties and device performance.

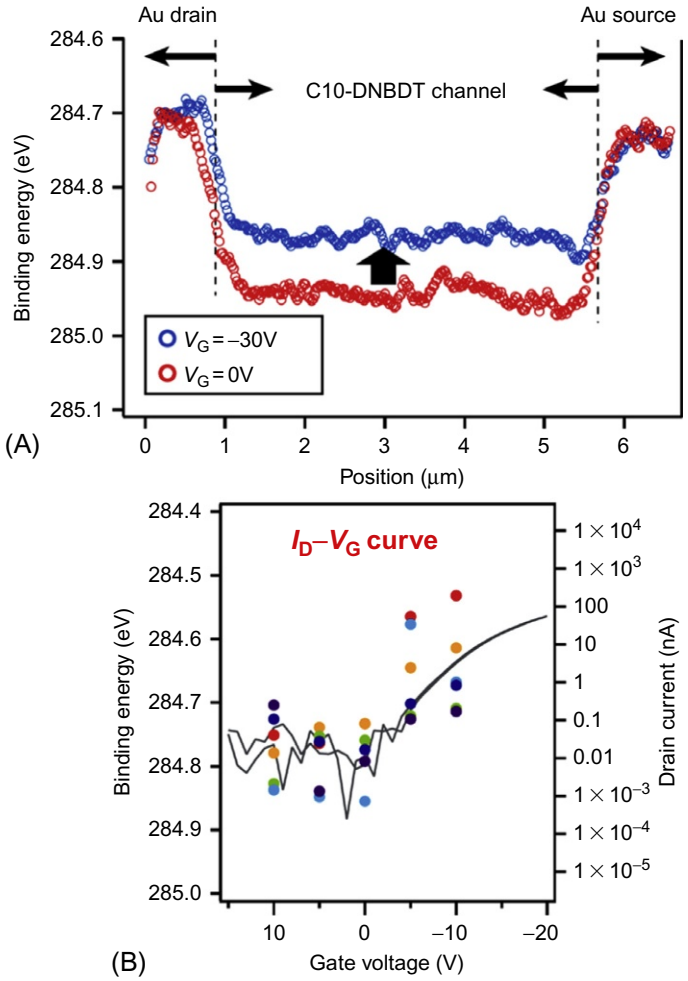

Fig. 8.39

(A) *Operando* measurements of line profiles of C 1*s* photoelectron binding energy across a single-crystalline OFET. (B) Gate bias voltage dependence of C 1*s* photoelectron binding energy in the channel and that of drain current. *Reproduced from N. Nagamura, Y. Kitada, I. Honma, K. Horiba, M. Oshima, H. Matsui, J. Tsurumi, J. Takeya, Chemical potential shift in organic field-effect transistors during operation revealed by soft X-ray operando nano-spectroscopy, Appl. Phys. Lett. 106 (2015) 251604, with the permission of AIP Publishing.*

8.9 Summary and Future Prospects

PES has been utilized to analyze chemical and electronic structures in materials science, solid-state physics, and chemistry, and so on after the development of XPS by Kai Siegbahn in 1957. Recently the PES technique has been much improved thanks to the rapid progress of synchrotron radiation sources and precisely designed electron analyzers with a

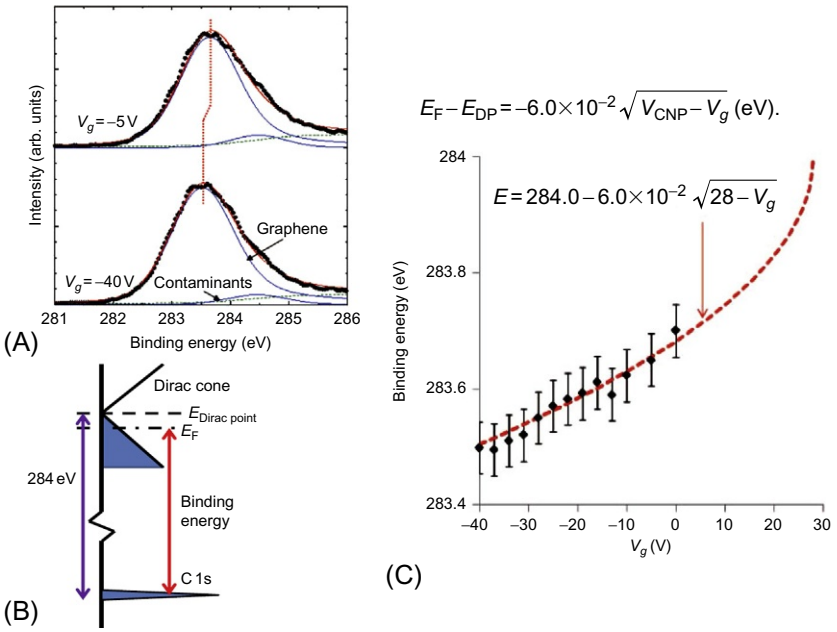

Fig. 8.40

(A) *Operando* pinpoint C 1*s* core-level spectra taken at the center of the graphene channel under the gate biasing of −5 and −40 V. (B) Schematic diagram of density of states and C 1*s* core level of graphene. (C) Plot of the binding energy (E_B) of the graphene peak against the gate bias (*V*g). *Reproduced from H. Fukidome, K. Nagashio, N. Nagamura, K. Tashima, K. Funakubo, K.Horiba, M. Suemitsu, A. Toriumi, M. Oshima, Pinpoint operando analysis of the electronic states of a graphene transistor using photoelectron nanospectroscopy, Appl. Phys. Express 7 (2014) 065101, with the permission of The Japan Society of Applied Physics.*

two-dimensional detector. In addition to materials science, solid-state physics, and chemistry, highly sensitive and high-resolution PES is becoming inevitable also for various kinds of industrial applications especially in green chemistry and green technology.

These strong demands to PES from science and technology would enhance the progress of PES toward much higher energy resolution (sub meV), higher angle resolution (sub 0.1 degrees), higher time resolution (femtosecond), higher spin resolution, higher spatial resolution (several nm), and combined analysis of these by developing a more sensitive analyzer and much brighter SR beam including X-ray free electron laser (XFEL) with higher coherency and shorter pulse structure.

Furthermore, industrial applications would request *operando* PES more than before, because they need electronic structure of real devices such as fuel cells and LIBs under operating condition in order to correlate electronic structure with properties and functions. Since industry users deal with nanolayers and nanostructures for real devices and green chemistry, electronic

structure analysis of nanolayers and nanostructures under real device conditions is strongly required. For that purpose, nanobeam HAXPES with higher photon energy than 15 keV even at ambient pressure might become more important as the "first target." In order to characterize electronic structure of nanolayers and nanostructures, ambient pressure *operando* nano-ARPES with SXs under real device conditions would be the "second target." As described in Section 8.6), the use of about 100-nm SX beam for photoemission spectroscopy is not so difficult at present. However, since much smaller nanostructures than 100 nm have been used for practical nanodevices (LSI, MRAM, ReRAM, etc.) and green chemistry (catalysts, fuel cells, LIB, etc.), nanospectroscopy with less than 10-nm spatial resolution would be required. Furthermore, research on dynamics in chemical reactions taking advantage of short pulse X-rays and femtosecond lasers would be the "third target."

On the other hand, there is a trend from hard materials like Si and ceramics to soft materials like organic films for OFET, which are vulnerable to intensive radiation damage. Therefore the development of highly sensitive two-dimensional detectors with higher time resolution is strongly required.

Based on these advanced technologies in PES, three-dimensional analysis (x, y, z) would become six-dimensional analysis together with energy-resolved (E *or* ω), angle-resolved (k), and time-resolved (t) analysis. In addition to analytical techniques, rapid progress in theoretical calculations significantly accelerates the progress in PES.

References

[1] S. Huefner, Photoelectron spectroscopy: principles and applications, in: M. Cardona (Ed.), Solid-State Science, Springer, Berlin, 1994.
[2] L. Ley, M. Cardona, Photoemission in Solids I: General Principles, vol. 26, Springer-Verlag, Berlin, 1978.
[3] L. Ley, M. Cardona, Photoemission in Solids II, vol. 27, Springer-Verlag, Berlin, 1979.
[4] C.D. Wanger, W.M. Riggs, L.E. Davis, J.F. Moulder, G.E. Muilenberg, Handbook of X-ray Photoelectron Spectroscopy, Perkin-Elmer Corp., Physical Electronics Division, Eden Prairie, MN, 1979.
[5] P. van der Heide, X-ray Photoelectron Spectroscopy: An Introduction to Principles and Practices, John Wiley & Sons, Hoboken, NJ, 2012.
[6] M. Watanabe, S. Sato, I. Munro, G.S. Lodha, A Guide to Synchrotron Radiation Science, Narosa Publishing House, New Delhi, 2016.
[7] H. Wiedemann, Synchrotron Radiation, Springer, Berlin, 2003.
[8] P. Willmott, An Introduction to Synchrotron Radiation: Techniques and Applications, John Wiley & Sons, Hoboken, NJ, 2011.
[9] E. Landemark, C.J. Karlsson, Y.-C. Chao, R.I.G. Uhrberg, Core-level spectroscopy of the clean Si(001) surface: charge transfer within asymmetric dimers of the 2×1 and $c(4 \times 2)$ reconstructions, Phys. Rev. Lett. 69 (1992) 1588.
[10] S. Huefner, Very High Resolution Photoelectron Spectroscopy, Springer, Berlin, Heidelberg, 2007.
[11] H. Ding, J.C. Campuzano, A. Bellman, T. Yokoya, M.R. Norman, T. Takahashi, H. Katayama-Yoshida, T. Mochiku, K. Kadowaki, G. Jennings, Momentum dependence of the superconducting gap in $Bi_2Sr_2CaCu_2O_8$, Phys. Rev. Lett. 74 (1995) 2784–2787.

[12] A. Ohtomo, D.A. Muller, J.L. Grazul, H.Y. Hwang, Artificial charge-modulation in atomic-scale perovskite titanate superlattices, Nature 419 (2002) 378.
[13] K. Yoshimatsu, R. Yasuhara, H. Kumigashira, M. Oshima, Origin of metallic states at the heterointerface between the band insulators $LaAlO_3$ and $SrTiO_3$, Phys. Rev. Lett. 101 (2008) 026802.
[14] T. Yajima, Y. Hikita, M. Minohara, C. Bell, J.A. Mundy, L.F. Kourkoutis, D.A. Muller, H. Kumigashira, M. Oshima, H.Y. Hwang, Controlling band alignments by artificial interface dipoles at perovskite heterointerfaces, Nat. Commun 6 (2015) 6759.
[15] K. Horiba, S. Ito, S. Kurosumi, N. Nagamura, S. Toyoda, H. Kumigashira, M. Oshima, N. Furuta, S. Nishimura, A. Yamada, N. Mizuno, Electronic structure of $Li_2Fe_{1-x}Mn_xP_2O_7$ for lithium-ion battery studied by resonant photoemission spectroscopy, J. Phys. Conf. Ser. 502 (2014) 012004.
[16] S. Toyoda, H. Kamada, T. Tanimura, H. Kumigashira, M. Oshima, T. Ohtsuka, Y. Hata, M. Niwa, Annealing effects of in-depth profile and band discontinuity in TiN/LaO/HfSiO/SiO_2/Si gate stack structure studied by angle-resolved photoemission spectroscopy from backside, Appl. Phys. Lett. 96 (2010) 042905.
[17] K. Siegbahn, Preface to hard X-ray photo electron spectroscopy, Nucl. Instrum. Meth. A 547 (2005) 1–7.
[18] J.C. Woicik, Hard X-ray photoelectron spectroscopy (HAXPES), Springer Ser. Surf. Sci. 59 (2016).
[19] H. Ding, T. Yokoya, J.C. Campuzano, T. Takahashi, M. Randeria, M.R. Norman, T. Mochiku, K. Kadowaki, J. Giapintzakis, Spectroscopic evidence for a pseudogap in the normal state of underdoped high-Tc superconductors, Nature 382 (1996) 51.
[20] S.Y. Zhou, G.-H. Gweon, A.V. Fedorov, P.N. First, W.A. de Heer, D.-H. Lee, F. Guinea, A.H. Castro Neto, A. Lanzar, Substrate-induced bandgap opening in epitaxial graphene, Nat. Mater. 6 (2007) 770–775.
[21] K. Horiba, H. Ohguchi, H. Kumigashira, M. Oshima, K. Ono, N. Nakagawa, M. Lippmaa, M. Kawasaki, H. Koinuma, A high-resolution synchrotron-radiation angle-resolved photoemission system combined with a laser molecular beam epitaxy, Rev. Sci. Instrum. 74 (2003) 3406–3412.
[22] A. Chikamatsu, H. Wadati, H. Kumigashira, M. Oshima, A. Fujimori, M. Lippmaa, K. Ono, M. Kawasaki, H. Koinuma, Gradual disappearance of the Fermi surface near the metal-insulator transition in $La_{1-x}Sr_xMnO_3$, Phys. Rev. B Rapid Commun. 76 (2007) 201103(R).
[23] K. Yoshimatsu, K. Horiba, H. Kumigashira, T. Yoshida, A. Fujimori, M. Oshima, Metallic quantum well states in artificial structures of strongly correlated oxide, Science 333 (2011) 319–322.
[24] Y. Ueoka, Y. Ishikawa, N. Maejima, F. Matsui, H. Matsui, H. Yamazaki, S. Urakawa, M. Horita, H. Daimon, Y. Uraoka, Analysis of electronic structure of amorphous InGaZnO/SiO_2 interface by angle-resolved X-ray photoelectron spectroscopy, J. Appl. Phys. 114 (2013) 163713.
[25] F. Matsui, Y. Hori, H. Miyata, N. Suganuma, H. Daimon, H. Totsuka, K. Ogawa, T. Furukubo, H. Namba, Three-dimensional band mapping of graphite, Appl. Phys. Lett. 81 (2002) 2556.
[26] M. Kobayashi, I. Muneta, T. Schmitt, L. Patthey, S. Ohya, M. Tanaka, M. Oshima, V.N. Strocov, Digging up bulk band dispersion buried under a passivation layer, Appl. Phys. Lett. 101 (2012) 202103.
[27] E. Kisker, K. Schröder, W. Gudat, M. Campagna, Spin-polarized angle-resolved photoemission study of the electronic structure of Fe(100) as a function of temperature, Phys. Rev. B 31 (1985) 329.
[28] J. Osterwalder, Spin-polarized photoemission, Lect. Notes Phys. 697 (2006) 95. (and references there in).
[29] R. Bertacco, D. Onofrio, F. Ciccacci, A novel electron spin-polarization detector with very large analyzing power, Rev. Sci. Instrum. 70 (1999) 3572.
[30] R. Bertacco, M. Merano, F. Ciccacci, Spin dependent electron absorption in Fe(001)-p(1x1)O: a new candidate for a stable and efficient electron polarization analyzer, Appl. Phys. Lett. 72 (1998) 2050.
[31] P.K. Das, D. Di Sante, I. Vobornik, J. Fujii, T. Okuda, E. Bruyer, A. Gyenis, B.E. Feldman, J. Tao, R. Ciancio, G. Rossi, M.N. Ali, S. Picozzi, A. Yadzani, G. Panaccione, R.J. Cava, Layer-dependent quantum cooperation of electron and hole states in the anomalous semimetal WTe_2, Nat. Commun. 7 (2016) 10847.
[32] K. Kuroda, G. Eguchi, K. Shirai, M. Shiraishi, Mao Ye, K. Miyamoto, T. Okuda, S. Ueda, M. Arita, H. Namatame, M. Taniguchi, Y. Ueda, A. Kimura, Tunable spin current due to bulk insulating property in the topological insulator $Tl_{1-x}Bi_{1+x}Se_{2-\delta}$, Phys. Rev. B 91 (2015) 205306.
[33] J.-H. Park, E. Vescovo, H.-J. Kim, C. Kwon, R. Ramesh, T. Venkatesan, Direct evidence for a half-metallic ferromagnet, Nature 392 (1998) 794.

[34] S. Yamamoto, I. Matsuda, Time-resolved photoelectron spectroscopies using synchrotron radiation: past, present, and future, J. Phys. Soc. Jpn. 82 (2013) 021003.
[35] M. Ogawa, S. Yamamoto, Y. Kousa, F. Nakamura, R. Yukawa, A. Fukushima, A. Harasawa, H. Kondoh, Y. Tanaka, A. Kakizaki, I. Matsuda, Development of soft x-ray time-resolved photoemission spectroscopy system with a two-dimensional angle-resolved time-of-flight analyzer at Spring-8 BL07LSU, Rev. Sci. Instrum. 83 (2012) 023109.
[36] K. Ozawa, M. Emori, S. Yamamoto, R. Yukawa, S. Yamamoto, R. Hobara, K. Fujikawa, H. Sakama, I. Matsuda, Electron–hole recombination time at tio$_2$ single-crystal surfaces: influence of surface band bending, J. Phys. Chem. Lett. 5 (2014) 1953.
[37] S. Gilbertson, G.L. Dakovski, T. Durakiewicz, J.-X. Zhu, K.M. Dani, A.D. Mohite, A. Dattelbaum, G. Rodriguez, Tracing ultrafast separation and coalescence of carrier distributions in graphene with time-resolved photoemission, J. Phys. Chem. Lett. 3 (2012) 64–68.
[38] D. Bröcker, T. Gießel, W. Widdra, Charge carrier dynamics at the SiO_2/Si(100) surface: a time-resolved photoemission study with combined laser and synchrotron radiation, Chem. Phys. 299 (2004) 247.
[39] J.A. Sobota, S.-L. Yang, A.F. Kemper, J.J. Lee, F.T. Schmitt, W. Li, R.G. Moore, J.G. Analytis, I.R. Fisher, P. S. Kirchmann, T.P. Devereaux, Z.-X. Shen, Direct optical coupling to an unoccupied dirac surface state in the topological insulator Bi_2 Se_3, Phys. Rev. Lett. 111 (2013) 136802.
[40] F. Schmitt, P.S. Kirchmann, U. Bovensiepen, R.G. Moore, L. Rettig, M. Krenz, J.-H. Chu, N. Ru, L. Perfetti, D. H. Lu, M. Wolf, I.R. Fisher, Z.-X. Shen, Effect of the amplitude mode and the transient melting of the charge density wave on the electronic structure of $TbTe_3$, Science 321 (2008) 1649.
[41] K. Horiba, Y. Nakamura, N. Nagamura, S. Toyoda, H. Kumigashira, M. Oshima, K. Amemiya, Y. Senba, H. Ohashi, Scanning photoelectron microscope system for three-dimensional spatial-resolved chemical analysis, Rev. Sci. Instrum. 82 (2011) 113701.
[42] K. Horiba, K. Fujiwara, N. Nagamura, S. Toyoda, H. Kumigashira, M. Oshima, H. Takagi, Observation of rebirth of metallic paths during resistance switching of metal nanowire, Appl. Phys. Lett. 103 (2013) 193114.
[43] R. Yasuhara, K. Fujiwara, K. Horiba, H. Kumigashira, M. Oshima, H. Takagi, Inhomogeneous chemical states in resistance-switching devices with a planar-type Pt/CuO/Pt structure, Appl. Phys. Lett. 95 (2009) 012110.
[44] M. Kotsugi, T. Wakita, T. Taniuchi, K. Ono, M. Suzuki, N. Kawamura, M. Takagaki, T. Nakamura, M. Taniguchi, K. Kobayashi, M. Oshima, N. Ishimatsu, H. Maruyama, Novel magnetic domain structure in iron meteorite induced by the presence of $L1_0$-FeNi, Appl. Phys. Express 3 (2010) 013001.
[45] T. Kojima, M. Mizuguchi, T. Koganezawa, K. Osaka, M. Kotsugi, K. Takanashi, Magnetic anisotropy and chemical order of artificially synthesized $L1_0$-ordered FeNi films on Au–Cu–Ni buffer layers, Jpn. J. Appl. Phys. 51 (2012) 010204.
[46] H. Fukidome, T. Ide, Y. Kawai, T. Shinohara, N. Nagamura, K. Horiba, M. Kotsugi, T. Ohkochi, T. Kinoshita, H. Kumigashira, M. Oshima, M. Suemitsu, Microscopically-tuned band structure of epitaxial graphene through interface and stacking variations using Si substrate microfabrication, Sci. Rep. 4 (2014) 5173.
[47] N. Nagamura, K. Horiba, A. Toyoda, S. Kurosumi, T. Shinohara, M. Oshima, H. Fukidome, M. Suemitsu, K. Nagashio, A. Toriumi, Direct observation of charge transfer region at interfaces in graphene devices, Appl. Phys. Lett. 102 (2013) 241604.
[48] J. Avila, I. Razado, S. Lorcy, R. Fleurier, E. Pichonat, D. Vignaud, X. Wallart, M.C. Asensio, Exploring electronic structure of one-atom thick polycrystalline graphene films: a nano angle resolved photoemission study, Sci. Rep. 3 (2013) 2439.
[49] L.I. Johansson, R. Armiento, J. Avila, C. Xia, S. Lorcy, I.A. Abrikosov, M.C. Asensio, C. Virojanadara, Multiple p-bands and Bernal stacking of multilayer graphene on C-face SiC, revealed by nano-angle resolved photoemission, Sci. Rep. 4 (2014) 4157.
[50] Y. Takata, M. Yabashi, K. Tamasaku, Y. Nishino, D. Miwa, T. Ishikawa, E. Ikenaga, K. Horiba, S. Shin, M. Arita, K. Shimada, H. Namatame, M. Taniguchi, H. Nohira, T. Hattori, S. Södergren, B. Wannberg, K. Kobayashi, Development of hard X-ray photoelectron spectroscopy at BL29XU in SPring-8, Nucl. Instrum. Methods Phys. Res., Sect. A 547 (2005) 50–55.

[51] H. Niwa, M. Kobayashi, K. Horiba, Y. Harada, M. Oshima, K. Terakura, T. Ikeda, Y. Koshigoe, J. Ozaki, S. Miyata, S. Ueda, Y. Yamashita, H. Yoshikawa, K. Kobayashi, Electronic structure analysis of carbon alloy cathode catalysts for polymer electrolyte fuel cells by hard X-ray photoemission spectroscopy, J. Power Sources 196 (2011) 1006–1011.

[52] T. Ikeda, M. Boero, S.-F. Huang, K. Terakura, M. Oshima, J. Ozaki, Carbon alloy catalysts: active sites for oxygen reduction reaction, J. Phys. Chem. 112 (2008) 14706.

[53] Z. Wei, Y. Kanzawa, K. Arita, Y. Katoh, K. Kawai, S. Muraoka, S. Mitani, S. Fujii, K. Katayama, M. Iijima, T. Mikawa, T. Ninomiya, R. Miyanaga, Y. Kawashima, K. Tsuji, A. Himeno, T. Okada, R. Azuma, K. Shimakawa, H. Sugaya, T. Takagi, R. Yasuhara, K. Horiba, H. Kumigashira, M. Oshima, Highly reliable TaO_x ReRAM and direct evidence of redox reaction mechanis, IEDM Tech. Dig. (2008) 293–296.

[54] K. Horiba, M. Taguchi, A. Chainai, Y. Takata, E. Ikenaga, H. Namatame, M. Taniguchi, A. Awaji, D. Miwa, Y. Nishio, K. Tamasaku, T. Ishikawa, H. Kumigashira, M. Oshima, N. Nakagawa, M. Lippmaa, M. Kawasaki, H. Koinuma, K. Kobayashi, S. Shin, Nature of well-screened state in hard x-ray Mn 2*p* core level photoemission of $La_{1-x}Sr_xMnO_3$ films, Phys. Rev. Lett. 93 (2004) 236401.

[55] K. Nomura, T. Kamiya, H. Yanagi, E. Ikenaga, K. Yang, K. Kobayashi, M. Hirano, H. Hosono, Subgap states in transparent amorphous oxide semiconductor, In–Ga–Zn–O, observed by bulk sensitive X-ray photoelectron spectroscopy, Appl. Phys. Lett. 92 (2008) 202117.

[56] M. Minohara, K. Horiba, H. Kumigashira, E. Ikenaga, M. Oshima, Potential profiling in depth for perovskite oxide heterojunctions using photoemission spectroscopy, Phys. Rev. B 85 (2012) 165108.

[57] B. Philippe, R. Dedryvère, M. Gorgoi, H. Rensmo, D. Gonbeau, K. Edstroem, Improved performances of nanosilicon electrodes using the salt LiFSI: a photoelectron spectroscopy study, J. Am. Chem. Soc. 135 (2013) 9829.

[58] N. Yabuuchi, K. Shimomura, Y. Shimbe, T. Ozeki, J.-Y. Son, H. Oji, Y. Katayama, T. Miura, S. Komaba, Graphite-silicon-polyacrylate negative electrodes in ionic liquid electrolyte for safer rechargeable Li-ion batteries, Adv. Energy Mater. 1 (2011) 759.

[59] F. Maeda, Y. Watanabe, M. Oshima, Realtime analysis of GaSb(001) during Sb desorption by core-level photoelectron spectroscopy, Phys. Rev. Lett. 78 (1997) 4233.

[60] Y. Enta, Y. Takegawa, D. Shoji, M. Suemitsu, Y. Takakuwa, H. Kato, N. Miyamoto, Band-dispersion-originated photoelectron intensity oscillations during Si epitaxial-growth on Si(100), J. Electron Spectro. Rel. Phenom. 80 (1996) 173.

[61] H.H. Rotermund, S. Jakubith, A. von Oertzen, G. Ertl, Solitons in a surface reaction, Phys. Rev. Lett. 66 (1991) 3083.

[62] S. Nemšák, A. Shavorskiy, O. Karslioglu, I. Zegkinoglou, A. Rattanachata, C.S. Conlon, A. Keqi, P.K. Greene, E.C. Burks, F. Salmassi, E.M. Gullikson, S.-H. Yang, K. Liu, H. Bluhm, C.S. Fadley, Concentration and chemical-state profiles at heterogeneous interfaces with sub-nm accuracy from standing-wave ambient-pressure photoemission, Nat. Commun. 5 (2014) 5441.

[63] C. Zhang, M.E. Grass, A.H. McDaniel, S.C. DeCaluwe, F. El Gabaly, Zhi Liu, K.F. McCarty, R.L. Farrow, M. A. Linne, Z. Hussain, G.S. Jackson, H. Bluhm, B.W. Eichhorn, Measuring fundamental properties in operating solid oxide electrochemical cells by using in situ X-ray photoelectron spectroscopy, Nat. Mater. 9 (2010) 944.

[64] H.S. Casalongue, S. Kaya, V. Viswanathan, D.J. Miller, D. Friebel, H.A. Hansen, J.K. Nørskov, A. Nilsson, H. Ogasawara, Direct observation of the oxygenated species during oxygen reduction on a platinum fuel cell cathode, Nat. Commun. 4 (2014) 2817.

[65] T. Masuda, H. Yoshikawa, H. Noguchi, T. Kawasaki, M. Kobata, K. Kobayashi, K. Uosaki, In situ x-ray photoelectron spectroscopy for electrochemical reactions in ordinary solvents, Appl. Phys. Lett. 103 (2013) 11605.

[66] N. Nagamura, Y. Kitada, I. Honma, K. Horiba, M. Oshima, H. Matsui, J. Tsurumi, J. Takeya, Chemical potential shift in organic field-effect transistors during operation revealed by soft X-ray *operando* nano-spectroscopy, Appl. Phys. Lett. 106 (2015) 251604.

[67] H. Fukidome, K. Nagashio, N. Nagamura, K. Tashima, K. Funakubo, K. Horiba, M. Suemitsu, A. Toriumi, M. Oshima, Pinpoint *operando* analysis of the electronic states of a graphene transistor using photoelectron nanospectroscopy, Appl. Phys. Express 7 (2014) 065101.

This page intentionally left blank

CHAPTER 9

Layer-by-Layer Nanolayers for Green Science

Katsuhiko Ariga[*,†]

[*]*National Institute for Materials Science (NIMS), Tsukuba, Japan* [†]*The University of Tokyo, Kashiwa, Japan*

9.1 Introduction

Functional materials with both nanosized functional units and macroscopic effects have to possess two extremely different structural dimensions, nanoscopic dimension and macroscopic dimension. Structurally controlled thin films can satisfy this demand, because they have macroscopic dimensions in lateral directions and nanoscopic dimension in thickness direction. Therefore, preparation of well-controlled thin films is one of the promising ways to utilize nanoscopic phenomena for practical applications. As fabrications for functional thin films with controlled nanoscopic thickness, the self-assembled monolayer (SAM) method [1–3], Langmuir-Blodgett (LB) technique [4–6], and layer-by-layer (LbL) assembly [7–10] have been widely used (Fig. 9.1).

The SAM method is an excellent method for providing organized monolayers strongly immobilized on a surface. This technique is regarded as a powerful strategy for surface modification of various kinds of materials. However, the SAM method is usually limited to fabricate single-layer structures and cannot provide controlled layered structures. It cannot be used as a technique to prepare well-organized multilayer films. On the other hand, the LB technique is good for fabrication of multilayer films. In the LB technique, a monolayer structure is first prepared on a liquid surface such as the air-water interface, which can be transferred onto a solid support under controlled surface pressures. However, this technique includes necessary process of formation of the monolayer at liquid interfaces. Therefore the LB technique is not always applicable to a wide range of materials, although many research efforts for application of various nanomaterials for the LB films have been made.

Another method for multilayer fabrication is the LbL assembly. Unlike films obtained from the former two methods, the LbL assembly provides multilayered films with rather disorganized or fuzzy structures [11]. However, the LbL assembly can be conducted by very simple procedures

Nanolayer Research. http://dx.doi.org/10.1016/B978-0-444-63739-0.00009-8

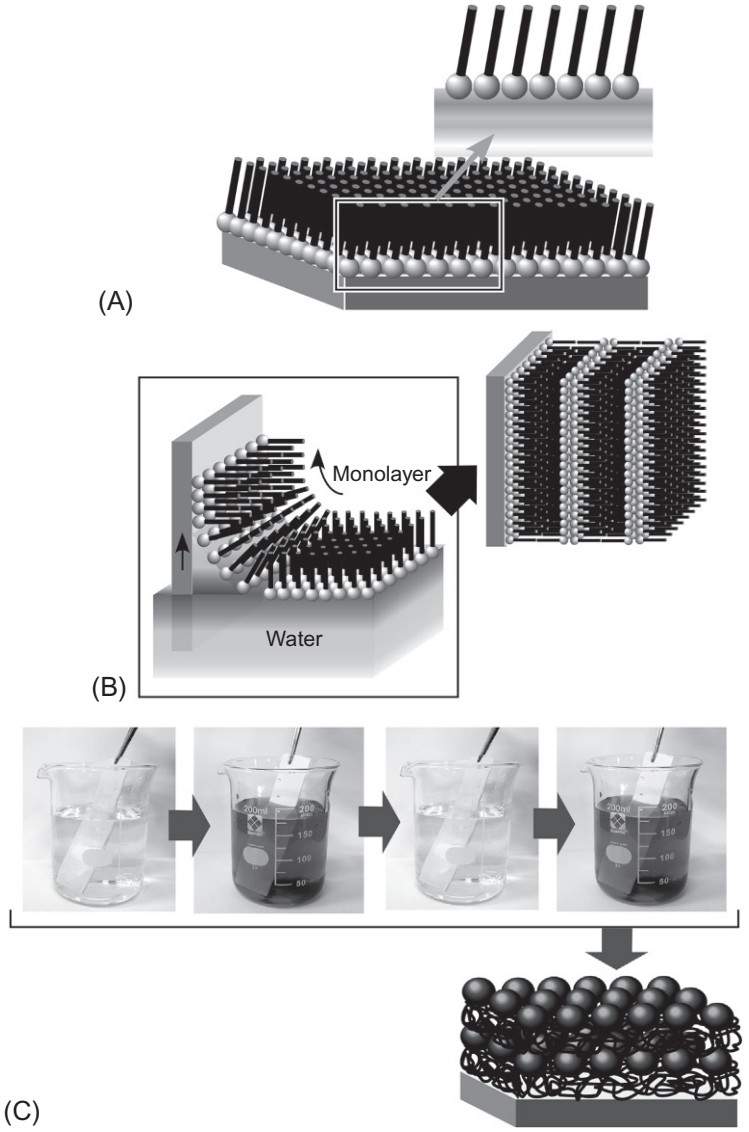

Fig. 9.1
Three representative functional thin films: (A) self-assembled monolayer (SAM); (B) Langmuir-Blodgett (LB); and film (C) layer-by-layer (LbL) assembly.

with inexpensive apparatuses. In addition, many kinds of materials can be used in the LbL assembly, because this assembling method is based on simple adsorption processes. Therefore, the LbL method can be regarded as a versatile technique for fabrication of multilayer thin films. In this chapter, basics of LbL assembly with some typical examples are first described. Then application examples of this technique for green sciences such as sensing and drug delivery are explained.

9.2 Basics of LbL Assembly

The LbL assembly is based on adsorption process between substrate surfaces and components in solution phases. Although various kinds of interactions possibly work on adsorption processes, initial proposals by Iler [12] and demonstration by Decher [13,14] relied on electrostatic interaction. In particular, Decher and coworkers successfully demonstrated basic examples of LbL assemblies using polyelectrolytes and/or bola-type amphiphiles through electrostatic adsorption. Based on their pioneering examples, many researchers demonstrated applicability of the LbL technique to various components such as inorganic nanomaterials [15–17], biomolecules [18–20], and supramolecular assemblies [21–23]. At the same time, uses of the other molecular interactions including biospecific interaction [24], metal coordination [25,26], hydrogen bonding [27,28], charge transfer [29], stereocomplex formation [30,31], and supramolecular inclusion [32] were demonstrated.

In order to explain the basic mechanism of the LbL assembly, one example of the LbL processes is depicted in Fig. 9.2, in which the LbL assembly process is done using cationic polyelectrolytes and anionic proteins. When a solid support with negatively charged surface is immersed into aqueous solution of the cationic polyelectrolyte, adsorption of the cationic polyelectrolyte to the solid surface occurs through electrostatic attraction. This adsorption process does not stop at charge neutral points; overadsorption to convert the surface charge to

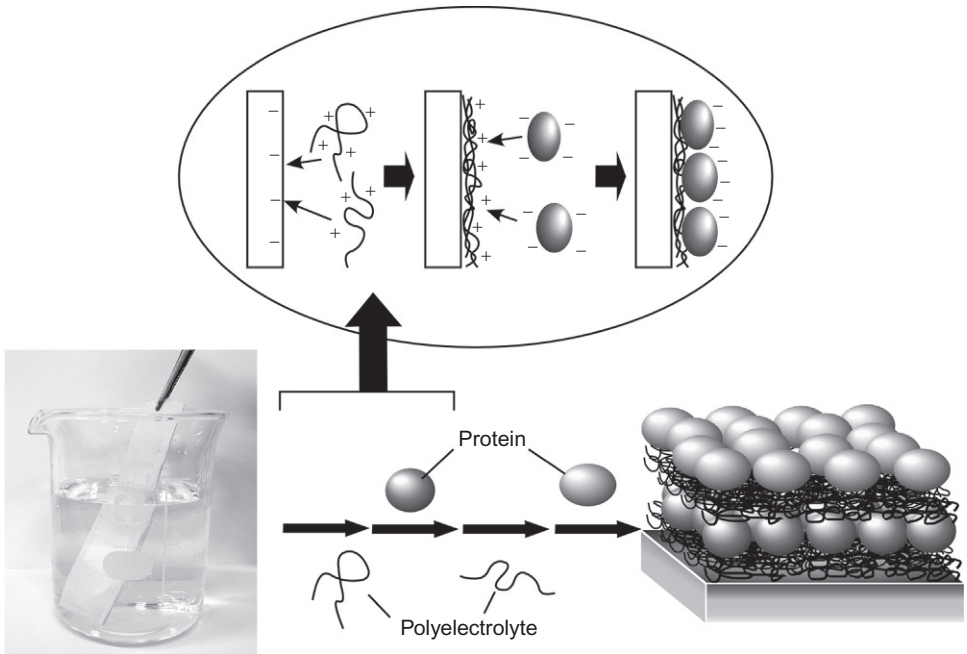

Fig. 9.2
One example of the LbL processes using cationic polyelectrolytes and anionic proteins.

positive always occurs. Therefore, the surface charge is reverted to positive after the adsorption of the cationic polyelectrolyte. The next immersion of the refuting film on the substrate into the aqueous solution of the anionic protein induces electrostatic adsorption of the protein onto positively charged surface. Again charge reversal occurs after the adsorption of the anionic protein, resulting in negatively charged surface. These processes can be repeated with alternation of surface charge, and continuous alternate adsorption between the components with different charges becomes possible.

According to this alternate adsorption mechanism, layered films with desirable thickness (desirable number of layers) can be assembled only with control of immersion cycles. If the charge alternation rule is kept, adsorption sequences can be freely modified, leading to fabrication of wide varieties of the layered films. Because these processes are based on very simple adsorption, the necessary apparatuses are only beakers and tweezers. In addition, adsorption of components in solution to the solid surfaces finishes within about 10 min. Therefore, LbL assembly can be done with nonexpensive elemental set-up and in a short time under ambient conditions. Because this mechanism can be applied to various charged substances, there is a vast choice of available fragile components such as biomaterials including proteins [33,34], nucleic acids [35], polysaccharides [36], and virus particles [37].

Media for the LbL assembly is not limited to solid substrate surfaces. The LbL assembly on microscopic colloidal particles is also possible, which can also result in formation of hollow capsules through destruction of central colloidal cores after the LbL assembly on them (Fig. 9.3) [38–41]. According to the strategy illustrated in this Figure, the LbL films are assembled sequentially on a colloidal core, and subsequent destruction of the central particle core results in hollow capsules. As a modified method, polyelectrolyte wrapping by the LbL assembly on enzyme crystals results in an extremely high enzyme loading in a nanosized capsule after dissolution of the enzyme crystals (Fig. 9.4) [42].

9.3 Application Example of LbL Assembly: Multienzyme Reactor

For environment-friendly green application of the LbL assembly, the functions of layered films with biomolecular components makes an attractive target. The LbL assembly process is carried out under mild conditions at low temperature. Therefore denaturation of biomolecules during assembling processes can be minimized. An increase in stability of biomolecules such as enzymes immobilized in the LbL film was also demonstrated [43]. Flexible but molecular-level interactions between polyelectolytes and biomolecules can prevent the immobilized biomolecules from unfavorable structural changes by external factors such as high temperature and low or high pH. Duration stability of biomolecules in the LbL structures is enhanced as compared with those in solution. In addition, the LbL multilayer films are generally more permeable than LB films with condensed structures. Therefore LbL assemblies are often advantageous on dynamic bioprocesses.

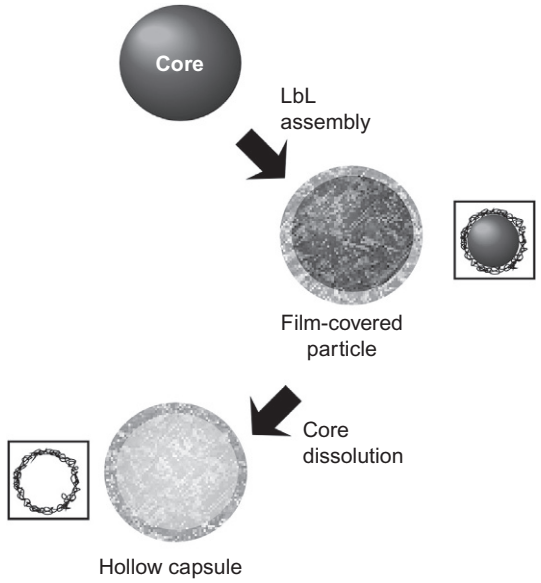

Fig. 9.3
The LbL assembly on microscopic colloidal particles and subsequent destruction of central colloidal cores to produce a hollow capsule.

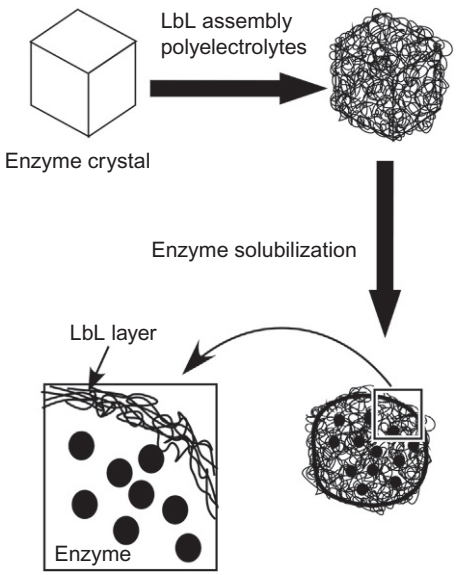

Fig. 9.4
Polyelectrolyte wrapping by the LbL assembly on enzyme crystals and formation of a hollow capsule with an extremely high enzyme loading after dissolution of the enzyme crystals.

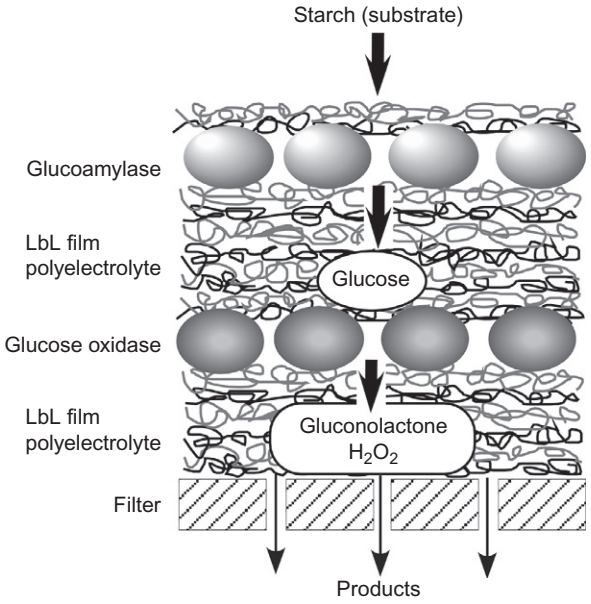

Fig. 9.5
Multienzyme reactor containing glucose oxidase and glucoamylase prepared on an ultrafilter.

One example of the advantages of the LbL structural features is application of multienzyme reactors (Fig. 9.5) [44]. This multienzyme reactor example was prepared from glucose oxidase and glucoamylase on an ultrafilter. Starch solution as reaction substrate was passed through the multienzyme reactor from the top. Glucoamylase can hydrolyze the glycoside bond in starch, resulting in glucose as the initial product. Glucose is then oxidized to gluconolactone by glucose oxidase accompanying production of H_2O_2 as a coproduct. Because of the ultrafilter below multienzyme film, the starting material, starch, cannot pass into the filtrate, which allows perfect separation between the starting materials and products. Wide applicability of solid supports for the LbL assembly leads to such advantages in reactor bioapplication

9.4 Environmental Sensor With Graphene LbL Assembly

One of the important issues in green science is detection and protection of surrounding environmental risks. Sensing of toxic and potentially toxic substances in environments is an important task of green science. For example, cesium detection is a crucial matter in Japan since the accident at the Fukushima Daiichi nuclear power plant. With the design of an appropriate molecular receptor, the presence of cesium in the earth [45] and in plant cells [46] can be visualized for sensing (Fig. 9.6). As seen in the following example, appropriate design of nanostructures and its fabrication are important factors in detecting environmental toxic substances.

In order to detect environmentally toxic aromatic hydrocarbons, fabrication of π-electron-rich nanospace on sensor surfaces was demonstrated. As shown in Fig. 9.7, reduced graphene oxide

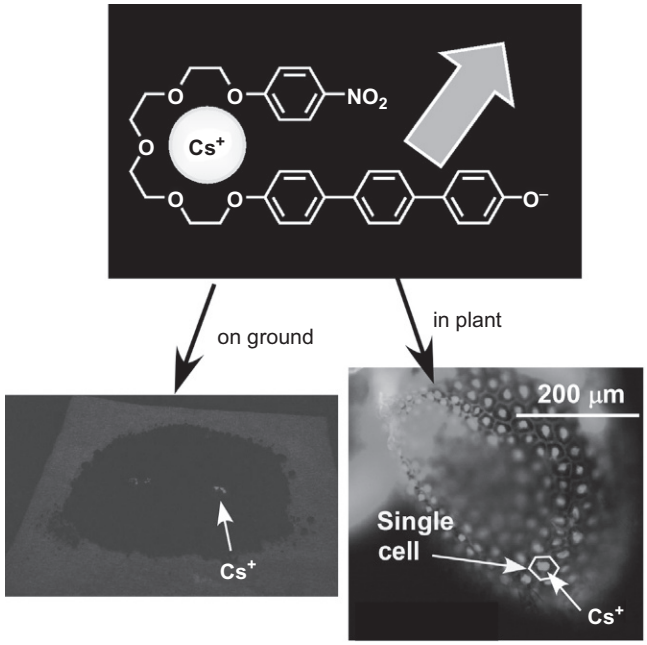

Fig. 9.6
Visualization of cesium on ground (left) and in plant cells (right).

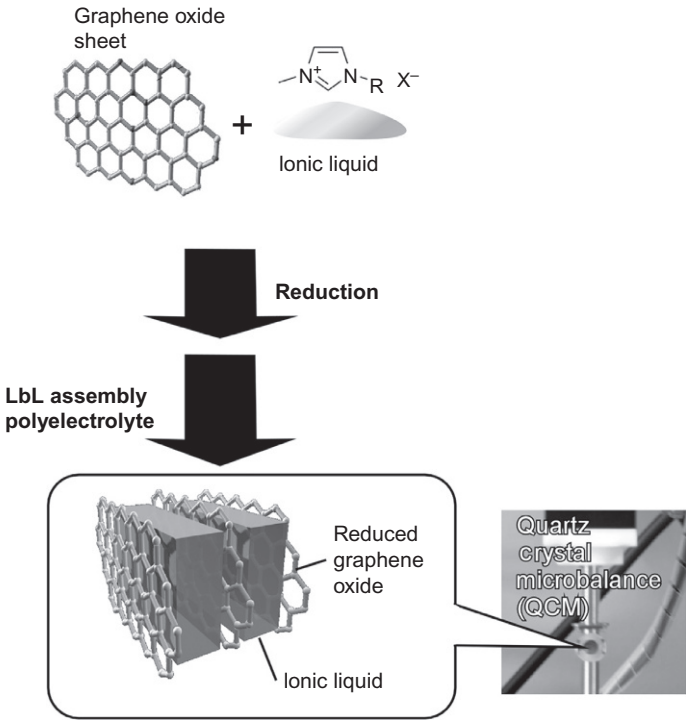

Fig. 9.7
Fabrication of π-electron-rich nanospace on a QCM sensor surface through LbL assembly of reduced graphene oxide in the presence of aromatic ionic liquids.

as two-dimensional π-electron materials and aromatic ionic liquids were assembled in LbL fashion on an electrode of quartz crystal microbalance (QCM) [47]. A QCM is widely known as a mass-sensitive sensor based on piezoelectric effects of quartz crystals [48–50]. Attachment and detachment of materials on the QCM electrode induces frequency decrease and increase, respectively, basically in proportion to changes of mass on its surface. With AT-cut 9 M Hz QCM sensor, a change of one nanogram can be detected with 1 Hz shift of the QCM frequency. Fabrication of nanostructures able to detect target substances on the QCM plate is a powerful method for sensor preparation for toxic gas substances.

For fabrication of graphene-based QCM sensor, pieces of graphene oxide nanosheets were first disassembled from graphite through oxidation of graphite materials under acidic conditions. The resulting graphene nanosheets were then reduced to reduced graphene oxide in the presence of immidazolium derivatives that can form ionic liquid in their condensed phase. This process leads to production of a complex of immidazolium cation and reduced graphene oxide, which can be assembled in LbL fashion with anionic polyelectrolytes poly(sodium styrenesulfonate) on QCM electrode. By several observation methods, aligned structure of reduced graphene oxides with enhanced spacing by filling with ionic liquid was confirmed.

Sensing capability of the fabricated structures was roughly examined by exposure of the graphene-based QCM sensor to solvent vapors under an ambient atmosphere. From decreases in frequency of the QCM sensor upon gas adsorption, selective and an in situ gas detection can be realized (Fig. 9.8). In particular, this sensor system exhibits enhanced sensitivity to aromatic gas substances. For example, significantly greater selectivity (more than 10 times) for benzene vapor over cyclohexane was observed in spite of their similar molecular sizes, molecular weights, and vapor pressures. The π-electron-rich two-dimensional nanospace in alternate layer structures of reduced graphene oxides and aromatic ionic liquid accommodate aromatic molecules preferentially.

In addition, adsorption of CO_2 gas from a saturated sodium hydrocarbonate solution can be detected by the same graphene-based QCM sensor, which suggests application of the fabricated sensor systems to global warming problems. Application of the LbL structures of reduced graphene-oxide and ionic liquid to electric resistance sensor is also possible. Difference of adsorption capability between benzene and cyclohexane can be converted to electric signals.

9.5 Environmental Sensor With LbL Assembly With Hierarchic Structure

As has been demonstrated, fabrication of guest-specific nanospace structures and assembly onto a sensor surface by the LbL technique is a useful method for sensing systems for detection of particular targets. As materials with controlled nanospaces, various mesoporous materials have much potential for sensing media because the size, geometry, and distribution of nanometer-scale pores are freely tuned as well as having a wide selection of pore components

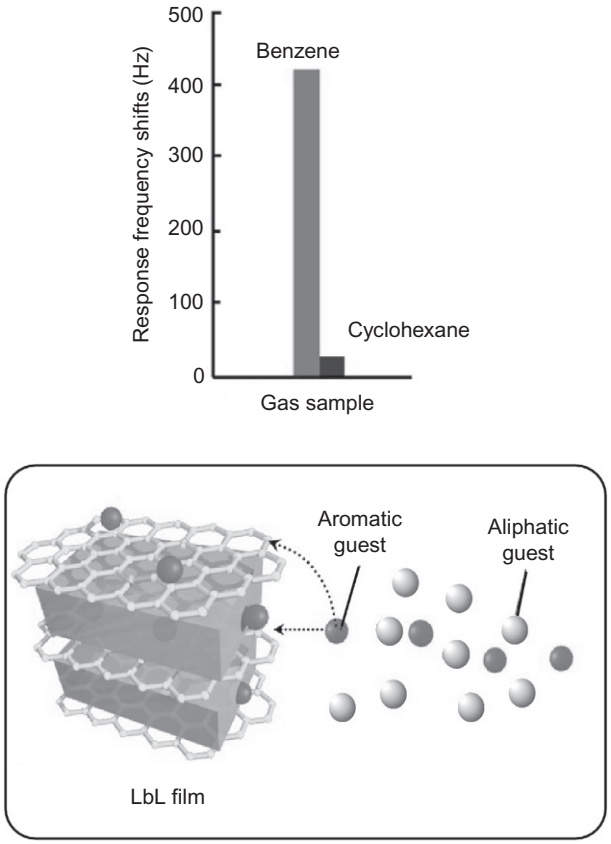

Fig. 9.8

Significantly greater selectivity for benzene vapor over cyclohexane at the π-electron-rich two-dimensional nanospace in alternate layer structures of reduced graphene oxides and aromatic ionic liquid.

and versatile surface modification [51,52]. Fabrication of hierarchic structure, mesoporous arrays in layered motif, is a powerful method for sensor design.

One example of sensors with LbL structures of mesoporous materials that uses mesoporous carbon materials as nanospace components is depicted in Fig. 9.9 [53]. In order to introduce surface charges on mesoporous carbon (CMK-3), mesoporous carbon materials were first treated by ammonium persulfate for surface oxidation to introduce negative carboxylate groups to mesoporous carbon. The resulting charged mesoporous carbon materials were assembled into the LbL films with cationic polyelectrolyte on the QCM electrode, and increasing surface coverage of the QCM electrode using the LbL process was confirmed. However, imperfect surface coverage on the QCM electrode is a better factor for sensing because of easier diffusion of guest gas molecules into mesopore channels. Therefore the LbL films of only two layers of mesoporous carbon materials were subjected to further sensing experiments in solution phase.

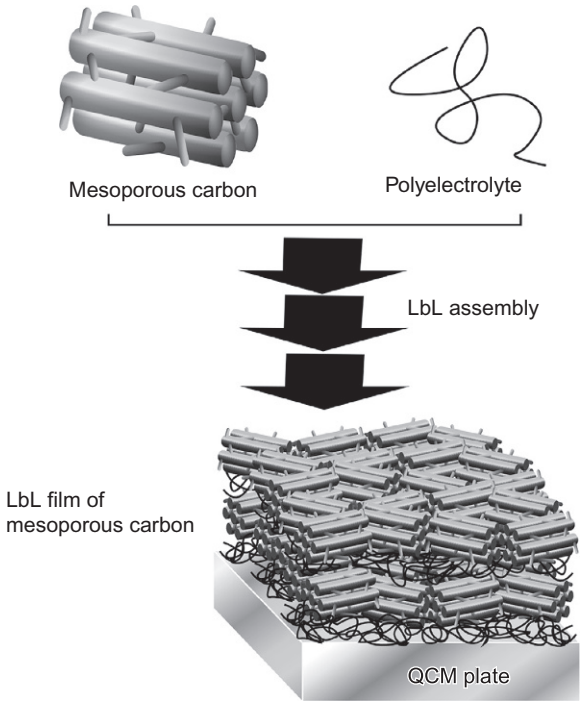

Fig. 9.9
LbL assembly of mesoporous carbon materials with cationic polyelectrolyte on the QCM electrode.

The QCM sensor plate covered with the LbL film of mesoporous carbon was immersed into aqueous solution and stabilized its resonant frequency. Injection of guest substances such as tannic acid into the aqueous phase induced frequency decreases of the QCM sensor upon adsorption of the guest onto mesoporous carbon materials. Frequency shifts of the QCM sensor with the mesoporous carbon LbL film upon adsorption of tannic acid were much greater than those observed for QCM sensors with octadecanethiol SAM structure or LbL films of polyelectrolytes alone, suggesting that mesopore structures have crucial importance for guest detection. Guest selectivity was also investigated using three guests: tannic acid, catechin, or caffeine. The QCM frequency response upon adsorption of tannic acid much exceeded those for catechin and caffeine guests. This clear guest selection resulted from size matching between mesopore host and guest molecules.

Interestingly, adsorption amount of tannic acid to the LbL films of mesoporous carbon showed a sigmoidal profile as a function of guest concentration at low concentration regions. The observed behavior originated from some kinds of cooperative phenomena. Probably, it can be explained by enhanced guest-guest interaction, because the adsorbed tannic acid can have effective hydrophobic interactions and/or π-π interaction within confined mesoporous nanospaces (Fig. 9.10). Although cooperative adsorption is often observed for gas molecules to

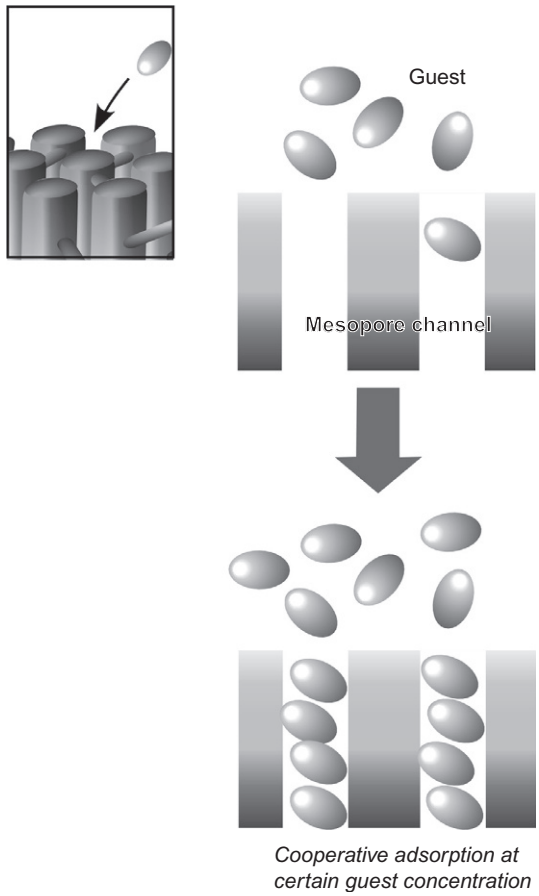

Fig. 9.10
Cooperative phenomena of guest adsorption into mesopore channels.

nanopores upon capillary condensation in gas phase, the similar cooperative adsorption upon guest inclusion in liquid phase has not been well explored. This finding can enhance understanding of molecular interactions within nanosized confined spaces; in particular, cooperative guest binding with nonspecific interactions in liquid media may be related to important phenomena including those observed in biological systems.

Sensor systems with further integrated hierarchic structures were also investigated. The system illustrated in Fig. 9.11 has hierarchic structures where hollow capsules are assembled into LbL structures, and every capsule has mesopore structures at its external walls [54]. Synthesis of mesoporous carbon capsules is based on template synthesis with use of zeolite crystals as templates. The carbon capsule structures with well-defined homogeneous dimensions ($1000 \times 700 \times 300$ nm^3) with 35-nm-thick walls and empty pore were synthesized. The capsule walls are made from carbon and have mesoporous structures with a uniform pore size

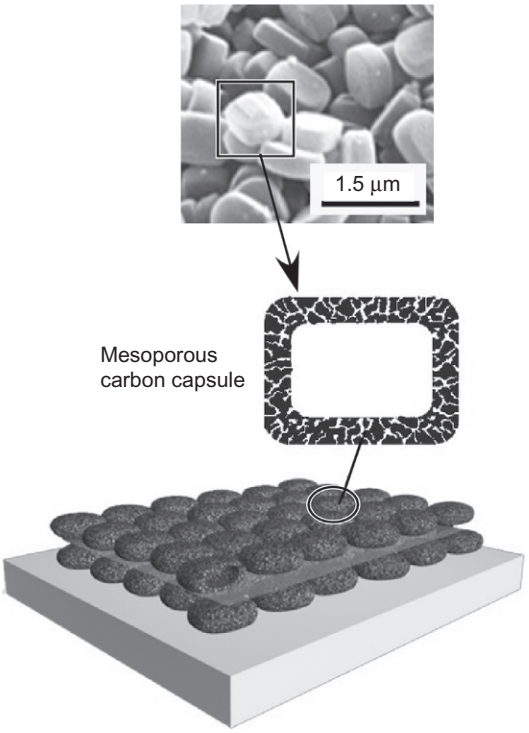

Fig. 9.11
Hierarchic LbL structures of hollow capsules with mesopore structures at its external walls.

distribution centered at 4.3 nm in diameter, and a specific surface area of 918 $m^2\ g^{-1}$. Although the carbon capsules do not essentially have surface charges, introduction of surface charge can be done through covering the capsule with charged surfactants, which can be further assembled alternately with counterionic polyelectrolyte onto a QCM sensor electrode.

Detection of various volatile substances onto the LbL films of the mesoporous carbon capsules was similarly examined through in situ frequency decrease of the QCM sensor upon exposure of the mesoporous carbon capsule QCM plate to saturated vapors of target substances. Among tested substances (water, cyclohexane, pyridine, aniline, benzene, and toluene), sensitivities for aromatic substances (pyridine, aniline, benzene, and toluene) are much higher than water and cyclohexane. In addition, noncharged aromatic hydrocarbon (benzene and toluene) exhibits the highest sensitivity. The amount of benzene adsorbed at equilibrium is ca. 5 times larger than that of cyclohexane, although these two substances have very similar physical properties including vapor pressures, molecular weights, and structures. This result strikingly indicates the crucial importance of the role of π-π interactions for selective detection of volatile organic compounds.

As shown in Fig. 9.12, this hierarchic structure is useful for modulating sensing selectivity. Modification of detection selectivity was made upon doping modulation elements into interior

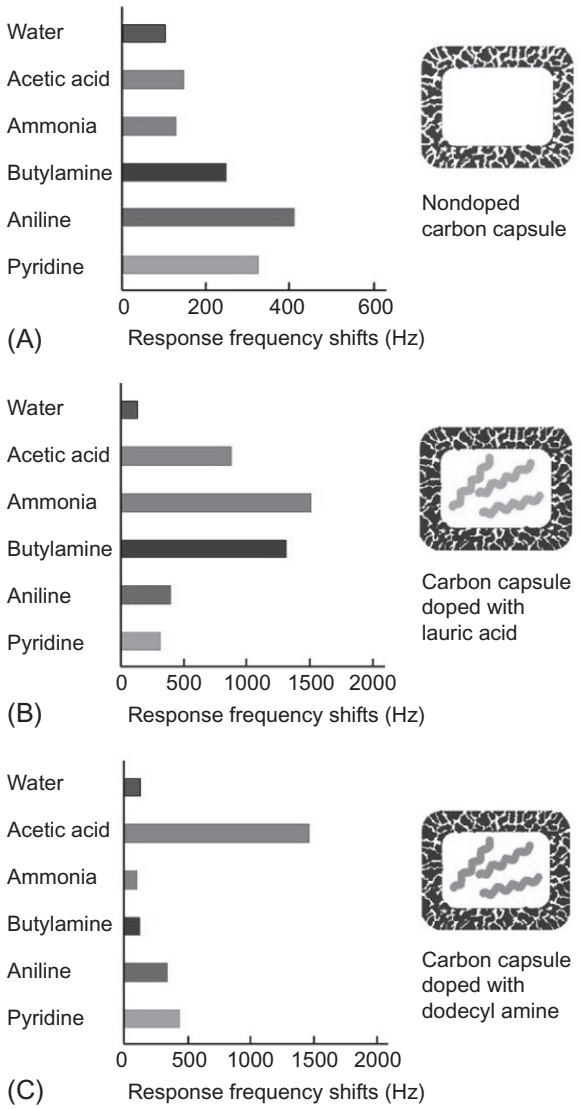

Fig. 9.12

Modified guest selectivity by doping modulation elements into interior spaces of the capsules in the LbL films.

spaces of the capsules in the LbL films. Adsorption preference was easily tuned by impregnation with additional recognition components (the second element). Wide ranges of guests (water, acetic acid, ammonia, butylamine, aniline, and pyridine) were investigated. Sensors with nondoped carbon capsules exhibited high affinity to aromatic compounds (aniline and pyridine). When lauric acid was doped as the second element, the sensors showed the greatest affinities for non-aromatic amines (ammonia and butylamine) and the second highest affinity for acetic acid were observed. Acid-base interactions are strong enough to alter the

sensing selectivity from aromatic compounds to basic substances. This concept was realized in reversed way through doping with acid second elements. Doping of dodecylamine into the carbon capsule films led to a strong preference for acetic acid. This strategy for modulation of sensing selectivity by doping with the second recognition elements into the capsule interiors within LbL films will enhance versatility of sensor design. Because carbon background materials are stable in water and various media, this sensing system can be used for detection of various toxic substances at biological environments.

9.6 Stimuli-Free Material Release From LbL Assembly

Control of release of materials to environments is one of the important tasks in green science. Some of them play important roles in biomedical fields such as drug delivery. As described in this section, hierarchic LbL structures of mesoporous silica capsule show unusual stimuli-free control of materials release from the assembled capsule. It may become an eco-friendly system for controlled materials supply.

In this case, mesoporous silica capsules were similarly synthesized using zeolite crystals as templates. The prepared mesoporous silica capsule with negative charges on the surface were assembled with cationic polyelectrolytes with the aid of anionic silica nanoparticles as a coadsorber (Fig. 9.13) [55,56]. Scanning electron microscopic observation on the fabricated LbL films confirmed that the mesoporous silica capsules were well dispersed among the silica particles within the film.

The LbL films of mesoporous silica capsules were prepared on a QCM plate in order to evaluate materials release from the capsule films. As standard experiments, incorporation and evaporation of water from the LbL films of mesoporous silica capsules. The QCM plate with the LbL film was first immersed into water phase in order to introduce water within the mesoporous capsule. Then, quantitative in situ evaluation of water evaporation from the capsules in the LbL films was made in the air phase. Surprisingly, an increase in QCM frequency corresponding to water release from the interior of the silica capsule within the compartment film exhibited a stepwise profile of repeated release and stop even though any external stimuli were not applied (Fig. 9.14).

A plausible mechanism for the observed stimuli-free automatic stepwise of water release from the mesoporous silica capsule films can be assumed to originate from combination of two processes. Balances of water evaporation from the pores and capillary penetration into the pores resulted in automodulated release of water. Probably, water entrapped in mesopore channels initially evaporates. The first water evaporation process occurs based on this evaporation. When the most of the water evaporates from the mesopore parts, water evaporation speed becomes much slower. Then water supply from the capsule interior to mesopore regions was made through rapid capillary penetration. Again, water evaporates from mesopore to exterior as the second evaporation step starts automatically.

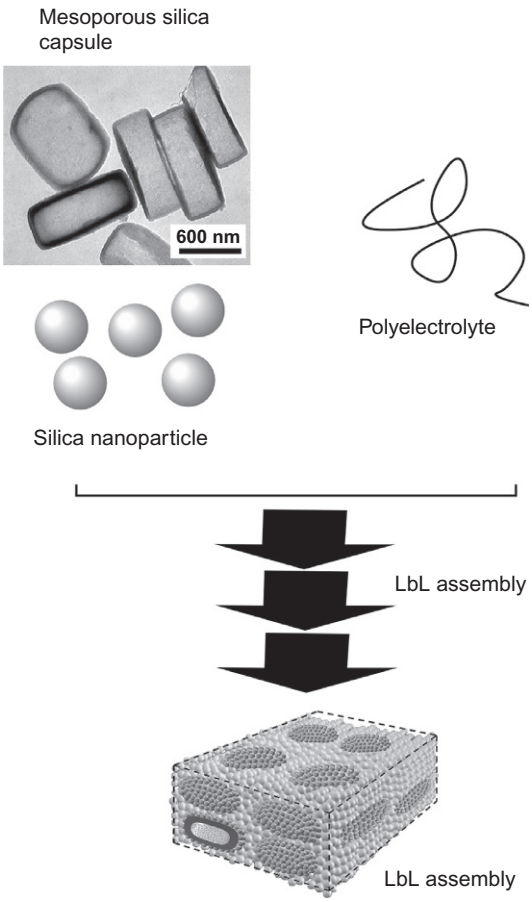

Fig. 9.13
A LbL film of mesoporous silica capsule with cationic polyelectrolytes with the aid of anionic silica nanoparticles as a co-adsorber.

The stimuli-free control of materials release is not limited to water evaporation. For example, the similar release profiles were commonly observed for various fluid drugs such as fragrance molecules. This is a rare example of a stimulus-free controlled release medium. This finding might be useful for materials supply in a stepwise manner and/or prolonged release efficiency.

9.7 Conclusions: Toward Nanoarchitectonics

This chapter briefly introduced several uses of LbL assemblies. Assembling well-defined nanostructures into controlled structures is surely a powerful way for various functional systems including green science-related applications. Fabrication of multienzyme reactors, highly selective sensors, selectivity-tunable sensors, and stimuli-free control of materials release were exemplified.

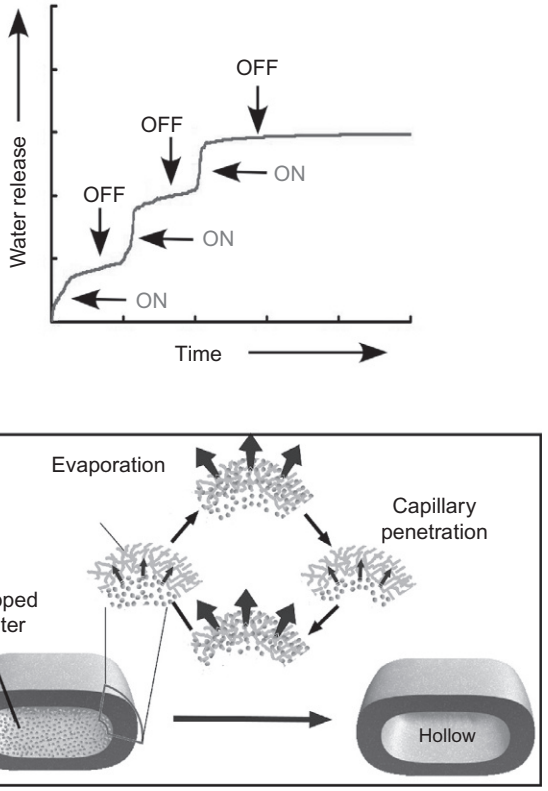

Fig. 9.14
QCM frequency changes corresponding to water release with a stepwise profile of repeated release and stop even witout any external stimuli.

Assembling nanoscale building blocks into functional systems corresponds to architecting functional systems in nanoscale. This feature is indeed similar to the emerging concept of nanoarchitectonics [57–59]. This terminology was first proposed by Masakazu Aono and involves the preparation of functional materials and fabrication of advanced systems by the harmonization of various actions such as atomic and molecular manipulation, self-assembly/organization, and control over the structure through the application of various physical stimuli and actions. This concept is expected to be used in various applications including catalysis [60], photocatalytic removal of pollutants [61,62], environmental remediation [63], optoelectronic applications [64,65], sensors [66–68], capacitors [69], and batteries [70,71] as well as functional materials [72–74] and systems [75–77]. The LbL fabrications match well with this basic concept of nanoarchitectonics. In addition, green science and green chemistry are included in target of nanoarchitectonics. This chapter discussed LbL strategy for green science. However, these approaches should be included for the more advanced concept of nanoarchitectonics for further future developments.

Acknowledgments

This study was partially supported by JSPS KAKENHI Grant Number JP16H06518 (Coordination Asymmetry) and the World Premier International Research Center Initiative (WPI Initiative), MEXT, Japan.

References

[1] Y. Okahata, K. Ariga, O. Shimizu, Langmuir 2 (1986) 538.
[2] K. Ariga, T. Nakanishi, T. Michinobu, J. Nanosci. Nanotechnol. 6 (2006) 2278.
[3] M.V. Lee, D. Enders, T. Nagao, K. Ariga, Langmuir 26 (2010) 4594.
[4] S. Acharya, J.P. Hill, K. Ariga, Adv. Mater. 21 (2009) 2959.
[5] K. Ariga, Y. Yamauchi, T. Mori, J.P. Hill, Adv. Mater. 25 (2013) 6477.
[6] K. Sakakibara, P. Chithra, B. Das, T. Mori, M. Akada, J. Labuta, T. Tsuruoka, S. Maji, S. Furumi, L. K. Srestha, J.P. Hill, S. Acharya, K. Ariga, A. Ajayaghosh, J. Am. Chem. Soc. 136 (2014) 8548.
[7] K. Ariga, J.P. Hill, Q. Ji, Phys. Chem. Chem. Phys. 9 (2007) 2319.
[8] K. Ariga, Y. Yamauchi, G. Rydzek, Q. Ji, Y. Yonamine, K.C.-W. Wu, J.P. Hill, Chem. Lett. 43 (2014) 36.
[9] G. Rydzek, Q. Ji, M. Li, P. Schaaf, J.P. Hill, F. Boulmedais, K. Ariga, Nano Today 10 (2015) 138.
[10] M.B. Zakaria, C. Li, Q. Ji, B. Jiang, S. Tominaka, Y. Ide, J.P. Hill, K. Ariga, Y. Yamauchi, Angew. Chem. Int. Ed. 55 (2016) 8428.
[11] G. Decher, Science 277 (1997) 1232.
[12] R.K. Iler, J. Colloid Interface Sci. 21 (1966) 569.
[13] G. Decher, J.D. Hong, J. Schmitt, Thin Solid Films 210 (1992) 831.
[14] Y. Lvov, G. Decher, H. Möhwald, Langmuir 9 (1993) 481.
[15] Y. Lvov, K. Ariga, I. Ichinose, T. Kunitake, Langmuir 12 (1996) 3038.
[16] Y. Lvov, K. Ariga, M. Onda, I. Ichinose, T. Kunitake, Langmuir 13 (1997) 6195.
[17] H. Wang, S. Ishihara, K. Ariga, Y. Yamauchi, J. Am. Chem. Soc. 134 (2012) 10819.
[18] F. Caruso, N.D. Furlong, K. Ariga, I. Ichinose, T. Kunitake, Langmuir 14 (1998) 4559.
[19] K. Ariga, Q. Ji, J.P. Hill, Adv. Polym. Sci. 229 (2010) 51.
[20] K. Ariga, J.P. Hill, Q. Ji, Macromol. Biosci. 8 (2008) 981.
[21] K. Ariga, Y. Lvov, T. Kunitake, J. Am. Chem. Soc. 119 (1997) 2224.
[22] K. Katagiri, R. Hamasaki, K. Ariga, J. Kikuchi, Langmuir 18 (2002) 6709.
[23] K. Katagiri, R. Hamasaki, K. Ariga, J. Kikuchi, J. Am. Chem. Soc. 124 (2002) 7892.
[24] Y. Lvov, K. Ariga, I. Ichinose, T. Kunitake, J. Chem. Soc., Chem. Commun. (1995) 2313.
[25] H. Lee, L.J. Kepley, H.-G. Hong, T.E. Mallouk, J. Am. Chem. Soc. 110 (1988) 618.
[26] S.W. Keller, H.-N. Kim, T.E. Mallouk, J. Am. Chem. Soc. 116 (1994) 8817.
[27] W.B. Stockton, M.F. Rubner, Macromolecules 30 (1997) 2717.
[28] L. Wang, Z. Wang, X. Zhang, J. Shen, L. Chi, H. Fuchs, Macromol. Rapid Commun. 18 (1997) 509.
[29] Y. Shimazaki, M. Mitsuishi, S. Ito, M. Yamamoto, Langmuir 13 (1997) 1385.
[30] T. Serizawa, K. Hamada, T. Kitayama, N. Fujimoto, K. Hatada, M. Akashi, J. Am. Chem. Soc. 122 (2000) 1891.
[31] T. Serizawa, K. Hamada, M. Akashi, Nature 429 (2004) 52.
[32] A. Ikeda, T. Hatano, S. Shinkai, T. Akiyama, S. Yamada, J. Am. Chem. Soc. 123 (2001) 4855.
[33] Y. Lvov, K. Ariga, T. Kunitake, Chem. Lett. (1994) 2323.
[34] Y. Lvov, K. Ariga, I. Ichinose, T. Kunitake, J. Am. Chem. Soc. 117 (1995) 6117.
[35] Y.M. Lvov, Z.Q. Lu, J.B. Schenkman, X.L. Zu, J.F. Rusling, J. Am. Chem. Soc. 120 (1998) 4073.
[36] Y. Lvov, M. Onda, K. Ariga, T. Kunitake, J. Biomater. Sci. Polym. Ed. 9 (1998) 345.
[37] Y. Lvov, H. Haas, G. Decher, H. Möhwald, A. Mikhailov, Y. B. Mtchedlishvily, E. Morgunova, B. Vainshtein, Langmuir 10 (1994) 4232.

[38] G.B. Sukhorukov, E. Donath, S. Davis, H. Lichtenfeld, F. Caruso, V.I. Popov, H. Möhwald, Polym. Adv. Technol. 9 (1998) 759.
[39] E. Donath, G.B. Sukhorukov, F. Caruso, S.A. Davis, H. Möhwald, Angew. Chem. Int. Ed. 37 (1998) 2201.
[40] F. Caruso, R.A. Caruso, H. Möhwald, Science 282 (1998) 1111.
[41] K. Ariga, Y.M. Lvov, K. Kawakami, Q. Ji, J.P. Hill, Adv. Drug Deliv. Rev. 63 (2011) 762.
[42] F. Caruso, D. Trau, H. Möhwald, R. Renneberg, Langmuir 16 (2000) 1485.
[43] M. Onda, K. Ariga, T. Kunitake, J. Biosci. Bioeng. 87 (1999) 69.
[44] M. Onda, Y. Lvov, K. Ariga, T. Kunitake, J. Ferment. Bioeng. 82 (1996) 502.
[45] T. Mori, M. Akamatsu, K. Okamoto, M. Sumita, Y. Tateyama, H. Sakai, J.P. Hill, M. Abe, K. Ariga, Sci. Technol. Adv. Mater. 14 (2013) 015002.
[46] M. Akamatsu, H. Komatsu, T. Mori, E. Adams, R. Shin, H. Sakai, M. Abe, J.P. Hill, K. Ariga, ACS Appl. Mater. Interfaces 6 (2014) 8208.
[47] Q. Ji, I. Honma, S.-M. Paek, M. Akada, J.P. Hill, A. Vinu, K. Ariga, Angew. Chem. Int. Ed. 49 (2010) 9737.
[48] Y. Okahata, K. Ariga, J. Chem. Soc. Chem. Commun. (1987) 1535.
[49] K. Ariga, K. Isoyama, O. Hayashida, Y. Aoyama, Y. Okahata, Chem. Lett. (1998) 1007.
[50] K. Ariga, K. Endo, Y. Aoyama, Y. Okahata, Colloid Surf. A 169 (2000) 177.
[51] K. Ariga, A. Vinu, Y. Yamauchi, Q. Ji, J.P. Hill, Bull. Chem. Soc. Jpn. 85 (2012) 1.
[52] V. Malgras, Q. Ji, Y. Kamachi, T. Mori, F.-K. Shieh, K.C.-W. Wu, K. Ariga, Y. Yamauchi, Bull. Chem. Soc. Jpn. 88 (2015) 1171.
[53] K. Ariga, A. Vinu, Q. Ji, O. Ohmori, J.P. Hill, S. Acharya, J. Koike, S. Shiratori, Angew. Chem. Int. Ed. 47 (2008) 7254.
[54] Q. Ji, S.B. Yoon, J.P. Hill, A. Vinu, J.-S. Yu, K. Ariga, J. Am. Chem. Soc. 131 (2009) 4220.
[55] Q. Ji, M. Miyahara, J.P. Hill, S. Acharya, A. Vinu, S.B. Yoon, J.-S. Yu, K. Sakamoto, K. Ariga, J. Am. Chem. Soc. 130 (2008) 2376.
[56] Q. Ji, S. Acharya, J.P. Hill, A. Vinu, S.B. Yoon, J.-S. Yu, K. Sakamoto, K. Ariga, Adv. Funct. Mater. 19 (2009) 1792.
[57] K. Ariga, Q. Ji, W. Nakanishi, J.P. Hill, M. Aono, Mater. Horiz. 2 (2015) 406.
[58] M. Aono, K. Ariga, Adv. Mater. 28 (2016) 989.
[59] K. Ariga, M. Aono, Jpn, J. Appl. Phys. 55 (2016) 1102A6.
[60] H. Abe, J. Liu, K. Ariga, Mater. Today 19 (2016) 12.
[61] C.M. Puscasu, G. Carja, C. Zaharia, Int. J. Mater. Prod. Technol. 51 (2015) 228.
[62] C.-M. Puscasu, E.M. Seftel, M. Mertens, P. Cool, G. Carja, J. Inorg. Organomet. Polym. Mater. 25 (2015) 259.
[63] K. Ariga, S. Ishihara, H. Abe, M. Li, J.P. Hill, J. Mater. Chem. 22 (2012) 2369.
[64] X. Chen, P. Li, H. Tong, T. Kako, J. Ye, Sci. Technol. Adv. Mater. 12 (2011) 044604.
[65] M. Pandeeswar, T. Govindaraju, J. Inorg. Organomet. Polym. Mater. 25 (2015) 293.
[66] K. Ariga, Y. Yamauchi, Q. Ji, Y. Yonamine, J.P. Hill, APL Mater. 2 (2015) 030701.
[67] S. Ishihara, J. Labuta, W. Van Rossom, D. Ishikawa, K. Minami, J.P. Hill, K. Ariga, Phys. Chem. Chem. Phys. 16 (2014) 9713.
[68] K. Ariga, K. Minami, L.K. Shrestha, Analyst 141 (2016) 2629.
[69] R. Rajendran, L.K. Shrestha, R.M. Kumar, R. Jayavel, J.P. Hill, K. Ariga, J. Inorg. Organomet. Polym. Mater. 25 (2015) 267.
[70] K. Takada, Langmuir 29 (2013) 7538.
[71] K. Takada, N. Ohta, Y. Tateyama, J. Inorg. Organomet. Polym. Mater. 25 (2015) 205.
[72] K. Ariga, M. Li, G.J. Richards, J.P. Hill, J. Nanosci. Nanotechnol. 11 (2011) 1.
[73] K. Ariga, K. Minami, M. Ebara, J. Nakanishi, Polym. J. 48 (2016) 371.
[74] K. Ariga, V. Malgras, Q. Ji, M.B. Zakaria, Y. Yamauchi, Coord. Chem. Rev. 320–321 (2016) 139.
[75] K. Ariga, M.V. Lee, T. Mori, X.-Y. Yu, J.P. Hill, Adv. Colloid Interface Sci. 154 (2010) 20.
[76] K. Ariga, J. Li, J. Fei, Q. Ji, J.P. Hill, Adv. Mater. 28 (2016) 1251.
[77] K. Ariga, ChemNanoMat 2 (2016) 333.

CHAPTER 10

Graphene-Based Nanolayers Toward Energy Storage Device

Mahmoud M.M. Ahmed, Toyoko Imae[1]

National Taiwan University of Science and Technology, Taipei, Taiwan
[1]*Corresponding author*

10.1 What Is Graphene?

Graphene [1,2], the rising star among carbon materials, is a sheet of atomic thickness consisting of hexagonally honeycomb-packed sp^2 carbon and forming a two-dimensional structure. It is a unit layer of parent graphite, which is the layered accumulation of graphenes interacting with each other mainly by π-π stacking. It is considered to be the master structure of the other nanocarbons, for example, fullerene, carbon nanotube, and carbon ribbon. Recently, graphene has occupied the minds of many scientists [3], since it is a zero-band gap semiconductor in which the valence and conduction bands are shaped like an inverted pair of cones that meet at a single point in the momentum space. Due to its structure, graphene has outstanding electronic [4] and thermal properties [5–7]. In addition, graphene is considered "the strongest material ever" as its breaking strength is 42 N/m and Young's modulus is ∼1.0 TPa [8]. Due to these properties, especially the electronic properties, it can be applied to various systems: Graphene has been applied to solar energy devices [9], semiconductors [10], ultracapacitors [11,12], gas sensors [13], biosensors [14], and diagnostic treatments [15,16]. It has also been used recently in flexible and organic light emitting diode displays [17] with better performance than that of the indium tin oxide. Its large surface area also enables it to be used for various catalytic reactors including fuel cell devices [18], biomedical therapy [19], and solar cell systems. All these excellent properties and new applications of graphene make its synthesis procedure a hot (fundamental) topic in the nanotechnology field. In this chapter, the preparation of graphene is focused mainly on the top-down and bottom-up methods to promote mass production. Its layer characterization and application to energy storage, particularly to the supercapacitor field, are described.

10.2 Synthesis of Graphene

Graphene can be prepared via one of two major ways, the top-down and bottom-up methods [20,21]. Fig. 10.1 illustrates the schematic diagram of graphene preparation methods via

Nanolayer Research. http://dx.doi.org/10.1016/B978-0-444-63739-0.00010-4

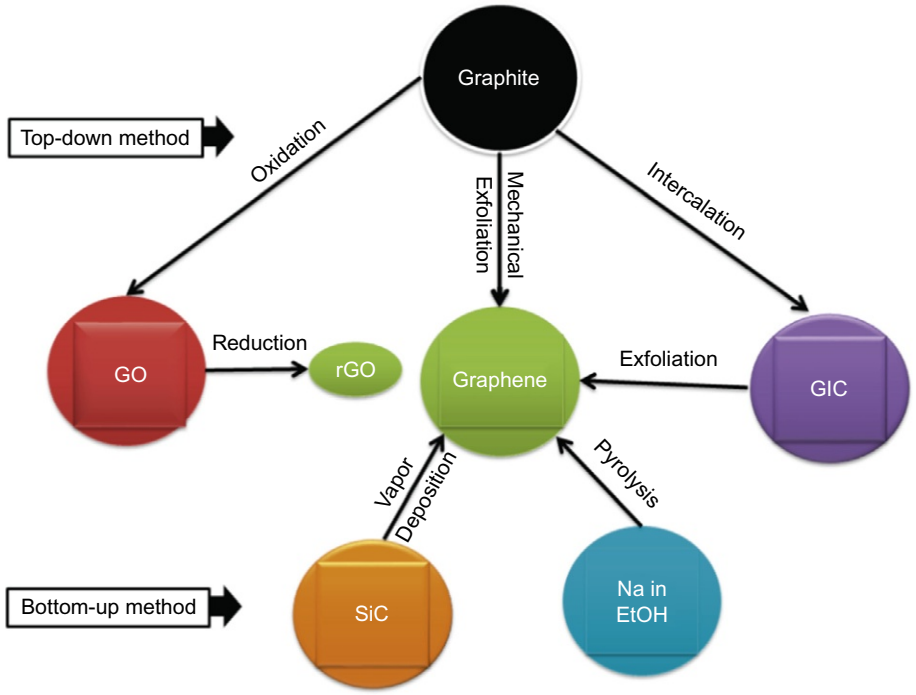

Fig. 10.1
Schematic diagram of graphene preparation via different methods.

different routes. The top-down methods include graphene preparation through mechanical exfoliation, oxidation-reduction [graphene oxide (GO)] and intercalation-exfoliation [graphite intercalation compound (GIC)]. The bottom-up methods are the pyrolysis of sodium in ethanol and chemical vapor deposition of silicon carbide (SiC). Since any method has its own advantages and disadvantages in terms of yield, quality, mass production, and applications of the produced graphene, the procedure for each preparation method is introduced with its characteristics in the following sections.

10.2.1 Top-Down Methods

10.2.1.1 Mechanical exfoliation

One of the top-down methods is the mechanical exfoliation of graphite, which had been one of the most frequently used methods. The Ruoff group [22] in 1999 used a tip of an atomic force microscope (AFM) to exfoliate highly oriented pyrolytic graphite (HOPG), yielding a thickness of ~200 nm. In 2010, Geim and Novoselov [1] used Scotch tape to exfoliate 1-mm-thick HOPG, and succeeded in yielding graphene of single or few layers. Thus, the Nobel Prize in Physics was awarded to them due to their amazing discovery that opened the door to excellent

development of graphene research. The mechanically exfoliated graphene is efficiently used in various applications including field effect transistors. This method using Scotch tape was also applied to other 2D materials, for example, boron nitride, molybdenum sulfide, and others [23]. Although this procedure is effective for exfoliation, the increase of product yield is still ongoing since the work is tedious and time consuming.

Mechanical exfoliation is also possible by dispersing or dissolving pristine or expanded graphite in aqueous organic solvents or polymer solutions [24–26], which have high affinity for graphene. This method allows the π-π interaction between graphite layers to be diminished by means of a bath-type sonicator for a long time [27] or a powerful tip homogenizer for a shorter time. This procedure has several advantages. For instance:

(1) The method is facile and one step.
(2) The procedure is suitable for large-scale production.
(3) The obtained graphene dispersion is stabilized by solvation for a relatively long time.
(4) The procedure does not induce strong functionalization or severe defects in the graphene sheets [28].

In addition, this method can be performed in single or mixed solvents [29], ionic liquids [30,31], and/or surfactant solutions [32]. The stable dispersions of graphene sheets [33] can be attained in the solvent or at the interface of immiscible solvents [34]. This procedure does not include any harmful chemical reaction or unrecovered functionalization, since it is only a physical exfoliation process. Few procedures have recently been reported with different interpretations for the mechanisms. Thus these methods can be promising techniques for investigating the exfoliation [35,36]. Meanwhile, since the dispersed graphene suffers from instability, fragmentation, long sonication time, and less-than-desired yield, there are issues yet to be solved (which is not the case with the procedure via GO described later). In addition, small fragments can affect graphene's unique properties, and sometimes surfactants are not easily washed out or removed from the surface of graphene. When the stacked graphite is dispersed in certain solvents and stimulated mechanically, it will become deformed to break the π-π interaction force between its layers, and cause the exfoliation to graphene of a few layers. This mechanism depends on specific characteristics of the solvent that enable stabilization of the exfoliated graphite in the dispersion.

The stability of the dispersion is the key parameter of the best exfoliation [28]. Hansen solubility parameters [37,38] can be used to predict the ability of various solvents to disperse graphene [39]. The dispersion parameters generally define the stability of materials in solutions and are contributed by three parameters of dispersion, polarity, and hydrogen bonding between molecules (solute and solvent). These parameters are described as vectors in the three-dimensional space (Hansen space). The ideal solvent that can cause exfoliation of graphite to graphene should have dispersion force of ∼18 MPa, polarity of ∼9.3 MPa, and hydrogen bonding of 7.7 MPa [40]. Thus 1-methylpyrrolidone is considered one of the best solvents in

terms of exfoliation and stability, since this solvent satisfies the conditions of an ideal solvent. Moreover, this solvent causes exfoliation with high yield after a mild continuous sonication for a few weeks [35,36].

The use of organic solvents to exfoliate graphite is considered undesirable due to problems associated with organic solvents, e.g., possessing high boiling point and high toxicity. This disadvantage can be avoided by using a surfactant-water system instead. Various surfactants, including sodium dodecylsulphate [41] and sodium cholate [42], have been used for dispersion of carbon nanotubes [43] and of other carbon materials as well [33,44]. For graphene [45], similar surfactants were also used [42] with water [46] or other solvents for long sonication time [47]. The use of surfactants can cause easy exfoliation and stabilization of graphene [45] and enables the obtained graphene to be used in different applications [48] such as a conductive film with high quality. Thus the graphite exfoliation using surfactants has several advantages as following:

(1) The method is nonoxidative, and the quality of obtained graphene is high.
(2) The procedure doesn't require high-temperature treatment or chemical posttreatments.
(3) Safe (nontoxic), user-friendly, and low-boiling-point solvents can be used.

The dispersibility of graphene depends on the type of surfactants used. Several nonanionic surfactants [49] have been investigated to exfoliate graphene directly from graphite via sonication for a short time in a mild condition [50]. A stable suspension of graphene solution is formed in an organic solvent (dimethylformamide) dissolved in a cationic surfactant [45]. Although the sonication method can be considered an efficient method for the dispersion of graphene, it has some disadvantages including the very long sonication time, which causes fragmentation to graphene flakes with the difficulty of removing surfactant and with the less reproducibility. Therefore other methods are essentially required to improve the reproducibility of the produced graphene and decrease its fragmentation.

10.2.1.2 Oxidation-reduction (via GO)

One of the most traditional procedures used in the top-down method is the oxidation-reduction reaction. Although different procedures have been reported, the differences among these methods consist in a variation of the oxidizing agents, or the reaction circumstances. These treatments allow an efficient oxidation process, and hence effective exfoliation procedures can be performed. Table 10.1 lists various methods of graphite oxidation and compares their advantages and disadvantages. The oxidation methods of the natural graphite to graphite oxide were first developed by Brodie in 1859 [51] and Staudenmaier in 1898 [52]. In 1958 Hummers and Offeman [53] modified the method. They had successfully obtained graphite oxide as a product of graphite oxidation by using potassium permanganate, sodium nitrate, and sulfuric acid, which were not the chemicals used by Brodie and Staudenmaier. Since the development and use of the Hummers procedure to synthesize graphite oxide, other oxidation schemes have

Table 10.1 Comparison of oxidation procedures of graphite

Inventor	Chemical	Advantage	Disadvantage
Brodie 1859 [51]	$KClO_3$ HNO_3	• High yield • Dispersibility in water • Effective oxidation	• Reaction is explosive • Chlorate is difficult to wash out • Products are fragmented
Staudenmaier 1898 [52]	$KClO_3$ HNO_3 H_2SO_4	• Oxidative procedure • Suitability for large scale • Effective oxidation and exfoliation	• Reaction is explosive • Washing/heating processes are time consuming • Chlorate is difficult to wash out
Hummers and Offeman 1958 [53]	$KMnO_4$ $NaNO_3$ H_2SO_4	• No chlorate contamination • Mass production • High purity	• Oxidation is incomplete • Separation process is time consuming • Ice bath is necessary
Kovtyukhova et al. 1999 [54] (modified Hummers method)	$K_2S_2O_3$ P_2O_5 H_2SO_4	• Higher oxidation	• Processes are time consuming • Temperature is difficult to control
Marcano et al. 2010 [55] (improved Hummers method)	$KMnO_4$ H_3PO_4 H_2SO_4	• Improved oxidation efficiency and production amount • No toxic gases • Reaction at room temperature	• Yield is less and cost is high • Washing steps are time consuming • Amount of hydrophilic oxidized graphene is increased
Yu et al. 2016 [56] (based on the improved Hummers method) Lin et al. 2016 [57], Dong et al. 2016 [58]	$KMnO_4$ K_2FeO_4 H_2SO_4 CrO_3 $(NH4)_2S_2O_8$ H_2SO_4	• Less consumption of oxidants/intercalators • Shorter reaction time • Large sheets	• Oxidation occurs mostly only at the edges of the graphene plane • Graphene is hybridized with chromium oxides difficult to wash out

been developed. One method was reported by Kovtyukhova et al. [54] in 1999. They succeeded in oxidizing graphite via mixing sulfuric acid with a blend of potassium thiosulfate and phosphorous pentaoxide to allow the complete oxidation of the whole layers. The improved Hummers method for the synthesis of GO was developed by Marcano et al. [55] in 2010. They improved the Hummers method by excluding $NaNO_3$ and increasing the amount of $KMnO_4$. In addition, they performed the reaction in a mixture of H_2SO_4/H_3PO_4 (9:1). When the improved Hummers method [55] is compared to the Hummers [53] and modified Hummers [54], some advantages are found regarding the products. In contrast to the Hummers method, the improved method does not generate toxic gases, and the temperature can be easily

controlled without an ice bath, which was needed in the Hummers method. These important advantages improve the efficiency of the oxidation process and produce a greater amount of hydrophilic graphene material as compared to the Hummers method and its modified method. Although the improved method provides large-scale GO with higher quality, the poor yield and high cost sometimes prevent its practical application. Therefore a new method was established based on the improved method [56]. This method diminishes oxidative chemicals by partially replacing $KMnO_4$ by K_2FeO_4 and reducing the amount of concentrated sulfuric acid. Although this enhanced method provides the large scale and efficient oxidation of the graphite layers, the oxidation occurs mostly at the edge of the graphene plane. In other words, the method did not extend the oxidation on the whole sheet surfaces, as might be expected. Therefore other methods were recently developed to allow the expansion of the sheets before performing the oxidation process. This method was examined at room temperature by Lu's group [57,58]. They used chromic acid–intercalated expanded graphite to be oxidized by ammonium persulfate in sulfuric acid. The technique provided a large-scale production of GO with ultralow density. When the strong oxidative reagents are used, various hydrophilic functional groups are produced including carboxylic, epoxy, and hydroxyl groups [59]. These functional groups induce a hydrophilic nature of the produced graphite oxide and allow water molecules to be easily intercalated between the layers via simple sonication process, separating graphite oxide into partially exfoliated GO layers.

The obtained graphite oxide or GO has a variety of important properties and applications not only as a cathode for lithium-ion batteries but also as electrode materials for supercapacitors and fuel cells, because its large surface area makes it more suitable [60,61]. Furthermore, the hydrophilicity of GO allows it to be uniformly deposited in the form of thin film onto hydrophilic substrates, because the aspect of thin film is necessary for electronic applications [9]. Thus the GO itself is a useful material. Importantly, the functional groups on GO assist in preventing the restacking of the graphene layers. In addition, they can also be successfully linked to different molecules or polymers [62] with other functionalities that are added to the functionality of GO [63]. This progressive functionalization changes the electronic structure of GO and makes it further connected to various mechanical [64], chemical [65], biological [66], and electrochemical [67] applications. The hybridization of GO with conductive polymers including polyaniline [68,69], polyacrylic acid [70–72], polypyrrole [73], and others [74] is especially fascinating because of the variety of possible utilizations particularly in energy transfer systems.

When the GO is used as the precursor of graphene, the oxidized groups of GO must be reduced to form reduced graphene oxide (rGO), so procedures were developed to reduce the functional groups on the surface of GO. Since different types of functional groups on GO make it difficult to completely reduce it to graphene, the reported methods mainly adopted less harmful reducing agents, for example, vitamin C [75,76], Zn/HCl [77,78], $NaBH_4$ [79,80], or aluminum powder [81], instead of using the conventional strong reducing agent "hydrazine," to reduce the

Table 10.2 Comparison of reduction methods of GO

Chemical Method			
Inventor	**Chemical**	**Advantage**	**Disadvantage**
Dimiev et al. 2011 [77], Dey et al. 2012 [78]	Zn/HCl	• Scalability and facility • Reaction at room temperature	• More defects (increase of sp^3)
Fernnández-Merino et al. 2010 [75], Zhang et al. 2010 [76]	Vitamin C	• Nontoxicity • Solubility in aqueous/organic solvents • No contamination of heteroatoms	• Very long reaction time
Si et al. 2008 [79], Shin et al. 2009 [82]	$NaBH_4$	• High conductivity	• Broken and crumbled sheets
Fan et al. 2010 [81]	Aluminum powder	• Short reaction time • Less toxicity • High conductivity	• Extremely vigorous reaction
Physical Method			
Inventor	**Method**	**Advantage**	**Disadvantage**
Eswaraiah et al. 2011 [83]	Focused solar radiation	• Easy scalability • Cost effectiveness • High electrical conductivity	• Inhomogeneous power distribution
Eigler et al. 2012 [84]	Laser beam	• Large area graphene sheets	• Higher Sp^3 than Sp^2
Wang et al. 2013 [85]	Gamma radiation	• Eco-friendly reaction • Reaction at room temperature	• Higher Sp^3 than Sp^2
Lee et al. 2011 [86]	Heating at 1900°C under vacuum	• Less Sp^3, more Sp^2	• Reaction at very high temperature

severe defects caused by the hydrazine reduction. Table 10.2 summarizes different chemical and physical reduction procedures performed to effectively convert GO into graphene with fewer defects. The reduction step should be carried out in polymer or surfactant solution(s) to produce a stable dispersion of rGO [87,88], because the restacking of the fewer hydrophilic reduced layers could be inhibited. This is essential for the stable dispersion of rGO.

The rGO suffers from many defects in the sp^2 (graphene) structure, and the sp^2 structure cannot be recovered in adding incomplete reduction of all functional groups on its surface. After the reduction of the GO, the properties particular to rGO negatively affect some applications. For instance, rGO has slightly lower efficiency than graphene in the electrical conductivity and energy system. However, even though the GO produced by hydrazine is more oxidized than the product by Hummers method, both products at the same condition result in similar electrical conductivities to each other [55]. Therefore other schemes were essentially required

to improve the conductivity and reduce functionalities and defects of the obtained graphene material. Furthermore, reduction methods have several disadvantages in view of the difficulties in chemical waste and temperature control. In order to make the reduction process more eco-friendly [89], performing the reduction process without additional chemicals is required.

Physical methods have been investigated for reducing the functional groups on the GO surface without any chemical reactions. Eswaraiah et al. [83] in 2011 reduced the GO with the very simple idea of solar radiation condensed by focusing lens. Other reduction procedures have been done via laser beam [84] and gamma radiation [85]. Also in 2011, Jin et al. [86] heated GO at 290°C to reduce its functional groups and exposed it subsequently to higher temperature (1900°C) at low pressure (10^{-6} Torr) to exfoliate it. The obtained rGO sheets had higher conductivity than rGO obtained by the other methods and original graphite. However, it should be noted that although the modifications on GO synthesis improve the quality of rGO, there are still severe defects of sp^2 structure in the obtained rGO. Thus the other approach should be developed for the production of effective graphene.

10.2.1.3 Intercalation-exfoliation (via GIC)

Over the past hundred years, the most common way to prepare graphene has been through a GIC, but this procedure has caused a lot of concern. Generally, this method consists of two steps, that is, the intercalation to form the GIC and the expansion and exfoliation of the GIC. On the first step of the intercalation to form the GIC, the beginning of the idea of "the intercalation procedure" is quite old [90], and the procedure was used to expand the graphite as the "expanded graphite." The small molecules can be inserted between the graphite layers, and this reaction results in an expansion of interlayer distance of graphite. There are two different groups of intercalation compounds, that is, the donor type [91] and the acceptor type [92]. Table 10.3 summarizes two main intercalators used for GIC preparation and their exfoliation.

Table 10.3 Comparison of different types of GICs

Intercalator	Donor Type	Acceptor Type
Chemicals	• Li, Na, K, Ca (Lewis base), mixed metallic salts, alloys, eutectic mixtures	• HF, I_2, Br_2, $FeCl_3$ (Lewis acid)
Exfoliation	• Hydrogen gas evolution	• Hydrogen gas evolution • Further intercalation with Lewis base • High temperature
Advantage	• Nonoxidative preparation • Large-scale production • Wide utilization to lithium batteries	• Nonoxidative preparation • Easy handling and preparation • Large-scale production • High-yield production
Disadvantage	• Vacuum condition for GIC preparation • Explosive exfoliation • Hybridization with metal ions	• Hybridization with metal ions

In the first (donor) type of GIC, the intercalation compounds can donate electrons to graphite and expand graphite layers. Acceptor-type GIC is manufactured by intercalating compounds, which accept electrons from graphite. These intercalation procedures have been widely used for exploration of GICs functionalization and enormous application possibilities [93–97]. The second step in GIC preparation of graphene is the subsequent expansion and exfoliation of the GIC [98]. In order to cause the expansion/exfoliation after intercalation into the graphite layers, the intercalation compounds need stimulation [99].

To accomplish the first step (GIC formation), many procedures have been investigated for how to cause the intercalation of different molecules into the graphite layers, since the intercalation of small molecules should be the key point in exfoliation. Among many studies reported for GICs synthesis [100–104], several researches have applied the donor-type intercalators, for example, lithium [105,106], potassium [107], calcium [108], and sodium [109] metals or mixture of metals [110,111]. Although this procedure has recently been used in lithium ion batteries [105], the reaction must be performed in a dry box/vacuum to avoid the vigorous reaction of the alkali metals, although the reaction temperature is relatively low (200°C). Acceptor-type intercalation [112] has also been investigated by applying fluoride [113,114], iodide [115], iron chloride [116], and other metal chloride salts [117] either alone or mixed with other salts [118–120]. Some advantages can be considered for the GICs of metal chlorides, since they are easy to handle and chemically stable in comparison with the GICs of other alkali metals. These are important aspects from the viewpoint of mass production. Historically, GICs (donor/acceptor types) have been prepared via intercalation of Bronsted acids, for example, HNO_3, H_2O_2, and H_2SO_4 through direct reaction with graphite at room temperature. These acids allow intercalation as well as oxidation of the graphite layers. On the other hand, the intercalation of Lewis acids/bases is performed via vapor intercalation of the alkali metal into graphite layers, after the temperature is increased above the melting point of the intercalator. One important aspect of the GIC formation especially via Lewis acids/bases intercalation is that the intercalated molecules are not covalently bonded to or strongly interacting with the carbon atoms. In other words, the electron donor-acceptor interaction between the intercalator and graphite is a weak interaction. Therefore there is no direct functionalization of the obtained graphene that can damage its unique properties.

For the second step, expansion and exfoliation of the GIC, different procedures have been proposed [92,101,121,122], and they can be classified into two types:

(1) Gas expansion [123].
(2) Intercalation-induction [110,124].

The gas expansion procedures can be performed through the chemical reaction of the intercalated alkaline metals. The metals react vigorously with protic solvents to generate H_2 gas, which can cause the expansion of graphite layers. The acceptor-type GICs are less active compared to the donor-type GICs but can increase expansion of the graphite layers. The typical case is the donor-type H_2SO_4-GIC treated with H_2O_2. The GIC can be expanded by

decomposition of H_2O_2 at high temperature. It is important to note that H_2O_2 can be successfully used for the exfoliation of acceptor-type $FeCl_3$-GIC as well [123]. The procedure shows the possibility of scaled-up production and excellent battery performance. When ethanol is used as an exfoliating solvent for a donor-type (potassium) intercalator, ethanol can act for the gas expansion procedure and also release the produced H_2 gas [92], although a safe procedure in case of or to prevent explosion still needs to be investigated. An explosion caused by the gas reaction could bring severe defects to the produced graphene. Therefore the achievement of a mild method that provides fewer defects in graphene is highly required. This mild method was also used on the oxidation of the graphite layers when the intercalation of the oxidative molecules into the interlayer of the graphite lattice produced wormlike exfoliated graphite [125].

In the intercalation-induction procedure, the alkali metal halides accept electrons from graphite and induce the further intercalation of larger molecules to cleave the graphite layers. This process can allow the mild exfoliation of graphite without undesired reactions. Primary amine can successfully intercalate into the layers of the acceptor-type $FeCl_3$-GIC due to its electron lone pair and linear molecular structure, causing the interlayer structure of graphite to be more expanded (see Fig. 10.2A) [116]. In this process, a lone pair of amine can make Lewis acid-base interaction with $FeCl_3$, which is already intercalated into graphite layers by Lewis acid-base interaction with graphite, and complexes of iron and amine are removed with halide counterions from graphite. It is important to note that the tertiary amine cannot penetrate into the stacked layers of the $FeCl_3$-GIC due to the steric hindrance by the three-dimensional structure. However, the alkyl chain of primary amine should change its configuration to be bulky to expand the graphite layers as a wedge. The idea of co-intercalation was recently attempted to intercalate crown ether [126] and pyrrolidinium cation in donor-type Na-GIC [127], but the exfoliation of the donor-type GIC did not occur [109], perhaps due to little or no intercalation of bulky molecules. Thus the primary amine treatment of acceptor-type $FeCl_3$-GIC is a remarkably facile procedure for producing expandable graphene sheets without producing any significant defects in the basal plane of graphene.

The intercalation of graphite and the exfoliation processes of $FeCl_3$-GIC can be characterized by the G band of Raman spectra (Fig. 10.2B), where a G band ($\sim$1580 cm^{-1}) of graphite shifted to a band ($\sim$1625 cm^{-1}) of $FeCl_3$-GIC after the intercalation [116]. This shift represents the charge transfer from graphite (donor) to $FeCl_3$ (acceptor), lowering the Fermi energy level. On the other hand, the reaction of the $FeCl_3$-GIC with dodecylamine shifts the G band back to $\sim$1581 cm^{-1}, which is close to the G band of the original graphite [128], and this band shift indicates an increase of the Fermi energy level. The same processes were also confirmed by X-ray diffraction (XRD) (Fig. 10.2C). The $FeCl_3$-GIC showed a lattice distance corresponding 0.92 nm, which is longer than 0.34 nm of pristine graphite. The amine-treated process displayed the disappearance of the Bragg peaks in this angle region but the appearance of a spacing distance of 4–6 nm in the small-angle region, which is much larger than the distance by GO oxidation expansion [129]. These results confirm that the treatment of $FeCl_3$-GIC by

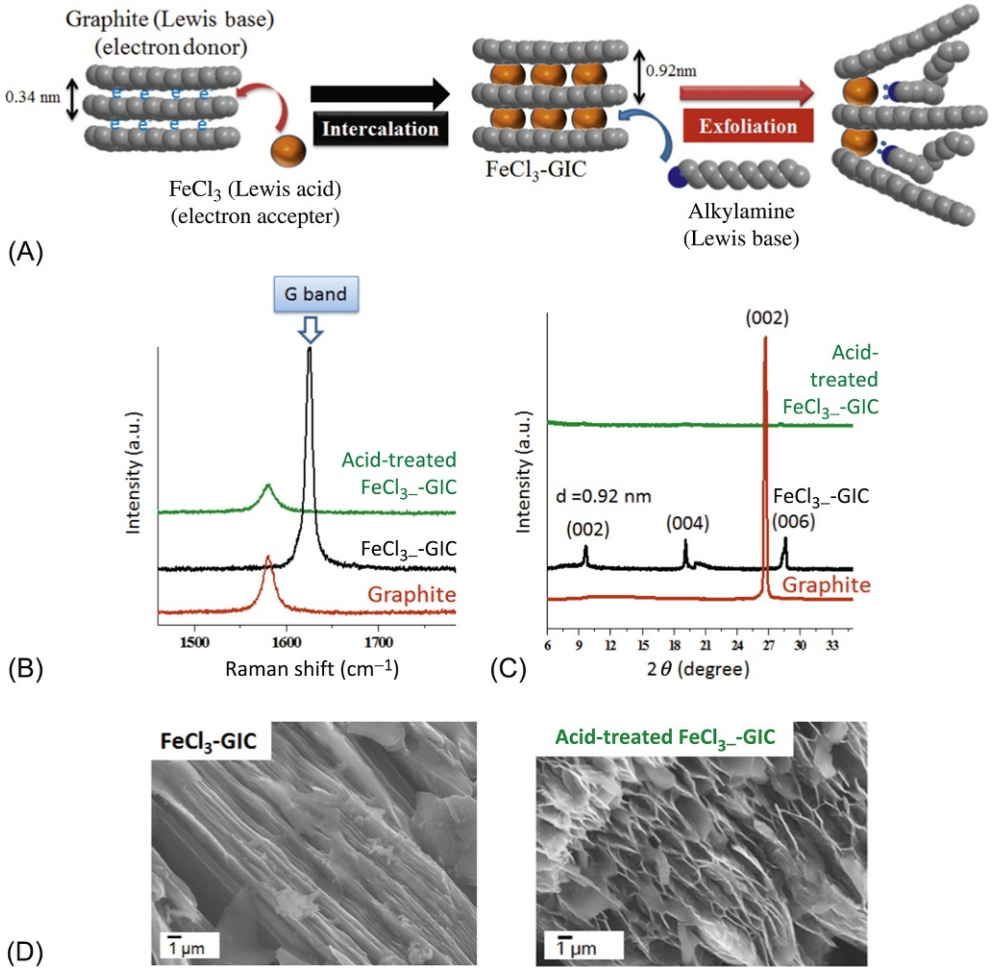

Fig. 10.2

(A) Schematic illustration for formation of $FeCl_3$-GIC and amine-treated $FeCl_3$-GIC, (B) Raman spectra, and (C) TGA of graphite, $FeCl_3$-GIC, and dodecylamine-treated $FeCl_3$-GIC, and (D) SEM images of $FeCl_3$-GIC and dodecylamine-treated $FeCl_3$-GIC [116]. *Reproduced with permission from M. Ujihara, M.M.M. Ahmed, T. Imae, Y. Yamauchi, Massive-exfoliation of magnetic graphene from acceptor-type GIC by long-chain alkyl amine, J. Mater. Chem. A 2(12) (2014) 4244–4250.*

primary amine has yielded an irreversible opening of the graphite layers (as shown in scanning electron microscope (SEM) images in Fig. 10.2D). Additionally, since the partially expanded graphite exhibits a strong magnetic property due to the remaining iron oxide onto the graphene sheets, the product is magnetic graphene composite (MGC).

The manipulation at higher temperatures helped to further expand the graphite layers of MGC, as clearly observed by an astonishing massive volume increase even at visual observation and on SEM images after heating at 900°C compared to 400°C (Fig. 10.3A) [129]. Similar

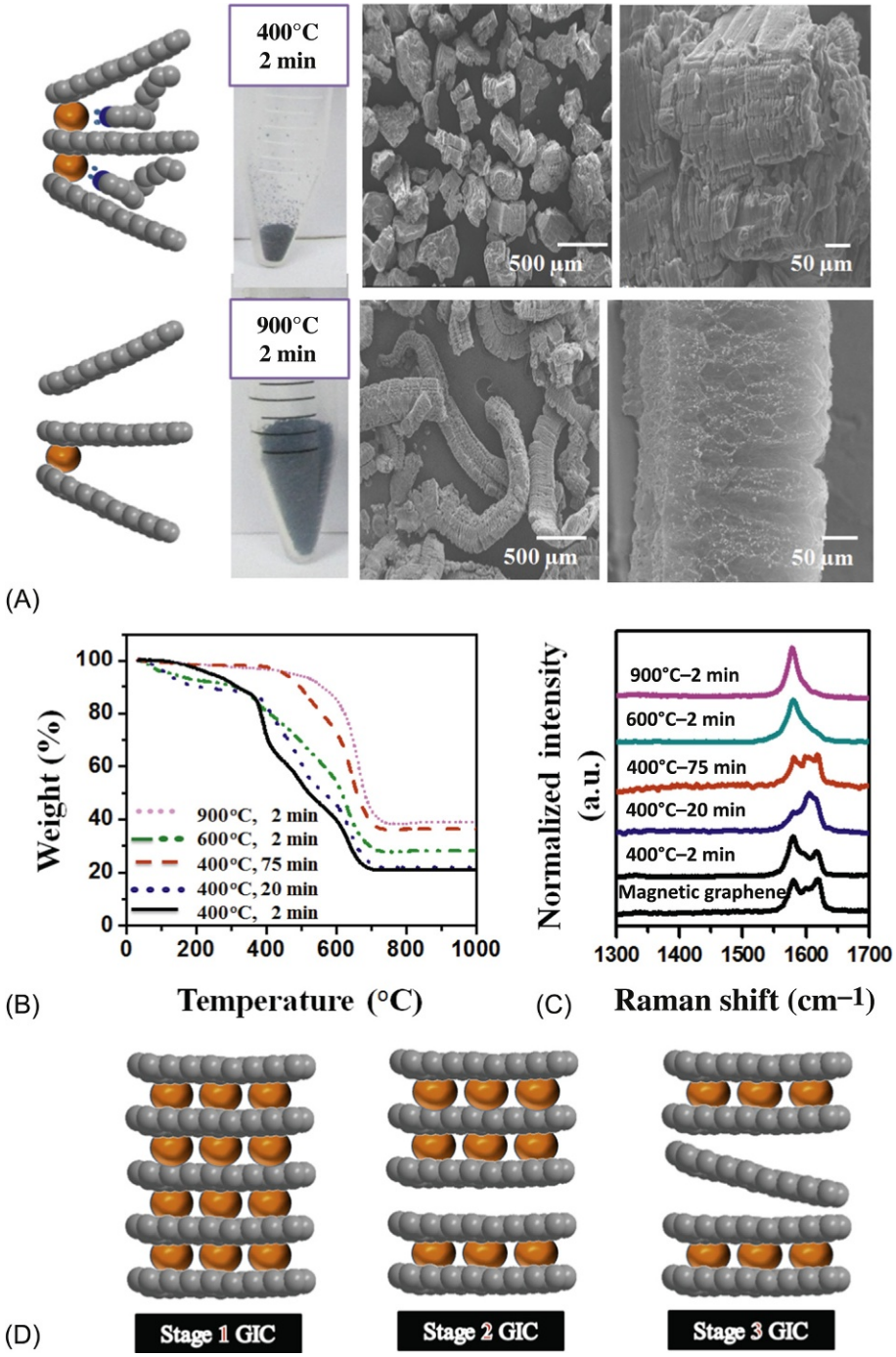

Fig. 10.3

(A) Photographs and SEM images (at low and high magnifications), (B) TGA and (C) Raman spectra of MGC and heat-treated MGC at different temperatures and time periods, and (D) classification of stage number (1–3) in GIC [148]. *Reproduced with permission from M.M.M. Ahmed, T. Imae, Electrochemical properties of a thermally expanded magnetic graphene composite with a conductive polymer, Phys. Chem. Chem. Phys. 18(15) (2016) 10400–10410.*

volume expansion phenomena were observed for different GICs with various intercalators, for example, paraffin [130], iron [131], polyethylene terephthalate [132], phase transition materials [133], mixture of potassium permanganate and perchloric acid [134], and mixture of acetic anhydride and other strong oxidizing agents [135–140]. The expansion of graphite as a result of aggressive heating is considered an imperative characteristic of thermal energy storage material [141]. Additionally, roll milling is efficient for expanding aluminum oxide-intercalated graphite [142]. A more sophisticated method is laser irradiation on sulfuric acid-intercalated graphite [143] and sodium-intercalated graphite [144]. Other GICs, including alumina and silica, also provide similar expanded morphology [145], while volume expansion of GIC via microwave reactions is becoming more popular [146,147].

The expansion of the layers may be caused by the complete decomposition/removal of the amine compound accompanied by the heating at 900°C, as seen in thermogravimetric analysis (TGA) results, although the incomplete decomposition of the amine compound was observed at lower temperatures like 400°C and 600°C (Fig. 10.3B) [148]. The heating procedure has an effect even on fullerene, which introduced a new family of carbon tubes when it was heated at 2000°C in vacuum condition [149]. Additionally, G bands of Raman spectra of MGC (Fig. 10.3C) showed clear splitting but not a single band ($\sim$1625 cm^{-1}) like $FeCl_3$-GIC (Fig. 10.2B). Any splitting (>2 bands between $\sim$1580 and $\sim$1625 cm^{-1}) of the G band indicates inhomogeneous amine-removal process with various stages. Although heat-treated MGC at 400°C showed similar splitting, the bands at higher Raman shift decreased on heat-treated MGC at 600°C and only a single band at $\sim$1580 cm^{-1} was observed in heat-treated MGC at 900°C. $FeCl_3$-GIC takes stage 1 and shows a $\sim$1625-cm^{-1} Raman band, higher stages occur at lower Raman shift, and then wholly expanded graphene takes a $\sim$1580-cm^{-1} band, as shown in Fig. 10.3D, denoting that the intercalators are being removed while the exfoliation process is acting.

10.2.2 Bottom-Up Methods

The bottom-up method of graphene preparation can be carried out by vapor deposition of precursors. One of the precursors is carbon materials, which have been deposited on a substrate of copper film [150]. Another is silicon carbide, which has been thermally decomposed [151,152]. The advantages of this bottom-up method are high purity and homogeneity of the products at large dimension. Meanwhile, this method still involves low yield and high equipment investment.

Another bottom-up method is performed by the pyrolysis of ethanol with sodium metal [153]. This procedure allows the formation of highly defected graphene. Despite the low quality of the obtained graphene with defects, this method is considered a facile one-step method for mass production of graphene. However, the graphene synthesis by this method still requires high vacuum, and it should be processed with caution because of the vigorous reaction of alkali metals.

10.3 Characterization of Graphene

Like other carbonaceous nanomaterials, graphene can be characterized via various techniques [154]. Microscopic techniques involve transmission electron microscopy and SEM. They can provide clear contrast images. The number of the layers can also be assumed via either technique of scanning tunneling microscope and AFM. On the other hand, Raman scattering spectroscopy can be valuable for studying the status of the carbon hybridization, defects, and number of graphite layers. Meanwhile, X-ray photoelectron spectroscopy can be efficiently used for studying the carbon structure. Additionally, Brunauer-Emmett-Teller (BET) adsorption analysis can evaluate the specific surface area of the carbon materials. TGA can also be used to assess the decomposition of graphene and its composites. In this section, the characterization of graphene is introduced through description of the different techniques.

10.3.1 Morphology of Graphene

Microcopy is considered one of the most important techniques that can be used to accurately visualize mono- and multilayered materials, for example, graphene, GO, rGO, their derivatives and composites. AFM plays a significant role in the characterization of graphene and its derivatives, especially in determining their accurate surface morphology, thickness, roughness, and anchoring properties. These properties are essential for characterization and interpretation of graphene properties and functionalities. During the past decades, in some attempts AFM has been used as a standard technique for analyzing graphene and its related materials [155]. Table 10.4 compares the thickness of graphite and related products with the techniques producing them.

Note that the use of various exfoliation techniques yields different thicknesses of the obtained graphene materials. For instance, GO has larger thickness (~2 nm) than other graphene products (~1 nm). This fact can be explained by the functional groups attached on its surface. The thickness of graphene decorated with metals and/or metal oxides, like gold or TiO_2, showed larger thickness due to the doping effect, which increases the average layer size due to the electron cloud. Similarly, boron- and nitrogen-doped and oxygen plasma graphene showed larger thickness (~4 nm). On the other hand, rGO and graphene from GIC showed less thickness (~1 nm). This height is considered the thinnest among other graphene products. Moreover, graphene produced from GIC also provided scalable and higher yield than other production methods. Due to these advantages, graphene production via GIC should be given more attention.

10.3.2 Electronic Structure of Graphene

Since graphene mainly consists of carbon atoms connected via sp^2 orbitals, the direct method of detecting the electronic structure of graphene is Raman spectroscopy based on the group theory. There are two remarkable characteristics of sp^2 hybridization: strong bonding to the

Table 10.4 Comparison of thickness of graphite and related products with production techniques

Technique	Product	Thickness (nm)	Reference/Year
Exfoliation of HOPG by AFM tip	Graphene	~200	[22]/1999
Mechanical exfoliation by Scotch tape	Graphene	~3	[1]/2004
Modified Hummers method: hydrazine reduction in different solvents	GO	>3	[156]/2008
Modified Hummers method: hydrazine reduction in water	rGO	1	[157]/2008
Hummers method	GO	1–1.4	[158]/2008
Staudenmaier procedure	Chemically converted graphene	1.8–2.2	[159]/2008
Staudenmaier procedure	Au-anchored graphene	~4	[160]/2008
Hummers method	TiO_2-GO composite	2	[161]/2008
Hummers method	Graphene	2–3	[162]/2008
Rapid heating of graphite	Graphene nanoribbon	1–1.8	[163]/2008
Acid treatment of graphite	Graphene	~1	[164]/2008
Oxygenation of exfoliated graphite oxide	Graphene	~1	[165]/2008
Oxygen plasma exposure in chemical vapor deposition	Graphene	5	[166]/2013
Exfoliation of $FeCl_3$-GIC	Magnetic graphene compound	1.5	[116]/2014
Acid treatment of commercial GO	GO	<5	[167]/2015
Chemical vapor deposition	Hexagonal boron nitride-graphene composite	~4	[168]/2015
Hydrothermal and freeze-drying method	MoO_3/graphene nanosheets	~2	[169]/2015

neighboring atoms and the electron cloud around *P*z axis. For graphene, the Raman spectrum consists of two main bands. The first important band is the G band, which appears around 1580 cm^{-1} [170]. The G band is the only band that does not depend on the excitation wavelength in graphene. Meanwhile, two other (D and G′) bands depend on the excitation wavelength due to the forbidden transition. The Raman shift of G band is considered the most important key factor for graphene analysis, because the G band results from a first-order Raman scattering with intraprocess for electron-phonon interaction [171]. Meanwhile, it only depends on the composition of the material with sp^2 orbital. It is also remarkable that any distortion of sp^2 orbital energy can directly shift the G band position. This shift is upwards or downwards

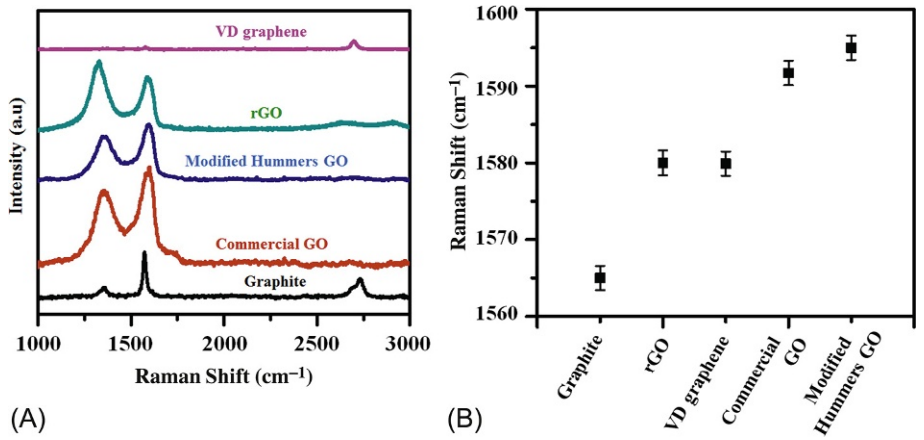

Fig. 10.4

(A) Raman spectra and (B) G band position of graphite, GO obtained from modified Hummers method (modified Hummers GO), commercial GO, rGO, and graphene synthesized from vapor deposition method (VD graphene) [172]. *Reproduced with permission from M.M.M. Ahmed, Preparation of graphene from graphite using physical and chemical methods (MS thesis), National Taiwan University of Science and Technology, 2013.*

(toward higher or lower wavenumber, respectively), depending on lowering or raising the Fermi energy level, respectively [171]. Fig. 10.4A shows the Raman spectra of graphite, GO (commercial and modified Hummers method products), rGO and graphene prepared by vapor deposition procedure, and the G band positions are plotted in Fig. 10.4B. The G band positions of rGO and graphene are higher than graphite but lower than both GOs. The change in Fermi energy level from graphite to graphene originates from the variation of π electron state, and the change from graphite/graphene to oxidized graphene is associated with the introduction of acceptor-type functions [170].

In addition, if the graphene has some defects in the structure, sp^3 carbon coexists, and then the spectrum has another band called a D band, which appears around 1350 cm^{-1} as a breathing mode of sp^2 orbitals due to the functionalization [173]. This band is a mode of a second-order Raman scattering with intraprocess of the electron-phonon interaction. The third important band is the G´ band, called 2D band because its position is almost double that of the D band. This band appearing at 2700 cm^{-1} arises as the second-order Raman scattering in interprocess of electron-phonon interaction [174].

In the case of graphite, the common precursor of the top-down method for graphene, the Raman spectrum consists of only two main bands (G and G′) with a lack of D band. Different origins of graphite provide different spectra. If the graphite has some sp^3 carbons, it has a small D band. Meanwhile, the oxidized graphite always has a strong D band due to the functionalization by different functional groups including carboxylic, hydroxyl, and epoxy groups. For the intercalation-exfoliation process utilizing $FeCl_3$ intercalator, no D band could be detected [116]. This means that there are no defects in the sp^2 orbital of this graphene.

The intercalation in graphite and the exfoliation of GIC can be significantly characterized by Raman spectrometry [175]. The intercalation is classified by the stage number, which is the number of graphite layers sandwiched between two layers of the intercalaters (see Fig. 10.3D) [176]. The intercalation induces a redshift of the G band due to the lower Fermi energy level and shifts the band gap due to the doping effect [177]. The intercalation step is followed by an explosive reaction to achieve the exfoliation step [178]. The lower the stage number, the more efficiently exfoliation can be performed. The exfoliation allows the GIC to be dissociated or cleaved to form the graphene sheets. Then this exfoliation process of GIC should not allow the layers to be restacked. After exfoliation, it blueshifts back to a position close to the graphite G band because of removal of dopant, increasing the Fermi energy level and shifting the band gap [110]. Moreover, the area ratio (I_D/I_G) between D band and G band indicates defects of the materials, since it shows the number ratio between the sp^2 to sp^3 carbons. Therefore, when GO possesses stronger D band than G band, it is considered a highly defective carbon material due to functional groups on it including carboxyl, hydroxyl, carbonyl, and others. However, after performing reduction reaction, D band area usually decreases compared to G band area, indicating the reduction of these functional groups. The I_D/I_G values of GO and rGO obtained from Fig. 10.4A are 1.3 and 0.3, respectively. This indicates the recovery of defects that resulted from the oxidation process.

The area ratio between G′ and G bands ($I_{G'}/I_G$) indicates the number of graphene layers. When this ratio is approximately 0.3, the graphene is a monolayer, and if this ratio increases, the number of the layers increases [179,180], and the shape and symmetry of the G′ band reflect the layer numbers and the electron-phonon interaction. However, the ($I_{G'}/I_G$) ratio would be a better parameter. Thus area ratios ((I_D/I_G) and ($I_{G'}/I_G$)), band shifts and band shapes are essential information for electronic characterizations of graphene structure like defects, quality, hybridization, doping, Fermi level, and layer number. Therefore they can be considered strong characterization indicators that express the quality of graphene and related compounds.

10.3.3 Surface Property of Graphene

One of the most important surface properties of graphene is its surface area. The surface area of graphene plays a vital role in the various applications in electrochemistry [181], adsorption [182], water purification [183], catalysis, sensing, and others [184,185]. The high surface area of the graphene electrodes could open new pathways for electron accessibility. Graphene exhibits a very high, theoretical, specific surface area reaching 2630 $m^2\ g^{-1}$ [186]. This value is much higher than that of other carbon materials, for example, carbon nanotubes, activated carbon, and carbon black [187]. This ultrahigh specific surface area made graphene one of the hottest materials in various fields, especially in electrochemistry [188].

Table 10.5 compares specific surface areas of various carbon materials. Well-exfoliated graphene exhibits a high surface area that is close to theoretical one. However, if the exfoliation

Table 10.5 Specific surface area and capacitance of various carbon materials

Material	Specific Surface Area ($m^2 g^{-1}$)	Capacitance (Fg^{-1})	Condition	References
N-doped mesoporous carbon	3300	160	1 Ag^{-1}	[189]
KOH-activated GO	3269	326	1 Ag^{-1}	[190]
Activated carbon	2681	172	5 mVs^{-1}	[191]
Graphene aerogel	2211	410	0.1 Ag^{-1}	[192]
N-doped hierarchical porous carbon	2196	192	10 Ag^{-1}	[193]
N-doped carbon	2150	198	1 Ag^{-1}	[194]
GO porous carbon hybrid	2143	270	1 Ag^{-1}	[195]
Graphene/activated carbon	2106	210	1 mVs^{-1}	[196]
Porous carbon	1810	305	0.5 Ag^{-1}	[197]
N-rich graphene composite	1646	300	0.1 Ag^{-1}	[198]
Supershort carbon nanotube/rGO	370	244	50 mVs^{-1}	[199]
Graphene/ polyaniline	268	257	0.1 Ag^{-1}	[200]
Mesoporous carbon	81.7	341	1 mVs^{-1}	[201]

procedure is not performed properly, the obtained surface area will be less. Therefore, the surface area of graphene was boosted by N-doping [189] or potassium hydroxide (KOH) activation [190]. Graphene and related compounds/composites could be highly favored for many fields, especially in electrochemical performance and electronic applications. Table 10.5 also includes the capacitance values from different carbon materials, but it was not easy to obtain the relation between surface area and capacitance because reports differ on the conditions of capacitance measurements.

10.4 Graphene-Based Supercapacitor

10.4.1 Basics of Electric Double Layer

Supercapacitors are among the top priorities for energy storage devices due to their high-power density. When graphene is applied for supercapacitor, an efficient electrochemical supercapacitor is behaved. Its concept is based on the electric double layer existing at the boundary between a conductor and its contacting electrolyte solution. The earliest electric double layer theory was proposed by Helmholtz and further supplemented and developed by

Gouy, Chapman, Grahame, and Stern. It regulates the electrochemical processes occurring at the electrostatic interface between a charged electrode material and an electrolyte. Many electrochemical theories and technologies have been presented since the double layer theory was established, including electrochemical supercapacitors, batteries, and fuel cells. The rapid growth of mobile electronics and alternative energy vehicles created a need for advanced electrochemical energy storage devices with high power capabilities. This demand led to substantial research and development of supercapacitors. In the early 1990s, the US Department of Energy strongly advocated funding for battery and supercapacitor research, creating an international awareness of the potential of supercapacitors. Since then, great effort has focused on supercapacitor research and its development in terms of electrode materials, composites, hybridizations, and suitable electrolytes to improve performance and to reduce expenses. At the same time, the fundamental understanding, design, operation, and component optimization of supercapacitors has led to improvements in performance, particularly by increasing the energy density. To further increase energy density, more advanced supercapacitors called pseudocapacitors, in which the electroactive materials are merged with carbon particles to form composite electrode materials, were developed. The electrochemical reaction of the electroactive material in a pseudocapacitor takes place at the interface between the electrode and electrolyte via adsorption, intercalation, or reduction-oxidation (redox) mechanism. In this way, the capacitance and the energy density are increased significantly [202].

10.4.2 Electric Double Layer at Interface of Electrode and Electrolyte Solution

The electric double layer is a very important concept for understanding the supercapacitor performance of various carbon materials. The electric double-layer models representing the relation between the electrode material and the electrolyte started with aqueous solutions. The laws were broadened to engage ionic liquids and other electrolytes as well. In the electric double layer, the positive (or negative) charge buildup at the interface of the electrode and electrolyte solution is partially neutralized by the gathering of counterions in the solution through the action of Coulomb's force, resulting in a structured electric double layer. The electric double layer consists of two layers. The first, called the Stern layer, results from accumulating the counterions on electrode surface. Then the diffusion layer extends outward from the Stern surface; this second layer is called the Gouy-Chapman layer. The thickness of the double layer reflects the electric double layer capacitor (EDLC). The deeper the electric double layer, the higher capacitance behavior is observed.

Supercapacitors can be systematized into two major sorts of EDLCs and pseudocapacitors depending on the charge storage mechanism. EDLC materials stock up charge mainly in an electrochemical double layer formed on the surface of the electrode but not in its bulk. Therefore the capacitance mainly depends on the surface area of electrode, which can be

accessed by the electrolyte ions. The important factors controlling the electrochemical activity of electrodes are the specific surface area, pore size distribution, pore shape, morphology, conductivity, and surface functionality. Among these, the pore size of electrode materials should be very close to the ion size of the electrolyte to yield maximum double layer capacitance. Meanwhile, if the sizes do not match, it leads to capacitance drop [203].

On the other hand, pseudocapacitors store charges mainly via fast and reversible faradic reactions occurring on metal oxides or conducting polymers. Normally, pseudocapacitors can generate the capacitance value of one order higher magnitude than EDLCs. However, limited cyclability always exists because of the nature of redox reactions. Therefore hybrid systems offer an alternative to conventional pseudocapacitors or EDLCs. In this case, materials for pseudocapacitors (batterylike, energy source) and EDLCs (capacitorlike, power source) are hybridized on one electrode substrate. By designing electrolytes with the most advantageous performance and by using such hybrid capacitance composition, the enormous demand for high-voltage operation with high stability and long-term cyclability can be accomplished [204]. Three types of materials for capacitors [205] are discussed thoroughly in the following sections.

10.4.3 Materials for Supercapacitors

10.4.3.1 Materials for EDLCs

It has been established that the high energy and power density of EDLC materials can contribute to high surface area, high conductivity, accessibility, and morphology, which are key factors for accomplishing high capacitance through charging of the double layers [206,207]. Carbon materials exhibit many required properties, including electrochemical stability, conductivity, and porosity [208], and thus different carbon materials have been investigated as EDLC materials. Materials include activated carbons, carbon aerogels, porous carbons, carbide-derived carbons [209], carbon nanotubes, graphenes [210], templated carbons [211], onionlike carbons [212,213], carbon nanofibers [214], carbon microcoils [215,216], and carbon nanohorns [217].

Among these, activated carbons are one of the commonly used materials in the market. They have many advantages like being inexpensive, easy processing, easy manufacturing, high surface area, and high chemical stability. Activated carbons are prepared via controlled oxidation of various bulk carbon materials derived from many organic materials such as woods, coals, nutshells, etc. [218]. Depending on the activation process and the carbon precursor [219], activated carbons with high surface areas can be manufactured. These activated carbons have broad pore size distribution consisting of micropores (<2 nm), mesopores (2–50 nm), and macropores (>50 nm), which result in the high specific surface area of activated carbons [220]. However, if the pores are not accessible to the electrolyte, then the specific capacitance does not linearly increase with increasing the specific surface area of the electrode [207]. For instance, KOH activation of high surface area carbon (1180 $m^2\ g^{-1}$) yielded a capacitance of only

160 Fg^{-1}. In addition, the oxygen-containing functional groups on the surface of activated carbons resulting from the activation procedure decrease conductivity. Therefore different activation procedures have been investigated especially via electrochemical [221–223] and thermal [224] methods. So the activation process and the precursor are essential factors for achieving higher capacitance values.

Onionlike carbons are zero-dimensional graphitic spheres with concentric layers of a few nanometers in diameter [225]. They are usually produced by annealing of diamond powders in vacuum at 1800°C. The produced onionlike carbons exhibit a surface area of 500–600 $m^2\ g^{-1}$. This high surface area and high electrical conductivity result in high power EDLC [213,218,225,226], although the capacitance was limited to 30 Fg^{-1}. Carbon aerogels are composed of relatively high surface area carbon material ranging from 400 to 1000 $m^2\ g^{-1}$ and specific capacitance of 20 to 100 Fg^{-1} [227]. Therefore they are used as an efficient electrode material in EDLC. Porous carbons are produced from a wide variety of resources including glucose [228], hexylamine [229], cellulose [230,231], silica nanospheres [232], coffee [233], and lignin [234] to optimize the produced energy density [235–237]. They exhibit porous structure and large surface area [238,239]. The unique three-dimensional morphology was controlled to allow better accessibility to electrolytes [240–243].

Special attention is given to flexible devices [244–246]. Carbide-derived carbon [209] is a type of carbon material that can be prepared by passing chlorine gas on metals to etch them at elevated temperatures [247]. This process allows the synthesis of microporous carbons with surface area of 1000–3000 $m^2\ g^{-1}$ and narrow pore size distributions [248]. When selective choosing of a particular metal and a carbonization temperature can effectively organize the pore size within 0.6 to 1.1 nm, the capacitance can reach up to 180 Fcm^{-3}; however, this value drastically decreases as the film depth is enlarged. Carbon nanotubes have been investigated for EDLC applications [249]. Their high electrical conductivity and accessibility of electrolytes are key points in their electronic applications [250]. Their energy densities are quite large compared to ACs, although their specific surface area is not so large (generally $<500\ m^2\ g^{-1}$) [220]. Recently, carbon dot and other carbon materials including carbon nanohorns have also been investigated in the supercapacitor field [251].

Graphene is considered one of the most efficient carbon materials and has widely been investigated as an EDLC material [252–254]. Graphene can be produced using a variety of techniques, including laser scribing [255–257], reduction of GO [258], surfactant intercalation, microemulsion [259], iron oxide reduction [260], and other methods [116]. Among these techniques, the laser scribing method and flash converted method for reducing GO to rGO are efficient and facile for production [255,261] and the resultant rGO showed better energy performance, namely, ultrahigh power supercapacitance, than rGO prepared by inkjet printing and thermal reduction reaction [262,263]. Moreover, the laser scribing technique was efficiently utilized in flexible wearable devices [264,265]. Therefore improving graphene synthesis procedure would be a key point for producing highly capacitive material [265].

In addition, graphene provided great stability and excellent performance for efficient EDLC [266].

The surface area of graphene is also considered one of the most important features for EDLC, especially a high surface area of graphene; for example, 1000 $m^2\ g^{-1}$ produced a high specific energy density value of 65 $WhKg^{-1}$ [267]. Similarly, KOH-activated graphene yielded a surface area of 3100 $m^2\ g^{-1}$, which led to a breakthrough in the graphene supercapacitor field [268]. Therefore preparing high-quality and high surface area graphene is considered the most important factor for establishing an efficient EDLC. The performance of graphene has also been investigated in various electrolytes such as aqueous [269], organic [270], and ionic liquid [271]. It is important to note that the use of ionic liquid and organic electrolytes enables a wide potential window, which enhances the produced energy density. In addition, graphene was coupled with carbon nanotubes [272] to boost the energy density along with the enhancing of the EDLC effect. Although various methods have been investigated for producing high energy density graphene, the obtained density is not sufficient for powerful applications. Therefore, in order to enhance the produced energy value, other materials need to be investigated.

10.4.3.2 Materials for pseudocapacitors

While EDLC materials cannot sufficiently stock up energy density, pseudocapacitor materials increase the energy density and allow the storage of energy density in the bulk of electrode materials as well as at their surface. Being electrically conductive or having two oxidation states in a specific potential window is the most vital characteristic of pseudocapacitor materials. Conducting polymers and metal oxides are the main materials applied for pseudocapacitors. Conducting polymers such as polythiophene [273], polypyrrole [274], polyaniline [275], and their derivatives can store charges along the reactive groups in the polymer backbones. Thus various conducting polymers have been investigated in various aqueous and organic electrolytes [208,220,276–278].

On the other hand, transition metal oxide materials can change redox states. Therefore metal oxides are also considered to be an alternative practical material in pseudocapacitors. Ruthenium oxide is one of the most commonly used materials for pseudocapacitors due to its capacitance characteristics. The strong capability of ruthenium oxide results from its fast and reversible electron-transfer reactions coupled with the adsorption of protons near its surface. Controlled redox conditions and factors can accomplish a capacitance of 720 Fg^{-1} [279]. However, ruthenium is a rare metal and extremely expensive, indicating the limit of its supply and applications [280]. Therefore other metal oxides such as manganese [281], nickel [282], cobalt [283], gold [284], aluminum [285], and iron [286] oxides have also been investigated in aqueous electrolytes. Special attention is given to manganese oxide [287,288] due to its promising and theoretically higher capacitance value. However, none of these materials has been utilized in commercial applications yet.

10.4.3.3 Materials for hybrid supercapacitors

Hybrid supercapacitors are considered the most sophisticated type of supercapacitors, because they combine the advantages of EDLC and pseudocapacitors. The fascinating electrical properties of graphene make it attractive for various hybrid materials. Graphene works as a smooth pathway for electron transport. Moreover, the hybridization with pseudocapacitor materials can efficiently contribute to the capacitance value as well as the energy density. The energy density of the devices fabricated with graphene composites can achieve more efficient storage and better cyclability than conventional batteries. This enhancement is a major breakthrough compared to standard EDLC. In addition to the excellent stability and long life cycles of graphene, the hybridization can show an enhancement of energy density: On the hybridization with EDLC materials to improve their energy density, metal oxides including ruthenium oxide [289–291], cobalt oxide [292], iron oxide [293], manganese oxide [294], and vanadium oxide [295] as well as mixed oxides [296–299] are most frequently used as pseudocapacitor materials.

Hybrid supercapacitors with conducting polymers with different morphologies and structures are also widely explored to optimize their resulting energy density [300]. Oxidation polymerization techniques are the top selected methods for polymerization [301]. Other procedures for polymerization have also been studied electrochemically [302] or through vapor deposition [303]. Polyaniline is one of the best candidates for hybridization with graphene [304,305]. Other conducting polymers like poly(3,4-ethylenedioxythiophene) have also been studied for supercapacitor performance with graphene [306]. Although composites with conductive polymers can help to produce higher energy density values than graphene, cracks and decomposition of the electrodes occur. Therefore another hybridization scheme was investigated; that is, graphene was doped by electron donor or acceptor such as boron and nitrogen [304]. These doping effects enabled a synergistic effect with graphene energy performance. Various metals and conducting polymers have been hybridized with graphene to facilitate electron transport and enhance the obtained energy density. The National Aeronautics and Space Administration (NASA) has cleared a sustainable supercapacitor device using cobalt and magnesium oxides covered by graphene with high surface area, being effectively used in various energy recourses [307]. This invention will boost both energy density and power density compared to batteries. This hybrid can also be used for various applications such as space missions and chargeable cars.

10.5 Conclusions and Future Directions

Graphene possesses the unique monolayer structure of two-dimensional carbon sheet and thus attracts a lot of attention due to its excellent properties. However, in its applications, mass production and high purity are demanded. Therefore scientists have exerted their efforts for the high-scale production of graphene with high quality. In the first part of this chapter, the

preparation procedures of graphene were explained in detail by comparison with each other, although it will be difficult to select better procedures because of their various merits and demerits. Moreover, produced materials depend on their applications.

On the characterization of graphene, morphology observed by microscopy was introduced. The thickness of as-produced graphene determined by AFM was mostly a few layers of graphene, but GO displayed thicker value because of the existence of oxidized functional groups. The electronic structure of graphene is best examined with Raman spectroscopy. The characteristic three bands (G, D, and G′ bands) and their area ratios are indicative of layer numbers, defects, and hybridization besides electronic states. The surface area of graphene and its derivatives or composites may predict the electrochemical performance.

Graphene and related compounds can provide various applications. They are among the most adequate components of EDLC consisting of carbon materials. After the explanation of the principle of EDLC, the efficiency of graphene-based electrodes on EDLC supercapacitors was compared with other electrodes on pseudocapacitors and hybrid capacitors. On the development of effective supercapacitors, it becomes apparent that the hybridization of graphene-based materials with pseudocapacitive materials is dispensable. Thus composites with graphene-based materials are expected to develop extraordinary energy and power sources with durable performance.

References

[1] K.S. Novoselov, A.K. Geim, S.V. Morozov, D. Jiang, Y. Zhang, S.V. Dubonos, et al., Electric field effect in atomically thin carbon films, Science 306 (5696) (2004) 666–669.

[2] K.S. Novoselov, Graphene: materials in the Flatland, Microwave Conference (EuMC), 2011 41st European: IEEE, 2011, pp. 1–348.

[3] A.K. Geim, K.S. Novoselov, The rise of graphene, Nat. Mater. 6 (3) (2007) 183–191.

[4] R.M. Westervelt, Applied physics. Graphene nanoelectronics, Science 320 (5874) (2008) 324–325.

[5] B. Balandin, A. Alexander, S. Ghosh, W. Bao, I. Calizo, D. Teweldebrhan, F. Miao, et al., Superior thermal conductivity of single-layer graphene, Nano Lett. 8 (3) (2008) 902–907.

[6] C. Faugeras, B. Faugeras, M. Orlita, M. Potemski, R.R. Nair, A.K. Geim, Thermal conductivity of graphene in Corbino membrane geometry, ACS Nano 4 (4) (2010) 1889–1892.

[7] A.A. Balandin, Thermal properties of graphene and nanostructured carbon materials, Nat. Mater. 10 (8) (2011) 569–581.

[8] C. Lee, X. Wei, J.W. Kysar, J. Hone, Measurement of the elastic properties and intrinsic strength of monolayer graphene, Science 321 (5887) (2008) 385–388.

[9] K.S. Novoselov, V.I. Fal'ko, L. Colombo, P.R. Gellert, M.G. Schwab, K. Kim, A roadmap for graphene, Nature 490 (7419) (2012) 192–200.

[10] O. Yaw, P. Srinivasan, Graphene: is it the future for semiconductors? An overview of the material, devices, and applications, Electrochem. Soc. Interface 20 (1) (2011) 47–52.

[11] J. Luo, H.D. Jang, J. Huang, Effect of sheet morphology on the scalability of graphene-based ultracapacitors, ACS Nano 7 (2) (2013) 1464–1471.

[12] L. Peng, X. Peng, B. Liu, C. Wu, Y. Xie, G. Yu, Ultrathin two-dimensional MnO_2/graphene hybrid nanostructures for high-performance, flexible planar supercapacitors, Nano Lett. 13 (5) (2013) 2151–2157.

[13] M. Zhou, Y.-H. Lu, Y.Q. Cai, C. Zhang, Y.P. Feng, Adsorption of gas molecules on transition metal embedded graphene: a search for high-performance graphene-based catalysts and gas sensors. Nanotechnology 22 (38) (2011) 385502. http://dx.doi.org/10.1088/0957-4484/22/38/385502.

[14] L.-M. Lu, H.-B. Li, F. Qu, X.B. Zhang, G.-L. Shen, R.-Q. Yu, In situ synthesis of palladium nanoparticle-graphene nanohybrids and their application in nonenzymatic glucose biosensors, Biosens. Bioelectron. 26 (8) (2011) 3500–3504.
[15] Y. Lu, B.R. Goldsmith, N.J. Kybert, A.T.C. Johnson, DNA-decorated graphene chemical sensors, Appl. Phys. Lett. 97 (8) (2010) 083107.
[16] Y. Bo, W.Q. Wang, J.F. Qi, S.S. Huang, A DNA biosensor based on graphene paste electrode modified with Prussian blue and chitosan, Analyst 136 (9) (2011) 1946–1951.
[17] B.J. Kim, G. Yang, M.J. Park, J.S. Kwak, K.H. Baik, D. Kim, et al., Three-dimensional graphene foam-based transparent conductive electrodes in GaN-based blue light-emitting diodes, Appl. Phys. Lett. 102 (16) (2013) 083107.
[18] H. Ming, X. Li, Y. Wei, L. Bu, Z. Kang, J.W. Zheng, Facile synthesis of ionic-liquid functionalized graphite oxide nanosheets for a highly efficient fuel cell, RSC Adv. 3 (11) (2013) 3655–3660.
[19] J.T. Robinson, S.M. Tabakman, Y.Y. Liang, H.L. Wang, H.S. Casalongue, D. Vinh, et al., Ultrasmall reduced graphene oxide with high near-infrared absorbance for photothermal therapy, J. Am. Chem. Soc. 133 (17) (2011) 6825–6831.
[20] R.Y.N. Gengler, K. Spyrou, P. Rudolf, A roadmap to high quality chemically prepared graphene, J. Phys. D. Appl. Phys. 43 (37) (2010) 374015.
[21] S. Park, R.S. Ruoff, Chemical methods for the production of graphenes, Nat. Nanotechnol. 4 (4) (2009) 217–224.
[22] X. Lu, M. Yu, H. Huang, R.S. Ruoff, Tailoring graphite with the goal of achieving single sheets, Nanotechnology 10 (3) (1999) 269–272.
[23] X. Li, H. Zhu, Two-dimensional MoS_2: properties, preparation, and applications, J. Materiomics 1 (1) (2015) 33–44.
[24] A. Pénicaud, C. Drummond, Deconstructing graphite: graphenide solutions, Acc. Chem. Res. 46 (1) (2013) 129–137.
[25] J.Y. Lee, I. In, Enhanced solvent exfoliation of graphite to graphene dispersion in the presence of polymer additive, Chem. Lett. 40 (6) (2011) 567–569.
[26] J. Dong, B. Zeng, Y. Lan, S. Tian, Y. Shan, X. Liu, Z. Yang, H. Wang, Z.F. Ren, Field emission from few-layer graphene nanosheets produced by liquid phase exfoliation of graphite, J. Nanosci. Nanotechnol. 10 (8) (2010) 5051–5055.
[27] Y. Hernandez, V. Nicolosi, M. Lotya, F.M. Blighe, Z.Y. Sun, S. De, et al., High-yield production of graphene by liquid-phase exfoliation of graphite, Nat. Nanotechnol. 3 (9) (2008) 563–568.
[28] J.N. Coleman, Liquid exfoliation of defect-free graphene, Acc. Chem. Res. 46 (1) (2013) 14–22.
[29] M. Yi, Z.G. Shen, S.L. Ma, X.J. Zhang, A mixed-solvent strategy for facile and green preparation of graphene by liquid-phase exfoliation of graphite. J. Nanopart. Res. 14 (8) (2012), http://dx.doi.org/10.1007/s11051-012-1003-5.
[30] X. Wang, P.F. Fulvio, G.A. Baker, G.M. Veith, R.R. Unocic, S.M. Mahurin, et al., Direct exfoliation of natural graphite into micrometre size few layers graphene sheets using ionic liquids, Chem. Comm. 46 (25) (2010) 4487–4489.
[31] S. Ravula, S.N. Baker, G. Kamath, G.A. Baker, Ionic liquid-assisted exfoliation and dispersion: stripping graphene and its two-dimensional layered inorganic counterparts of their inhibitions, Nanoscale 7 (10) (2015) 4338–4353.
[32] S.M. Notley, Highly concentrated aqueous suspensions of graphene through ultrasonic exfoliation with continuous surfactant addition, Langmuir 28 (40) (2012) 14110–14113.
[33] M. Lotya, Y. Hernandez, P.J. King, R.J. Smith, V. Nicolosi, L.S. Karlsson, et al., Liquid phase production of graphene by exfoliation of graphite in surfactant/water solutions, J. Am. Chem. Soc. 131 (10) (2009) 3611–3620.
[34] Z. Tang, J. Zhuang, X. Wang, Exfoliation of graphene from graphite and their self-assembly at the oil – water interface, Langmuir 26 (11) (2010) 9045–9049.
[35] U. Khan, A. O'Neill, M. Lotya, S. De, J.N. Coleman, High-concentration solvent exfoliation of graphene, Small 6 (7) (2010) 864–871.
[36] J.N. Coleman, Liquid exfoliation of defect-free graphene, Acc. Chem. Res. 46 (1) (2013) 14–22.

[37] C.M. Hansen, Solubility parameters—an introduction, in: Hansen Solubility Parameters, CRC Press, Boca Raton, FL, 2007, , pp. 1–26. http://dx.doi.org/10.1201/9781420006834.ch1.
[38] C.M. Hansen, Theory_the Prigogine corresponding states theory, the X_{12} interaction parameter and the Hansen solubility parameters, in: Hansen Solubility Parameters, CRC Press, Boca Raton, FL, 2007, pp. 27–43. http://dx.doi.org/10.1201/9781420006834.ch2.
[39] K.F. Kelly, W.E. Billups, Synthesis of soluble graphite and graphene, Acc. Chem. Res. 46 (1) (2013) 4–13.
[40] Y. Hernandez, M. Lotya, D. Rickard, S.D. Bergin, J.N. Coleman, Measurement of multicomponent solubility parameters for graphene facilitates solvent discovery, Langmuir 26 (5) (2010) 3208–3213.
[41] H. Dominguez, Structure of the SDS/1-dodecanol surfactant mixture on a graphite surface: a computer simulation study, J Colloid Interf. Sci. 345 (2) (2010) 293–301.
[42] M. Lotya, P.J. King, U. Khan, S. De, J.N. Coleman, High-concentration, surfactant-stabilized graphene dispersions, ACS Nano 4 (6) (2010) 3155–3162.
[43] S. Lin, Carbon nanotubes and graphene in aqueous surfactant solutions: molecular simulations and theoretical modeling (PhD), Massachusetts Institute of Technology, 2012.
[44] M.Z. Cai, D. Thorpe, D.H. Adamson, H.C. Schniepp, Methods of graphite exfoliation, J. Mater. Chem. 22 (48) (2012) 24992–25002.
[45] S. Vadukumpully, J. Paul, S. Valiyaveettil, Cationic surfactant mediated exfoliation of graphite into graphene flakes, Carbon 47 (14) (2009) 3288–3294.
[46] M.D. Doganci, B.U. Sesli, H.Y. Erbil, B.P. Binks, I.E. Salama, Liquid marbles stabilized by graphite particles from aqueous surfactant solutions, Colloid Surf. A: Physicochem. Eng. Asp. 384 (1–3) (2011) 417–426.
[47] Y. Sim, J. Park, Y.J. Kim, M.J. Seong, S. Hong, Synthesis of graphene layers using graphite dispersion in aqueous surfactant solutions, J. Korean Phys Soc. 58 (4) (2011) 938–942.
[48] M.S. Kang, K.T. Kim, J.U. Lee, W.H. Jo, Direct exfoliation of graphite using a non-ionic polymer surfactant for fabrication of transparent and conductive graphene films, J. Mater. Chem C 1 (9) (2013) 1870–1875.
[49] R. Atkin, G.G. Warr, Self-assembly of a nonionic surfactant at the graphite/ionic liquid interface, J. Am. Chem. Soc. 127 (34) (2005) 11940–11941.
[50] L. Guardia, M.J. Fernández-Merino, J.I. Paredes, P. Solís-Fernández, S. Villar-Rodil, A. Martínez-Alonso, et al., High-throughput production of pristine graphene in an aqueous dispersion assisted by non-ionic surfactants, Carbon 49 (5) (2011) 1653–1662.
[51] B.C. Brodie, On the atomic weight of graphite, Philos. Trans. R. Soc. Lond. 149 (1859) 249–259.
[52] L. Staudenmaier, Verfahren zur Darstellung der Graphitsäure, Ber. Dtsch. Chem. Ges. 31 (2) (1898) 1481–1487.
[53] W.S. Hummers, R.E. Offeman, Preparation of graphitic oxide, J. Am. Chem. Soc. 80 (6) (1958) 1339.
[54] N.I. Kovtyukhova, P.J. Ollivier, B.R. Martin, T.E. Mallouk, S.A. Chizhik, E.V. Buzaneva, et al., Layer-by-layer assembly of ultrathin composite films from micron-sized graphite oxide sheets and polycations, Chem. Mater. 11 (3) (1999) 771–778.
[55] D.C. Marcano, D.V. Kosynkin, J.M. Berlin, A. Sinitskii, Z. Sun, A. Slesarev, et al., Improved synthesis of graphene oxide, ACS Nano 4 (8) (2010) 4806–4814.
[56] H. Yu, B. Zhang, C. Bulin, R. Li, R. Xing, High-efficient synthesis of graphene oxide based on improved Hummers method. Sci. Rep. 6 (2016), http://dx.doi.org/10.1038/srep36143.
[57] S. Lin, L. Dong, J. Zhang, H. Lu, Room-temperature intercalation and ~1000 fold chemical expansion for scalable preparation of high-quality graphene, Chem. Mater. 28 (7) (2016) 2138–2146.
[58] L. Dong, Z. Chen, S. Lin, K. Wang, C. Ma, H. Lu, Reactivity-controlled preparation of ultralarge graphene oxide by chemical expansion of graphite, Chem. Mater. 29 (2) (2017) 564–572.
[59] K.N. Kudin, B. Ozbas, H.C. Schniepp, R.K. Prud'homme, I.A. Aksay, R. Car, Raman spectra of graphite oxide and functionalized graphene sheets, Nano Lett. 8 (1) (2008) 36–41.
[60] K. Feng, B. Tang, P. Wu, "Evaporating" graphene oxide sheets (GOSs) for rolled up GOSs and its applications in proton exchange membrane fuel cell, ACS Appl. Mater. Interf. 5 (4) (2013) 1481–1488.
[61] S. Mayavan, J.B. Sim, S.M. Choi, Simultaneous reduction, exfoliation and functionalization of graphite oxide into a graphene-platinum nanoparticle hybrid for methanol oxidation, J. Mater. Chem. 22 (14) (2012) 6953–6958.

[62] H.-H. Chang, C.-K. Chang, Y.-C. Tsai, C.-S. Liao, Electrochemically synthesized graphene/polypyrrole composites and their use in supercapacitor, Carbon 50 (6) (2012) 2331–2336.
[63] N. Yousefi, X. Lin, Q. Zheng, X. Shen, J.R. Pothnis, J. Jia, et al., Simultaneous in situ reduction, self-alignment and covalent bonding in graphene oxide/epoxy composites, Carbon 59 (2013) 406–417.
[64] A. Satti, P. Larpent, Y. Gun'ko, Improvement of mechanical properties of graphene oxide/poly(allylamine) composites by chemical crosslinking, Carbon 48 (12) (2010) 3376–3381.
[65] S. You, J. Yu, B. Sundqvist, L.A. Belyaeva, N.V. Avramenko, M.V. Korobov, et al., Selective intercalation of graphite oxide by methanol in water/methanol mixtures, J. Phys. Chem. C 117 (4) (2013) 1963–1968.
[66] X. Dong, W. Huang, P. Chen, In situ synthesis of reduced graphene oxide and gold nanocomposites for nanoelectronics and biosensing. Nanoscale Res. Lett. 6 (60) (2011), http://dx.doi.org/10.1007/s11671-010-9806-8.
[67] L. Lai, L. Chen, D. Zhan, L. Sun, J. Liu, S.H. Lim, et al., One-step synthesis of NH_2-graphene from in situ graphene-oxide reduction and its improved electrochemical properties, Carbon 49 (10) (2011) 3250–3257.
[68] T. Remyamol, H. John, P. Gopinath, Synthesis and nonlinear optical properties of reduced graphene oxide covalently functionalized with polyaniline, Carbon 59 (2013) 308–314.
[69] G. Ning, T. Li, J. Yan, C. Xu, T. Wei, Z. Fan, Three-dimensional hybrid materials of fish scale-like polyaniline nanosheet arrays on graphene oxide and carbon nanotube for high-performance ultracapacitors, Carbon 54 (2013) 241–248.
[70] Y. Hu, R.-F. Ding, J.-Y. Xu, Q.-A. Wang, Z.-Y. Chen, W.-C. Fan, Synthesis and characterization of poly acrylic acid/graphite oxide nanocomposite, Trans. Nonferrous Met. Soc. China 13 (2) (2003) 285–288.
[71] F.T. Cerezo, C.M.L. Preston, R.A. Shanks, Structural, mechanical and dielectric properties of poly(ethylene-co-methyl acrylate-co-acrylic acid) graphite oxide nanocomposites, Compos. Sci Technol. 67 (1) (2007) 79–91.
[72] J. Wu, Q. Tang, H. Sun, J. Lin, H. Ao, M. Huang, et al., Conducting film from graphite oxide nanoplatelets and poly(acrylic acid) by layer-by-layer self-assembly, Langmuir 24 (9) (2008) 4800–4805.
[73] Y. Han, Y. Lu, Preparation and characterization of graphite oxide/polypyrrole composites, Carbon 45 (12) (2007) 2394–2399.
[74] W. Li, X.-Z. Tang, H.-B. Zhang, Z.-G. Jiang, Z-Z. Yu, X-S. Du, Y-W. Mai, Simultaneous surface functionalization and reduction of graphene oxide with octadecylamine for electrically conductive polystyrene composites, Carbon 49 (14) (2011) 4724–4730.
[75] M.J. Fernández-Merino, L. Guardia, J.I. Paredes, S. Villar-Rodil, P. Solís-Fernández, A. Martínez-Alonso, et al., Vitamin C is an ideal substitute for hydrazine in the reduction of graphene oxide suspensions, J. Phys. Chem. C 114 (14) (2010) 6426–6432.
[76] J. Zhang, H. Yang, G. Shen, P. Cheng, J. Zhang, S. Guo, Reduction of graphene oxide vial-ascorbic acid, Chem. Commun. 46 (7) (2010) 1112–1114.
[77] A. Dimiev, D.V. Kosynkin, A. Sinitskii, A. Slesarev, Z. Sun, J.M. Tour, Layer-by-layer removal of graphene for device patterning, Science 331 (6021) (2011) 1168–1172.
[78] R.S. Dey, S. Hajra, R.K. Sahu, C.R. Raj, M. Panigrahi, A rapid room temperature chemical route for the synthesis of graphene: metal-mediated reduction of graphene oxide, Chem. Commun. 48 (12) (2012) 1787–1789.
[79] Y. Si, E.T. Samulski, Synthesis of water soluble graphene, Nano Lett. 8 (6) (2008) 1679–1682.
[80] D.R. Dreyer, S. Park, C.W. Bielawski, R.S. Ruoff, The chemistry of graphene oxide, Chem. Soc. Rev. 39 (1) (2010) 228–240.
[81] Z. Fan, K. Wang, T. Wei, J. Yan, L. Song, B. Shao, An environmentally friendly and efficient route for the reduction of graphene oxide by aluminum powder, Carbon 48 (5) (2010) 1686–1689.
[82] H.-J. Shin, K.K. Kim, A. Benayad, S.-M. Yoon, H.K. Park, I.-S. Jung, et al., Efficient reduction of graphite oxide by sodium borohydride and its effect on electrical conductance, Adv. Func. Mater. 19 (12) (2009) 1987–1992.
[83] V. Eswaraiah, S.S.J. Aravind, S. Ramaprabhu, Top down method for synthesis of highly conducting graphene by exfoliation of graphite oxide using focused solar radiation, J. Mater. Chem. 21 (19) (2011) 6800–6803.
[84] S. Eigler, C. Dotzer, A. Hirsch, Visualization of defect densities in reduced graphene oxide, Carbon 50 (10) (2012) 3666–3673.

[85] S. Wang, Y. Zhang, H.-L. Ma, Q. Zhang, W. Xu, J. Peng, et al., Ionic-liquid-assisted facile synthesis of silver nanoparticle-reduced graphene oxide hybrids by gamma irradiation, Carbon 55 (2013) 245–252.
[86] M. Jin, T.H. Kim, S.C. Lim, D.L. Duong, H.J. Shin, Y.W. Jo, et al., Facile physical route to highly crystalline graphene, Adv. Funct. Mater. 21 (18) (2011) 3496–3501.
[87] H. Feng, Y. Li, J. Li, Strong reduced graphene oxide–polymer composites: hydrogels and wires, RSC Adv. 2 (17) (2012) 6988–6993.
[88] Y.W. Zhu, M.D. Stoller, W.W. Cai, A. Velamakanni, R.D. Piner, D. Chen, et al., Exfoliation of graphite oxide in propylene carbonate and thermal reduction of the resulting graphene oxide platelets, ACS Nano 4 (2) (2010) 1227–1233.
[89] Z. Sui, X. Zhang, Y. Lei, Y. Luo, Easy and green synthesis of reduced graphite oxide-based hydrogels, Carbon 49 (13) (2011) 4314–4321.
[90] M.S. Dresselhaus, G. Dresselhaus, P.C. Eklund, D.D.L. Chung, Lattice vibrations in graphite and intercalation compounds of graphite, Mater. Sci. Eng. 31 (1977) 141–152.
[91] E. Widenkvist, D.W. Boukhvalov, S. Rubino, S. Akhtar, J. Lu, R.A. Quinlan, M.I. Katsnelson, K. Leifer, H. Grennberg, U. Jansson, Mild sonochemical exfoliation of bromine-intercalated graphite: a new route towards graphene. J. Phys. D: Appl. Phys. 42 (11) (2009) 112003. http://dx.doi.org/10.1088/0022-3727/42/11/112003.
[92] L.M. Viculis, J.J. Mack, O.M. Mayer, H.T. Hahn, R.B. Kaner, Intercalation and exfoliation routes to graphite nanoplatelets, J. Mater. Chem. 15 (9) (2005) 974–978.
[93] J.M. Englert, K.C. Knirsch, C. Dotzer, B. Butz, F. Hauke, E. Spiecker, et al., Functionalization of graphene by electrophilic alkylation of reduced graphite, Chem. Commun. 48 (41) (2012) 5025–5027.
[94] T. Kuila, S. Bose, A.K. Mishra, P. Khanra, N.H. Kim, J.H. Lee, Chemical functionalization of graphene and its applications, Prog. Mater. Sci. 57 (7) (2012) 1061–1105.
[95] J.O. Besenhard, E. Theodoridou, Electrochemical applications of graphite intercalation compounds, Syn. Met. 4 (3) (1982) 211–223.
[96] M. Inagaki, Applications of graphite intercalation compounds, J. Mater. Res. 4 (06) (1989) 1560–1568.
[97] A. Hirsch, J.M. Englert, F. Hauke, Wet chemical functionalization of graphene, Acc. Chem. Res. 46 (1) (2013) 87–96.
[98] K. Feiyu, I. Michio, T. Masahiro, Exfoliation of graphite via intercalation compounds. Chem. Phys. Carbon (2004), http://dx.doi.org/10.1201/9780203997031.ch1.
[99] M. Inagaki, F. Kang, M. Toyoda, Exfoliation of graphite via intercalation compounds, Chem. Phys. Carbon 29 (2004) 1–69.
[100] E. Stumpp, The intercalation of metal chlorides and bromides into graphite, Mater. Sci. Eng. 31 (1977) 53–59.
[101] M.S. Dresselhaus, G. Dresselhaus, Intercalation compounds of graphite, Adv. Phys. 51 (1) (2002) 1–186.
[102] D.D.L. Chung, Review graphite, J. Mater. Sci. 37 (8) (2002) 1475–1489.
[103] N. Usha, B. Viswanathan, V.R.K. Murthy, J. Sobhanadri, X-ray photoelectron spectroscopic study of some pure stages of graphite ferric chloride intercalation compounds, Spectrochim. Acta A Mol. Biomol. Spectrosc. 53 (11) (1997) 1761–1765.
[104] Z. Yan, Z. Zhuxia, L. Tianbao, L. Xuguang, X. Bingshe, XPS and XRD study of $FeCl_3$–graphite intercalation compounds prepared by arc discharge in aqueous solution, Spectrochim. Acta A Mol. Biomol. Spectrosc. 70 (5) (2008) 1060–1064.
[105] H. Huang, Y. Xia, X.Y. Tao, J. Du, J.W. Fang, Y.P. Gan, et al., Highly efficient electrolytic exfoliation of graphite into graphene sheets based on Li ions intercalation-expansion-microexplosion mechanism, J. Mater. Chem. 22 (21) (2012) 10452–10456.
[106] S. Pruvost, C. Herold, A. Herold, P. Lagrange, Structural study of novel graphite-lithium-calcium intercalation compounds, Eur. J. Inorg. Chem. (8) (2004) 1661–1667.
[107] J. Kwon, S.H. Lee, K.-H. Park, D.-H. Seo, J. Lee, B.-S. Kong, et al., Simple preparation of high-quality graphene flakes without oxidation using potassium salts, Small 7 (7) (2011) 864–868.
[108] K. Kanetani, K. Sugawara, T. Sato, R. Shimizu, K. Iwaya, T. Hitosugi, et al., Ca intercalated bilayer graphene as a thinnest limit of superconducting C_6Ca, PNAS 109 (48) (2012) 19610–19613.
[109] W. Sirisaksoontorn, A.A. Adenuga, V.T. Remcho, M.M. Lerner, Preparation and characterization of a Tetrabutylammonium graphite intercalation compound, J. Am. Chem. Soc. 133 (32) (2011) 12436–12438.

[110] J.M. Englert, C. Dotzer, G. Yang, M. Schmid, C. Papp, J.M. Gottfried, et al., Covalent bulk functionalization of graphene, Nat. Chem. 3 (4) (2011) 279–286.
[111] K.H. Park, B.H. Kim, S.H. Song, J. Kwon, B.S. Kong, K. Kang, et al., Exfoliation of non-oxidized graphene flakes for scalable conductive film, Nano Lett. 12 (6) (2012) 2871–2876.
[112] T. Abe, Y. Mizutani, Y. Yokota, M. Inaba, Z. Ogumi, Raman scattering study of $FeCl_3$ based graphite bi-intercalation compounds, Mol. Cryst. 340 (1) (2000) 173–178.
[113] J.H. Lee, D.W. Shin, V.G. Makotchenko, A.S. Nazarov, V.E. Fedorov, Y.H. Kim, et al., One-step exfoliation synthesis of easily soluble graphite and transparent conducting graphene sheets, Adv. Mater. 21 (43) (2009) 4383–4387.
[114] V.M. Paasonen, P.P. Semyannikov, A.S. Nazarov, Use of fluorinated graphite intercalation compounds as two-dimensional microreactors, Dokl. Chem. 381 (4–6) (2001) 359–361.
[115] K. Kobayashi, S. Suzuki, H. Oshima, K. Sugihara, C-axis thermoelectric power of stage-2 graphite intercalation compound with iodine monobromide, J. Phys. Soc. Jpn. 68 (6) (1999) 2006–2009.
[116] M. Ujihara, M.M.M. Ahmed, T. Imae, Y. Yamauchi, Massive-exfoliation of magnetic graphene from acceptor-type GIC by long-chain alkyl amine, J. Mater. Chem. A 2 (12) (2014) 4244–4250.
[117] K.C. Kwon, K.S. Choi, S.Y. Kim, Increased work function in few-layer graphene sheets via metal chloride doping, Adv. Funct. Mater. 22 (22) (2012) 4724–4731.
[118] S.S. Tzeng, M.H. Nien, Distribution of intercalant in copper chloride and iron chloride graphite intercalation compounds, J. Mater. Res. 14 (1) (1999) 302–307.
[119] T. Abe, Y. Mizutani, E. Ihara, M. Asano, T. Harada, Preparation of $FeCl_3$-IBr-H_2SO_4-graphite multi-intercalation compounds, J. Mater. Res. 9 (2) (1994) 377–382.
[120] L. Yang, H. Liu, Y. Chen, H. He, H. Chen, Formation process of $FeCl_3$-$NiCl_2$-graphite intercalation compounds, J. Mater. Eng. Perform. 21 (3) (2012) 339–344.
[121] T. Enoki, Intercalation and guest-host interaction in nano-graphite, J. Phys. Chem. Solids 65 (2–3) (2004) 103–108.
[122] L.M. Viculis, J.J. Mack, R.B. Kaner, A chemical route to carbon nanoscrolls, Science 299 (5611) (2003) 1361.
[123] X. Geng, Y. Guo, D. Li, W. Li, C. Zhu, X. Wei, et al., Interlayer catalytic exfoliation realizing scalable production of large-size pristine few-layer graphene. Sci. Rep. 3 (2013), http://dx.doi.org/10.1038/srep01134.
[124] H. Mazurek, G. Ghavamishahidi, G. Dresselhaus, M. Dresselhaus, Low temperature X-ray diffraction study of stage 1 graphite-$FeCl_3$, Carbon 20 (5) (1982) 415–418.
[125] W. Gu, W. Zhang, X. Li, H. Zhu, J. Wei, Z. Li, et al., Graphene sheets from worm-like exfoliated graphite, J. Mater. Chem. 19 (21) (2009) 3367–3369.
[126] H. Zhang, M.M. Lerner, Preparation of graphite intercalation compounds containing crown ethers, Inorg. Chem. 55 (17) (2016) 8281–8284.
[127] H. Zhang, Y. Wu, W. Sirisaksoontorn, V.T. Remcho, M.M. Lerner, Preparation, characterization, and structure trends for graphite intercalation compounds containing pyrrolidinium cations, Chem. Mater. 28 (3) (2016) 969–974.
[128] T. Maluangnont, W. Sirisaksoontorn, M.M. Lerner, A comparative structural study of ternary graphite intercalation compounds containing alkali metals and linear or branched amines, Carbon 50 (2) (2012) 597–602.
[129] J. Chen, B. Yao, C. Li, G. Shi, An improved Hummers method for eco-friendly synthesis of graphene oxide, Carbon 64 (2013) 225–229.
[130] J. Zhang, H. Zhu, M. Wang, W. Wang, Z. Chen, Electrochemical determination of sunset yellow based on an expanded graphite paste electrode, J. Electrochem. Soc. 160 (8) (2013) H459–H462.
[131] X. Yue, K. Yu, L. Ji, Z. Wang, F. Zhang, L. Qian, et al., Effect of heating temperature of expandable graphite on amorphization behavior of powder expanded graphite-Fe mixtures by ball-milling, Powder Tech. 211 (1) (2011) 95–99.
[132] S. Paszkiewicz, A. Szymczyk, Z. Špitalský, J. Mosnáček, Z. Rosłaniec, Morphology and thermal properties of expanded graphite (EG)/poly(ethylene terephthalate)(PET) nanocomposites, Chemik 66 (1) (2012) 21–30.
[133] B. Zalba, J.M. Marín, L.F. Cabeza, H. Mehling, Review on thermal energy storage with phase change: Materials, heat transfer analysis and applications, Appl. Thermal Eng. 23 (3) (2003) 251–283.

[134] Y. Xiujuan, Q. Liwen, Preparation for graphite materials and study on electrochemical degradation of phenol by graphite cathodes, Adv. Mater. Phys. Chem. 2 (2012) 63–68.
[135] J.-H. Li, L.-L. Feng, Z.-X. Jia, Preparation of expanded graphite with 160 μm mesh of fine flake graphite, Mater. Lett. 60 (6) (2006) 746–749.
[136] J. Li, H. Da, Q. Liu, S. Liu, Preparation of sulfur-free expanded graphite with 320 μm mesh of flake graphite, Mater. Lett. 60 (29–30) (2006) 3927–3930.
[137] J. Li, H. Shi, N. Li, M. Li, J. Li, Ultrasound-assisted preparation of alkaline graphite intercalation compounds, Ultrason. Sonochem. 17 (5) (2010) 745–748.
[138] S.H. Ba, C.H. Jiang, K.B. Sun, Z.X. Sun, Prepared and infrared extinction characteristics of micron expanded graphite, Adv. Mater. Res.: Trans. Tech. Pub. 308 (2011) 710–714.
[139] S. Gambhir, R. Jalili, D.L. Officer, G.G. Wallace, Chemically converted graphene: scalable chemistries to enable processing and fabrication, NPG Asia Mater. 7 (6) (2015) e186.
[140] Q.-L. Yan, M. Gozin, F.-Q. Zhao, A. Cohen, S.-P. Pang, Highly energetic compositions based on functionalized carbon nanomaterials, Nanoscale 8 (9) (2016) 4799–4851.
[141] Z. Zhang, X. Fang, Study on paraffin/expanded graphite composite phase change thermal energy storage material, Energy Convers. Manag. 47 (3) (2006) 303–310.
[142] X.-X. Wu, H.-X. Li, G.-Q. Liu, C.-C. Niu, G. Wang, J.-L. Sun, Nanocarbon-coated α-al$_2$o$_3$composite powders synthesized by high-energy ball milling, J. Inorg. Mater. 28 (3) (2013) 261–266.
[143] G. Carotenuto, A. Longo, L. Nicolais, S. De Nicola, E. Pugliese, M. Ciofini, et al., Laser-induced thermal expansion of H_2SO_4-intercalated graphite lattice, J. Phys. Chem. C 119 (28) (2015) 15942–15947.
[144] Y. Wen, K. He, Y. Zhu, F. Han, Y. Xu, I. Matsuda, et al., Expanded graphite as superior anode for sodium-ion batteries. Nat. Commun. 5 (2014), http://dx.doi.org/10.1038/ncomms5033.
[145] W.F. Mohamad, F. Ahmad, S. Ullah, Effect of inorganic fillers on thermal performance and char morphology of intumescent fire retardant coating, Asian. J. Sci. Res. 6 (2) (2013) 263.
[146] M. Matsumoto, Y. Saito, C. Park, T. Fukushima, T. Aida, Ultrahigh-throughput exfoliation of graphite into pristine 'single-layer' graphene using microwaves and molecularly engineered ionic liquids, Nat. Chem. 7 (9) (2015) 730–736.
[147] Y. Kim, E.-S. Cho, S.-J. Park, S. Kim, One-pot microwave-assisted synthesis of reduced graphene oxide/nickel cobalt double hydroxide composites and their electrochemical behavior, J. Ind. Eng. Chem. 33 (2016) 108–114.
[148] M.M.M. Ahmed, T. Imae, Electrochemical properties of a thermally expanded magnetic graphene composite with a conductive polymer, Phys. Chem. Chem. Phys. 18 (15) (2016) 10400–10410.
[149] L.K. Shrestha, R.G. Shrestha, Y. Yamauchi, J.P. Hill, T. Nishimura, M. Ki, et al., Nanoporous carbon tubes from fullerene crystals as the π-electron carbon source, Angew. Chem. Int. Ed. 54 (3) (2015) 951–955.
[150] X.S. Li, W.W. Cai, J.H. An, S. Kim, J. Nah, D.X. Yang, et al., Large-area synthesis of high-quality and uniform graphene films on copper foils, Science 324 (5932) (2009) 1312–1314.
[151] R. Zhang, Y.L. Dong, W.J. Kong, W.P. Han, P.H. Tan, Z.M. Liao, et al., Growth of large domain epitaxial graphene on the C-face of SiC, J. Appl. Phys. 112 (10) (2012)104307.
[152] B. Dlubak, M.B. Martin, C. Deranlot, B. Servet, S. Xavier, R. Mattana, et al., Highly efficient spin transport in epitaxial graphene on SiC, Nat. Phys. 8 (7) (2012) 557–561.
[153] M. Choucair, P. Thordarson, J.A. Stride, Gram-scale production of graphene based on solvothermal synthesis and sonication, Nat. Nanotechnol. 4 (1) (2009) 30–33.
[154] H. Wang, T. Maiyalagan, X. Wang, Review on recent progress in nitrogen-doped graphene: synthesis, characterization, and its potential applications, ACS Cat. 2 (5) (2012) 781–794.
[155] S. Park, R.S. Ruoff, Chemical methods for the production of graphenes, Nat. Nanotechnol. 4 (4) (2009) 217–224.
[156] Y. Xu, H. Bai, G. Lu, C. Li, G. Shi, Flexible graphene films via the filtration of water-soluble noncovalent functionalized graphene sheets, J. Am. Chem. Soc. 130 (18) (2008) 5856–5857.
[157] S. Park, J. An, R.D. Piner, I. Jung, D. Yang, A. Velamakanni, et al., Aqueous suspension and characterization of chemically modified graphene sheets, Chem. Mater. 20 (21) (2008) 6592–6594.

[158] J.I. Paredes, S. Villar-Rodil, A. Martínez-Alonso, T. JMD, Graphene oxide dispersions in organic solvents, Langmuir 24 (19) (2008) 10560–10564.
[159] J.R. Lomeda, C.D. Doyle, D.V. Kosynkin, W.-F. Hwang, J.M. Tour, Diazonium functionalization of surfactant-wrapped chemically converted graphene sheets, J. Am. Chem. Soc. 130 (48) (2008) 16201–16206.
[160] R. Muszynski, B. Seger, P.V. Kamat, Decorating graphene sheets with gold nanoparticles, J. Phys. Chem. C 112 (14) (2008) 5263–5266.
[161] G. Williams, B. Seger, P.V. Kamat, TiO2-graphene nanocomposites. UV-assisted photocatalytic reduction of graphene oxide, ACS Nano 2 (7) (2008) 1487–1491.
[162] R. Hao, W. Qian, L. Zhang, Y. Hou, Aqueous dispersions of TCNQ-anion-stabilized graphene sheets, Chem. Commun. (48) (2008) 6576–6578.
[163] X. Li, X. Wang, L. Zhang, S. Lee, H. Dai, Chemically derived, ultrasmooth graphene nanoribbon semiconductors, Science 319 (5867) (2008) 1229–1232.
[164] X. Li, G. Zhang, X. Bai, X. Sun, X. Wang, E. Wang, et al., Highly conducting graphene sheets and Langmuir-Blodgett films, Nat. Nanotechnol. 3 (9) (2008) 538–542.
[165] X. Fan, W. Peng, Y. Li, X. Li, S. Wang, G. Zhang, et al., Deoxygenation of exfoliated graphite oxide under alkaline conditions: a green route to graphene preparation, Adv. Mater. 20 (23) (2008) 4490–4493.
[166] A. Zandiatashbar, G.-H. Lee, S.J. An, S. Lee, N. Mathew, M. Terrones, et al., Effect of defects on the intrinsic strength and stiffness of graphene, Nat. Commun. 5 (2014) 3186.
[167] A. Siriviriyanun, M. Popova, T. Imae, L.V. Kiew, C.Y. Looi, W.F. Wong, et al., Preparation of graphene oxide/dendrimer hybrid carriers for delivery of doxorubicin, Chem. Eng. J. 281 (2015) 771–781.
[168] T. Gao, X. Song, H. Du, Y. Nie, Y. Chen, Q. Ji, et al., Temperature-triggered chemical switching growth of in-plane and vertically stacked graphene-boron nitride heterostructures. Nat. Commun. 6 (2015) 6835, http://dx.doi.org/10.1038/ncomms 7835.
[169] K. Zhou, W. Zhou, X. Liu, Y. Sang, S. Ji, W. Li, et al., Ultrathin MoO_3 nanocrystalsself-assembled on graphene nanosheets via oxygen bonding as supercapacitor electrodes of high capacitance and long cycle life, Nano Energy 12 (2015) 510–520.
[170] L.M. Malard, M.A. Pimenta, G. Dresselhaus, M.S. Dresselhaus, Raman spectroscopy in graphene, Phys. Rep. 473 (5–6) (2009) 51–87.
[171] M.S. Dresselhaus, A. Jorio, R. Saito, Characterizing graphene, graphite, and carbon nanotubes by Raman spectroscopy, Annu. Rev. Cond. Matt. Phys. 1 (2010) 89–108.
[172] M.M.M. Ahmed, Preparation of graphene from graphite using physical and chemical methods (MS thesis), National Taiwan University of Science and Technology, 2013.
[173] A. Jorio, M.S. Dresselhaus, R. Saito, G. Dresselhaus, Raman Spectroscopy in Graphene Related Systems, Wiley, Weinheim, 2010.
[174] O. Frank, M. Mohr, J. Maultzsch, C. Thomsen, I. Riaz, R. Jalil, et al., Raman 2D-band splitting in graphene: theory and experiment, ACS Nano 5 (3) (2011) 2231–2239.
[175] J.C. Chacón-Torres, L. Wirtz, T. Pichler, Raman spectroscopy of graphite intercalation compounds: charge transfer, strain, and electron–phonon coupling in graphene layers, Phys. Status Solidi B 251 (12) (2014) 2337–2355.
[176] Y. Geng, Q.B. Zheng, J.K. Kim, Effects of stage, intercalant species and expansion technique on exfoliation of graphite intercalation compound into graphene sheets, J. Nanosci. Nanotechnol. 11 (2) (2011) 1084–1091.
[177] A. Jorio, M. Dresselhaus, R. Saito, G. Dresselhaus, Raman Spectroscopy in Graphene Related Systems, John Wiley & Sons, Weinheim, 2011.
[178] M. Inagaki, R. Tashiro, Y. Washino, M. Toyoda, Exfoliation process of graphite via intercalation compounds with sulfuric acid, J Phys. Chem. Solids 65 (2–3) (2004) 133–137.
[179] D. Graf, F. Molitor, K. Ensslin, C. Stampfer, A. Jungen, C. Hierold, et al., Spatially resolved Raman spectroscopy of single-and few-layer graphene, Nano Lett. 7 (2) (2007) 238–242.
[180] A. Ferrari, J. Meyer, V. Scardaci, C. Casiraghi, M. Lazzeri, F. Mauri, et al., Raman spectrum of graphene and graphene layers, Phys. Rev. Lett. 97 (18) (2006)187401.

[181] Z. Li, X. Hu, D. Xiong, B. Li, H. Wang, Q. Li, Facile synthesis of bicontinuous microporous/mesoporous carbon foam with ultrahigh specific surface area for supercapacitor application, Electrochim. Acta 219 (2016) 339–349.
[182] T. Maneerung, J. Liew, Y. Dai, S. Kawi, C. Chong, C.-H. Wang, Activated carbon derived from carbon residue from biomass gasification and its application for dye adsorption: kinetics, isotherms and thermodynamic studies, Bioresource Tech. 200 (2016) 350–359.
[183] G.D. Jimenez, T. Monti, J.J. Titman, V. Hernandez-Montoya, S.W. Kingman, E.R. Binner, New insights into microwave pyrolysis of biomass: preparation of carbon-based products from pecan nutshells and their application in wastewater treatment, J. Anal. Appl. Pyrolysis 124 (2017) 113–121.
[184] N. Baig, A.-N. Kawde, A cost-effective disposable graphene-modified electrode decorated with alternating layers of Au NPs for the simultaneous detection of dopamine and uric acid in human urine, RSC Adv. 6 (84) (2016) 80756–80765.
[185] A.-N. Kawde, N. Baig, M. Sajid, Graphite pencil electrodes as electrochemical sensors for environmental analysis: a review of features, developments, and applications, RSC Adv. 6 (94) (2016) 91325–91340.
[186] M. Pumera, Electrochemistry of graphene: new horizons for sensing and energy storage, The Chem. Record. 9 (4) (2009) 211–223.
[187] F. Bonaccorso, L. Colombo, G. Yu, M. Stoller, V. Tozzini, A.C. Ferrari, et al., Graphene, related two-dimensional crystals, and hybrid systems for energy conversion and storage, Science 347 (6217) (2015) 1246501.
[188] M.F. El-Kady, Y. Shao, R.B. Kaner, Graphene for batteries, supercapacitors and beyond, Nat. Rev. Mater. 1 (2016)16033.
[189] A.B. Fuertes, M. Sevilla, High-surface area carbons from renewable sources with a bimodal micro-mesoporosity for high-performance ionic liquid based supercapacitors, Carbon 94 (2015) 41–52.
[190] C. Yin, T. C-A, F. Cai, C. Song, H. Gong, J. Wang, Effects of activation temperature on the deoxygenation, specific surface area and supercapacitor performance of graphene, Carbon 109 (2016) 558–565.
[191] K. Le Van, T.T. Luong Thi, Activated carbon derived from rice husk by NaOH activation and its application in supercapacitor, Prog. Nat. Sci.: Mater. Int. 24 (3) (2014) 191–198.
[192] T.-T. Chen, W.-L. Song, L.-Z. Fan, Engineering graphene aerogels with porous carbon of large surface area for flexible all-solid-state supercapacitors, Electrochim. Acta 165 (2015) 92–97.
[193] Y. Ma, C. Ma, J. Sheng, H. Zhang, R. Wang, Z. Xie, et al., Nitrogen-doped hierarchical porous carbon with high surface area derived from graphene oxide/pitch oxide composite for supercapacitors, J. Col. Inter. Sci. 461 (2016) 96–103.
[194] X. Hong, K.S. Hui, Z. Zeng, K.N. Hui, L. Zhang, M. Mo, et al., Hierarchical nitrogen-doped porous carbon with high surface area derived from endothelium corneum gigeriae galli for high-performance supercapacitor, Electrochim. Acta 130 (2014) 464–469.
[195] X. Li, J. Zhou, W. Xing, F. Subhan, Y. Zhang, P. Bai, et al., Outstanding capacitive performance of reticular porous carbon/graphene sheets with super high surface area, Electrochim. Acta 190 (2016) 923–931.
[196] C. Zheng, X. Zhou, H. Cao, G. Wang, Z. Liu, Synthesis of porous graphene/activated carbon composite with high packing density and large specific surface area for supercapacitor electrode material, J. Power Sources 258 (2014) 290–296.
[197] Y. Li, Z. Li, P.K. Shen, Simultaneous formation of ultrahigh surface area and three-dimensional hierarchical porous graphene-like networks for fast and highly stable supercapacitors, Adv. Mater. 25 (17) (2013) 2474–2480.
[198] X. Fan, C. Yu, J. Yang, Z. Ling, J. Qiu, Hydrothermal synthesis and activation of graphene-incorporated nitrogen-rich carbon composite for high-performance supercapacitors, Carbon 70 (2014) 130–141.
[199] F. Zeng, Y. Kuang, N. Zhang, Z. Huang, Y. Pan, Z. Hou, et al., Multilayer super-short carbon nanotube/reduced graphene oxide architecture for enhanced supercapacitor properties, J. Power Sources 247 (2014) 396–401.
[200] Z.-F. Li, H. Zhang, Q. Liu, L. Sun, L. Stanciu, J. Xie, Fabrication of high-surface-area graphene/polyaniline nanocomposites and their application in supercapacitors, ACS Appl. Mater. Interfaces 5 (7) (2013) 2685–2691.

[201] J. Hu, Z. Kang, F. Li, X. Huang, Graphene with three-dimensional architecture for high performance supercapacitor, Carbon 67 (2014) 221–229.
[202] V. Chabot, J. Zhang, Electrochemical Supercapacitors for Energy Storage and Delivery, CRC Press, Boca Raton, FL, 2013.
[203] C. Largeot, C. Portet, J. Chmiola, P.-L. Taberna, Y. Gogotsi, P. Simon, Relation between the ion size and pore size for an electric double-layer capacitor, J. Am. Chem. Soc. 130 (9) (2008) 2730–2731.
[204] D.H. Doughty, P.C. Butler, A.A. Akhil, N.H. Clark, J.D. Boyes, Batteries for large-scale stationary electrical energy storage, The Electrochem. Soc. Inter. 19 (3) (2010) 49–53.
[205] R. Xue, J. Yan, X. Liu, Y. Tian, B. Yi, Effect of activation on the carbon fibers from phenol–formaldehyde resins for electrochemical supercapacitors, J. Appl. Electrochem. 41 (11) (2011) 1357–1366.
[206] A. Yu, V. Chabot, J. Zhang, Electrochemical Supercapacitors for Energy Storage and Delivery: Fundamentals and Applications, CRC Press, Boca Raton, FL, 2013.
[207] G. Wang, L. Zhang, J. Zhang, A review of electrode materials for electrochemical supercapacitors, Chem. Soc. Rev. 41 (2) (2012) 797–828.
[208] P. Simon, Y. Gogotsi, Materials for electrochemical capacitors, Nat. Mater. 7 (11) (2008) 845–854.
[209] P.-L. Taberna Sr., P. Simon, C. Lethien, P. Huang, et al., Mechanically stable carbide derived carbon nanoporous films for micro-supercapacitors, PRiME 2016/230th ECS Meeting (October 2–7, 2016), ECS, 2016. Abstract MA2016–02 945.
[210] M. El-Kady, Graphene Supercapacitors: Charging Up the Future, University of California, Los Angeles, CA, 2013.
[211] J. Xu, Z. Tan, W. Zeng, G. Chen, S. Wu, Y. Zhao, et al., A hierarchical carbon derived from sponge-templated activation of graphene oxide for high-performance supercapacitor electrodes, Adv. Mater. 28 (2016) 5222–5228.
[212] M. Zeiger, N. Jäckel, V.N. Mochalin, V. Presser, Review: carbon onions for electrochemical energy storage, J. Mater. Chem. A 4 (9) (2016) 3172–3196.
[213] D. Pech, M. Brunet, H. Durou, P. Huang, V. Mochalin, Y. Gogotsi, et al., Ultrahigh-power micrometre-sized supercapacitors based on onion-like carbon, Nat. Nanotechnol. 5 (9) (2010) 651–654.
[214] F. Miao, C. Shao, X. Li, K. Wang, Y. Liu, Flexible solid-state supercapacitors based on freestanding nitrogen-doped porous carbon nanofibers derived from electrospun polyacrylonitrile@ polyaniline nanofibers, J. Mater. Chem. A 4 (11) (2016) 4180–4187.
[215] T. Wang, Y. Zhu, Z. Xing, G. Tang, H. Fan, The specific capacitive performances of the manganese oxyhydroxide/carbon microcoil electrodes for supercapacitors, Electrochim. Acta 151 (2015) 134–139.
[216] P.D. Adhikari, M. Ujihara, T. Imae, P.-D. Hong, S. Motojima, Reinforcement on properties of poly (vinyl alcohol) films by embedding functionalized carbon micro coils, J. Nanosci. Nanotechnol. 11 (2) (2011) 1004–1012.
[217] M. Ujihara, T. Imae, A review of hydrophilization of oxidized nanocarbons, in: Recent Progress in Colloid and Surface Chemistry with Biological Applications, American Chemical Society, Washington DC, 2015, pp. 25–41.
[218] P. Simon, Y. Gogotsi, Capacitive energy storage in nanostructured carbon–electrolyte systems, Acc. Chem. Res. 46 (5) (2012) 1094–1103.
[219] V.B. Kumar, A. Borenstein, B. Markovsky, D. Aurbach, A. Gedanken, M. Talianker, et al., Activated carbon modified with carbon nanodots as novel electrode material for supercapacitors, J. Phys. Chem. C 120 (2016) 13406–13413.
[220] L.L. Zhang, X. Zhao, Carbon-based materials as supercapacitor electrodes, Chem. Soc. Rev. 38 (9) (2009) 2520–2531.
[221] M. Sullivan, B. Schnyder, M. Bärtsch, D. Alliata, C. Barbero, R. Imhof, et al., Electrochemically modified glassy carbon for capacitor electrodes characterization of thick anodic layers by cyclic voltammetry, differential electrochemical mass spectrometry, spectroscopic ellipsometry, X-ray photoelectron spectroscopy, FTIR, and AFM, J. Electrochem. Soc. 147 (7) (2000) 2636–2643.
[222] M. Beidaghi, W. Chen, C. Wang, Electrochemically activated carbon micro-electrode arrays for electrochemical micro-capacitors, J. Power Sources 196 (4) (2011) 2403–2409.

[223] H. Xu, X. Fan, Y. Lu, L. Zhong, X. Kong, J. Wang, Preparation of an electrochemically modified graphite electrode and its electrochemical performance for pseudo-capacitors in a sulfuric acid electrolyte, Carbon 48 (11) (2010) 3300–3303.
[224] A. Jänes, H. Kurig, E. Lust, Characterisation of activated nanoporous carbon for supercapacitor electrode materials, Carbon 45 (6) (2007) 1226–1233.
[225] C. Portet, G. Yushin, Y. Gogotsi, Electrochemical performance of carbon onions, nanodiamonds, carbon black and multiwalled nanotubes in electrical double layer capacitors, Carbon 45 (13) (2007) 2511–2518.
[226] G. Sun, L. Ma, J. Ran, X. Shen, H. Tong, Incorporation of homogeneous Co_3O_4 into a nitrogen-doped carbon aerogel via a facile in situ synthesis method: implications for high performance asymmetric supercapacitors, J. Mater. Chem. A 4 (2016) 9542–9554.
[227] P. Simon, A. Burke, Nanostructured carbons: double-layer capacitance and more, The Electrochem. Soc. Inter. 17 (1) (2008) 38.
[228] R.R. Devarapalli, S. Szunerits, Y. Coffinier, M.V. Shelke, R. Boukherroub, Glucose-derived porous carbon-coated silicon nanowires as efficient electrodes for aqueous micro-supercapacitors, ACS Appl. Mater. Interfaces 8 (7) (2016) 4298–4302.
[229] B.B. Garcia, S.L. Candelaria, G. Cao, Nitrogenated porous carbon electrodes for supercapacitors, J. Mater. Sci. 47 (16) (2012) 5996–6004.
[230] Y. Jiang, J. Yan, X. Wu, D. Shan, Q. Zhou, L. Jiang, et al., Facile synthesis of carbon nanofibers-bridged porous carbon nanosheets for high-performance supercapacitors, J. Power Sources 307 (2016) 190–198.
[231] G. Zu, J. Shen, L. Zou, F. Wang, X. Wang, Y. Zhang, et al., Nanocellulose-derived highly porous carbon aerogels for supercapacitors, Carbon 99 (2016) 203–211.
[232] J. Liu, X. Wang, J. Gao, Y. Zhang, Q. Lu, M. Liu, Hollow porous carbon spheres with hierarchical nanoarchitecture for application of the high performance supercapacitors, Electrochim. Acta 211 (2016) 183–192.
[233] Y.S. Yun, M.H. Park, S.J. Hong, M.E. Lee, Y.W. Park, H.-J. Jin, Hierarchically porous carbon nanosheets from waste coffee grounds for supercapacitors, ACS Appl. Mater. Interfaces 7 (6) (2015) 3684–3690.
[234] H. Li, D. Yuan, C. Tang, S. Wang, J. Sun, Z. Li, et al., Lignin-derived interconnected hierarchical porous carbon monolith with large areal/volumetric capacitances for supercapacitor, Carbon 100 (2016) 151–157.
[235] C. Liu, J. Wang, J. Li, M. Zeng, R. Luo, J. Shen, et al., Synthesis of N-doped hollow-structured mesoporous carbon nanospheres for high-performance supercapacitors, ACS Appl. Mater. Interfaces 8 (11) (2016) 7194–7204.
[236] S.-K. Kim, E. Jung, M.D. Goodman, K.S. Schweizer, N. Tatsuda, K. Yano, et al., Self-assembly of monodisperse starburst carbon spheres into hierarchically organized nanostructured supercapacitor electrodes, ACS Appl. Mater. Interfaces 7 (17) (2015) 9128–9133.
[237] J. Chen, J. Xu, S. Zhou, N. Zhao, C.-P. Wong, Nitrogen-doped hierarchically porous carbon foam: a free-standing electrode and mechanical support for high-performance supercapacitors, Nano Energy 25 (2016) 193–202.
[238] M.F. El-Kady, R.B. Kaner, J.Y. Hwang, Porous interconnected corrugated carbon-based network (ICCN) composite, US Patent 20,160,148,759, 2016.
[239] K. Wang, Y. Cao, X. Wang, M.A. Castro, B. Luo, Z. Gu, et al., Rod-shape porous carbon derived from aniline modified lignin for symmetric supercapacitors, J. Power Sources 307 (2016) 462–467.
[240] C. Zhang, X. Zhu, M. Cao, M. Li, N. Li, L. Lai, et al., Hierarchical porous carbon materials derived from sheep manure for high-capacity supercapacitors, ChemSusChem 9 (9) (2016) 932–937.
[241] G. Hasegawa, K. Kanamori, T. Kiyomura, H. Kurata, T. Abe, K. Nakanishi, Hierarchically porous carbon monoliths comprising ordered mesoporous nanorod assemblies for high-voltage aqueous supercapacitors, Chem. Mater. 28 (11) (2016) 3944–3950.
[242] Y. Tan, Q. Gao, J. Xu, Z. Li, 1D nanorod-like porous carbon with simultaneous high energy and large power density as a supercapacitor electrode material, RSC Adv. 6 (56) (2016) 51332–51336.

[243] J. Huang, J. Wang, C. Wang, H. Zhang, C. Lu, J. Wang, Hierarchical porous graphene carbon-based supercapacitors, Chem. Mater. 27 (6) (2015) 2107–2113.
[244] W.K. Chee, H.N. Lim, Z. Zainal, N.M. Huang, I. Harrison, Y. Andou, Flexible graphene-based supercapacitors: a review, J. Phys Chem. C 120 (8) (2016) 4153–4172.
[245] P. Huang, C. Lethien, S. Pinaud, K. Brousse, R. Laloo, V. Turq, et al., On-chip and freestanding elastic carbon films for micro-supercapacitors, Science 351 (6274) (2016) 691–695.
[246] Y. Qiu, G. Li, Y. Hou, Z. Pan, H. Li, W. Li, et al., Vertically aligned carbon nanotubes on carbon nanofibers: a hierarchical three-dimensional carbon nanostructure for high-energy flexible supercapacitors, Chem. Mater. 27 (4) (2015) 1194–1200.
[247] J. Chmiola, C. Largeot, P.-L. Taberna, P. Simon, Y. Gogotsi, Monolithic carbide-derived carbon films for micro-supercapacitors, Science 328 (5977) (2010) 480–483.
[248] V. Presser, M. Heon, Y. Gogotsi, Carbide-derived carbons from porous networks to nanotubes and graphene, Adv. Func. Mater. 21 (5) (2011) 810–833.
[249] Y. Zhu, H. Hu, W.-C. Li, X. Zhang, Cresol–formaldehyde based carbon aerogel as electrode material for electrochemical capacitor, J. Power Sources 162 (1) (2006) 738–742.
[250] Y. Zhai, Y. Dou, D. Zhao, P.F. Fulvio, R.T. Mayes, S. Dai, Carbon materials for chemical capacitive energy storage, Adv. Mater. 23 (42) (2011) 4828–4850.
[251] A. Izadi-Najafabadi, T. Yamada, D.N. Futaba, M. Yudasaka, H. Takagi, H. Hatori, et al., High-power supercapacitor electrodes from single-walled carbon Nanohorn/nanotube composite, ACS Nano 5 (2) (2011) 811–819.
[252] M.F. El-Kady, V. Strong, S. Dubin, R.B. Kaner, Laser scribing of high performance and flexible graphene-based electrochemical capacitors, Science 335 (6074) (2012) 1326–1330.
[253] P.J. Mackey, M.D. Hogue, M.R. Johansen, M.F. El-Kady, et al., Graphene-based ultracapacitors for aeronautics applications. 247th ACS National Meeting and Exposition: Two-Dimensional Materials for Energy and Fuel, American Chemical Society, Washington DC.
[254] M.F. El-Kady, R.B. Kaner, Scalable fabrication of high-power graphene micro-supercapacitors for flexible and on-chip energy storage, Nat. Commun. 4 (2013) 1475.
[255] M.F. El-Kady, R.B. Kaner, Direct laser writing of graphene electronics, ACS Nano. 8 (9) (2014) 8725–8729.
[256] M.F. El-Kady, V. Strong, S. Dubin, R.B. Kaner, Laser Scribing of High-Performance and Flexible Graphene-Based Electrochemical Capacitors, Science 335 (6074) (2012) 1326–1330.
[257] V. Strong, S. Dubin, M.F. El-Kady, A. Lech, Y. Wang, B.H. Weiller, et al., Patterning and electronic tuning of laser scribed graphene for flexible all-carbon devices, ACS Nano 6 (2) (2012) 1395–1403.
[258] Z. Lei, N. Christov, X. Zhao, Intercalation of mesoporous carbon spheres between reduced graphene oxide sheets for preparing high-rate supercapacitor electrodes, Energy Environ. Sci. 4 (5) (2011) 1866–1873.
[259] B. Wei, L. Wang, Q. Miao, Y. Yuan, P. Dong, R. Vajtai, et al., Fabrication of manganese oxide/three-dimensional reduced graphene oxide composites as the supercapacitors by a reverse microemulsion method, Carbon 85 (2015) 249–260.
[260] Z.-J. Fan, W. Kai, J. Yan, T. Wei, L.-J. Zhi, J. Feng, et al., Facile synthesis of graphene nanosheets via Fe reduction of exfoliated graphite oxide, ACS Nano 5 (1) (2011) 191–198.
[261] M.F. El-Kady, The promise of laser scribed graphene supercapacitors. 7th Annual CAFE Electric Aircraft Symposium, CAFE Foundation.
[262] L.J. Wang, M.F. El-Kady, S. Dubin, J.Y. Hwang, Y. Shao, K. Marsh, et al., Flash converted graphene for ultra-high power supercapacitors. Adv. Energy Mater. 5 (18) (2015) 1500786, http://dx.doi.org/10.1002/aenm.201500786.
[263] L.T. Le, M.H. Ervin, H. Qiu, B.E. Fuchs, W.Y. Lee, Graphene supercapacitor electrodes fabricated by inkjet printing and thermal reduction of graphene oxide, Electrochem. Commun. 13 (4) (2011) 355–358.
[264] M. El-Kady, V. Strong, S. Dubin, J. Wassei, J. Torres, R. Kaner, Synthesis and patterning of laser converted graphene for flexible energy storage devices. Meeting Abstracts: The Electrochem. Soc.:1364.
[265] Y. Shao, M.F. El-Kady, L.J. Wang, Q. Zhang, Y. Li, H. Wang, et al., Graphene-based materials for flexible supercapacitors, Chem. Soc. Rev. 44 (11) (2015) 3639–3665.

[266] C.X. Guo, C.M. Li, A self-assembled hierarchical nanostructure comprising carbon spheres and graphene nanosheets for enhanced supercapacitor performance, Energy Environ. Sci. 4 (11) (2011) 4504–4507.
[267] H. Li, Y. Tao, X. Zheng, J. Luo, F. Kang, H.-M. Cheng, et al., Ultra-thick graphene bulk supercapacitor electrodes for compact energy storage, Energy Environ. Sci. 9 (10) (2016) 3135–3142.
[268] Y. Zhu, S. Murali, M.D. Stoller, K.J. Ganesh, W. Cai, P.J. Ferreira, et al., Carbon-based supercapacitors produced by activation of graphene, Science 332 (6037) (2011) 1537–1541.
[269] L.L. Zhang, R. Zhou, X.S. Zhao, Graphene-based materials as supercapacitor electrodes, J. Mater. Chem. 20 (29) (2010) 5983–5992.
[270] Z. Wen, X. Wang, S. Mao, Z. Bo, H. Kim, S. Cui, et al., Crumpled nitrogen-doped graphene nanosheets with ultrahigh pore volume for high-performance supercapacitor, Adv. Mater. 24 (41) (2012) 5610–5616.
[271] Z. Lin, P.-L. Taberna, P. Simon, Graphene-based supercapacitors using eutectic ionic liquid mixture electrolyte, Electrochim. Acta 206 (2016) 446–451.
[272] Q. Cheng, J. Tang, J. Ma, H. Zhang, N. Shinya, L.-C. Qin, Graphene and carbon nanotube composite electrodes for supercapacitors with ultra-high energy density, Phys. Chem. Chem. Phys. 13 (39) (2011) 17615–17624.
[273] A. Laforgue, P. Simon, C. Sarrazin, J.-F. Fauvarque, Polythiophene-based supercapacitors, J. Power Sources 80 (1) (1999) 142–148.
[274] F. Wolfart, D.P. Dubal, M. Vidotti, P. Gómez-Romero, Hybrid core–shell nanostructured electrodes made of polypyrrole nanotubes coated with Ni $(OH)_2$ nanoflakes for high energy-density supercapacitors, RSC Adv. 6 (18) (2016) 15062–15070.
[275] Y. Gawli, A. Banerjee, D. Dhakras, M. Deo, D. Bulani, P. Wadgaonkar, et al., 3D polyaniline architecture by concurrent inorganic and organic acid doping for superior and robust high rate supercapacitor performance. Sci. Rep. 6 (2016), http://dx.doi.org/10.1038/srep21002.
[276] G.A. Snook, P. Kao, A.S. Best, Conducting-polymer-based supercapacitor devices and electrodes, J. Power Sources 196 (1) (2011) 1–12.
[277] J. Zhang, X.S. Zhao, Conducting polymers directly coated on reduced graphene oxide sheets as high-performance supercapacitor electrodes, J. Phys. Chem. C 116 (9) (2012) 5420–5426.
[278] S. Lehtimäki, M. Suominen, P. Damlin, S. Tuukkanen, C. Kvarnström, D. Lupo, Preparation of supercapacitors on flexible substrates with electrodeposited PEDOT/graphene composites, ACS Appl. Mater. Interfaces 7 (40) (2015) 22137–22147.
[279] A. Burke, Ultracapacitors: why, how, and where is the technology, J. Power Sources 91 (1) (2000) 37–50.
[280] J.W. Long, D. Bélanger, T. Brousse, W. Sugimoto, M.B. Sassin, O. Crosnier, Asymmetric electrochemical capacitors stretching the limits of aqueous electrolytes, MRS Bull. 36 (07) (2011) 513–522.
[281] M. Jana, J.S. Kumar, P. Khanra, P. Samanta, H. Koo, N.C. Murmu, et al., Superior performance of asymmetric supercapacitor based on reduced graphene oxide–manganese carbonate as positive and sono-chemically reduced graphene oxide as negative electrode materials, J. Power Sources 303 (2016) 222–233.
[282] B. Yuan, C. Xu, D. Deng, Y. Xing, L. Liu, H. Pang, et al., Graphene oxide/nickel oxide modified glassy carbon electrode for supercapacitor and nonenzymatic glucose sensor, Electrochim. Acta 88 (2013) 708–712.
[283] Y. Xu, L. Wang, P. Cao, C. Cai, Y. Fu, X. Ma, Mesoporous composite nickel cobalt oxide/graphene oxide synthesized via a template-assistant co-precipitation route as electrode material for supercapacitors, J. Power Sources 306 (2016) 742–752.
[284] Z. Yu, S. Sun, M. Huang, Electrodeposition of gold nanoparticles on electrochemically reduced graphene oxide for high performance supercapacitor electrode materials, Int. J. Electrochem. Sci. 11 (5) (2016) 3643–3650.
[285] H. Zhan, D.J. Garrett, N.V. Apollo, K. Ganesan, D. Lau, S. Prawer, et al., Direct fabrication of 3D graphene on nanoporous anodic alumina by plasma-enhanced chemical vapor deposition. Sci. Rep. 6 (2016), http://dx.doi.org/10.1038/srep19822.
[286] Q. Qu, S. Yang, X. Feng, 2D sandwich-like sheets of iron oxide grown on graphene as high energy anode material for supercapacitors, Adv. Mater. 23 (46) (2011) 5574–5580.
[287] W. Wei, X. Cui, W. Chen, D.G. Ivey, Manganese oxide-based materials as electrochemical supercapacitor electrodes, Chem. Soc. Rev. 40 (3) (2011) 1697–1721.

[288] M.B. Sassin, C.N. Chervin, D.R. Rolison, J.W. Long, Redox deposition of nanoscale metal oxides on carbon for next-generation electrochemical capacitors, Acc. Chem. Res. 46 (5) (2012) 1062–1074.
[289] W. Wang, S. Guo, I. Lee, K. Ahmed, J. Zhong, Z. Favors, et al., Hydrous ruthenium oxide nanoparticles anchored to graphene and carbon nanotube hybrid foam for supercapacitors. Sci. Rep. 4 (2014) 4452, http://dx.doi.org/10.1038/srep04452.
[290] J.Y. Hwang, M.F. El-Kady, Y. Wang, L. Wang, Y. Shao, K. Marsh, et al., Direct preparation and processing of graphene/RuO_2 nanocomposite electrodes for high-performance capacitive energy storage, Nano Energy 18 (2015) 57–70.
[291] X. Lang, A. Hirata, T. Fujita, M. Chen, Nanoporous metal/oxide hybrid electrodes for electrochemical supercapacitors, Nat. Nanotechnol. 6 (4) (2011) 232–236.
[292] S.G. Mohamed, C.-J. Chen, C.K. Chen, S.-F. Hu, R.-S. Liu, High-performance lithium-ion battery and symmetric supercapacitors based on $FeCo_2O_4$ nanoflakes electrodes, ACS Appl. Mater. Interfaces 6 (24) (2014) 22701–22708.
[293] H.D. Liu, J.L. Zhang, D.D. Xu, L.H. Huang, S.Z. Tan, W.J. Mai, Easy one-step hydrothermal synthesis of nitrogen-doped reduced graphene oxide/iron oxide hybrid as efficient supercapacitor material, J. Solid State Electrochem. 19 (1) (2015) 135–144.
[294] I. Aldama, V. Barranco, T.A. Centeno, J. Ibañez, J.M. Rojo, Composite electrodes made from carbon cloth as supercapacitor material and manganese and cobalt oxide as battery one, J. Electrochem. Soc. 163 (5) (2016) A758–A765.
[295] J. Chu, Z. Kong, D. Lu, W. Zhang, X. Wang, Y. Yu, et al., Hydrothermal synthesis of vanadium oxide nanorods and their electrochromic performance, Mater. Lett. 166 (2016) 179–182.
[296] A.S. Adekunle, K.I. Ozoemena, Electrosynthesised metal (Ni, Fe, Co) oxide films on single walled carbon nanotube platforms and their supercapacitance in acidic and neutral pH media, Electroanalysis 23 (4) (2011) 971–979.
[297] M.F. Montemor, S. Eugénio, N. Tuyen, R. Silva, T. Silva, M. Carmezim, Nanostructured transition metal oxides produced by electrodeposition for application as redox electrodes for supercapacitors, in: Handbook of Nanoelectrochemistry: Electrochemical Synthesis Methods, Properties, and Characterization Techniques, Springer Link, New York, 2016, pp. 681–714.
[298] B. Zhu, S. Tang, S. Vongehr, H. Xie, X. Meng, Hierarchically MnO_2–nanosheet covered submicrometer-$FeCo_2O_4$-tube forest as binder-free electrodes for high energy density all-solid-state supercapacitors, ACS Appl. Mater. Interfaces 8 (7) (2016) 4762–4770.
[299] S.T. Senthilkumar, N. Fu, Y. Liu, Y. Wang, L. Zhou, H. Huang, Flexible fiber hybrid supercapacitor with $NiCo_2O_4$ nanograss@carbon fiber and bio-waste derived high surface area porous carbon, Electrochim. Acta 211 (2016) 411–419.
[300] S. Chen, W. Ma, H. Xiang, Y. Cheng, S. Yang, W. Weng, et al., Conductive, tough, hydrophilic poly (vinyl alcohol)/graphene hybrid fibers for wearable supercapacitors, J. Power Sources 319 (2016) 271–280.
[301] A.K. Sharma, P. Bhardwaj, S.K. Dhawan, Y. Sharma, Oxidative synthesis and electrochemical studies of poly (aniline-co-pyrrole)-hybrid carbon nanostructured composite electrode materials for supercapacitor, Adv. Mater. Lett. 6 (5) (2015) 414–420.
[302] R. Wang, Q. Wu, X. Zhang, Z. Yang, L. Gao, J. Ni, et al., Flexible supercapacitors based on polyaniline nanowires-infilled 10 nm-diameter carbon nanotube porous membrane by in-situ electrochemical polymerization, J. Mater. Chem. A 4 (32) (2016) 12602–12608.
[303] J.M. D'Arcy, M.F. El-Kady, P.P. Khine, L. Zhang, S.H. Lee, N.R. Davis, et al., Vapor-phase polymerization of nanofibrillar poly (3,4-ethylenedioxythiophene) for supercapacitors, ACS Nano 8 (2) (2014) 1500–1510.
[304] N.A. Kumar, J.-B. Baek, Doped graphene supercapacitors, Nanotechnology 26 (49) (2015)492001.
[305] M. Moussa, M.F. El-Kady, H. Wang, A. Michimore, Q. Zhou, J. Xu, et al., High-performance supercapacitors using graphene/polyaniline composites deposited on kitchen sponge, Nanotechnology 26 (7) (2015)075702.
[306] Z. Zhiheng, F.R. Georgia, M. Qingshi, Z. Shenmin, K. Hsu-Chiang, M. Jun, PEDOT-based composites as electrode materials for supercapacitors, Nanotechnology 27 (4) (2016)042001.
[307] National Aeronautics and Space Administration (NASA), Case Number ARC-16812-1.

This page intentionally left blank

Index

Note: Page numbers followed by *f* indicate figures.

O

P

Q

R

S

T

U

V

W

X

Y

Z

This page intentionally left blank

NANOLAYER RESEARCH

METHODOLOGY AND TECHNOLOGY FOR GREEN CHEMISTRY

TOYOKO IMAE

Nanolayer Research: Methodology and Technology for Green Chemistry introduces the topic of nanolayer research and current methodology from basic to application for green science. Each chapter is written by a specialist in the specific research area and offers deep coverage of the topic. Nanofilms are explained with the application in mind for electronic devices for smart grids, units for cells, electrodes for butteries, and sensing systems for environmental purposes on the applicable subjects. Therefore, readers can use this book not only as a textbook for basic knowledge but also as a reference book for practical research.

- Outlines basic principles of nanolayers
- Includes the methodology and technology of nanolayers
- Includes numerous nanolayer applications

ELSEVIER

elsevier.com/books-and-journals

ISBN 978-0-444-63739-0

9 780444 637390